

**PROCESS MEASUREMENT AND CONTROL FOR EXPOSURE  
CONTROLLED PROJECTION LITHOGRAPHY**

A Dissertation  
Presented to  
The Academic Faculty

by

Xiayun Zhao

In Partial Fulfillment  
of the Requirements for the Degree  
Ph.D. in the  
School of Mechanical Engineering

Georgia Institute of Technology  
May 2017

**COPYRIGHT 2017 BY XIAYUN ZHAO**

**PROCESS MEASUREMENT AND CONTROL FOR EXPOSURE  
CONTROLLED PROJECTION LITHOGRAPHY**

Approved by:

Dr. David W. Rosen, Chair  
School of Mechanical Engineering  
*Georgia Institute of Technology*

Dr. Thomas Kurfess  
School of Mechanical Engineering  
*Georgia Institute of Technology*

Dr. Jun Ueda  
School of Mechanical Engineering  
*Georgia Institute of Technology*

Dr. Martha Grover  
School of Chemical & Biomolecular  
Engineering  
*Georgia Institute of Technology*

Dr. Jerry H. Qi  
Mechanical Engineering  
*Georgia Institute of Technology*

Date Approved: April 05, 2017

Dedicated lovingly to my dear children who keep challenging and inspiring me

—  
Lawrence Hongrui Zhao  
and  
Jerry Hongqing Zhao.

*"Before the great responsibility is bestowed from the Heaven, the person's resolve will be tormented, his body labored, his flesh starved, his possessions deprived, and his works disrupted; so that through the pounding of the outer afflictions, and the maturing of inner perseverance, his capacity could be expanded."*

— a Mencius (Mengzi) quote.

## ACKNOWLEDGEMENTS

I would like to express my sincere thanks to my PhD advisor Dr. David W. Rosen for providing me such a wonderful opportunity to challenge myself and to achieve higher than I could think possible. His willingness to share and help, his understanding and confidence in my abilities, along with his rich experiences and insights, have navigated me through the completion of my graduation study. He sets an excellent role model for me, and I will cherish forever such a memorable PhD journey with his guidance.

I deeply thank Dr. Martha Grover, Dr. Thomas Kurfess, Dr. Jerry Qi, and Dr. Jun Ueda, for being my reading committee professors. I am grateful to their valuable time and effort in helping me improve my research and dissertation.

I would like to acknowledge Dr. Amit Jariwala, one former labmate who worked on the same project, for his significant research achievement. I was fortunate to have the opportunity to work with the other labmates including Harrison Jones, Changxuan Zhao, Jenny Wang and Ying Zhang, who contributed to this project.

I am grateful to Dr. Yan Wang who mentored nicely my teaching practicum, as well as to Dr. Wayne E. Whiteman who provided me various help and advice during my graduate study. I was also delighted to be a part of Dr. Rosen's research team at Georgia Tech. The diverse group of people (Chad Hume, Sang-in Park, Jane Kang, Namin Jeong, Narumi Watanabe, Yeming Xian, Dazhong Wu, Ningrong Lei, Wenchao Zhou and everyone else), all smart and kind, helped and enriched greatly my PhD student life.

I am greatly indebted to my college advisor Dr. Yan Deng at Tsinghua University (Beijing, China), whose generosity and support allowed me to be where I am today.

I, specially, appreciate the tremendous support and care I have been receiving from my husband Yanjun Zhao. I have no words to express my endless love for him - a

most capable and highly committed man, as well as a very kindhearted father to our precious children. Meanwhile, I would like to thank my dearest children Larry Zhao and Jerry Zhao - my best treasure in life, without whose inspirations I would have never started nor finished my PhD study.

Last but not least, I wish to thank my parents, to whom I own an enormous debt of gratitude. I'd also like to extend my thoughts and thanks to all my other loving family members.

# TABLE OF CONTENTS

ACKNOWLEDGEMENTS	iv
LIST OF TABLES	xv
LIST OF FIGURES	xvii
LIST OF SYMBOLS AND ABBREVIATIONS	xxvi
SUMMARY	xxx
Chapter 1 Introduction and Motivation	1
1.1 Background	1
1.1.1 Additive manufacturing process monitoring and measurement	1
1.1.2 Real-time control in commercial AM systems	2
1.2 ECPL System Overview	3
1.3 ICM System Overview	4
1.4 Motivation	5
1.5 Dissertation Organization	6
Chapter 2 Existing ECPL Process Measurement and Control	8
2.1 Process Control Method Developed by Zhao	8
2.1.1 Process Model	8
2.1.2 Process Control	8
2.1.3 Critics and Summary	9
2.2 Process Control Method Developed by Jariwala	10
2.2.1 Process Model	10
2.2.2 Process Control	11

2.2.3	Critics and Summary	12
2.3	Process Control Developed by Jones	13
2.3.1	Process Model	13
2.3.2	Process Control	14
2.3.3	Critics and Summary	15
2.4	Summary of existing ECPL controls	16
Chapter 3 Literature Review on Controls of Manufacturing Processes Relevant to		
ECPL		18
3.1	ECPL Property Space	18
3.2	Controls of Polymerization	19
3.2.1	Challenges in polymerization modeling and optimization: A population balance perspective	19
3.2.2	Measurement and control of polymerization reactors	20
3.3	Controls of Lithography	22
3.3.1	Model-based Adaptive Control of Photolithography [23]	23
3.3.2	Run-to-run control of DUV lithography [27]	25
3.3.3	Run-to-run controls of photolithography [28]	26
3.4	Frequency Domain Control of Laser Metal Deposition [29]	27
3.5	Adaptive Neural Network Control of a Class of Unknown Nonlinear System	27
3.6	Literature summary	28
3.7	Proposed Advanced Process Control Schemes	30
3.7.1	Evolutionary Cycle-to-Cycle Control	30
3.7.2	Hierarchical Framework of Control Methods for ECPL	31

3.8	Chapter summary	33
Chapter 4 Research Gaps, Goals and Questions		35
4.1	Issues of Real-time Measurement with ICM System	35
4.2	Issues of Controlling ECPL Process	39
4.3	Research Gaps of ECPL Process Measurement and Control	41
4.4	Research objective	43
4.5	Research Questions and Hypothesis	43
4.5.1	Research Question 1	44
4.5.2	Research Question 2	46
4.6	Chapter summary	47
Chapter 5 ECPL Process Measurement: ICM&M Sensor Model and Algorithms		48
5.1	Monitoring polymerization reactions	49
5.2	Overview of Metrology for ECPL	51
5.2.1	Need and Requirement for online Metrology	51
5.2.2	Offline Metrology for material properties and process characterization	51
5.3	ICM&M model	54
5.3.1	Phase extraction technique for ICM&M	54
5.3.2	ICM&M sensor model	56
5.3.3	ICM&M Calibration Model	66
5.4	Parameter estimation for ICM&M model	68
5.4.1	Curve Fitting with One-term Fourier Model	69
5.4.2	Online Parameters Estimation	69
5.5	Summary of the developed ICM&M sensor method	74



5.6	Initial experimental validation for the ICM&M method	75
5.6.1	Calibration in test measurement	76
5.6.2	Validation Experiment	79
5.7	Chapter summary	88
Chapter 6 Data Algorithms in the ICM&M System for Measuring the ECPL Process		90
6.1	Objective and organization of the chapter	90
6.2	The ICM&M method from data perspective	92
6.2.1	Data analytics in manufacturing	92
6.2.2	To materialize the ICM&M method with data techniques	92
6.2.3	Data mining approach for realizing the ICM&M system	94
6.2.4	Scope and overview of ICM&M data mining	94
6.3	Data preprocessing for ICM&M	95
6.4	Identifying ECPL process stages	99
6.4.1	Classification of the ECPL process stages	99
6.4.2	Rule-based classification for identifying curing window	100
6.4.3	Effect of critical value	102
6.4.4	Exception handling with multiclass classification	105
6.4.5	Ensemble method based on majority voting for robust identification of the curing window across ROI	110
6.4.6	Summary and recommendation	114
6.5	Mining curing window data's oscillating pattern for instantaneous frequency	115
6.5.1	Fit options for "fourier1" curve fit to ICM&M data	115
6.5.2	Data window and weight	118

6.5.3	Outlier frequency detection and treatment	124
6.5.4	Summary and recommendation	126
6.6	Evaluating the total phase change	126
6.6.1	Integration timestep	127
6.6.2	Integration method	128
6.6.3	Error analysis of ICM&M numerical integration	131
6.6.4	Summary and recommendation	133
6.7	Validating the ICM&M data mining algorithms for estimating the phase angle in sensor model	134
6.8	Measurement intervals	138
6.8.1	Spatial size reduction: adjacent pixels group together	138
6.8.2	Measurement period	138
6.9	Aggregating data for final height estimation	140
6.9.1	Outliers in cured height	141
6.9.2	Robust statistics used to estimate the average height	143
6.9.3	Summary and recommendation	147
6.10	Summary of the data analysis algorithms for ICM&M	148
6.11	Chapter summary	150
Chapter 7 Computer Implementation for the ECPL process measurement & control		153
7.1	General design of software used in metrology	153
7.2	Design a software for the integrated system of ECPL and ICM&M	153
7.3	Development of the ECPL-M&C software	156
7.3.1	Software tasks	156

7.3.2	Modularity and scalability	157
7.3.3	Graphical user interface	160
7.3.4	Data structure	162
7.3.5	Parallel computing	163
7.3.6	Computation environment	170
7.4	Chapter summary	170
Chapter 8 Experimental Validation and Characterization, of the ICM&M System for		
ECPL Process Measurement		
8.1	Experiment design	173
8.1.1	Design philosophy and experiment plan	173
8.1.2	ICM&M implementation	175
8.1.3	Microscope measurement practice	177
8.2	Results and discussion	178
8.2.1	Material formulation	178
8.2.2	Calibration experiment	179
8.2.3	Validation experiment group #1: varying exposure time	185
8.2.4	Validation experiment group #2: varying exposure intensity	195
8.3	Measurement characteristics of ICM&M	204
8.3.1	Traceability	204
8.3.2	Comparability and accuracy	211
8.3.3	Repeatability	212
8.3.4	Sensitivity, resolution and range	213
8.3.5	Summary of the ICM&M characteristics	214

8.4	Utility of the ICM&M system	215
8.4.1	Local vs. global measurement for the ECPL process	215
8.4.2	Lateral measurement potentiality	216
8.4.3	ICM&M for ECPL process dynamics, modeling, and control	217
8.5	Chapter summary	218
Chapter 9 Real-time ECPL Process Measurement and Control		220
9.1	Background and introduction	220
9.1.1	Research in process modeling, measurement and control for AM	220
9.1.2	Real-time control in commercial AM systems	222
9.1.3	Objective of this chapter	223
9.2	Parallel computing software for real-time process measurement and control	223
9.3	Implementation of the ICM&M in real time	224
9.4	Design of a closed-loop controller	225
9.4.1	The control scope	225
9.4.2	The control mode	226
9.4.3	The actuator	226
9.4.4	System delays	227
9.4.5	The control scheme	229
9.5	Offline measurement methods	234
9.5.1	Microscope measurement	235
9.5.2	Robust ICM&M method off line	238
9.6	Experiment design for real-time ECPL process measurement and control	244
9.7	Experiment results and implications	247

9.7.1	Offline measurement	248
9.7.2	Real-time in-process measurement	256
9.7.3	Examine the performance of real-time feedback control for exposure height	263
9.7.4	Examine the performance of real-time control for total height	269
9.7.5	Error analysis for the real-time process measurement and control system	273
9.8	Discussion and recommendation	276
9.8.1	Online compensation for the measurement latency	277
9.8.2	A predictive on-off feedback control to address discrete measurement issue	278
9.8.3	Control dark curing in the ECPL process	280
9.9	Chapter summary	282
Chapter 10 Closure and Future Work		285
10.1	Revisiting Research Questions	285
10.2	Conclusion	291
10.3	Contribution	294
10.3.1	Summary of novelty	295
10.3.2	Overall contribution	296
10.3.3	Contributions to the particular AM process - ECPL	297
10.3.4	Contributions to the general AM research	298
10.4	Limitations	303
10.5	Future work	304
10.5.1	Long-term goal	304

10.5.2	Recommendation for Future Work	304
APPENDIX A	Offline ICM&M analysis result for the samples cured in the real-time	
Control experiments		317
A.1	Voting scheme for identifying curing window in global measurement	317
A.2	Measured region and results by the offline ICM&M method	326
A.3	Selected example pixel measured by the offline ICM&M method	333
APPENDIX B	Real-time ICM&M Data Acquisition and analysis result for the samples	
cured in the real-time	Control experiments	340
B.1	Real-time data acquisition and logging	340
B.2	Online measured pixels' time sequence and measurement results	341
B.3	Real-time measurement latency and control system delays	345
APPENDIX C	ECPL-M&C Software	360
C.1	Software Manual	360
C.2	MATLAB Codes	362
1.	Function: "icmFit2.m"	362
2.	Function: "Real_Time_ICM_processMeasureTimer.m"	370
3.	Function: "icm_main_worker.m"	373
4.	Function: "icm_init_measure_ret.m"	384
5.	Function: "icm_init_mem_file.m"	386
6.	Function: "icm_init_fit_ret.m"	388
7.	Function: "icm_set_uv_status.m"	388
REFERENCES		390
VITA		397

## LIST OF TABLES

Table 1. Summary of Existing Process Controls .....	16
Table 2. Summary of Literature Review on Controls of Processes Relevant to ECPL....	29
Table 3 Research Gaps Identification for ECPL Control .....	42
Table 4 Research Gaps in ICM real-time measurement .....	43
Table 5. Phase component analysis of the ICM&M multi-beam interference optics model .....	60
Table 6. Instantaneous frequency of the multi-beam interference optics model in ICM&M .....	61
Table 7. Effects of MHL in prediction accuracy .....	119
Table 8. Comparing integration methods for profile line measurement .....	130
Table 9. Experimental design matrix for validating ICM&M in offline mode .....	174
Table 10. Calibration Experiment Results .....	184
Table 11. Measurement results of validation experiments varying exposure time.....	194
Table 12. Measurement results of validation experiments varying exposure intensity ..	202
Table 13. ICM&M measurement results using growth-dependent refractive index for the validation group varying exposure time .....	209
Table 14. ICM&M measurement results using growth-dependent refractive index for the validation group varying exposure intensity .....	210
Table 15. Measurement repeatability.....	213
Table 16. ICM&M characteristics.....	215
Table 17. Evaluate a sample cured part's height profile with its microscope data.....	236
Table 18. Experimental design for real-time ECPL process measurement and control .	247

Table 19. Offline measurement results for the samples cured in the real-time measurement & control experiments .....	249
Table 20. Real-time measurement results for the samples cured in the real-time measurement & control experiments .....	257
Table 21. Real-time measurement and control system delays and resultant errors in the process output of cured height .....	269
Table 22. Error analysis for the real-time measurement and control of the ECPL process .....	275



## LIST OF FIGURES

Figure 1: Exposure Controlled Projection Lithography Process Overview [17] .....	4
Figure 2: ICM System.....	5
Figure 3. An integrated ECPL System with Real-Time Measurement and Control.....	6
Figure 4: ECPL Open-loop Process Control Scheme by Zhao [19] .....	9
Figure 5. ECPL Open-loop Process Control Scheme by Jariwala [17] .....	12
Figure 6: Flow Diagram of the Control System Proposed by Jones [20] .....	15
Figure 7. Literature Survey on Controls of Processes Relevant to ECPL .....	19
Figure 8. MPC block diagram (Seborg, Edgar [26]) .....	22
Figure 9. Adaptive control of photolithography using the nonlinear model [23].....	24
Figure 10. Run to Run Control Architecture for DUV Lithography [27].....	26
Figure 11. Hierarchical framework of control methods for ECPL.....	32
Figure 12. Issues in ECPL Process Control .....	40
Figure 13 ECPL System from the Perspective of Control Design.....	41
Figure 14. Multi-beam Interference Optics Model for ICM&M .....	57
Figure 15. Multi-layer thin film reflectance in the ICM&M sensor model .....	63
Figure 16. The need for exponentially weighted curve fitting to improve the curve fitting for most recent data (Top: unweighted fitting; Bottom: exponential weighted fitting)....	70
Figure 17. Scheme of ICM&M measurement method: models and algorithms .....	75
Figure 18. Initial ICM&M validation (calibration part): the DMD bitmap pattern for curing a square part with the ECPL process (Note: the dashed outline indicates the edge of the DMD which consists of 1024×768 micromirrors).....	77

Figure 19. Initial ICM&M validation (calibration part): select a line in the acquired video of interferograms to measure the cured part heights with the ICM&M method. ....	77
Figure 20. Initial ICM&M validation (calibration part): estimate the individual and average total phase angles for 25 pixels from Pixel (245, 220) to (365, 220) at an interval of five pixels in the selected horizontal line. ....	78
Figure 21. Initial ICM&M validation (calibration part): measure the sample line profile with the Olympus 3D confocal microscope. ....	78
Figure 22. Initial ICM&M validation: DMD exposure pattern in (a) Experiment #1: 150X150 pixels square bitmap; (b) Experiment #2: 50X50 pixels square bitmap. ....	79
Figure 23. Initial ICM&M validation: selected line of horizontal pixels to measure with ICM&M in (a) Experiment #1; (b) Experiment #2. ....	81
Figure 24. Initial ICM&M validation: time sequence of grayscale for (Left) Pixel (275, 230) in Experiment #1; (Right) Pixel (290, 225) in Experiment #2. ....	82
Figure 25. Initial ICM&M validation: estimated instantaneous frequency for (a) Pixel (275, 230) in Experiment #1; (b) Pixel (290, 225) in Experiment #2. ....	83
Figure 26. Initial ICM&M validation: estimated cured height for the voxel on (a) Pixel (275, 230) in Experiment #1; (b) Pixel (290, 225) in Experiment #2. ....	83
Figure 27. Initial ICM&M validation: ICM&M measured horizontal line heights profile for voxels on (a) 22 pixels of (250:5:355, 230) in Experiment #1; (b) 9 pixels of (265:5:305, 225) in Experiment #2. ....	85
Figure 28. Initial ICM&M validation: microscope measured line profile for (a) sample cured in Experiment #1; (b) sample cured in Experiment #2. ....	85

Figure 29. Initial ICM&M validation: measuring a vertical line profile for Experiment #2  
(a) selected line in the interferogram: Pixel (300, 200) to Pixel (300, 240); (b) ICM&M  
measurement result; (c) microscope measurement. .... 87

Figure 30. Data-driven ICM&M Method for ECPL process and product measurement.. 94

Figure 31. ICM&M data preprocessing - Top graph: a good pixel; Bottom graph: a bad  
pixel which needs filter. .... 97

Figure 32. ICM&M data preprocessing - ICM&M estimated total phase angle for the  
ECPL cured part with (a) raw data; (b) data preprocessed by a 5×5 image median filter 98

Figure 33. Effect of the critical range  $R_{i,c}$  for incubation stage identification in the  
ICM&M estimation (a) black curve: preprocessed data; red curve: fitted data with  $R_{i,c} =$   
10; (b) estimated frequency and phase angle by ICM&M method with  $R_{i,c} = 10$ ; (c)  
estimated frequency and phase angle by ICM&M method with  $R_{i,c} = 20$ . .... 104

Figure 34. ICM&M data of time sequence: filtered raw data (black) and curve fitted data  
(red) for (a) a pixel with spurious waves in incubation stage; (b) a neighboring pixel with  
good data shows relatively straight pattern in incubation stage. .... 106

Figure 35. Instantaneous frequency and total phase angle estimated by the ICM&M  
method (a) false alarms are triggered in incubation stage with only statistical detection in  
the classification algorithm; (b) false alarms with low amplitude oscillation are  
suppressed and curing start is correctly identified with exception handling embedded into  
the algorithm ..... 107

Figure 36. Challenge in differentiating incubation and curing stages (a) time sequence of  
grayscale in an example problematic pixel compared with its good neighboring pixel; (b)

estimated instantaneous frequency and total phase angle for the problem pixel and neighboring pixel. ....	110
Figure 37. The voting mechanism helps identify the process stages correctly as demonstrated in three problematic pixels which have noisy data at incubation stage: 1(a), 2(a), 3(a) ICM&M data analysis and measurement results without voting; 1(b), 2(b), 3(b) ICM&M data analysis and measurement results with voting. ....	112
Figure 38. Estimation of full-field cured height profile (a). without (b) with the ensemble majority voting assisted classification method. ....	113
Figure 39. Effects of applying frequency bounds in the curve fitting for ICM&M data: red curve – unbounded fitting, blue curve – bounded fitting. ....	118
Figure 40. MHL effect in ICM&M estimation for low intensity ECPL process (a) a typical pixel’s time sequence of grayscale in the ECPL process with UV iris level at 5%, black curve is the preprocessed raw data and red curve is the fitted data; (b) estimated frequency and phase angle using MHL (32 or 48 adaptively) as in ECPL process with 10-40% UV iris level; (c) estimated frequency and phase angle using double MHL (64 or 96 adaptively). ....	125
Figure 41. Integration methods: ICM&M data of a representative pixel .....	128
Figure 42. Phase evaluation: time integral of the frequencies which are estimated by the ICM&M data mining .....	129
Figure 43. Selected ROI pixels in the interferogram - profile line to measure. ....	130
Figure 44. Phase evaluated at individual pixel in ROI by two integration methods .....	131
Figure 45. Error analysis of integration method .....	133

Figure 46. ICM&M data mining for online estimation of frequency and phase angle with adaptive rolling fit in ECPL experiments (a) UV iris level: 20%, Exposure time: 12s; (b) UV iris level: 10%, Exposure time: 12s; (c) UV iris level: 5%, Exposure time: 26s. ....	135
Figure 47. Causes and classification of outliers in cured height.....	142
Figure 48. Regular statistics vs. Robust statistics: ICM&M estimated height for 22 cured samples – average with error bar (standard deviation across the cured part) .....	145
Figure 49. Measurement dispersion using ICM&M method .....	147
Figure 50. ICM&M data mining approach: data flow and algorithms .....	149
Figure 51. The integrated ECPL system: ECPL process, ICM&M module, and MATLAB software for ECPL M&C .....	154
Figure 52. MATLAB application for the ECPL process measurement & control: functional modules.....	157
Figure 53. MATLAB application for the ECPL process measurement & control: Graphical User Interface .....	161
Figure 54. Flow Chart: Parallel Computing of Real-time measurement and control for the ECPL process.....	170
Figure 55. DMD pattern: 1024×768 pixels binary bitmap displaying a black square of 250×250 pixels in the center .....	179
Figure 56. Calibration: outline of the cured part in the last interferogram – ROI of Pixels (235:5:385, 140:5:290) to be measured .....	180
Figure 57. Calibration: estimated individual and average total phase angles for 31×31 pixels in the ROI of Pixels (235:5:385, 140:5:290).....	181

Figure 58. Calibration: measured typical profile lines in two lateral dimensions (X and Y) to estimate the height of the cured sample..... 182

Figure 59. A 2<sup>nd</sup> calibration sample: (a) outline of the cured part in the last interferogram – ROI of Pixels to be measured; (b) estimated individual and average total phase angles for 30×30 pixels in the ROI; (c) and (d): measured typical profile lines in two lateral dimensions (X and Y) to estimate the height of the cured sample. .... 183

Figure 60. Selected ROI pixels (red dashed lines: estimated entire cured area; cyan line: an example profile line) to measure with ICM&M in the 1<sup>st</sup> sample ..... 187

Figure 61. Illustration of implementing the ICM&M algorithms using the 1<sup>st</sup> samples in the experiments varying exposure time: (a) typical time sequence of grayscale; (b) estimated instantaneous frequency along timeline; (c) evolving cured height of the voxel on the selected the pixel..... 189

Figure 62. ICM&M result VS. microscope measurement for the 1<sup>st</sup> set of samples in exposure time experiment. Each sample’s (a) entire cured area height profile estimated by ICM&M; (b) horizontal profile line in the confocal microscope. .... 192

Figure 63. Measurement results for experiments varying exposure time..... 195

Figure 64. ICM&M implementation and process dynamics in the experiments varying exposure intensity: (a) representative pixel’s time sequence of grayscale; (b) estimated instantaneous frequency; (c) evolving cured height of the voxel on the selected the pixel. .... 197

Figure 65. Selected ICM&M result VS. microscope measurement for the 1<sup>st</sup> set of samples in exposure intensity experiment: (a) Selected in the last interferogram the approximated cured area (enclosed within the red dashed lines) to measure with ICM&M;

(b) ICM&M measured heights profile for voxels on the pixels within the cured area; (c) Microscope measured horizontal line profile. ....	201
Figure 66. Comparing the ICM&M measurement results with the microscope measurement in experiments varying exposure intensity .....	203
Figure 67. Model of the evolving effective refractive index $nm$ .....	208
Figure 68. Improved ICM&M accuracy by using growth-dependent (previously constant) effective refractive index in the sensor model (a) validation experiments varying exposure time; (b) validation experiments varying exposure intensity. ....	211
Figure 69. On-Off control input in the ECPL process .....	227
Figure 70. Statistics of the ratio of dark cured height over exposed cured height.....	231
Figure 71. Scheme diagram of feedback control for real-time cured height in ECPL process.....	234
Figure 72. Measuring multiple profile lines across a sample cured part with microscope .....	237
Figure 73. ICM&M without vs. with voting: selected region of pixels to be measured	241
Figure 74. ICM&M without (a) vs. with (b) voting: estimated height profile.....	242
Figure 75. ICM&M without (a) vs. with (b) voting: measuring a pixel with noisy incubation signal .....	242
Figure 76. ICM&M voting for ECPL process stage (a) incubation; (b) resting. ....	243
Figure 77. An example of final height profile estimated by the ICM&M with voting and outlier removal schemes .....	244
Figure 78. Ratio of dark height to exposure height for the parts cured in the real-time measurement and controls experiments .....	252

Figure 79. Explore the ICM&M method’s utility in ECPL process modeling: (a) capability of identifying the curing window; (b) vivid correlation between the estimated cured window length and the actual cured height.....	255
Figure 80. Measurement results of exposure height for the parts cured in the real-time measurement and control experiments Group #1 .....	258
Figure 81. Measurement results of exposure height for the parts cured in the real-time measurement and control experiments Group #2 .....	258
Figure 82. Measurement results of total height for the parts cured in the real-time measurement and control experiments Group #1 .....	259
Figure 83. Measurement results of total height for the parts cured in the real-time measurement and control experiments Group #2 .....	259
Figure 84. Real-time feedback control results for exposure height in the real-time measurement and control experiments Group #1 .....	265
Figure 85. Real-time feedback control results for exposure height in the real-time measurement and control experiments Group #2 .....	265
Figure 86 Delays in the real-time process measurement and control experiments.....	267
Figure 87. Overall process control results for the parts cured in the real-time measurement and control experiments Group #1 .....	272
Figure 88. Overall process control results for the parts cured in the real-time measurement and control experiments Group #2 .....	272
Figure 89. Error analysis for the real-time process measurement and control system ...	276



Figure 90. Confocal microscope (Objective Lens Magnification 25×, edges could be clearly imaged and measured under a higher magnification lens e.g. 50×) measured centerline profile for the ECPL cured microlens (a) Sample #1; (b) Sample #2..... 307

Figure 91. ICM&M estimation results for the center voxel in the EPCL cured microlens (a) Sample #1; (b) Sample #2. .... 307

Figure 92. Process simulation by COMSOL and measurement by the ICM&M method for the center voxel in the EPCL cured microlens (a) Sample #1; (b) Sample #2..... 308

## LIST OF SYMBOLS AND ABBREVIATIONS

ECPL	Exposure Controlled Projection Lithography
DMD	Digital Micromirror Device
UV	Ultraviolet
AM	Additive Manufacturing
ICM	Interferometric Curing Monitoring
ICM&M	Interferometric Curing Monitor & Measurement
$\mu$ SL	micro Stereolithography
EC2C	Evolutionary Cycle to Cycle
MSE	Mean Square Errors
MHL	Moving Horizon Length
QCM-D	Quartz Crystal Microbalance with Dissipation
OPLD	Optical Path Length Difference
ROI	Region of Interest
$E$	Optical wave
$A$	Real positive amplitude of the optical wave
$\emptyset$	Interferogram phase change (rad)
$\Phi$	Interferogram phase change ( <i>unit: cycle, i.e., <math>2\pi</math> rad</i> )
$I$	Irradiance
$\delta_{jk}$	Difference of the two optical waves' phase angles $\emptyset_j$ and $\emptyset_k$
$n_l$	Refractive index of liquid resin
$n_s$	Refractive index of cured solid part
$n_{cf}$	Refractive index of the curing front
$n_m$	Mean, i.e., effective refractive index of the curing part

$\Delta n$	The difference between the effective refractive index $n_m$ and the liquid resin's refractive index $n_l$
$Z$	Cured height ( $\mu\text{m}$ )
$\dot{Z}$	Curing velocity ( $\mu\text{m/s}$ )
$IF$	Instantaneous Frequency
$\lambda$	Wavelength
$I_M$	The directly measured intensity by CCD camera
$f$	Instantaneous frequency (Hz)
$\omega$	Instantaneous angular frequency (rad/s)
$T_i$	Time step of integration
$f_i$	Instantaneous frequency in the $i^{\text{th}}$ run of parameter estimation
$\omega_i$	Instantaneous angular frequency in the $i^{\text{th}}$ run of parameter estimation
$\sum_i T_i \omega_i$	Total phase angle (unit: rad) changed during the curing process
$\sum_i T_i f_i$	Total phase angle (unit: cycle, i.e., 1 cycle = $2\pi$ rad) changed during the curing process
$t$	time variable
$MTI$	Measurement Time Interval (s)
$R_i$	Range of an interferogram pixel's grayscale data segment from the start of the ECPL process to the current datapoint
$\sigma_i$	Standard deviation of an interferogram pixel's grayscale data segment from the start of the ECPL process to the current datapoint
$R_{i,c}$	Critical value of the range of interferogram grayscale data for a pixel determined being at the ECPL incubation stage
$\sigma_{i,c}$	Critical value of the standard deviation of interferogram grayscale data for a pixel determined being at the ECPL incubation stage
$R_r$	Range of an interferogram pixel's grayscale data segment from the time when UV lamp is shut down to the current datapoint

$\sigma_r$	Standard deviation of an interferogram pixel's grayscale data segment from the time when UV lamp is shut down to the current datapoint
$R_{i,r}$	Critical value of the range of interferogram grayscale data for a pixel determined being at the ECPL resting stage
$\sigma_{i,r}$	Critical value of the standard deviation of interferogram grayscale data for a pixel determined being at the ECPL resting stage
$E_a$	Approximate error in cured height estimation with the first-order Euler's method
$\overline{f''}$	Average second derivative of instantaneous frequency
$Z_{cycle}$	the sensitivity of ICM&M system – ratio of the change in the height $Z$ to the change in the interferogram phase change $\Phi$
$T_{Process}$	Estimated Period (s) of the data detected by the ICM&M system during the ECPL process
$Z_{Total}$	Total height in the entire curing process
$Z_{Exp}$	Cured height under exposure
$Z_{Dark}$	Cured height in dark curing
$r_{D/T}$	ratio of dark cured height $Z_{Dark}$ to total cured height $Z_{Total}$
$r_{D/E}$	ratio of dark cured height $Z_{Dark}$ to exposed cured height $Z_{Exp}$
$\tau_{meas}$	Measurement latency - the lag between the two parallel threads of real-time interferogram acquisition and online measurement analysis
$\tau_{ctrl}$	feedback control delay
$\tau_s$	feedback control delay caused by the missed sensing of the target trigger point due to discrete measurement
$\tau_{sc}$	feedback control delay caused by sensor-to-controller time lapse for transmitting measurement result
$\tau_c$	feedback control delay caused by time for implementing control algorithms in controller
$\tau_{act}$	actuation delay
$\tau_{ca}$	controller-to-actuator time delay for transferring the control signal

$\tau_a$	delay in mechanically operating the actuator
$Z_{oc}$	Over-cured height due to extended exposure
$Z_{OC\_RT}$	Over-cured Height inferred from Real-time Measurement
$Z_{OC\_ICM}$	Over-cured Height estimated by the ICM&M Characteristic of sensitivity

## SUMMARY

The Exposure Controlled Projection Lithography (ECPL) is an additive manufacturing process, in which liquid photopolymer monomers cross-link into solid polymer with controlled ultraviolet irradiation. Unlike other types of stereolithography processes, the ECPL system cures a 3D part by projecting from beneath a stationary and transparent substrate ultraviolet radiation, which is modulated by a sequence of DMD bitmaps varying the exposure intensities, patterns and durations. It has become promising in fabrication of micro optics and fluidics components.

Due to the complex chemical & physics interactions in photopolymerization process, unavailable in-situ metrology and the unmeasurable time-varying disturbances such as oxygen inhibition and light source fluctuations, a common practice in stereolithography process planning is to use experimental characterization and statistics models in an open-loop control mode, which cannot effectively control the nonlinear black/grey-box process. Hence, the ECPL system still suffers loss of accuracy, which limited it from becoming a more capable micro manufacturing method for wider applications. A potential solution for controlling the not-fully-known ECPL process is the methodology of closed-loop control, which requires measurement feedback to link input and output variables. An in-situ interferometric curing monitoring (ICM) system has been developed to monitor the ECPL process, but it is not accurate or ready for real-time measurement yet and only able to provide interferograms for posterior analysis of cured heights combined with offline microscope measurements. In all, to improve the ECPL

process accuracy and precision involves with extensive research in process modeling, measurement and control.

A new research is needed to realize an automated, accurate and precise ECPL system. To attain this goal, two research questions will be investigated by this research.

- How to develop a real-time metrology based on the existing in-situ interferometric curing monitoring system to measure the cured part dimensions, specifically the cured height profile across the curing area?
- As a baseline control, without a constitutive process model of first principle differential equations, what is an applicable ECPL process control approach, which could utilize the real-time measurement system to improve the process accuracy?

The intellectual merit of this research lies in developing real-time measurement and control methods for the ECPL process, with answers for the research questions. The scientific and engineering outcomes from this research will help achieve better manufacturing accuracy and precision thereby facilitating applications of the ECPL system in micro fabrication, and will offer an exemplification of the applicability and benefits of real-time feedback control methodologies for unknown nonlinear processes in other additive manufacturing methods.

# CHAPTER 1 INTRODUCTION AND MOTIVATION

The following sections introduces the Exposure Controlled Projection Lithography (ECPL) process which is a stereolithography based rapid prototyping process. As a metrology for the ECPL process, the developed interferometric curing measurement (ICM) system is also presented. The knowledge gap involved in utilizing the ECPL as a reliable manufacturing process is presented. This provides a foundation for investigation of the research issues associated with the measurement and control of the ECPL process.

## 1.1 Background

### 1.1.1 Additive manufacturing process monitoring and measurement

Additive manufacturing (AM), as a process for fabricating parts directly from a three-dimensional digital model, has tremendous potential for producing high-value, complex, individually customized parts. There are lots of individual AM processes which vary in material and machine technology [7]. AM offers multiple advantages over traditional manufacturing techniques, including reduced material waste, lower energy intensity, reduced time to market, just-in-time production, and construction of structures not possible with traditional manufacturing processes. While the use of AM has been growing, a number of challenges continue to impede its more widespread adoption, particularly in the areas of measurement science and standardization [8, 9].

Currently most AM processes do not employ feedback protocols based on multi-scale measurement and modeling. Awareness and interest in research of AM process monitoring and measurement has been most vibrant for metal-based AM processes [8]. In 2012, the National Institute of Standards and Technology (NIST) held a workshop entitled “Measurement Science Roadmap for Metal-Based Additive Manufacturing” to



understand and address the hurdles faced by the hard matter (metal) community from the perspective of measurement science [8]. Some sample research includes traceable thermal [10], meltpool shape [11] and dimensional metrology, which however remain mainly in fundamental measurement theory without real-time exploration yet. In-situ metrology modules available from AM machine manufacturers and measurement specialists include equipment such as pyrometer and camera [12], as well as technologies such as coherent imaging and X-ray tomography [13]. Many in-process sensing technologies have primarily focused on monitoring melt pool signatures, and to date correlations between process measurements, process parameter settings, and quality metrics have been primarily qualitative [14]. To facilitate and expand research on process monitoring and measuring for other AM processes, in 2016, NIST is focusing further on metrology development for additive manufacturing of polymer-based materials [6].

Generally, there still lacks substantial research and literature on real-time sensors and measurement along with control methods for AM processes especially for polymer-based AM processes which usually involve complicated multidisciplinary physics phenomena and chemical photopolymerization. The measurement need for additive manufacturing of polymer-based materials is urgent because such soft materials present great processability and range of properties that enable applications across numerous industrial sectors [6].

### **1.1.2 Real-time control in commercial AM systems**

From a commercial manufacturing standpoint, in-process sensing technology for additive manufacturing is still in its infancy [14]. Process monitoring and controls for additive manufacturing are still in research and development phase [15], with metal additive manufacturing predominating the specific research area of measurement science and feedback control [8, 9] and the counterpart research for non-metal such as polymer and soft materials AM processes has just set out recently [6]. Status of real-time control

in commercial metal additive manufacturing systems is summarized in a most recent review literature [15], which found that continuous feedback control in commercial systems is more easily realized in directed energy deposition systems than in laser powder bed fusion (LPBF) systems due to the much lower processing speeds and larger melt pool size. The Optomec LENS (Laser Engineered Net Shaping) MR-7 offers the option of closed loop control, which is being tested and optimized by university collaborators [16]. In commercial LPBF systems, high-speed closed-loop control based on melt pool monitoring is not yet realized, however, layer-wise monitoring and control have been demonstrated. For example, Concept Laser's QM coating module images newly formed powder layer surfaces, and actively detects and compensates for powder layer thickness variation [15].

## 1.2 ECPL System Overview

Various micro fabrication applications in microelectronics, micro-optics, micro-fluidics, MEMS and MEMOS demand smaller and smaller devices. Driven by the trend, micro stereolithography ( $\mu$ SL) is required to deliver photo-curable micro structures with decreasing feature sizes. Improved control of  $\mu$ SL is critical in realizing better manufacturing resolution and reproducibility.

A prototypical  $\mu$ SL process consists of the following basic steps - substrate and chamber setup, photopolymerizable material preparation, photo exposure curing, post-developing and washing.  $\mu$ SL machines can be classified into two main categories laser scan and mask projection. The Digital Micromirror Device (DMD) based Exposure Controlled Projection Lithography (ECPL) system falls into the category of non-stacking mask projection stereolithography apparatus. It has promising applications in fabrication of microfluidics and micro optics components for biomedical devices. Different from a conventional laser scan projection stereolithography process, ECPL cures a 3D feature by projecting radiation through a stationary, transparent substrate and by varying exposure

patterns and durations with a timed sequence of DMD bitmaps. As illustrated in Figure 1, in the ECPL process, when the resin is exposed to a patterned light beam from DMD for certain time, photopolymerization takes place and a layer of liquid resin is cured. Each layer has a target cured height, and the cumulative layers form the final cured part.

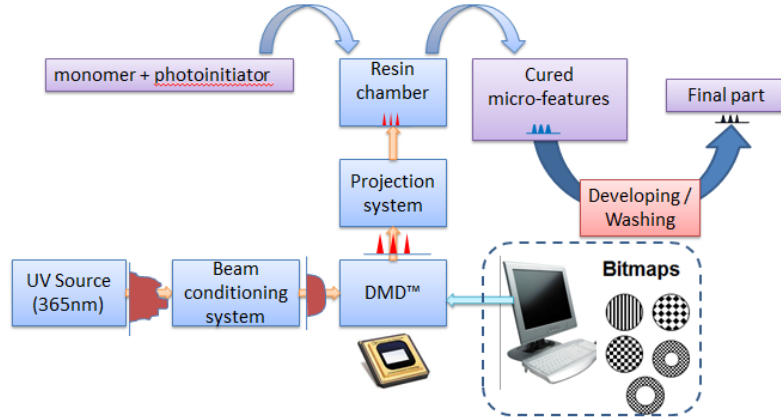


Figure 1: Exposure Controlled Projection Lithography Process Overview [17]

### 1.3 ICM System Overview

To identify the inherent variations of cured height with on-going exposure and provide reference to identify fabrication errors induced by post-cure process such as washing and final part measurement, Jariwala [17] designed an in-situ interferometric curing monitor (ICM) system for the ECPL process. The (ICM) system, as seen in Figure 2, is based on a Mach-Zehnder interferometer and is described in detail in Jariwala, Schwerzel [18]. A coherent laser is directed, through a beam expander, moveable iris, and beam splitter, at the resin chamber. Light reflecting off the interface surfaces of the resin chamber reflect through the beam splitter and into the camera. Due to the optical path differences between the light beams reflected from different interface surfaces an interference pattern is observed by the camera.

The laser source is a small, low-power, 532 nm wavelength laser diode, which provides the coherent laser light required for interferometry. The beam expander expands the narrow beam produced by the laser source such that the light output could cover the

entire curing area in the resin chamber and the camera can capture a full-field interferogram. The movable iris can adjust the size of the incident beam and selectively illuminate a specific location on the curing plane. The beam splitter reflects the laser source downward into the resin chamber while, at the same time, allowing for light coming from the resin chamber to pass through to the camera above. The camera captures the intensity of incoming laser light from the resin chamber, and provides an interference pattern of intensity profile across the shined chamber area.

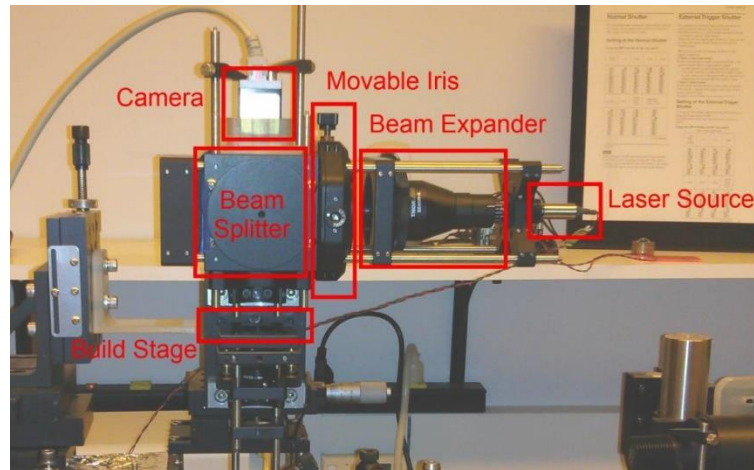


Figure 2: ICM System

#### 1.4 Motivation

ECPL systems have been evolving since our first generation prototype in 2008, and the process has been continuously improved, resulting in a smaller and smaller fabrication error, from 25% [19] to 15% [17] to recently 10% [20]. However, to become a more capable micro manufacturing method for wider applications, ECPL still has limited process accuracy, which sparks a new study area of interest - advanced process control methods as will be investigated in this dissertation.

Another motivation is the development of an in-situ measurement system - , the interferometric curing monitoring (ICM) system, proposed by Jariwala et al. ([18], [21]) in an attempt to build a more precise ECPL system. The plateau of current open-loop

process accuracy might be changed with a more mature interferometric curing monitor and measurement (ICM&M) system, which will be able to provide real-time measurement output enabling a closed-loop control. It is reasonable to think that advanced control methods with real-time closed-loop feedback could improve significantly ECPL process accuracy, as envisioned in Figure 3.

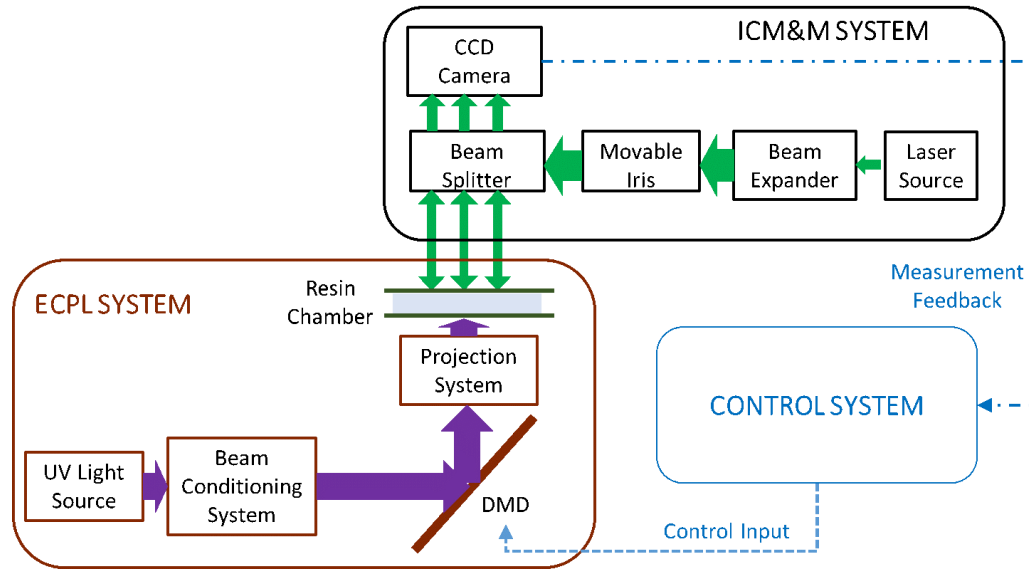


Figure 3. An integrated ECPL System with Real-Time Measurement and Control

This research aims to upgrade the ICM system into a real-time metrology, and to develop some advanced control system, defined under this particular scenario as closed-loop real-time feedback control, for the ECPL system.

## 1.5 Dissertation Organization

A brief introduction to the ECPL process and ICM system is presented in Chapter 1. This chapter also presents the motivation for the ECPL process measurement and control. Chapter 2 presents the limitations in the existing ECPL process control methods, and Chapter 3 reviews some advanced control methods for processes relevant to the ECPL process. A detailed explanation of the research gaps, research questions and hypothesis is presented in Chapter 4. Chapter 5 presents the development of the interferometric curing monitoring and measuring (ICM&M) sensor model and online

parameter estimation algorithms, with some initial experimental validations during the course of this research. Chapter 6 explores the data analysis methods underpinning of the ICM&M method for ECPL process measurement. A data mining approach for evaluating the ICM&M sensor model was developed and verified to be intelligent, accurate, robust and efficient for handling. To implement the ICM&M method for the ECPL process measurement, an application program – the ECPL M&C software - is designed and created in MATLAB as presented in Chapter 7. Chapter 8 designs and implements experiments for validation of the ICM&M method offline, and its measurement characteristics are also presented. Herein, the first research question and its hypothesis is validated in this chapter. To further evaluate the first research hypothesis and to validate the second research hypothesis, Chapter 9 demonstrates a real-time implementation of the ICM&M method for measuring and controlling the ECPL process with a developed feedforward-feedback control method. The real-time experiments results are interpreted and an error analysis is elaborated for evaluating the process control performance. In Chapter 10, the research questions are revisited and the contributions resulting from this work are summarized. The limitations of this work and directions for future work are also discussed.

## CHAPTER 2 EXISTING ECPL PROCESS MEASUREMENT AND CONTROL

Primarily due to the complicated nature of photopolymerization and stereolithography process, so far no comprehensive control strategy exists yet except for some basic use of offline open-loop process control technology. This technique relies on characterization experiments, which are used to quantify the effects of exposure dose on the cured heights. Our group has worked extensively in an effort to realize an automated and precise ECPL system. This chapter provides the related previous research in order to identify gaps between the research goal and previous works.

### 2.1 Process Control Method Developed by Zhao

#### 2.1.1 Process Model

Zhao [19] found a process model (Equation ( 1 )) relating the exposure dose  $E$  to the final cured height  $Z$  by curve fitting of measurement data from many cured parts. Experiments were performed beforehand to determine the values of critical exposure  $E_c$ , and penetration depths of liquid ( $D_{pL}$ ) and of solid resin ( $D_{pS}$ ). This model was an analytical solution of the ordinary differential equation of a transient layer curing model developed by Limaye and Rosen [22], which was based on Beer-Lambert's Law ( $E_c$ - $D_{pS}$ , i.e., threshold exposure model). Before solving, it was simplified by applying Taylor series expansion with higher order terms omitted.

$$Z(E) = D_{pS} \ln \left[ \frac{D_{pL} E}{D_{pS} E_c} + 1 - \frac{D_{pL}}{D_{pS}} \right] \quad (1)$$

#### 2.1.2 Process Control

Based on the process model above, an open-loop process control for ECPL was developed and the control scheme is summarized as shown in Figure 4. Given a 3D part

profile, based on the inverse process model, a timed sequence of bitmaps was generated to minimize the mean squares of errors between all voxels' actual exposure dose to their required dose in order to cure the desired part.

The process control method was implemented on a few examples of lenses fabrication by Jariwala [17]. The desired diameter was 200 $\mu\text{m}$  and the sag height was 120 $\mu\text{m}$ . It was observed that the process control failed to adequately cure the heights and the overall diameter of the part. The height was under-cured by almost 20  $\mu\text{m}$  and the diameter mismatch was up to 50 $\mu\text{m}$ , which corresponded to around 30%.

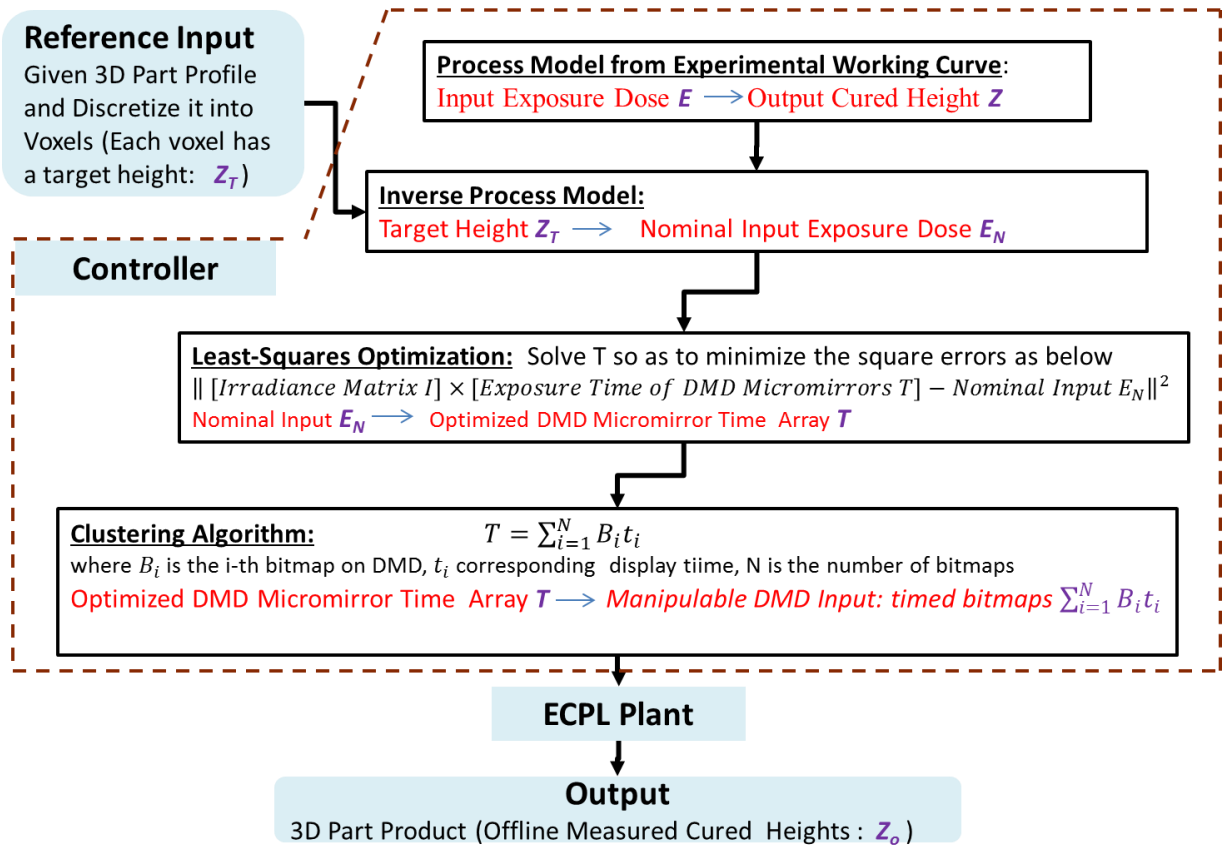


Figure 4: ECPL Open-loop Process Control Scheme by Zhao [19]

### 2.1.3 Critics and Summary

Below lists some critical factors which prohibited an accurate process.



- 1) Admittedly the algorithms of least squares optimization and clustering were limited in only approximating rather than equating the ideal process input receipt, however it was not fair to account heavily on the algorithms for the errors because process uncertainties might be more devastating.
- 2) The ECPL process is not well known and susceptible to unmeasurable material / equipment variations and disturbances and operational errors.
- 3) Another critical error source could be the assumption that voxel curing behavior follows the part curing characteristics. That is, the working curve relating exposure dose to part cured height might be inaccurately or wrongly applied to the voxel curing, because in the process model ignored possible voxel-voxel interactions such as mechanics which might have induced surface shrinkage.

As a summary, this process control has a virtue in terms of process automation development, but could not achieve good accuracy due to an over-simplified process model and process inherent challenges. This is a common problem of open-loop control.

## **2.2 Process Control Method Developed by Jariwala**

### **2.2.1 Process Model**

To come up with a more accurate process model, Jariwala [17], investigated the photopolymerization chemical reaction kinetics and conducted both 1D and 2D simulations in COMSOL Multiphysics® to generate a semi-empirical material model based on the well-known Beer Lambert's law of attenuation. This chemical kinetics based material model was validated to be able to estimate better the shape of a cured part than the experimental working curve above, because it added oxygen inhibition and diffusion effects.

The semi-empirical model, still based on the basic threshold exposure model, was revised by incorporating the idea that both  $E_c$  and  $D_p$  rather than remain constant, could actually change with the distance between substrate pixel and substrate center. In order to find out the functions of  $E_c$  and  $D_p$  with the substrate pixel's distance away from the substrate center, a response surface named as material model was generated with COMSOL simulation data (note: not physical experiment, which was verified to agree with COMSOL simulation result with some acceptable errors).

The final form of this process model is as shown in Equation (2), where  $R$  is the maximum radius ( $\mu\text{m}$ ) of the part to be cured,  $r$  is the distance ( $\mu\text{m}$ ) of the point of interest from the center  $E(r)$  is the irradiance energy ( $\text{mJ}/\text{cm}^2$ ) incident at the point of interest and is obtained from the material parameter database and  $Z$  is the cured part height at the point of interest.

$$Z(r, R) = \begin{cases} 0, & \text{for } E(r) < E_c(r, R) \\ D_p(r, R) \times \ln\left(\frac{E(r)}{E_c(r, R)}\right), & \text{for } E(r) \geq E_c(r, R) \end{cases} \quad (2)$$

### 2.2.2 Process Control

With the process model in the equation above, a process control scheme was formulated by interplaying the empirical response surface with COMSOL simulation of polymerization reaction kinetics to estimate the manufacturing process input required to cure a part with desired shape and dimensions.

The process-planning problem, which was actually also an open-loop control, was split into two steps – estimating first bitmap and exposure time using material model database, and estimating subsequent bitmaps and exposure time based on simulated slicing techniques. Figure 5 shows the flow chart for estimating the subsequent bitmaps and exposure times.

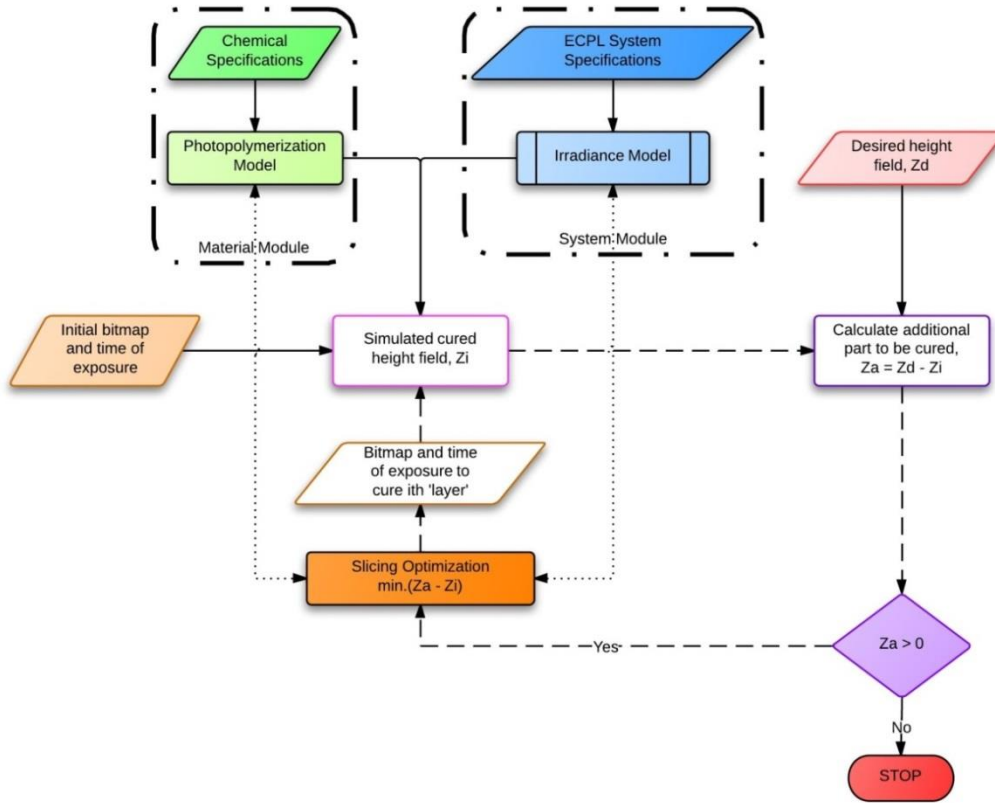


Figure 5. ECPL Open-loop Process Control Scheme by Jariwala [17]

In micro-lens curing experiments, Jariwala’s process control method yielded an error of about 15% between the cured part geometry and the desired part geometry, both in sag height and diameter.

### 2.2.3 Critics and Summary

Compared with Zhao’s control, this one outperformed in terms of less error due to the use of COMSOL simulation of the photopolymerization process. The process control method has following strengths and weakness.

1. It is noted that in Figure 5, there is a closed loop in the control using the COMSOL simulation result as a feedback. The error between feedback simulated height and desired height was used to adjust both the bitmap and exposure time. Hence, it was closed-loop control which might be one reason other than improved process model that the control yielded better result.

However, because the time-consuming COMSOL simulation could not provide in-situ feedback, the controller calculated the input offline which was later implemented in an open-loop mode. Consequently, such kind of controller is incapable of dealing with process variations and disturbances.

Hence, it is still an open-loop control system embedded with an offline closed-loop controller implemented in an open-loop mode. Generally, we could define it as semi-closed-loop.

2. It didn't unveil explicitly the exact formulation of process model, but merely relied on COMSOL simulation of chemical reactions and 2D finite element method to estimate the cured part. Without an analytical model, it was hard to claim that new knowledge about the ECPL process model was obtained except for some chemical kinetics rate constants. The part of finite element analysis by COMSOL indicated the analytical model if any is very complex and could be addressed only by numerical methods thus far. Even though the solution is challenging, the analytical model itself should have an explicit form, which was however not established by the author.
3. A practical issue lies in the unrepeatable experiments which were tried by following researchers. The process control method seemed instable or unreliable.

## **2.3 Process Control Developed by Jones**

### **2.3.1 Process Model**

Jones [20] experimented with a real-time sensor, an interferometric curing monitoring (ICM) system, to fit a model relating time ( $t$  in seconds) and phase angle ( $\Phi$  and  $\Phi_c$  in degrees) with part height ( $Z$  in  $\mu\text{m}$ ) so that a comparison between the direct control of time and the control with measured phase angle could be performed. The time

to part height relationship, Equation. (3), was experimentally determined by curing a single square for a known amount of time, washing the sample, and then measuring its height.

$$Z(t) = 36.85 \times \ln(t) + 22.707 \quad (3)$$

The relationship, as shown in Equation (4), between phase angle and part height was also found using the same dataset.

$$Z(\phi_c) = 30.144 \times \ln(\phi_c) - 159.83 \quad (4)$$

### 2.3.2 Process Control

Corresponding to model in Equation (3), a simple open-loop controller, working like a stopwatch, was used to control the curing time so as to achieve a desired height. A second control method was proposed based on Equation (4) with the aid of ICM which could provide in-situ measurement. Equation (4) maps the in-situ measurement of interferogram phase angle with the ICM to the off-line measurement of cured part height with microscopy. The objective was that after characterizing the in-situ ICM measurement, real-time inference of cured height would be available to advance the controls towards real-time closed loop feedback control, which was proposed in Figure 6. This controller aimed to achieve real-time control by turning bitmaps on and off in response to ICM measurements of phase angle.

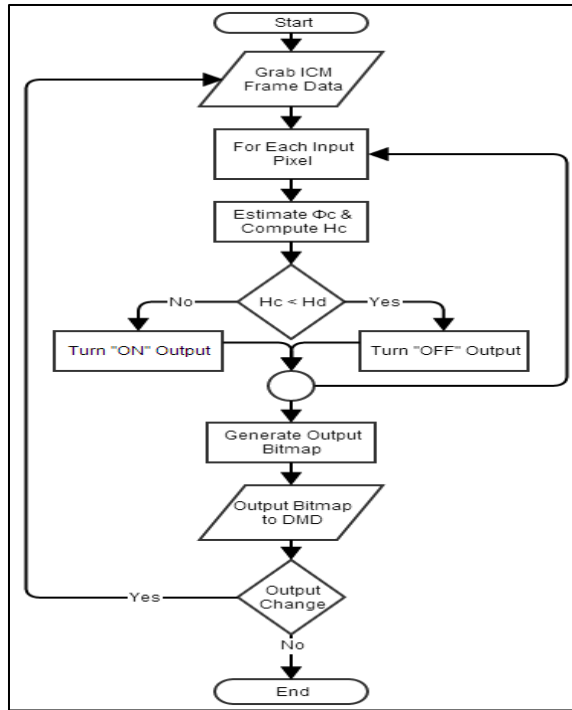


Figure 6: Flow Diagram of the Control System Proposed by Jones [20]

### 2.3.3 Critics and Summary

The stopwatch type of control is simple and straightforward, and its accuracy depends on the model accuracy in Equation (3).

As to the proposed control scheme in Figure 6, it is a quasi closed loop controller because it compares feedback with setpoint just to decide when to stop displaying the given bitmap, but can not adjust accordingly the exposure intensity or pattern. Another limitation is that it achieves control only in a conditioned scenario where the bitmap is known and all that needs control is just the bitmap's display time. Simple examples of squares curing using only single or two bitmaps were conducted experimentally and the results demonstrated better accuracy than the use of open-loop, time-based control. However, more complete closed-loop feedback control across the entire build chamber for a 3D part is still needed. Furthermore, the controller performance depends heavily on the accuracy of the empirical model, and was constrained by a lacking of well-developed analysis of real time measurement data.

Jones' work was more about development of a sensor rather than a controller. His research is meaningful in showing that the interferogram pixel intensity - time curve has potential to calculate the cured height thereon to provide a real-time feedback.

## 2.4 Summary of existing ECPL controls

The existing ECPL process control methods introduced above are summarized in Table 1. Such existing process controls suffer noticeable loss of accuracy because of the inherent weakness of the offline process model and open-loop control mode, which cannot track the changes in process, material and equipment.

Table 1. Summary of Existing Process Controls

Control Methods		Zhao (2009)	Jariwala (2013)	Jones (2014)
Process Model	Measurement	Offline (Microscopy)	Offline (Microscopy)	Offline (Microscopy), <b>Online (ICM)</b>
	Operation	<b>Offline</b>	<b>Offline</b>	<b>Offline</b>
	Methods	<b>Physical</b> (Analytical Transient Layer Curing Model) + <b>DOE</b> (to build Working Curve)	<b>Physical</b> (Revised Exposure Threshold Model) & <b>Chemical</b> Kinetics COMSOL Simulation + <b>DOE</b> (to build Material Database)	<b>DOE</b> (Purely Experiments Data Curve Fitting using Logarithmic Regression)
	Process Knowledge	<b>Preliminary</b>	<b>Intermediate</b>	<b>None</b>
	Parameters	1. Offline Preset. 2. Uniform all across time and space. <b>No variation or dynamics considered.</b>	1. Offline Preset. 2. Changing radially. <b>Spatial variation but no dynamics considered</b>	1. Offline Preset. 2. Constant Curve slope and interceptions (No physical meaning). <b>No variation or dynamics considered.</b>
	Variables	<b>Exposure dose E</b> (both bitmap and exposure time)	<b>Exposure dose E</b> (both bitmap and exposure time)	Requiring Bitmap be given, Model #1: <b>exposure time t</b> ; Model #2: <b>exposure time t</b> (by comparing measured and desired Phase angle $\Phi$ )
Equations	$Z(E) = D_{ps} \ln \left[ \frac{D_{pL} E}{D_{pS} E_c} + 1 - \frac{D_{pL}}{D_{pS}} \right]$	$Z(r, R) = \begin{cases} 0, & \text{for } E(r) < E_c(r, R) \\ D_p(r, R) \times \ln \left( \frac{E(r)}{E_c(r, R)} \right), & \text{for } E(r) \geq E_c(r, R) \end{cases}$	Model #1: $Z(t) = 36.85 \times \ln(t) + 22.707$ Model #2: $Z(\phi_c) = 30.144 \times \ln(\phi_c) - 159.83$	
Controller	Algorithms	1. Offline 2. Optimization & Clustering to calculate process input from the model	1. Offline 2. Incremental Trial and error based on simulation feedback	<b>Controller #1</b> : Simple stopwatch type of time control using Model #1. <b>Controller #2</b> : Feedback time control using Model #2.
	Implementation Mode	implement the pre-calculated input in an <b>open-loop</b> mode	implement the pre-calculated input in an <b>open-loop</b> mode	Controller #1: Open-loop Controller #2: <b>Quasi Closed-loop</b>
Fabrication Error		<b>~ 25%</b>	<b>~ 15%</b>	<b>~ 10%</b>
Notes		1. "Offline" means the model parameters or controllers inputs are calculated ahead of the process. Oppositely, "Online" means the calculations are done during the process. 2. "DOE": Design of Experiments 3. Parameter "Dynamics" means its changes or evolution with time.		

Despite their effectiveness to some extent, the existent process controls suffer noticeable loss of accuracy because they cannot track the changes in process, material

and equipment. The techniques have some common limitations of the inherent weakness of the offline process model and non-closed-loop control mode.

1) Offline process model

It is noted that all the existent process controls are based on offline process model, which couldn't address the online process variations and disturbances. The process input has been preset by the process model, whose parameters are obtained offline and prone to become oversimplified or obsolete due to the varying material properties and equipment conditions along with some stochastic phenomena present in the photopolymerization. Thus, offline static process model would undermine a desired accurate process control.

2) Open-loop control mode

On top of all, under the existing strategies it is common practice to operate the ECPL process in an open-loop mode. The fabrication process would go thru without adjusting the process input according to online process variations and disturbances.



## **CHAPTER 3 LITERATURE REVIEW ON CONTROLS OF MANUFACTURING PROCESSES RELEVANT TO ECPL**

Many of the limitations of the existing ECPL controls mentioned stem from the fact that fundamental understanding of photopolymerization based stereolithography is still incomplete; therefore an open-loop control cannot effectively address all the process control problems of concern. An advanced method for controlling processes, which are only partially understood, is closed-loop control where input and output variables are linked through information feedback [23]. Very few literature reports application of advanced control methods to micro stereolithography ( $\mu$ SL) process, not to mention to the specific kind of non-stacking DMD-based  $\mu$ SL process as is the ECPL case. This chapter presents some relevant research on the control technologies in other manufacturing processes which are similar to ECPL in one or another way, and thereby proposes at the end a few feasible control strategies for ECPL process.

### **3.1 ECPL Property Space**

There is quite a lot of research effort on the control technologies in other manufacturing processes which are similar to ECPL in one or another way. Perusing literature in these process control methods could shed some light onto the guidelines or approaches of developing an improved ECPL control system. Figure 7 depicts the surveyed control strategies in a wide spectrum of processes linked to the ECPL process of our interest. The literature review started from the properties space of ECPL and reached out to similar processes in terms of a particular property. We wish to learn various controls and identify these suitable to ECPL.

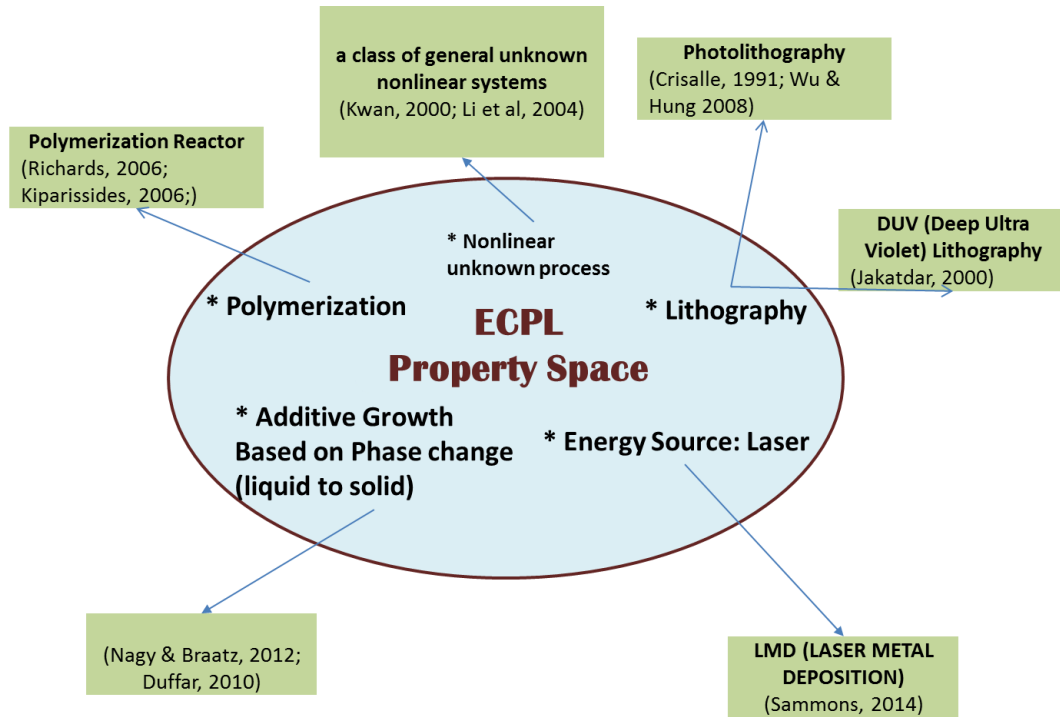


Figure 7. Literature Survey on Controls of Processes Relevant to ECPL

### 3.2 Controls of Polymerization

First of all, ECPL could be deemed as a miniature polymerization reactor, specifically, a free radical chain-growth photo-polymerization process, which is one of various polymerization kinds. A polymerization process usually undergoes disturbances, which move the process away from the desired trajectories. In order to obtain in-specification end-use polymer properties such as final form and shape, for the intended application, process measurement and control systems must be designed and implemented.

#### 3.2.1 Challenges in polymerization modeling and optimization: A population balance perspective

Kiparissides [24] surveyed a unified population balance approach to follow the time evolution of molecular and morphological polymer properties in batch and

continuous polymerization reactors. The numerical methods as well as the computational issues related with the solution of the dynamic population balance equation were critically assessed. The orthogonal collocation on finite elements (OCFE) method and the fixed-pivot technique (FPT) are then applied to a free-radical batch polymerization reactor to calculate the dynamic evolution of the molecular weight distribution (MWD). Moreover, theoretical and experimental results were shown on the dynamic evolution of particle size distribution (PSD) in a suspension polymerization reactor.

The numerical solution of the dynamic population balance equation (PBE) for a particulate system, especially for a reactive one, is a notably difficult problem due to both numerical complexities and model uncertainties regarding the particle nucleation, growth, aggregation and breakage mechanisms that are often poorly understood. Usually, the numerical solution of the PBE requires the discretization of the particle volume domain into a number of discrete elements that results in a system of stiff, nonlinear differential or algebraic/differential equations that is solved numerically.

Recent advances in on-line monitoring of “polymer quality” were briefly discussed in the context of available hardware and software sensors. The problem of real-time optimization of polymerization processes under parametric uncertainty is also examined. Finally, new issues related with the modeling, numerical solution and control of multidimensional population balance equations were conferred.

### **3.2.2 Measurement and control of polymerization reactors**

Richards and Congalidis [25] presented a hierarchical approach to the control system design and reviewed traditional regulatory techniques as well as advanced control strategies for batch, semi-batch, and continuous reactors. The paper focused on process control in a complex industrial environment of free radical copolymerization reactor with environmental conditions (Pressure, Temperature, Level, and Flow) regulation, and material property (viscosity, MWD and PSD) measurement. This process had been used

as a benchmark to test various control and estimation schemes. It represents a wide class of free radical polymer reactors with no less challenge in general polymer industry than in ECPL. The logic is that if the control methods introduced in the literature could address the polymerization with more complex issues, they or their variations might also be applicable to ECPL, because the polymerization process is more aggressive than ECPL in terms of high nonlinearity, multiple inputs-outputs, multiple sensors and deadtime issues.

The industrial measurement techniques are not applicable to ECPL micro process, however, as rationalized above, the controls methods might be leveraged to ECPL.

Richards [25] started reviewing controls with a comparison of generic control methodologies as below.

1) PID feedback control

Very widely used because it requires minimal process knowledge. In particular, it doesn't require a mathematical model of the process. If properly tuned, the PID controller can be quite robust in maintaining good steady state in the face of unmeasured disturbances. However, it has a serious limitation: the PID controller requires control variables to be measured online so that the control action can occur after detecting a deviation between the set point and the measured variable. Perfect control is not possible because PID feedback control is reactive and compromising.

2) Feedforward control

It relies on the fidelity and accuracy of the process model, based on which it compensates the measured disturbances.

3) Feedforward - feedback control

A combination of feedforward and feedback control utilizes the best of both approaches by being able to provide compensation for both measured and

unmeasured disturbances as well as model inadequacy and measurement inaccuracies.

As expected, the authors recommended feedforward-feedback control, which includes distinct control schemes based on different control algorithms. Academic researchers have established prominent nonlinear MPC (Model Predictive Control) technology for tough control problems in polymerization reactors. A nonlinear MPC control might be designed for ECPL, given real-time measurement and based on a reasonably accurate process model that can capture the interactions between input, output, and disturbance variables. The scheme of MPC is shown in the block diagram in Figure 8. If Jariwala's [17] output prediction with COMSOL simulation could be fast enough to be in pace with real-time ICM measurement, a nonlinear MPC model might be interesting and applicable.

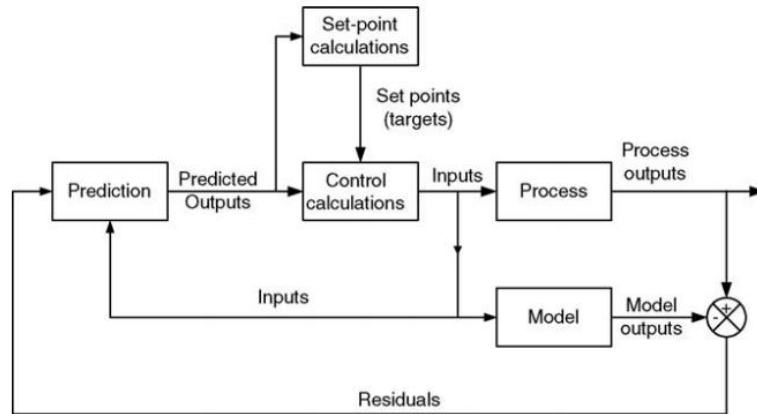


Figure 8. MPC block diagram (Seborg, Edgar [26])

### 3.3 Controls of Lithography

Lithography such as photolithography, DUV lithography and electronic beam lithography in semiconductor manufacturing all have some commonality with micro stereolithography in that they involve photo induced chemical process and need exposure dose control.

### 3.3.1 Model-based Adaptive Control of Photolithography [23]

Adaptive control techniques, with their capability for providing satisfactory control even when the process changes with time, are promising candidates for dealing with common problems encountered in photolithography processing such as batch-to-batch variations in resist properties, inconsistencies in resist curing, etc. Crisalle, Soper [23] proposed and evaluated an adaptive control strategy for the photolithography process. The design utilizes a reduced-order lithography model, an on-line parameter estimator, and a nonlinear model-inversion controller (NMIC).

A crucial output of photolithography - the width of the printed resist lines - was controlled by automatically adjusting the exposure energy. In the calculation of the appropriate exposure adjustment, the controller uses both measured critical dimensions as well as estimated values produced by the process model. The control system is capable of tracking changes in the photolithography process by automatic updating of key model parameters as the process evolves in time. Simulation studies of the closed-loop adaptive control strategy using the PROLITH simulation package to represent the lithography process demonstrate the feasibility of this approach.

The lumped-parameter model (LPM) of Hershel and Mack defines an explicit relationship between the critical dimension (a controlled variable) of the line or space feature, and the exposure energy (a manipulated input variable) by means of the integral equations.

$$\left[ \frac{E}{E_0} \right]^{\gamma_e} = 1 + \frac{1}{D_e} \int_0^x \left[ \frac{I(\xi)}{I(0)} \right]^{-\gamma_e} d\xi$$

where, CD = critical dimension (nm), E = exposure energy (mJ/cm<sup>2</sup>), E<sub>0</sub> = effective photosensitivity (mJ/cm<sup>2</sup>), D<sub>e</sub> = effective film thickness (nm), γ<sub>e</sub> = effective resist contrast (dimensionless), I(ξ) = aerial intensity distribution (mW/cm<sup>2</sup>), and ξ = horizontal location on the mask (nm).

The model-based adaptive control strategy proposed for photolithography consists of the concerted operation of the parameter estimation technique, the nonlinear controller, and the LPM equation. The relationship between these three elements is shown in the block diagram of Figure 9. At a given sampling instant the estimator first makes use of the measured input-output data N-tuples to calculate updated values of three model parameters  $D_e$ ,  $\gamma_e$  and  $E_0$  which minimize the least-squares error. Next, the updated LPM parameters are used to calculate the estimated critical dimension  $CD(t)$ . Finally, the nonlinear controller makes use of all available information— the updated LPM parameters, the estimated critical dimension, the desired set point, and the actual critical dimension measurement— to calculate the prescribed exposure energy according to inverse of LPM.

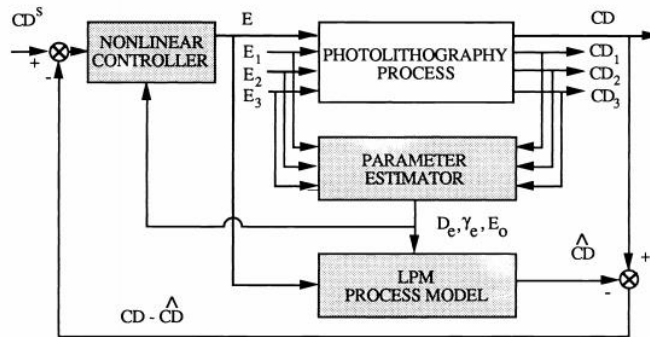


Figure 9. Adaptive control of photolithography using the nonlinear model [23]

The performance of the overall adaptive control structure is enhanced by including the data filtering operations and by adopting the deadband policy. Since commercial projection step-and-repeat steppers have a bound on the fastest reproducible shutter speed (typically of the order of 3 msec), exposure adjustments less than this limit are therefore not possible. This limitation in the control action is expressed in terms of a deadband variable,  $E_{mm}$ , the minimum allowable exposure energy change. No attempt is made to adjust the exposure dose when this threshold is violated. The control policy is then ruled by the logical condition as below.

If  $|E(t_k) - E(t_{k-1})| \leq \Delta E_{min}$ , then  $E(t_k) = E(t_{k-1})$ .

The control deadband  $\Delta E_{min}$  may be arbitrarily set to values greater than the resolution of the optical shutter. Such a choice prevents the controller from making small exposure adjustments that would have only a minor effect on the critical dimensions. The performance of the control loop is thus markedly enhanced.

Similarly in ECPL, the UV light shutter and DMD flip time also limit exposure adjustment. This limitation in the control action could be expressed in terms of a deadband variable,  $\Delta E_{min}$ , the minimum allowable exposure energy change.

Deadband consideration can be an improvement in our proposed control method of ECPL compared with Jariwala's method [17].

It is necessary to clarify that “adaptive” control in this paper [23] is actually a recursive least squares digital control. By the term “adaptive,” the paper meant online parameter estimation. There are different forms of adaptive control, which is generally a broad class.

### **3.3.2 Run-to-run control of DUV lithography [27]**

To achieve enhanced predictive model as well as to facilitate control of deep ultra violet (DUV) lithography, Jakatdar [27] presented a framework that integrates the metrology of wafer level observables with a physical model. For simulation, he proposed a dynamic physical model for volume shrinkage in chemically amplified photo resists. He also designed an in-line run-to-run control with sensors. A static model of the DUV (Deep Ultra Violet) lithography process was obtained using regression on a design of experiment to predict the output CD (critical dimensions) in terms of exposure dose and bake time. Based on the static model, a process drift model was developed to attribute CD variability to wafer reflectivity variation, batch to batch resist variation and exposure and thermal dose variation, as well as measurement noises.



In a scenario with one sensor, the in-line reflectometer measures the resist thickness before and after the exposure and baking steps, in order to calculate the deprotection induced thickness loss (DITL). This DITL value is used to estimate the post-develop CD which is then used in conjunction with a standard RtR control algorithm, to prescribe a recipe for the subsequent wafer. A schematic of the control architecture and notation is shown in Figure 10.

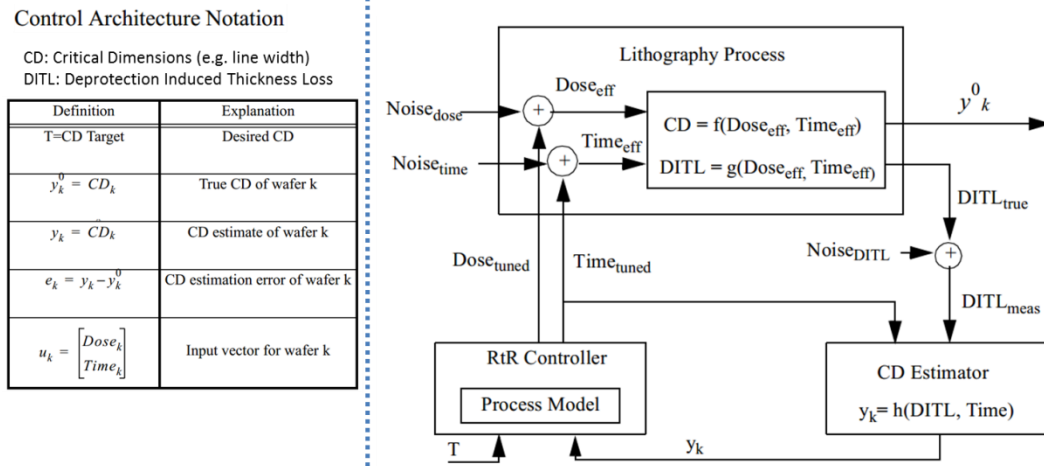


Figure 10. Run to Run Control Architecture for DUV Lithography [27]

The controller uses a Kalman Filter to provide estimates of the noise and uses process models based on a statistical design of experiments technique. Two scenarios were considered, differing in the type of metrology as well as the frequency of measurements available. The simulation results indicate the efficacy of using such a scheme for a real-world lithography sequence.

### 3.3.3 Run-to-run controls of photolithography [28]

Wu, Hung [28] described two run-to-run controllers, a nonlinear multiple exponential-weight moving-average (NMEWMA) controller and a dynamic model-tuning minimum-variance (DMTMV) controller, for critical dimensions (CD) control in

photolithography processes. The experimental design and a multiple regression analysis were used to form relationships between the factors (exposure dose and focus) and the output quality property (critical dimension). Both controllers could easily update the dynamic model and obtain the optimal inputs for the next run. The simulation results demonstrated that the DMTMV controller was more powerful than the NEWMA controller for rejecting disturbances and increasing yields. Quantified improvements were obtained from simulations and real photolithography processes.

### **3.4 Frequency Domain Control of Laser Metal Deposition [29]**

Also using laser to deposit material as ECPL does, the Laser Metal Deposition (LMD) process is an established additive manufacturing process which is comprised of melting powdered metal material with a laser to fabricate metal structures. While the process is usually modeled and controlled via pure temporal models and algorithms, the process is more aptly described as a repetitive process with two sets of dynamic processes: one that evolves in time and one that evolves in part layer. Therefore, it is advantageous to derive a model of the LMD process that captures these two dominant phenomena. Although first principles models are capable of capturing both phenomena, simpler models can be derived and characterized using system identification methods. Therefore, a Hammerstein model describing the LMD process is derived [29], which captures the two dominant aspects of the process and reproduces a common description of the melt pool shape. The model is then transformed into the frequency domain and the unknown dynamics are identified and validated using system identification techniques. The phase and magnitude properties of the model are also examined.

### **3.5 Adaptive Neural Network Control of a Class of Unknown Nonlinear System**

Kwan and Member [30] proposed a robust controller for backstepping control of a class of general nonlinear system using neural network (NN). All errors and weight are

guaranteed to be bounded. The tracking error can be reduced to arbitrarily small values by choosing certain gains large enough. Several practical systems, including an induction motor and a RLFJ robot, were used to demonstrate the effectiveness of the proposed controller. The method does not require the system dynamics to be exactly known or require any off-line learning phase.

A similar but more powerful control algorithm was presented by Yahui Li [31]. Two different backstepping neural network (NN) control approaches were presented for a class of affine nonlinear systems in the strict-feedback form with unknown nonlinearities. By a special design scheme, the controller singularity problem is avoided perfectly in both approaches. The closed loop signals are guaranteed to be semiglobally uniformly ultimately bounded and the outputs of the system are proved to converge to a small neighborhood of the desired trajectory. The control performances of the closed-loop systems can be shaped as desired by suitably choosing the design parameters. Simulation results obtained demonstrate the effectiveness of the approaches proposed.

Although it still requires further research to check if ECPL could be really modeled into a backstepping system with a particular form of equations as described in literature [31] and [30], the salient feature of such model and robust adaptive neural network control algorithm for a class of general unknown nonlinear system is very interesting.

### **3.6 Literature summary**

The literatures, as summarized in Table 2, have relevance to aspects of ECPL process control, but could not be applied directly due to the differences in material, equipment and approach. For example, the traditional lithography control design cannot be directly used for ECPL because the processes are fairly different in nature - the former is subtractive while the latter is additive.

Actually, system control is challenging and requires careful development across several levels of detail. There is no panacea control method and each class of system might have its own unique characteristics that require a special algorithm for stability and robustness. Hence, there is still no handy solution to ECPL advanced process control, which demands further research work on both the real-time measurement and process modeling. Even so, the literature review has tremendous value in providing inspirational insights into feasibility of advanced control for ECPL.

Table 2. Summary of Literature Review on Controls of Processes Relevant to ECPL

Literature Process	Process Measurement	Process Model	Controller	Enlightenment to ECPL
Polymerization Modeling & Optimization (Kiparissides, 2006)	Online Hardware Sensors (e.g. spectroscopy) and Software Sensors (e.g. Nonlinear State Estimator)	Dynamics of population balance equations (PBE): nonlinear, high-dimensional	Dynamics optimization and control of particulate polymerization processes	1. A PBE (Population Balance Equation) approach of ECPL model and optimization might be possible. This might provide more insight of the photopolymerization mechanisms. Challenges are huge in mathematical formulation and solution algorithms. 2. State observer (i.e. estimator) might be needed and could be designed based on PBE model to complement with the insufficient in-situ metrology.
Polymerization Reactor (Richards, et al, 2006)	1. Environmental conditions: Pressure, Temperature, Level, and Flow. 2. Material property: viscosity, MWD and PSD Note: many still offline.	Not specifically given. Could be DOE or Chemical Kinetics and Dynamics	Nonlinear Model Predictive Control (MPC)	If Jarivak's [1] output prediction with COMSOL simulation could be fast enough to be in pace with real-time ICM measurement, a nonlinear MPC model might be interesting and applicable.
PhotoLithography (Crisalle, et al, 1991)	PROLITH simulation only	Reduced order Lumped Parameter Model	Run-to-Run: Model Parameters online estimation	1. Run-to-Run controller could be adapted for ECPL. 2. Deadband: minimum allowable exposure dose change. 3. Data filtering to reduce the measurement error effect.
PhotoLithography (Wu, et al, 2008)	Offline measurement	DOE (factorial design of experiments: two factors, seven levels)	Two Run-to-Run controllers: 1. exponential-weight moving average 2. recursive least squares (RLS)	1. Both Simulation and Experiments demonstrated Run-to-Run control could automatically regulate the model coefficients and could be applied to nonlinear models to reject disturbances and increase yields. 2. Double confirmed that Run-to-Run controller might be applicable to ECPL, especially a variation of Run-to-Run controller with RLS system identification.
Deep Ultra Violet (DUV) Lithography (Jakatdar, 2000)	in-line Reflectometer	Dynamic physical model for volume shrinkage, DOE	Run-to-Run controller uses a Kalman Filter to provide estimates of the noise and uses process models based on a statistical design of experiments technique.	1. Suggest that Run-to-Run controller with Kalman Filter could work for ECPL.
Laser Metal Deposition (Sammons, 2014)	Offline measurement	a Hammerstein model: a combination of a static nonlinear process in series with a linear dynamic process.	No controller design, but only Frequency Domain System Identification techniques.	Indicate possibility of applying frequency domain techniques in system identification for ECPL process dynamics, based on which a controller could be designed.
a class of general unknown nonlinear systems e.g. robot, motor (Kvan, 2000; Li et al, 2004)	simulation only, no experiments done.	1. No preliminary dynamical analysis is needed. 2. No need for the off-line experimental learning phase	Adaptive Backstepping using Neural Network	This general adaptive neural network controller for robust backstepping control of a class of unknown nonlinear systems, which might include ECPL as long as it could be fit into such a backstepping model.

As we could see from the literature, Run-to-Run (R2R) control has been used extensively in lithography processes and actually other semiconductor processes as well. The R2R control literature is based on the processes where fundamental or first principles model are not available or are very difficult to obtain. In addition, large numbers of off-line experiments are required for the generation of linear or nonlinear empirical models from experiments. All the features enable R2R to be a good candidate for ECPL because

currently we lack a first principles model for ECPL but already did lots of experiments and have empirical models. Obviously, considering the unique constraints of ECPL, we need a variation of R2R; one candidate variant has been developed, called evolutionary cycle-to-cycle (EC2C) control, which will be introduced in the next section.

Additionally, adaptive neural network (ANN) methods also appear to be promising, based on their successful application in other process governed by unknown nonlinear systems. Hence, it seems that applying advanced control technologies, such as EC2C and ANN, to ECPL is promising but requires further conclusive investigation and more specific detailed design of the control system. In the following section, we will explore more about the ECPL process control.

### **3.7 Proposed Advanced Process Control Schemes**

The overall objective of an ECPL control system is to ensure that the final outputs of the process (i.e. the cured height and shape) conform to established specifications. Although all the final outputs are important, the cured height has been a most prominent concern because cured heights of discretized voxels define the shape.

Considering the process control issues above, we focus the search space of advanced control methods on these which could update online process dynamics modeling and thus track the process evolution with various disturbances more accurately.

#### **3.7.1 Evolutionary Cycle-to-Cycle Control**

We proposed a digital control method – evolutionary cycle to cycle (EC2C) control method- based on the R2R literature. The name, changed from “Run” to “Cycle”, clarifies that the proposed controller works per measurement cycle instead of per experiment run. There is an essential difference between our EC2C approach and traditional R2R approaches. In semiconductor processes, run-to-run usually means wafer-to-wafer, lot-to-lot or batch-to-batch, which is more of a statistical process control, even

though there are a broader classification of R2R including statistics, estimation and artificial intelligence [32]. In our proposed cycle-to-cycle control, we dive into a smaller scale and smaller time step, and focus on a single part fabrication process, that is, to control a single “Run” of process instead of “Run-to-Run” in a batch process.

The EC2C control will inherit the advantages of present R2R control methodologies and adapt well to our ECPL process special issues. Furthermore, if physical (first principles) models can be developed, EC2C control might be extended by synthesizing both physical and empirical models for optimization to overcome the limitations and disadvantages of classical R2R. A recursive least squares (RLS) system identification and Kalman filters could be used in the EC2C for ECPL to enhance the controller performance.

### **3.7.2 Hierarchical Framework of Control Methods for ECPL**

We already looked into a search space of ECPL-like process control methods. There is no panacea or all-purpose control method, but only myriad control methods dealing with various types of systems. Worse still, terminologies and definitions of various control methods seem to clutter in vast literature. It is confusing that there are a number of control methods which differ despite similar name or resemble despite different names. For example, in some paper adaptive control might mean a run-to-run control, which again could also be called as a cycle-to-cycle control or recursive least square digital control. Hence, we need clarify our candidate control methods.

Furthermore, under the scenario of ECPL, which kind of control is suitable totally depends on the process model and measurement capability. It is always easier to start with a simple model and develop a baseline control. As our knowledge of the process develops along with improved in-situ measurement to provide real-time feedback, we might be able to progress towards a more and more complex process model based on

which a more advanced control algorithm will become enabled. Hence, it is better to summarize the candidate methods in a hierarchical manner.

Inspired by literature, tailored for ECPL, a hierarchical framework of control methods is put forward for different stages. The development stage of control methods is defined in two status coordinates: degree of process knowledge and degree of measurement capability. The hierarchical framework of control methods, both existing and potential in our research scope, is presented in Figure 11.

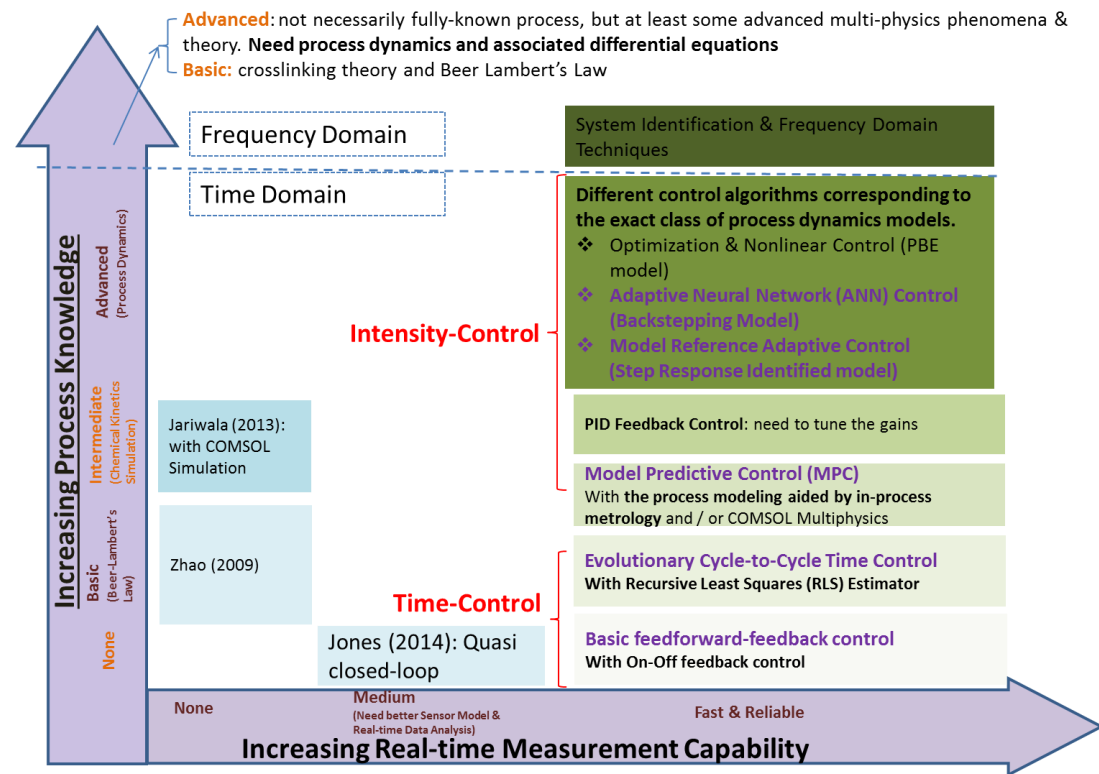


Figure 11. Hierarchical framework of control methods for ECPL

As shown in the control methods hierarchy in Figure 11, only when the in-situ, real-time measurement capability is fast and reliable can we attempt, in increasing order of complexity, the implementation of more advanced control strategies, dynamics model based control algorithms, and on-line optimization strategies to compute input recipes for the ECPL.

Considering current development of ECPL and ICM, we will investigate two most viable candidate controls, evolutionary cycle-to-cycle (EC2C) control and adaptive neural network (ANN) control, which are mostly likely to satisfy the search criteria - capability of adaptive learning and control of unknown or uncertain process.

As shown in the hierarchical framework, the two proposed control methods adopt different theory and architecture, and can be applied under different development stages depending on the knowledge of the process dynamics. EC2C is basically a kind of digital control based on recursive least squares estimates. It can be used at the initial stage when we still have no good fundamental knowledge of the physical relationships among the ECPL photopolymerization variables. The EC2C digital control is envisioned as a baseline controller, which serves as both a guideline for controller tuning and a system identification tool for modeling the ECPL process dynamics in forms of sophisticated differential equations. As the research moves forward with better knowledge of the photopolymerization mechanism and ECPL process dynamics, a more advanced control strategy – adaptive neural network control- with developed process ordinary differential equations could be designed to manipulate the process input directly.

### **3.8 Chapter summary**

Investigation of instrumentation and control methodologies, which will be needed to meet the evolving needs of photopolymerization based processes and other additive manufacturing processes, could be a challenging and vibrant area for academic researchers and industrial practitioners alike.

The chapter reviewed existing control methods for processes relevant to ECPL. Advanced control methods for the ECPL process were identified and a search space of relevant literature was surveyed to reveal promising techniques. Inspired by literature, tailored for ECPL, a hierarchical framework of control methods is proposed. Candidates



include basic feedforward-feedback control, evolutionary cycle-to-cycle control, model predictive control, adaptive neural network control, and frequency domain techniques.

Future work includes detailed design and physical implementation of some advanced control system onto the real ECPL system to further verify and explore their capability.

## CHAPTER 4 RESEARCH GAPS, GOALS AND QUESTIONS

It is common that for all micro manufacturing processes, in order to effectively achieve process control and quality enhancement, improved real-time metrology systems and sensors are needed along with models that describe the various manufacturing processes at the micro level such that true process control can be enabled [33]. This chapter presented the existing issues relevant to measurement and control of the ECPL process. The research gaps from existing literature were identified and presented. It was found that the existing literature lacks adequate models and effective closed-loop controls that could precisely fabricate the cured part. In order to accomplish the research objective, research questions and hypotheses were formulated. The main research question in this study is how to control ECPL with more accuracy and robustness. And our research hypothesis is that advanced control methods in unison with real-time metrology could provide effective and satisfactory control of ECPL process. We will break the process control question into two research questions in terms of metrology and control system.

### 4.1 Issues of Real-time Measurement with ICM System

To realize in-situ sensing of the ECPL process, Jariwala et al [18] and Jones et al [21] developed an interferometric curing monitoring (ICM) system. Various interferometry techniques and applications exist; however, there is no handy solutions to the real-time ICM measurement because:

- 1) The ICM measurand – photopolymerization process cured part dimensions, involve complex unknown material properties and variations. Hence, a measuring principle model, i.e., an ICM model, is needed in order to interpret the interferogram accurately and to extract the desired measurement variables. The ICM model consists of two sub-models: interference optics model and

calibration model, both of which decide the unique issues and inherent challenges in real-time measurement with the ICM system.

- 2) Many existent techniques of interferogram signal processing deal with spatial interferograms instead of temporal interferogram as in the ECPL case.

Techniques for phase measurement can be split into two basic categories: electronic method which utilizes hardware of phase modulator, and analytical method of fringe pattern analysis such as Fourier transform which commonly adopts a phase shifter in one beam [34]. A different approach, based on a 1D unwrapping along the time axis rather than on a 2D spatial unwrapping, is needed for an important subclass of interferometry applications [35]. For the ICM, one is interested in phase changes rather than absolute phase values occurring over time and a sequence of incremental phase maps can be obtained leading up to the final phase-difference map of interest.

- 3) Existing literature provides two approaches of temporal phase measurement: temporal phase shifting with a carrier modulation and Fourier analysis of time-dependent intensity signal [36, 37]. However, the ICM is not configured to be able to add a temporal carrier in the coherent light to modulate the intensity. If the last method is used, it is possible to measure the phase without introducing a carrier, but the sign of the displacement cannot be deduced.
- 4) Even though there are some research in temporal phase unwrapping for interferogram, real-time measurement is rarely addressed and most of the algorithms are for posterior offline analysis. Gao, Huyen [38] proposed a parallel algorithm with a special GPU (Graphics Processing Unit) card and achieved only 4 fps for  $256 \times 256$  digital fringe patterns real-time windowed Fourier filtering. Real-time measurement demands both hardware and software to sufficiently be fast and precise [39].

- 5) Some literature even requires the measured object to have special characteristics to implement its approach. For instance, Huntley and Saldner [35] assumed implicitly that the deformation rate was sufficiently low for negligible phase change to occur over the time scale required to digitize one set of phase-stepped images. This doesn't apply to ECPL process measurement which is fast and cannot use a four-step interferometer where four intensity values at a phase increment of  $\pi/2$  are required.

The existing ICM system could potentially provide an in-situ metrology to aid advanced controllers design. It has already provided insights into the real-time photopolymerization process, interferogram of which demonstrated vividly the stages of incubation period, exposure curing and dark reaction in ECPL process. However, Jariwala [1] used ICM for process monitoring process only, because it was only a qualitative and non-direct visualization of the curing process. Jones [20] mainly employed some data filtering and maximas estimation codes to quantitatively count the phase after obtaining entire interferogram and calculated cured heights from the empirical curve of phase vs height, hence it still remained at offline analysis rather than online measurement.

Both existing approaches of using ICM to obtain information of cured heights are limited in the following aspects [40].

- 1) An interference optics model [17, 18, 20, 21, 41] as shown in Equation ( 5 ), which models a linear relationship of phase angle  $\emptyset$  and refractive index change  $\Delta n$ . However, to obtain the cured height, an empirical logarithmic curve is used to fit the cured height from phase shift  $\emptyset$  as Equation ( 6 ) [20]. The two equations together imply a logarithmic relation between the two compounding variables of overall resin refractive index change  $\Delta n$  and cured height  $Z$ . This logarithmic relationship needs justification otherwise an improved or modified model will be required.

$$\text{Phase Angle } \varnothing = 2\pi \cdot \left( \frac{2 \cdot \Delta n \cdot t}{\lambda} \right) \quad (5)$$

$$\text{Cured Height } Z = 78.96 \cdot \ln(\varnothing) - 259 \quad (6)$$

where  $\Delta n$  is the change in overall refractive index,  $t$  is the fixed chamber height,  $\lambda$  is the coherent laser wavelength.

- 2) The calibration by curve fitting an empirical model of intensity oscillation phase angle and cured height lacks a firm basis in physical phenomena and is not amenable in practice due to batch-by-batch and operator-by-operator variations.
- 3) The simple method of phase angle counting of extrema is problematic in both accuracy and real-time implementation. By identifying a half-cycle from peak and valley extrema, the method has limited resolution fixed at  $\pi$ , and phase angle less than  $\pi$  is prone to interpolation errors, which might be significant especially in the case of non-constant periods and amplitudes. The unknown process variations and irregular oscillation patterns also makes it difficult to predict the next peak or valley.
- 4) Considering the intensity dynamics of a single point could be highly biased, because it is not necessarily representative or comprehensive across the entire part. Accuracy is limited by the unwanted irradiance variations arising from nonuniform light reflection or transmission by the test object spatially.

Consequently, ICM still confronts some modeling and software issues to be completely eligible as real-time measurement of cured heights to provide output feedback for advanced controller.

No direct literature method is available for the unique ICM measurand and system. A mature ICM measurement method needs some research from scratch.

- 1) Need an ICM model to interpret the interferogram accurately and to extract the desired measurand.

- 2) Need fast and robust algorithms to estimate the ICM model's dynamic parameters online.
- 3) Need experimental calibration to obtain reliable values of the ICM model's static parameters.
- 4) Need handle measurement noises in the camera and process.

## 4.2 Issues of Controlling ECPL Process

Kiparissides [24] summarized several valid reasons for the lack in closed-loop “quality” control applications for particulate polymerization processes. These reasons also well explained why herein no closed-loop control methods have been used in projection lithography such as ECPL and other photo polymerization based additive manufacturing. Like all other complex polymerization processes, ECPL also faces challenges on both issues of model formulation as well as control computation.

### 1) Nonlinear process

The photo polymerization process is highly nonlinear, involving a large number of time-varying kinetics and transport parameters.

### 2) Lack of “Friendly” Differential Equations

From a population balance perspective [24], modeling of particulate polymerization systems might lead to nonlinear integral-differential equations. Their infinite-dimensional nature does not allow their direct use for the design of nonlinear controllers that can be easily implemented in real-time.

### 3) Unavailable or Non-direct On-line measurement

So far it is very difficult to measure online of the cured part height, or in polymerization jargons – MWD (Molecular Weight Distribution) and PSD (Particle Size Distribution) which might be useful to model the cured height. Moreover, formulation of a meaningful objective function of cured heights in terms of distributed molecular and morphological properties (e.g., MWD, PSD, etc.) is not easy. The only promising in-situ

metrology – ICM [18], which is still under development, might be available in future, but it has foreseeable limitations as secondary measurements do. ICM might be insufficient for the accurate inference of the entire cured voxels heights.

Like all other complex polymerization processes, ECPL also faces challenges on both issues of model formulation as well as control computation.

Foremost, process knowledge, preferably in-depth, is very important in controller design. The nonlinear process involves multi physics such as photonics, chemistry and mechanics, which interact in a complex and unknown way. Consequently, no process dynamics has been modeled yet, not to mention control it.

Another factor detrimental to process control is unmeasured or unmeasurable process variations including exposure UV light source intensity fluctuation, batch-to-batch inconsistencies in photo material formulation, etc.

Worse still, ECPL is vulnerable to external disturbances such as oxygen inhibitor distribution, and unquantified effects on cured thickness and shape caused by downstream operations such as post-curing developing and washing.

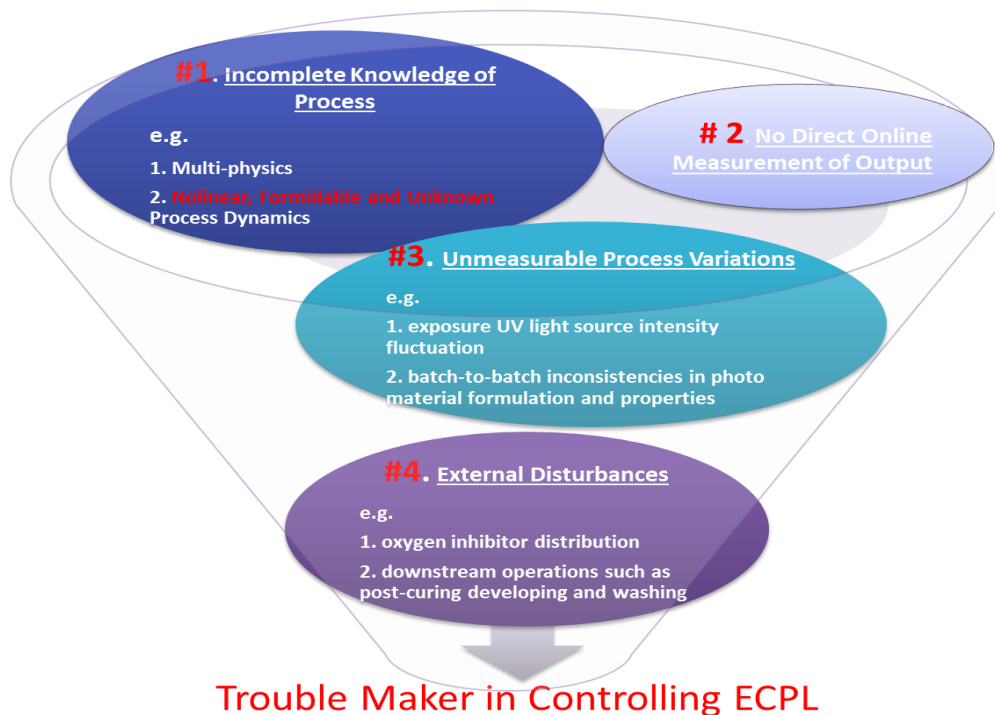


Figure 12. Issues in ECPL Process Control

Therefore, it is difficult to control ECPL process because of the specific issues depicted in Figure 12, which become motivations for new research. The study aims to handle some controls of the corresponding unknown process with adequate design and appropriate measurements.

### 4.3 Research Gaps of ECPL Process Measurement and Control

To identify the research gaps in ECPL process control, we firstly review the system from the perspective of controls design. Control terminologies are adopted to lineate the ECPL controls skeleton as shown in Figure 13.

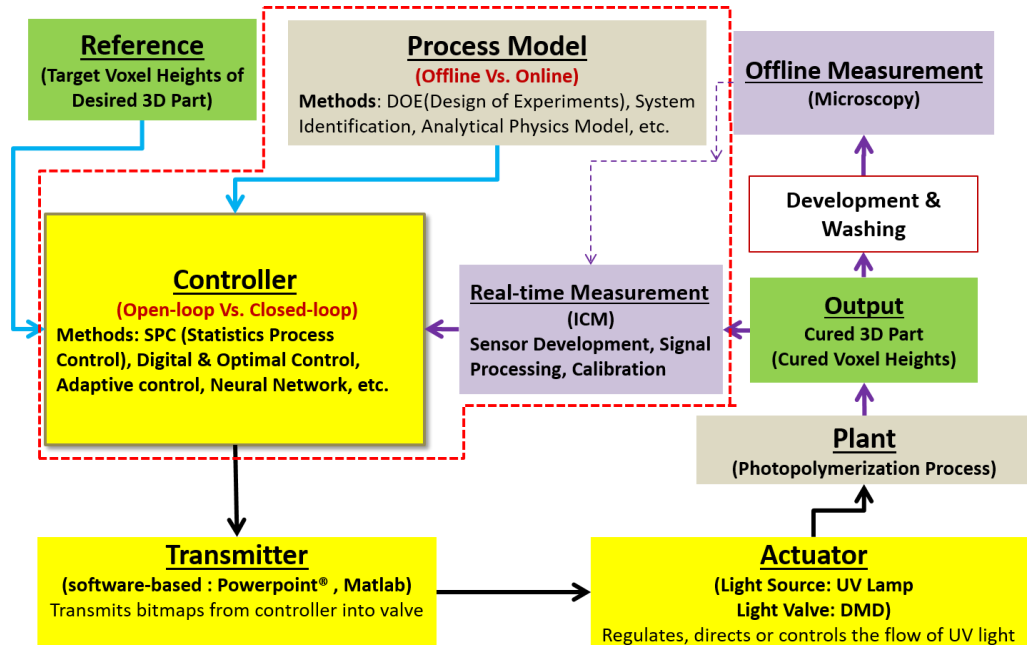


Figure 13 ECPL System from the Perspective of Control Design

With the help of the control system skeleton in Figure 13, we compare in Table 3 the status quo and thereby identify research gaps to improve the process control for ECPL. Comparing with the current controls, we envision to fill the research gaps by developing an advanced control, which in future work is to be designed to possess the desired characteristics as highlighted in the table below for better control performance.



Specifically, to address the challenging issues in previous section, an advanced control method should be able to conduct online adaptive learning and dynamics control with real-time measurement.

Table 3 Research Gaps Identification for ECPL Control

Control Methods	Process Model		Measurement	Controller				Transmitter		
	Mode			Operation Mode		Algorithms	Manipulated Input (DMD Bitmaps)			
	Offline	Online	Method	Offline	Online Real-time				Open-loop	Closed-loop
Zhao (2009)	✓		DOE & Simple Physical Model	✓		✓		Optimizataion & Clustering	1. Binary Bitmaps 2. Dispay time of Each Bitmap	PowerPoint
Jariwala (2013)	✓		DOE & Chemical Kinetics with COMSOL 2D Finite Element Simulation	✓		✓		Incremental Trial and error based on offline simulation	1. Binary Bitmaps 2. Dispay time of Each Bitmap	PowerPoint
Jones (2014)	✓		DOE & Logarithmic Curve Fitting	✓	✗ (Immature)		✗ (Semi-)	Monitor the height indirectly by the phase angle. Can NOT adjust accordingly the exposure intensity or pattern.	1. Only Dispay time of Bitmap (Binary Bitmap Given)	MATLAB
Advanced (Proposed to Fill Gaps)		✓ (Online Estimation & Update)	DOE, Advanced Multi-Physics Models, System Identification	✓	✓	✓	✓	Advanced control algorithms with measurement feedback e.g. PID control, adaptive, neural network.	1. Binary / Grayscale Bitmaps 2. Display time of Each Bitmap 3. Exposure intensity 4. Chemical composition	Candidate: LabVIEW MATLAB

It is worth noting that a close-up of the specific research gaps in the real-time measurement as presented in Section 2.4.2 and also highlighted in Table 3, are summarized in Table 4.

Conclusively, to address the challenging issues in previous sections, a real-time metrology need be developed and an advanced control method should be able to conduct online adaptive learning and dynamics control with measurement feedback.

Table 4 Research Gaps in ICM real-time measurement

ICM Methods	Sensor Model	Calibration Model	Measurement Mode (Online Vs. Offline)	Data Analysis Method	Measured Area
Existing	<b>Implicit model</b> confounding two critical variables: the changes in effective refractive index and cured height.	Arbitrarily use logarithmic curve fitting of Experimental data of cured height Vs. phase angle. <b>Lack physics justification</b> , and reproducibility.	Mainly Offline. Slow and Inaccurate online measurement, <b>NOT ready in Real-time</b> Execution.	Count phase angle by <b>peak-valley extremas</b> in an increment of pi. <b>Inaccurate, and impractical</b> in real-time implementation.	<b>Single point</b>
Proposed	Elaborated optics model with <b>explicit</b> parameters and variables.	An <b>established mathematical method</b> to calculate cured height from the sensor model with more confidence.	Online and <b>Mature</b> Real-time.	Extract the phase angle information <b>robustly</b> by a <b>sensor model</b> . <b>Online parameter estimation</b> , and numerical integration.	<b>Multiple point , Full field</b>

#### 4.4 Research objective

Key to a successful application of control to a manufacturing process is the availability of real-time measurement and appropriate models, which range from empirical forms such as from design of experiments and system identification to analytical forms such as detailed fundamental mechanistic and first principle differential equations.

The overall research objective is to improve the ECPL manufacturing process accuracy and precision, which consist of three aspects - process measurement, process modeling and control. The research will focus on developing a real-time metrology to provide sufficient feedback, with which the research will further focus on applying advanced control methods based on appropriate process modeling. In summary, the research objective is abstracted as follows:

*To develop a real-time process measurement and control method for ECPL.*

#### 4.5 Research Questions and Hypothesis

Kiparissides [24] pointed out that the weakest link in polymer reactor control is undoubtedly the on-line instrumentation, the lack of understanding of the process dynamics, the highly sensitive and nonlinear behavior of polymer reactors and the lack of

well structured control strategies all contribute to the impediment of advanced control applications to polymer manufacturing. As a special polymer reactor, the photopolymerization based ECPL process, similarly confronts the following problems to be addressed in the development of a control policy.

- 1) Ability to measure and characterize the cured polymer part dimensions via on-line sensors and/or nonlinear estimation algorithms.
- 2) Better understanding of process dynamics via mechanistic/data-based modeling and experimentation.
- 3) Development of closed-loop model-based controllers with emphasis on achieving superior performance and disturbance handling.

In response to research gaps identified in Table 3, we generally need to divide the research into three parts, process measurement, process modeling and process control, each of which presents some challenging research question. However, the process modeling and control are closely related, and each model associates with a specific control strategy, thus we would pursue a control-oriented modeling as we study a certain control method. The research questions of process modeling and process control are combined into a broader research question of process control issue as presented in the following sub-sections.

To achieve the research goal, two research questions and hypotheses are proposed to formulate detailed problems of this research. Methods will be developed in order to answer the research questions and to validate the answers by testing the hypotheses.

#### **4.5.1 Research Question 1**

**Research Question 1:** How to develop a real-time metrology for the ECPL process based on the existing in-situ interferometric curing monitoring system to measure the cured part dimensions, specifically the cured heights across the curing area?

**Hypothesis 1:** A real-time metrology for cured part dimensions could be achieved by processing a time series of pixel intensities in a sequence of interferograms, which are provided by the existing in-situ interferometric curing monitoring (ICM) system, based on interference optics and online parameter estimation algorithms.

**Rationale:** The ICM system aims to utilize the principles of interferometry to measure the dimensions, particularly the height at the current research stage, of the part cured in the resin chamber. In future work, it could be extended to 2D and 3D measurement. The sequential acquisition of a large number of interferograms and its postprocessing facilitate the recovery of the phase distribution, so that the whole-field dynamic displacement field can be determined [42]. In this framework, the phase distribution is commonly recovered using a temporal phase shifting algorithm, and the unwrapping is performed as a function of time. For ICM, the camera records frames of spatial interferogram produced by the optical path lengths differences of the light reflecting from the interface surfaces thru the resin chamber. A temporal intensity oscillation in the interferogram sequence is evident for pixels across the curing area, because the optical path length of the light reflecting from the top and bottom surfaces of cured part is changing with time as the photopolymerized resin cures in the chamber. The resultant temporal interference pattern presents a time series of intensity for each pixel across the chamber. The curing process causes the resin refractive index to change from  $n_l$  to  $n_s$  as it crosslinks from liquid into solid. Meanwhile, it changes the height of liquid resin and solid resin in the chamber. Both changes in medium refractive index and height lead to a change in optical path length thus in the interferogram phase. Transform-based or reference-based approaches could be used to retrieve optical phase distributions coded in the temporal intensity [36, 43, 44]. Hence, signal processing of the pixel intensity time series could recover the cured height, based on a well-established ICM model which consists of two sub-models. One sub-model is the sensor model of interference optics that explains the intensity dynamics in the interferogram sequence. The other sub-model is the

calibration model that calculates the measured variable of cured height from ex-situ microscope measurement and estimated parameters in the sensor model.

#### **4.5.2 Research Question 2**

**Research Question 2:** As a baseline control, without a constitutive process model of first principle differential equations, what is an applicable ECPL process control approach, which could utilize the real-time measurement system to improve the process accuracy?

**Hypothesis 2:** A basic On-Off control approach with the online measurement feedback, is applicable in ECPL process to control the height of cured part in real time without requiring sophisticated process model.

**Rationale:**

In one simplest control of the ECPL process operated by just switching the UV lamp, because of the discontinuous operating mode (i.e., on/off) of the exposure source, a discontinuous controller is a natural implementation choice over continuous controllers that may need to be applied by means of identifying the ECPL process model and carefully modulating the exposure intensity. It can be as simple as a switching between two states in the form of an On-Off controller [45]. In general, On-Off control is widely used in industry, especially for discontinuous actuators which have to be switched fully off if the output reaches a limit [46]. Previous ECPL experiments found that exposure time plays a significant role in determining the height of ECPL cured part. As a basic feedback control strategy, the ECPL process could adopt such a two-level control scheme that simply turning on or off the UV lamp, particularly by turning off the UV lamp when the feedback of measured height reaches the setpoint of cured height.

A more advanced version of on-off controller could be designed by incorporating predictive model to enhance its robustness. As seen from the literature, Run-to-Run (R2R) control has been used extensively in lithography and other semiconductor

processes [23, 27, 47, 48]. It is based on processes where fundamental or first principles models are not available or are very difficult to obtain, and requires offline experiments for the generation of empirical models. All the features enable R2R to be a good candidate for ECPL under a black-box situation where a first principles model is not yet available except for only some experiments and empirical models. A variation of R2R, Evolutionary Cycle to Cycle (EC2C) time control, which is suitable for the ECPL process will be needed due to the unique constraints of ECPL. The name, changed from “Run” to “Cycle”, clarifies that the proposed controller works per measurement cycle instead of per experiment run. There is an essential difference between the EC2C method and traditional R2R approaches. In semiconductor processes, run-to-run usually means wafer-to-wafer, lot-to-lot or batch-to-batch, which is more of a statistical process control [32]. This proposed cycle-to-cycle control adopts a smaller scale and smaller time step, and focus on a single part fabrication process, that is, to control a single “Run” of the process instead of “Run-to-Run” in a batch process. The EC2C could inherit the advantages of conventional R2R control methodologies and adapt well to the ECPL process.

#### **4.6 Chapter summary**

This chapter firstly identified the challenges in realizing the desired real-time ICM based metrology and an accurate ECPL process control system, respectively. The research gaps for ECPL process control were presented. It was found that the existing research lacks adequate measurement and control methods that could precisely monitor the height profile of the cured part in real time. In order to accomplish the research objective, two research questions and hypotheses were formulated.

# **CHAPTER 5 ECPL PROCESS MEASUREMENT: ICM&M SENSOR MODEL AND ALGORITHMS**

For monitoring the polymerization based ECPL process, this chapter begins with an overall review of existing state-of-art monitoring for general polymerization reactions in Section 5.1. The molecular level reactions monitoring is not directly applicable to the mesoscale observation of cured part dimensions in ECPL, however, the literature helps understand the current design scope of metrology for ECPL real-time monitoring and helps orient the future research for advanced multi-sensor instrumentation system.

To enable advanced closed-loop control for ECPL, an in-situ interferometric curing monitoring (ICM) system has been developed to infer the output of cured height. However, the existing ICM method based on an implicit model and rough phase counting is not fast and accurate enough. This chapter develops an interferometric curing monitoring and measuring (ICM&M) method which addresses the sensor modeling and algorithms issues. A physical sensor model for ICM&M is derived based on interference optics utilizing the concept of instantaneous frequency. The associated calibration procedure is outlined for ICM&M measurement accuracy. To solve the sensor model, particularly in real time, an online evolutionary parameter estimation algorithm is developed adopting moving horizon exponentially weighted Fourier curve fitting and numerical integration. As a preliminary validation, simulated real-time measurement by offline analysis of a few videos of interferograms acquired in the ECPL process is presented. The agreement between the cured height estimated by ICM&M and that measured by microscope indicates that the measurement principle is promising as real-time metrology for global measurement and control of the ECPL process.

## 5.1 Monitoring polymerization reactions

Various studies on polymer analysis and characterization, as well as mechanistic and kinetic studies of polymers have been reported [49]. Much effort has been devoted to study polymerization processes and modern experimental techniques have improved their understanding. As new stimuli-responsive and "intelligent" polymers continue to be developed, the ability to monitor reactions will become increasingly important. Polymer scientists and engineers can take full advantage of the latest monitoring strategies to optimize reactions in both the lab and the manufacturing plant. Monitoring polymerization reactions enables laboratory researchers to optimize polymer reactions by providing them with a better understanding of the underlying reaction kinetics and mechanisms. Moreover, it opens the door to improved industrial-scale reactions, including enhanced product quality and reduced harmful emissions.

Principles and applications of important polymer characterization tools include light scattering, gel permeation chromatography, calorimetry, rheology, and spectroscopy. Among various fundamental and recent advanced developments in characterization and analysis of polymers, spectroscopy has, over the years, proved itself to be the most popular family of techniques in providing information at molecular levels, such as the reaction kinetics rate constants, rate of polymerization, and molecular weight distribution (MWD). For instances, microstructure of synthetic copolymers is obtained by NMR spectroscopy; monomeric composition and structure can be obtained via pyrolysis mass spectrometry; both structural and dynamical properties of a wide range of physiologically relevant biopolymer (e.g. noncovalent protein complexes) can be determined in real time by Nano Electrospray Ionization Mass Spectrometry.

Automatic continuous online monitoring of polymerization (ACOMP) reactions, is a flexible platform that enables characterization tools to be employed simultaneously during reactions in order to obtain a complete record of multiple reaction features [49]. The first work on automatic continuous online monitoring of polymerization reactions



(ACMOP) was published in 1998 [49]. It is not straightforward to apply the characterization tools for ACMOP. For example, Raman and near infrared techniques are difficult to calibrate and both invasive requiring in situ probes to be inserted into the reactor leading to fouled measurement data.

With the various scientific metrology tools being able to monitor a wide range of polymerization processes at molecular level, higher level observation of mesoscale and macroscale polymerized structures is desired, especially in polymerization based manufacturing processes such as photo-lithography and stereolithography. Microscopic and macroscopic monitoring and measuring polymerization processes might utilize the reported molecular-based characterization and analysis above, which however demands sophisticated process models to scale up the determined kinetics reaction rates, molecular weights, chain lengths and particle size.

In manufacturing plants, direct characterization tools could be helpful to measure and control the final cured polymer parts. Particularly, as polymerization-based additive manufacturing processes continue to be developed, in-situ or real-time monitoring tools are necessitated to improve the process accuracy and product quality and to fulfill their potential applications in a great diversity of industry sectors [1]. Reflectance real time infrared spectroscopy was reported to quantify photopolymerization reactions in a time range of millisecond and monitor the isothermal cure profiles with application to stereolithography resins [50]. The photopolymerization reaction data for different combinations of conditions (chemical composition, radiation intensity and temperature), obtained from the time-resolved infrared technique, could shed some light on monitoring the photopolymerization based AM process at molecular level and help establish some constitutive process models to predict the cured part's dimensions, mechanical and optical properties.

## **5.2 Overview of Metrology for ECPL**

In this chapter, with the interferometric curing monitoring (ICM) system initiated by former lab colleagues [17], the author developed a physics sensor model and online algorithms to address the compelling issues of real-time process monitor and measurement for the ECPL.

### **5.2.1 Need and Requirement for online Metrology**

Metrology is essential to the development and improvement of new processes and tools for future technology generations (Jakatdar, 2000) [19]. Metrology can potentially reduce the cost of manufacturing and time-to-market for new products through better characterization of process tools and processes. As device dimensions shrink, the challenge for physical metrology will be to keep pace with online testing that provides critical performance data. Manufacturing sub-micron devices will require the availability of robust in-situ equipment and online analysis tool, i.e. both hardware and software.

For the ECPL process, measurement would supply information on the current state of the plant. It forms the basis to control the process for optimal output. An indirect method to obtain a measure of cured height that is quick and inexpensive is the in-house designed interferometric curing monitoring (ICM) system. It must have adequate repeatability, reproducibility and calibration capability to provide the necessary real time information for fault detection and process control. This would need the development of increasingly faster data acquisition and computational algorithms for converting sensor data into useful information.

### **5.2.2 Offline Metrology for material properties and process characterization**

Besides online measurement, offline measurement is also critical to complement the system characterization. For the ECPL, as is also typical in industry polymerization reactor, it is still difficult to have online direct measurements of the cured polymer part

properties such as refractive index, molecular weight and composition, so the control design has to incorporate some available offline cured sample properties measured at the laboratory.

Refractive index is one of the most interesting properties measured offline to calibrate the online ICM&M measurement. Some typical metrology which could serve as offline characterization tools for the ECPL process were tried, including ellipsometer and reflectometry, which however were not able to detect signal from the ECPL cured sample and failed to obtain the desired solid cured part's refractive index. One possible reason is because the cured part was transparent and too thin (less than 100  $\mu\text{m}$ ). Perhaps in future, we could try some more advanced techniques for refractive index distribution over the cured part.

It is worthy to note another promising offline instrument, the Q-Sense E4 Quartz Crystal Microbalance with Dissipation (QCM-D), which is a four module instrument used to measure bulk-surface interactions for materials, chemistry, and life sciences research. A wide range of crystal surfaces are available for flexible immobilization of proteins, nucleotides, cells, and polymers. The provided modeling and analysis software enables quantification of viscosity, elasticity, and thickness of any soft film, while reaction kinetics can be extracted as well.

Many literatures report research findings and progress on photopolymerization process characterization and modeling with the QCM-D equipment. Duner, Thormann [51] followed the QCM response due to the in situ growth of a polymer layer on the sensor surface, and compared the measured response with predictions from one continuum viscoelastic model that describes the polymer layer response in terms of a spring and a dashpot coupled in parallel. Jeon, Schmidt [52] used QCM-D to measure polymer thickness (nanometer) over time and found linear growth of the living radical polymerization, ensuring the smooth, uniform films necessary for consistent laser ablation. The QCM-D measurement helped determine the chemical, physical, and optical

parameters necessary to pattern methacrylate-based polymer thin films at sub-diffraction resolutions, and helped provide precise control over the film thickness and uniformity, particularly important parameters for patterning nanoscale features [52].

We also tried to use the QCM-D sensor [53] to characterize the photo-polymerization process which is essential in the ECPL process by trying to measure the curing thickness and refractive index while the liquid material was photo cured into solid. Normally, QCM-D enables real-time, label free measurements of molecular adsorption and/or interactions on various surfaces. Unfortunately, we could not proceed with QCM-D to measure and model the photo-polymerization process in this study. The abnormality and failure was probably due to the ECPL material hardness, viscosity or weight or large cured thickness. Nevertheless, it is a good lesson that in future if we want to use ECPL machine to cure smaller (a few microns or sub micros) parts or if we use other materials for the ECPL process, it would be interesting to utilize the QCM-D for process characterization and modeling as described in the QCM-D application literatures [51, 52, 54], which may benefit the process control and applications as well.

In this study, ECPL cured product size is of top priority and the major control concern. After considering the candidates above, it turns out that one available and feasible offline metrology is the Olympus LEXT 3D Material Confocal Microscope which could measure film thickness and cured micro part profile. It is chosen as the offline calibration metrology for the online ICM&M measurements. We will use it to compare with the online measurement thereby calibrating the ICM&M measurement parameters specifically the refractive index.

## 5.3 ICM&M model

### 5.3.1 Phase extraction technique for ICM&M

The ICM&M system aims to utilize the principles of interferometry to measure the dimensions, particularly the height at the current research stage, of the part cured in the resin chamber. In future work, it could be extended to 2D and 3D measurement. The sequential acquisition of a large number of interferograms and their postprocessing facilitates the recovery of the phase distribution, so that the whole-field dynamic displacement field can be determined [42].

There are quite a lot of phase extraction techniques for interferometric fringe patterns and these are classified into three categories: phase shifting methods, transform-based methods, and others [55]. The phase-shifting techniques can be classified into temporal and spatial phase shifting. In the temporal phase shifting technique, at least three phase-shifted fringe patterns are collected. In order to keep the phase nearly unchanged during the phase shifting, a fast phase shifter and a high capturing rate are necessary. In the spatial phase-shifting techniques, several phase shifted fringe patterns are captured in one shot at different locations by either different cameras or on different areas of a camera. Transform-based techniques are the predominant phase extraction methods in the imaging-based IDM. These techniques include Fourier transform, Hilbert transform, windowed Fourier transform, wavelet transform, and a combination of Fourier and windowed Fourier transform. Like the phase-shifting techniques, the transform-based phase extraction methods can be applied in the spatial domain, temporal domain, or even spatial-temporal domain. The only requirement is that a carrier has to be introduced along one axis in the processing domain to avoid the phase ambiguity.

In a common interferometric dynamics measurement framework, reference-based or transform-based approaches could be used to retrieve optical phase distributions coded in the temporal intensity [36, 43, 44, 55]. However, the ICM&M system does not feature

the required frequency carriers in its hardware configuration, and cannot adopt the abovementioned phase-shifting or transform algorithms.

There exist phase extraction methods other than the two broad classes of phase-shifting and transform algorithms [55]. For example, Li, Soh [56] proposed two phase demodulation methods to measure the thin film large deflection - time sequence phase method and sequence pulse counting method. Although the methods are a variant of max-min or peak-valley scanning method similar to what has been used in the previous ICM system [20], they are more sophisticated and are able to process the interferograms sequence in decimal when the detected phase changes are smaller than  $\pi$ . Especially, compared with phase-shifting or transform methods, the temporal phase extraction algorithm of time sequence analysis is more simple but fairly efficient by retrieving the phase from the grayscales variation. However, the literature time sequence phase methods are still too rough for analysis of the relatively fast ECPL curing and we need investigate a more suitable and accurate phase extraction method for ICM&M.

Conclusively, since the ICM&M optical setup is simple and does not require phase shifting or carrier devices, a new generation of ICM&M measurement method can be achieved by developing a better time sequence analysis based phase detection method. A time sequence phase method is based on the point-wise comparison of the change of intensity in time domain to obtain the continuous phase map, which is then converted to determine the real displacement of the specimen tested [56]. It involves a segment of time when a number of frames are to be processed. Signal processing of the pixel intensity time series could recover the cured height, based on a well-established ICM&M model which consists of two sub-models. One sub-model is the sensor model of interference optics that explains the intensity dynamics in the interferogram sequence. The other sub-model is the calibration model that calculates the measured variable of cured height from ex-situ microscope measurement and estimated parameters in the sensor model.

### 5.3.2 ICM&M sensor model

For ICM&M, the sensor of camera records frames of the spatial interferogram produced by the optical path length differences of the light reflecting from the interface surfaces thru the resin chamber. A temporal intensity oscillation in the interferogram sequence is evident for pixels across the curing area, because the optical path length of the light reflecting from the top and bottom surfaces of the cured part changes with time as the photopolymerized resin cures in the chamber. The resultant temporal interference pattern presents a time series of intensity for each pixel across the chamber. The curing process causes the resin refractive index to change from  $n_l$  to  $n_s$  as it crosslinks from liquid into solid. Meanwhile, it changes the height of liquid resin and solid resin in the chamber. Both changes in medium refractive index and height lead to a change in optical path length thus in the interferogram phase.

#### 5.3.2.1 Multi-beam interference optics

Firstly, a prototype sensor model based on multiple beams interference optics is built for ICM&M. An example case of the interference of five optical waves is illustrated in Figure 14, where it is assumed that the waves interfere above any curing point in space after reflection and refraction in the resin chamber. It is noted that due to the special configuration of perpendicular incidence in ICM&M, the waves are assumed to be linearly polarized at the same plane and travelling in the vertical direction. Meanwhile, other possible beams are omitted because chances are these beams have been attenuated greatly and become insignificant after multiple reflections, scattering and absorption.

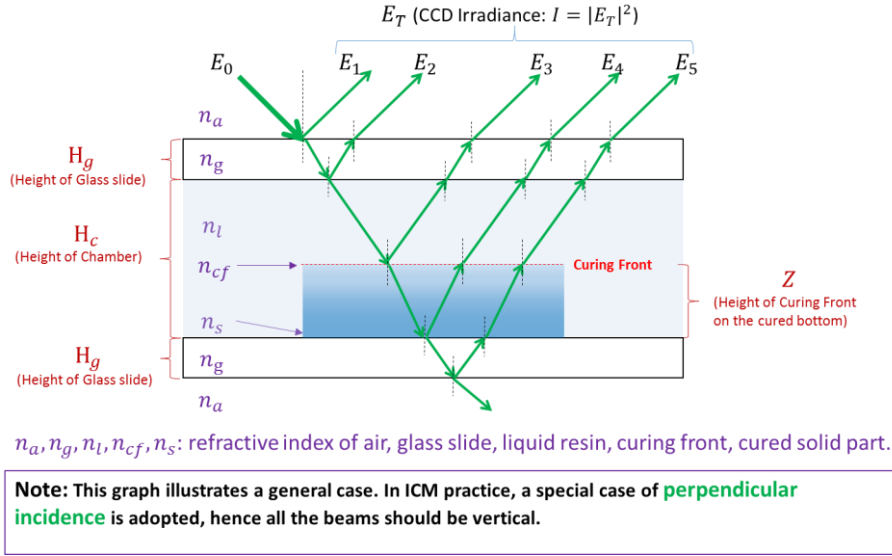


Figure 14. Multi-beam Interference Optics Model for ICM&M

Furthermore, a key simplifying factor in the analysis of the interference optics model in Figure 14 is the use of a virtual interface; that is, curing front to extract values of both the refractive index and growth rate of a film [57]. It has been shown that multiple-layer film is mathematically the same as a single layer on an “effective interface”, which is the case for compound semiconductor films where both chemical composition and growth rate need to be determined [57]. The concept of single virtual interface could also be applied in the ECPL resin curing process with the same assumption that each thin cured layer is homogeneous and isotropic with fixed refractive index and growth rate in the plane normal to the incidence direction.

The phenomenon of interference occurs when multiple waves overlap. In Figure 14, mathematically the vector addition of the wave components in Equation ( 7 ) results in a total wave of Equation ( 8 ).

$$E_n = A_n e^{i\phi_n}, n = 1, 2, \dots, 5 \quad (7)$$

where,  $A_n$  is the real positive amplitude,  $\phi_n$  is the wave phase angle.

$$E_T = \sum_{n=1}^5 E_n = \sum_{n=1}^5 A_n e^{i\phi_n} \quad (8)$$



In the interference field, each camera sensor pixel receives the coherent superposition of the multiple beams. When the field is observed by a CCD camera, the result is the average of the field energy by area unit during the integration time of the camera, that is, the irradiance  $I$  [58], which is proportional to the squared module of the amplitude as shown in Equation ( 9 ).

$$I = |E_T|^2 = \left| \sum_{n=1}^5 A_n e^{i\phi_n} \right|^2 = \sum_{n=1}^5 |A_n|^2 + 2 \sum_{j=1}^5 \sum_{\substack{k=1 \\ k \neq j}}^5 A_j A_k \cos(\delta_{jk}) \quad (9)$$

where,  $\delta_{jk} = \phi_j - \phi_k$ , is the relative phase difference between the component of each wave (for simplicity, the temporal and spatial dependencies have been omitted in the general expression here but will be taken into consideration in the analysis later).

The phase differences  $\delta_{jk}$  in Equation ( 9 ) are caused by optical path length differences between each set of two wave components. The stationary items such as  $\delta_{21}$  stem from beams such as  $E_1$  and  $E_2$ , which have constant path length difference - a product of the glass slide height and refractive index in the case of  $\delta_{21}$ . Hence, the term of  $\delta_{21}$  in Equation ( 9 ) will contribute to the average, i.e., DC (direct current), term in the detected intensity signal. Only the changing optical path length will contribute to the detected cycling of interferogram intensity. The oscillation, i.e., AC (alternative current), terms come from the beams  $E_3$ ,  $E_4$  and  $E_5$ , whose optical path are affected by the curing block in the chamber.

The ICM&M aims to measure the ECPL process dynamics, thus the oscillation of intensity signal is of interest. It is worth noting that the AC terms in the intensity signal convey information about the optical path length difference (OPLD) coupling both varying height and refractive index in the curing block. As noted in the virtual interface in the optics model, the curing front is an imaginary interface between the uncured liquid resin and curing part, which is defined as the whole curing block that might consist of intermediate phases between liquid and solid depending on the curing degree – portion of

cross linked monomers [59]. Thus the cured height is defined as the height of the curing front relative to the cured solid bottom. As shown in Equation ( 10 ), one can use the integral form of the cured height and refractive index to calculate the OPLD between the beams  $E_3$  and  $E_4$  thru the curing part with a curing front at height  $z$ . The vertical distribution of refractive index is assumed continuous as the curing proceeds, and thus according to the mean value theorem of integration, there exists an intermediate value  $n_m$  between  $n_s$  and  $n_{cf}$  such that the OPLD is a product of the height  $z$  and  $n_m$ .

$$OPLD_{E_4-E_3} = \int_0^z n(x)dx = n_m z, \quad (10)$$

where  $n(0) = n_s, n(z) = n_{cf}$

where,  $n_s$  and  $n_{cf}$  are the refractive indices of cured solid bottom and curing front respectively,  $n_m$  is the mean, i.e., effective refractive index of the curing part. All are assumed to be constant.

Theoretically, the ICM&M method is able to detect the product of cured/curing bulk height and refractive index. With a bulk effective refractive index being calibrated beforehand, the cured height could be estimated without involving the curing degrees in molecular reactions. This is a macroscopic measurement of part height (unit: microns). It does not utilize conventional concept in chemical engineering of curing degree to identify the specific cured part of certain crosslinking degree. The ICM&M is developed to focus on measuring the cured part at micro scale. Experiments will be performed to demonstrate its capability of measuring the height of cured part, or inferring where the liquid resin becomes solid without knowledge of curing degrees.

According to the model in Figure 14 and Equation. ( 9 ) - ( 10 ), the phase difference components are analyzed as shown in Table 5. The red items highlight time-varying items which induce the oscillations in intensity captured by the CCD camera in ICM&M.

Table 5. Phase component analysis of the ICM&M multi-beam interference optics model

No.	Phase Difference	Source Beams	Role
1	$\delta_{21} = \frac{4\pi}{\lambda} n_g H_g$	$E_1, E_2$	Constant DC term
2	$\delta_{31} = -\frac{4\pi}{\lambda} n_l Z + \frac{4\pi}{\lambda} n_l H_c + \delta_{21}$	$E_1, E_3$	Oscillating AC term
3	$\delta_{41} = \frac{4\pi}{\lambda} (n_m - n_l) Z + \frac{4\pi}{\lambda} n_l H_c + \delta_{21}$	$E_1, E_4$	Oscillating AC term
4	$\delta_{51} = \frac{4\pi}{\lambda} (n_m - n_l) Z + \frac{4\pi}{\lambda} n_l H_c + 2\delta_{21}$	$E_1, E_5$	Oscillating AC term
5	$\delta_{32} = -\frac{4\pi}{\lambda} n_l Z + \frac{4\pi}{\lambda} n_l H_c$	$E_2, E_3$	Oscillating AC term
6	$\delta_{42} = \frac{4\pi}{\lambda} (n_m - n_l) Z + \frac{4\pi}{\lambda} n_l H_c$	$E_2, E_4$	Oscillating AC term
7	$\delta_{52} = \frac{4\pi}{\lambda} (n_m - n_l) Z + \frac{4\pi}{\lambda} n_l H_c + \delta_{21}$	$E_2, E_5$	Oscillating AC term
8	$\delta_{43} = \frac{4\pi}{\lambda} n_m Z$	$E_3, E_4$	Oscillating AC term
9	$\delta_{53} = \frac{4\pi}{\lambda} n_m Z + \delta_{21}$	$E_3, E_5$	Oscillating AC term
10	$\delta_{54} = \frac{4\pi}{\lambda} n_g H_g = \delta_{21}$	$E_4, E_5$	Constant DC term

### 5.3.2.2 Instantaneous frequency analysis

The phase components listed in Table 5 reveal that the oscillating phases are all attributed to the cured height  $Z$ , the change rate of which is the curing velocity. Because the nonlinear ECPL process is known to exhibit non-constant curing velocity, the ICM&M signal in Equation ( 9 ) has frequency content that changes over time. The instantaneous frequency (IF) represents one of the most important parameters in the analysis of such signals with time-varying frequency [60]. Despite the possibility that light intensity and material properties (e.g.  $n_l, n_s, n_{cf}, n_m$ ) are subject to change with time during the process, for a short duration, these factors may be assumed to be constant. With the assumption that all the process parameters are momentarily invariant, the only varying factor is the cured height, and thus the IF, defined as the time differential of

phase, is only associated with the curing velocity  $\dot{Z}$ . As shown in Table 6, the IF components based on the phase components in Table 5 are analyzed.

Table 6. Instantaneous frequency of the multi-beam interference optics model in ICM&M

Instantaneous Frequency (Hz)	Corresponding Phase	Estimated Value (Hz)
$f_0 = 0$	$\delta_{21}, \delta_{54}$	0
$f_1 = \frac{2}{\lambda} n_l \dot{Z}$	$\delta_{31}, \delta_{32}$	31.5
$f_2 = \frac{2}{\lambda} n_m \dot{Z}$	$\delta_{43}, \delta_{53}$	32.1
$f = \frac{2(n_m - n_l) \cdot \dot{Z}}{\lambda}$	$\delta_{41}, \delta_{51}, \delta_{42}, \delta_{52},$	0.6

A rough estimation of the IF values is performed using the experimental data obtained by Jones, Jariwala [20], who cured a 51.5  $\mu\text{m}$  part in 9 seconds with the same material composition and exposure intensity. Hence, the average curing velocity  $\dot{Z}$  is about 5.7 ( $\mu\text{m/s}$ ). The interferograms intensity signal is about 0.6 Hz, which is obviously the lowest non-zero frequency component  $f$  in Table 6. Since the refractive index of resin  $n_l$  is 1.4723 [41], one could back-calculate  $(n_m - n_l) = 0.0279$  by plugging the average  $\dot{Z}$  of 5.7 into  $f = \frac{2(n_m - n_l)(5.7)}{0.532} = 0.6$  Hz. Hence, the mean effective refractive index  $n_m$  was estimated to be 1.5002. Furthermore, the other two frequency components could be estimated as below.

$$f_1 = \frac{2}{\lambda} n_l \dot{Z} \cong \frac{2}{0.532} (1.4732)(5.7) = 31.5 \text{ Hz}$$

$$f_2 = \frac{2}{\lambda} n_m \dot{Z} \cong \frac{2}{0.532} (1.5002)(5.7) = 32.1 \text{ Hz}$$

Exposure time and exposure intensity are the two main process parameters, and the frequency is mainly determined by exposure intensity. Intuitively, higher exposure intensity means a faster curing process and, larger instantaneous frequency. Please note that the 9s curing process under normal exposure intensity (UV iris level at 22% in this study) was presented to estimate roughly the magnitude of the frequencies, especially to

disclose that low frequency item dominates the signal, in order to come up with a sensor model in the subsequent section. The IF values in Table 6 are subject to change with the actual exposure parameters, but found to show similar phenomenon as analyzed below.

The IF analysis above concludes that three non-zero instantaneous frequencies exist in the ICM&M intensity signal. However, the actually observed ICM&M intensity signal frequency is low about 0.6 Hz. Two possible reasons could explain that only the low frequency component  $f$  is detected in the captured signal. Firstly,  $f_1$  and  $f_2$  are about 30Hz and cannot be detected by the CCD camera with a sampling frequency of 30Hz, which could detect up to 15 Hz signal according to the Nyquist theorem. Secondly, both  $f_1$  and  $f_2$  involve the beam wave  $E_3$ , which is modeled to reflect from the vague virtual curing front that has a refractive index close to the liquid resin and thus has very small amplitude due to a weak reflectivity.

Even if the high-frequency items of  $f_1$  and  $f_2$  could be detected with high-speed camera, since they have similar values, it requires computation effort to distinguish one from the other in the signal. From the viewpoint of practicability, the high frequency items are not easily observable and worse still could only provide redundant information about  $\dot{Z}$ . The primary goal of the sensor is to measure the curing velocity and thereby height. In sharp contrast to  $f_1$  and  $f_2$ , the low frequency component  $f$  has been shown to be able to provide vivid signal pattern which could form an adequate sensor model about  $\dot{Z}$ .

The presence of  $f_1$  and  $f_2$  could add up to the amplitude of  $f$  signal, but would not affect its phase angle - the real thing that matters in the target measurand. Besides, a filter will be used to reduce the amplitude effects of high frequency oscillation including  $f_1$ ,  $f_2$  and noise. In that regard, it is assumed in the sensor model that the potential error caused by  $f_1$  and  $f_2$  is negligible.

Furthermore, to validate the abovementioned assumption that high-instantaneous-frequency interference beams are truly negligible, reflectance is estimated as shown in Figure 15.

Assuming lossless dielectric media, the intensity of the incident beam is divided into reflected and transmitted parts [61]. In this rough estimation, nominal values are used for the quantities listed in Figure 14, specifically,  $n_a = 1$ ,  $n_g = 1.52$ ,  $n_l = 1.4723$ ,  $n_m = 1.4945$ ,  $H_g = 200 \mu m$ , and for a cured part of 50 microns high,  $Z = 50 \mu m$  and  $H_c = 150 \mu m$ . Given an incident beam ( $E_0$ ), part of it gets reflected by the top and bottom surfaces of the glass lid, and the other part transmitted into the layer of liquid resin can get reflected by the top and bottom (i.e., curing front) surfaces of the liquid layer and transmitted upward thru the glass lid to the interference field (e.g., camera). Similarly, further transmission - reflections - transmissions happen in the layers of cured part and glass substrate. Fresnel equations are used to compute the reflectivity at each interface, and thereby reflectance is calculated for each layer of thin film [61]. Please note that, the reflectance means the ratio of the reflected intensity back from the entire chamber to the original incident intensity, and the reflected intensity includes all the reflections and transmissions along the pathway from original incidence to the layer then upward to above the glass lid.

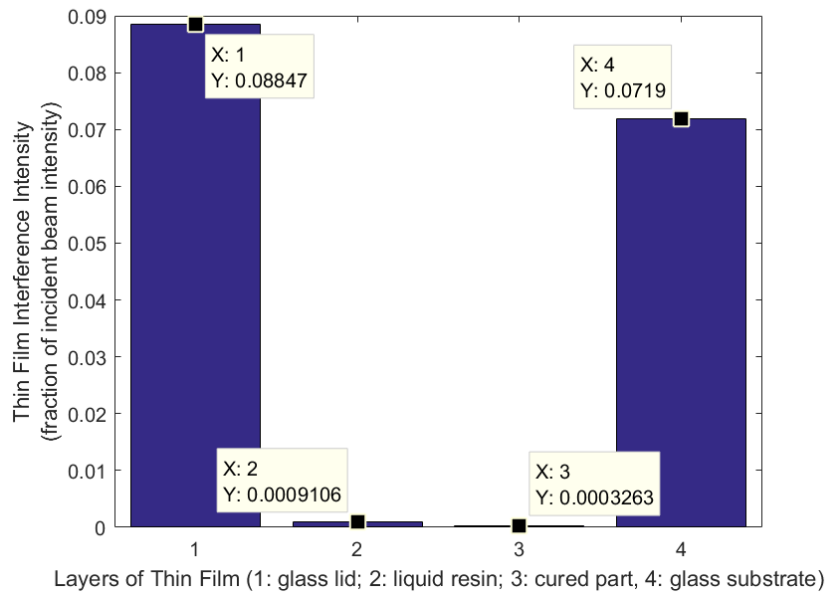


Figure 15. Multi-layer thin film reflectance in the ICM&M sensor model

As a result, a total of about 16.16% of original incident beam ( $E_0$ ) intensity is reflected upward to the top area (above the glass lid) forming multi-beam interferences that are then captured by the camera, while the other part (83.84% of irradiance) is transmitted downward thru the resin chamber to the air beneath the substrate. Only a tiny fraction of incident intensity is found to be reflected by the internal chamber. Clearly, 0.091% and 0.033% of  $E_0$  intensity are reflected by the liquid resin layer and the cured part layer, respectively, in sharp contrasts with that 8.847% and 7.19% are from the glass lid and substrate, respectively. The low quantitative value of reflectance from liquid and cured resins provide a convincing evidence that the amplitude (square root of intensity) of beam wave  $E_3$  is very small and therefore its resultant high-frequency modes  $f_1$  and  $f_2$  are really negligible.

### 5.3.2.3 Established ICM&M sensor model

As a summary, the ICM&M directly-measured intensity  $I_M$  is modeled as a sum of the reference and all the low instantaneous frequency  $f$  components in the multi-beam interference optics model. Note that all the cosine terms with frequency  $f$  but different amplitudes and phase offset can add up to a single cosine wave, which still preserves the same frequency but possesses different phase offset and amplitude. The multi-beam interference optics model in Equation ( 9 ) ends up with a lumped single-frequency cosine formula, which resembles what has been observed from the ICM&M interferogram signal.

As shown in Equation ( 11 ), an implicit model interprets the observed interferogram intensity ( $I_M$ ) in terms of the cured height ( $Z$ ), refractive indices ( $n_m, n_l$ ), amplitudes ( $I_0, I_1$ ) and phase offset  $\varphi$ , all of which are unknown and dynamically changing.; hence the cured height  $Z$  is unsolvable by a single observation of intensity at one time point. However, the time derivative of the phase component in Equation ( 11 ), termed as instantaneous angular frequency, essentially corresponds to the curing velocity

– the temporal derivative the cured height, i.e.,  $\dot{Z}$ , and can help derive a further implicit sensor model as shown in Equation ( 12 ).

The implicit ICM&M sensor model is derived as shown in Equation ( 11 ) and ( 12 ).

$$I_M = I_0 + I_1 \cos(\delta + \varphi) = I_0 + I_1 \cos\left(\frac{4\pi(n_m - n_l)}{\lambda} \cdot Z + \varphi\right) \quad (11)$$

$$\omega = 2\pi f = \frac{d(\delta + \varphi)}{dt} = \frac{d\delta}{dt} = \frac{4\pi(n_m - n_l)}{\lambda} \cdot \frac{dZ}{dt} + \frac{4\pi Z}{\lambda} \cdot \frac{d(n_m)}{dt} \quad (12)$$

$$\cong \frac{4\pi(n_m - n_l)}{\lambda} \cdot \frac{dZ}{dt}$$

where,  $I_M$  is the directly measured intensity by CCD camera;  $I_0$  is the overall average intensity;  $I_1$  is the superposed intensity of all the interference beams with the same instantaneous frequency  $f$ ;  $\delta$  is the time-varying phase component in the intensity model;  $\varphi$  is the static superposed phase offset of all the interference beams with the same frequency;  $f$ ,  $\omega$  are the instantaneous frequency and instantaneous angular frequency, respectively;  $\lambda$  is the laser wavelength  $0.532\mu\text{m}$ ,  $n_m$  and  $n_l$  are mean cured and liquid part refractive index.

With the implicit ICM&M sensor model that illustrates the intensity signal, we desire to further infer the measurand – cured height from it. Hence, an explicit sensor model for ICM&M is required to calculate the cured height from the estimated parameters of instantaneous frequency in the model along with the calibrated parameters of refractive index in the ex-situ measurements.

By rewriting Equation ( 12 ), a differential form of the cured height is derived in Equation ( 13 ). The model of curing rate incorporates both the nonlinearity in the numerator part of instantaneous frequency, and nonlinearity due to the potential changes in refractive index. In future work, the nonlinearity of cured rated due to the refractive index changes will be investigated.



$$\frac{dZ}{dt} = \frac{\omega\lambda}{4\pi(n_m - n_l)} = \frac{f\lambda}{2(n_m - n_l)} \quad (13)$$

To evaluate the cured height from the differential form in Equation ( 13 ), a numerical integration approach using Euler's Method is proposed as below in Equation ( 14 ), which forms the final ICM&M sensor model. The one-step method is used for computation efficiency. Potential error due to the first-order integration would be elaborated in subsequent experiment analysis and shown to be at an insignificant submicron level.

$$Z = \frac{\lambda}{4\pi(n_m - n_l)} \sum_i T_i \omega_i = \frac{\lambda}{2(n_m - n_l)} \sum_i T_i f_i \quad (14)$$

where  $T_i$  is the time step of integration,  $f_i$  (or  $\omega_i$ ) is the instantaneous (angular) frequency in the  $i^{\text{th}}$  run of parameter estimation. The refractive index difference term  $\Delta n = (n_m - n_l)$  requires calibration with ex-situ microscope measurements of cured height. It is noted that the cumulative sum term  $\sum_i T_i \omega_i$  is essentially the total phase angle that has changed during the curing process; and so is  $\sum_i T_i f_i$  but has a unit referred as cycle (one cycle is  $2\pi$  rad).

As a result, Equation ( 13 ) is an explicit ICM&M sensor model in derivative form for curing velocity, and Equation ( 14 ) is an explicit ICM&M sensor model in integral form for cured height.

### 5.3.3 ICM&M Calibration Model

Fundamentally, metrology calibration is required to maintain the quality of measurement as well as to ensure the proper working of the instrument. As shown in the ICM&M sensor model, one primary uncertainty is the difference  $\Delta n$  between the refractive index of the effective solid resin  $n_m$  and that of the liquid resin  $n_l$ , which provides the instrument design capacity for holding a calibration. Having a design with these characteristics increases the likelihood of the actual measuring instruments performing as expected. Specifically, in the ICM&M sensor model, Equations ( 13 ) and (

14 ), the difference between refractive indexes  $n_m$  and  $n_l$ , assumed to be natural physical constants, is unknown and should be quantified with known standard metrology. In this study, the Olympus LEXT OLS4000 3D material confocal microscope [62] is used as a scientifically sound measurement apparatus to transfer the primary standard value of sample heights profile to the ICM&M measured object – ECPL cured part heights profile.

With such measurement assurance methodology by comparing the in-house ICM&M to the commercial microscope, a calibration process for cured height is achieved by solving the unknown or uncertain refractive index difference term  $\Delta n$  in a test measurement, which can be used in subsequent measurements for cured heights. The equation for deriving refractive index difference  $\Delta n$  in the calibration process is referred as the calibration model. By inverting the ICM&M sensor model in Equations ( 14 ), the calibration model is available as shown in Equation ( 15 ).

$$\Delta n = n_m - n_l = \frac{\lambda \sum_i(T_i \omega_i)}{4\pi Z} = \frac{\lambda \sum_i(T_i f_i)}{2Z} \quad ( 15 )$$

To implement the measurement and control in 3D printing practice with the ECPL system, the ICM&M calibration procedure should be performed beforehand. The ICM&M calibration process is introduced as the following steps.

1. Firstly, cure a test sample with the in-situ ICM&M system recording the interferograms video simultaneously.
2. Secondly, measure the test sample with the ex-situ confocal microscope and obtain the cured height  $Z$  as a reference standard.
3. Thirdly, estimate the instantaneous frequencies and thus the total phase angle  $\sum_i(T_i \omega_i)$  by analysing the process video with the ICM&M algorithm as presented in the following section.
4. Finally, compute the refractive index term  $\Delta n$  by substituting the previous results of  $Z$  and  $\sum_i(T_i \omega_i)$  to the calibration model in Equation ( 15 ).

During ECPL curing, to compute cured height, the ICM&M estimated parameters should be plugged into the sensor model in Equation ( 14 ), along with  $\Delta n$  derived in the calibration process.

Refractive index is subject to change with photopolymerization process dynamics (e.g. crosslinking degree and density), as well as with environment conditions variations (e.g. temperature and oxygen diffusion). Regardless of the underlying causes, it is surely important to consider about the changes in refractive index into the sensor model. By calibration against the microscope measurement, the derived refractive index is supposed to incorporate the in-process variations and can provide an effective group refractive index for succeeding measurements using the ICM&M method. The calibrated refractive index could work best for ECPL processes under similar settings to the calibration conditions, which makes sense in minimizing the effects of refractive index changes. Generally, the calibration should be performed for every new batch of photopolymer resin, and whenever necessary as the material refractive index tends to vary under different process conditions including exposure time and intensity.

#### **5.4 Parameter estimation for ICM&M model**

In the ICM&M model, the cured height of a voxel is coded in the temporal intensity dynamics observed in the corresponding camera pixel. It is discovered that adjacent voxels, which are expected to have close if not identical cured heights, share similar phase angles across the curing area. Hence, Fourier analysis along the time-axis is one candidate method to evaluate the phase map [36], but the Fourier transform based analysis is efficient only when the frequency content of the analyzed signal does not change over time. In the ICM&M application, one deal with signals where the cured height information is conveyed within time-variations of the signal's instantaneous frequency that corresponds to the curing velocity. Hence, a method of time-frequency

analysis [60] is needed to solve the ICM&M model, which requires estimation of the unknown parameter of instantaneous frequency  $f$  or  $\omega$  to calculate the cured height.

#### 5.4.1 Curve Fitting with One-term Fourier Model

A curve fitting method is adopted to minimize the square errors between the sensor model prediction and measurement. Because there is only one outstanding frequency in the ICM&M sensor model, the method of 'fourier1' - a Fourier series model with only one frequency item as shown in Equation ( 16 ), is used in the curve fitting to estimate the instantaneous frequency locally.

$$y = f(t) = a_0 + a_1 \cdot \cos(\omega t) + b_1 \cdot \sin(\omega t) \quad (16)$$

It could be written into the trigonometric form as shown in Equation ( 17 ).

$$y = f(t) = a_0 + \sqrt{a_1^2 + b_1^2} \cdot \cos(\omega t + \theta), \quad (17)$$

$$\text{where } \theta = \tan^{-1}\left(-\frac{b_1}{a_1}\right)$$

The one-term Fourier model in Equation ( 17 ), can be mapped to the ICM&M sensor model, and used to estimate the instantaneous angular frequency  $\omega$ .

#### 5.4.2 Online Parameters Estimation

##### 5.4.2.1 Estimation method of moving horizon exponentially weighted fitting: rolling fit

The conventional least squares method that assumes constant parameters over the entire curing period may not work in this case [63], because the assumption of static parameters is only valid in a short time. During the entire curing period, the growth velocity of the cured part tends to change with the temperature, composition, and microstructure. An in situ sensor must be able to deal with a time-varying process if feedback control is to be used. In on-line parameter estimation, a model is fitted optimally to the past and present process measurements while the process is in operation [64]. For the ICM&M application, parameter estimation via on-line optimization can be

performed by solving online a minimization problem such as sum of squared errors in the abovementioned ‘Fourier 1’ curve fitting. This parameter estimator can have an increasing (with time) or constant horizon. An estimator with an increasing horizon has been referred to as batch estimator and one with constant horizon as moving horizon estimator. A solution to the ICM&M model with varying instantaneous frequency is to fit the parameters over a short window of data, i.e., a moving horizon.

Exponential weighting is typically used in a recursive update procedure for parameter estimation. Figure 16 compares curve fitting without and with weights. The top graph displays an unweighted fitting which fits a much shorter length of latest data and could not estimate the current frequency as well as the weighted fitting did in the bottom graph. This demonstrates the necessity of applying exponential weights to fit the Fourier model for the most recent set of data, which is critical in estimating the latest instantaneous frequency.

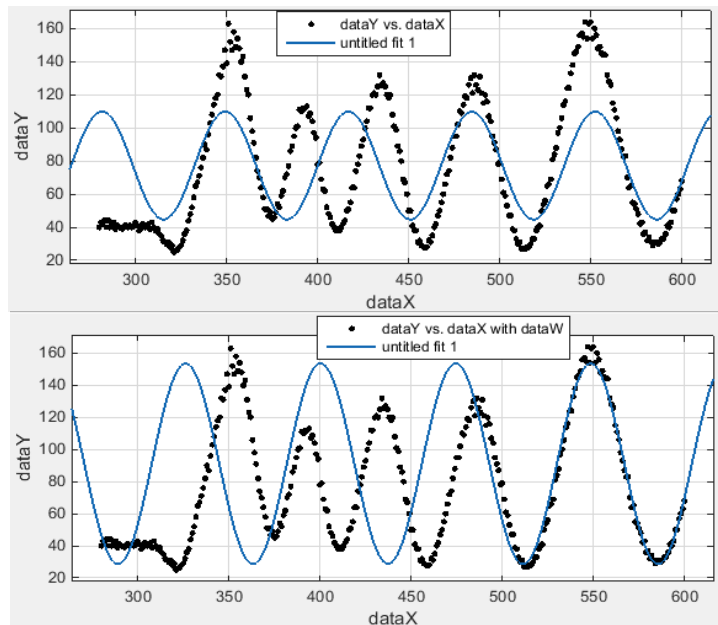


Figure 16. The need for exponentially weighted curve fitting to improve the curve fitting for most recent data (Top: unweighted fitting; Bottom: exponential weighted fitting)

Conclusively, a windowed exponentially weighted curve fitting with moving horizon, is developed for ICM&M parameter estimation. With the one-term Fourier model in Equation ( 17 ), and given a sequence of measurements in a window size  $m$

starting from  $j - m + 1$  up to  $j$  along with exponential decay half life, the parameters in this window can be estimated by solving the following minimization problem in Equation ( 18 ). Note that “half life” means the width decaying weight to one half, and it is related to the exponential decay constant  $\tau$  by a factor of  $\ln(2)$ .

$$\min \sum_{l=j-m+1}^j e^{-\frac{j-l}{\tau}} (y_{l_{meas}} - y_{l_{fitted}})^2 \quad (18)$$

where  $\tau = half\_life / \ln(2)$ , and  $y_{l_{meas}}, y_{l_{fitted}}$  is the  $l^{th}$  measured and fitted data respectively in the curve fitting with one-term Fourier model.

When new measurement data are acquired, the window is shifted to include these new data and at the same time part of the old data is discarded using a suitable forgetting factor – exponential weights in this case. The training data set is used to estimate the sensor model parameters, and succeeding (or test set) data are used to validate the accuracy of the parameters. In other words, the estimated parameters in the current run of rolling fit are applied to a rolling prediction for upcoming measurement data, in order to verify the estimation accuracy and prediction capability, which is critical for real-time measurement and control.

#### 5.4.2.2 Estimation Performance Evaluation: Goodness of Fit

After fitting data with the ICM&M model online, we should evaluate the goodness of fit. As is common in statistical literature, the term goodness of fit (GOF) could be used here in the following sense to assess the online parameter estimation. A "good fit" means the above-proposed ICM&M model and parameter estimator could reasonably, given the assumptions of least-squares fitting, explain a high proportion of the variability in the interferograms sequence of grayscale data, and is able to predict new observations with high certainty.

MATLAB Curve Fitting Toolbox™ software supports the goodness-of-fit statistics for the parametric model [65].

R-square is defined as the ratio of the sum of squares of the regression (SSR) and the total sum of squares (SST). SSR and SST are defined as in Equation ( 19 ). Please note that SST is actually the sum of SSR and SSE (sum of squared errors). Given these definitions, R-square is expressed as in Equation ( 19 ).

$$R - square = \frac{SSR}{SST} = \frac{\sum_{i=1}^n w_i (\hat{y}_i - \bar{y})^2}{\sum_{i=1}^n w_i (y_i - \bar{y})^2} \quad (19)$$

where, n is the number of datapoints,  $w_i$  is the weight of the  $i^{\text{th}}$  data  $y_i$ ,  $\hat{y}_i$  is the  $i^{\text{th}}$  estimated value by regression, and  $\bar{y}$  is the average of all datapoints.

R-square can take on any value between 0 and 1, with a value closer to 1 indicating that a greater proportion of variance is accounted for by the model. For example, an R-square value of 0.85 means that the fit explains 85% of the total variation in the data about the average.

We use R-square defined as above to examine the ICM&M model estimation accuracy. The higher R-square in a run of curve fitting, the more confident we are at the estimated model parameters. Obviously, R-square of 0.9 is a good fit, while 0.1 is a bad fit. However, in-between it is hard to gauge a watershed value of R-square to distinguish a good fit and a bad fit.

On one hand, one could always adjust the watershed value to guard a fitting pass or failure, and to meet the experimental result. In practical sense, an R-square of 0.8 or so could suggest that the estimated parameters in the ICM&M model is acceptable.

On the other hand, R-square is affected by multiple factors such as data length and weights; hence one can increase R-square by changing these factors to get a better fitting result.

#### 5.4.2.3 Another method of estimation performance evaluation: rolling prediction

Besides the R-square for goodness of fit, to verify the online estimation accuracy and prediction capability, which is critical for real-time control, another method is to perform rolling prediction. In such a validation procedure, the training data set, i.e., the

windowed data by moving horizon in a run of rolling fit, is used to estimate the sensor model parameters; and the test data set, i.e., measurement data in the succeeding run, could be used to validate the accuracy of the estimated parameters. The prediction is based on an existing fit to the data. Specifically, one can use the estimated parameters in the current run of rolling fit to predict the upcoming measurement data in next run, and then compare the predicted data set with the test data set by metrics of the mean square errors (MSE). Thereby, a rolling fit is accompanied and validated with a rolling prediction while acquiring a real-time video online or replaying an acquired video offline. Please note that the estimated parameters for an offline video should be the same as the online estimated parameters for a real-time video, because the same ICM&M model and algorithms as previously presented are employed in an identical way. The less rolling prediction MSE is, the more accurate the parameters estimation is.

One assumption behind the validation method with rolling prediction MSE is that the process remains fairly constant in the two consecutive runs, that is, the parameters in this time segment won't change too much in the next run of fitting. It holds when the duration of each run is sufficiently short so that the process could be regarded as constant for a brief instant. In practice, the time interval of each run may be fairly long, e.g. hundreds of milliseconds, limited by the hardware speed; hence the rolling prediction MSE may not be a valuable or valid metrics for estimation performance in the nonlinear and varying ECPL process.

Nevertheless, given fast enough rolling, the rolling prediction provides a fair evaluation of the estimated parameters during the ECPL curing process and could help predictive process control. The rolling prediction MSE is supposed to spike when the process transitions to dark curing. Large rolling prediction MSE at this transition time doesn't necessarily mean that the previous estimation fails; instead it might serve as a flag for the process transition.



Please note that in this study for metrology, the ICM&M method adopts R-square (Equation ( 19 ) in Section 5.4.2.2) as a criterion for goodness of fit in the curve fitting algorithm both online and offline. The rolling prediction introduced in this section, could be employed as a predictive model for real-time control but not real-time measurement. It is only suitable for offline evaluation but not feasible for real-time measurement as it requires information from future data.

### **5.5 Summary of the developed ICM&M sensor method**

As a summary, the ICM&M sensor should sense the local change in the interference pattern, estimate the instantaneous frequency of the interference pattern, and estimate the resulting change in part cure height. This procedure needs to be repeated for each subsequent time period as the part is being fabricated. When part fabrication is completed, an estimate of total cured part height and total interferogram phase angle are produced.

The relationships among the CCD camera sensor, the interferograms sequence, the ICM&M model and algorithms presented in Sections 4.2 and 4.3, are shown in Figure 17. As stated, the ICM&M model includes a sensor model and calibration model, which provide formulated problems for the parameter estimation and cured height algorithms to solve. The algorithm of parameter estimation by moving horizon exponentially weighted “Fourier1” curve fitting is developed to estimate the instantaneous frequency  $f$  in the sensor model. Note that all the blue symbols in Figure 17 denote frequency items and conversions between the model and algorithms. The calibration model will be used to estimate the key index of refraction difference between solid and liquid resin off-line, then used to compute cured height during on-line operation. The overall scheme of the developed ICM&M measurement method with evolutionary estimation and incremental accumulation enables a promising real-time implementation.

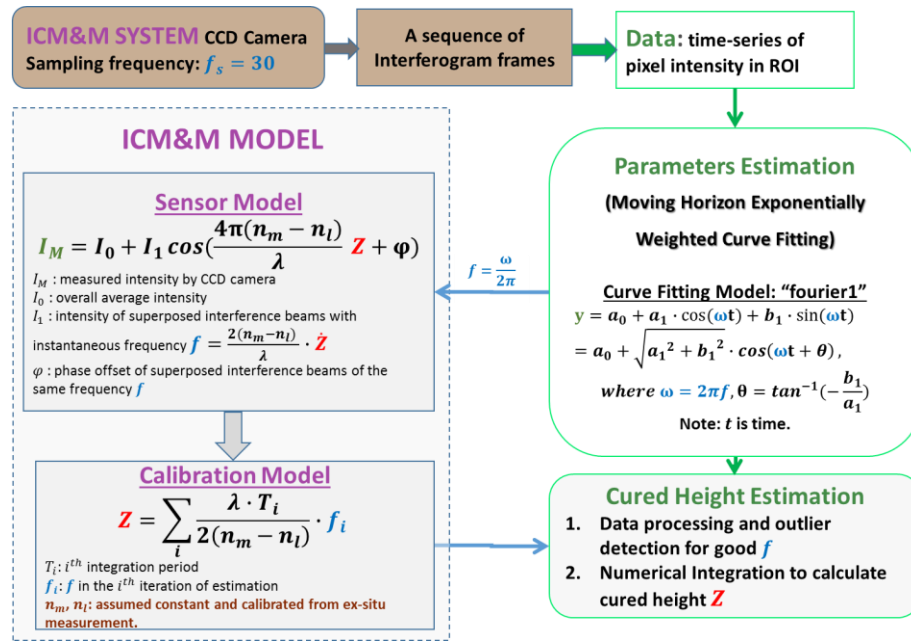


Figure 17. Scheme of ICM&M measurement method: models and algorithms

## 5.6 Initial experimental validation for the ICM&M method

To study the feasibility of the ICM&M method above, we initially validate it through an offline approach – the offline ICM&M, which applies the measurement method onto a video of interferograms recorded by the camera with an acquisition speed of 30 frames per second during the curing experiment. Please note that in the offline ICM&M, the videos are always acquired in real-time, and only the measurements are done off line in order not to demand sophisticated computing power. Implementing the ICM&M method in offline mode is actually a simulated real-time process measurement as the measurement analysis is conducted while playing a video which exactly displays the curing process monitored by the in-situ ICM&M system.

In this preliminary validation experiment, a new batch of photopolymer resin was made and calibrated first, followed by a sequence of validation experiments curing square blocks of different widths. For best ICM&M performance, it is recommended that the calibration conditions, especially the exposure time and intensity, should be the same as will be used in the to-be-measured process conditions. Both calibration and validation experiments in the section of work adopted a normal exposure intensity at UV lamp iris

level 22% and exposure time 12 seconds. The cured parts heights were measured by both the proposed offline ICM&M method and a confocal microscope, which comparison demonstrates the qualification of the ICM&M method as an offline and real-time metrology for the ECPL printed 3D parts.

### 5.6.1 Calibration in test measurement

For the calibration, a square block part was cured by the ECPL system. A 200×200 pixels square bitmap as shown in Figure 18 was displayed on DMD for 12 seconds while the UV lamp (OmniCure® S2000) was on with the lamp iris level being 22%. The ICM&M camera captured the video of interferograms. In Figure 19, A line of 120 pixels in the interferograms was selected for ICM&M analysis, and the pixel info at the bottom of the figure shows that the rightmost pixel of the line is (365, 220) - pixel width being 365 and height 220 in the interferogram. The cured part is supposed to have a uniform heights profile due to ideally uniform UV light intensity and material properties across the curing area; hence the adjacent pixels are supposed to have very similar if not identical changed phase angles during the curing process. It is found that to evaluate the line profile of heights, measuring heights for pixels in the line at an interval of five pixels would not affect the accuracy significantly but requires much less computation expense than measuring every pixel for the whole line. In this particular case, the ICM&M method was applied to a horizontal line of 25 pixels starting from Pixel (245, 220) to Pixel (365, 220) with 5 pixels between each two neighbouring measured pixels; and the measured horizontal pixels line is denoted as Pixels (245:5:365, 220). The ICM&M model and algorithm estimated the total phase angle,  $\sum_i(T_i f_i)$  in Equation ( 15 ), for each measured pixel; and the average total phase angle is 6.175 cycles (i.e.,  $6.175 \times 2\pi$  rad) as shown in Figure 20. Figure 21 presents the line profile measured by the laser confocal microscope and the average height was 73.866  $\mu\text{m}$ , which substitutes  $Z$  in Equation ( 15 ). The calibration process is completed by solving the calibration model of

Equation ( 15 ) for  $\Delta n = n_m - n_l = \frac{\lambda \sum_i (T_i f_i)}{2Z} = \frac{(0.532)(6.175)}{2(73.866)} = 0.022237$ , which value will be used in the following experiments to calculate some example parts heights to validate the ICM&M measurement capability and accuracy.

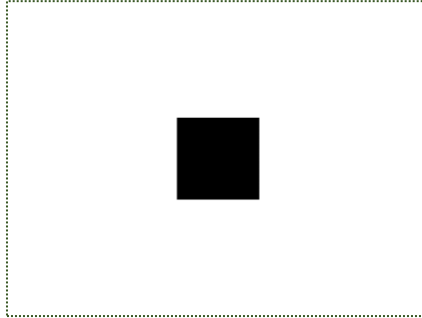


Figure 18. Initial ICM&M validation (calibration part): the DMD bitmap pattern for curing a square part with the ECPL process (Note: the dashed outline indicates the edge of the DMD which consists of 1024×768 micromirrors).

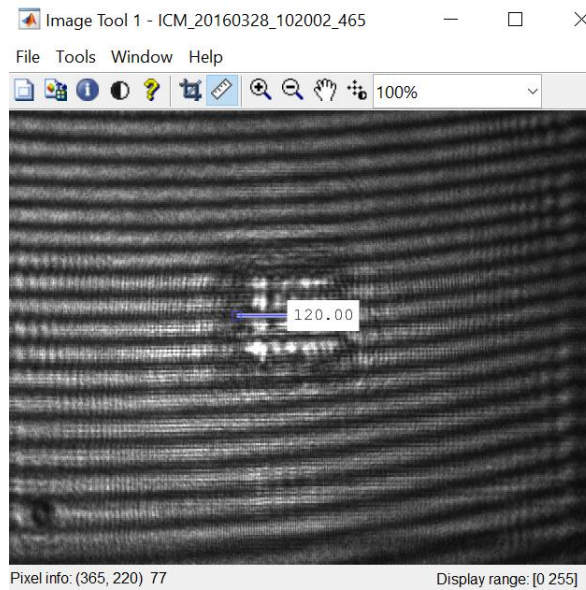


Figure 19. Initial ICM&M validation (calibration part): select a line in the acquired video of interferograms to measure the cured part heights with the ICM&M method.

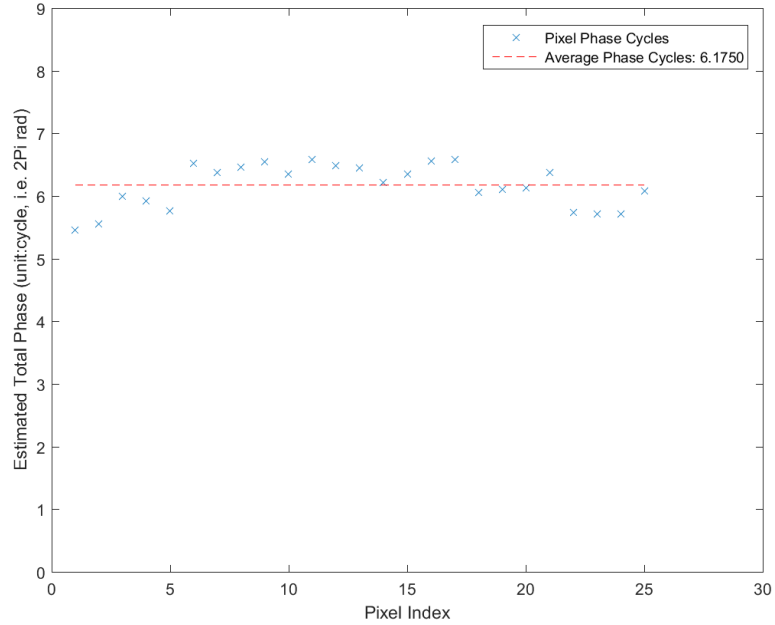


Figure 20. Initial ICM&M validation (calibration part): estimate the individual and average total phase angles for 25 pixels from Pixel (245, 220) to (365, 220) at an interval of five pixels in the selected horizontal line.

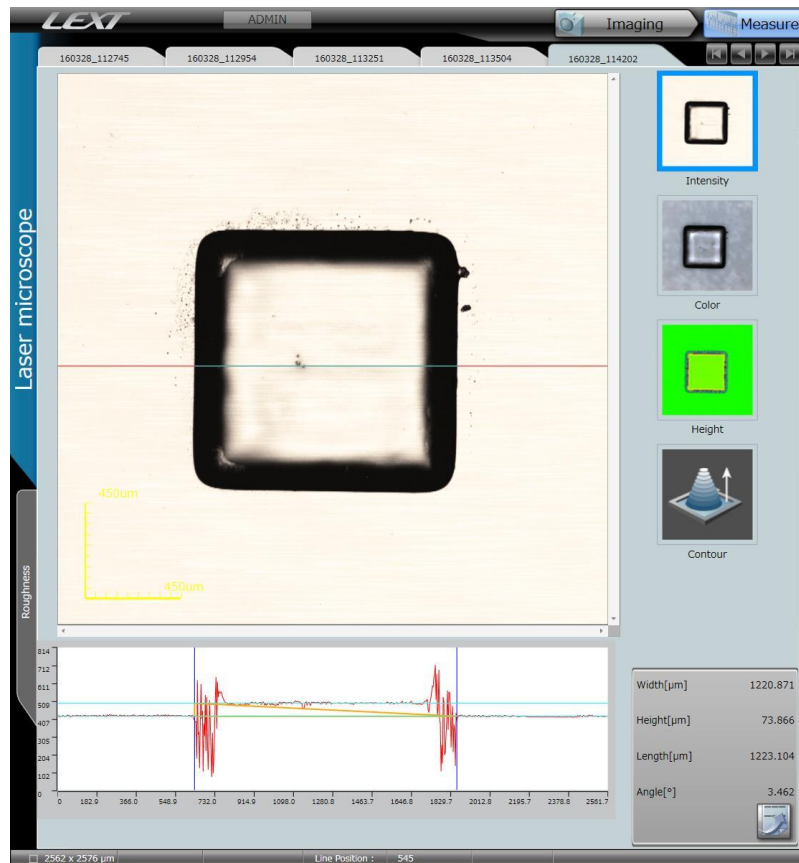


Figure 21. Initial ICM&M validation (calibration part): measure the sample line profile with the Olympus 3D confocal microscope.

### 5.6.2 Validation Experiment

After the calibration which results in a known refractive indexes difference  $\Delta n = n_m - n_l = 0.022237$ , the same batch of resin material was used in the following experiment to validate the ICM&M model and algorithms in previous sections. In the validation experiments, we cured two square blocks of different widths by changing the DMD bitmap size to  $150 \times 150$  pixels and  $50 \times 50$  pixels in two experiments, respectively, while all the other conditions were kept the same, that is, all the parts were cured under UV exposure for 12 seconds with the same UV lamp (OmniCure® S2000) iris level as in the calibration process. The purposes of the two experiments are: (1) to validate that the above-described ICM&M model and algorithms can successfully measure the height of ECPL fabricated part with accuracy; (2) to demonstrate that the measurement technology is repeatable and versatile in measuring parts of a range of lateral sizes; (3) to verify that ICM&M measurement is consistent and precise in universal measurement for heights all over a part, particularly by the second experiment measuring both lateral and vertical profiles; (4) as a by-product to show the potentiality of the ECPL process for applications in manufacturing micro parts.

Figure 22 shows the DMD masks used in the the two experiments - Experiment #1 and #2.

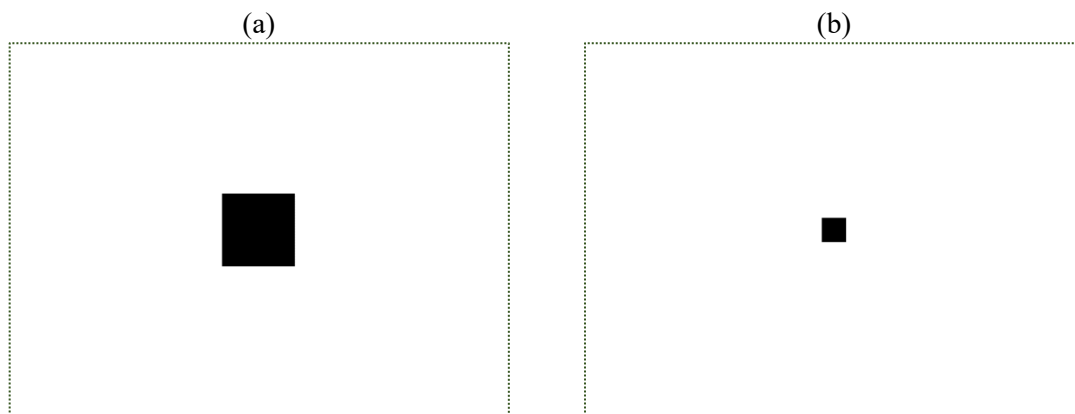


Figure 22. Initial ICM&M validation: DMD exposure pattern in (a) Experiment #1:  $150 \times 150$  pixels square bitmap; (b) Experiment #2:  $50 \times 50$  pixels square bitmap.

To apply the ICM&M method in an off line mode, we replayed the curing process video, and in the last frame of the interferogram that presents a better shape of the cured part we selected a line of pixels as the region of interest (ROI) to measure. Since the cured parts analysed in this study are cuboid, theoretically it should not matter much which line to choose for measuring the height; however considering the not-perfectly-uniform UV irradiation in the ECPL system, and also for easy visual match with the microscope measurement in later comparison of results, it is recommended to choose lines in the central cured area. Figure 23 displays the lines of ROI for measurement in the experiments, and the information at the bottom provides the pixel coordinates of (Width, Height) for one end pixel in the selected line; e.g., Pixel (356, 230) denotes the right end pixel at width of 356 and height 230 in the interferogram. As noted in Figure 23, the interferogram of Experiment #1 shows a clear square shape corresponding to the desired square block, while that of Experiment #2 displays a tiny area which resembles a circle instead of a square. The number on the line, i.e., “106” in Figure 23(a) and “41.05” in Figure 23(b), indicates the lengths in pixels of the selected line. As in the calibration process, for each line only these pixels at an interval of every five pixels are measured to save computation time at little expense of accuracy. Hence, the measured pixels, in the selected horizontal lines in figure 23, are actually pixels (250:5:355, 230) in Experiment #1, denoting the pixels located at the width ranging from 250 to 355 at an interval of 5 and at height of 230, and in Experiment #2, the pixels are given as (265:5:305, 225).

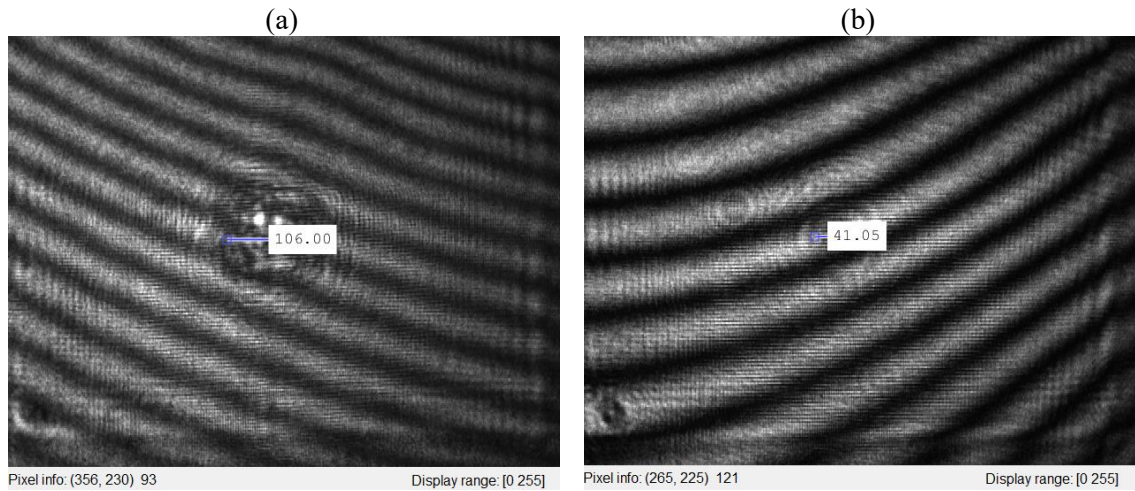


Figure 23. Initial ICM&M validation: selected line of horizontal pixels to measure with ICM&M in (a) Experiment #1; (b) Experiment #2.

After setting the measured object (pixels in the ROI), we simulated the real-time ICM&M metrology by replaying the video and extracting the time series of grayscales for all the measured pixels in the same time, thereby immediately estimating the instantaneous frequency and summing up the total changed phase leading to the final computing of the cured heights as per the algorithms presented in Section 5.4.2.1. To illustrate the process of implementing ICM&M algorithms, the sequence of figures from Figure 24 to Figure 26 depicts the time sequence of grayscales, estimated instantaneous frequency, and curve of cured height for a typical pixel in each experiment, specifically, Pixel (275, 230) in Experiment #1 and Pixel (290, 225) in Experiment #2. In Figure 24, the grayscale has a range of [0, 255] expressing the intensity of the pixel in the interferograms captured by the CCD camera in the ICM&M system. It is not exactly sinusoidal due to the nonlinear curing process and stochastic noises including the nonlinear response of camera electronics [37]. The black dots in the figure depict the raw data and the red dotted line is correspondingly the fitted curve by the online parameter estimation algorithm. The fitted curve agrees very well with the raw data, demonstrating the effectiveness of the moving horizon curve fitting and capability of real-time measuring.



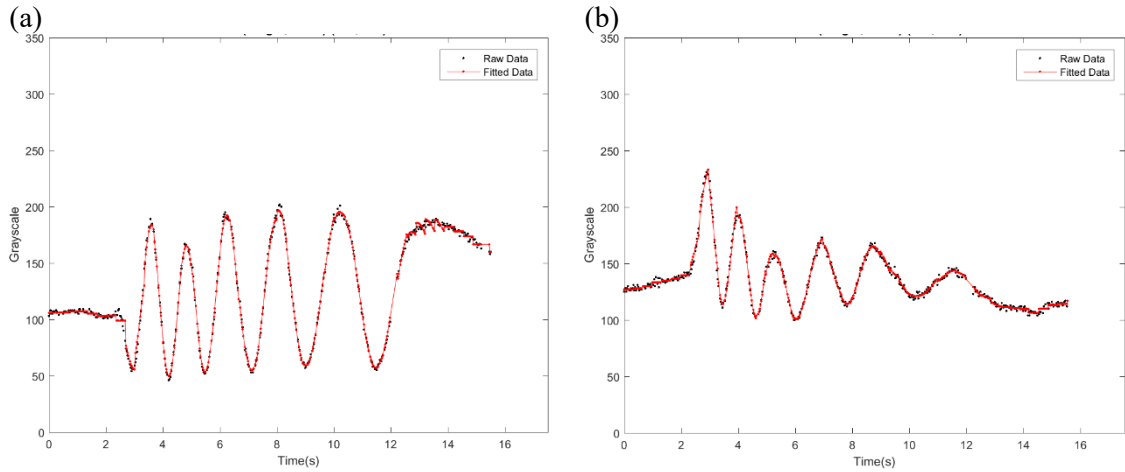


Figure 24. Initial ICM&M validation: time sequence of grayscale for (Left) Pixel (275, 230) in Experiment #1; (Right) Pixel (290, 225) in Experiment #2.

In Figure 25, the instantaneous frequency is estimated consecutively after playing every 10 frames of the video and obtaining a new batch of 10 raw grayscale data points. Please note that the measurement period, 10 samples (frames) per run of measurement in this study, could be changed as the computation power supports; and a sufficiently fast measurement is expected to be more accurate because it can capture the process dynamic better. Figure 25 also shows the cumulative sum of total phase change during the curing process, which is used to replace the item of  $\sum_i T_i f_i$  in Equation ( 14 ) for calculation of the voxel cured height as shown in Figure 26. The total phase angle is estimated to be 6.0469 cycles producing the cured height of 72.36  $\mu\text{m}$  for the voxel on Pixel (275, 230) in Experiment #1. Similarly, as to the voxel on Pixel (290, 225) in Experiment #2, the total phase angle is 5.7804 cycles resulting an estimated height of 69.14  $\mu\text{m}$ . As will be reported in Figure 28, the measured cured heights for the two experiments were 72.42  $\mu\text{m}$  and 69.48  $\mu\text{m}$ , respectively.

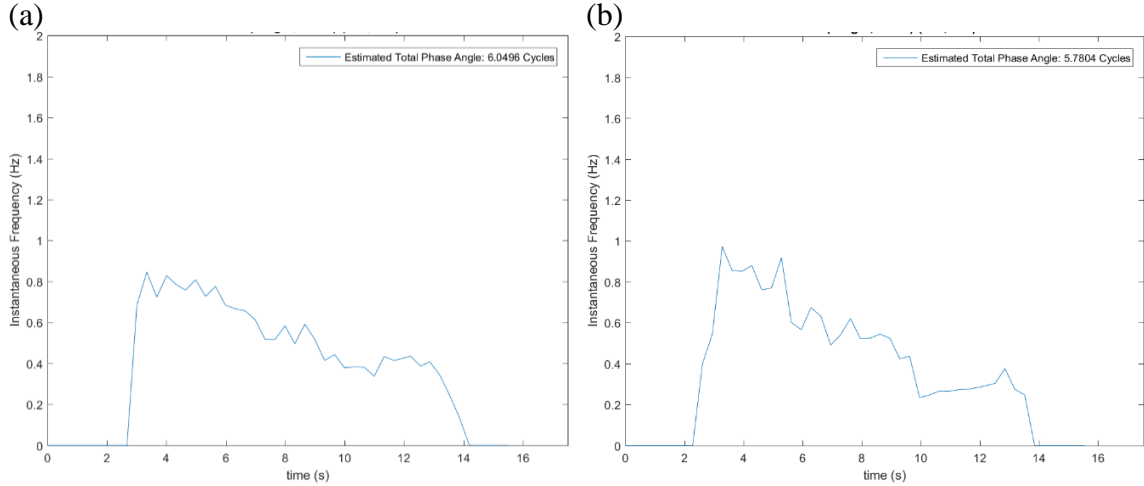


Figure 25. Initial ICM&M validation: estimated instantaneous frequency for (a) Pixel (275, 230) in Experiment #1; (b) Pixel (290, 225) in Experiment #2.

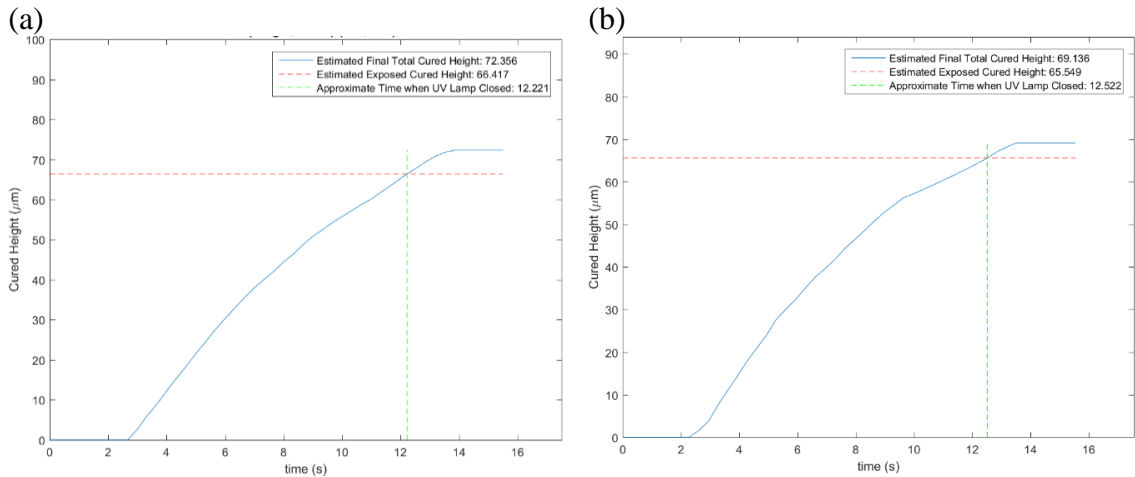


Figure 26. Initial ICM&M validation: estimated cured height for the voxel on (a) Pixel (275, 230) in Experiment #1; (b) Pixel (290, 225) in Experiment #2.

Figure 26 also indicates the exposed cured height before the time when the UV lamp was closed. It is worth to point out that a stereolithographic cure process involves mass and energy transport during the curing process, incorporating exposure and dark reaction [59], which is vividly shown in Figure 24 by that the pixel grayscales oscillation still persists for a while after the UV light is turned off at about 12 seconds. As continued “dark” gelation is expected in photopolymerization [66], the cured height by the ECPL

process can also be classified into exposed and dark cured height. The ECPL process is continuous while the ICM&M measurement is discrete with the digital signal of grayscales measured every 10 frames – 0.333 second with the camera acquisition speed being 30 frames per second. Hence, the UV close time is approximated instead of being determined with an error up to 0.333 second.

The same procedure was repeated to calculate the cured height for all the other voxels on the selected line of pixels in Figure 23, and the average height is evaluated as the final result which can be compared with the microscope measurement for accuracy check. As a result, the measured line profile is represented by the 22 pixels in Experiment #1 and 9 pixels in Experiment #2 as shown in Figure 27. The cured parts in the experiments were measured with the Olympus 3D confocal microscope as shown in Figure 28. The black outer frame corresponding to the edges in the sample imparts an uncertainty in the lateral dimensions of the cured part, but doesn't affect the height we are interested in measuring. Attention is focused on the dimensions especially "Height" result at the right-bottom box of the confocal microscope screenshot in Figure 28. For Experiment #1, the cured height is 73.140  $\mu\text{m}$  by the ICM&M method, and 72.424  $\mu\text{m}$  by the confocal microscope, yielding to a relative error of 0.99%; for Experiment #2, the cured height is 69.790  $\mu\text{m}$  by ICM&M, and 69.480  $\mu\text{m}$  by microscope, yielding to a relative error of 0.45%. The good agreement between the ICM&M method and the confocal laser microscope measurements demonstrates that the ICM&M method developed in this dissertation is capable of measuring the vertical height for parts cured by the ECPL process.

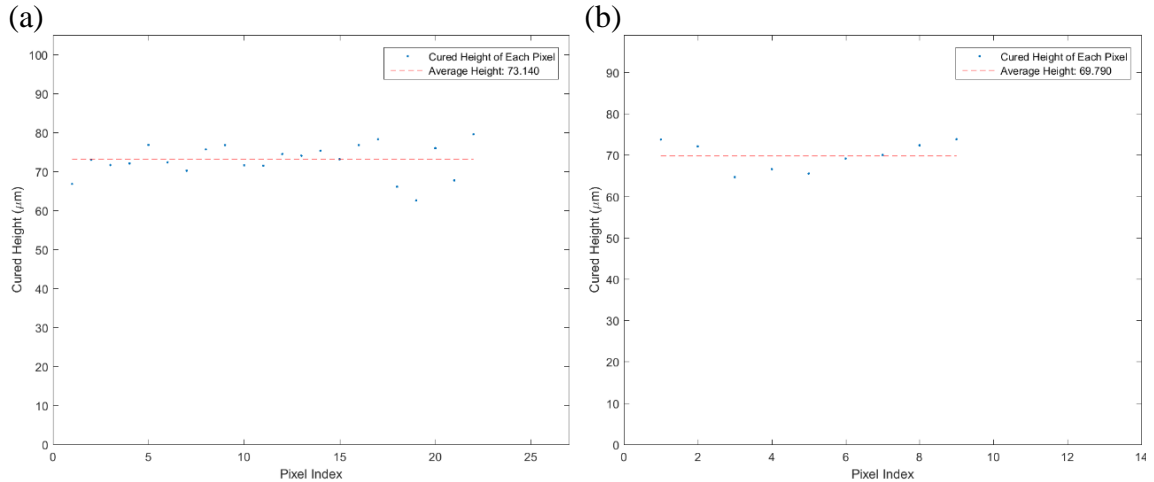


Figure 27. Initial ICM&M validation: ICM&M measured horizontal line heights profile for voxels on (a) 22 pixels of (250:5:355, 230) in Experiment #1; (b) 9 pixels of (265:5:305, 225) in Experiment #2.

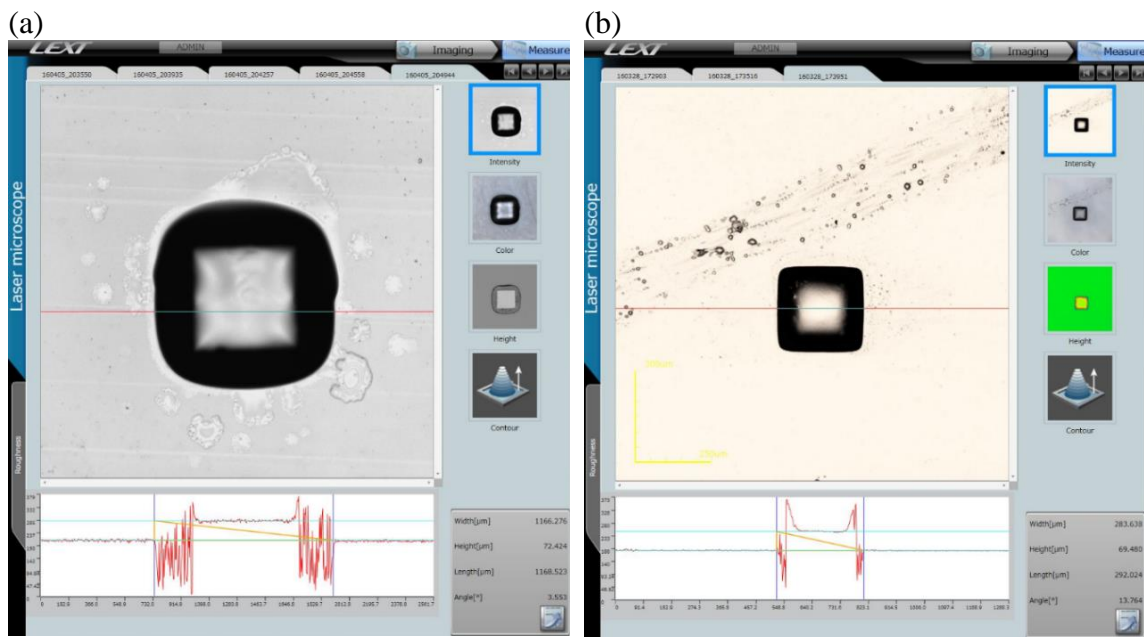


Figure 28. Initial ICM&M validation: microscope measured line profile for (a) sample cured in Experiment #1; (b) sample cured in Experiment #2.

The variations of the cured height in Figure 27 are not unusual due to the inherent stochastic factors in the chemical reactions, uneven UV irradiation for photopolymerization process, and non-uniform material properties, all of which could contribute to the actual spatial roughness. Other than the inherent process characteristics, another possible cause of the varying cured height is the measurement errors due to the

noise in the interferograms and ICM&M algorithms deficiency. However, it is noted that in Figure 28 the microscope measured line profile also presents fluctuations for the cured part (white part within the black frame), which could justify the variations measured by the ICM&M method to some extent.

Herein we have validated that the ICM&M method is accurate and feasible as both an ex-situ and real-time metrology. To further demonstrate that the ICM&M is versatile in full-field measurement, we continued to use the sample cured in Experiment #2 and measured a vertical line Pixels (300, 200:5:240) with the same method. Measuring a horizontal line and a vertical line together can serve as an effective validation for 2-dimensional area's heights profile measurement with easy computation effort. The reason we just chose the second experiment sample for validation of universal measurement capability is that the part is much smaller and more difficult to measure. If the ICM&M method could measure all over a small part, it can also easily measure a bigger part. Figure 29 shows the selected vertical line to measure, ICM&M and microscope measurement results. The average height for this vertical line profile was calculated as  $68.93 \mu\text{m}$  using the ICM&M method, while the microscope measurement was  $69.19 \mu\text{m}$ , resulting in a relative error of 0.59%.

Graphs (b) in Figure 23 to Figure 28 for a horizontal line in Experiment #2, and Figure 29 for a vertical line in Experiment #2, provide encouraging results of comprehensive multi-voxel heights profile, verifying that the ICM&M method is not restricted to a single point or a single line measurement and promising in achieving the desired full-field measurement capability.

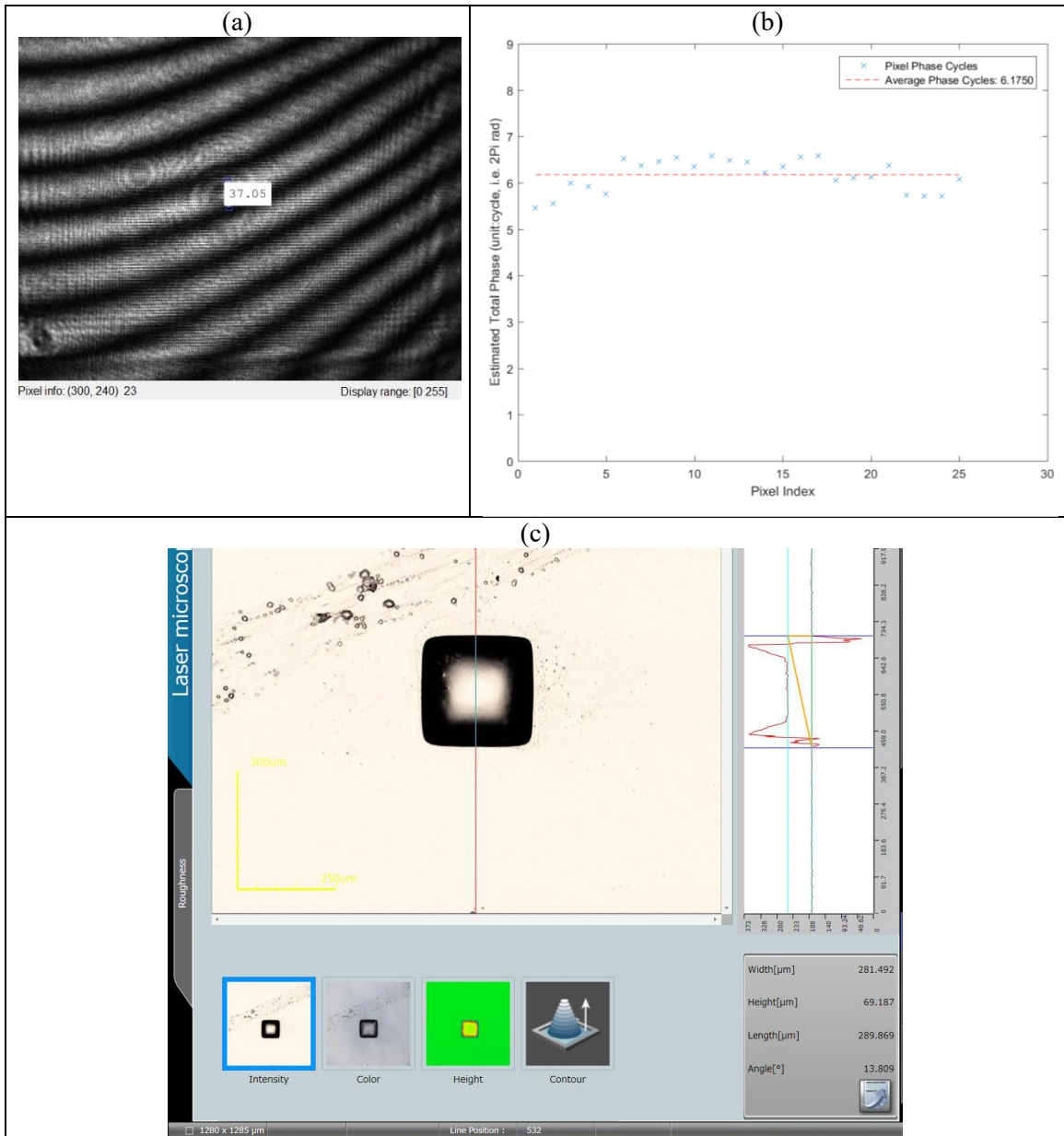


Figure 29. Initial ICM&M validation: measuring a vertical line profile for Experiment #2 (a) selected line in the interferogram: Pixel (300, 200) to Pixel (300, 240); (b) ICM&M measurement result; (c) microscope measurement.

In this study, the lateral boundary in the interferograms was approximated manually by human eyes, and the chosen ROI was aimed to measure the main part height for a direct comparison with the microscope measurement. Theoretically, by measuring voxels height profile, the lateral shape could be defined naturally and compared with

microscope images, as in Figure 28. In future, if desired, image segmentation and pattern recognition techniques could be applied to help detect the curing area automatically.

Conclusively, the ICM&M measurement method is in accordance with the microscope in terms of both average height and observed deviations. It features real-time and full-field measurement capabilities with accuracy and precision.

## 5.7 Chapter summary

An interferometric curing monitoring and measuring (ICM&M) method was developed and successfully applied to measure the height of part cured by an in-house stereolithographic apparatus – Exposure Controlled Projection Lithography (ECPL) system. The ICM&M sensor model of instantaneous frequency based on interference optics is built to interpret the fringes in-situ automatically, and algorithms of online parameter estimation adopting moving horizon exponentially weighted Fourier curve fitting and numerical integration is developed to extract the phase change underlying the fringes so as to measure cured object shape and height. It is used to calculate the phase from a sequence of interferogram images for dynamic cured height measurements on the continuous growing surfaces produced by ECPL. The proposed ICM&M method is promising to enable real-time, full-field shape measurements, specifically, of the evolving vertical growth that occurs during photopolymerization based ECPL process. Based on this principle of ICM&M model and algorithm, the original primarily monitoring system can be upgraded into a real-time metrology equipment for the ECPL process.

To validate, experiments were performed with an established calibration procedure as introduced with the sensor model, followed by two experiments curing two square blocks of different widths. Accurate estimation of the cured parts height profile was provided by the ICM&M method. It is proven to be repeatable and universal, making it a method of choice for both in-situ and ex-situ height tracking and lateral sizing in the

ECPL process. The ICM&M algorithms may need elaboration to reduce the effect of measurement noise in the upcoming ICM&M validation and characterization experiments. The designs of the ICM&M sensor model and algorithms have incorporated the consideration for real-time deployment. The algorithms of measurement analysis take less than 0.2 second, which is smaller than the measurement period of 0.333 second, indicating that the developed ICM&M method is qualified for real-time process measurement.

This chapter is aimed to address Research Question 1 by developing a sensor model based on interference optics and the corresponding online parameter estimation algorithms. The initial experiments which are aimed to test the developed ICM&M method, provide a preliminary validation of Research Hypothesis 1.

Research about the ICM&M algorithms and parameters is elaborated in Chapter 6. A software of real-time image acquisition and analysis should be developed to implement the model and algorithms, and Chapter 7 presents the development of the software. More validation and characterization results are presented in Chapter 8. Furthermore, Chapter 9 presents more research of implementing real-time measurement with the developed ICM&M method, which is sensitive to the process and sensor noises and depend upon the speed of the ECPL process as well as the ICM&M sampling and computation time [67].



## **CHAPTER 6 DATA ALGORITHMS IN THE ICM&M SYSTEM FOR MEASURING THE ECPL PROCESS**

In the previous chapter, an in-situ interferometric curing monitoring and measuring (ICM&M) system has been developed to infer the output of cured height. Successful ICM&M practice of data acquisition and analysis for retrieving useful information is central to the success of real-time measurement and control for the ECPL process. As the photopolymerization phenomena occur continuously over a range of space and time scales, the ICM&M data analysis is complicated with computation speed and cost. The large amount of video data, which is usually noisy and cumbersome, requires efficient data analysis methods to unleash the ICM&M capability.

In this chapter, we designed a pragmatic approach of ICM&M data mining to intelligently decipher part height across the cured part. As a data-driven measurement method, the ICM&M algorithms are strengthened by incorporating empirical values obtained from experimental observations to guarantee realistic solutions, and they are particularly useful in real time when limited resource is accessible for online computation. Experimental results indicate that the data-enabled ICM&M method could estimate the height profile of cured parts with accuracy and precision. The study exemplifies that data mining techniques can help realize the desired real time measurement for AM processes, and help unveil more insights about the process dynamics for advanced modeling and control.

### **6.1 Objective and organization of the chapter**

To upgrade the original primarily monitoring system into a real-time measurement equipment, we have created a sensor model based on interference optics to interpret the dynamic fringes in-situ automatically as presented in Chapter 5. With the

sensor model, for measuring the continuous growing surface of the part produced by the ECPL machine, online parameter estimation algorithms have been developed by adopting moving horizon exponentially weighted Fourier curve fitting and numerical integration to extract the phase change underlying the evolving interferograms [68, 69]. The developed sensor model and measurement algorithms, together, establish a methodology of interferometric curing monitoring and measuring, and provide a feasible metrology system promising to enable real-time and full-field measurement of the photopolymer part dimensions.

This chapter continues the authors' research initiative in seeking for real-time measurement method for the dimensions, primarily the vertical height, of additively manufactured photopolymer parts made by the ECPL process. With the ICM&M sensor model and algorithms established in previous chapter [68], the main practical aspects, data processing and effects of algorithms and algorithm parameters, which are critical for effective implementation of the ICM&M method, remain unresolved. Based on the developed ICM&M method resultant from previous research on sensor modeling and algorithms [68, 69], this study is aimed at the potential of harnessing the rich but usually noisy data from video of interferograms with data mining techniques to realize a real-time metrology of cured part height for advanced process control [70].

To start, Section 6.2 identifies the research issues raised by the real and rich data in physical implementation of the ICM&M. Sections 6.3 - 6.9 are focused on addressing the practical issues from the data perspective with the aid of a data mining approach to fulfill the ICM&M's role as a reliable metrology for the ECPL process. The developed ICM&M data analysis algorithms are summarized in Section 6.10 followed by conclusions in Section 6.11.

## **6.2 The ICM&M method from data perspective**

### **6.2.1 Data analytics in manufacturing**

Enormous literature is available in the area of data analysis techniques, and solution approaches are often adjusted or rediscovered for the specific application domain such as manufacturing processes and materials development. Data analysis is pervasive in scientific simulations, experiments and observations with the aim of finding useful information [71], and is used extensively to improve the performance of manufacturing systems at different levels. The focus of the research so far is on data mining techniques as well as on the stages before and after data mining, including data collection, processing, cleaning, transformation and decision making based on data [72]. Developing data enabled sensing and control techniques is an emerging research line for advanced manufacturing with higher efficiency and lower cost [72].

### **6.2.2 To materialize the ICM&M method with data techniques**

The ICM&M method, consisting of sensor model and algorithms, is by nature a data-driven measurement method, developed to gain insights for the ECPL curing process and to infer with confidence about the final height of the cured product. In practice, the conceptual level of the ICM&M sensor models and algorithms should be embedded into the context of real data environment during data acquisition, algorithms implementation, model evaluation, and final decision making. Employing the data science process [73], a diagram as shown in Figure 30 illustrates from the data perspective the implementation level of the ICM&M method with yellow highlights (1) to (4) identifying the nodes where substantial data analysis may be performed.

Firstly, during image acquisition, the video often has missing frames. Worse still, the images may be of low quality, for instance, interferograms are low contrast and noisy

due to camera electronics issues [37]. Preprocessing and classification (yellow highlight (1) in Figure 30) could help obtain a clean dataset for ICM&M analysis.

Furthermore, the ECPL process parameters and the ICM&M algorithm parameters will affect the accuracy and robustness of the ICM&M method for ECPL cured part measurement. The ECPL process parameters such as the exposure intensity and exposure time would be important considerations in dealing with the stream data from the ICM&M camera. The algorithm parameters in the rolling fit (yellow highlight (2) in Figure 30) would be highly critical in outputting a realistic and meaningful estimation of the dependent curing process variables. Afterwards, evaluating the mean instantaneous frequency for each iteration (yellow highlight (3) in Figure 30), which corresponds to outlier removal and choices of different numerical integrations while translating the instantaneous frequency information into the cured height result, could also change the outcome to some extent. In the end (yellow highlight (4) in Figure 30), the statistics algorithm used to derive the final measurement quantity of the cured height from the multiple voxels height profile require careful handling of the outliers in the resultant dataset of estimated voxels height; otherwise the distribution of the measured height could be mischaracterized in case with noisy raw data.

In addition, the raw data streaming from the camera in the ICM&M system varies at both spatial and temporal scales. The large amounts of data being generated and made available by the ICM&M system for the ECPL process continue to grow with the measurement region and part size. Mining the dynamic data stream which is massive and fast changing presents additional computation difficulty [74] and requires more computation power. Consequently, the ICM&M data that features mounting quantity and unsatisfying quality drives the need for efficient data analysis tools to enable large-scale, high-fidelity and real-time measurement for ECPL process and product.

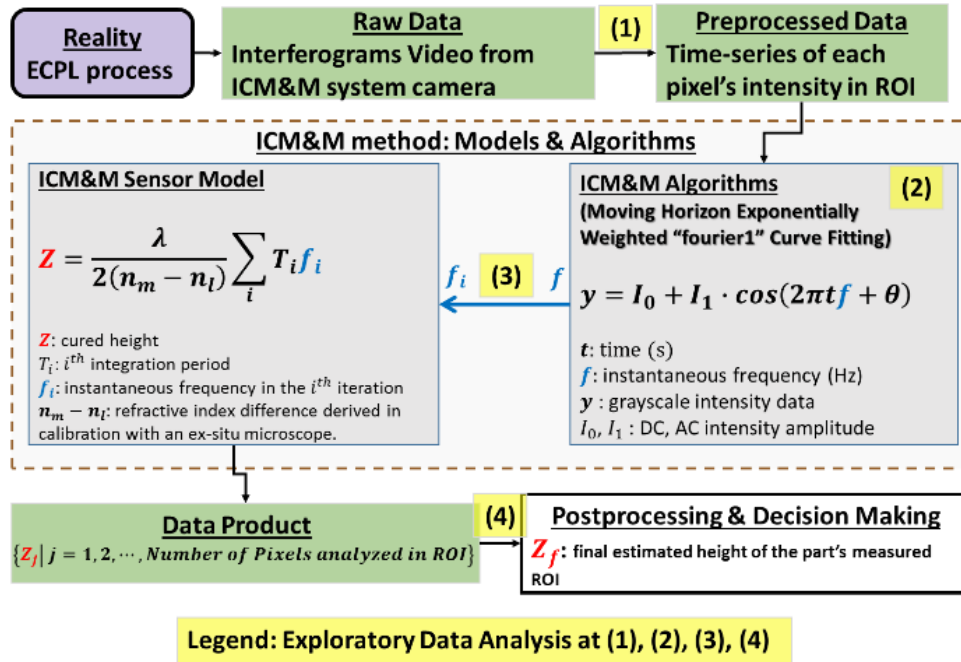


Figure 30. Data-driven ICM&M Method for ECPL process and product measurement

### 6.2.3 Data mining approach for realizing the ICM&M system

This section casts the primary measurement problem of deriving online information of cured height from acquired interferogram video into a data mining problem, and presents how a data mining approach is applied in order to realize the full potential of the ICM&M method. The entire data analysis and algorithms study was conducted in an offline mode with real-time acquired videos of the ECPL curing process.

### 6.2.4 Scope and overview of ICM&M data mining

Data mining is the extraction of implicit, previously unknown, and potentially useful information from data. Fundamentally, data mining could be viewed as one essential step where intelligent methods are applied to extract data patterns in the knowledge discovery process. However, the term data mining has been widely used to refer to the entire knowledge discovery process including data preprocessing, traditional data mining, pattern evaluation, visualization and presentation of mined knowledge [75].

Therefore, this study adopts a broad view of data mining functionality, which is the process of discovering interesting patterns of oscillating greyscales and mine the knowledge of the ECPL process in terms of cured part's dimensions from large amounts of interferogram data.

The idea of ICM&M video data mining is to develop a mature online algorithm that can sift through the real-time acquired data of pixels' greyscales automatically, identifying the ECPL process stages - incubation, exposed curing, dark curing and resting - and estimating the associated instantaneous frequencies and curing heights. The proposed data mining approach is expected to serve the purpose, boost the procedure, and exert the potential of the ICM&M method as a real-time metrology for the ECPL process.

### **6.3 Data preprocessing for ICM&M**

Removing objects that are noise is an important goal of data preprocessing as noise hinders most types of data analysis [76]. Due to the ECPL process noise and the ICM&M equipment noise, the acquired interferograms sometimes have unwanted temporal burrs and spatial speckles. Temporally, one may use a low pass filter algorithm of moving average to smooth the time sequence of greyscales [77]. The goal of smoothing is to produce slow changes in value so that it is easier to see trends in data. To remove the spatial salt and pepper noise, one solution is image median filtering which replaces the noise pixel by the median value of the neighbors [78]. When filtering the image spatially, one needs to specify the size of the filter. Since filters are centered on a particular pixel (the center of the filter) the size of the filter is uneven and often has equal dimensions, i.e.,  $3 \times 3$ ,  $5 \times 5$ ,  $7 \times 7$ , etc. For example,  $5 \times 5$  span means the pixel grayscale is the median value within  $5 \times 5$  square centering the pixel. Please note that "pixel" in this study means pixel in the interferogram captured by CCD camera, not that in DMD bitmaps or resin chamber substrate.

Some interferogram pixels receive small amount of exposure and display low-amplitude sinusoidal signal of grayscales which could be not apparent enough for the ICM&M algorithm to recognize as an effective cycle. Another situation is that some pixels have low signal-to-noise ratio (SNR) and their oscillation patterns in the curing process are buried by noise. In both cases, a pixel's data sequence of grayscales is not informative enough and requires referring to good pixels around it. As a demonstration, pixels' raw grayscale intensity data were extracted from an interferogram video captured in an ECPL experiment of curing a square block for 12 seconds under ultraviolet light exposure. Ideally, the pixels were supposed to display similar phase change. A typical and good pixel that presents an appealing oscillation pattern is shown at the top of Figure 31, and it could directly provide friendly data for the ICM&M algorithm which estimated the total phase angle was 8.712 cycles. However, the video has some troublesome pixels, and one such challenging pixel is shown as the blue line at the bottom graph in Figure 31 to have a total phase of 6.265 cycles, which is short of 2.5 cycles compared with the good neighboring pixel at the top of Figure 31. Obviously, the ICM&M was unable to recognize some suppressed waves in the bad pixel's raw data and underestimated the total phase angle, indicating a need for data preprocessing.

As shown at the bottom graph in Figure 31, the image median filter helps resolve the small-amplitude oscillations around 4s and 9s, respectively, and helps recover a buried wave around 6s in the pixel's original time sequence of raw grayscale data. Among the tested three filter sizes,  $3 \times 3$  and  $9 \times 9$  do not enhance the data as much as  $5 \times 5$  and  $7 \times 7$  filters. Besides, there is a turn point in the filter size regarding the filtered signal's fidelity. If it spans too narrow, stochastic noise dominates; if it spans too wide, inherent spatial difference dominates. It is found that the  $9 \times 9$  filter spans so wide that it distorts the signal and misled the algorithm to a wrong estimation of 7.218 cycles phase angle. The more neighbors included, the more strongly the image is filtered; and a wider filter will consume more computation time [78]. Conclusively speaking, for the ICM&M

application, the  $5 \times 5$  image median filter is shown to be an efficient preprocessor, and will be used in this study.

It is worth to point out that occasionally the filter would do harm on the curing period's signal by straightening the small amplitude alternating current (AC) signal. Nevertheless, most of the time, the chosen  $5 \times 5$  filter will assist differentiating the process stages as will be discussed later.

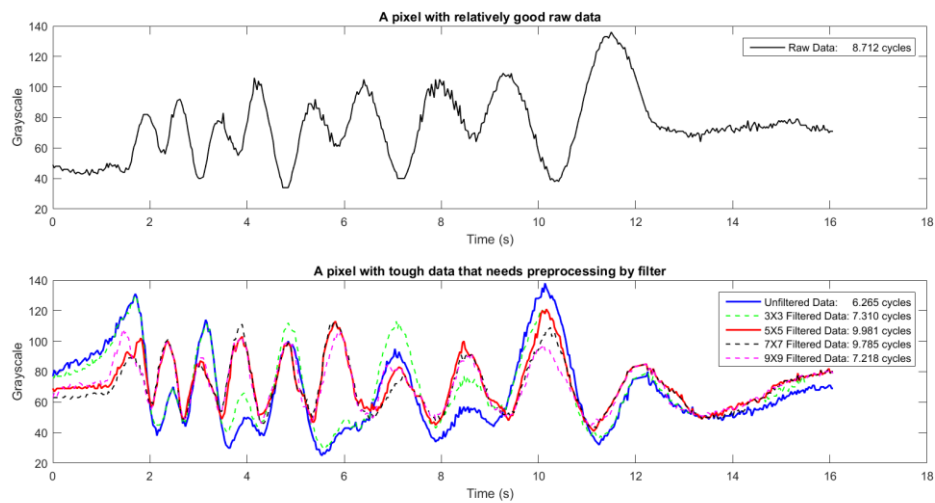


Figure 31. ICM&M data preprocessing - Top graph: a good pixel; Bottom graph: a bad pixel which needs filter.

Secondly, preprocessing the ICM&M raw data with an image median filter can improve the ICM&M measurement accuracy and precision across the curing area. A more comprehensive way of verifying the filtering effect is to examine the entire cured area's distribution of phase angle estimated by the ICM&M method. Figure 32 shows the result of ICM&M analysis for the same video of interferograms but with raw data and filtered data, respectively. The video was recorded while curing a square block on the ECPL machine, and the cured part was supposed to have uniform height across the horizontal dimensions. In Figure 32 (a), the average phase cycle over the entire curing area is shown to be 7.787 cycle with a standard deviation of 1.277 cycle, while in Figure



32 (b) the average is 8.562 cycle with deviation of 0.606 cycle. The calibrated refractive index difference  $\Delta n = 0.0231$ , which was plugged in Equation ( 14 ) along with the total phase angle 7.787 and 8.562, respectively, and the cured height was computed to be 90.84 $\mu\text{m}$  with the raw data and 98.46 $\mu\text{m}$  with the filtered data. The cured part was measured by a confocal microscope and the actual height was 97.00 $\mu\text{m}$ . Comparing the results, it is found that the filtered data could not only result in a more uniform (i.e., smaller deviation) height profile that conforms to the flat-top cured part, but also provides a more accurate measurement of the average height.

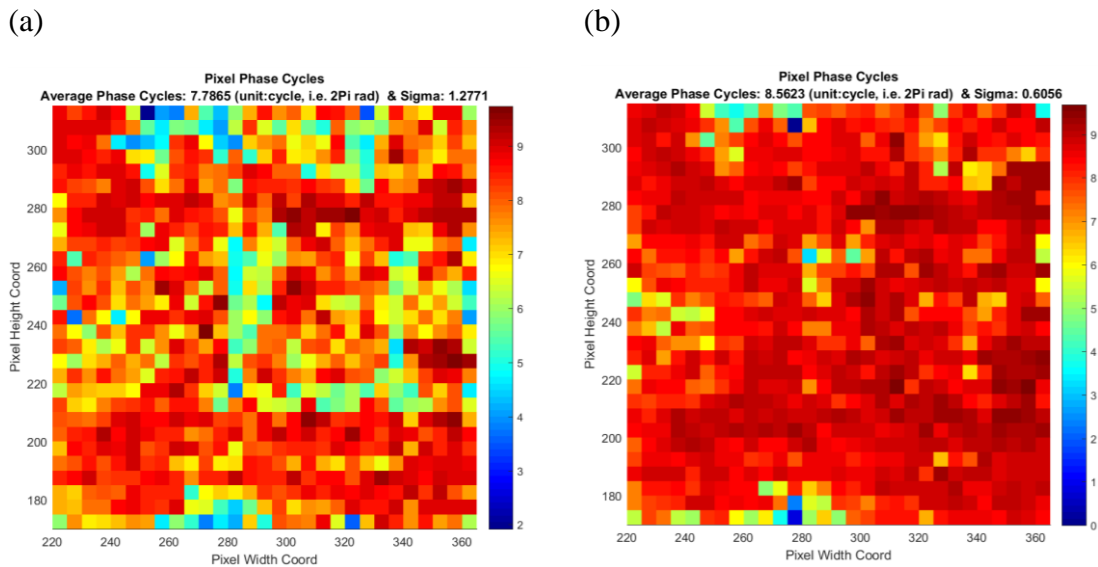


Figure 32. ICM&M data preprocessing - ICM&M estimated total phase angle for the ECPL cured part with (a) raw data; (b) data preprocessed by a 5×5 image median filter

Lastly, for the ultimate purpose of real-time process control, it is more practical but also risky to sample only one single or a limited number of pixels as online measurement feedback due to the computing power constraint. The chosen pixel(s) is vulnerable to noise and might provide severely biased measurement misleading the process control. By applying image median filter, the time sequence of measured pixel is actually a median of a group of neighboring pixels (25 pixels in case of 5×5 filter), thus the filtered data is more robust and representative enabling a more reliable measurement and control real time.

The image median filter is a double-edged sword in that it sometimes resolves some small-amplitude oscillations correctly and sometimes flattens some small magnitude supposed-to-be sinusoidal signal during the curing process. Nevertheless, it is found that in terms of the overall ROI height profile measurement, the median filter does more good than harm for the ICM&M method.

It is noted that the filter is effective often but not always. Sometimes, even filtered data sequence still possesses bad signals that mislead the ICM&M algorithm. Such problematical pixels would be handled as outliers in the data product at the end of data aggregation process.

## **6.4 Identifying ECPL process stages**

### **6.4.1 Classification of the ECPL process stages**

Like a traditional stereolithography process [79], the photopolymerization based ECPL process involves mass and energy transport, and consists of incubation, exposed curing, dark curing and resting stages [17, 59]. The incubation stage is the period prior to start of crosslinking, and it is conventionally explained by the exposure threshold model where a critical amount of exposure energy is needed by the liquid monomers to get solidified [79]. The exposed curing stage is the primary curing period when chemicals and photons interact actively and a 3D object is formed. The dark curing stage is a continued “dark” gelation after the exposure light is turned off [80]. Theoretically, an ICM&M data of pixel intensity time-curve should present a leading flat line, vividly oscillating curve, gradual tail, and flat line again, corresponding to the incubation, exposed curing, dark curing and resting periods, respectively. Such a pattern is observed well in the top graph of Figure 31, despite some sawtooth throughout the timeline. The pixel grayscales oscillation started at about 1.5s, and still persisted for a while after 12s when the UV light was turned off.

It is a major task to identify different process stages and could be a daunting challenge especially in the real-time implementation due to the process uncertainty and noises. Data mining techniques are needed to learn the ECPL process from the ICM&M data. Correct and timely classification of the streamed ICM&M data into the ECPL process stages, particularly the start and the end of curing, is crucial for online estimation accuracy and computation efficiency. Only the curing period, including both exposed curing and dark curing stages, requires the ICM&M algorithm of moving horizon “fourier1” curve fitting to estimate the evolving instantaneous frequency thereby the cured height. The other two stages, pre- and post- curing, i.e., incubation and resting period, would not contribute to the part growth, but still are an integral part of the natural photopolymerization process and should be detected in order not to affect the cured height estimation.

#### **6.4.2 Rule-based classification for identifying curing window**

A statistic approach is employed to dynamically monitor the range and deviation of the windowed data and determine if it approximates a straight line with a reasonably small spread. The statistical learning algorithm adopts a rule-based classification using “IF-THEN” rules [81, 82] to identify the curing window by analyzing the preprocessed data of interferograms pixel intensity. The presence of incubation is determined by satisfying all three heuristic rules as below. Please note that the symbol “ $R$ ” means the range of the interferogram grayscale data for the pixel measured, the subscript “ $i$ ” means “incubation stage”, the subscript “ $r$ ” means “resting stage”, and the subscript “ $c$ ” means critical value. For example,  $R_{i,c}$  denotes the critical value of the range of interferogram grayscale data for a pixel determined being at the ECPL incubation stage.

Rule 1: the range ( $R_i$ ) of the entire dataset available so far is smaller than an empirical critical value  $R_{i,c}$ , i.e.,  $R_i < R_{i,c}$ .

Ideally, during incubation there is no curing, no thickness change, thus no greyscale change, i.e.,  $R_i = 0$ . A tolerance of noise is needed for disclosing the constant pattern in the data fluctuating within  $R_{i,c}$ . In this study,  $R_{i,c} = 20$ .

Rule 2: the standard deviation ( $\sigma_i$ ) of the latest segment of data acquired after last run of measurement analysis is smaller than an empirical critical value  $\sigma_{i,c}$ , i.e.,  $\sigma_i < \sigma_{i,c}$ .

No drastic variation is expected within the latest dataset; otherwise, a significant increase of deviation is a good indication of curing trend. The second rule helps judge whether curing starts or not with more confidence.

In this study,  $\sigma_{i,c} = 5$ .

Rule 3: the previous iteration of analysis estimated that the process was in incubation.

Enforcing the third rule is based on process continuity and helps the code bypass this identification algorithm if the process is not in incubation anymore.

Breaking any one of these rules will indicate a termination of the incubation and trigger a “fourier1” curve fitting for the current dataset as it is supposed to be done in the curing stage. It usually means that the process has entered into exposed curing, however exceptions could occur due to data noise and will be discussed later.

The start of dark curing could be identified easily by receiving a signal of UV lamp shutdown. Ideally, the curing tail will last for a while and gradually rest down, but it is prone to process noise and usually features spurious rippling frequencies. Hence, it is challenging to find the exact time when dark curing stops. A similar set of heuristic rules is designed to identify the end of the curing. Either satisfying Rules 1, 2 and 3 together, or satisfying Rule 4, will indicate that the dark curing ends and resting stage begins.

Rule 1: the UV lamp is closed.

Rule 2: the range ( $R_r$ ) of the windowed (window length is  $w_r$ ) dataset is smaller than an empirical critical value  $R_{r,c}$ , i.e.,  $R_r < R_{r,c}$ .

Firstly, one needs to set the window length  $w_r$  for resting period detection based on experimental observation. For the ECPL process typically has about 3 second dark curing, given 30 frames per second acquisition rate, 45 interferograms data is produced during a 1.5 second time window. Hence, in this study,  $w_r = 45$  is used.  $R_{r,c}$  is chosen to be 10 for low UV intensity curing (e.g., UV iris level is 5%) and 20 for higher UV intensity curing, because low UV intensity curing tend to have low SNR.

Rule 3: the standard deviation ( $\sigma_r$ ) of the latest segment of data acquired after last run of measurement analysis is smaller than an empirical critical value  $\sigma_{r,c}$ , i.e.,  $\sigma_r < \sigma_{r,c}$ .

The critical value  $\sigma_{r,c}$  is set to be 5, same as that ( $\sigma_{i,c}$ ) used in incubation stage.

Rule 4: the previous iteration of analysis estimated that the dark curing was over.

If previous iteration decides that curing has ended, the succeeding iterations will just average the data and fit it into line segments with zero frequency, even though sometime the tailing data could present appealing oscillations which are still disregarded as noises by referring to knowledge from previous iteration.

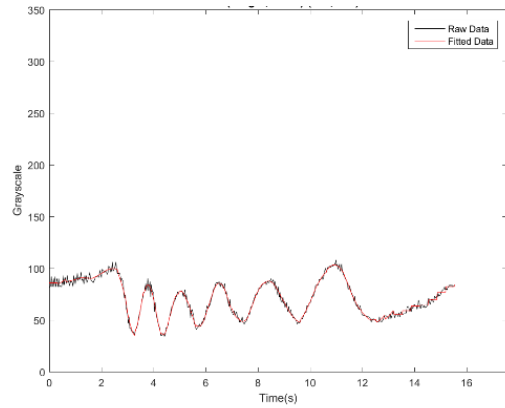
### 6.4.3 Effect of critical value

Caution must be taken in setting the critical value of  $R_{i,c}$ . As the spurious noises in incubation data may be mistaken as curing signal, it could be detected by raising the critical values of range  $R_{i,c}$  and standard deviation  $\sigma_{i,c}$  for incubation grayscale data. Increasing the critical values in the statistical learning could predict a longer than actual incubation period and underestimate the total phase angle. In this study, we primarily adjust  $R_{i,c}$  and keep  $\sigma_{i,c}$  as constant, which might just play similar role. In an experiment curing a square block with a DMD pattern of 150×150 square bitmap under UV exposure (22% iris level) for 12 second, the critical value  $R_{i,c} = 10$  was able to distinguish 80% of the 21 pixels' incubation well. Raising the critical range to 20, all the points can have a

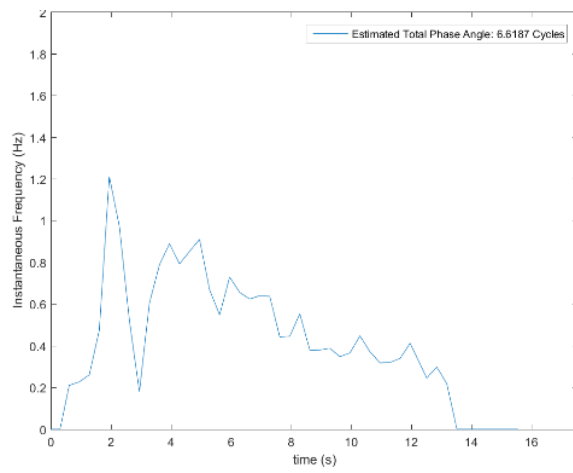
reasonable incubation period by comparing with the result from manually examining the grayscale data curve.,

An example is presented as below to demonstrate the effect of the critical range value  $R_{i,c}$  in the ICM&M estimation of phase angle. For the pixel (W=310, H=220) in a sample video which was captured while curing a square block with a DMD pattern of 50×50 square bitmap under UV exposure (intensity at 22% iris level) for 12 second, the grayscale time sequence is show in Figure 33 (a). With a critical range of 10 the estimated frequency, as shown in Figure 33 (b), is 6.61 cycles and is obviously wrong because the signal peak and valley cycles are visually less than 6. The curing started immediately which is untrue because the signal shows vividly a threshold period of about 2 seconds. After increasing the critical range from 10 to 20, as shown in Figure 33 (c), the algorithm detects the curing time on time, and the estimated total phase angle is 5.47 cycles which is in accordance with the visual observation by counting from the signal plot in Figure 33 (a).

(a)



(b)



(c)

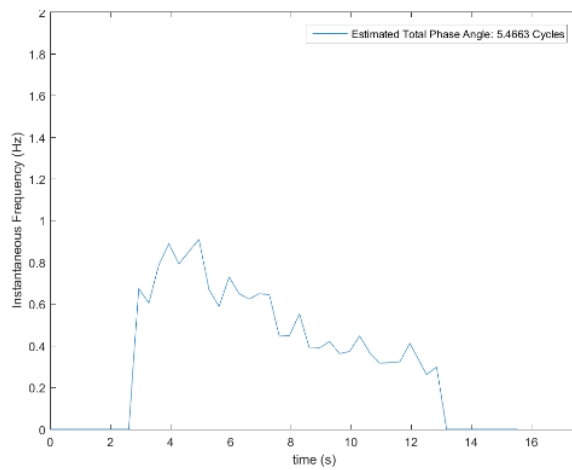


Figure 33. Effect of the critical range  $R_{i,c}$  for incubation stage identification in the ICM&M estimation (a) black curve: preprocessed data; red curve: fitted data with  $R_{i,c} = 10$ ; (b) estimated frequency and phase angle by ICM&M method with  $R_{i,c} = 10$ ; (c) estimated frequency and phase angle by ICM&M method with  $R_{i,c} = 20$ .

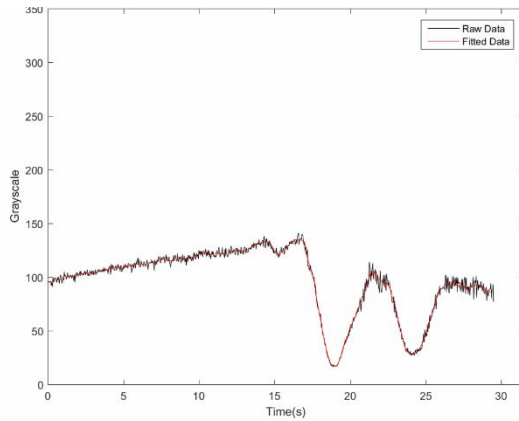
#### 6.4.4 Exception handling with multiclass classification

The statistical inference from the data magnitude establishes a base classifier for identifying the start of curing throughout the incubation. However, sometimes, the data make it very difficult to decide whether a detected wave represents a blip in incubation or a trend in curing. Ensemble methods can be used to increase overall accuracy by combining multiple classifiers, and its major advantage is high tolerance of noisy data. This section adds a new classifier of monitoring the AC amplitude to fix the misclassified data by the previous statistical classifier.

The following example necessitates monitoring of the fitted frequency on the way of looking for the start of curing. It is not uncommon that the incubation stage has a sequence of sloping or jaggling data, which sways away from the statistics range and triggers the curve fitting algorithm to estimate the frequency because it is mistaken as a signal of curing start. For example, in an experiment curing a square part under UV exposure for 26 seconds with the exposure intensity at 5% UV lamp iris level, as shown in Figure 34 (a), a pixel's grayscale data sequence (black curve) displays an obvious dip after 15 seconds, which however based on the signal of its neighboring pixel as shown in Figure 34 (b) should be actually flat. Figure 34 (b) displays a relatively good time sequence which shows that the curing occurred around 16 second, and peaks and valleys are manually counted as roughly 2 cycles. However, in Figure 34 (a), the small wave is misclassified into curing period, and the estimated total phase angle is 3.387 cycles, which is an obvious outlier considering its proximity similarity to Figure 34 (b). Too early start of curing misidentified by the algorithm, defined as false alarm, leads to overestimation of the total phase angle.



(a) Pixel Coordinate  
(Width, Height) = (305, 260)



(b) Pixel Coordinate  
(Width, Height) = (305, 270)

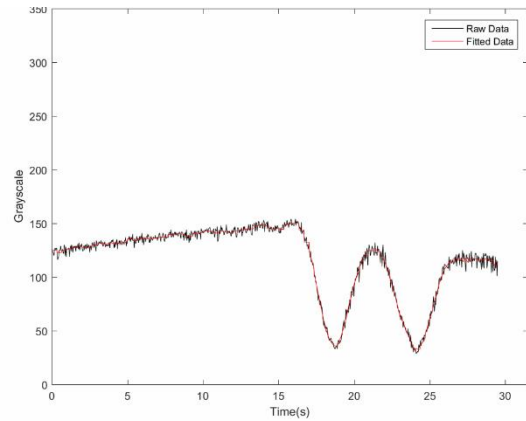


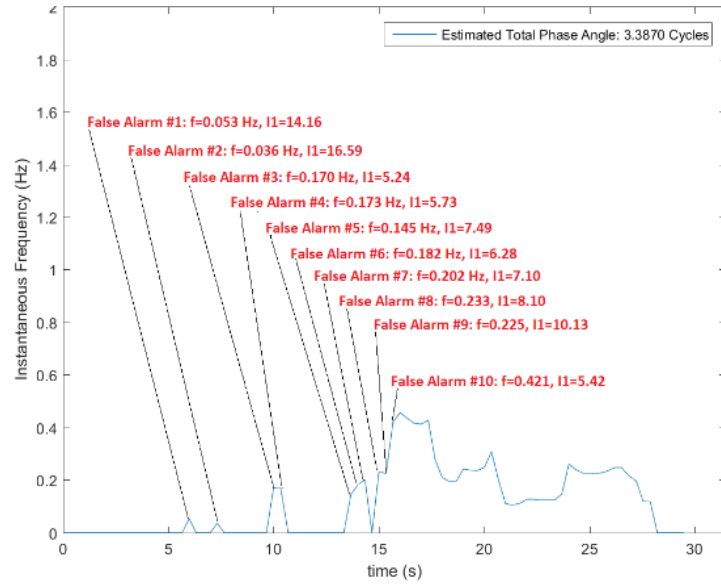
Figure 34. ICM&M data of time sequence: filtered raw data (black) and curve fitted data (red) for (a) a pixel with spurious waves in incubation stage; (b) a neighboring pixel with good data shows relatively straight pattern in incubation stage.

The false alarm outputs a curve fitting result with nonzero frequency, which is a result of fitting the spurious noises. Figure 35 (a) shows the ICM&M estimated frequency along the process time, all the nonzero frequencies before 16s should be false alarms for curing start. To gain some insight about how the false alarms could affect ICM&M accuracy, one could sum up the false alarms frequencies:

$$0.170+0.173+0.145+0.182+0.202+0.233+0.225+0.421=1.751 \text{ Hz,}$$

and multiply it by the time stepsize between consecutive measurements (in this case 10 frames per measurement / 30 frames per second = 1/3 second per measurement), coming up to 0.584 cycle. Please note the timestep is not constantly 1/3 due to the fluctuating image acquisition rate and it is just a quick estimation. Part of the overestimated phase angle is induced directly by false alarms as calculated to be 0.584 cycle. Besides, the false alarms could indirectly affect the phase angle estimation by influencing the choice of start point for the succeeding iterations of “fourier1” curve fitting algorithm which induce additional errors in the phase angle estimation.

(a)



(b)

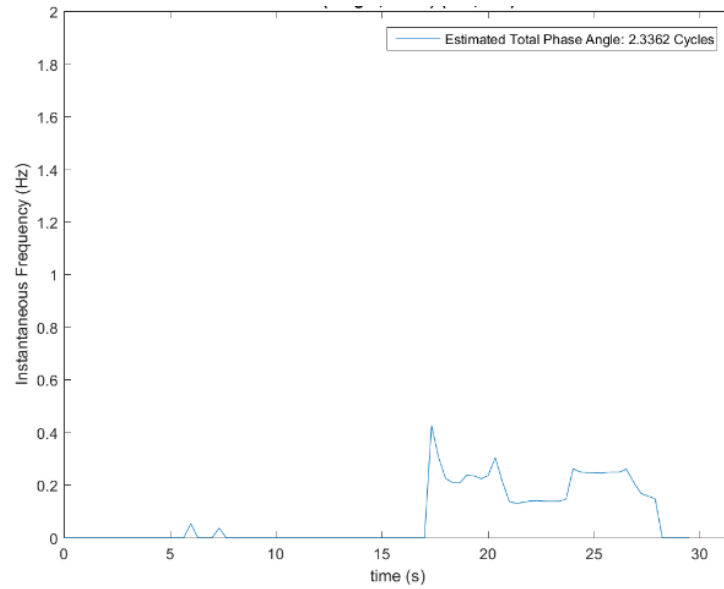


Figure 35. Instantaneous frequency and total phase angle estimated by the ICM&M method (a) false alarms are triggered in incubation stage with only statistical detection in the classification algorithm; (b) false alarms with low amplitude oscillation are suppressed and curing start is correctly identified with exception handling embedded into the algorithm

Most of the false alarms (#3 to # 10) feature lower than 10 oscillating amplitude ( $I_1$  in Figure 30), hence, we may apply an exception handling method of screening  $I_1 \leq I_{1c}^i$ , where the critical AC amplitude value for incubation stage  $I_{1c}^i = 10$ , and artificially

zero out its associated frequency. After applying the outlier detection and removal, the start of curing was correctly identified to occur around 17s and total phase angle was 2.336 cycles, which agree with what is seen directly with the data in Figure 35 (b) shows the improved result with the method of outlier detection and removal. Such scheme is especially useful in low intensity curing process (such as 5% UV iris level in this case) when the incubation period is longer and more susceptible to noise.

The false alarm might output a high amplitude and low frequency, less than 0.1Hz, as False Alarms #1 and #2 shown in Figure 35 (a), which are acceptable to be counted into the phase angle but should still be marked as incubation period to help continue identify the possibly remaining incubation in the succeeding data. The reason that we keep the small frequency is sometimes the curing period really starts with such small frequency and if we eliminate it wrongly, it could delay the detection of curing period and causes underestimation of total phase angle.

As a second example to validate the classification algorithm, a sample video will be studied here, and it was captured while curing a square block with a DMD pattern of 250×250 square bitmap under UV exposure (intensity at 22% iris level) for 15 seconds. The pixel (Width: 235, Height: 220) has a spurious wave around 2 s between the two orange lines, as shown in Figure 36 (a), raising false alarms with small oscillating amplitude ( $I_1$  as shown in Figure 30), but high frequency as shown in Figure 36 (b). If the segment of spurious wave is misidentified as the curing period, the associated error in the estimation of total phase angle is calculated using the frequency and time numbers in Figure 36 (a) as below:

$$1.024 \text{ Hz} \times (1.643 \text{ s} - 1.309 \text{ s}) + 0.832 \text{ Hz} \times (1.977 \text{ s} - 1.643 \text{ s}) + 0.983 \text{ Hz} \times (2.311 \text{ s} - 1.977 \text{ s}) = 0.95 \text{ cycle.}$$

By investigating its neighboring pixels, for example, pixel (Width 240, Height 220) as shown in Figure 36, the curing start point appears around 2 second. The estimated total phase angle for the good neighboring pixel is 7.14 cycles, which should be

close to the actual phase angle for the pixel under investigation, hence the error due to misclassification of the curing stage could be estimated as  $0.78/7.14 = 10.92\%$ . By applying an exception handling method of screening  $I_1 \leq I_{1c}^i$ , where the critical AC amplitude value  $I_{1c}^i$  is set to 10, the false alarms were detected and removed, the algorithm is able to predict the curing stage and estimate the phase angle more consistently with its adjacent pixel as shown in Figure 36 (b). Note a difference of  $(7.74 - 7.14) = 0.6$  cycle, as shown in Figure 36 (b), between the two neighboring pixels, which may be attributed to the true spatial height variation or simply the process noise.

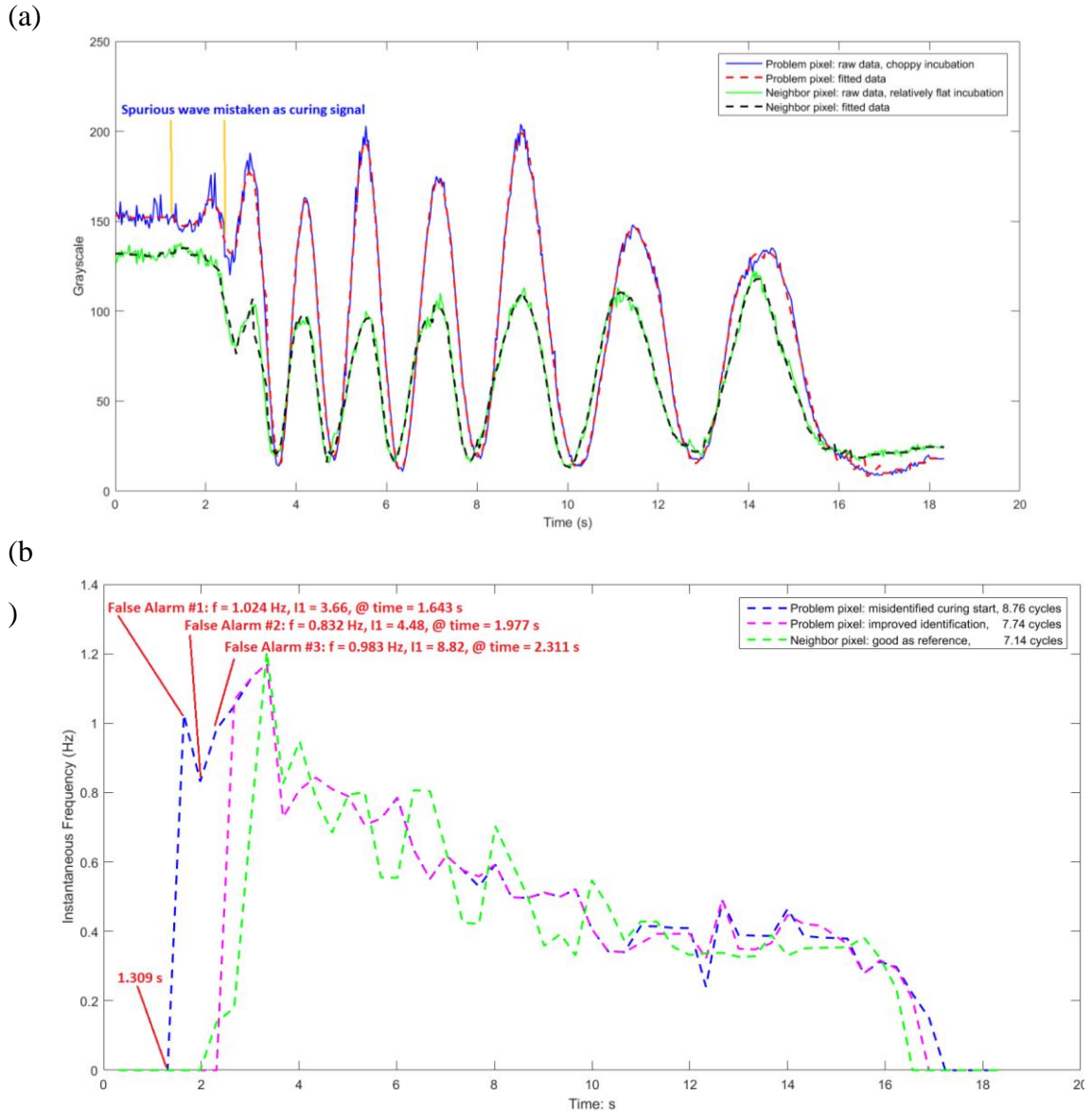


Figure 36. Challenge in differentiating incubation and curing stages (a) time sequence of grayscale in an example problematic pixel compared with its good neighboring pixel; (b) estimated instantaneous frequency and total phase angle for the problem pixel and neighboring pixel.

#### 6.4.5 Ensemble method based on majority voting for robust identification of the curing window across ROI

An ensemble tends to be more accurate than its base classifiers [75]. To ensure that all pixels across ROI have consistent curing start, an ensemble that performs majority

voting for curing start is considered. That is, given a tuple of greyscale data sequences for all pixels in the ROI to classify, it collects the number of pixels that are labeled as incubation pixels based on the classifiers introduced in previous sections, and decides that all pixels are in incubation if majority pixels vote for incubation as the current process stage. The multiclass classification method above may make mistakes in predicting the end of incubation (i.e., the start of curing) due to misleading noises, but the ensemble will correct the misclassified pixels and yield more accurate detection of curing start.

If any pixel makes an error, it can affect the vote count, and there is a better chance that one may still be able to predict the right curing start for the pixel because of the redundancy gained by having additional pixels. Error-correcting codes are used to force these misclassified pixels back to incubation stage thereby improving the accuracy of measurement, not just for each individual pixel, but for the entire ROI to attain a smooth and consistent cured profile.

An example experiment that cured square block with  $250 \times 250$  square DMD pattern under exposure intensity of 10% iris level for 12 seconds is presented to demonstrate the usefulness of the majority voting based ensemble method in identifying correctly the curing window across ROI.

It is noted that threshold is very vulnerable to bad signals and could introduce severe errors into final results as shown in Figure 37. Three problematic pixels that have too much misleading noise at the incubation stage showed significant errors in the estimated phase angle and cured height in the left column of Figure 37.

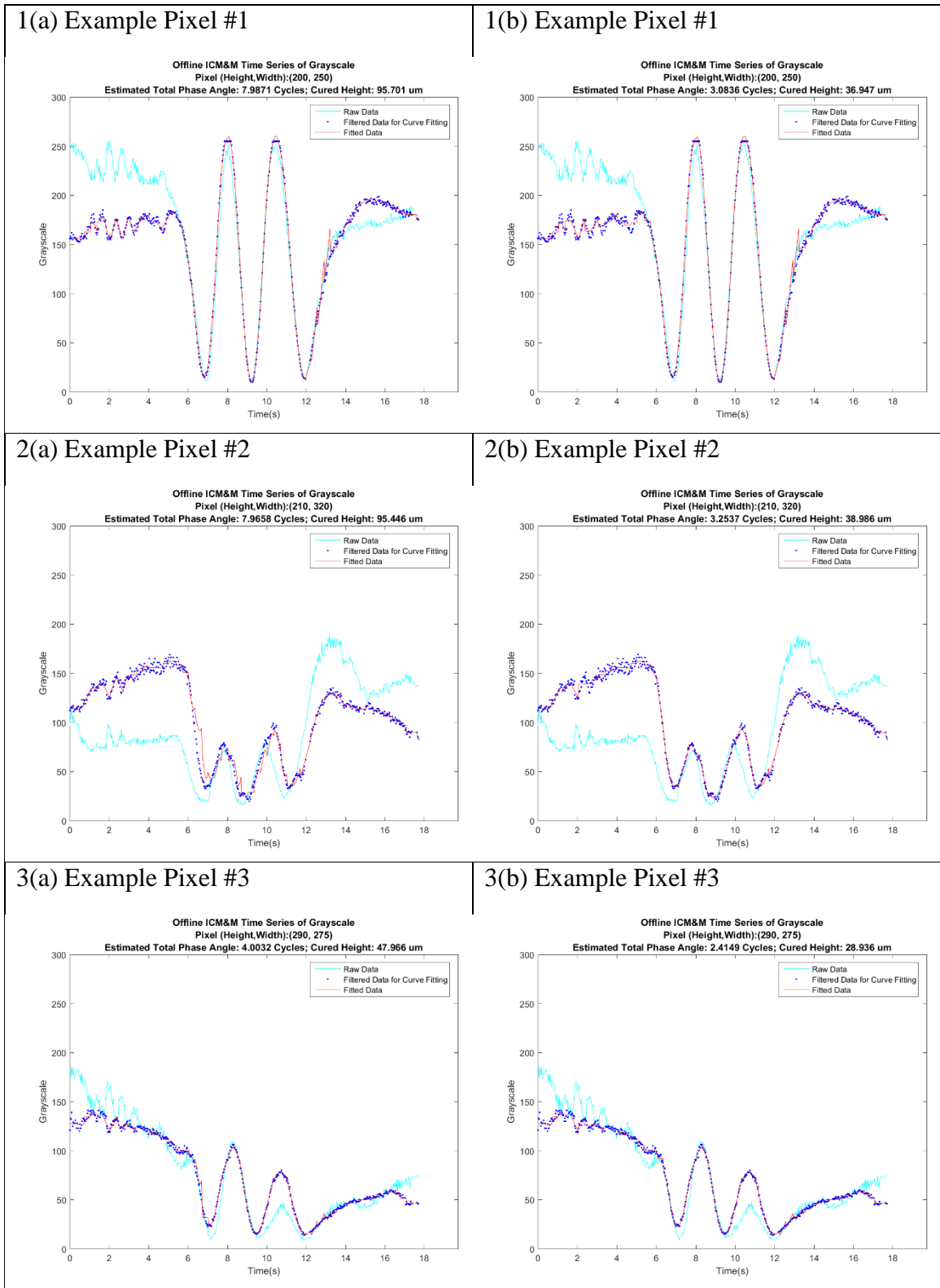


Figure 37. The voting mechanism helps identify the process stages correctly as demonstrated in three problematic pixels which have noisy data at incubation stage: 1(a),

2(a), 3(a) ICM&M data analysis and measurement results without voting; 1(b), 2(b), 3(b) ICM&M data analysis and measurement results with voting.

If most pixels have entered curing period, force the other pixels to curing period. Contrarily, if most pixels are still in the threshold, other pixels which may suffer noisy and bad signals are forced to stay in threshold period no matter how fiercely the signal fluctuates. This strategy would mitigate the bad signal problems a lot. With the ensemble method based on majority voting mechanism in identification of curing period start and end, they were correctly measured as shown in the right column in Figure 37. This method could be extremely effective in multi-pixel, especially full-field, measurement as compared in Figure 38. Despite similar average height, the standard deviation is reduced significantly - 3.5 microns less deviation in Figure 38 (b) than in Figure 38 (a), with the estimated deviation being 3.87  $\mu\text{m}$  which is closer the microscope measured deviation of 4.98 $\mu\text{m}$ . Please note that Figure 37 and Figure 38 are results for the same experiment, with the former investigating individual pixel measurement and the latter full-field measurement, to demonstrate the benefit of the ensemble majority voting method.

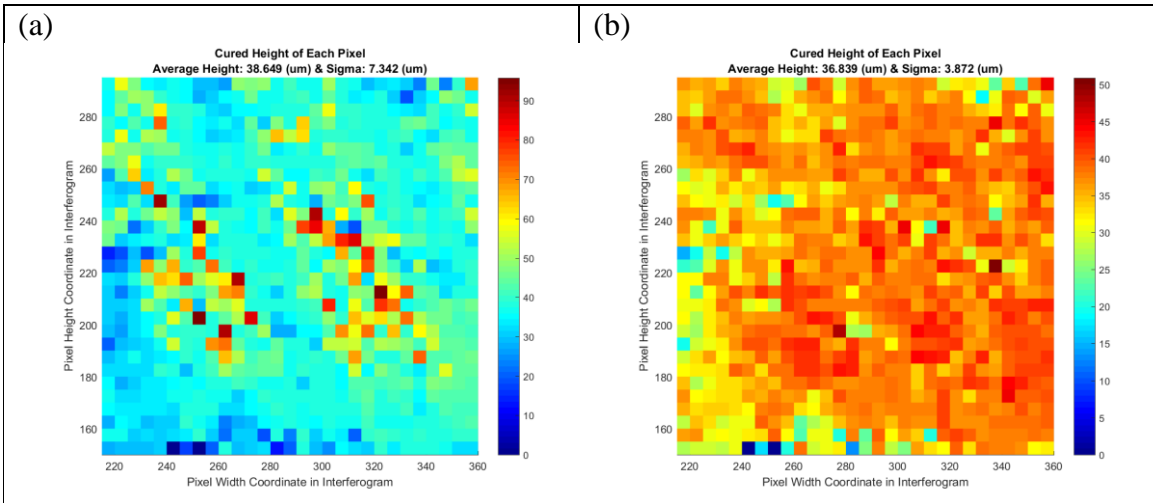


Figure 38. Estimation of full-field cured height profile (a). without (b) with the ensemble majority voting assisted classification method.



#### 6.4.6 Summary and recommendation

Misidentification of the curing window could cause significant errors in the frequency estimation by introducing large noise frequencies in the incubation and resting periods. The identification of incubation is more vulnerable to outliers which would alarm falsely about the onset of the curing process. A too conservative algorithm might delay the detection and bring up measurement error.

Conclusively, the classification algorithm based on statistical inference rules and exception handling could effectively identify the start of curing, and a similar algorithm is used to detect the end of dark curing after the UV lamp is closed. The critical values for grayscale data range ( $R_{i,c}$ ,  $R_{r,c}$ ) and standard deviation ( $\sigma_{i,c}$ ,  $\sigma_{r,c}$ ), and for the AC amplitude ( $I_{1c}^i$ ) are all chosen based on straightforward experimental observation and basic statistics. The empirical experience has been shown to be representative and effective, but still could be a potential error source in scenarios with low-SNR image grayscale data.

As the exception handling could suppress false alarms effectively, it may be overactive sometimes to cause missed alarms which result in a delayed identification of the curing start. Both false alarms and missed alarms contribute to the final ICM&M measurement error, and there could be more advanced algorithms to differentiate false alarms and missed alarms for accurate identification of the curing window.

The statistical learning rules may perform well on most cases, but less well on some noisy data. In future, to compensate for this, one can prune the rules online if the pruned version of rules has greater quality. Various pruning strategies can be used such as the pessimistic pruning approach described in the reference book [83].

For exception handling, in addition to screening out the low AC amplitude frequencies, the ensemble method based on voting scheme could be used for detection of the curing start and stop as well as to enhance the robustness of the overall ICM&M

algorithm. More details about the voting scheme and effects for identifying process stages will be presented in Section 9.5.2.1 while dealing with a more challenge data streamed from real-time implementation of the process measurement and control.

## **6.5 Mining curing window data's oscillating pattern for instantaneous frequency**

### **6.5.1 Fit options for “fourier1” curve fit to ICM&M data**

Without sufficient constraints, multiple fittings using the same data and model might lead to different fitted coefficients. The MATLAB curve fitting algorithm use goodness of fitting such as R-square to decide the optimal fitting model result [84]. However, mathematically the optimal solution may not be the physically best solution in engineering practice. To avoid this, in the specific application of ICM&M, the curve fitting algorithm need tuning with some domain expertise input to the fit options. This section mainly provides some guidance to set tolerances, start points and bounds, which are critical for realizing real-time measurement with realistic fitting results. Other default fit options could be explored further for improving the fitting in future work.

#### **6.5.1.1 Tolerances**

The termination tolerances (1.0e-6 by default) on model value (“TolFun”) and coefficient values (“TolX”) decides directly the number of iterations used for fit to the desired tolerances thereby affect the computation time. Hence, the default tolerance values should be adjusted to a proper order. In the ICM&M method, the curve fit model value is the interferogram image grayscale - an integer value ranging from 1 to 256, and a tolerance of 1.0e-3 could be good enough. The fitted coefficient of frequency (Hz) is the target fit result which will be used for the cured height calculation and should be more accurate.

A MATLAB code performance profiler was run to compare the computation time for curve fitting with different sets of tolerances. When the fitting options used the

default (TolFun = 1.0e-6 grayscale; TolX = 1.0e-6 Hz), each run of curve fitting took about 234 ms. When the tolerances decreased (TolFun = 1.0e-3 grayscale; TolX = 1.0e-5 Hz), the fitting time was reduced to 180 ms and an error in total phase angle relative to previous default tolerances result was 0.79%. When the tolerances decreased further (TolFun = 1.0e-3 grayscale; TolX = 1.0e-4 Hz), the fitting time is about 143 ms and the phase error was 1.56% relative to the results with default tolerances. As a compromise between computation time and accuracy, this study chose an options of (TolFun = 1.0e-3 grayscale; TolX = 1.0e-5 Hz).

#### 6.5.1.2 Start point

In curve fitting, start point is a vector of initial values for the coefficients to be fitted. If no start points, the default value of an empty vector is passed to the fit function, and might lead to some impractical solution. Starting points for the model could be determined heuristically. In the rolling fit for ICM&M data, the fitted result from previous run of measurement analysis, if good enough (heuristically, R-square is larger than 0.75), will be used as a start point for the current run of curve fitting. The scheme of assigning start point by inheriting a previous decent fitting to data from the last time window, reflects the continuity in the curing process, and enables a consistent estimation. Besides, providing a start point could help reduce the computation effort and enhance the speed.

It is noted that previous fitted coefficients to be used as start point for current run of new data measurement analysis, could sometimes mislead the algorithm to a wrong or unrealistic solution, because the seemingly good coefficients are actually for spurious patterns. This issue would be mitigated by applying coefficient bounds.

### 6.5.1.3 Coefficients bounds

The curve fitting would run into a bad estimation despite pretty good confidence with high R-square, especially in situations where the algorithm finds a local solution that reflects the noise instead of a global solution that captures the grand pattern of data trends. Worse still, the subsequent curve fitting would follow this bad estimation by using its result of fitted coefficients values as starting points, and so on. Consequently, the rolling fit could bog down to a stagnation where the algorithm gets stuck in the local solutions.

One solution is to apply empirical values to guide the curve fitting toward realistic values. Firstly, the first curve fitting at the detected beginning of curing should impose a constraint to the fitted frequency so as to get a good start point for the succeeding runs of curve fitting. From experiment observations, an empirical frequency range was derived to be the lower and upper bounds for fitted frequency: [0.4 Hz, 1.2 Hz] for curing above a UV intensity iris level equal or larger than 10%, and [0.1 Hz, 0.5 Hz] for curing at smaller than 10% UV iris level exposure intensity. Afterwards, in the succeeding curve fittings to the remaining exposed curing stage, [0.1 Hz, 15Hz] is set as bounds for the curing frequency estimation to avoid local solutions due to noise.

For instance, in an experiment of curing a square block with 250×250 pixels DMD bitmap for 26 seconds under UV exposure intensity at 5% iris level, the grayscale time-curve of Pixel (H: 210; W: 305) is shown in the top graph in Figure 39, which shows raw data (cyan curve), preprocessed data (black dots), fitted data (red curve) without setting bounds for the fitted coefficients of frequency in the “fourier1” model, and fitted data (blue curve) with coefficient bounds set for frequency. It shows both curve fitting, without or with frequency bounds could fit the data similarly well though the latter fit was slightly better. However, the underlying fitted frequency values are much different as shown in the bottom graph in Figure 39. The red curve of estimated frequency shows a severe underestimation and mistake compared with the blue curve.

The former yields a total phase of 1.464 cycles, while the latter has a much more accurate result of 2.462 cycles which agrees with the visible oscillations in the time sequence at the top graph.

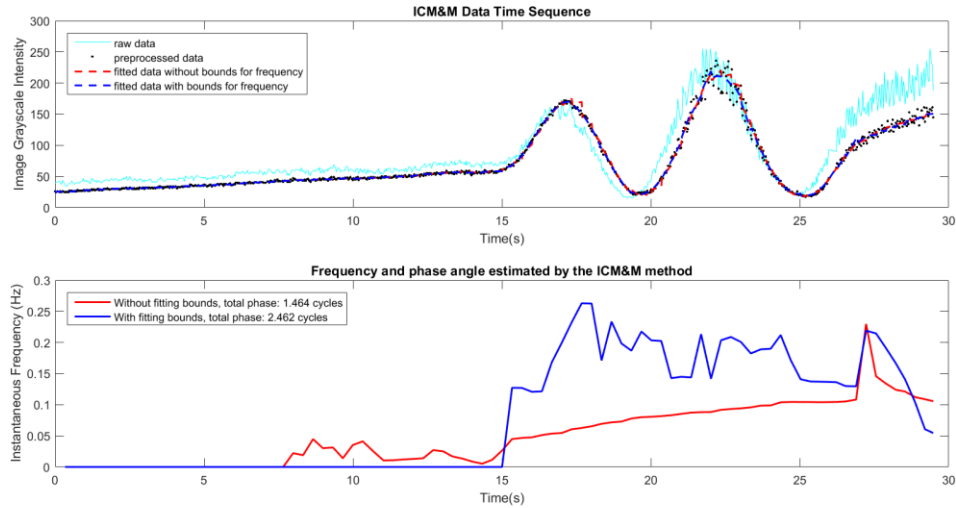


Figure 39. Effects of applying frequency bounds in the curve fitting for ICM&M data: red curve – unbounded fitting, blue curve – bounded fitting.

This example demonstrates vividly the difference between unbounded fitting and bounded fitting in ICM&M results. The accuracy of fitted frequency could avalanche, resulting in a big error in the finally estimated phase angle and cured height. In this sample ICM&M video, there were quite many such example pixels poorly estimated because of blind fitting without realistic bounds for the to-be-fitted coefficients of frequency in the cosine function in Equation ( 17 ), and the proposed bounded curve fitting helped estimate them all correctly.

### 6.5.2 Data window and weight

The basic idea of rolling fit is a sliding window model that runs computations only on recent data rather than all of the data seen so far [74]. At every time of measurement, the ICM&M uses a segment of the most recent  $w$  data points, where  $w$  is the window size or moving horizon length (MHL). Horizon length was demonstrated to

have a significant effect in the moving horizon estimator [63, 64]. This section investigates practical horizon lengths for the ECPL process measurement.

Accompanied with the MHL is another parameter in the rolling fit, “half life”, which means the width decaying weight to one half [69]. In this study, online measurement is run every 10 new data points acquired, to capture the most recent process dynamics, the half life is basically set to 10 allowing sufficient weight for new data. Its effect is not as significant as MHL; hence the study is focused on MHL.

Both MHL and half life are subject to change with data trends due to process dynamics and or noise vivid in some cases, as will be addressed later, so that the curve fitting could fit into the desired global pattern of oscillation rather than getting stuck to local optima or spurious noise. Also, it has been found that with the same MHL, curve fitting with larger half life tends to output higher estimation for the instantaneous frequency, which is understandable because larger half life weights more historic data corresponding to faster curing.

#### 6.5.2.1 Consideration from the prediction prospect

In an initial study with ECPL curing with the UV exposure intensity at 22% iris level [69], different values of window length were investigated in the rolling fit as shown in Table 7.

Table 7. Effects of MHL in prediction accuracy

<b>Moving Horizon Length</b>	<b>MSE of Rolling Prediction</b>
Entire Segment of data	6.54
70	6.56
60	6.32
50	6.10
40	5.95
36	5.61
<b>32</b>	<b>5.57</b>
30	5.71

For the long-term purpose of real-time EPCL process control which requires a good predictive measurement model, a metric of accuracy in the fitted model's prediction for the succeeding batch (five data points) of grayscales, i.e., the mean square error of the predicted data and actual acquired data was used to evaluate the effects of rolling fit MHL. It was found that a window length of "32" yields the lowest mean square error (MSE) in the rolling prediction as shown in Table 7.

One possible explanation is that despite non-constant oscillation cycles, for the ECPL curing at 22% UV iris level, the interferograms intensity data has roughly average periods of about 60 sampling data points and it requires at least half cycle to estimate the period and frequency accurately. A window length that is too long will slow the algorithm and yield a poor fitting. Hence, a window length of "32" turns out to be a reasonable option for real-time computation, good estimation accuracy and prediction performance as well, especially in that the signal peaks and valleys are observed to be fitted much better in the rolling prediction while other window lengths result in serious overshoot (undershoot) at peaks (valleys).

#### 6.5.2.2 Adaptive estimation for process dynamics

The initial study recommending 32 as MHL and provides a good rule of thumb for choosing MHL, which needs to be refined for improving algorithm accuracy. As a matter of fact, different curing stages (e.g., exposed curing and dark curing), and different UV intensities in terms of iris level (e.g., 5% to 95%, with a normal operation at 22%,) induces various curing velocities. Thereby, a range of instantaneous frequencies needs to be estimated, and MHL should be adjusted according to the process dynamics so as to estimate the frequency more accurately. In the following study, different MHL derived from empirical observation will be applied during the ICM&M implementation, realizing an intelligent algorithm – adaptive estimator - that fits to different process stages and conditions.

### 6.5.2.3 MHL for different process stages

It was experimentally found that for the ECPL process under UV exposure with a medium UV intensity (e.g., UV lamp iris level between 10% to 40%), the frequency approximately ranges from 0.5 Hz to 1.5 Hz. The authors' lab specifies a normal operating exposure intensity with UV iris level at 22%, which outputs instantaneous frequency in the ICM&M data up to 1 Hz. The minimal number of data points (or frames in the case of video processing),  $w_m$ , is estimated as in Equation ( 20 ), based on a principle that at least one half cycle of the signal should be included to identify the peak and valley for estimating the frequency with more confidence. Please note that  $w_m$  is sufficient but not necessary for MHL to be estimated, because values smaller than  $w_m$  could also evaluate the frequency well though might not with that much accuracy, confidence or robustness.

$$w_m \cong (T_p \times f_a) / 2 = \frac{f_a}{2f_p} \quad ( 20 )$$

where,  $w_m$  is the minimal window length,  $T_p$  and  $f_p$  are the ECPL curing process signal's period and frequency,  $f_a$  is the ICM&M camera's acquisition frequency (unit: frames per second).

Given an acquisition rate of 30 frames per second (fps), one full cycle of the ICM&M data would consist of approximately 20 (30 fps/1.5 Hz) to 60 (30 fps/0.5 Hz) data points depending on the process curing rate. By Equation ( 20 ) the MHL should be at least 30, which is the greater of 10 and 30 to detect the entire segment signal for various UV intensities. Combined with the result from Section 6.5.2.1, MHL is chosen to be 32 as a bootstrapping window length.

While measuring online, the data window for the first run of curve fitting at the detected beginning of curing would inevitably involve some incubation samples which are usually flat and might drag down the estimated curing frequency. The MHL of 32 has been found in experiments to be able to provide a decent sample size with appropriate



proportion of data from both incubation and curing stages for the initial “fourier1” curve fitting. Besides, the exponential weights in rolling fit also helps up-weight the most recent data in curing stage and down-weight the incubation data in incubation, so as to estimate the initial frequency better.

As the curing goes on, the process slows down gradually and the process signal’s period increases (e.g., to about 3 seconds), by Equation ( 20 ), MHL should be extended accordingly. A wider window of data, e.g., 48 data points corresponding to about 1.5 seconds time window, could aid the estimation of frequency towards the end of exposed curing. For real-time data analysis, it is hard to tell exactly when the process is slowing down or when the MHL should be increased, because the estimated frequency usually jumps up and down due to the process variations and noises. Therefore, throughout the exposed curing, an ensemble [85] of several curve fittings with different sets of MHL and half life is adopted to decide which MHL is better for the specific data set by comparing the goodness of fitting (GOF) using R-square metric [84]. For computation efficiency, the algorithm will start curve fitting with MHL of 32 and half life of 10 first; if the GOF R-square is above 0.95, it will determine that the fitting is successful and no need for a second fitting with longer MHL. If the R-square is lower than 0.95, a second run of curve fitting with MHL of 48 and half life of 10 would be performed, then the R-square values for the two runs are compared and the result with greater R-square value is used. The adaptive approach gives the algorithm flexibility and intelligence in choosing a better window length for more accurate estimation.

For the dark curing period, it is observed that usually half cycle takes about 5 seconds, i.e., the frequency is about 0.1 Hz, the previous moving horizon of 32 or 48 cannot estimate such low frequency, and MHL needs be increased further, by Equation ( 20 ), to 150. However, in practice 150 frames span a too long time window which might be even longer than the duration of dark curing itself. The estimated MHL of 150 could just provide a guidance and in practice MHL of 96 could estimate low frequency around

0.1 Hz as well for normal UV exposure curing. After the UV lamp shuts down, the curing process transitions to the resting stage, and the curing frequency drops gradually and there is no clear dividing line when to extend the MHL. Hence, a similar approach was used for comparing several fittings with different sets of (MHL, half life), e.g., (64,20) and (96, 30) in this study. The fitting that yields the highest R-square value will be adopted. It is found that the extended window length and half life could predict well the flattening tendency of decreasing frequency at dark curing period.

#### 6.5.2.4 MHL for low intensity ECPL process

In this study, low exposure intensity means the UV lamp iris level is smaller than 10%, e.g., 5%. The reason such low intensity ECPL process stands alone is that it features lower curing frequency about 0.2 Hz and the normal MHL of 32 and 48 could not estimate the frequency correctly. By Equation ( 20 ), the low intensity curing requires 75 data points, hence MHL values of 64 and 96 will be used in the adaptive curve fitting to exposed curing window. The dark curing period will adopt some value around 150 (e.g., 128 and 192 in this study) to estimate frequencies around 0.1Hz. Below is an example illustrating the need for applying a different set of MHL values for low intensity ECPL processes.

An ICM&M video was captured while curing a square block with a DMD pattern of 250×250 square bitmap under UV exposure (intensity at 5% iris level) for 26 seconds. In Figure 40 (a), about 2.5 cycles could be seen with a naked eye. Two sets of MHL were applied for rolling fit, and both could fit the raw data well as shown in the red curve. However, the ICM&M using MHL of 32 or 48 adaptively as previously presented would estimate the total phase angle to be 4.02 cycles as shown in Figure 40 (b), and the insufficient window wrongly estimated the frequency around 0.35 Hz, which is higher than the naked-eye observation of about 0.2 Hz. Therefore, a longer MHL is proposed as a solution to provide an accurate estimation of curing frequency. Figure 40 (c) shows the

result of applying a set of (MHL, half life): (64,10) or (96, 20) adaptively for the curing window and (128,20) or (192,30) adaptively for dark curing, and the estimated frequency was correctly around 0.2 Hz totaling to 2.3 cycle which agrees with the visible counts in the grayscale plot.

### 6.5.3 Outlier frequency detection and treatment

The instantaneous frequency is the most critical key in height computation, however it is not uncommon to encounter some computation limitations due to process noise and algorithm inefficiency, which may cause failed and/or unrealistic values.

Throughout the process, an outlier detection scheme was used to filter out the small-amplitude oscillations which are most likely stochastic noise rather than curing frequency. A critical oscillation amplitude for the curing window,  $I_{1c}^c$ , is used as a gauge to aid the frequency outlier detection in the curing window. A criterion of  $I_1 < I_{1c}^c$  is used to determine and remove outlier frequency. In this study,  $I_{1c}^c$  is chosen as 5, smaller than the critical AC amplitude in the incubation stage  $I_{1c}^i = 10$ , because unlike the incubation stage, the curing window sometimes does feature small amplitude (around 10) oscillation and too bold removal of false outliers risks a big loss of measurement accuracy.

As a recommendation for future work, instead of simply zeroing out the detected meaningless frequency, one may replace it with a prediction inferred from previous reference data using outlier treatment methods such as nearest neighbor classification and moving average [82].

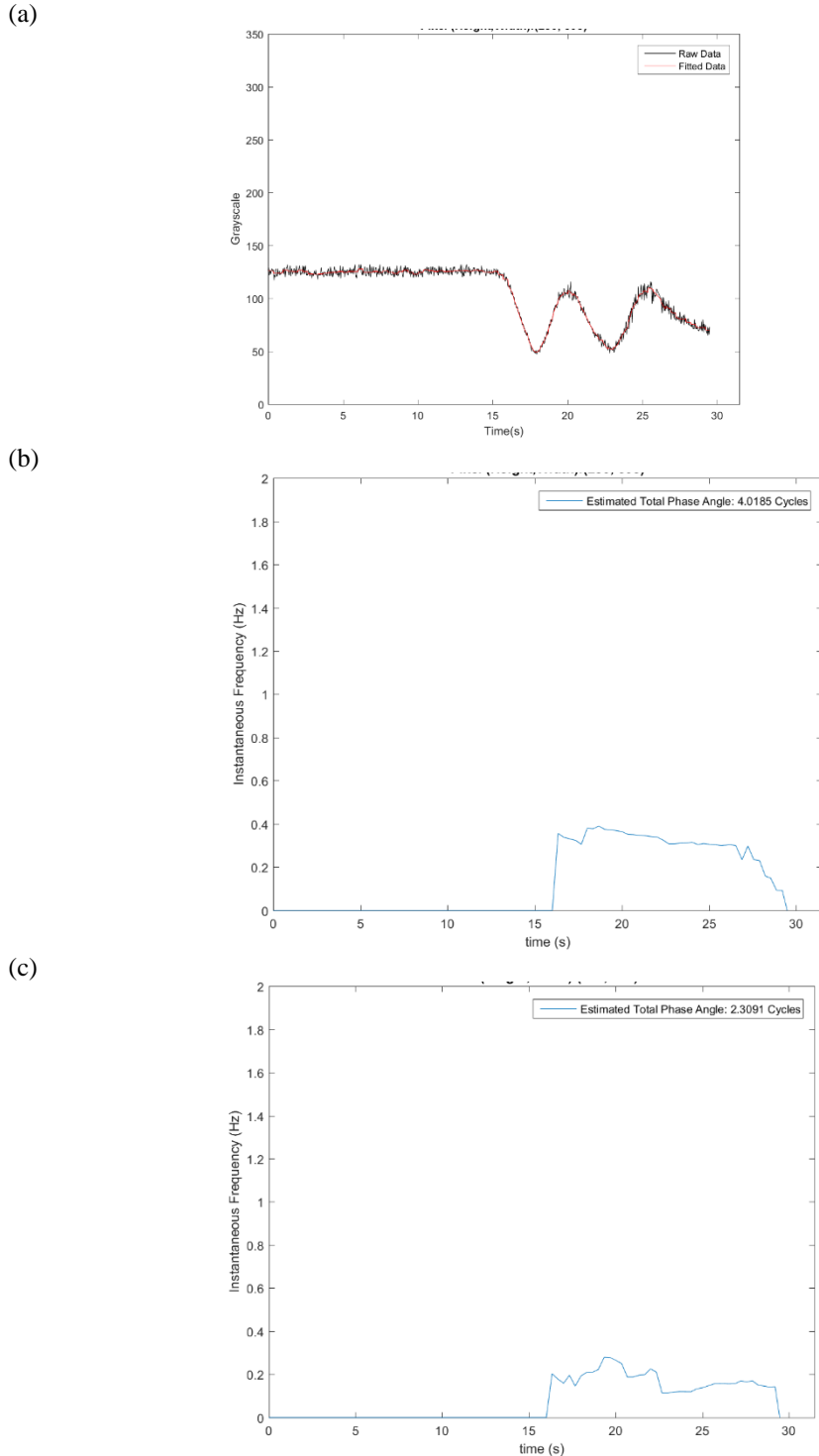


Figure 40. MHL effect in ICM&M estimation for low intensity ECPL process (a) a typical pixel's time sequence of grayscale in the ECPL process with UV iris level at 5%, black curve is the preprocessed raw data and red curve is the fitted data; (b) estimated frequency and phase angle using MHL (32 or 48 adaptively) as in ECPL process with 10-40% UV iris level; (c) estimated frequency and phase angle using double MHL (64 or 96 adaptively).

#### 6.5.4 Summary and recommendation

Herein, with the adaptive curve fitting and outlier removal for the curing window data on a rolling basis, frequencies have been obtained.

It is noted that the adaptive curve fitting scheme using R-square as criterion can not necessarily guarantee the true frequency to be fitted. The issue is evident in Figure 39 (bottom graph), where the estimated frequency, rather than falling continuously, abnormally hikes up to about 0.2 Hz, at the tailing period. It was because the initial curve fitting used 128 as MHL for fitting to the dark curing data and it automatically stopped after the first trial due to a satisfied R-square (above 0.95) achieved. However, it was found that had the algorithm proceeded with a longer MHL of 192, the frequency could be fitted to be lower, about 0.1 Hz, which matches the resting period data better. Hence, the adaptive mechanism for judging a good fitting should be improved further not to just considering about the R-square value, but also the true nature underlying the data. It is recommended to use a distance-based algorithm to sift the good fitting by comparing the currently fitted frequency with a reference, which could be derived with another data mining task of exploring the secondary dataset of online fitted frequencies. As a complement with the R-square criterion, the computationally learned reference frequency from previous data could enable a more powerful adaptive estimator for current frequency. The advanced algorithms could be more computationally expensive; hence the study would stick to the current pragmatic and effective algorithms for ICM&M.

#### 6.6 Evaluating the total phase change

With the instantaneous frequency estimated by the ICM&M data mining, numerical integration is adopted to evaluate the total phase changed during the EPCL process as the cumulative term  $\sum_i T_i f_i$  in Equation ( 14 ).

### 6.6.1 Integration timestep

In the ICM&M data collection, the nominal acquisition rate is set at 30 fps. However, the image acquisition is not a guaranteed equally spaced sampling process. One reason is that the camera could capture faster or slower depending on the system operation, hence it adjusts frequently to meet the preset timer. Another reason is that the high acquisition throughput could force the system to drop some frames occasionally due to the data transmission and memory buffer constraints. Furthermore, in real-time implementation, the acquisition rate could be varying more easily due to potential interrupts by online data analysis. Consequently, it would be inaccurate to apply a constant integration time step by simply assuming evenly spaced acquisition and inverting it.

The actual time interval between consecutive frames should be calculated using timestamp of the acquired frame. By recording the time when each frame is captured by camera, i.e., the image's timestamp, the integration time interval for the term  $T_i$  in sensor model Equation ( 14 ) could be calculated. This practice ensures that the analysis is immune to the unevenly sampled data or missing frames during acquisition.

In MATLAB, there are two methods to time the image acquisition. The real time measurement uses a timer of "tic toc" to calculate the elapsed time from the first frame to each new frame. MATLAB also provides a function of "getdata" to get the exact timestamp of each image acquired, which function however takes significant long time of about 27ms compared with "tic toc" that takes only a few milliseconds. For the sake of computation speed, the study used the timer function of "tic toc", which was found to output time intervals very close to the values from the "getdata" function, but still could be an error source reside in the software application.

## 6.6.2 Integration method

The phase angle is time integral of the frequency. Algorithms for one-step techniques such as Euler's method are extremely simple to program. Both specified rectangle (also Backward Euler's method) and trapezoidal methods have the general form:  $\text{New value} = \text{old value} + \text{slop} \times \text{step size}$ . The only way in which the methods differ is the calculation of the slope [86].

To demonstrate, the section presented an example ICM&M video that was recorded while a square block was curing under 22% UV iris level exposure for 12 seconds with a DMD mask of  $200 \times 200$  pixels. bitmap. A representative pixel (height 220, width 310) was analyzed, and its grayscale data is shown in Figure 41.

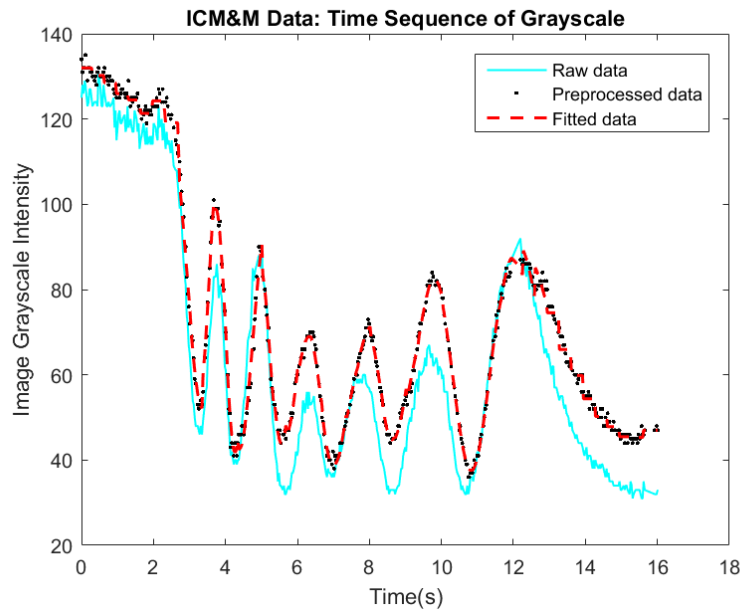


Figure 41. Integration methods: ICM&M data of a representative pixel

The estimated instantaneous frequencies from the pixel's time sequence of grayscale are shown in Figure 42 (black circles). It is noted that the time intervals between consecutive estimations, which were run every 10 frames, are not necessarily constant, especially at 12 second when the hardware operation of shutting down UV lamp interrupted the acquisition.

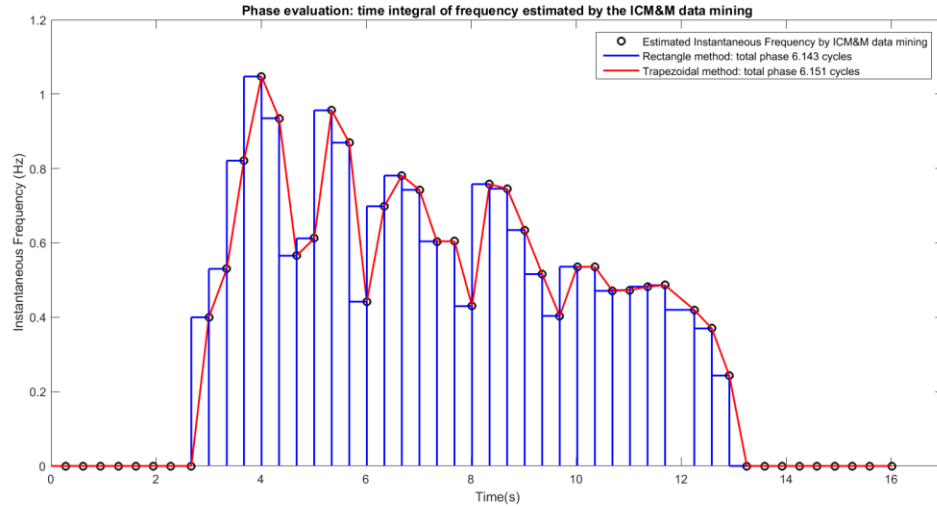


Figure 42. Phase evaluation: time integral of the frequencies which are estimated by the ICM&M data mining

Geometrically, the phase is the area under the frequency time curve. Integration with rectangle rule is straightforward, for it directly adds up the product of the fitted frequency from the current window of data and the time duration of the window, as shown with the blue lines in Figure 42. The rectangle method for ICM&M frequency-time curve approximates the area by drawing rectangles using the right corner of the divided strips, and could be pretty accurate within small time step. Integration with trapezoidal rule approximates the region under the frequency graph with the average of current frequency and previous frequency, as shown with the red lines in Figure 42. The trapezoidal rule utilizes frequencies derived from data points in both current and previous time windows, that is, involves more history data, hence, it might not reflect the current window's dynamics as much as the rectangle rule could. However, trapezoidal rule could provide robustness in case that outlier occurs in the current estimation and previous estimation could mitigate the error. In Figure 42, the two methods resulted in very similar phase values.

A broader comparison was made by measuring a horizontal profile line. Figure 43 shows the last interferogram of the video. The pixels located at height 220 and width



from 245 to 365 at an interval of 5 pixels, totally 25 pixels, were measured by the ICM&M method with the two different integration methods. In Figure 44 all the pixels' phases are plotted comparing the two integration methods, and it is clear that the resulted phase from rectangle rule and trapezoidal rule are very close to each other. As shown in Table 8, the two integration methods have very similar output of average phase and thus similar final measured height by Equation ( 14 ), and the rectangle slightly outperformed the trapezoidal in terms of the error relative to microscope measurement.

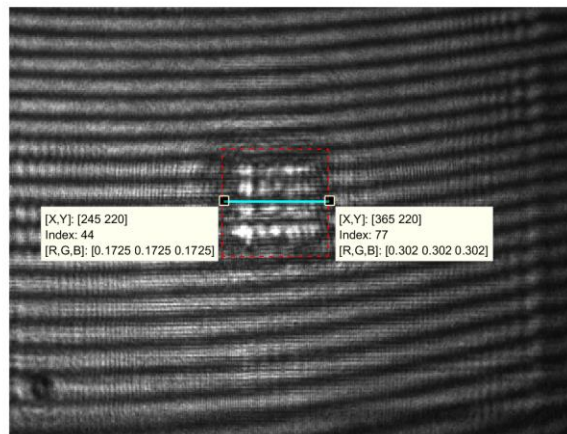


Figure 43. Selected ROI pixels in the interferogram - profile line to measure

Table 8. Comparing integration methods for profile line measurement

Integration Method	ICM&M Phase (cycle)	ICM&M Measured Height ( $\mu\text{m}$ )	Microscope Measured Height ( $\mu\text{m}$ )	Relative Error
Trapezoidal	6.156	73.756	74.643	-1.19%
Rectangle	6.162	73.834	74.643	-1.08%

As a conclusion, the example analysis has demonstrated that, between the rectangle and trapezoidal rules, each method's strength seemed to offset its weakness, and one is not particularly preferable than the other in current ICM&M practice. However, in future, with more computation power available and more advanced estimation algorithms, the rectangle rule might dominate as it could fulfill better the concept of instantaneous frequency which is the core of the ICM&M sensor model.

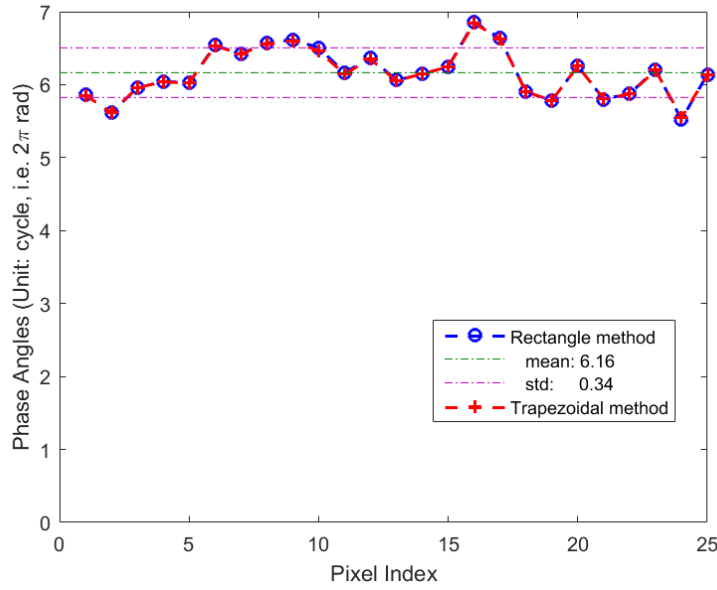


Figure 44. Phase evaluated at individual pixel in ROI by two integration methods

### 6.6.3 Error analysis of ICM&M numerical integration

The ICM&M estimated instantaneous frequency time curve, which embodies the first derivative of the curing height, is varying, indicating that there could be some measurement errors due to the Euler's method. Please note that there is no explicit curing height function available for the continuous ECPL process and the derivative is only estimated discretely. Since there is no true value available a priori for the curing velocity and height, the true value of second order derivative of the curing rate  $\dot{Z}''(\xi)$  is unknown but needed to estimate the global error associated with the Euler's method. One must apply techniques such as average second derivative of the curing velocity function  $\overline{\dot{Z}''}(t)$  to obtain an indirect estimate of the errors involved [86].

Hence, the approximate error  $E_a$  in cured height estimation with the first-order Euler's method is calculated as below Equation ( 31 ) [86].

$$E_a \cong -\frac{T}{12} \cdot \dot{Z}''(\xi) \cdot (T_i)^2 \cong -\frac{T}{12} \cdot \overline{\dot{Z}''}(t) \cdot (T_i)^2 \cong -\frac{T}{12} \cdot \frac{\overline{f''}\lambda}{2(n_m - n_l)} \cdot (T_i)^2 \quad (21)$$

where  $T$  is the total curing time,  $T_i$  is the average time interval,  $Z$  is the cured height,  $f$  is the instantaneous frequency,  $\overline{f''}$  is the average second derivative of instantaneous frequency,  $\xi$  and  $t$  are time variables,  $\lambda$  is the laser wavelength,  $n_m$  and  $n_l$  are mean solid and liquid refractive index, respectively.

Centered finite divided differences are used to estimate the derivative for each interval between the data points of estimated instantaneous frequency. The first and second derivatives of instantaneous frequency,  $f'$  and  $f''$  are approximated by divided differences of the ICM&M estimated instantaneous frequencies as shown in Equations ( 22 ) and ( 23 ). Thereby, the average second derivative of instantaneous frequency  $\overline{f''}$  required by Equation ( 21 ) is estimated as shown in Equation ( 24 ).

$$f'(t_i) \cong \frac{f(t_{i+1}) - f(t_i)}{t_{i+1} - t_i} \quad (22)$$

$$f''(t_i) \cong \frac{f'(t_{i+1}) - f'(t_i)}{t_{i+1} - t_i} \quad (23)$$

$$\overline{f''} \cong \frac{\sum_{i=1}^n f''(t_i)}{n} \quad (24)$$

Taking the same pixel analyzed in Figure 41 and Figure 42 as an example, the error caused by the first-order integration method is estimated with the aid of Equations ( 21 ) - ( 24 ) as below.

$\overline{f''} \cong \frac{\sum_{i=1}^n f''(t_i)}{n} = -0.011374 \text{ Hz/s}^2$ , plugged into the following,

$$E_a \cong -\frac{T}{12} \cdot \frac{\overline{f''}\lambda}{2(n_m - n_l)} \cdot (T_i)^2 \cong -\frac{(12 \text{ s})}{12} \cdot \frac{(-0.011374 \frac{\text{Hz}}{\text{s}^2})(0.532 \mu\text{m})}{2(0.0222)} \cdot (0.3419 \text{ s})^2 = 0.016 \mu\text{m}.$$

The resultant error of only 0.016  $\mu\text{m}$ , compared to the microscope measurement of 74.643  $\mu\text{m}$ , is negligible. The entire line of pixels analyzed in Figure 44 is also investigated with the same error analysis, and the result is shown in Figure 45. It shows that the approximate error caused by first-order integration is within 0.05  $\mu\text{m}$ , not quite notable.

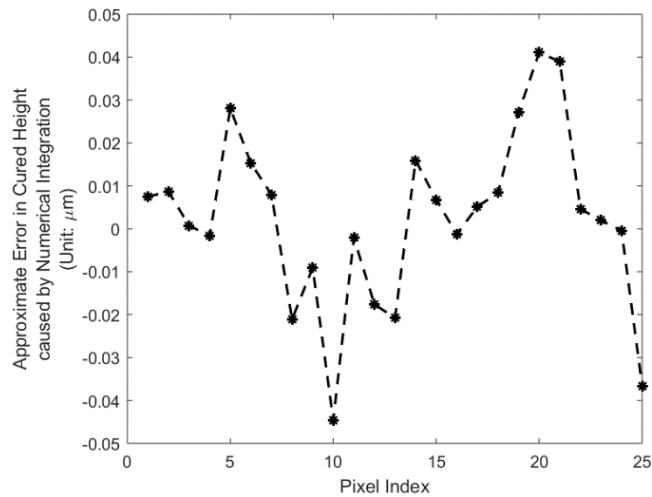


Figure 45. Error analysis of integration method

#### 6.6.4 Summary and recommendation

The Euler method will provide error-free predictions if the underlying function is linear, because for a straight line the second derivative would be zero [86]. Although the curing process is known to be nonlinear, the curing velocity reflected by the instantaneous frequency shows some downslope trend. The zig-zag in estimated instantaneous frequency time curve is primarily caused by the process noise, and the fluctuations could be statistically fit into an almost linear curve, which lead to a near-zero average second derivative  $\overline{f''}$  in Equation ( 24 ). That is why the error analysis result above is very small.

The small integration error could imply that in the curing process the part grows upward with an asymptotically uniform retarded motion, which could be observed from the instantaneous frequency as shown in Figure 33 and Figure 36. In theory [79], the curing process should be slowing down strictly, that is, the instantaneous frequency curve is expected to be a strictly decreasing function. However, the curve fitting sometimes might be fooled by the noise to fit into an irrational frequency, and the ICM&M estimated frequency curve could provide confusing up-and-downs as shown in Figure 42.

Nevertheless, the fluctuations could still be neutralized in statistical sense, as is resulted in the near-zero average second derivative  $\overline{f''}$  in Equation ( 24 ). Furthermore, during ICM&M practice, there are a good many pixels which present quality signal and are estimated properly by the algorithms to output a frequency curve nicely reducing along the time. These positive results help greatly verify the inference about the curing velocity pattern and the conclusion about the insignificant integration error.

Besides, a fundamental source of error in Euler's method is that the derivative at one end of the interval is assumed to apply across the entire interval. With the ICM&M approach, the instantaneous frequency is not estimated specifically at the endpoint of the interval, but evaluated using the entire segment of new data within that interval. Hence the estimated interval-wise frequency could be more representative than a point-specific derivative as used in the conventional Euler's method. Therefore, the numerical algorithm used in the ICM&M method would not expect as much error as one could think for traditional Euler's method.

The error may be reduced by decreasing the step size. However, too-small step size may lead to overfitting of the noise. Current measurement period of 0.333 second has shown proven accuracy, and experiments showed that half of it could improve a little bit, but no need to reduce further because it would not improve accuracy significantly anymore.

The Euler's method is a first-order technique, but works very well. Higher-order Runger-Kutta methods could be explored if necessary, however more computational effort will be needed.

## **6.7 Validating the ICM&M data mining algorithms for estimating the phase angle in sensor model**

To demonstrate how the overall data mining scheme of various data analysis algorithms presented above works behind the scene for ICM&M, this section presents

analysis result of three ICM&M videos which were captured while curing a square block with a DMD pattern of  $250 \times 250$  square bitmap under UV exposure, with intensity at 20%, 10% and 5% iris level, respectively. The first two samples were exposed by UV for 12 seconds, the third 26 seconds due to a low intensity.

A representative pixel was chosen in each sample video for the analysis. Figure 46 shows for each sample, in the upper-left graph the ICM&M data (raw data, preprocessed data and fitted data), in the bottom-left graph the estimated frequency evolution and total phase angle, in the upper-right graph the varying MHL and half life in the adaptive rolling fit, and in the bottom-right graph the R-square value as an indication for goodness of fitting.

(a)

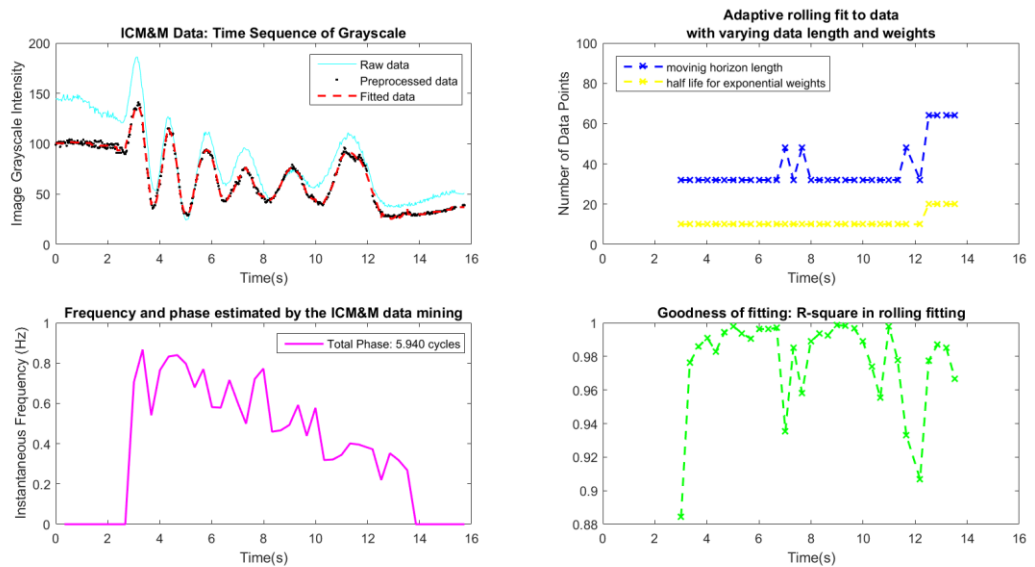
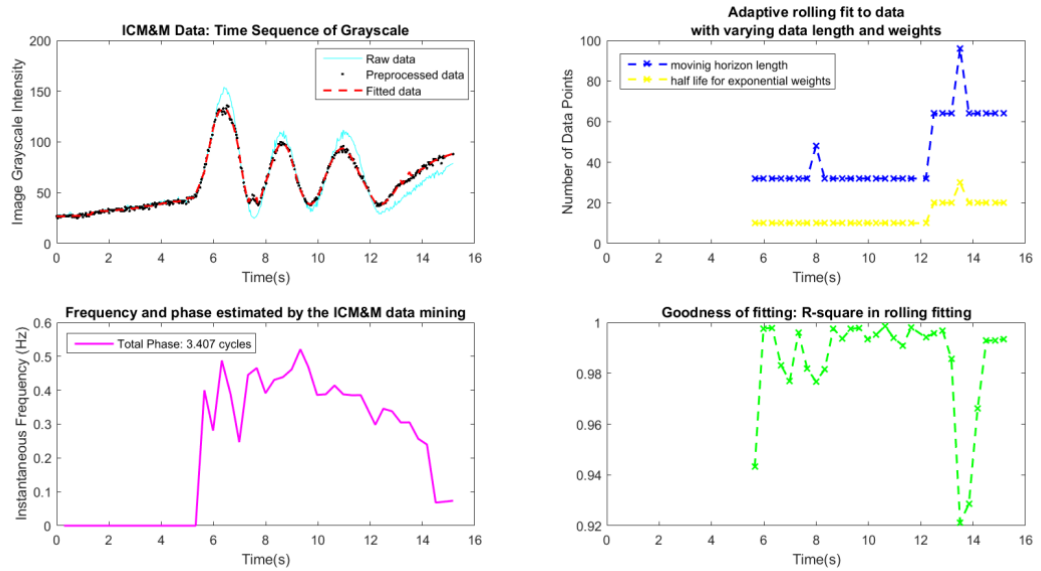


Figure 46. ICM&M data mining for online estimation of frequency and phase angle with adaptive rolling fit in ECPL experiments (a) UV iris level: 20%, Exposure time: 12s; (b) UV iris level: 10%, Exposure time: 12s; (c) UV iris level: 5%, Exposure time: 26s.

(b)



(c)

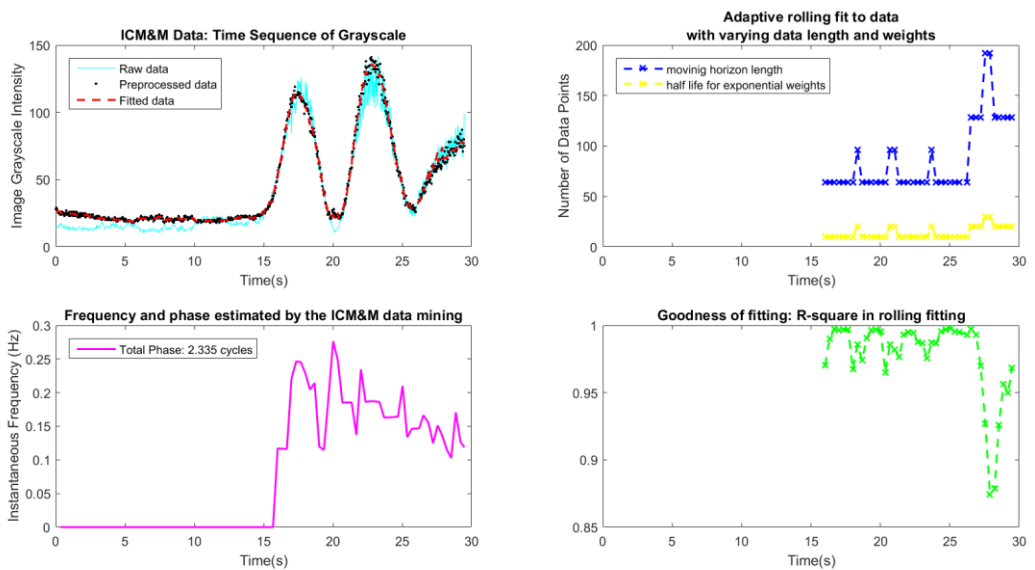


Figure 45 (continued). ICM&M data mining for online estimation of frequency and phase angle with adaptive rolling fit in ECPL experiments (a) UV iris level: 20%, Exposure time: 12s; (b) UV iris level: 10%, Exposure time: 12s; (c) UV iris level: 5%, Exposure time: 26s.

Firstly, in the plot of ICM&M data, generally speaking, the preprocessed data are smoother than raw data, and straighten out the incubation and resting stages. In Figure 46 (a), the preprocessed data enhances the pattern of oscillation at 10 seconds; while in Figure 46 (b), the preprocessed data do not model the signal well at 7.5 seconds by

creating a tiny bump. It confirms that the image median filter could bring in some undesired noise and affect the accuracy, and a more advanced filter could be used in future to solve this problem. Herein, the benefits outweigh the harm by using the presented preprocessing method in the dissertation.

Secondly, the data mining results of evolving frequency (magenta curves) in Figure 46, show that the statistics based classification algorithm could detect the curing window that is consistent with the grayscale plots. Please note that the “fourier1” curve fitting is only employed for the curing process, hence in the MHL and R-square plots, the identified incubation and resting stages are blank.

Thirdly, the moving horizon exponentially weighted “fourier1” curve fitting, equipped with the adaptive scheme of changing MHL (blue lines in Figure 46) with thoughtful values works in all the three examples to maintain high R-square (mostly above 0.95 and almost all above 0.9 as shown in green curves in Figure 46), ensuring good fitting throughout the process. Identifying when the MHL requires adjustment completely depends on the data and the process. It mainly works at the transition time from exposed curing to dark curing, e.g., when the UV lamp was turned off at 12 seconds for the first two experiments and 26 seconds for the third, as one could see from blue curves in Figure 46, respectively. The half life is also adjusted based on the MHL as shown in the yellow curve.

The extended MHL and half life in dark curing are especially useful when the resting period is not present or could not be identified. A near zero frequency estimated in the tailing region would help mitigate the issue. In Figure 46 (b) and (c), the resting stage was not identified out due to the sloping tail, but low frequency was fitted at the end of curing thus the noise in the supposed-to-be flat resting period would not introduce significant frequencies in the phase calculation.



Lastly, the numerically integrated phase angle, geometrically the area under the magenta curve in the frequency plot, agrees well with the counts of visible cycles in the grayscale plot.

## **6.8 Measurement intervals**

From the point of view of studying the potential accuracy of measurements, it is important to emphasize that all physical systems accuracy studied have a finite extent both in space and time, and all measurands are averaged with respect to these space volume and time interval [87]. Applying the ICM&M method for measuring part height, also needs considering about issues from measurement intervals, both spatially and temporally, particularly in order to strike a compromise between measurement accuracy and speed for the ultimate goal of real-time process measurement under realistic constraints of hardware speed and computation power. This section discusses about choosing appropriate spatial interval and adequate temporal interval to increase measurement efficiency without affecting accuracy significantly.

### **6.8.1 Spatial size reduction: adjacent pixels group together**

Spatial interval could be determined by the filter span (e.g.,  $5 \times 5$ ) used in the preprocessing, and it was experimentally found that measuring every five pixels would not affect the accuracy significantly due to proximity similarity especially in the studied case of curing flat top parts. Neighboring pixels are similar and would provide too much redundant information. It is acceptable to skip the redundant measurements by selectively measuring at an interval of every several pixels.

### **6.8.2 Measurement period**

First of all, in the ICM&M method, measurement period could be estimated by camera acquisition rate (e.g. 30 fps) and number of frames per run of measurement as shown in Equation ( 25 ). Both determine the signal quality and the measurement

accuracy. The base frequency less than 1 Hz means that measuring several times per second could be sufficient to capture the process dynamics. In this study, with approximately 30 fps acquisition, we measured the cured height by evaluating the instantaneous frequency after acquiring every 10 frames, i.e., measurement period is 10 frames per measurement / 30 fps = 0.333 second which could sufficiently detect a change in instantaneous frequency of the curing process.

$$T_{meas} \cong N_m / f_a \quad (25)$$

where,  $T_{meas}$  is the measurement period,  $N_m$  is the number of frames newly acquired in each run of measuring the current cured height with latest estimated frequency,  $f_a$  is the ICM&M camera's acquisition frequency (unit: frames per second).

Meanwhile, the basic scheme of rolling fit for instantaneous frequency requires sufficient sampling data points to evaluate the frequency for a brief time window. A higher than minimum sampling frequency would help greatly signaling the process dynamics, reduce the chance of aliasing frequency, and enables a more accurate estimation of the instantaneous frequency in the sensor model. We did try lower acquisition rate under 10 fps (about 1s per run of measurement based on Equation ( 25 )), and the signal of oscillating grayscales was skewed resulting in extensive measurement error. Even acquisition at 15 fps (about 0.667s per run of measurement based on Equation ( 25 )), performed better and under 10 fps, but still not as well as 30fps. Besides, in reality missing frames may happen due to hardware and software limitations, a slower acquisition would suffer more from the loss of frames and tend to distort the signal.

The ICM&M sensor model assumptions will hold better for smaller time steps. In mathematic theory, the smaller the measurement period is, the more precise the measurement is. In reality, a smaller sampling window in a single run of estimation could be more vulnerable to noise and could not represent a larger-scale trend. Besides, frequent measurement in real time would demand for fast computation so as not to hinder the simultaneous data acquisition. A compromise is made between principle and practice

by setting the measurement period to be 10 samples of data points (i.e. frames) per run of measurement for the study with a nominal image acquisition rate at 30 frames per second. Please note that the measurement period in this study is in terms of the number of samples per measurement, rather than conventionally time interval per measurement. Since the image acquisition rate is subject to change, the sampling space is therefore not uniform, and the measurement period has a fixed number of samples but non-constant time step. In the offline ICM&M experiments as presented in Chapter 8, a rough estimation of measurement period in terms of time is  $10/30 = 0.333$  second per measurement.

### **6.9 Aggregating data for final height estimation**

Aggregate data are commonly used for measuring practice improvement. In statistics, when data are aggregated, groups of observations are replaced with summary statistics based on those observations. In this study, aggregate data are defined as ICM&M resultant data of cured heights not limited to one single voxel, but all the voxels that are tracked across the region of interest (ROI). Without aggregate data, outcomes from mining multiple pixels' ICM&M data cannot be compared to a standard measurement of a cured part's height profile from a confocal microscope. There are several issues that complicate the gathering of aggregate data, including outlier data and the process of comparison to microscope images.

In this study, the average height of the ROI is of the greatest interest and is the easiest to be compared with the microscope measured height profile. In future, if a close-up profile for each voxel is needed, outlier detection and treatment algorithms such as proximity-based approaches [83] are recommended for a robust estimation of individual voxel height.

Given a dataset of estimated voxel heights derived from the abovementioned ICM&M method, this section aims to retrieve the attribute of the cured part height by computing an aggregate numeric representation.

### **6.9.1 Outliers in cured height**

There are several definitions for outliers. One of the more widely accepted interpretations on outliers is “an observation (or subset of observations) which appears to be inconsistent with the remainder of that set of data [88]”. However, the identification of outliers in data sets is far from clear given that suspicious observations may arise from low probability values from the same distribution or perfectly valid extreme values (tails) for example.

Figure 47 illustrates the causes and classification of outliers in cured height. In the real world, non-outliers in the ECPL output of cured part height are from the normal process variations that are present as real surface roughness. Outliers in the ECPL process output are produced from abnormal process failures (e.g. DMD mask defection and optical setup misalignment) that induce physical defects in cured parts. With the ICM&M estimated height data, suspicious outliers could be either positive outliers or negative outliers but prone to be falsely identified. The false positive and negative outliers stem from bad signal data from interferograms, and or wrong estimation for example obviously wrong counts of the phase cycles.

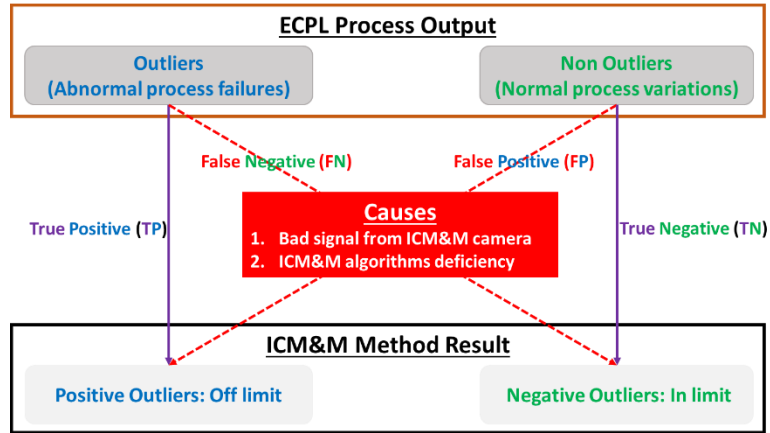


Figure 47. Causes and classification of outliers in cured height

The root cause of discrepancies in ICM&M estimated heights is the acquired low-quality interferograms, which might be disguised with speckles due to multiple scattering within the glass substrate and resin material leading to extra peaks that can skew the fitted result [89]. Noise could be caused by micro particles reaction and interaction that influences the optical behavior in the ECPL process. Another cause is the hardware camera which fails to record high-quality interferograms, due to for example heating that affects the electronics. Regardless of the noise source, artificial data techniques can only remedy to a certain extent but cannot completely remove the bad signal issues.

Another significant source of outliers is the ICM&M sensor model, which is subject to some physical principle limits. The natural limitations are due to the fluctuation phenomena connected with molecular-kinetic substance structure and probably a more fundamental character connected with nano-scale material properties in the ECPL photopolymerization process.

Besides, the presented algorithms employed in the ICM&M system also produce some outliers. Like any concrete measurement needs some priori information [87], the ICM&M method needs a definite value of the refractive index in the sensor model, as well as empirical critical or bounding values for guiding the algorithms towards realistic solutions. The uncertainty in the pre-defined parameters for the ICM&M model and

algorithms can propagate into the measurement errors of final cured height resulting in outliers.

Outliers could be examined by comparing the ICM&M result against microscope measurement of the cured part, however it is impractical to compare voxel by voxel. Especially, for real-time ICM&M, there is neither time nor in-situ standard reference such as microscope for checking outliers. Therefore, a statistics based outlier detection method is needed to determine outliers in the ICM&M resultant data of cured heights. This study proposes a solution to reduce the effect of outliers in final average height estimation using robust statistics, which would mitigate the dilemma of removing/modifying observations that appear to be suspicious outliers.

### **6.9.2 Robust statistics used to estimate the average height**

While implementing ICM&M for the height of a cured part, to use multi-pixel average height is more representative and reliable than to use single pixel height because sometimes single pixel measurement may not be accurate due to low data quality or algorithm deficiency. Groups of pixels working in ensembles can create better predictions than one pixel alone. Therefore, robust multi-pixel measurement is applied for the ensemble average to infer the height of the cured block. To capture the grand average in the data, robust regression is an elegant candidate solution which up-weights the well-predicted cases and down-weights the poorly predicted cases [90].

Depending on the time and computing power constraints, it is often possible to make an informal assessment of the impact of the outliers by carrying out the analysis with and without the suspicious outliers [83]. As this study adopted offline analysis which was exempt from the computation constraints, regular statistics with equal weight to all data and robust statistics with discretion to outliers were both used to estimate the measurement distribution of cured height. Specifically, provided an ICM&M resultant dataset of estimated heights for ROI voxels, the regular statistics adopts traditional least

squares fitting by calculating the normal average and deviations with “mean” and “std” functions in MATLAB. The robust statistics is performed in MATLAB by a robust regression algorithm -“robustfit” [91], which also estimates the standard deviation ( $\sigma$ ) with the larger of robust estimate of  $\sigma$  and a weighted average of the root mean square errors (RMSE) from least square fitting and robust estimated  $\sigma$ .

To illustrate the usefulness of the robust statistics method, results from a series of experiments, which cured a square block with a DMD pattern of 250×250 square bitmap under various settings of UV exposure intensity and time, are presented in Figure 48. The experiment was designed to study exposure time and exposure intensity effects, and each experiment setting was repeated once to test the repeatability also. Please note that all cured parts were expected to be flat-top square blocks. More research results about the experiment were reported in Chapter 8 [92], and this dissertation reports only the result of robust regression for postprocessing the ICM&M resulted multiple voxel heights. The ICM&M video for each curing experiment was analyzed with a 145×145 pixels square ROI that approximated the cured shape in the interferogram. The ROI was measured with a measurement period at 10 frames per run and a spatial interval of five pixels. Hence, totally 900 pixels were measured for each cured part, and each pixel’s time series of grayscale were analyzed by the same ICM&M data mining procedure presented in the dissertation. All the cured part heights were also measured by an ex-situ confocal microscope, which did not directly provide variation in the height profile but only average values as shown in Figure 48 (green cross).

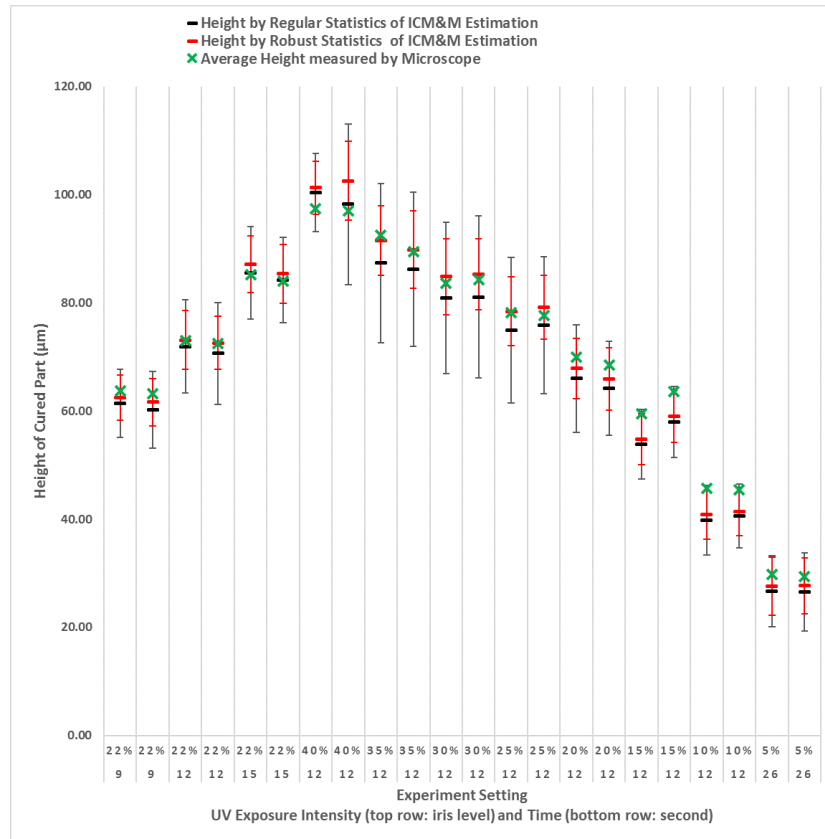


Figure 48. Regular statistics vs. Robust statistics: ICM&M estimated height for 22 cured samples – average with error bar (standard deviation across the cured part)

As shown in Figure 48, only in four out of the twenty-two experiments did the regular statistics give more accurate average height (bold black line) than the robust statistics did (bold red line). Although regular statistics could predict average height well sometimes, it is still inferior to robust statistics which is far more likely to provide less biased estimation of the average height.

Furthermore, by examining the exported microscope measurement data for some ECPL cured samples' representative profile lines, it was found that the sample standard deviation was around 8 µm. Though the study lacks comprehensive microscope data to get exact variation over the entire cured area for each sample, the statistics of variation of sampled line profiles measured for ECPL cured parts with the same setting and similar surface could offer a fairly good reference for the population standard deviation values.



In Figure 48, in each of the experiments, the regular statistics yielded a larger standard deviation (black error bar) than the robust statistics did (red error bar), confirming that the outliers could induce unnecessarily drastic variations in the heights. The robust statistics method estimated that all the samples have less than  $8\mu\text{m}$  deviation, which allows some room for the variations introduced by post-curing operations such as washing and cleaning, thus reaching the generally observed surface variation of  $8\mu\text{m}$  under microscope. For instance, the six experiments of 35%, 30% and 20% iris level curing had about  $14\mu\text{m}$  deviations by regular statistics and about  $6.6\mu\text{m}$  by robust statistics. Therefore, the robust statistics provide a more reasonable and realistic evaluation of the variations in cured height profile.

Since the robust regression estimation has proven accurately compared to the microscope measurement as demonstrated in Figure 48, the method of robust regression has been chosen to estimate the average and standard deviation of ICM&M measured height profile. Figure 49 shows, for each experiment presented as in Figure 48, the ICM&M resultant measurement dispersion, which reveals in some sense the measurement capability and uncertainty of the ICM&M method. The 1-sigma percentage means the portion of the total number of measured pixels (900 in this set of experiments) that has an ICM&M estimated height within one standard deviation away from the average height. In all the experiments, the 1,2 and 3 sigma distributions display quite consistent values around 68.7%, 89.8% and 94.2%, respectively as shown in Figure 49. The heights within one standard deviation have been found to agree with the cured part's actual height profile average and variations under the microscope. Hence, in the ICM&M estimation, data within one standard deviation are supposed to be true negative outliers, data off one standard deviation are assumed to be outliers that could be most likely true positive outliers. Improved hardware and software could help reduce the chance of false positive outliers which could be estimated better by the ICM&M data mining algorithms, and thereby increase its measurement capability.

The one-sigma percentage disclosed in Figure 49 has an important implication. From the perspective of measurement capability, for entire part measurement, it could mean that about 70% of the cured area could be measured accurately by the ICM&M method. In terms of measurement uncertainty, for individual voxel measurement; 70% chance is that its height could be measured accurately by the ICM&M method.

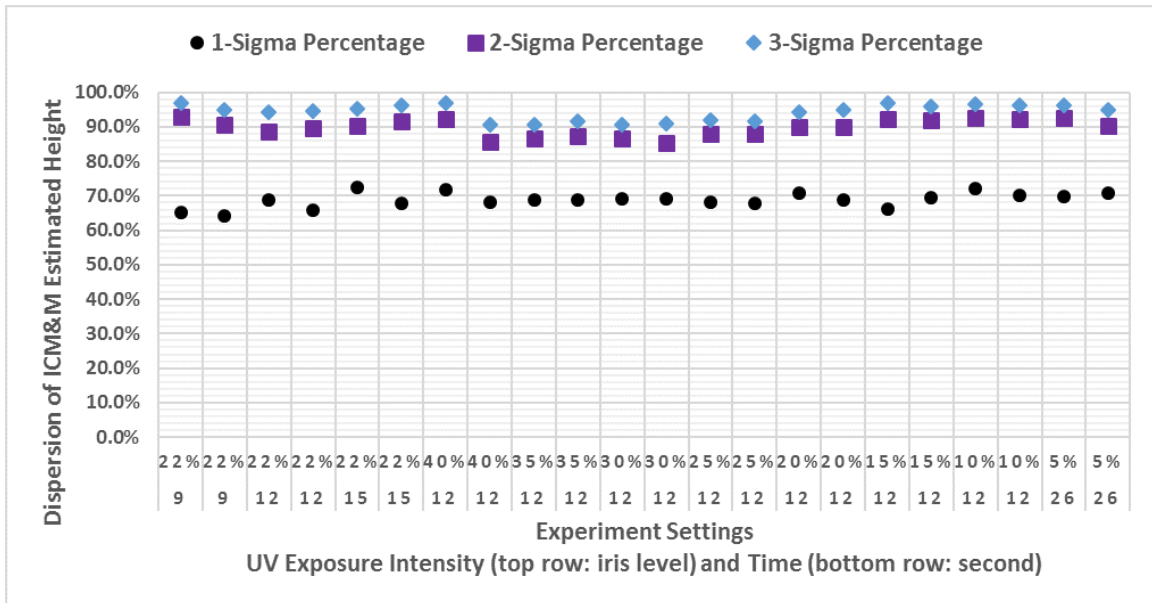


Figure 49. Measurement dispersion using ICM&M method

### 6.9.3 Summary and recommendation

It is important to investigate the causes of the possible outliers, removing only the data points clearly identified as outliers. Situations where the outliers' causes are only partially identified require sound judgment and a realistic assessment of the practical implications of retaining outliers. Given that their causes are not clearly determined, they should still be used in the data analysis. There are different techniques to identify suspicious observations that would require further analysis and also tests to determine if some observations are outliers. Nevertheless, it would be dangerous to blindly accept the result of a test or technique without the judgment of an expert given the underlying assumptions of the methods that may be violated by the real data [83].

In this study, for overall height profile measurement of a flat top square block, robust statistics is used to aggregate the data for average height measurement without examining every pixel's height. In the future, for individual voxel height measurement, one might apply outlier detection and treatment by the nearest neighbor method to enable a robust estimation of close-up height profiles. Investigation and implementation of such an outlier detection and correction for individual voxel measurement is presented in Section 9.5.2.2 while dealing with a more challenge data streamed from real-time implementation of the process measurement and control.

### **6.10 Summary of the data analysis algorithms for ICM&M**

The study successfully developed a feasible framework of ICM&M data mining algorithms, which was experimentally validated as being accurate enough to extract useful information as well as being robust enough to cope with imperfect data. The dissertation presents the detailed techniques and analysis about the ICM&M data mining algorithms, in order to provide insights into how the ICM&M method arrives at a measurement result and to provide greater confidence in the upcoming use of the ICM&M method for ECPL process measurement and control.

The entire chain of data mining that drives the methodology of ICM&M for the ECPL process and product measurement, as shown in Figure 50, consists of data filtering in preprocessing, classification methods to identify the process stages, adaptive curve fitting to estimate the instantaneous frequency of the curing window data, numerical integration to evaluate the total phase angle, conversion of the total phase angle with the sensor model to the desired result of cured height, and robust regression with outlier detection and treatment to estimate the average height profile in final aggregation of multiple voxels measurement. In Figure 50, green boxes represent the data flow, yellow boxes mark the algorithms, and gold boxes provide empirical input of some algorithm parameters.

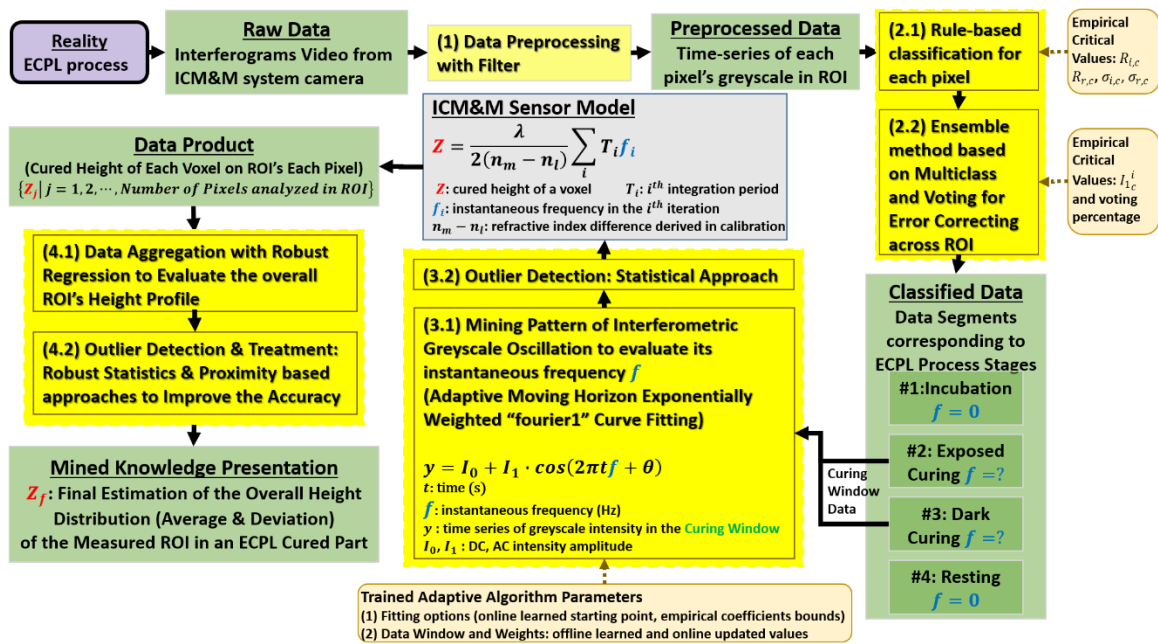


Figure 50. ICM&M data mining approach: data flow and algorithms

For the ICM&M data mining algorithms, there could be multiple fitting solutions to the same data if not enough constraints given. In order to improve the performance in data mining problems, one should build in as much prior knowledge as possible [81]. The techniques of specifying some empirical critical values for the statistical learning of the non-curing process stages, and applying updated empirical values for the adaptive curve fitting to the data in curing stages, contribute positively and significantly to force these algorithms to search for a more realistic analysis other than stopping at an arbitrary seemingly good result. It requires domain knowledge as well as explorative experiment to set practical guidance for the ICM&M data mining [81], which is critical in fulfilling the ICM&M method as both real-time and offline measurement system for the ECPL process. The system configurations and process parameters could affect the process dynamics, therefore, the empirical values might require tuning accordingly. Nevertheless, the fundamental principle and scheme of ICM&M algorithms are expected to be valid. Please note that all the empirical values used in this study were effective for the current ECPL

and ICM&M systems setup, and it is recommended that users conduct test experiments as necessary for identifying the specific system under investigation.

For the data-enabled ICM&M method, this study employed a modest number of basic data mining techniques and demonstrated the effectiveness and potential of the data mining approach in real-time monitoring and measurement for the ECPL process. The essential nature of our data analysis approach underlying the ICM&M method also subjects its real-time implementation to computation power limits. In future work, to enhance the accuracy and robustness and to realize real-time applications of the ICM&M method, more advanced data mining technologies including high performance computing could be utilized.

## **6.11 Chapter summary**

Both manufacturing and measurement are among the myriad of application fields where data mining applies. In this chapter, challenged by the size and noise of data, we explored the data analysis underpinning of the ICM&M method for ECPL process measurement.

A data mining approach for evaluating the interferometric curing monitoring and measuring (ICM&M) sensor model was developed, to enable a real-time measurement method of a photopolymer additive manufacturing process. The ICM&M algorithms were designed and verified to be intelligent, accurate, robust and efficient for handling large volume of stream data with process dynamics and noises. Algorithm parameter effects were studied, and empirical values obtained from experimental observations were incorporated to guarantee realistic solutions. The measurement characteristics of ICM&M accuracy, precision, capability and uncertainty were revealed by experiment data analysis.

Examples were provided to illustrate how each algorithm works for the specific goal at different ECPL process stages. Effectiveness and limitations were presented at the

end of each section to provide more insights about the algorithms. Data from a batch of twenty-two experiments were analyzed at the end, demonstrating that the overall data mining scheme could succeed in measuring the total cured height with good accuracy (mostly less than 5% relative errors) and more details about the measurement characteristics of the ICM&M method would be reported in Chapter 8. The reported algorithms, working together, enable about 70% of 900 voxels in each of the 22 cured parts being measured within reasonable deviation, and the 30% outliers turned out to not affect the accuracy of average height estimation due to the virtue of the robust algorithms. Improvements in hardware and software can definitely enhance the ICM&M performance. Besides, it was found that the computing time with all the algorithms for each run of frequency estimation is below 200 milliseconds depending on the data quality. Compared to the measurement period of around 330ms, the running time indicates that the developed algorithms can provide a feasible real-time measurement solution.

The ICM&M system combines information from raw camera data, insight from the sensor model and intelligence from data mining algorithms to reveal the ECPL process dynamics of evolving cured part dimensions, especially the vertical height profile. It benefits from the established sensor model with well-trained algorithms for the ICM&M data analysis. The developed ICM&M method visualizes the process dynamics, which is useful for modeling of photopolymerization based additive manufacturing processes. The real-time accessible sensor technology with the thoughtful ICM&M algorithms can enable deployment of advanced control technologies into the ECPL process, and can enhance the quality of fabricated parts.

Given the rather large number of data analysis algorithms that are currently available, there may not be a single best algorithm that produces the most accurate result with ICM&M. We selected these algorithms which are easy to understand, fast and interpretable, balancing the computation accuracy and computation expense.

Recommendations are made constantly during the presentation in hope to motivate further investigation for alternative algorithms given enhanced computation power and hardware performance is available in the future.

To conclude, this chapter develops a paradigm of merging the advances in data mining technologies with the urgent need for improvement of AM processes with real-time measurement and control. It is aimed to elaborate on how the time series of data is processed for addressing Research Question 1, specifically, the online parameter estimation algorithms that underpins the Research Hypothesis 1.

# **CHAPTER 7 COMPUTER IMPLEMENTATION FOR THE ECPL PROCESS MEASUREMENT & CONTROL**

The task of this chapter is to introduce an integral part for ECPL process measurement and control (M&C) – the software, denoted as “ECPL-M&C software” in this study. Both general and specific design requirements for metrology software are presented in Section 7.1 and 7.2, respectively. Taking into account the considerable effort required on creating, developing, debugging, studying and applying the code, the thesis presents detailed design and development of the ECPL-M&C software in Section 7.3. Motivation and visions for the software is revisited and conclusions are made in Section 7.4.

## **7.1 General design of software used in metrology**

For solving problems in metrology, software has been increasingly used for data acquisition and processing, transmitting, storing and presenting measurement results, along with auxiliary infrastructural device and information [87]. Requirements for measurement software include compatibility with hardware, adequacy of computation resource, integrity of code and configuration parameters. In real time scale, the permissible latency time for getting a measurement result is another important consideration. Errors of the software itself should be insignificant as compared to the transformed errors of input data and to the methodical errors of the algorithm.

## **7.2 Design a software for the integrated system of ECPL and ICM&M**

For ECPL process measurement and control, a software is needed to interface the ECPL system’s hardware equipment including the UV lamp, DMD and CCD camera for process operation, measurement and control. In Figure 51, the brown dashed lines indicate the communication between the software and hardware. The double arrows



between the app and the camera mean that the software could both send instructional signals to the camera and receive image data from it. The one-way arrow to UV light source and to DMD, respectively, means that it only write into the lamp and DMD without data feedback. As a console for transmitting commands and data, the software is also intended for all numerical computing needed for the process control.

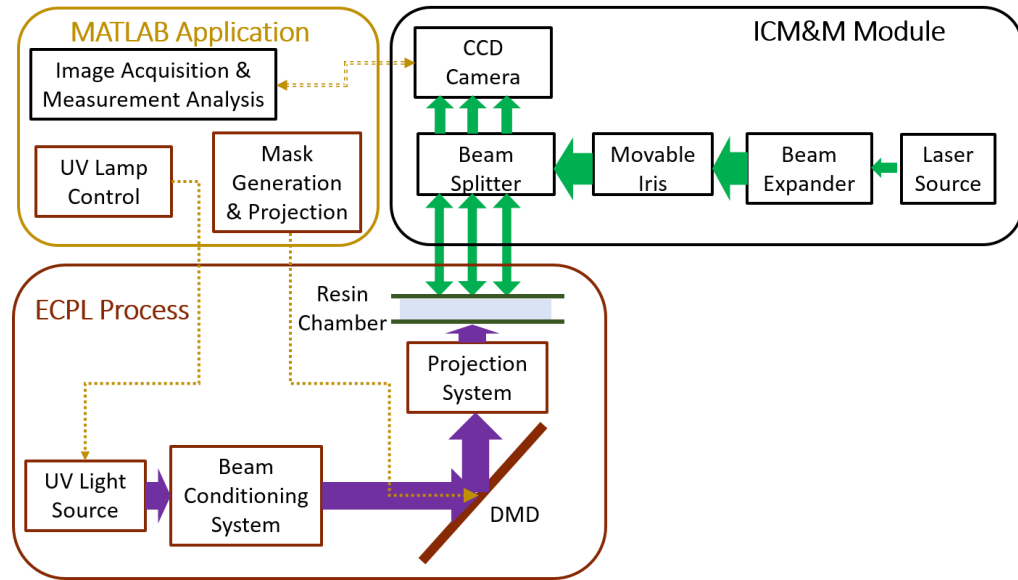


Figure 51. The integrated ECPL system: ECPL process, ICM&M module, and MATLAB software for ECPL M&C

The MATLAB application is referred to as “ECPL-M&C software” in the study, and designed with the specific functions as below.

1. Provides a human machine interface (HMI) to operate the whole system.
  - (1) For the ECPL process
    - a) Turns on / off the ECPL UV lamp (OmniCure® S2000) to start / stop the curing process.
    - b) Sets the UV iris level to manipulate the irradiation intensity for ECPL curing.
    - c) Generates cross-section bitmaps for the target 3D object.
    - d) Projects the time sequence of bitmaps onto DMD to obtain the specified thickness for each part cross-section.

- (2) For the ICM&M module
  - a) Starts / Stops the ICM&M camera.
  - b) Selects a region of interest (ROI) to analyze and measure.
  - c) Starts / stops image acquisition and analysis.
  - d) Writes the acquired images into a video file for recording the ECPL process dynamics.
  - e) Reports and saves process data and measurement results.
- 2. Performs all the computation for the ECPL process measurement and control.
  - (1) For measurement
    - a) Implement the ICM&M sensor model and algorithms to measure the ROI pixels cured height
    - b) Complement the ICM&M algorithms with data analysis of the estimated parameters and the resultant measurements to evaluate the cured height more accurately.
  - (2) For control
    - a) Implement the time control algorithm to derive the control input of exposure time for each bitmap.
    - b) Implement the intensity control algorithm to derive the control input of exposure intensity (i.e., UV iris level) for each bitmap.  
This task is out of the work scope of the research and will be incorporated in the future work.

## 7.3 Development of the ECPL-M&C software

### 7.3.1 Software tasks

A graphical user interface using the graphical user interface development environment (GUIDE) of MATLAB was created to implement the ICM&M method for the ECPL process. The application was designed to perform the following tasks.

- Visualization  
Build a graphical user interface to visualize the process interferograms and online measurement results.  
  
Provide user control components such as pushbuttons and edit boxes to operate the ECPL process and to streamline the process with the ICM&M acquisition and measurement analysis.
- Hardware connectivity  
Connect and communicate between the software application and hardware equipment including the ultraviolet (UV) lamp and DMD in the ECPL system as well as the CCD camera in the ICM&M system.
- Data management  
Create a MATLAB memory map file to log the acquired interferograms data and timestamps, process parameters such as the UV lamp iris level and exposure duration, and measurement parameters such as measurement period and calibrated refractive indices.
- Numerical computation  
Implement the ICM&M algorithms, and perform data analysis required for best estimation of the cured height profile of the ECPL cured part.
- Report generation  
Document and save into MAT-files all the data, curve fitting estimated parameters for the sensor model, along with the measurement results of the cured heights. Display and save the results of time-height curve and ROI height profile in figures.

### 7.3.2 Modularity and scalability

As shown in Figure 52, the application can be functionally modularized into two main parts – process measurement with ICM&M (green parts in the figure) and process control of ECPL (blue parts in the figure). The ICM&M part is further divided, based on usage, into offline ICM&M (brown in the figure) and real-time ICM&M (purple in the figure), both of which employ the same algorithms to analyze the interferograms data extracted from offline replay and real-time acquisition, respectively. The ECPL process part can be broken down into lateral control and vertical control sections. Each module is designed with considerable scalability to extend the software capability in future for full-field measurement and comprehensive control in fabricating complex 3D objects for real-world applications.

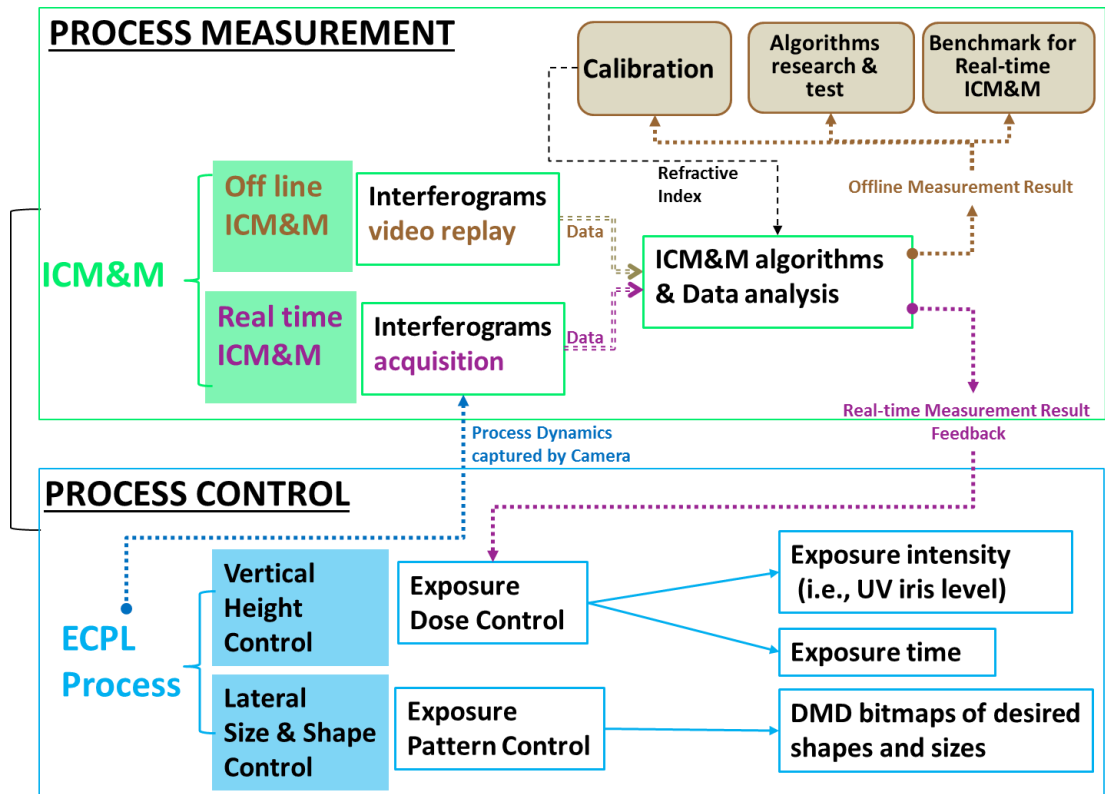


Figure 52. MATLAB application for the ECPL process measurement & control: functional modules

### 7.3.2.1 Software module for the ICM&M

The offline ICM&M utilizes a video record of interferograms captured when the ECPL process was curing a part to measure that cured part. The three brown blocks on the upper-right corner of Figure 52 states that the three main uses of the offline measurement result: 1) to calibrate the refractive index as explained in the ICM&M sensor model and calibration process; 2) to serve as a simulation analysis tool for the ICM&M algorithms development as shown in the “Algorithms research & test”; 3) to provide a benchmark unveiling the full measurement capability and accuracy without computation power limits effects that would make the real-time ICM&M underperform.

The real-time ICM&M features in-situ interferograms acquisition. In MATLAB, the “Image Acquisition Tool” provides an efficient workflow to solve the challenging imaging acquisition problem using the ICM&M system’s GigE vision camera. To use the specific ICM&M camera in MATLAB, the right hardware support packages for both “IP Camera” and “Gige Camera” must be installed so that the software can recognize the camera correctly and access to its attributes settings properly. It is worthy to point out that we initially used the "OS Generic Camera" hardware package which assumes wrongly the camera as "winvideo" and could not access fully or correctly to its attributes; and consequently we couldn't capture the whole curing area with a reasonable resolution. Another issue with the camera misidentification was that it was not stable in the camera output formats which cause trouble in our experiment of ICM&M. Appropriate handling of the ICM&M camera as a Gige IP camera helps integrate the ICM&M hardware with the ECPL system neatly in the software app. The application was ultimately programmed to be able to configure the camera attributes and acquire images with triggers. For the image acquisition, a timer function is used to regulate the acquisition speed in MATLAB.

The “ICM&M algorithms & Data analysis” section is coded to execute the ICM&M algorithms of moving horizon exponentially weighted Fourier curve fitting and numerical integration, along with some necessary data processing and analysis to better

estimate the cured height. It can analyze the intensity data for all pixels within the preset region of interest (ROI), which could be selected interactively by mouse dragging a rectangle on the interferogram or specified programmable by defining a matrix of interesting pixels' coordinates. For instances, after an interactive placement of a rectangle on the current axes, the analysis module can automate the data processing and measurement analysis for the rectangle's center pixel or corner pixels or horizontal centerline or vertical centerline or all of them at the same time. Alternatively, if an area of pixels is specified as the ROI in the code, the analysis module can output the area height profile correspondingly. It is worth to note that specifying ROI pixels in the code beforehand instead of in the GUI platform in real-time can facilitate continuous acquisition and logging. Conclusively, the application features wide measurement types including single point, discrete multi-point, line profile and area profile vertical height. It is scalable to full-field measurement as long as the computer has sufficiently fast processor and large memory.

#### 7.3.2.2 Software module for the ECPL: principle and practice

As stated, the ECPL process control consists of two general dimensions' control: the lateral control and the vertical control. This research focuses mainly on the vertical control and would address the lateral control only to some extent as necessary, because the vertical control is not as straightforward as the lateral control and presents more research interest and challenges. Besides, in cases of curing a 3D parts which can be discretized into vertical voxels, controlling the vertical height profile would have virtually rendered the lateral shape and surface profile.

The lateral control module aims to manipulate the size and shape of bitmap displayed on DMD which determines the cross-section of the cured part. It can provide a sequence of bitmaps with different sizes and/or shapes required to form a complex 3D object. In this study, experiment of curing rectangle blocks is used to test and validate the

process, but please be noted that a wide range of geometrical shapes bitmaps (e.g., circles) could be generated and employed in real applications and the software can easily be adapted and extended for more complex 3D objects curing.

The vertical control module, which is the primary research objective, controls the cured height of a voxel. A voxel is defined as a block growing on the resin substrate which is divided into pixels that are mapped to the interferogram pixels, so that the lateral size of the cured part corresponding to one interferogram pixel determines the lateral area resolution for a voxel.

In the study, a lateral control session with rectangle bitmap specification and generation, and a simple on-off control with the real-time ICM&M feedback intended for the vertical height control are included in the software application.

### **7.3.3 Graphical user interface**

Figure 53 shows the application's graphical user interface (GUI). To start with the application, one should select from the left-bottom dropdown menu "Real-time Measurement" or "Offline Measurement", for the former involves with real-time interferograms acquisition and simultaneous online measurement while the later replays off line an already acquired video of interferograms and performs ex-situ measurement.

"Measurement Parameters" as shown in the upper-right panel are always required beforehand and one can use the "Default" parameters which may provide a good set of starting values but may still need modifications, especially for the refractive indices values which are subject to change with materials and disturbances (e.g. oxygen diffusion and inhibition).

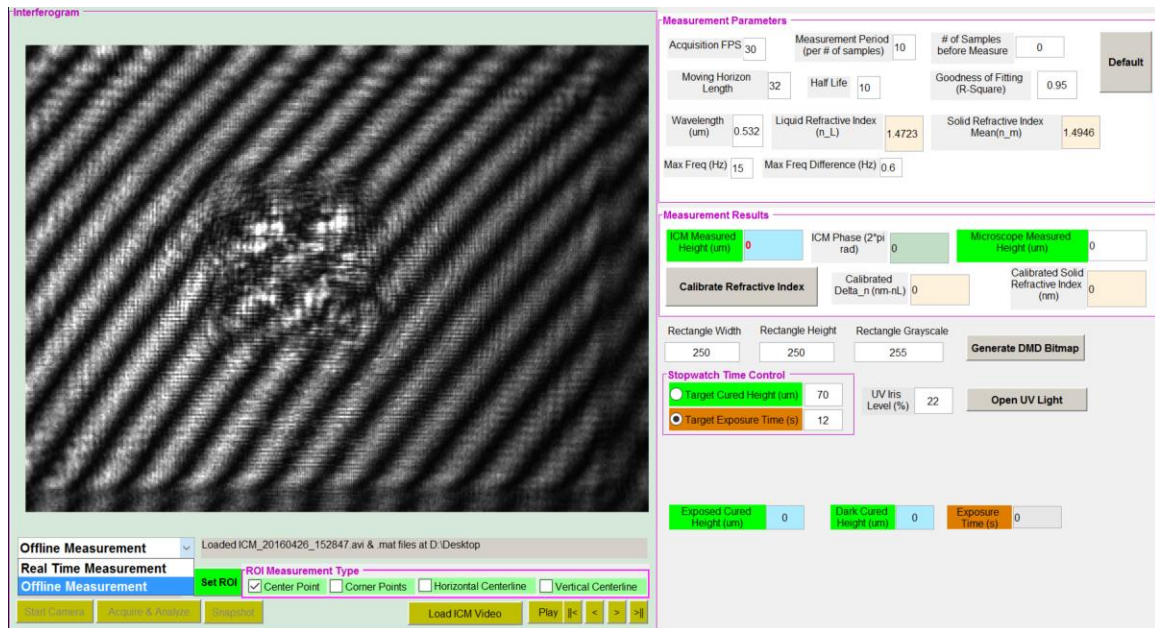


Figure 53. MATLAB application for the ECPL process measurement & control: Graphical User Interface

In the “Real-time Measurement” practice, one firstly presses the button “Start Camera” to set up the video input object in MATLAB and to configure the ICM&M camera setting, and can immediately preview images in the GUI axes. Secondly, click “Set ROI” to notify the application the pixels of interest for measurement analysis. Herein the ICM&M part is ready and the ECPL process part should be started with inputting the bitmap size and grayscales into the “Rectangle Width” and “Rectangle Height” boxes followed by pushing buttons of “Generate DMD Bitmap”. Please note that the application provides a rectangle bitmap of user-specified width, height and grayscale, for the sake of experiment simplification and validation efficiency, and can be easily extended to a series of various shape bitmaps in future. Two methods of exposure time control are provided for deciding when to turn off the UV lamp. One is simply a stopwatch control with preset target exposure time, the other a basic negative feedback control - “On/Off” control decided by whether or not the measured cured height has reached the setpoint of cured height. The user must select one of them in the experiment. Also, the UV iris level should be specified, otherwise “22” is used by default. Thirdly,



press “Acquire & Analyze” to get ready the image acquisition and measurement computation. Lastly, user needs to click “Open UV” to turn on the UV lamp, the UV light beam will be shaped by the DMD displaying the previously generated rectangle bitmap, and a rectangle block will be cured in the resin chamber. Meanwhile, the entire ECPL process should have been captured by the ICM&M module.

If the ROI is empty, only real-time acquisition without online measurement will be performed. In the validation of ICM&M method, due to the computer limitation, we did not set ROI for online ICM&M which would cause severe loss of frames during image acquisition and impair the performance evaluation of the ICM&M method. However, we later improved the software code with parallel computing and presented the real-time ICM&M results in the thesis.

In case of “Offline Measurement”, instead of starting camera, one firstly should load an acquired video of interferograms and associated timestamp file by pressing the button “Load ICM Video”. A toolbar of replaying video is provided for user to play or stop, and to play the first frame, the previous frame, next frame and last frame as shown at the bottom of GUI. Click “Play” and stop at the desired starting frame for measurement analysis, click “Set ROI” and “Play” again. Then the application will perform measurement analysis while playing the frames, which could be taken as a simulation of the “Real-time ICM&M” doing acquisition and analysis simultaneously.

#### **7.3.4 Data structure**

In MATLAB, “struct” and “cell” arrays are the most commonly used containers for storing heterogeneous data of different types and sizes. One most important data structure – the resultant data structure in the software program is introduced as below.

The measurement result, as stored in the variable “MeasureRet”, returns all the rolling fit coefficients, processed coefficients and online estimated heights. It is an nPOI-

by-1 structure array of all points measurement. Specifically, the result variable "MeasureRet" is a structure array including the following data:

- 1) nPOI: number of points of interest
- 2) RunNo: number of runs of online parameter estimation
- 3) "PixelHeightWidth": pixel's coordinate vector [height; width]
- 4) "PixelGrayscalesData": point data, i.e., time-series of pixel grayscale  
"PixelGrayscalesData\_Smooth": smooth data using a moving average filter.
- 5) "FittedCoeffs": coefficients returned by each run of rolling fit for each POI

"fourier1" returns 4 coefficients  $y=a_0+a_1*\cos(px)+b_1*\sin(px)$

Note: first set of coefficients is the initial values

The length of coefficients =  $4*(RunNo + 1)$  due to the initial value

FittedCoeffs = [a0; a1; b1; p].

6) "ProcessedCoeffs": Processed coefficients, will grow to be a 3-by-RunNo matrix

"ProcessedCoeffs" = [I0; I1; p], where I0 is the estimated baseline amplitude (DC), I1 is the estimated fringe amplitude (AC), and p is the estimated frequency.

Note:  $y=I_0+I_1*\cos(px+\phi)$ , the phase angle  $\phi$  is not of interest here, hence not stored in the data.

- 7) "CureFlags": Flag the curing window, i.e., mark the beginning of curing
- 8) "Times": RunNo-by-1 matrix, array of run time for each POI
- 9) "Heights": RunNo-by-1 matrix, estimated height at each run for each POI
- 10) "Freq\_w": RunNo-by-1 matrix, the real frequency " $\omega$ " of  $I_m = I_0 +$

$I_1*\cos(\omega t+\phi)$  at each run for each POI

### 7.3.5 Parallel computing

An easy and efficient data-parallel programming is essential and desired to fulfill the performance of real-time ICM&M and ECPL process control. MATLAB®

provides two main ways to take advantage of multicore and multiprocessor computers. By using the full computational power of your machine, one can run the MATLAB applications faster and more efficiently. One can run multiple MATLAB workers (MATLAB computational engines) on a single machine to execute applications in parallel, with “Parallel Computing Toolbox™” [93]. This approach allows one more control over the parallelism than with built-in multithreading, and is often used for coarser grained problems such as running parameter sweeps in parallel.

#### 7.3.5.1 Some key variables

##### (1) “**status**”

“status” is a global variable which conveys three important statuses – “measurement status”, “lastWriteFrameIdx” and “workerReady”.

- “measurement status”. 1: running, 0 stopped.
  1. Used in the timer function “processMeasureTimer”: if measurement is stopped, stop acquisition and writing frames and just preview.
  2. Used in "icm\_main\_worker.m" while loop, if measurement is running, keep the loop of measurement analysis.
  3. In "pb\_AcquireAVI\_Callback.m", set to be "0" when push button "Stop Acquisition"
  4. In "pb\_AcquireAVI\_Callback.m", set to be "1" when push button "Acquire & Analyze" and calls the function "icm\_init\_mem\_file.m" which actually initialize the status to be "1"
- “lastWriteFrameIdx”:

Used to mark the index number of previous frame for continue numbering the subsequently acquired frame.
- “workerReady”

In "pb\_AcquireAVI\_Callback.m", set to be "0" when push button "Acquire & Analyze" and calls the function "icm\_init\_mem\_file.m" which actually initialize the status to be "0".

Then still in "pb\_AcquireAVI\_Callback.m", it creates the batch job "icm\_main\_worker.m" which gets started and when ready tells GUI that worker is ready by setting the status to be "1".

In "pb\_AcquireAVI\_Callback.m", it waits until the status is set to be "1" and continues to proceed to notify the timer function for image acquisition by initializing the frame index, uvStatus and acquiring status, and image data matrix, and by enabling the UV Lamp Switch Button. Only when UV lamp is turned on, the acquisition would really start in the video timer function so that it can acquire the entire process from UV curing start till after curing stop.

## (2) “**handles.mmf**”

Memory-mapping is a mechanism that maps a portion of a file, or an entire file, on disk to a range of memory addresses within the MATLAB® address space. Then, MATLAB can access files on disk in the same way it accesses dynamic memory, accelerating file reading and writing. Memory-mapping allows you to work with data in a file as if it were a MATLAB array. In the real-time ICM&M app, the memory map file "icm\_comm.dat" plays a role of cache. The cache file is used for temporary storage of data and can be accessed more quickly than the main memory.

The global accessible variable "handles.mmf" stores the acquired images data and can be retrieved immediately by parallel thread for measurement analysis. It is initialized in the pushbutton "Acquire & Analyze" callback function, and written in the video timer function, and read in the batch job for measurement analysis.

### 7.3.5.2 Flow chart

Below presents a flowchart of the software to achieve real-time acquisition and measurement analysis of the interferograms from the ICM&M system for the ECPL process.

1. Before acquiring images using the Image Acquisition Toolbox, create a video input object.
2. Firstly, start camera and initialize acquisition parameters, region of interest (ROI) to measure, UV Lamp Status.
3. To generate timer events, we specify two things: what happens when it occurs, and how often it should occur. The TimerFcn property specifies the callback function to execute when a timer event occurs. A timer event occurs when the time period specified by the TimerPeriod property expires.

The callback function is responsible for triggering the acquisition and storing the frame into the AVI file. More details on how to use this callback can be found in the documentation.

#### 4. The Timer Callback Function

The following is a description of the callback function executed for each timer event.

- Snapshot a single frame
- Determine whether to keep the frame for analysis. If user has not pushed the button to start analyze and to open UV light yet, just preview without saving the frame for measurement analysis.
- In the timer function, when GUI pushbutton of "Acquire and Analyze" is pressed, the acquisition is officially started, and the GUI data "handles.dp.acquiring" is set true notifying the timer function to start acquisition rather than preview only. The timer function acquires latest frame by snapshot and display it on GUI axes, meanwhile it writes the

memory map file "handles.mmf" which data include image frame data, frame index, frame time stamp (time elapsed from the 1st frame), UV iris level (a metric for UV light intensity), UV lamp status of "On" or "Off", "snapTic" which starts a stopwatch timer to measure the delay between writing and reading the frame.

5. The pushbutton "Set ROI" will allow user to specify the region of interest (ROI) which include all the pixels to be measured for height profile. The ROI is a matrix of pixels coordinates [Height; Width]. The app will extract the time series of grayscales of the ROI pixels and measured the corresponding voxels height.

6. The pushbutton "Acquire & Analyze" will perform the following tasks.

- Initialize memory map file for GUI: "handles.mmf"
- Start a batch processing job as a main worker for data analysis and measurement calculation : "handles.job", which runs MATLAB script "icm\_main\_worker.m" with the curve fitting function "icmFit2.m" on the main worker.
- To expedite the measurement related analysis and computation, more workers may be needed to make into a parallel pool for the job in addition to the main worker running the batch job itself. The script "icm\_main\_worker.m" uses this pool for execution of statements "parfor" that is inside the batch code. The "parfor" loop iterates online parameter estimation for each pixel calling the core function of curve fitting "icmFit2.m" which is the most time-consuming.

Because the pool requires  $N$  (e.g.,  $N=2$  in this study) workers in addition to the worker running the batch, there must be at least  $N+1$  workers available on the cluster. One does not need a parallel pool already running to execute batch; and the new pool that batch creates is not related to a pool one might already have open. The default value is 0,

which causes the script or function to run on only a single worker without a parallel pool [94].

Therefore, a number of workers are assigned in the batch job as fitters to do the online parameter estimation by curve fitting for pixels in parallel loops. The fitters number is recommended to be the number of computer cores in local cluster to optimize the computer resource without causing adverse effect of overhead cost such as communication time. In this study, two fitters are assigned for "parfor" loop in MATLAB to calculate two pixels' cured height simultaneously. If multi-core computer with more computation power is provided, more workers might be available to accelerate the computation for more pixels in ICM&M analysis.

- Initialize the acquired frame index, UV status to be "0" which means the UV is not on yet, and acquiring status to "1" which will notify the video timer function to start acquisition.

The main worker function measures the height of each ROI pixel in a timely fashion per measurement period (e.g., 10 frames per run of measurement) and reports the time delay from writing to reading each frame, i.e., from acquiring to analyzing each frame, so as to provide insight about how the measurement is keeping in pace with the data acquisition. It also saves the metadata of ICM&M constant parameters, dynamic data including all frame data - time sequence of grayscales and frame index, measurement results including all curve fitting parameters and results, and matrix of time delays.

7. The pushbutton "Stop Acquisition" will perform the following tasks.
  - If the real-time measurement is running, notify the video timer function to stop acquisition and meanwhile notify the main worker to stop measurement

- Stop the camera and write the acquired images into a video file
- Save the constant parameters
- Wait for the batch job to be completed and display the result diary
- Denounce the mask of selected region of interest for measurement

8. When user stops the camera, all the frames are written into a video file by the writeVideo function.

The flowchart diagram is illustrated in Figure 54. The blue shape represents MATLAB graphical user interface (GUI) controls such as push buttons, edit boxes, and plot axes. The blue arrows depict the typical user manual operation that implements the ICM&M for an ECPL curing process which is shown in the brown block. The purple arrows direct toward the associated key functions. There are two main computing threads (shaded green boxes in the figure) running in the MATLAB: one is the video timer function for image acquisition at specified frequency, the other the batch process job which off-loads the execution of long-running computations of scripts and functions for online measurement analysis and controller computation in the background. The red fonts and arrows denote the key data of a memory map file that enables the communication between the parallel computing blocks. As shown in the brown shaded box related directly to the ECPL process, the user turns on the UV lamp by pushbutton “Open UV”, the ECPL process gets started, the image acquisition is also triggered, the memory map file is written and immediately read by the batch job for measurement. The online measurement is feedback into the controller which would calculate the input for the actuation. After the UV lamp is closed, dark curing occurs in place of exposed curing in the ECPL process, and the user could wait for a few seconds before stopping the acquisition to capture the entire process including the dark curing.



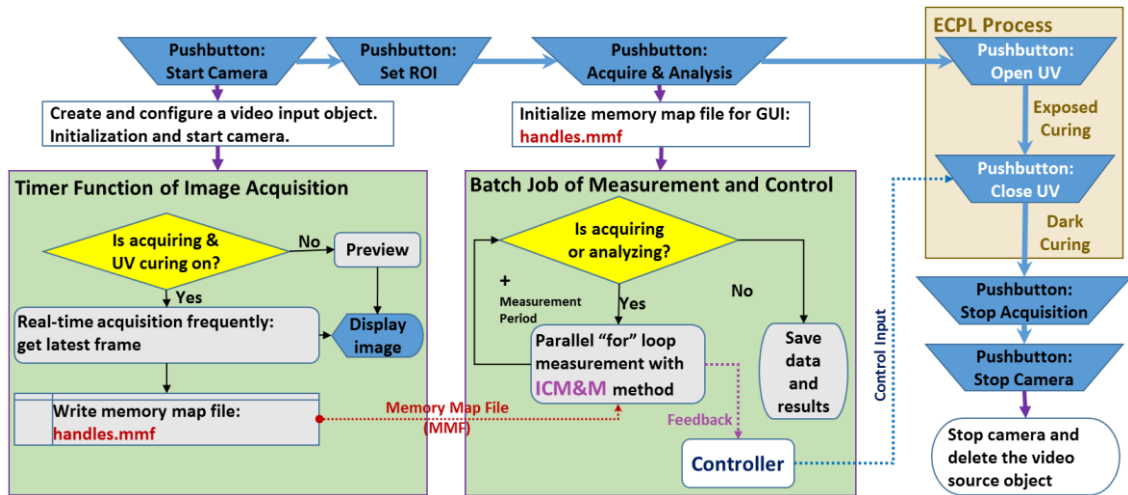


Figure 54. Flow Chart: Parallel Computing of Real-time measurement and control for the ECPL process

### 7.3.6 Computation environment

The application is executable in MATLAB R2015b for 64-bit Operating System and can be used in both experiment and post analysis. The real-time acquisition of the ECPL process was done in-situ on the lab desktop computer with a processor of Intel® Core(7M) i7 CPU 870 @2.93GHz 2.94GHz and an installed memory (RAM) of 16.0 GB (8.00 GB usable). All the offline ICM&M analysis was done on an ex-situ Lenovo laptop with Intel(R) Core(TM) i7-4510U CPU @ 2.00GHz 2.6 GHz and an installed memory (RAM) of 8.00 GB. Provided a more powerful multi-core processor and a high-speed camera, the ICM&M is expected to be able to run faster and more accurate measurement online with a full-field measurement capability if necessary.

## 7.4 Chapter summary

To implement ICM&M method, an application program – ECPL M&C software - was designed and created in MATLAB Graphical User Interface Development Environment (GUIDE). The app can be deployed onto the physical system integrating the ECPL and ICM&M automating the ECPL process by controlling the ultraviolet lamp and

DMD mask display as well as synchronizing the ICM&M which acquires and analyzes interferograms online. The parallel computing toolbox was employed in MATLAB to accelerate the computation.

This chapter documents the development of a comprehensive MATLAB-based software platform for measurement and control of the ECPL process. Importantly, the display of interferogram frames is temporally precise and is achieved without a substantial sacrifice in temporal performance of other key functions such as data acquisition and ICM&M analysis.

The implementation of the software in MATLAB is a significant advantage because of the wide adoption of MATLAB as a tool for data analysis in engineering field. Similar systems that are implemented using a low-level programming language (e.g., C or C++) require nontrivial computer programming skills, which can be discouraging or even prohibitive for researchers that do not have a strong programming background [95].

The ECPL process measurement and control benefits from the developed MATLAB application, a comprehensive and automatic platform for effortless operation of the AM process and online monitoring and measurement in just a few clicks. It is hoped that this software will enable physical experiments and testing for the research hypothesis. Additional information about the software can be found at the Appendix C.

## **CHAPTER 8 EXPERIMENTAL VALIDATION AND CHARACTERIZATION, OF THE ICM&M SYSTEM FOR ECPL PROCESS MEASUREMENT**

The previous chapters have reported an ICM&M method which consists of a sensor model (Chapter 5) for the ICM&M system and online parameter estimation algorithms based on instantaneous frequency (Chapter 6). In Chapter 7, an application program was created in MATLAB to integrate the ECPL and ICM&M systems and to acquire and analyze interferograms online. This chapter details our initial efforts to validate the ICM&M model and algorithms developed in Chapter 5 and Chapter 6. Given the limited equipment configurations, to validate and characterize the ICM&M system better, the implementation of real-time ICM&M is mainly performed in a mimic form by playing a real-time acquired interferogram video and simultaneously performing estimation of cured height, which simulated real-time ICM&M practice is called in this research “offline ICM&M”, essentially a post-analysis of acquired video. Please note that the real-time ICM&M and offline ICM&M share exactly the same sensor model and algorithms.

Given the limited computing power, the ECPL process interferograms were acquired real time and analyzed off line. A series of experiments was performed curing square samples by varying exposure time and intensity. Results show that the ICM&M can provide a cost-effective measurement for cured heights with excellent accuracy and reliability, and possess decent capability of estimating lateral dimensions. The offline ICM&M is a convincing demonstration and benchmark for the real-time ICM&M metrology, providing a comprehensive evaluation of the ICM&M system’s measurement characteristics as well as its utilities in modeling and control of the additive manufacturing process dynamics.

## **8.1 Experiment design**

The MATLAB application, equipped with the ICM&M method, provides a user-friendly platform for streamlining the ECPL process and the ICM&M implementation as well as a powerful tool for testing the ICM&M method. According to the ICM&M sensor model and calibration process [68], the experiment design incorporates a calibration experiment and a set of validation experiment.

### **8.1.1 Design philosophy and experiment plan**

As presented in Chapter 5 [68], a calibration procedure is required to determine the uncertain material property of refractive index in the ICM&M method. The design of ICM&M method possesses measurement traceability by relating its measurements to a known standard – an existing well-characterized measurement system. In this study, the Olympus LEXT OLS4000 3D material confocal microscope [62] is used as a scientifically sound measurement apparatus to transfer the primary standard value of sample heights profile to the ICM&M measured object – ECPL cured part heights profile. For each new batch of material, calibration is performed once at the beginning and more times later if necessary, for instance, the material has been exposed in air too long and is likely to change in properties with oxygen diffusion etc. The derived refractive index value from calibration is assumed to be constant under the normal ECPL operating conditions so that the ICM&M measurement results are within engineering tolerance over some reasonable period of time. In this study, a bottle of material resin was prepared and used in all the experiments which were done over a period about two weeks.

To validate the feasibility and explore the capability of the developed ICM&M method, two series of validation experiments were designed to cure 3D square blocks for various exposure time and under different UV intensities, respectively. Each experiment category above has its own particular purpose; meanwhile together they serve to provide a thorough investigation with one common theme - to demonstrate that the ICM&M

method is reproducible and robust in measuring cured parts with precision and accuracy. Table 9 presents the overall scheme of the designed experiment that consists of one calibration experiment and two validation groups. The varying process conditions for each validation group are highlighted in red.

Table 9. Experimental design matrix for validating ICM&M in offline mode

		Experiment Groups		
		Calibration	Validation Group #1: Varying Exposure Time	Validation Group #2: Varying Exposure Intensity
Experiment Setting	Exposure Time (s)	12 s	9 s, 12 s, 15 s	12 s
	Exposure Intensity (UV Iris level)	22%	22%	40%, 35%, 30%, 25%, 20%, 15%, 10%, 5%
	Exposure Pattern Bitmap Size (Pixels×Pixels)	250×250	250×250	250×250
Particular Attributes to Assess for the ICM&M method		Traceability	Temporal stability	Sensitivity
Common Attributes to Assess for the ICM&M method		<ol style="list-style-type: none"> <li>1. External &amp; Internal Comparability</li> <li>2. Precision and Accuracy</li> <li>3. Resolution and Range</li> <li>4. Repeatability.</li> </ol>		

For each individual experiment that cures a square block within certain conditions (i.e., DMD bitmap size, UV intensity, and exposure time), the curing process was captured by the ICM&M camera in real-time with an acquisition speed of 30 frames per second, and saved into a video file along with the process data including the UV lamp close time. Thereafter, in the “Offline Measurement” module in the MATLAB application, the video of interferograms and all process data were loaded ex-situ at a laptop computer, and analyzed to obtain the cured height profile for a selected Region of Interest (ROI). The cured part was also measured by the confocal microscope, of which the measurement result was used as the actual height to compare with the offline ICM&M measurement result for error analysis.

### 8.1.2 ICM&M implementation

In the implementation and investigation of the ICM&M method, there are a few practical thoughts to address in the experiment design.

First of all, choosing square blocks as target 3D objects in the experiments is because the resultant cured part with lateral aspect ratio close to if not equal 1:1 from the square bitmap projection could vividly demonstrate that ECPL process is isotropic and homogeneous and that the ICM&M method is omnidirectional. Besides, square blocks provide a simple and efficient way of testing the accuracy of ICM&M by presenting obviously flat height profiles. In principle, one can always use various DMD bitmaps to cure customized parts and utilize the same ICM&M method which should be universally applicable for measuring cured heights profile regardless of the part shape.

To apply the ICM&M method in an off line mode, we replayed the curing process video, and in the last frame of the interferogram that presents a better shape of the cured part we selected a line or an area of pixels as the region of interest (ROI) to measure. Since the cured parts analyzed in this study are cuboid, theoretically it should not matter much which line to choose for measuring the height. However, considering the not-perfectly-uniform UV irradiation and stochastic process variations in the ECPL system along with some possible defects due to post-curing operation, as well as for easy visual match with the microscope measurement in later comparison of results, it is recommended to choose some features such as center lines or entire area with edge lines. The larger the ROI is chosen to be measured, the more computational time the ICM&M method needs. In the calibration, the entire area would be selected as ROI for a comprehensive analysis because its result forms the critical foundation for subsequent measurement. In the validation experiment, to speed up the analysis without influencing the results significantly, a representative profile line would be chosen as the ROI to be measured by ICM&M.

Ideally, measuring a height profile with ICM&M means measuring the cured heights of all voxels based on all the pixels in the ROI, which would be computationally tedious and costly especially in real-time ICM&M. The cured part is supposed to have a uniform heights profile due to ideally uniform UV light intensity and material properties across the curing area; hence the adjacent pixels are supposed to have very similar if not identical changed phase angles during the curing process. Pixels' time sequences of grayscale in interferograms were compared, confirming the assumption of the proximity similarity in neighboring pixels' profile. It has been found that to evaluate the height profile, measuring heights for pixels in the ROI at an interval of five pixels would not affect the accuracy significantly but requires much less computation expense than measuring every pixel for the whole area. Specifically, we measured every 5 pixels because: (1) a 5-by-5 image median filter was used to denoise the raw data, hence measuring every five pixels does not omit or overlap any raw data; (2) it turns out that measuring every one pixel does not improve the accuracy significantly but requires far more computation. According to the recommended practice, the pixels in measured area's lines profile is denoted in the form of Pixels (starting pixel width coordinate: interval: ending pixel width coordinate, starting pixel height coordinate: interval: ending pixel height coordinate). For example, Pixels (245:5:365, 220) denotes a horizontal line of 25 pixels starting from Pixel (245, 220) to Pixel (365, 220) with 5 pixels between each two neighboring measured pixels.

Since the non-uniform acquisition is averagely 30 frames per second, this study performed measurement every 10 frames of interferogram, correspondingly at a temporal measurement period of approximately 1/3 second.

Lastly, because the UV lamp in the ECPL system is designed for users to adjust its intensity in percentage scale of the "iris level"; for example, 100% means a fully open iris and maximum intensity, and 0% means completely closed and no irradiation at all.

Hence, we used the iris level as a nominal indication of the exposure intensity applied in the ECPL process.

### **8.1.3 Microscope measurement practice**

In both calibration and validation experiments, we need measure the cured part using a microscope, specifically the Olympus LEXT OLS4000 3D material confocal microscope [62], which displays directly the profile of a selected line with height measurement result. Since the cured part is designed to be a flat-top block, a profile line is supposed to be able to reveal the sample's height regardless of the its position. In practice, however, cured samples are sometimes impacted by the post ECPL operations (e.g. removing and washing) and cannot present a perfectly smooth surface as will be seen in the experiment results. Hence, one should locate the to-be-measured line in a proper position where the surface is as intact as possible to obtain the actual height of the cured part. Preferably, profile lines in X and Y directions (i.e. length and width dimensions), respectively, are measured and the average result is used as a better estimation of the actual height.

It is recommended to use higher magnification microscope for better image quality and measurement accuracy, which higher magnification scanning however could take much longer time (dozens of minutes to scan about 90 $\mu$ m high sample in the confocal microscope). Nevertheless, it has been found that, while measuring ECPL samples in confocal microscope measurement, using low magnification lens (5X) or higher magnification (20X) lens yield the quantitative value of measured height in only a couple of microns' deviation, hence no significant affect in heights measurement. In this study the major benefit of higher magnification microscope measurement is that it can output higher quality sample image, shedding light into the features such as the edging area and rendering clear and more smooth.



Besides, the confocal microscope can export abundant measurement data for all profile lines in a spreadsheet file, which could provide overall height profile for the entire sample. Of course one can choose to export merely part of the measurement data, for example, one exports the data for the line selected in the software user interface to measure just one profile line. Some postprocessing of the exported data, i.e. analysis of the average and deviation, is required to attain the final measurement area. This measurement approach dealing with data is also more objective than manually selecting a measurement line by cursor on the software bench, though it requires more time and effort.

As a well-characterized scientific metrology equipment, the confocal microscope provides a standard reference but could also present some measurement uncertainty due to equipment operation and sample properties. In this study, to get as accurate result as possible, we tried to use higher magnification for all the sample measurement, and used multiple lines average as microscope measurement result.

## **8.2 Results and discussion**

### **8.2.1 Material formulation**

As specified in earlier research [17], a trifunctional acrylate monomer - trimethylolpropane triacrylate (TMPTA, SR-351) obtained from Sartomer was used as obtained, with the photoinitiator 2, 2-dimethoxy-1, 2-diphenylethan-1-one (DMPA, IRGACURE-651) obtained from Ciba Specialty Chemicals, as the resin composition for the ECPL process. The DMPA photoinitiator concentration in the TMPTA monomer was recommended to be 20% by weight to ensure a homogenous solution. This specific formulation required less than 30 seconds to cure a thick (hundreds of microns) layer of resin. In principle, a resin formulation with higher sensitivity could have been appropriate

for ECPL. However, a fast curing resin system would impose a higher demand on faster and more accurate measurement and control; hence, the 20% resin formulation mentioned above was used. All the experiments done in this chapter used the same bottle of material which consists of a 4:1 ratio by weight of TMPTA monomer (16 gram) and DMPA initiator (4 grams). The mixture was stirred for approximately 4 hours to form a homogeneous solution.

### 8.2.2 Calibration experiment

According to the experiment design presented above, for the calibration, a moderate UV intensity corresponding to the UV lamp (OmniCure® S2000) iris level at 22% was chosen so that the ECPL process cured height would not grow too fast or too slow. A 250×250 pixels square as shown in Figure 55 was displayed on DMD for 12 seconds.

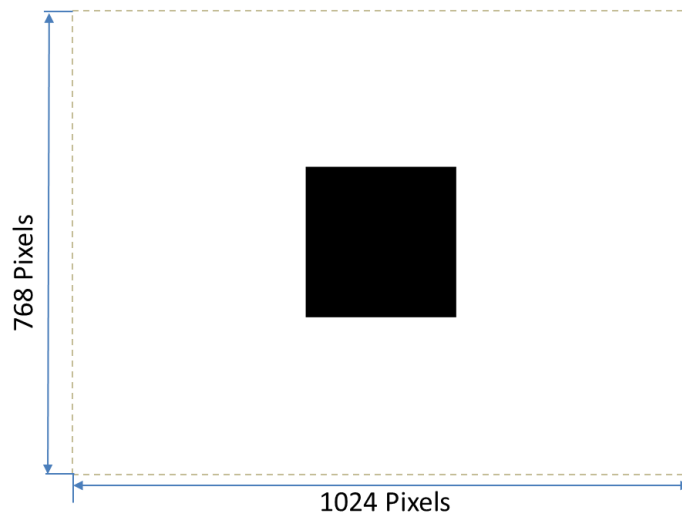


Figure 55. DMD pattern: 1024×768 pixels binary bitmap displaying a black square of 250×250 pixels in the center

The ICM&M camera captured the video of interferograms when the square block part was cured by the ECPL system. To start offline ICM&M analysis, firstly the

interferograms video was replayed in the MATLAB application, and the last frame of interferograms which shows the final cured part shape was extracted. In the video's last interferogram as shown in Figure 56, the ROI was selected by human eyes recognition of the cured part outline, approximated by an area of 150×150 pixels denoted as Pixels (235:385, 140:290) which is formed by the four corner pixels along with the outline (red dashed line).

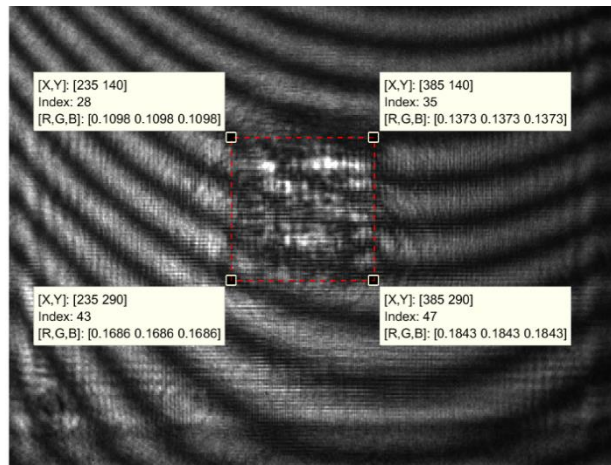


Figure 56. Calibration: outline of the cured part in the last interferogram – ROI of Pixels (235:5:385, 140:5:290) to be measured

The ICM&M method was applied to the square area of 31×31 (961) pixels designated as Pixels (235:5:385, 140:5:290), with 5 pixels between each two neighboring measured pixels in both width and height directions. The ICM&M model and algorithm estimated the total phase angle,  $\sum_i(T_i f_i)$  in Equation ( 14 ), for each measured pixel; and the average total phase angle is 6.150 cycles (i.e.,  $6.150 \times 2\pi$  rad) as shown in Figure 57.

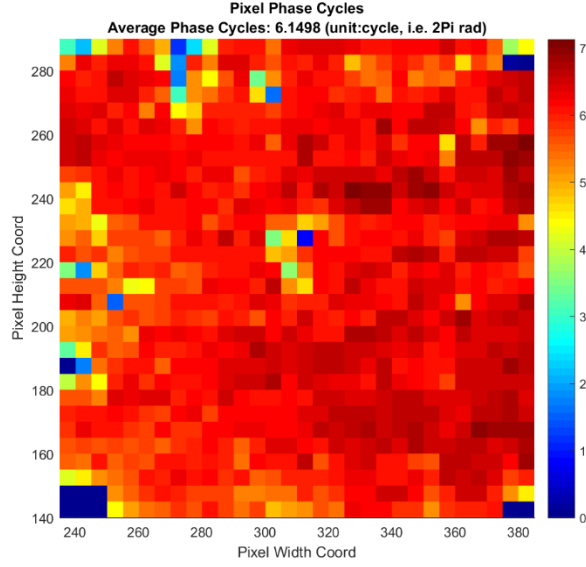


Figure 57. Calibration: estimated individual and average total phase angles for 31×31 pixels in the ROI of Pixels (235:5:385, 140:5:290)

The cured sample was measured by the laser confocal microscope, as shown in Figure 58, and the average height of two profile lines in X direction and Y direction is 73.492 μm, which substitutes Z in the calibration model in Equation ( 15 ). The calibration process is completed by solving the equation:

$$\Delta n = n_m - n_l = \frac{\lambda \sum_i (T_i f_i)}{2Z} = \frac{(0.532)(6.150)}{2(73.492)} = 0.02226. \text{ The corresponding mean solid part refractive index } n_m \text{ is derived to be 1.4946.}$$

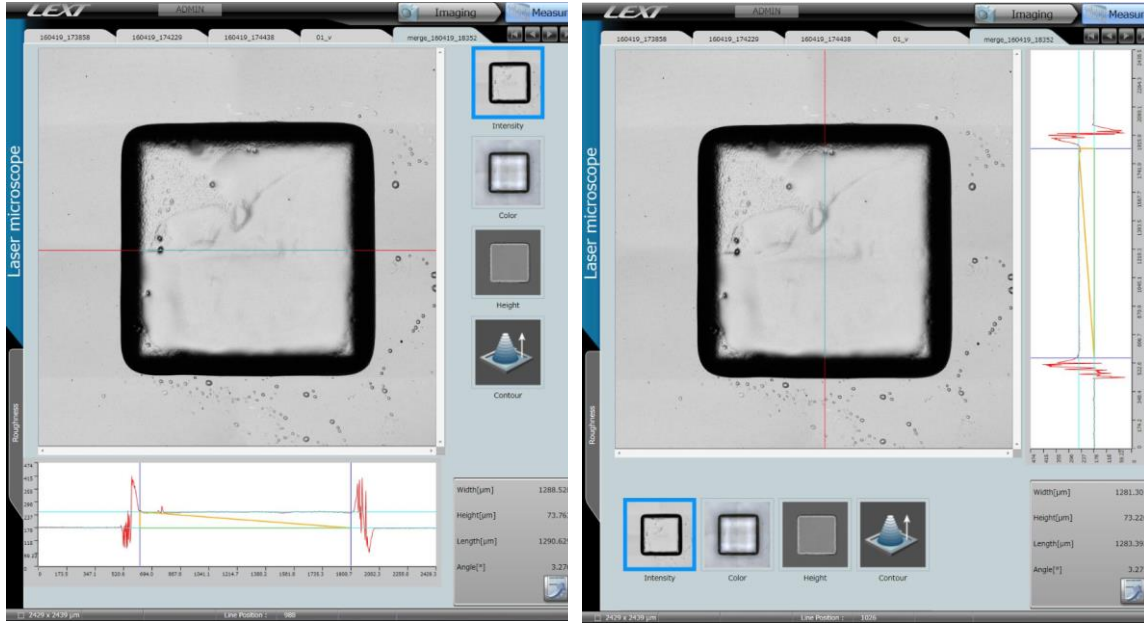


Figure 58. Calibration: measured typical profile lines in two lateral dimensions (X and Y) to estimate the height of the cured sample

To assess the calibration result, the experiment above was repeated, and a second sample was measured with the ICM&M method and the microscope as the first sample was done previously. Figure 59 depicts the results of the second calibration experiment. The cured area in the interferograms consist of roughly  $145 \times 145$  pixels enclosed by the pixels as shown in Figure 59, and a total of  $30 \times 30$  (900) pixels were measured with the offline ICM&M module, which estimated that the average total phase angle is 6.181 cycles. The microscope measurement is  $74.927 \mu\text{m}$  and  $73.650 \mu\text{m}$  for the selected lines in X and Y directions, respectively; hence the average measurement result is  $74.289 \mu\text{m}$ .

Applying the calibration model in Equation ( 15 ) [68], we got  $\Delta n = n_m - n_l =$

$$\frac{\lambda \sum_i (T_i f_i)}{2Z} = \frac{(0.532)(6.181)}{2(74.289)} = 0.0221, \text{ and } n_m = 1.4944.$$

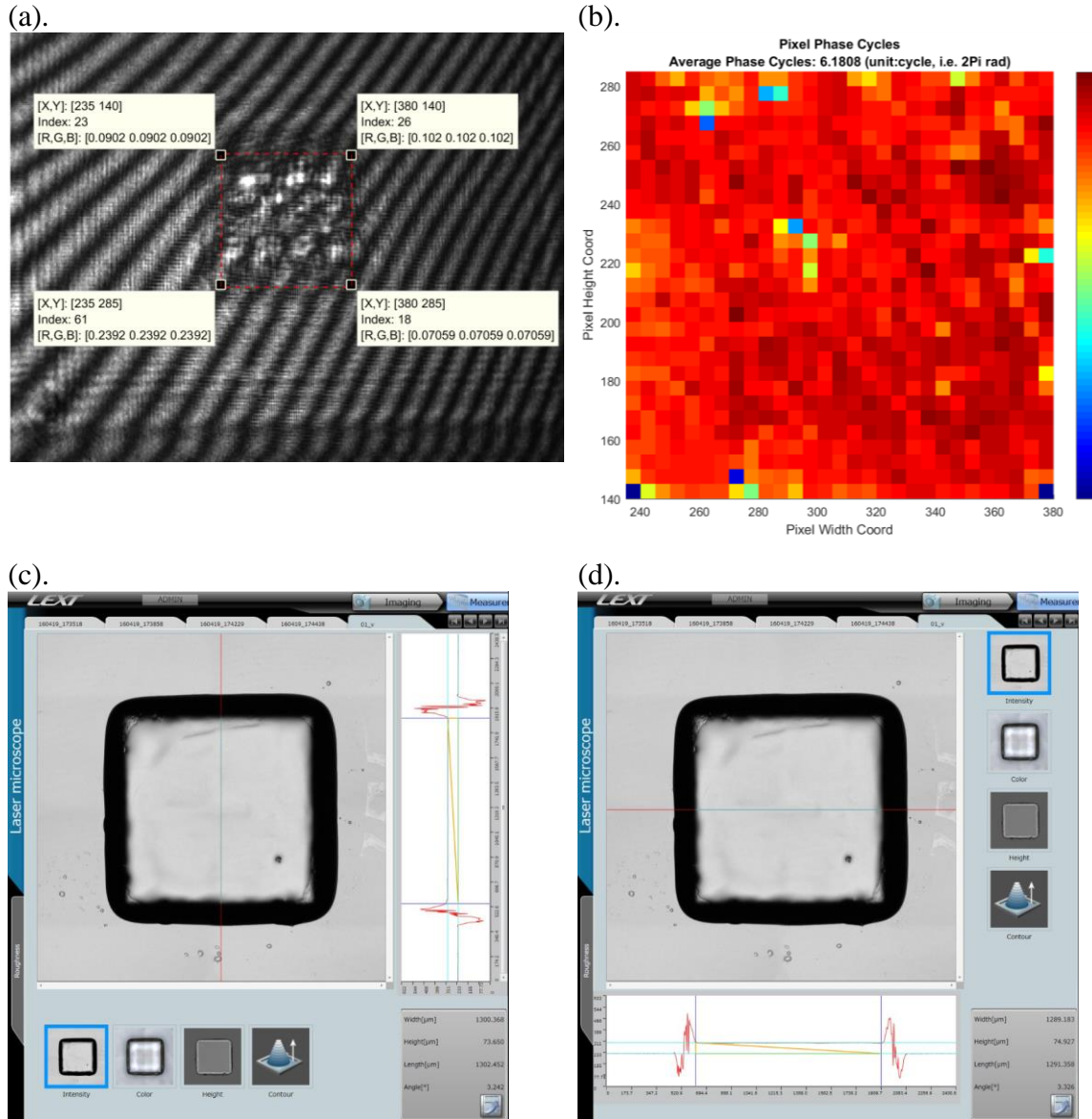


Figure 59. A 2<sup>nd</sup> calibration sample: (a) outline of the cured part in the last interferogram – ROI of Pixels to be measured; (b) estimated individual and average total phase angles for 30×30 pixels in the ROI; (c) and (d): measured typical profile lines in two lateral dimensions (X and Y) to estimate the height of the cured sample.

Please note that experiments are prone to operation errors and process noises. As one can see from the experiment above, there are some obvious defections in the cured part surface which might influence the microscope measurement results thereby induce calibration errors. The ICM&M measured heights profile present fluctuations are caused mainly by pixel grayscales signals noise.

The two calibration experiments are summarized in Table 10. The two samples demonstrate great reproducibility of the ECPL process and good consistency in ICM&M. The nuance in the phase angle and microscope measurement lead to a difference at the fourth decimal place of  $\Delta n$ . It is expected that there would be a dispersion of  $\Delta n$  ( $n_m$  as well) if one conducts more calibration experiments, because there are always some inevitable process variances and the calibration output of the refractive index is very sensitive to the inputs. The microscope can measure to the 3<sup>rd</sup> decimal, and ICM&M could estimate the phase angle to the 3<sup>rd</sup> decimal. Hence, it could be reasonable to assume that the calibrated refractive index (by the calibration model in Equation ( 15 )) could be also accurate to the 3<sup>rd</sup> decimal. Moreover, repeated calibrations show a subtle change starting at the 4<sup>th</sup> decimal of the refractive index value. Since the calibrated refractive index is to be used in subsequent measurements for height, a tailing 4<sup>th</sup> decimal is kept in the calibration of refractive index to provide a better estimation of the height at the 3<sup>rd</sup> decimal. Averaging the two calibration results and rounding it to the fourth decimal, we obtained  $\Delta n = 0.0222$  , correspondingly  $n_m = 1.4945$ , which value will be used in the category of validation experiments to calculate the example parts heights to validate the ICM&M measurement capability and accuracy.

Table 10. Calibration Experiment Results

Exp. No.	Number of ROI Pixels	Average of Total Phase Angle Estimated by ICM&M (rad)	Average Cured Height Measured by Microscope ( $\mu\text{m}$ )	Refractive index difference ( $\Delta n = n_m - n_l$ )	Cured part refractive index $n_m$
1	150×150	$6.150 \times 2\pi$	73.492	0.0223	1.4946
2	145×145	$6.181 \times 2\pi$	74.289	0.0221	1.4944

As a summary, in the calibration experiments, two sample parts were cured under the same conditions and measured with the offline ICM&M module in the MATLAB app. A large-scale calculation of most of (if not all yet) the voxels heights in the entire

cured area was performed for each sample to achieve as representative and robust as possible estimation of the refractive index value. Meanwhile, the between-sample similarity in total phase angle and microscope measured height thus in the estimated refractive index difference provides more confidence in the calibration result and critical guarantee for the measurement performance in subsequent experiments. As a byproduct, the calibration experiments has already demonstrated evidently that the ICM&M method has full-field measurement capability with good consistency and repeatability.

### **8.2.3 Validation experiment group #1: varying exposure time**

We used the same batch of resin material to further validate the ICM&M model and algorithms reported in a previous paper [68]. In the first set of validation experiments, we cured square blocks by displaying the same size (i.e., 250×250 pixels) DMD bitmap under the same UV lamp iris level of 22% as in the calibration process, but for different length of exposure time – 9 seconds (Experiment #1), 12 seconds (Experiment #2) and 15 seconds (Experiment #3), respectively.

Two samples were cured and measured in each subgroup of exposure time experiment. We will present one sample in each subgroup as an illustration of implementing the ECPL process and ICM&M measurement, and later introduce the other sample in each subgroup to demonstrate one important characteristics of process measurement – repeatability in both the ECPL process output and ICM&M measurement result with expected deviations.

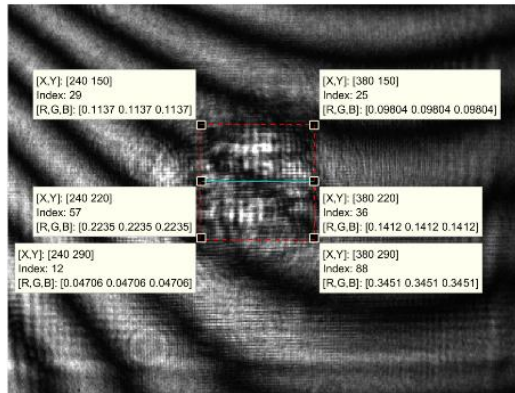
The first sample in each subgroup of experiment with various exposure time was introduced in this section. The offline ICM&M measurement procedure was illustrated via this set of samples and microscope measurement results were shown to verify the ICM&M results.

Figure 60 displays the ROI for measurement in the experiments, and the datatips provide the pixels coordinates (width and height) for the end pixels of the selected line

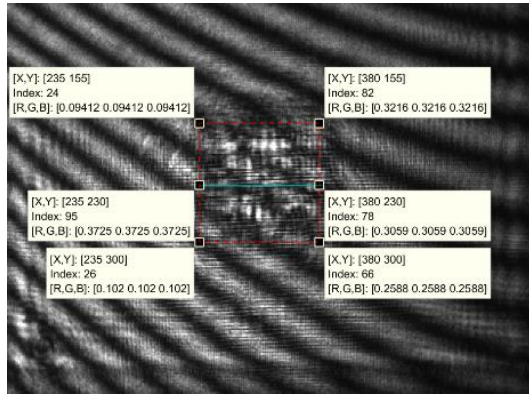


(cyan solid line in the figure) and the corner pixels of the approximated cured shape (red dashed line in the figure). As noted in Figure 60, the ending interferogram of each experiment shows a clear square shape of about 145 pixels, demonstrating that the ECPL process could preserve the cross-section shape and output a consistent size, which shape and size both can be well captured by the ICM&M system. As in the calibration process, for each ROI only these pixels at an interval of every five pixels are measured to save computation time at little expense of accuracy. The measured pixels are shown as the selected horizontal lines in Figure 60.

(a) Exp.#1: 9s exposure



(b) Exp.#2:12s exposure



(c) Exp. #3: 15s exposure

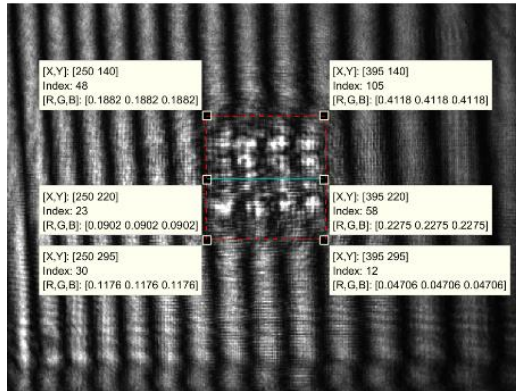


Figure 60. Selected ROI pixels (red dashed lines: estimated entire cured area; cyan line: an example profile line) to measure with ICM&M in the 1<sup>st</sup> sample

With the chosen ROI pixels corresponding to the to-be-measured voxels, we simulated the real-time ICM&M method by replaying the video and simultaneously extracting the time series of grayscales for all the measured pixels, followed immediately by estimating the instantaneous frequency and totaling the changed phase angle which leads to the final computing of the cured heights as per the algorithms presented in literature [68]. To illustrate the details of ICM&M algorithms implementation, the sequence of figures in Figure 61 depicts the time sequence of grayscale intensities, estimated instantaneous frequency along the time, and time curve of cured height for a typical pixel in each experiment, specifically, Pixel (220, 325), Pixel (230, 260) and Pixel (220, 280) in Experiments 1, 2 and #3, respectively.

In Figure 61 (a), the grayscale has a range of [0, 255] expressing the intensity of the pixel in the interferograms captured by the CCD camera. It is not exactly sinusoidal due to the nonlinear curing process and stochastic noises including the nonlinear response of camera electronics [37]. The blue dots in the figure depict the signal data and the red line is the fitted curve by the online parameter estimation algorithm. The fitted curve agrees very well with the data, demonstrating the effectiveness of the moving horizon curve fitting and capability of real-time measuring.

In Figure 61 (b), we estimated the instantaneous frequency consecutively every 10 frames which provided a new batch of 10 raw grayscale data points. The measurement period, e.g. 10 samples (frames) per run of measurement in this study, could be adjusted based on the computation power; and a sufficiently fast measurement is preferred to capture the process dynamic better so as to measure the process output more accurately.

Figure 61 (b) also shows the cumulative sum of total phase angle during the ECPL process. As the curing process proceeds, the running phase angle change is computed using the expression  $\sum_i T_i f_i$  in the ICM&M sensor model Equation ( 14 ) to calculate the voxel's cured height as shown in Figure 61 (c). The total phase angle is estimated to be 5.206 cycles producing the cured height of 62.38  $\mu\text{m}$  for the voxel on Pixel (220, 325) in Experiment #1. Similarly, in Experiment #2, the total phase angle is 6.060 cycles resulting an estimated height of 72.61  $\mu\text{m}$ . In Experiment #3, the total phase angle is 7.028 cycles and the estimated height is 84.21 $\mu\text{m}$ . These typical voxel heights estimated by the ICM&M are reasonably close to the microscope measurement as will be depicted in Figure 62.

Exp. #1: 9s exposure (a)	Exp. #2: 12s exposure (a)
-----------------------------	------------------------------

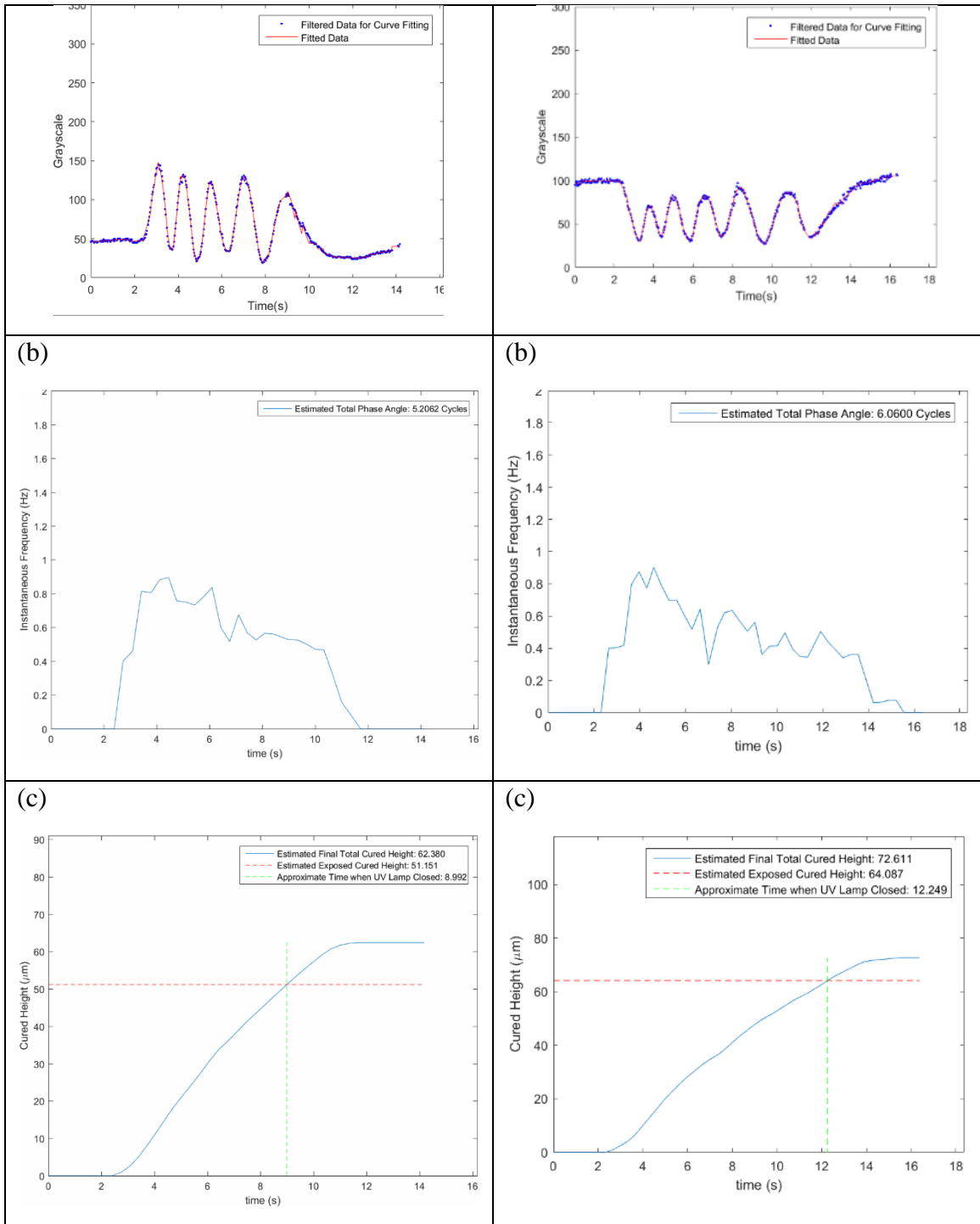


Figure 61. Illustration of implementing the ICM&M algorithms using the 1<sup>st</sup> samples in the experiments varying exposure time: (a) typical time sequence of grayscale; (b) estimated instantaneous frequency along timeline; (c) evolving cured height of the voxel on the selected the pixel.

Exp. #3: 15s exposure  
 (a)

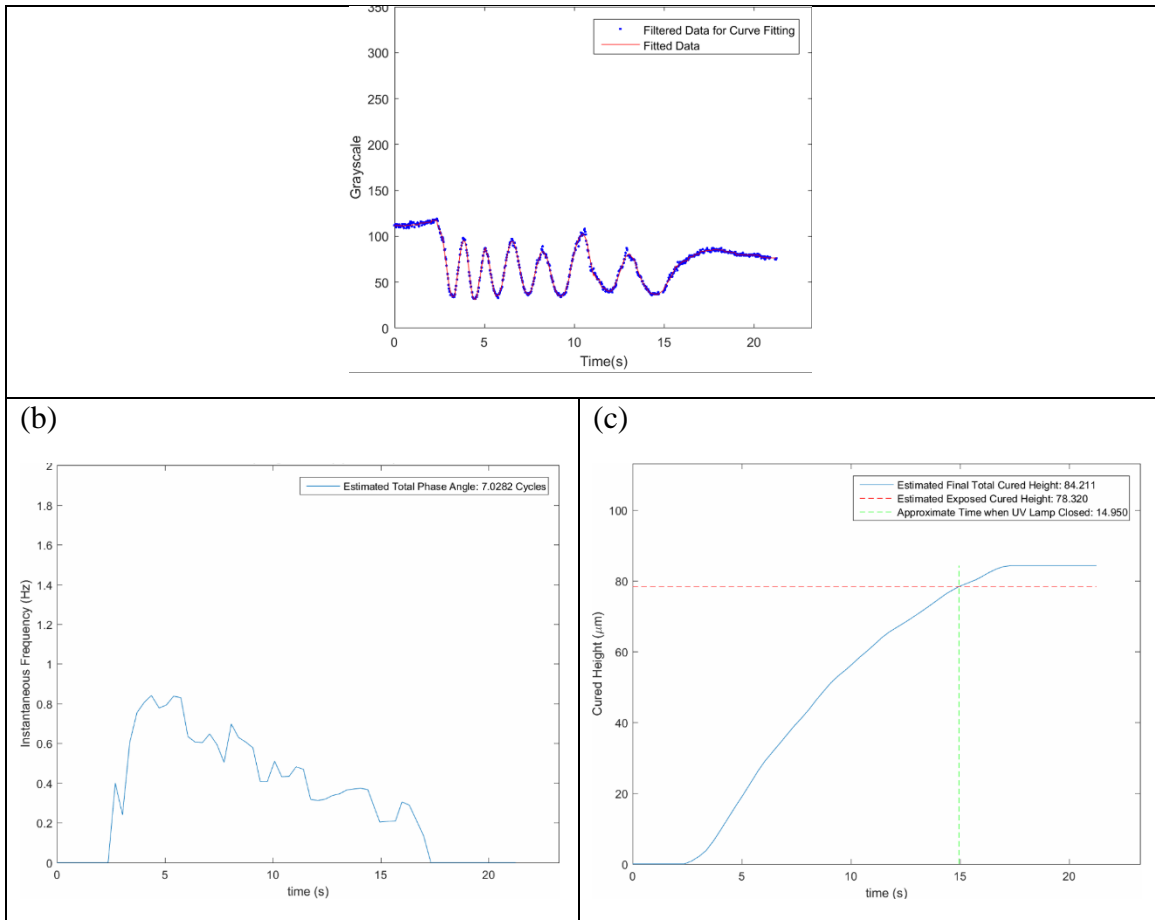


Figure 61 (continued). Illustration of implementing the ICM&M algorithms using the 1st samples in the experiments varying exposure time: (a) typical time sequence of grayscale; (b) estimated instantaneous frequency along timeline; (c) evolving cured height of the voxel on the selected the pixel.

In Figure 61 (b), another thing worthy to be pointed out is that the estimated instantaneous frequencies in the three experiments are shown to be alike in the first nine seconds, which makes sense because the 12-second and 15-second exposed curing experiments are actually a temporal extension of the 9-second curing under the same process conditions.

The stereolithographic cure process involves mass and energy transport during the curing process, incorporating exposure and dark reaction [59, 96], as it is vividly shown in Figure 61 (a) that the pixel grayscales oscillation still persisted for a while after the UV light was turned off at 9, 12 and 15seconds, respectively. As continued “dark” gelation is

expected in photopolymerization [66], the cured height by the ECPL process can also be classified into exposed and dark cured height. Figure 61 (c) marks the UV lamp shutdown time and displays the exposed cured height. The ECPL process is continuous while the ICM&M measurement is discrete with the digital signal measured every 10 frames – 0.333 second with the camera acquisition speed being 30 frames per second. Hence, there is an error up to 0.333 second in the approximated UV close time.

As explained in the design of experiment, a single pixel measurement could not be sufficient or conclusive. More pixels need to be measured for final height estimation with less bias. We carried out the same procedure illustrated above to calculate the cured height for all the other voxels on the selected line of pixels (cyan solid line) in Figure 60, evaluated the average height as the final result. As a result, the line height profile measured by ICM&M is represented by 30 pixels in all three experiments with an estimated average as detailed in Table 11.

To get a more comprehensive assessment of the ICM&M measurement capability, the entire cured area (enclosed by the red dashed line in Figure 60, approximated by  $145 \times 145$  pixels, was also measured at an interval of 5 pixels, thus the  $31 \times 31$  (961) voxels heights constitute the full field height measurement as shown in Figure 62 (a). The cured area height profile is evaluated with both average and deviation as presented in Figure 62 (a).

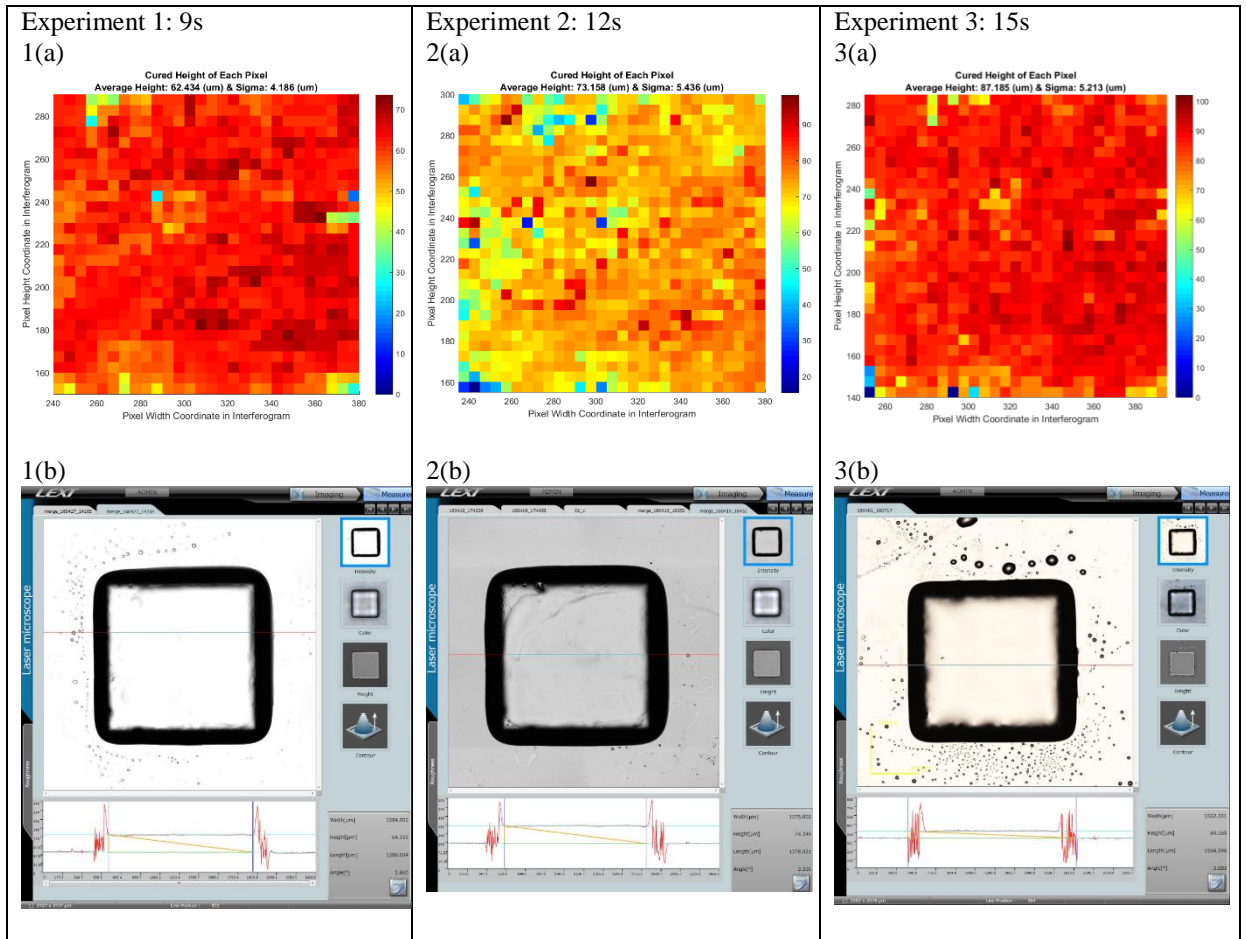


Figure 62. ICM&M result VS. microscope measurement for the 1<sup>st</sup> set of samples in exposure time experiment. Each sample's (a) entire cured area height profile estimated by ICM&M; (b) horizontal profile line in the confocal microscope.

The cured parts in the experiments were measured with the Olympus 3D confocal microscope as shown in Figure 62 (b). The “Height” value displayed at the right-bottom box of the confocal microscope screenshot in Figure 62 (b) indicates the measured height for the selected profile line. As pointed out in the experiment design, the average of measured heights for two lines in X-direction (horizontal) and Y-direction (vertical) is used as the final microscope measured height result to reduce the sample measurement bias. The same ECPL process and ICM&M method was repeated once to cure and measure a second square part in each experiment subgroup to investigate the ICM&M system's reproducibility and reliability. Sometimes the process signals might be too noisy

due to the camera hardware heating issue or sometimes the cured part suffered severe defects during washing. All the numerical results will be summarized in Table 11.

In Figure 62, some tiny holes and uneven surface with bumps and pits are seen in the microscope images of cured samples, which imply strongly that careful handling and postprocessing of the samples is needed. It is worth to point out that the observed sample defects would not affect the height measurement significantly as long as an intact profile line is chosen to measure under the microscope.

As noted in the ICM&M estimated cured heights profile in Figure 62 and Table 11, there is a deviation around  $5\mu\text{m}$  in each sample. The deviation was mainly caused by the process and signal noise which led to some deficiency in the ICM&M algorithm. Nevertheless, the average value demonstrates good accordance with the microscope measurement average and good agreement between the same-condition samples.

Table 11 compares quantitatively the measurement results in terms of absolute error and relative error. For each sample, the two rows in the table represent two different methods of estimating part height. The first row utilizes a method that averages two profile lines, while the second row averages heights across the entire cured area. The brown entries report these cured area height estimates and errors. Results show up to 2 microns' absolute deviation and less than 3% relative error. The agreement between the ICM&M estimation result (green column) and the confocal laser microscope measurements (gray column) demonstrates that the ICM&M method is capable of measuring the vertical height for ECPL cured parts with discernment for micron order difference and measurement range of about one hundred microns.

Furthermore, in Table 11, comparing the between-sample differences within the same subgroups, we obtained internal consistency for samples cured under the same conditions in ICM&M measurement results despite of microns' difference, which is also present in the microscope measurement results. The results show that ICM&M is capable



of measuring the height of parts cured for likely exposure durations with both accuracy and precision.

Table 11. Measurement results of validation experiments varying exposure time

Experiment Subgroup NO.	Exposure Time (s)	Sample NO.	ROI Pixels (Width, Height)	ICM&M Results			Microscope Measured Profile Line Height (μm)			Absolute Deviation (μm)	Relative Error
				Total Phase (cycle, i.e. 2π rad)	Cured Height (μm)	St.Deviation - Cured Height σ (μm)	X-direction	Y-direction	Average		
Experiment #1	9	Sample 1	Profile Line (240:380, 220)	5.175	62.01	4.19	64.192	63.211	63.70	-1.69	-2.66%
			Cured Area (240:380, 150:290)	5.211	62.43					-1.27	-1.99%
	9	Sample 2	Profile Line (225:370, 220)	5.037	60.35	4.37	63.031	63.335	63.18	-2.83	-4.48%
			Cured Area (225:370, 145:290)	5.144	61.63					-1.55	-2.45%
Experiment #2	12	Sample 1	Profile Line (235:380, 230)	6.065	72.67	5.44	74.349	71.775	73.06	-0.40	-0.54%
			Cured Area (235:380, 155:300)	6.106	73.16					0.10	0.13%
	12	Sample 2	Profile Line (235:380, 200)	6.102	73.11	4.95	72.760	72.299	72.53	0.58	0.80%
			Cured Area (235:380, 135:280)	6.062	72.63					0.10	0.14%
Experiment #3	15	Sample 1	Profile Line (250:395, 220)	7.086	84.91	5.21	84.160	86.329	85.24	-0.34	-0.40%
			Cured Area (250:395, 140:285)	7.276	87.19					1.94	2.28%
	15	Sample 2	Profile Line (225:370, 245)	7.066	84.67	5.45	84.305	83.772	84.04	0.63	0.75%
			Cured Area (230:375, 150:295)	7.129	85.42					1.38	1.64%

As shown in Figure 63, Experiment #2 with 12 seconds exposure had the smallest errors between ICM&M and microscope, which makes sense because of the identical process conditions as adopted in the calibration experiments. In Experiment #1 and #3 with 9 seconds and 15 seconds exposure, respectively, the ICM&M was still able to estimate the cured height with great accuracy, despite relatively larger errors. Reasons for the errors will be discussed later in Section 8.3.1.

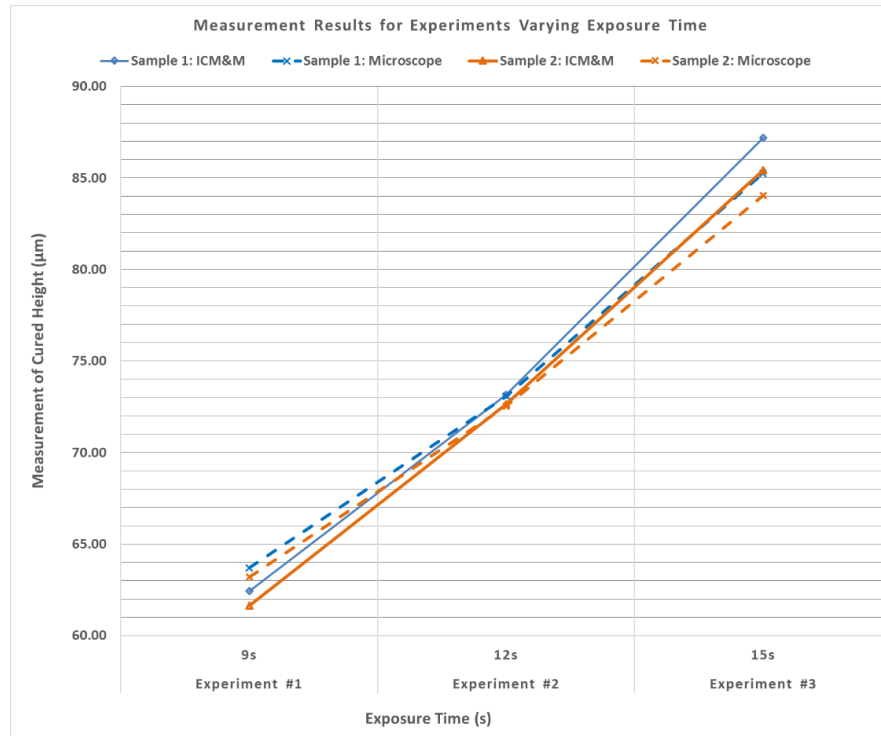


Figure 63. Measurement results for experiments varying exposure time

#### 8.2.4 Validation experiment group #2: varying exposure intensity

In the second set of validation experiments, we cured square blocks by displaying the same size (i.e., 250×250 pixels) DMD bitmap for the same length of exposure time (12 seconds), but under eight different UV intensities corresponding to the UV lamp iris levels at 40%, 35%, 30%, 25%, 20%, 15%, 10% and 5%, respectively. The procedure of ICM&M implementation and microscope measurement was the same as presented in the previous section about the experiments varying exposure time.

For each intensity level, we cured two samples and measured each sample with the offline ICM&M module in the developed MATLAB application and the confocal microscope. For validation purpose, we compared each individual ICM&M measurement with the microscope measurement result which is the average of two profile line measurement results for each sample.

To demonstrate the ECPL process difference under different intensities and how the ICM&M method responds to the process changes, we presented a representative pixel's interferogram grayscale signal and the ICM&M method's evolutionary estimation of the instantaneous frequency and cured height, as shown in Figure 64.

In Figure 64 (left column: 1a-8a), the grayscale signals vividly reflect the process dynamics difference due to the UV intensity variations. Conforming to the photopolymerization mechanism, the higher UV light intensity is provided, the more photo initiators are in the process, and the quicker the curing is. Within the same exposure time of 12 second, there was almost one more cycle in 40%-iris-level UV curing than in the 35%-iris-level curing, which had a about half cycle more than the 30%-iris-level UV curing did, and so on and so forth down to the 5%-iris-level curing.

The process dynamics change caused by varying intensity is further confirmed in Figure 64 (center column: 1b-8b), which shows that the estimated instantaneous frequencies is larger for higher UV intensity induced ECPL process. The time curves of cured height measured by the ICM&M are displayed in Figure 64 (right column: 1c-8c) with both exposed and dark cured height values determined by when the UV lamp was closed during the ECPL process. Examining into the curing start time in Figure 64 (b and c), one could see that the ICM&M estimated time curves of frequency and height have correctly reflected the trend of increasing threshold period in photopolymerization based AM process with decreasing exposure intensity [79]. As obviously shown in Figure 64 (b and c), the threshold period for 40%-iris UV curing is less than 2 seconds, while that for 5%-iris UV curing is about 14 seconds.

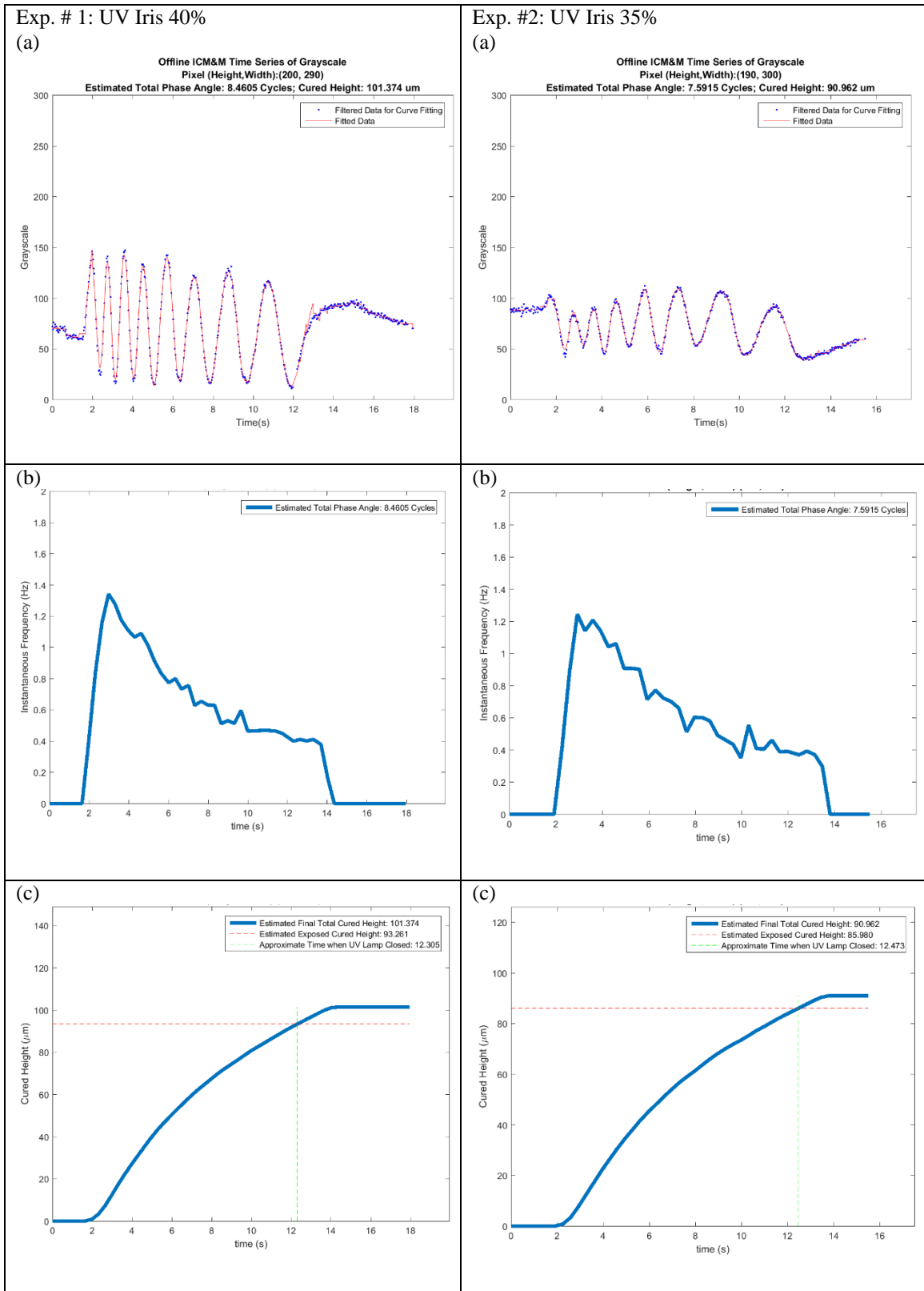


Figure 64. ICM&M implementation and process dynamics in the experiments varying exposure intensity: (a) representative pixel's time sequence of grayscale; (b) estimated instantaneous frequency; (c) evolving cured height of the voxel on the selected the pixel.

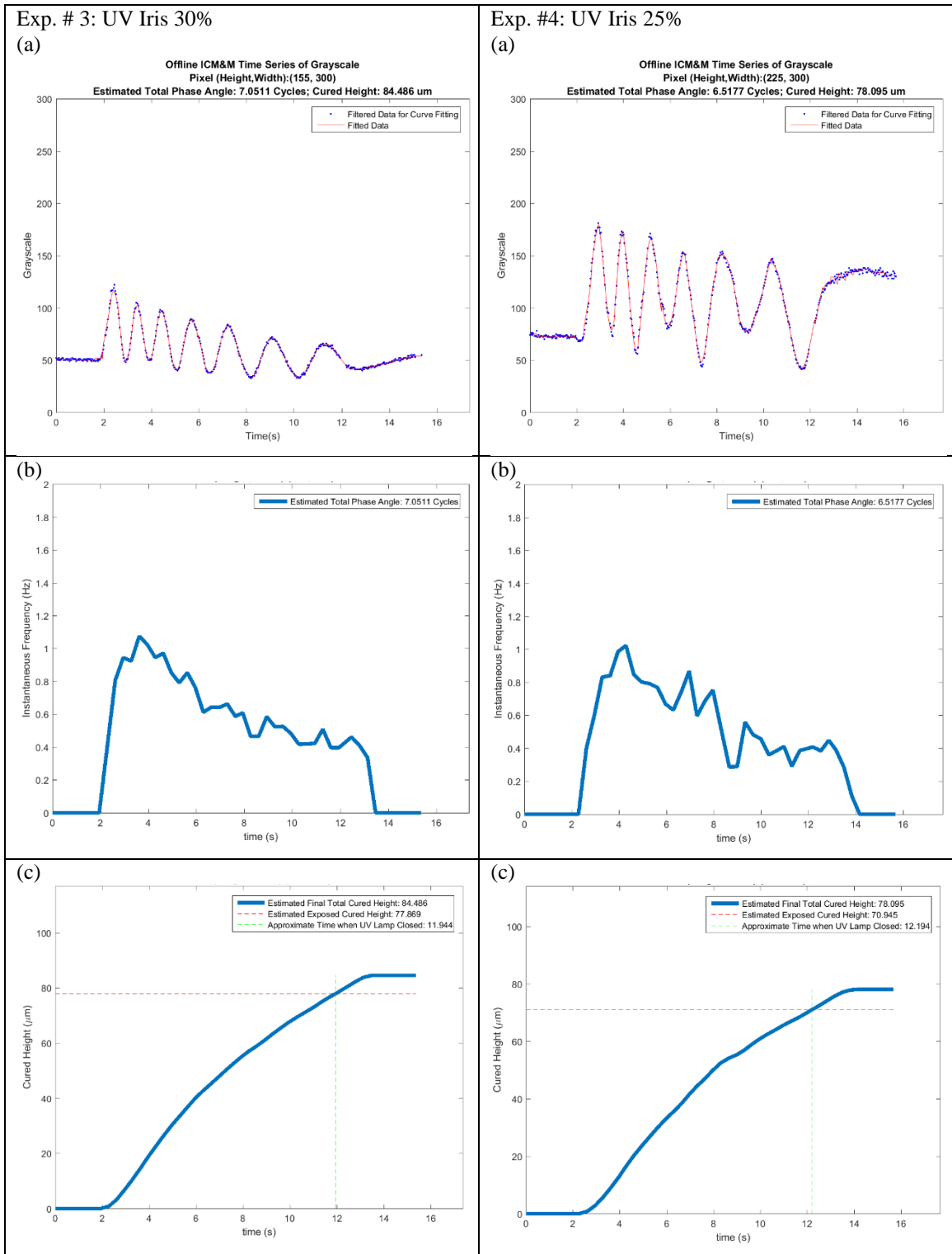


Figure 64 (continued). ICM&M implementation and process dynamics in the experiments varying exposure intensity: (a) representative pixel's time sequence of grayscale; (b) estimated instantaneous frequency; (c) evolving cured height of the voxel on the selected pixel.

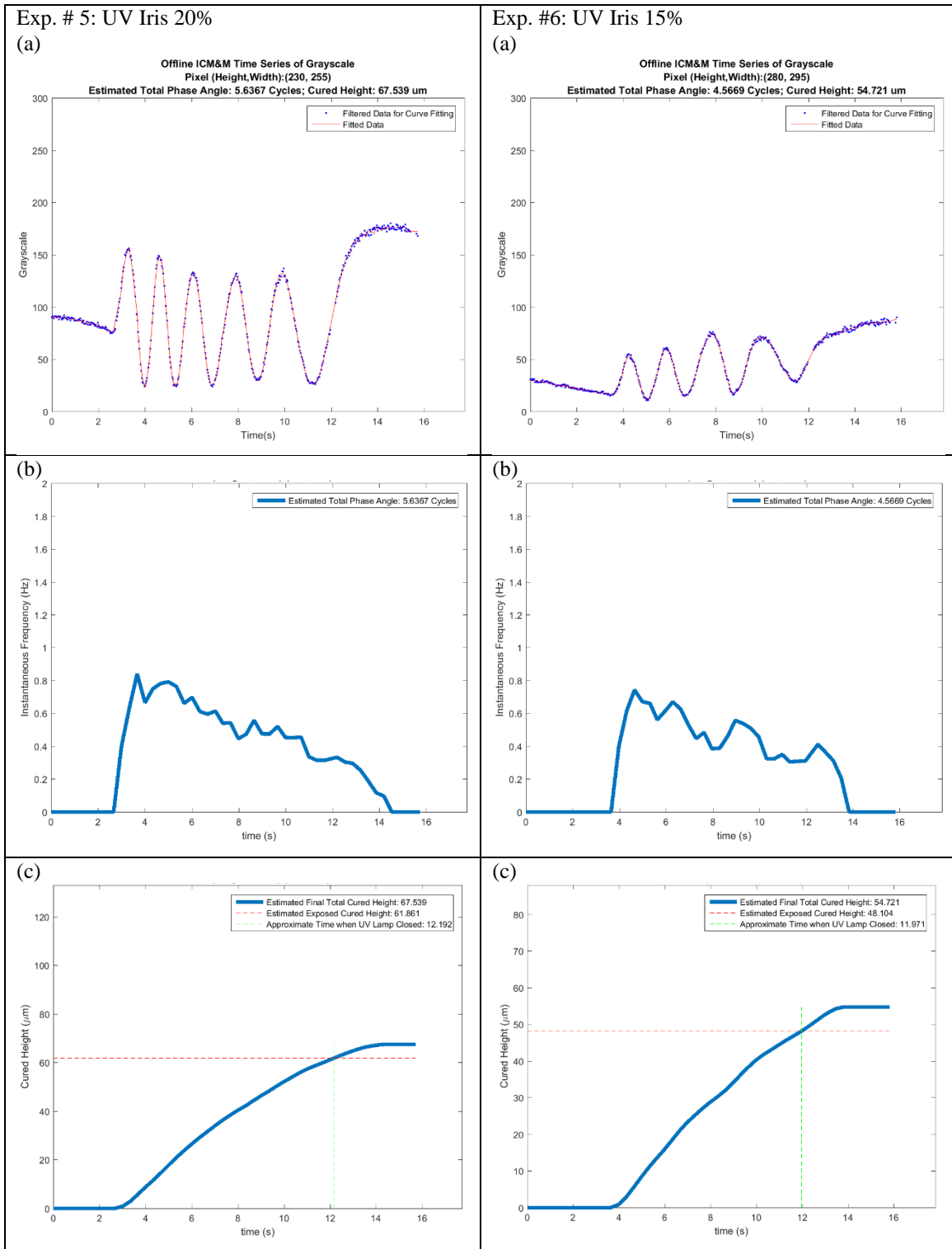


Figure 64 (continued). ICM&M implementation and process dynamics in the experiments varying exposure intensity: (a) representative pixel's time sequence of grayscale; (b) estimated instantaneous frequency; (c) evolving cured height of the voxel on the selected pixel.

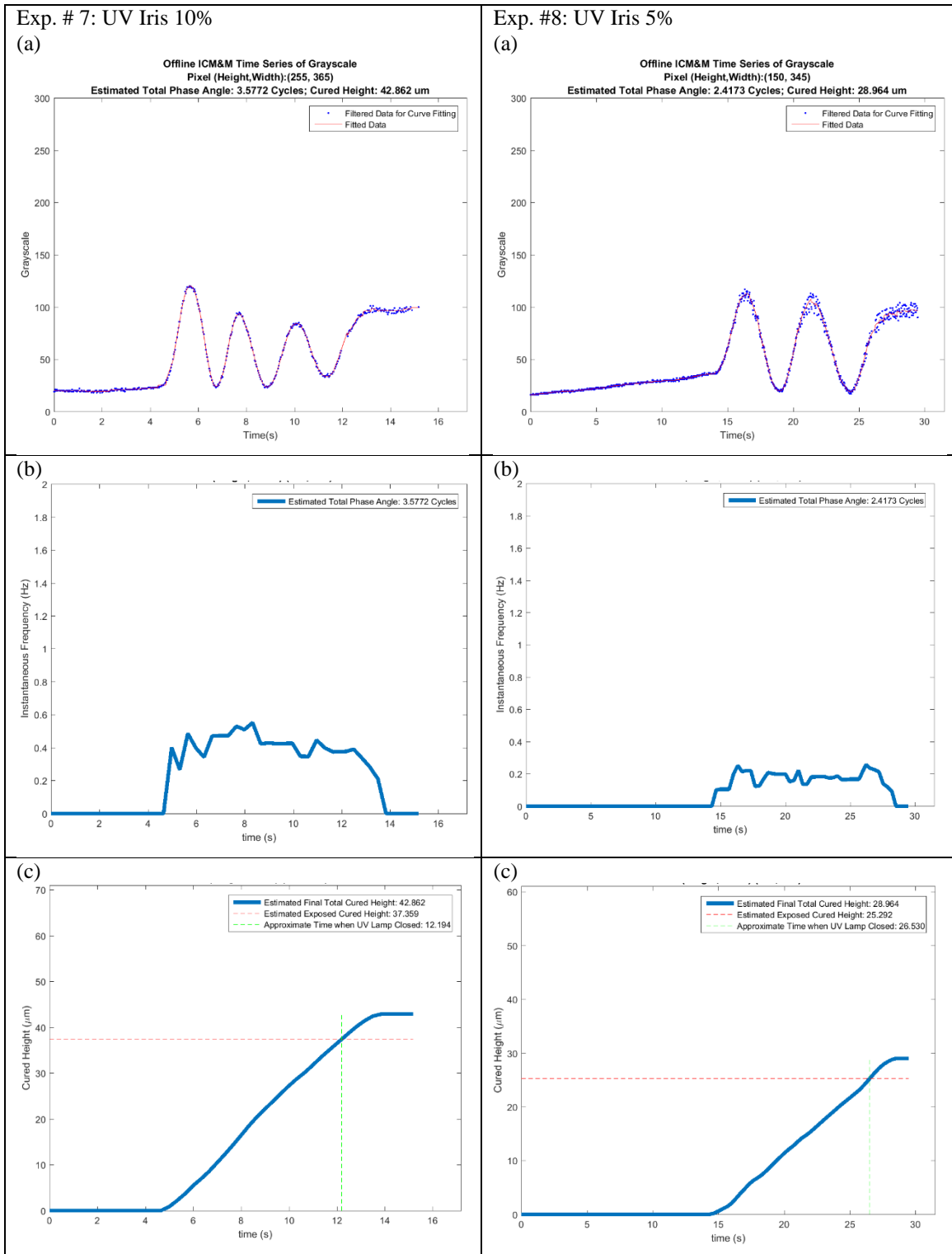


Figure 64 (continued). ICM&M implementation and process dynamics in the experiments varying exposure intensity: (a) representative pixel's time sequence of grayscale; (b) estimated instantaneous frequency; (c) evolving cured height of the voxel on the selected pixel.

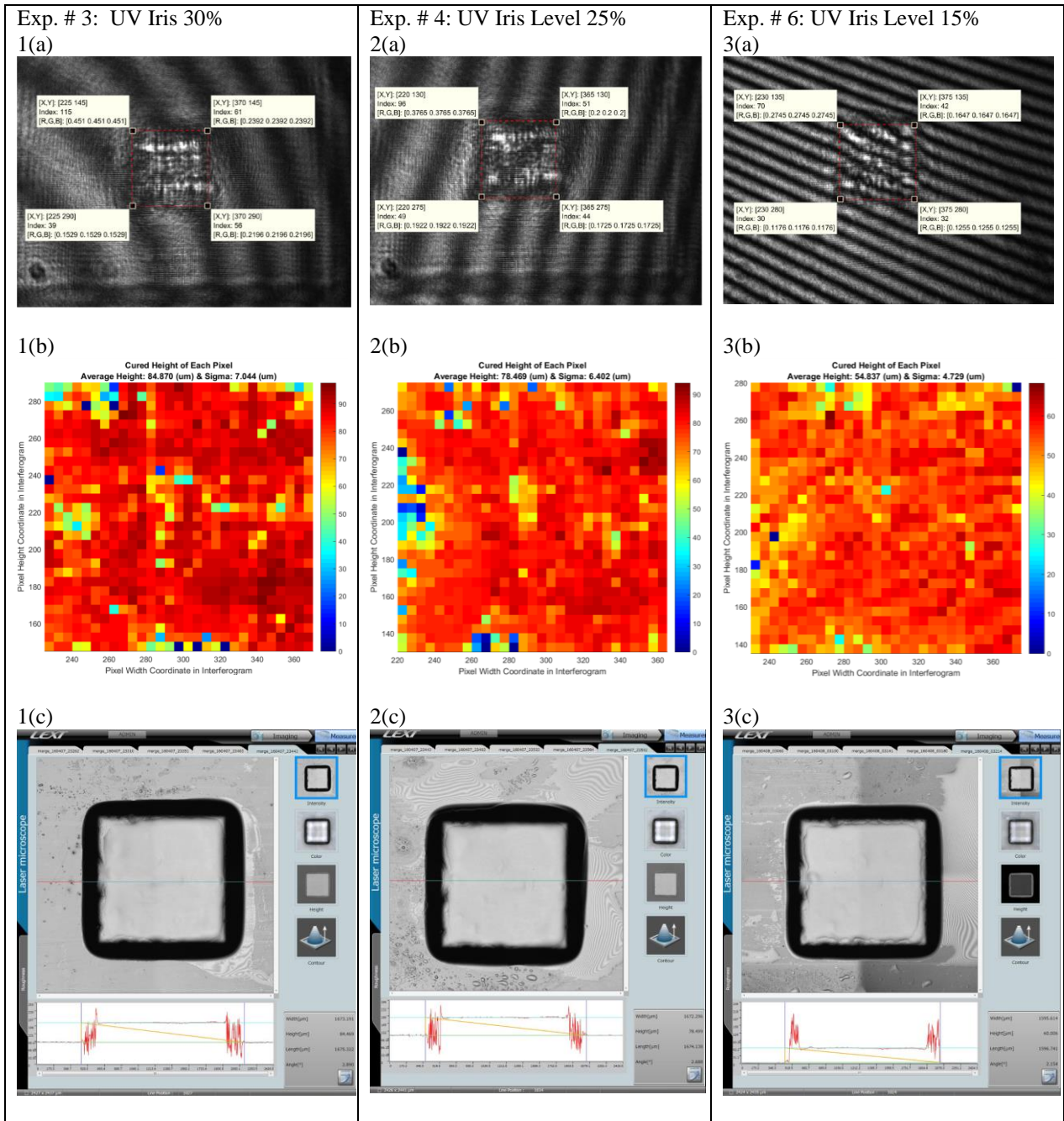


Figure 65. Selected ICM&M result VS. microscope measurement for the 1<sup>st</sup> set of samples in exposure intensity experiment: (a) Selected in the last interferogram the approximated cured area (enclosed within the red dashed lines) to measure with ICM&M; (b) ICM&M measured heights profile for voxels on the pixels within the cured area; (c) Microscope measured horizontal line profile.

Figure 65 depicts three experiments' heights profile measurement results for Experiment #3, #4 and #6 with UV iris level being 30%, 25% and 15%, respectively. The other subgroups of experiment were performed in a similar way and all the results will be



summarized at the end of this section. In Figure 65 (a), the selected ROI of approximated cured shape is shown in the ending interferogram of the sample in each experiment. Figure 65 (b) displays the ICM&M estimated heights for the pixels in the ROI at an interval of five pixels, and similar variations present in the heights profile as seen and explained in the previous validation experiment group. Figure 65 (c) shows the measured profile lines in X-direction, which demonstrate some variation of a few microns in the profile line; hence the average of two profile lines height values was used as an estimation of the actual cured height to assess the ICM&M results as shown in Table 12.

As a quantitative summary, Table 12 reports in details all the measurement results for the two sets of experiments varying exposure intensity. The experiments with exposure intensity at iris level of 20%, 25%, 30% and 35% had under 3 microns' deviation and less than 5% relative error, while the other experiments at high (40%) intensity and lower intensity (5%, 10% and 15%) had larger relative error virtually within 10%.

Table 12. Measurement results of validation experiments varying exposure intensity

Experiment Subgroup NO.	Exposure Intensity (iris level)	Sample NO.	ROI Cured Area Pixels (Width, Height)	ICM&M Results			Microscope Measured Profile Line Height ( $\mu\text{m}$ )			Absolute Deviation ( $\mu\text{m}$ )	Relative Error
				Total Phase (cycle, i.e. $2\pi$ rad)	Cured Height ( $\mu\text{m}$ )	St.Deviation - Cured Height $\sigma$ ( $\mu\text{m}$ )	X-direction	Y-direction	Average		
Experiment #1	40%	Sample 1	(220:365, 155:300)	8.453	101.29	4.86	95.939	94.620	95.28	6.01	6.30%
		Sample 2	(220:365, 170:315)	8.562	102.59	7.26	97.043	96.964	97.00	5.59	5.76%
Experiment #2	35%	Sample 1	(225:370, 165:310)	7.639	91.54	6.48	92.001	93.153	92.58	-1.04	-1.13%
		Sample 2	(220:365, 160:305)	7.500	89.87	7.20	88.997	90.060	89.53	0.34	0.38%
Experiment #3	30%	Sample 1	(225:370, 145:290)	7.083	84.87	7.04	84.469	82.695	83.58	1.29	1.54%
		Sample 2	(225:370, 150:295)	7.122	85.34	6.54	83.884	84.793	84.34	1.00	1.18%
Experiment #4	25%	Sample 1	(220:365, 130:275)	6.549	78.47	6.40	78.499	77.905	78.20	0.27	0.34%
		Sample 2	(225:370, 135:280)	6.611	79.22	5.91	77.958	77.368	77.66	1.55	2.00%
Experiment #5	20%	Sample 1	(235:380, 130:275)	5.665	67.87	5.59	69.762	70.258	70.01	-2.14	-3.05%
		Sample 2	(235:380, 135:380)	5.502	65.92	5.74	70.277	66.826	68.55	-2.63	-3.84%
Experiment #6	15%	Sample 1	(230:375, 135:280)	4.577	54.84	4.73	60.006	58.985	59.50	-4.66	-7.83%
		Sample 2	(230:375, 135:280)	4.923	58.98	4.83	62.812	64.431	63.62	-4.64	-7.29%
Experiment #7	10%	Sample 1	(230:375, 135:280)	3.409	40.84	4.50	45.653	45.658	45.66	-4.81	-10.54%
		Sample 2	(225:370, 135:280)	3.456	41.42	4.47	45.646	45.342	45.49	-4.08	-8.96%
Experiment #8	5%	Sample 1	(225:370, 140:285)	2.307	27.64	5.40	30.895	28.620	29.76	-2.12	-7.12%
		Sample 2	(235:380, 140:285)	2.312	27.70	5.20	30.019	28.666	29.34	-1.64	-5.61%

Figure 66 depicts the measurement results for visualized comparisons of the within-subgroup samples repeatability, between-subgroup trends of heights versus intensity levels, and ICM&M estimation accuracy against microscope measurements. As shown in Figure 66, in each subgroup of experiment, the ICM&M results are close within the two samples, and the microscope results are similar, but there seems to be a persistent gap between ICM&M and microscope results. The alarming relative errors might be an indication for the need of using modified refractive index rather than constant refractive index in the ICM&M sensor model, which will be investigated in more details in upcoming discussion about traceability in Section 8.3.1.

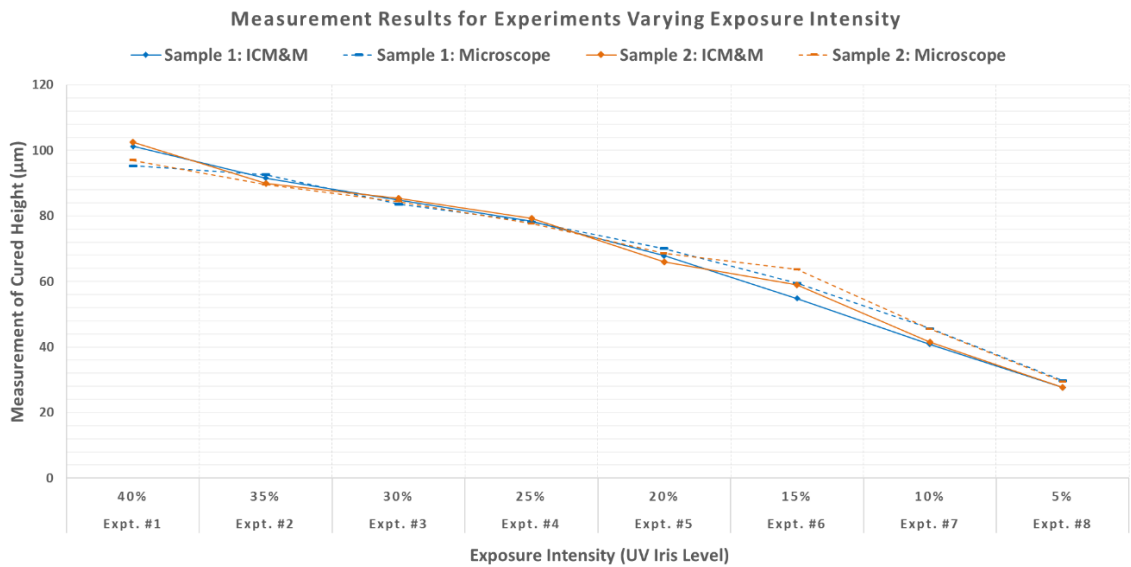


Figure 66. Comparing the ICM&M measurement results with the microscope measurement in experiments varying exposure intensity

The worst group which had the highest relative error is Experiment #7 at iris level 10%, but the absolute deviation is only about 4µm that could be partially attributed to the microscope error. It is not unusual for the microscope cursor measurement to have a  $\pm 3\mu\text{m}$  or sometimes even up to 7µm deviation from the average analysis of the microscope exported spreadsheet of data. The smoother sample we have, the less error the

microscope cursor measurement would have. The microscope error is more notable in the case of curing lower samples such as in Experiment #8 with iris level of 5%, only a 2- $\mu\text{m}$  deviation would induce 7% relative error.

### **8.3 Measurement characteristics of ICM&M**

#### **8.3.1 Traceability**

Metrological traceability is the property of a measurement result whereby the result can be related to a reference through a documented unbroken chain of calibrations, each contributing to the measurement uncertainty [97].

In the ICM&M practice, traceability is attained by careful calibration of measurement system using the ICM&M sensor model to estimate the effective solid part refractive index as the calibrated transfer basis and using the microscope as standard. With the experiment results above, the ICM&M traceability is reviewed and revised in this section to improve the overall measurement accuracy.

##### **8.3.1.1 Best traceability achieved for same-condition samples**

In the first set of validation experiment presented in Section 4.3, the 12-second experiment had the best result with minimal errors (0.1  $\mu\text{m}$  and less than 0.15%) in the full field cured height profile, in which the outcome is within the expectation because it adopted exactly the same process conditions as the calibration did. The experiment concludes that the ICM&M method could measure accurately for the ECPL process that is conducted with the same process conditions as the calibration experiment used.

### 8.3.1.2 To maintain traceability for different-conditions samples needs adjust the effective refractive index in the ICM&M sensor model

Except for the 12-second exposure experiment in the first validation experiment group, all the other experiments were conducted with settings different from these in the calibration experiments. It is notable that the ICM&M estimation errors in these different-conditions samples display an interesting pattern – near-zero deviation for samples cured around the calibration experiment setting, smaller-than-actual (microscope) measurement result for samples cured with less time or less intensity, and larger-than-actual result for samples cured with more time or more intensity.

Specifically, in the first set of experiment varying exposure time (Table 11), the 9 second exposure experiment had negative absolute deviation while the 15 second exposure experiments had positive value of absolute deviation. In the second set of experiment varying exposure intensity (Table 12) on one hand, the ICM&M tends to overestimate the cured height in experiments with iris level from 40% to 25%, which are all larger than the 22% iris level intensity as was used in the calibration. On the other hand, the ICM&M tends to underestimate the cured heights in the less than 22% (i.e., 20%, 15%, 10% and 5%) experiments.

The observed pattern of deviations could imply that the effective refractive index for higher cured parts should be larger and that for lower cured parts should be smaller than the calibrated value of 1.4945 in the calibration experiments above, so that the ICM&M results could be brought closer to the microscope results.

Upon reflection on the definition of the mean (i.e. effective) refractive index  $n_m$  in the sensor model [68], we found that it was the intermediate value between the fully cured solid part's refractive index and the thin curing front's refractive index based on the mean value theorem of integration. Intuitively, the effective (i.e. mean) refractive

index of the higher cured part could be larger as the cured part constitutes of more solid part - the previously cured part with larger curing degree and denser crosslinked polymers. As the part grows, the fresh cured thin layer occupies a less and less portion to the entire cured height, hence the mean refractive index defined in the sensor model is expected to become larger.

The mean refractive index  $n_m$  is actually correlated with the cured height, hence theoretically it is subject to change during the curing process. The higher the cured part is, the larger the mean refractive index  $n_m$  is. However, in the previous analysis as preliminary validation, for simplicity, we assumed that the mean refractive index was constant and modeled a linear relationship between the cured height and phase angle. The linear relationship due to the assumption of a constant refractive index sometimes does not hold well as one can see some nonlinearity present in the curing process from the dynamics curves in Figure 61 and Figure 64.

### 8.3.1.3 Literature research in dynamic change in refractive index during photopolymerization

Photopolymerization processes are accompanied by photoinitiator absorption, density changes and volumetric shrinkage, which alter optical properties and affects curing efficiency through depth. Spectral domain low coherence interferometry (LCI) was used to measure time-resolved changes in group refractive index and physical thickness throughout the photocure of a commercial dental composite [89], and the study revealed a linear relationship between the optical and physical density. Another reported investigation using LCI technique has found the change in optical characteristics through the bulk of curing photopolymers [98]. It has also demonstrated simultaneous evolution of optical (refractive index) and physical (shrinkage) properties throughout curing of photoactive monomers, and concluded that the extent and rate of refractive index change is dependent upon monomer formulation such as concentrations [98]. The mean

refractive index for resins with various resin composition ratios demonstrate a change at the magnitude order of  $10^{-2}$  between uncured and cured resin, and a change at the magnitude order of  $10^{-3}$  for the curing resin during the photopolymerization process with uncertainty of  $10^{-4}$  by two methods – LCI and a conventional Abbe refractometer.

Furthermore, a digital holographic microscopy based quantitative phase imaging system was used to measure the light-induced refractive index changes [96]. The most important advantage of quantitative phase imaging is the capability to measure the spatial distribution of the induced refractive index change. Further investigation is still needed concerning the spatial and temporal dynamics of the refractive index change in photopolymer. Nevertheless, experiments clarified that a rapid and steep change occurred in the refractive index at early stage of the reaction, and the total refractive index change during dark curing ranges from  $0.5 \times 10^{-3}$  to  $2.8 \times 10^{-3}$  for low to very high exposure intensity in that study.

All the reported research suggest that the effective refractive index is indeed changing as the resin cures and one should take it into account while implementing the ICM&M method.

#### 8.3.1.4 Improve the ICM&M method by incorporating simultaneous changes in both cured height and refractive index

For this specific ECPL material and process, to investigate quantitatively how the effective refractive index could be slightly changing as the photopolymerization curing goes on, we calculate the mean solid refractive index using the calibration model for all the samples and plots out the true effective refractive index against the ICM&M estimated phase angle as shown in Figure 67. The model of effective refractive index of the in-process curing part and solid cured part is shown as in Equation ( 26 ) and Figure 67. Both the trend and magnitude order (0.001) of the refractive index change found by the ICM&M analysis for the ECPL process conforms well with the literature reported

finding of a gradual increase in refractive index as the photopolymer resin cures [98], though different materials are used.

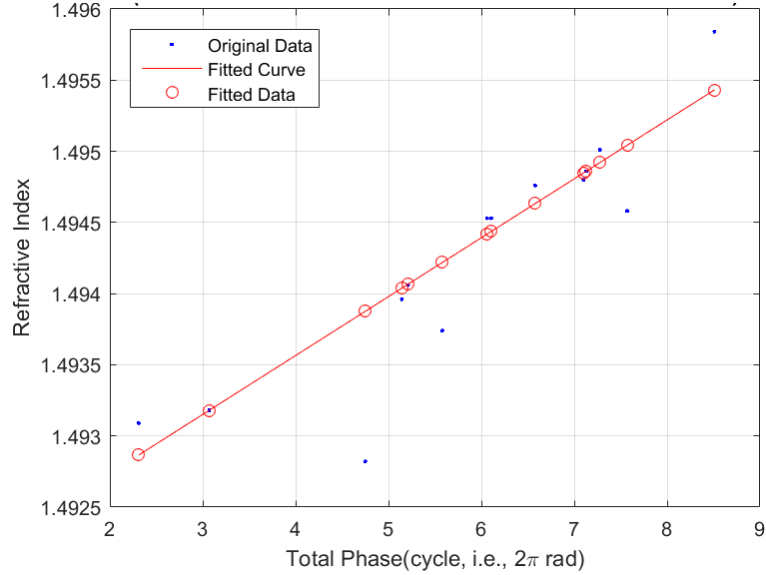


Figure 67. Model of the evolving effective refractive index  $n_m$

The reason we built the refractive index evolution curve against phase angle instead of cured height is because one would not have the height information available while implementing the ICM&M for heights measurement, whereas the temporal phase shifts conveyed by the interferogram signals are accessible to provide an alternative indication for cured part growth.

There are a few outliers, for example, the data point of phase angle 4.75 with a refractive index of 1.4928 is from the exposure intensity experiment with UV iris level at 15%, for which refractive index estimation we used the average of the two samples because it showed unusual discrepancy. The main reason for the outliers lies in the microscope measurement uncertainty to which the subtle changing calibrated refractive index is very sensitive. Nevertheless, the R-square of the linear curve fitting is 0.95866, indicating a fairly good fitting. The coefficients in Equation ( 30 ) show that the effective refractive index varies at the third decimal place, hence in the ICM&M method one

should use refractive index value accurate to at least the fourth digit after the decimal point.

$$n_m = 0.0004 \cdot \phi + 1.4919 \quad (26)$$

where  $n_m$  is the mean or effective refractive index of the cured part, and  $\phi$  is the total shifted phase angle. It is noted that the ICM&M method can support an accuracy to three decimal places and the 4<sup>th</sup> decimal point in this model only helps to round the estimation to that accuracy.

The initial ICM&M may be flawed in assuming constant effective refractive index, and we will recalculate the ICM&M estimation using evolving refractive index in this section. Firstly, we can obtain a modified refractive index value by plugging the ICM&M estimated phase value into Equation ( 26 ). In Table 13 and Table 14, the rightmost green columns show the modified refractive index and corresponding ICM&M results, which yield apparently better accuracy than previous results based on constant refractive index.

Table 13. ICM&M measurement results using growth-dependent refractive index for the validation group varying exposure time

Exposure Time (s)	Sample NO.	ROI Pixels (Width, Height)	ICM&M Results			Microscope Measured Profile Line Height (µm)			Absolute Deviation (µm)	Relative Error	Modified Effective Refractive Index	ICM&M Results (µm) with Modified Refractive Index	Absolute Deviation (µm)
			Total Phase (cycle, i.e. $2\pi$ rad)	Cured Height (µm)	St.Deviation - Cured Height $\sigma$ (µm)	X-direction	Y-direction	Average					
9s	Sample 1	Cured Area (240:380, 150:290)	5.211	62.43	4.19	64.192	63.211	63.70	-1.27	-1.99%	1.49407	63.68	-0.02
9s	Sample 2	Cured Area (225:370, 145:290)	5.144	61.63	4.37	63.031	63.335	63.18	-1.55	-2.45%	1.49404	62.94	-0.24
12s	Sample 1	Cured Area (235:380, 155:300)	6.106	73.16	5.44	74.349	71.775	73.06	0.10	0.13%	1.49444	73.37	0.31
12s	Sample 2	Cured Area (235:380, 135:280)	6.062	72.63	4.95	72.760	72.299	72.53	0.10	0.14%	1.49442	72.90	0.37
15s	Sample 1	Cured Area (250:395, 140:285)	7.276	87.19	5.21	84.160	86.329	85.24	1.94	2.28%	1.49492	85.56	0.32
15s	Sample 2	Cured Area (230:375, 150:295)	7.129	85.42	5.45	84.305	83.772	84.04	1.38	1.64%	1.49486	84.05	0.01

The overall ICM&M accuracy improvement with the evolving effective refractive index is shown in Figure 68. The previously most-errored (10% error) group of 10% UV iris level experiment is now able to measure with under 5% error. After applying the improved model, the highest ICM&M errors present in the 15% UV iris level experiment



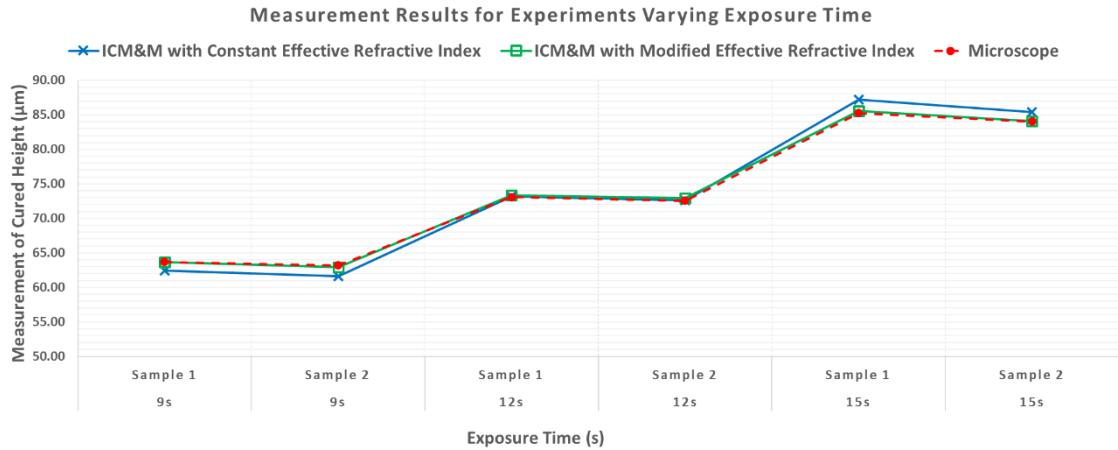
instead, which is understandable because its microscope measurements are the most inconsistent probably due to human error in the microscope practice.

Table 14. ICM&M measurement results using growth-dependent refractive index for the validation group varying exposure intensity

Exposure Intensity (iris level)	Sample NO.	ROI Cured Area Pixels (Width, Height)	ICM&M Results			Microscope Measured Profile Line Height ( $\mu\text{m}$ )			Absolute Deviation ( $\mu\text{m}$ )	Relative Error	Modified Effective Refractive Index	ICM&M Results ( $\mu\text{m}$ ) with Modified Refractive Index	Absolute Deviation ( $\mu\text{m}$ )
			Total Phase (cycle, i.e. $2\pi$ rad)	Cured Height ( $\mu\text{m}$ )	St.Deviation - Cured Height $\sigma$ ( $\mu\text{m}$ )	X-direction	Y-direction	Average					
40%	Sample 1	(220:365, 155:300)	8.453	101.29	4.86	95.939	94.620	95.28	6.01	6.30%	1.49543	97.21	1.93
40%	Sample 2	(220:365, 170:315)	8.562	102.59	7.26	97.043	96.964	97.00	5.59	5.76%	1.49543	98.46	1.46
35%	Sample 1	(225:370, 165:310)	7.639	91.54	6.48	92.001	93.153	92.58	-1.04	-1.13%	1.49504	89.35	-3.23
35%	Sample 2	(220:365, 160:305)	7.500	89.87	7.20	88.997	90.060	89.53	0.34	0.38%	1.49504	87.73	-1.80
30%	Sample 1	(225:370, 145:290)	7.083	84.87	7.04	84.469	82.695	83.58	1.29	1.54%	1.49485	83.56	-0.02
30%	Sample 2	(225:370, 150:295)	7.122	85.34	6.54	83.884	84.793	84.34	1.00	1.18%	1.49485	84.02	-0.32
25%	Sample 1	(220:365, 130:275)	6.549	78.47	6.40	78.499	77.905	78.20	0.27	0.34%	1.49463	78.00	-0.20
25%	Sample 2	(225:370, 135:280)	6.611	79.22	5.91	77.958	77.368	77.66	1.55	2.00%	1.49463	78.74	1.08
20%	Sample 1	(235:380, 130:275)	5.665	67.87	5.59	69.762	70.258	70.01	-2.14	-3.05%	1.49422	68.74	-1.27
20%	Sample 2	(235:380, 135:380)	5.502	65.92	5.74	70.277	66.826	68.55	-2.63	-3.84%	1.49422	66.77	-1.78
15%	Sample 1	(230:375, 135:280)	4.577	54.84	4.73	60.006	58.985	59.50	-4.66	-7.83%	1.49388	56.42	-3.07
15%	Sample 2	(230:375, 135:280)	4.923	58.98	4.83	62.812	64.431	63.62	-4.64	-7.29%	1.49388	60.69	-2.93
10%	Sample 1	(230:375, 135:280)	3.409	40.84	4.50	45.653	45.658	45.66	-4.81	-10.54%	1.49318	43.43	-2.23
10%	Sample 2	(225:370, 135:280)	3.456	41.42	4.47	45.646	45.342	45.49	-4.08	-8.96%	1.49318	44.03	-1.46
5%	Sample 1	(225:370, 140:285)	2.307	27.64	5.40	30.895	28.620	29.76	-2.12	-7.12%	1.49287	29.84	0.08
5%	Sample 2	(235:380, 140:285)	2.312	27.70	5.20	30.019	28.666	29.34	-1.64	-5.61%	1.49287	29.90	0.56

Considering the likely microscope errors, we just relax the curve fitting goodness and use a linear model to predict the varying effective refractive index as the part gets cured. Despite that roughly linear model of refractive index used, the problematic errors in lower and higher samples in Figure 63 and Figure 66 can still be well addressed as shown in Figure 68.

(a)



(b)

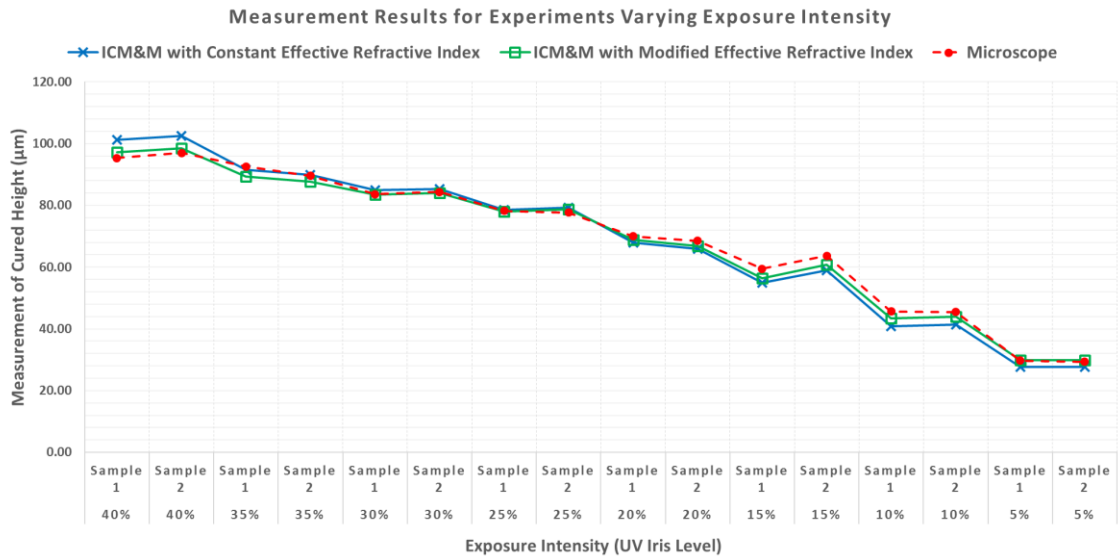


Figure 68. Improved ICM&M accuracy by using growth-dependent (previously constant) effective refractive index in the sensor model (a) validation experiments varying exposure time; (b) validation experiments varying exposure intensity.

### 8.3.2 Comparability and accuracy

External comparisons between the in-house ICM&M and a commercial microscope are an essential way to ensure commensurate measurements for evaluating the reliability of the developed ICM&M method. The experiments compare the ICM&M estimated height with the average of the microscope measured profile lines heights, resulting in absolute deviations and relative errors. The absolute errors of only a few

microns and the relative errors under 5%, prove that the ICM&M method has sufficient accuracy with a standard uncertainty of several microns for ECPL process measurement. The external comparison of ICM&M and microscope for each sample shows convincing accuracy of the ICM&M method.

Internal comparison results among the ICM&M measurements for various samples heights are also critical in the ICM&M validation to gain more confidence in its measurement capability. The samples in the calibration and validation experiments present consistency in the ECPL process output and ICM&M measurement results, which are shown to be good enough compared with the confocal microscope measurements.

All of the experiments including the ECPL process, ICM&M implementation and microscope measurement, taken together, have established reproducible results, and show comparability and consistency over space and time.

### 8.3.3 Repeatability

As shown in Table 11 and Table 12, the internal comparison of Sample 1 and Sample 2 in each subset of experiment shows quite identical ICM&M results of both phase angles and cured heights, which demonstrates the repeatability of the ICM&M method. In this study, the repeatability is computed as the square root of mean squared errors of the two samples in each experiment as shown in Equation ( 27 ). Table 15 shows the repeatability of the two groups of validation experiments, and we could conclude that the ICM&M measurement repeatability is 2 $\mu$ m, which means that one could expect a deviation of 2 $\mu$ m in measurements for repeatedly cured samples' heights.

$$\mathbf{Repeatability} = \sqrt{\frac{\sum_{i=1}^n (Z_{i1} - Z_{i2})^2}{n}} \quad ( 27 )$$

where  $n$  is the total number of experiment subsets,  $Z_{i1}$  and  $Z_{i2}$  are Sample 1 and Sample 2 heights, respectively.

Table 15. Measurement repeatability

Validation Experiment Group	Repeatability ( $\mu\text{m}$ )	
	ICM&M	Microscope
#1: varying exposure time	1.16	0.82
#2: varying exposure intensity	1.82	2.01

### 8.3.4 Sensitivity, resolution and range

Based on the ICM&M sensor model [68], the sensitivity of the measured height  $Z$  to a unit phase change  $\Phi$  ( $rad$ ) which is  $1/(2\pi)$  of 1 cycle  $\Phi$  (*unit: cycle, i.e.,  $2\pi rad$* ), is shown in Equation ( 28 ) and evaluated as below. It indicates that an error of  $\pm 0.5$  cycle in the phase estimation could induce an absolute deviation of  $\pm 6 \mu\text{m}$  in the height measurement. Due to the signal noise, the ICM&M algorithm sometimes could not identify the half cycle correctly, hence it happens that there could be a half cycle variation in the phase estimation which explains partial reason for the observed variations of about  $5 \mu\text{m}$  as shown in the ICM&M measurement results above (Figure 62 and Figure 65).

<p>hence,</p> $\frac{dZ}{d\Phi} = \frac{\lambda}{2(n_m - n_l)} \cong \frac{0.532\mu\text{m}}{2(0.0222)\text{cycle}} = 11.982 \frac{\mu\text{m}}{\text{cycle}}$ $\text{Sensitivity} = \frac{dZ}{d\Phi} = \frac{dZ}{(2\pi)d\Phi} = 1.907 \mu\text{m}/\text{rad}$ $Z_{\text{cycle}} = 1 (\text{cycle}) \times \frac{dZ}{d\Phi} \cong 11.982\mu\text{m}$	( 28 )
--	--------

The ICM&M resolution is dependent on both the ECPL process speed and the ICM&M measurement speed, and the smallest cured height ICM&M can resolve could be estimated by Equation ( 29 ).

$$\text{Resolution} = \frac{dZ}{d\Phi} \cdot (MTI \cdot IF) \cong 11.982 \cdot (MTI \cdot IF)\mu\text{m} \quad ( 29 )$$

where  $MTI$  is measurement time interval (s), and  $IF$  is the instantaneous frequency (Hz).

In this study, the measurement time interval is about 1/3 second, and the ICM&M estimated instantaneous frequency vary with the exposure time and intensity. As is shown Figure 61 and Figure 64,  $IF$  decreases as the curing goes on and as the intensity drops. In this study, the fastest curing occurs at the beginning of UV iris level 40% curing resulting in  $IF$  1.4 Hz and the resolution is  $11.982 \cdot \left(\frac{1}{3} \cdot 1.4\right) = 5.59\mu m$ . The curing rate will slow down to zero at the end of the curing process with the resolution being gradually reduced to a couple of microns to ultimately less than 1  $\mu m$ . For a mild exposure intensity such as 20%-25% UV iris level, the curing process has the instantaneous frequency averaging at 0.5 Hz corresponding to a resolution of  $11.982 \cdot \left(\frac{1}{3} \cdot 0.5\right) = 2.00 \mu m$ .

Generally speaking, the ICM&M method could discern vertical dimension measurement at a magnitude order of micron and has ability to dive into submicron discrimination given faster measurement speed.

The range characteristic of the ICM&M method is determined by the laser coherent length and the ECPL material property especially refractive index. In this study, it is obvious that the ICM&M method could measure part heights of up to at least 100  $\mu m$ .

### **8.3.5 Summary of the ICM&M characteristics**

Table 16 summarizes the characteristics of the ICM&M method from the previous experiment analysis and results.

Table 16. ICM&M characteristics

<ul style="list-style-type: none"> <li>✓ <b>Traceability</b></li> <li>✓ <b>Full-field global</b></li> <li>✓ <b>Real-time fashion</b></li> <li>✓ <b>Discernibility for Photo-polymerization Processes (Incubation, Exposure / Dark Curing)</b></li> <li>✓ <b>Time-resolved refractive index (Resolution: 0.001):</b> <math>n_m = 0.0004 \cdot \phi + 1.4919</math></li> <li>✓ <b>Repeatability: 2 <math>\mu\text{m}</math></b></li> </ul>	<ul style="list-style-type: none"> <li>✓ <b>Resolution: <math>11.982 \cdot (MTI \cdot IF) \mu\text{m}</math></b> Note: <i>MTI</i> is measurement time interval (s), and <i>IF</i> is the instantaneous frequency (Hz). (e.g., <i>MTI</i>=1/3s, <i>IF</i>=0.2Hz, Resolution ~1 <math>\mu\text{m}</math>)</li> <li>✓ <b>Range: 0 to <math>\geq 100 \mu\text{m}</math></b></li> <li>✓ <b>Sensitivity: <math>1.907 \mu\text{m}/\text{rad}</math> (i.e., <math>\pm 6 \mu\text{m}</math> / half cycle)</b></li> <li>✓ <b>Accuracy</b></li> <li>✓ <b>Precision</b></li> <li>✓ <b>Stability</b></li> </ul>
--	--

## 8.4 Utility of the ICM&M system

### 8.4.1 Local vs. global measurement for the ECPL process

In Table 11, the line height, the area height average and the microscope results are in good accordance for each sample, demonstrating two things (1) a line could be representative to measure the average height of the entire cured area's average height; (2) the ICM&M is capable of both local and full-field measurement for the average height of the cured part. However, the line profile results are shown to be sometimes worse than the area profile results in terms of accuracy, indicating the potential bias in sampling lines for estimating the average height of the cured part and the potential peril in controlling the cured part height with only a handful pixels' measurement average.

#### 8.4.2 Lateral measurement potentiality

Though we focused on measuring the cured height in this study, a byproduct of lateral dimensions measurement is also available. In all the experiments above, the resultant interferograms show similar size of cured shape, which have approximately 145 pixels in the line corresponding to the flat top part's width in the microscope. Please note that the black outer frames around the samples as shown in Figure 62 and Figure 65 are sloping edges and are not taken into account for the width measurement by ICM&M, but might have been included in the microscope profile line. It is found that the width of the flat top part in all samples is pretty close to  $1250\ \mu\text{m}$ , which could be directly seen in Figure 62 Exp #1 and Exp #2.

All the experiments used the same size bitmap as DMD pattern (250-by-250 pixels), and the ICM&M method could retain that information of size similarity. Other than being able to qualitatively measure the lateral shape, the ICM&M is found to be able to measure quantitatively lateral dimensions according to the following calculations, which estimated successfully the width of the cured squares.

In an interferogram, one pixel is actually a binning of four original pixels captured by the ICM&M camera. The camera pixel size is  $2.2\ \mu\text{m} \times 2.2\ \mu\text{m}$ , hence a pixel in the interferogram is  $8.8\ \mu\text{m} \times 8.8\ \mu\text{m}$ . Because the ICM&M optics adopts a vertical beam path reflected upward from the sample to the camera, in principal, it is 1:1 mapping. The ICM&M measured lateral size could be estimated by multiplying the value of  $8.8\ \mu\text{m}$  with the number of pixels in the width dimension of the cured part shown in the interferogram. Hence, the estimated width of the cured square part is calculated as  $145 \times 8.8 = 1276\ \mu\text{m}$ , which is in good accordance with the microscope measurement results of width:  $1247.5\ \mu\text{m}$  on average for the width of the flat top part in all the samples. The ICM&M width estimation result has 2.4% relative error with a deviation of

30  $\mu\text{m}$ , which corresponds to  $\pm 4$  interferogram pixels, which is acceptable for an initial study.

Conclusively, the ICM&M system has great potentiality in measuring the lateral dimensions of width and length as well as the vertical heights. We recommend in future work utilizing image analysis with image edge detection algorithms to measure the pixels length of cured shape for lateral dimensions information. This approach of measuring lateral dimensions for cured part is actually an alternative to the current plan of measuring the shape by measuring the heights profile across the curing area, which comes back to our research scope and priority in this study.

#### **8.4.3 ICM&M for ECPL process dynamics, modeling, and control**

Foremost, the two sets of experiment varying exposure time and intensity aim to verify the sensitivity of ICM&M method to the process input. The series of ICM&M detected grayscale signal and ICM&M estimated evolution of the instantaneous frequency and cured height in Figure 61 and Figure 64 exemplified that the ICM&M method could rapidly and accurately identify different ECPL process stages – threshold period, curing period and dark period, and meanwhile could capture in a real-time fashion the process dynamics in terms of the curing speed (instantaneous frequency) and cured height. Hence, the ICM&M can provide a powerful tool for visualizing the process dynamics, and help in future develop an insightful process model and thereby an effective process control system in the future.

In the validation experiments varying exposure time, the finding that the processes under all same conditions but different exposure time share similar instantaneous frequency in the grayscale signal confirms that exposure time adjustment cannot manipulate the process dynamics such as curing rate. Hence, the conventional



exposure time control of stereolithography-like additive manufacturing process is, strictly speaking, not a process dynamics control, but just a simple process on-off switch.

In the validation experiments varying exposure intensity, the evidence of the relationship between UV intensity and photo curing process dynamics can be utilized for photopolymerization-based additive manufacturing process modeling and control. The new thinking of exposure intensity control could be a ground-breaking complement to the traditional exposure time control, in order to realize an ultimate control of the ECPL process for better accuracy.

## **8.5 Chapter summary**

The lack of real-time sensors critical to process monitoring and control has been identified as one of the major challenges that are currently impeding large-scale deployment of AM processes and equipment. The interferometric curing monitoring and measuring (ICM&M) method, for the specific photopolymer based micro stereolithography machine is validated and characterized in this study.

In this dissertation, to validate and fulfill the developed ICM&M method, an application program was designed and created in MATLAB. The application was deployed onto the physical system integrating the ECPL and ICM&M to automate the ECPL process. In this study, given the limited equipment configurations and computation resource, the data analysis and measurement computation in ICM&M was performed off line. A coherent series of experiments were performed curing square samples by varying the factors of exposure time and intensity, and a representative full-field height profile was measured for each cured sample by both the in-house ICM&M and a commercial confocal microscope, to evaluate the measurement characteristics including traceability, comparability, accuracy, repeatability, sensitivity, resolution and range.

The experimental results demonstrate that the ICM&M method can measure multiple voxel heights consistently and simultaneously, and features the capability of

full-field measurement which is desired in global measurement and control of ECPL. The ICM&M provides a cost-effective metrology for cured heights with excellent accuracy and repeatability, and meanwhile features decent capability of estimating lateral dimensions. This offline ICM&M experimental report is a convincing demonstration and advocacy for real-time ICM&M, and can be used to benchmark the real-time ICM&M metrology. Once provided with real-time operating system and multi-thread parallel computation power, the real-time process measurement and control for ECPL can be achieved with the aid of ICM&M method.

The experiment results also suggested for the development of an enhanced ICM&M sensor model with growth-dependent effective refractive index to improve its measurement accuracy.

In addition, utility of the ICM&M in process dynamics modeling and control was discussed. The ICM&M method successfully illustrated the ECPL curing process dynamics in terms of instantaneous frequency which is associated with the curing velocity, i.e., growing rate in units of  $\mu\text{m}$  per second. It is responsive to the curing start / stop, curing speed, and curing area as shown in the designed experiment series varying exposure time, intensity and pattern size. The implementation with the well-developed MATLAB application demonstrates that the ICM&M is feasible and deployable in the physical system, and is well fit for the purpose for real-time ECPL process measurement, modeling and control. Additionally, the ICM&M system is efficient compared with potentially available commercial measurement tools, which however could be costly and need retrofit to become a qualified real-time metrology for monitoring online photopolymer AM processes.

This chapter answers Research Question 1 using a simulation approach by replaying an interferogram video and estimating cured heights simultaneously to mimic a real-time process measurement. A series of coherent experiments and in-depth evaluation of the developed ICM&M characteristics validate further Research Hypothesis 1.

# **CHAPTER 9 REAL-TIME ECPL PROCESS MEASUREMENT AND CONTROL**

The previous chapter provides a verification for Research Hypothesis 1 (Section 4.5.1) with the offline prototype of ICM&M method being validated and characterized. This chapter demonstrates a real-time implementation of the ICM&M method for measuring and controlling the ECPL process in order to evaluate further Research Hypothesis 1 and to validate preliminarily Research Hypothesis 2 as outlined in Chapter 4 (Section 4.5.2). In Section 9.2, the essential ECPL-M&C software is highlighted as an enabling tool and a potential error source for the subsequent real-time implementation experiment. Section 9.3 introduces the real-time implementation of the ICM&M system. A basic feedforward-feedback On-Off control scheme is developed in Section 9.4 for the real-time process control. Design of the real-time experiment is introduced in Section 9.6, followed by experiment results and discussions in Section 9.7. More discussion and recommendations about the preliminary and future real-time feedback control of ECPL process is presented in Section 9.8. Section 9.9 concludes the chapter with the benefits and challenges of applying real-time measurement for ECPL process control.

## **9.1 Background and introduction**

### **9.1.1 Research in process modeling, measurement and control for AM**

Currently, a gap exists between high-fidelity modeling research and real-time process measurement and online control efforts. The challenges involved in the sensing of AM processes include a lack of accessible metrology system and the need for intensive computing power. Generally speaking, the sensing of AM processes may require fast in situ measurements of the temperature, cooling rate, and residual stress; the calibration of fast optical sensors for high-accuracy measurements; and in-process monitoring of

geometric dimensions and the surface quality of finished layers [1]. Even if this is achieved, it is very challenging to use this information for the online process control of material composition and phase transformation, and for the repair of defects such as pinholes/porosity, micro cracks, and segregation. For commercial AM machines, integrating control algorithms with existing AM equipment through the machines' proprietary controllers creates another significant barrier to the cost-effective implementation of real-time AM process control.

A majority of current research on additive manufacturing has focused on metal AM process modeling and simulation for understanding the relationships between a material's process conditions and final properties [2-4], which are characterized into two main groups - mechanical properties (geometry, strength, hardness and residual stress) and microstructure properties (morphology, grain size, phase precipitation, etc.). A closed-loop control system based on infrared image sensing was built for control of the heat input and size of the molten pool in the laser based additive manufacturing process [4]. The closed loop control results showed a great improvement in the geometrical accuracy of the built features. The mechanical properties are dependent on microstructure properties that are controlled by thermal conditions at the onset of solidification and the cooling rate post solidification. Due to the high melt pool temperature and the rapid solidification process, there are currently no sensors available to monitor the microstructure in situ and in real-time. Thus, one needs to control the microstructure indirectly through other affecting parameters that can be monitored and controlled more easily. Assuming a correlation between the temperatures and cooling rate and deposition microstructure, in laser additive manufacturing (LAM), a real-time PID controller was designed to generate a consistent microstructure by manipulating the laser beam travel speed for maintaining certain cooling rate with feedback signals of surface temperatures monitored by an in-situ infrared imaging system [5].

Most studies present either a theoretical approach with little to no verification compared to that of real-life results [2], or semi-empirical approaches that may correlate well with specific experiments, but their results are not directly transferrable and expandable to other machines, requiring further experimentation. The AM processes could significantly benefit from accurate measurement systems, aided by process models in order to be able to back up the real measured data with model prediction.

Given the research progress in metal AM, the modeling, metrology and controls of polymer and soft materials AM are emerging as new research priorities for the monitored dimensional accuracy and materials and mechanics properties significantly affect the quality and performance of the final product [6]. The physics of polymers such as photopolymerization in additive lithography process and melting and recrystallization in plastic filament extrusion process are not adequately understood to develop robust mathematical models. Supercomputing can greatly impact such modeling efforts. Multi-physics complex process models need to be reduced to lower-order models for real-time parameter identification and control of AM processes [1]. For metal AM, only a few research groups have implemented closed-loop controllers to control the melt pool temperature, and even fewer literature report on closed-loop control rate or the microstructure [5]. As to the closed-loop control for non-metal additive manufacturing, to the authors' best knowledge, there is a scarcity of literature in real-time measurement and control for polymer and soft materials AM processes.

### **9.1.2 Real-time control in commercial AM systems**

From a commercial manufacturing standpoint, in-process sensing technology for additive manufacturing is still in its infancy [14]. Process monitoring and controls for additive manufacturing are still in research and development phase [15], with metal additive manufacturing predominating the specific research area of measurement science and feedback control [8, 9] and the counterpart research for non-metal such as polymer

and soft materials AM processes has just set out recently [6]. Status of real-time control in commercial metal additive manufacturing systems is summarized in a most recent review literature [15], which found that continuous feedback control in commercial systems is more easily realized in directed energy deposition systems than in laser powder bed fusion (LPBF) systems due to the much lower processing speeds and larger melt pool size. The Optomec LENS (Laser Engineered Net Shaping) MR-7 offers the option of closed loop control, which is being tested and optimized by university collaborators [16]. In commercial LPBF systems, high-speed closed-loop control based on melt pool monitoring is not yet realized, however, layer-wise monitoring and control have been demonstrated. For example, Concept Laser's QM coating module images newly formed powder layer surfaces, and actively detects and compensates for powder layer thickness variation [15].

### **9.1.3 Objective of this chapter**

The main objective of this chapter is to implement and validate the developed ICM&M system in real time, as well as to develop and demonstrate a real-time system for controlling the ECPL process output of cured part's vertical dimension.

## **9.2 Parallel computing software for real-time process measurement and control**

In the ECPL process, high-speed interferogram can be used to obtain imaging and optics data for dimensions prediction by determining the cured height resulting from grayscales signal analysis. In order to use such information for ECPL process control, images from the AM processes have to be processed at a speed sufficient to capture the process dynamics.

One prerequisite for implementing the ICM&M method in real time fashion to measure and control the cured height of part made by ECPL process is a high-

performance software that handles data acquisition and analysis for measurement and performs decision making and actuation for control.

A parallel computing software was developed in MATLAB with real-time acquisition in the foreground and online measurement running in the background. Details about the programming of the MATLAB software are presented in Chapter 7. This chapter validates the real-time metrology and control with the software whose functionality and limitation have been acknowledged in Chapter 7.

It is worth to point out upfront that the developed ECPL-M&C software could inevitably induce some error in the ECPL process output of cured sample's height, and on the other hand presents possible room for improvement in the future work.

### **9.3 Implementation of the ICM&M in real time**

The ICM&M method has proven capability of measuring the ECPL process cured part off line, and provided a benchmark for real-time measurement performance. For real-time execution, the sensor model and all the algorithms remain the same as in the previous offline implementation (Chapter 8). except for the integration method (rectangle method is used in Chapter 8). However, the integration methods are shown to be similar in estimation accuracy. The reason for using trapezoidal integral rather than rectangle integral in this chapter is that the real-time implementation encounters a longer measurement interval (0.55 s Vs. 0.33 s in Chapter 8 experiments), for which trapezoidal integral method might be more accurate. Particularly, the real-time ICM&M continues to use the following setting as the offline ICM&M does: (1) 5×5 filter in preprocessing; (2) trapezoidal integral; (3) evolving refractive index model in Equation ( 26 ) [92].

One significant difference between the real-time ICM&M and previous offline ICM&M is the acquisition rate. In real time, the interferogram data acquisition can be affected by the online measurement and control in the parallel computing; hence, the fidelity and quality of real-time data is not as high as that of the data acquired without

any online analysis as in the previous offline implementation of ICM&M. The average image data acquisition rate is 0.033 s per frame (i.e., 30 frames per second) for purely collecting process data that is later analyzed off line, while the average image acquisition rate is 0.055 s per frame (i.e., 18 frames per second) in real time along with online measurement analysis.

Furthermore, latency time between real time acquisition and measurement analysis is notable and critical in the overall process accuracy. In this study, it is estimated as the elapsed time between the instant when the image is written into the memory file and the instant when the image is read by the thread for measurement analysis. Ideally, each frame should be read immediately once it is acquired; however, if the analysis of previous frames takes excessive time, the latest frame cannot be analyzed until after the previous frame is analyzed thus the analysis is lagging behind the acquisition. The latency time could be reduced to minimum given high performance hardware and software. The effect of measurement latency will be discussed further with the experiment results.

## **9.4 Design of a closed-loop controller**

This section designs a negative feedback on-off scheme for controlling the photopolymer part growth in real-time during the ECPL process.

### **9.4.1 The control scope**

The ECPL process is a complex nonlinear system and there could be multiple control actions including manipulating the resin composition, temperature, UV exposure time, exposure intensity and exposure pattern for curing a target 3D object. In this preliminary study of real-time measurement feedback control, to simplify the multi-input control problem, a basic exposure time controller is designed to understand the real-time controllability of the vertical dimension, i.e., cured height in the ECPL process.



Manipulating other process factors, especially the chemical components (e.g. initiators, and oxygen inhibitors), exposure intensity and pattern, could be conceived in future work to complement the outcomes of these exposure time control for multiple output of desired properties such as lateral dimensions and mechanical properties.

#### **9.4.2 The control mode**

As a preliminary controller with ICM&M feedback, the ECPL exposure time controller under investigation involves some discrete switching concept which is a fundamental control method of On-Off control [99]. In control theory, an On-Off controller, is a discontinuous feedback controller that switches abruptly between two states [46]. These controllers may be realized in terms of any element that provides hysteresis. They are often used to control a plant that accepts a binary input. Such a control mode is easier to implement but expects some process tolerance or deviation. A typical example of On-Off controller is a thermostat which senses the temperature and maintains it near a desired set point by switching on / off the heater.

Similarly, with the ICM&M system available online, an On-Off control mode is designed to determine when to shut down the UV lamp for controlling the height of ECPL cured part. The On-Off controller employs a negative feedback to correct errors between the measured height and target height; thereby, when the cured height approaches the reference value, the UV lamp is switched off in order to terminate the curing.

#### **9.4.3 The actuator**

For controlling the ECPL process, the exposure source UV lamp that allows for control of overall exposure intensity across the chamber, and the pattern generator DMD that comprises an array of micromirrors to deliver spatial control of exposure intensity, could both be adopted as actuators. In this basic controller design, only UV lamp is used

to control the exposure for curing blocks in the upcoming validation experiments. The UV lamp could be either completely on or completely off. Please note that the UV lamp is equipped with an iris which could provide discrete percentage levels from 0% to 100% in an increment of 1% that fine tunes the exposure intensity. In this study of On-Off controller, only the two extreme limits of UV lamp shutter – fully on and fully off- are employed; and in the future design for more advanced control methods, the full range of UV source intensities along with the DMD could be utilized for more control flexibility and capability. In the on-off control for ECPL process, given a constant UV iris level and a fixed DMD bitmap, the input of UV light is a step function as shown in Figure 69.

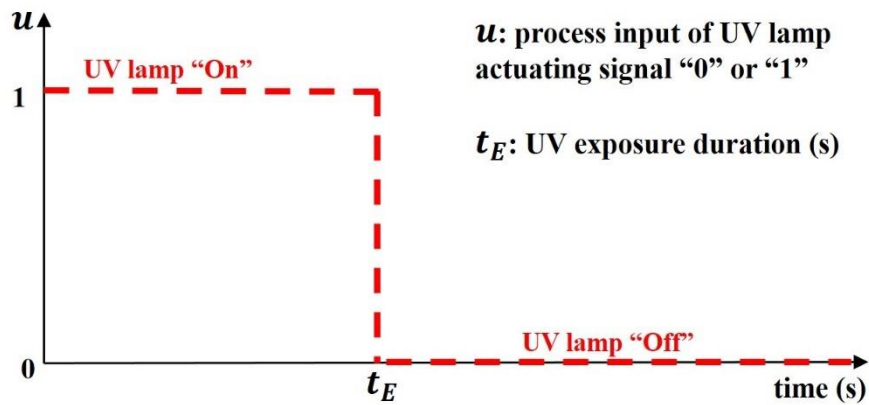


Figure 69. On-Off control input in the ECPL process

#### 9.4.4 System delays

As is common for real-time measurement and control systems [100], there exist in the ECPL On-Off feedback control system considerable delays in measurement  $\tau_{meas}$ , in feedback control  $\tau_{ctrl}$  and in actuation  $\tau_{act}$ , primarily due to the racing of multithreads in the parallel computing and in a real-time-unguaranteed operating system. The measurement latency  $\tau_{meas}$  resides between real-time acquisition and online analysis in the ICM&M system. The feedback control delay  $\tau_{ctrl}$  refers to various delays in the controller, including (1)  $\tau_s$  - the missed sensing of the target trigger point due to discrete

measurement, especially a significantly long measurement interval; (2) the sensor-to-controller time lapse  $\tau_{sc}$  for transmitting measurement result; and (3) the controller time  $\tau_c$  for implementing control algorithms. The actuation delay  $\tau_{act}$  includes (1) the controller-to-actuator time delay  $\tau_{ca}$  for transferring the control signal; and (2) the actuator delay  $\tau_a$  in mechanically operating the UV lamp.

To obtain information about the measurement latency  $\tau_{meas}$ , feedback control delays  $\tau_{ctrl}$  and actuation delay  $\tau_{act}$ , the ECPL-M&C software is equipped with two stopwatch timers – one for recording each interferogram’s timestamp when it is acquired and written into a file, the other for recording the timestamp when it is read from the file for analysis. The measurement latency of each frame can be estimated by calculating the time lapse between the image’s acquisition  $t_{acquire}$  and analysis  $t_{analyze}$  as shown in Equation ( 30 ). The timestamps are also used for tracing the measurement and control events, thus to capture the evolution of cured height. Investigating the timestamps of measurement and control footprints off line could also help identify the control delay  $\tau_{ctrl}$  which is estimated as a difference between the target point’s and trigger point’s timestamps. Meanwhile, the UV lamp status (on/off) is recorded every time when a new frame is acquired; thereby, the actuation delay could be derived by comparing the actuator status and corresponding timestamp.

Due to the limited computation resource in the parallel computing and execution for both measurement and control, the execution of controller and actuator can be impacted by an intensive measurement. It is expected that the feedback control delay  $\tau_{ctrl}$  would increase as the measurement interval is extended to allow sufficient time for measuring more pixels on line. The first part of control delay  $\tau_s$  which is referred as “measurement interval effect” could be estimated (denoted as  $\tau_{s\_interpolated}$ ) by a linear interpolation between the two consecutive discrete measurements that include the target point. The remaining part of control delay  $\tau_{sc}$  and  $\tau_c$ , which is referred as “transmission

delay” and “computation delay”, together, could be calculated as the difference between the time  $t_{sens}$  when measurement hits the trigger point and the actual trigger time  $t_{trg}$  when the controller receives the sensor’s signal after a possible delay due to some random disturbances in the computing environment. Therefore, the feedback control delay  $\tau_{ctrl}$  is estimated as shown Equation ( 31 ).

The actuation delay  $\tau_{act}$  is estimated via Equation ( 32 ) as the deviation between the actual instant of trigger point  $t_{trg}$  when the measured height  $z_m$  is detected to have hit the reference value  $z_t$  and the moment of shutdown point  $t_{shut}$  when the UV lamp is just confirmed to be turned off.

$$\tau_{meas} \cong t_{acquire} - t_{analyze} \quad ( 30 )$$

$$\tau_{ctrl} = \tau_s + (\tau_{sc} + \tau_c) \cong \tau_{s\_interpolated} + (t_{trg} - t_{sens}) \quad ( 31 )$$

$$\tau_{act} = \tau_{ca} + \tau_a \cong t_{shut} - t_{trg} \quad ( 32 )$$

The values of  $t_{acquire}$ ,  $t_{analyze}$ ,  $t_{sens}$ ,  $t_{trg}$  and  $t_{shut}$  are obtained from the image timestamp of the frame acquired, respectively, at the acquisition node, measurement node, decision-making control node and at the UV lamp switch node.

## 9.4.5 The control scheme

### 9.4.5.1 Compensator

A real-time monitoring of UV curing reaction rates of some stereolithography resin with a reflectance infrared spectrometry technique, revealed a significant additional conversion of reactive groups as the so-called dark curing, which means a post-irradiation polymerization process after termination of exposure [50]. Similarly, dark curing is expected in the ECPL process and cannot be neglected with the experimental materials in this study, as some extra vertical growth is observed from the interferogram changes detected by the ICM&M system.

In the ECPL On-Off control strategy, the inherent dark curing could introduce near the set point of the target total height a significant deadband, where no control actions are available to regulate the cured height after switching off the UV lamp. Consequently, the part of dark curing is uncontrollable by the simple on-off feedback controller, and should be accounted for upfront by a compensator which is aimed to reduce the cured height error attributed to dark curing. It is difficult to provide a kinetic model of the effects of dark curing. For simplification, in this study, the width of the On-Off control deadband is defined as a lumped ratio ( $r_{D/T}$ ) of dark cured height  $z_{Dark}$  to total cured height  $z_{Total}$ , which assumes linear dependency of dark cured height  $z_{Dark}$  on the leading exposed cured height  $z_{Exp}$  in the ECPL process with a constant ratio  $r_{D/E}$  as shown in Equation ( 33 ). Accordingly, Equation ( 34 ) is used to derive the lumped percentage ( $r_{D/T}$ ), which is also shown to be a constant, for quantifying the contribution of dark cured height  $z_{Dark}$  in the total cured height  $z_{Total}$ . The ratio value  $r_{D/T}$  could be identified experimentally with the specific material used in the process.

$$r_{D/E} = \frac{z_{Dark}}{z_{Exp}} \quad (33)$$

$$r_{D/T} = \frac{z_{Dark}}{z_{Total}} = \frac{z_{Dark}}{z_{Dark} + z_{Exp}} = \frac{r_{D/E} \times z_{Exp}}{z_{Dark} + r_{D/E} \times z_{Exp}} = \frac{r_{D/E}}{1 + r_{D/E}} \quad (34)$$

Provided a set point ( $z_s$ ) of desired total cured height of a target 3D part, the compensator estimates by Equation ( 35 ) a reference value, which will be input to the succeeding feedback controller serving as a trigger point ( $z_t$ ) for switching the UV lamp.

$$z_t = z_s \times (1 - r_{D/T}) \quad (35)$$

In previous study for ICM&M validation, experiments were conducted to cure multiple samples [92], and the ICM&M method were applied off line to measure out the dark cured height and total cured height of the 24 samples. Histogram of the resultant

ratios, in Figure 70, shows that the average ratio of dark cured height to exposed cured height was 0.108.

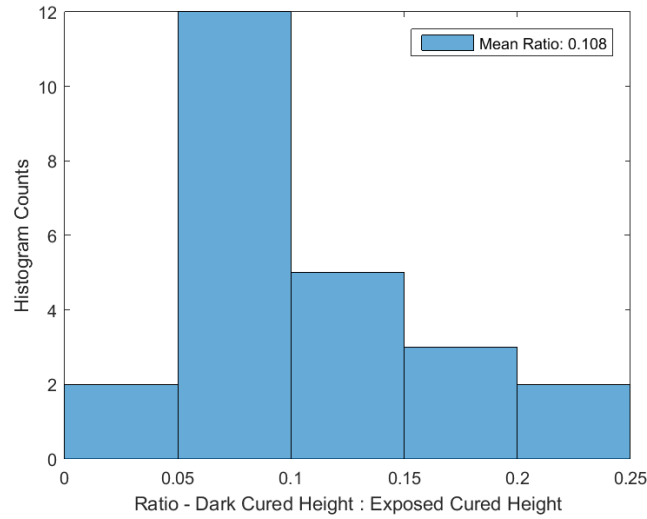


Figure 70. Statistics of the ratio of dark cured height over exposed cured height

As reported in literature [59], the dark reaction contributes to about 10% conversion of monomer at the locus where irradiation is received, which may explain why the dark cured height occupies around 9.75% of total height in the ICM&M measurement. Therefore, the lumped percentage of dark curing in the entire ECPL curing ( $r_{D/T}$ ) was estimated to be 10% which is to be used in the compensation for the part of dark curing in the real-time On-Off control experiments.

#### 9.4.5.2 Feedback controller

A closed-loop feedback controller is a key component in the On-Off control system. It compares the measured height  $z_m$  (feedback from the ICM&M system) with the reference value  $z_t$  (derived from the compensator), and calculates the difference as shown in Equation ( 36 ) for an error signal  $z_e$ .

$$z_e = z_m - z_t \quad ( 36 )$$

The measurement latency  $\tau_{meas}$  and control delay  $\tau_{ctrl}$  are subject to stochastic computing environment factors and more difficult to predict compared with the control delay that exhibit a more deterministic value and is easier to characterize. Consequently, the measurement latency and control delay is not specifically accounted for in this initial controller design. In other words, this controller design assumes negligible delays in measurement and control which actually can be well supported by an enhanced computing system in the future. To unveil the system's full potentiality, with the forward-looking assumption of insignificant delays in measurement and control, only the relatively predictable and physically inevitable delay in the actuation  $\tau_{act}$  is addressed in the feedback controller design.

Experiments can be conducted to quantify the actuation delay  $\tau_{act}$ , and a statistical mean delay of the measured delays for repeated experiments is used to estimate the dead zone  $z_{tol}$  in the controller for the specific experimental conditions (i.e., number of online measured pixels, and measurement interval). The initial characterization experiments that measure online one pixel at a measurement interval of about 0.55 second, indicate that it takes approximately 0.4 second for the control action is executed after the control decision is made.

The actuation delay can lead to a deadband in the controller, referred in the ECPL process as a tolerance of controlled height. The controller is supposed to shut down the UV lamp when the feedback error hits the non-zero tolerance rather than exactly zero so that the extended light curing due to the delay would bring the feedback error down to around zero. Therefore, the height control tolerance  $z_{tol}$  is estimated as one half of the over-cured height caused by the delayed termination of the UV exposure using the method of linear interpolation as shown in Equation ( 37 ). The symbol  $z_{cycle}$  denotes the cured height per oscillating cycle in the ICM&M detected time sequence of interferogram intensity at the measured pixel, and its value has been characterized to be approximately  $12 \mu\text{m}$  as shown in Equation ( 28 ).  $T_{process}$  is the period of the

interferogram intensity signal at the end of illuminated curing process, and is dependent on both the exposure time and intensity. In this study, a rough average value of  $T_{Process} \approx 5s$  could be used for estimating the controller tolerance. With an empirical value of  $\tau_{act} \approx 0.4s$ ,  $z_{tol}$  is estimated to be  $0.5 \mu m$  which is used in the real-time measurement and control experiments reported in this study.

$$z_{tol} \approx \frac{1}{2} \times \left( z_{cycle} \times \frac{\tau_{act}}{T_{Process}} \right) \quad (37)$$

With a proper setting of the tolerance  $z_{tol}$ , the controller algorithm for updating online the ECPL process input ( $u$ ) of UV lamp actuating signal is developed in Equation (38). Via switching off the UV lamp at an optimal time point decided by the algorithm, the controller is aimed to bring the final process output as close to the set point as possible.

$$u = \begin{cases} 1 \text{ ("On")}, & -z_e > z_{tol} \\ 0 \text{ ("Off")}, & -z_e \leq z_{tol} \end{cases} \quad (38)$$

#### 9.4.5.3 Overall integrated control system

As summarized in Figure 71, a real-time monitoring and control system for the ECPL process output of cured height is developed based on the classical feedback control theory [101]. The block diagram illustrates the control scheme with signals (shown as red symbols), control logic (shown as blue equations) and interpretations. The set point  $z_s$  means the desired total cured height, while the trigger point  $z_t$  means the reference value of cured height at which a control signal of cutting off the UV exposure is sent. It is noted that the trigger point flags the impending end (not immediate end due to the actuation delay  $\tau_{act}$ ) of exposed curing stage, only which the feedback controller can intervene. As explained previously, the feedback control loop cannot manipulate the dark curing stage, which is therefore compensated in the predefined calculation instead. The developed in-situ ICM&M system is used to sense the cured height in real time. With the measured information of cured height  $z_m$  under UV exposure, an On-Off feedback controller with a



deadband of height tolerance  $z_{tol}$  is used to determine the optimal time when to terminate illuminating the workpiece on the building platform.

Please note that  $r_{D/T}$  is tunable in the controller setting for better control accuracy if an empirical ratio obtained from the model in Equation ( 33 ) turns out to be inadequate. Another adjustable parameter in the controller is  $z_{tol}$ , whose value might be inaccurate as is roughly estimated by Equation ( 37 ).

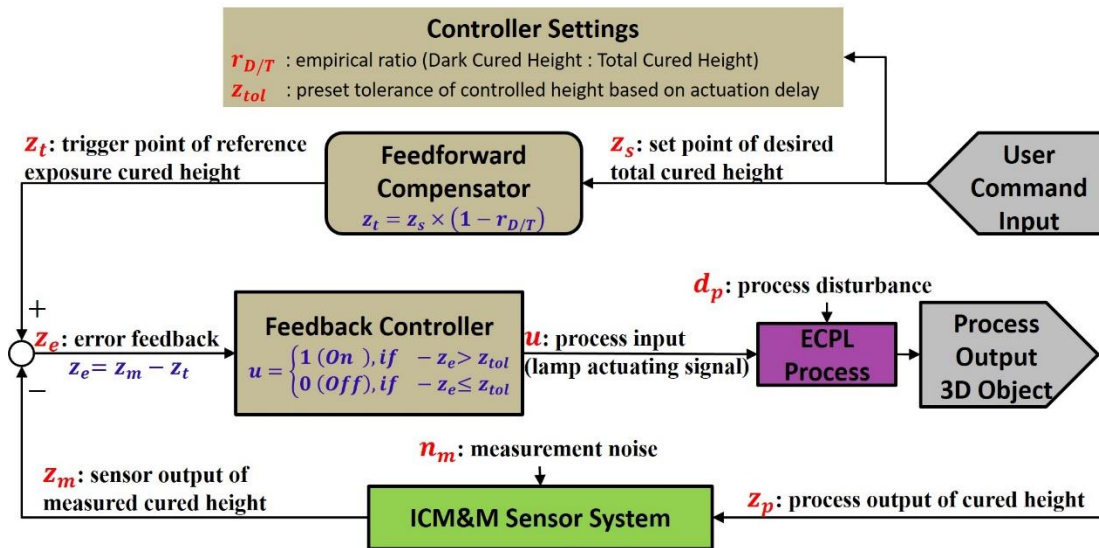


Figure 71. Scheme diagram of feedback control for real-time cured height in ECPL process

## 9.5 Offline measurement methods

In this study, the actual height profile of the cured flat-top parts is represented by the overall average and deviation values. This section describes in details how actual height profile is measured offline to bolster the upcoming interpretation and discussion about the experimental results in Section 9.7.

To measure the parts cured in the experiments, two methods are employed: an ex-situ confocal laser microscope (Olympus LEXT 3D Material Confocal Microscope) and an offline implementation of the developed ICM&M method. The microscope serves to

provide a standard measurement that is regarded as the actual process output  $z_p$ . The offline ICM&M method is performed in this post analysis as a validation tool to evaluate the potentiality of real-time ICM&M in an unrestricted computational environment, as well as to provide a further demonstration of the metrology's capability echoing with the previous offline characterization experiments. While the microscope cannot measure out the exposure height and dark height, the offline ICM&M method offers unique advantage in being able to estimate the exposure height and dark height across the cured part so that one can evaluate the accuracies of the compensator and the feedback controller (in Figure 71).

### **9.5.1 Microscope measurement**

To obtain a complete view of the overall heights profile under the microscope such that could be better compared with the ICM&M full-field measurement, for each cured block, several sampling horizontal and vertical profile lines across the part are measured under the microscope. However, a direct cursor measurement in microscope provides only average result without variation indication; worse still, it is prone to human error. Therefore, analysis of the exported measurement data is performed to calculate average and variance for each profile line.

According to the probability theory, the sum of two independent normally distributed random variables is normal with its mean being the sum of the two means and its variance being the sum of the two variances [102]. The measured single lines' heights are aggregated to provide an estimation for the overall average height of the cured part. To estimate the height variation across the entire part, firstly, the variances of sampled profile lines are averaged, and then the square root of the averaged variance is used as the average standard deviation – a metric for the overall roughness of the ECPL cured block.

For example, Figure 72 shows how the microscope is used to measure a cured part in one of the designed experiments (specifically, Group #2 Subset #2 in Table 18).

The measurement results shown in Figure 72 are the difference between the two cursors - one indicates the substrate and the other the sample surface – manually placed by the operator with naked eyes judgment. Thus, the cursor measurement is not necessarily an accurate measurement of the detected profile under microscope. The exact profile data are exported from the microscope and analyzed for a profile line’s average and variance height. In this instance, 5 horizontal lines and 5 vertical lines are measured. As shown in Table 17, the resultant overall height profile (with an average of 41.60  $\mu\text{m}$  and standard deviation of 4.79  $\mu\text{m}$  as shown in red bold numbers) is obtained by aggregating the 10 measured lines. Deviations of a few microns exist between the cursor measurement (Column 2) and microscope data average (Column 3), demonstrating the necessity of adopting the microscope data analysis approach, which meanwhile enables an estimation of the variance and deviation.

Table 17. Evaluate a sample cured part’s height profile with its microscope data

Sampling Profile Line #	Microscope Cursor Measurement ( $\mu\text{m}$ )	Microscope Data Average ( $\mu\text{m}$ )	Microscope Data Variance ( $\mu\text{m}$ )	Microscope Data Standard Deviation ( $\mu\text{m}$ )
1	42.93	40.40	33.79	5.81
2	42.93	44.34	16.37	4.05
3	42.93	44.04	19.32	4.40
4	42.93	44.29	14.74	3.84
5	37.22	35.88	27.03	5.20
6	35.01	39.04	21.22	4.61
7	43.86	45.01	24.60	4.96
8	40.86	43.02	24.08	4.91
9	40.86	42.25	23.48	4.85
10	35.01	37.72	24.76	4.98
<b>Overall</b>	40.45	<b>41.60</b>	22.94	<b>4.79</b>

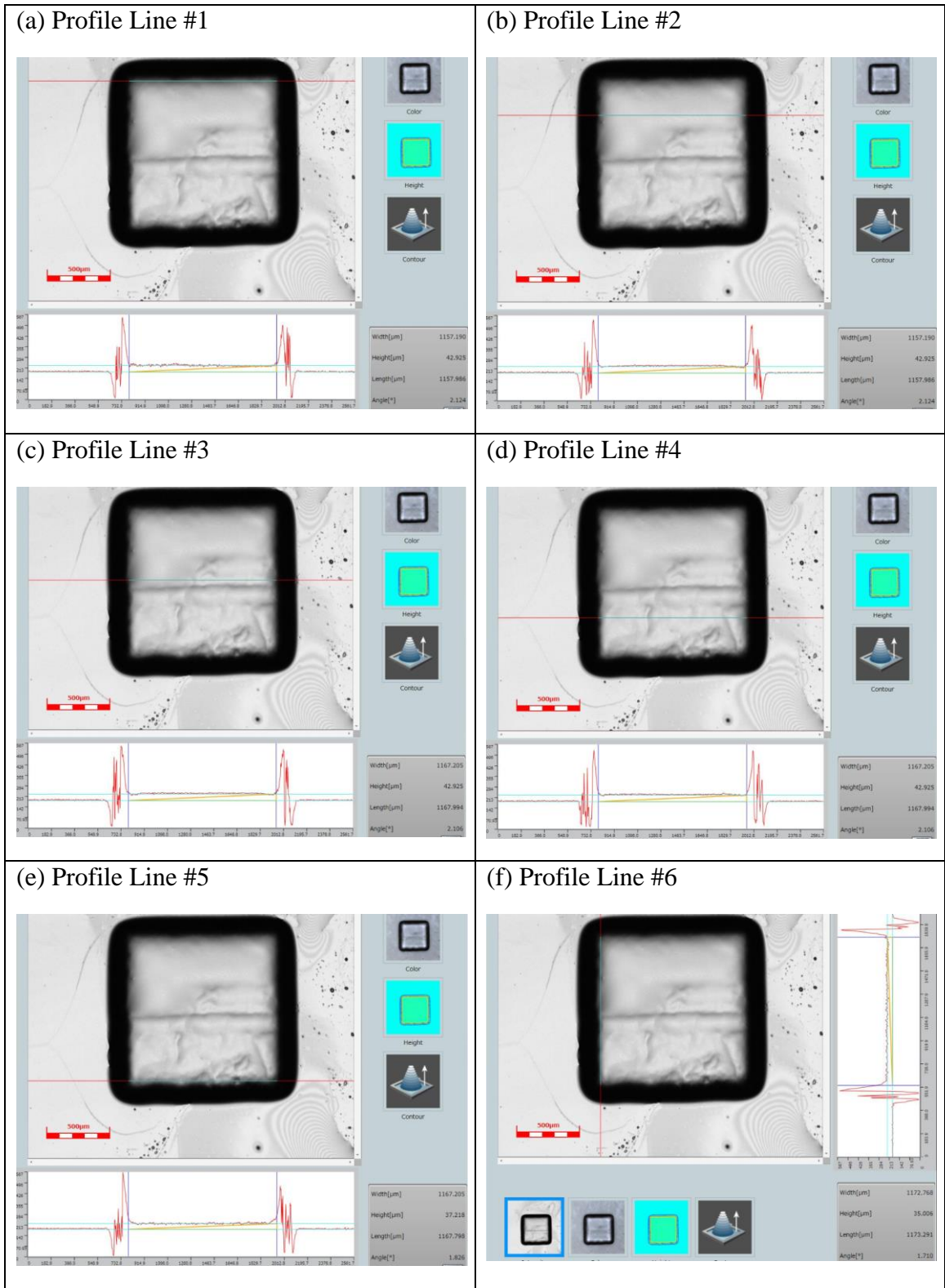


Figure 72. Measuring multiple profile lines across a sample cured part with microscope

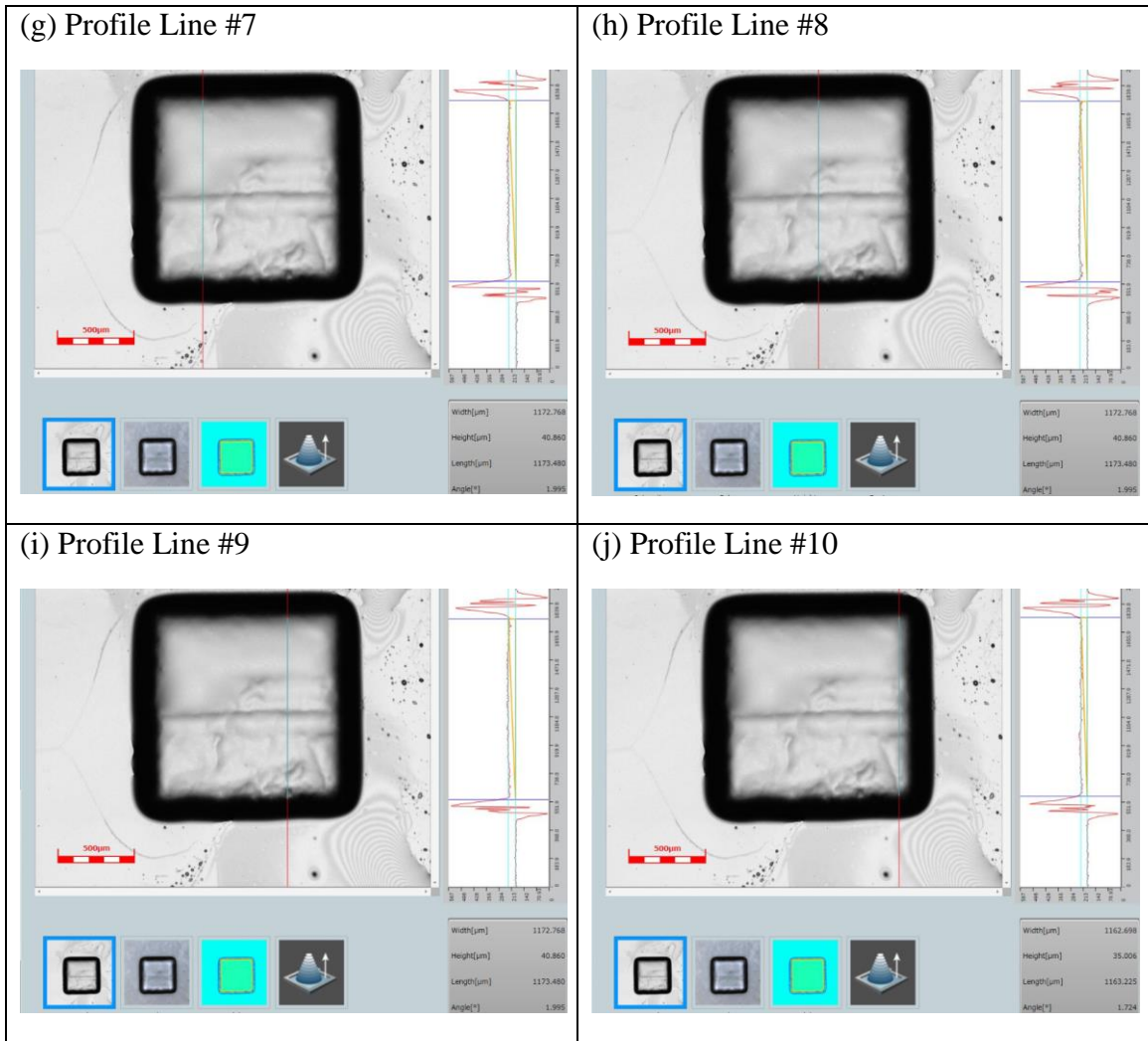


Figure 72 (continued). Measuring multiple profile lines across a sample cured part with microscope

### 9.5.2 Robust ICM&M method off line

Since the real-time measurement is subject to constraints in computation speed and power, an offline ICM&M analysis for the same interferogram dataset as analyzed online is used to measure the desired overall height profile of a cured part. The sensor model and fundamental algorithms are the same for both real-time and offline ICM&M, however, the later could tap into the full video resource for more pixels data to obtain results with less bias and less error. Moreover, due to smaller acquisition rates in the real-time experiments, the signal noise ratio (SNR) of the sampled interferogram data is fairly

lower, compared with that of the data collected without online analysis in a pure acquisition as in the previous work of offline ICM&M validation and characterization (Chapter 8) [92]. Therefore, a more robust ICM&M method, which equips the basic ICM&M algorithms (developed in Chapter 6) with a majority voting scheme and an outlier treatment technique, is exploited to enhance the measurement accuracy for the real-time experiment data.

Both the methods of voting and outlier treatment take the advantage of a rich dataset involving more sampling pixels. The majority voting method is called each run of measurement, during the execution of ICM&M, to identify the curing window coherently and easily (in case of noisy data) with the feedback of updated status from all the ROI pixels at large, and aims to improve an individual pixel measurement accuracy. After all ROI pixels are measured, the outlier treatment method would be employed as a postprocessing measure to detect and correct the outlier individual pixel within the initially resultant height profile statistics, and focus on ensuring a consistent and robust measurement for each individual pixel so as to provide a final height profile measurement with an improved overall estimation accuracy across the ROI.

#### 9.5.2.1 Voting scheme for identifying the curing window

A majority voting scheme is designed to identify the cure start and curing stop more consistently across the ROI. One base for determining the voting result is the percentage of pixels that are required for the algorithm to adopt a proposal that the process is at incubation period or dark period. The threshold percentage values are chosen based on experiments using two majority votings -  $2/3$  and  $4/5$ . It is found experimentally that  $2/3$  voting and  $4/5$  voting would not make a significant difference in the defined curing window. Increasing the voting percentage threshold from  $2/3$  to  $4/5$  could increase the average and deviation in cured heights slightly by less than 1  $\mu\text{m}$ . However, the deviation result from  $2/3$  voting is closer to the microscope measurement result, which

implies that 2/3 voting can output a smoother and more realistic height distribution. Therefore, for identifying pre-curing incubation period, it is decided to adopt 2/3 majority voting which is more robust and more accurate across the cured area despite possible underestimation for some individual pixels. For identifying resting period, 4/5 voting is proper, and even if it is not timely identified, the sufficiently long window used in the curve fitting for dark curing period could help alleviate the error.

In this study, if the number of pixels at incubation period drops below a threshold of 2/3 of the total pixels, the algorithm begins to allow individual pixel start curing; otherwise, all pixels are decided to be still at incubation despite some possible wavy signals existing in some pixels. Similarly, after the UV lamp is off, once 4/5 pixels are marked as have stopped curing already, the algorithm will artificially force all the other pixels into the resting stage, because the fluctuating tails in the unsettled pixels are likely noises instead of curing oscillations.

Generally speaking, this majority voting method is effective in suppressing false alarms in the should-be incubation stage and should-be resting stage, so that each pixel measurement would be immune to various spurious oscillations at the non-curing stages.

To demonstrate the benefit of the voting scheme, a cured part in one of the designed experiments (specifically, the target height is 40  $\mu\text{m}$ , Group #2 Subset #1 in Table 18) is measured by the ICM&M method, without and with the voting scheme, respectively. The ROI of measured pixels is shown in Figure 73 - a 100 $\times$ 100 pixels square (red dashed line) defined by the four corner pixels. The initial measurement without voting is displayed in Figure 74 (a), which shows a very large standard deviation of 11.5  $\mu\text{m}$ . One outstanding pixel that is located at [Width, Height] of [310, 170] is obviously overestimated to be 133  $\mu\text{m}$  and its time sequence of grayscale data is analyzed in Figure 75 (a). The grand pattern of the data shows approximately 3 cycles, but the ICM&M algorithm counts the misleading fluctuations within the time frame of [0, 17s] into the curing window. Supervised by the voting scheme, the ICM&M algorithm

estimate the curing window for the entire ROI to be [17.914s, 41.768s] as shown in Figure 76. In in Figure 76 (a), there are 441 pixels in total, and once the number of incubation pixels drops below 2/3 of that (i.e., 294), the time point is marked as the earliest allowable curing start time (i.e. 17.914 s) before which all the curing pixels determined by the ICM&M classification rules are forced artificially back to incubation stage. Similarly, in Figure 76 (b), the 4/5 voting for resting period uses the threshold number of 352 to find the latest allowable curing stop time (i.e., 41.768 s), after which all the curing pixels determined by the ICM&M classification rules are forced into resting stage so that the noises in tailing period would not induce error.

With the aid of voting, the ICM&M algorithm could easily discard the spurious waves, and correctly calculate the total phase angle for the problematic pixel is 3.15 cycles and the estimated height is 40.08  $\mu\text{m}$  which is right on target as shown in Figure 75 (b). The resultant height profile from the ICM&M with voting is more uniform and closer to reality as shown in Figure 74 (b); however, there is still improvement room to reduce the variation further and thus an outlier detection mechanism is introduced to address the issue (Section 9.5.2.2).

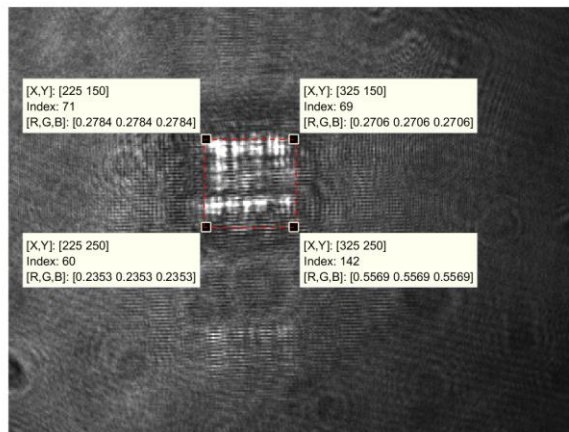
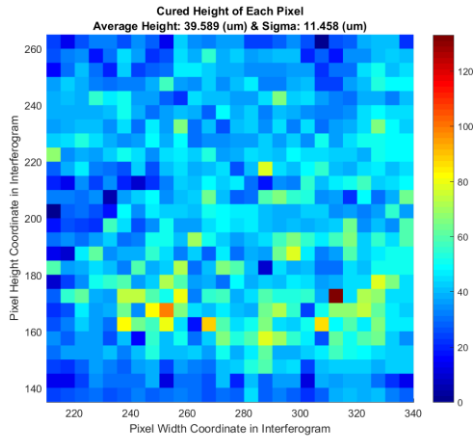


Figure 73. ICM&M without vs. with voting: selected region of pixels to be measured



(a)



(b)

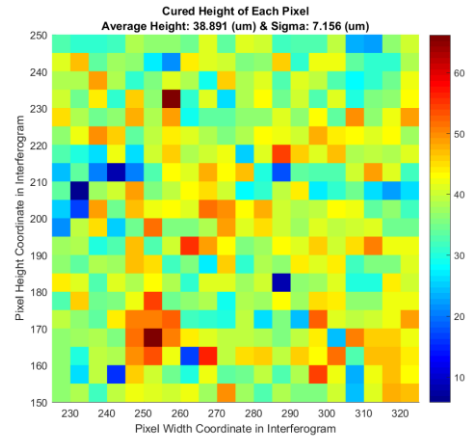
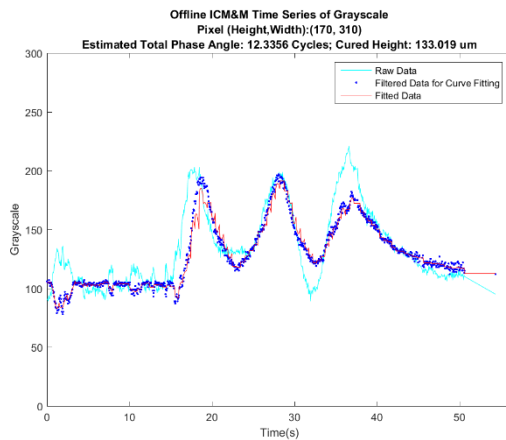


Figure 74. ICM&M without (a) vs. with (b) voting: estimated height profile

(a)



(b)

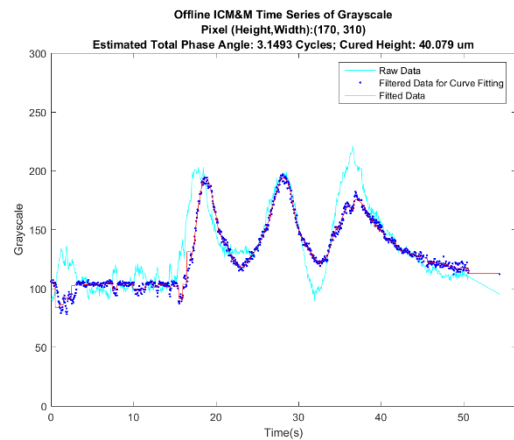
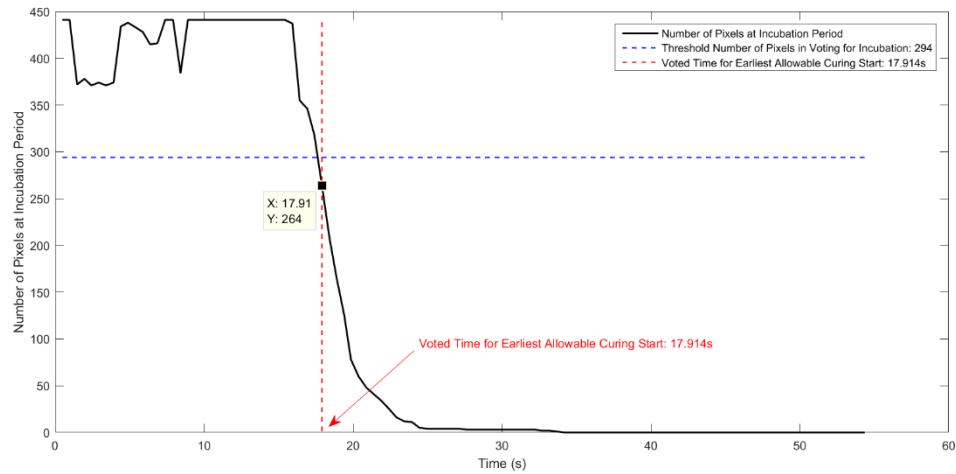


Figure 75. ICM&M without (a) vs. with (b) voting: measuring a pixel with noisy incubation signal

(a)



(b)

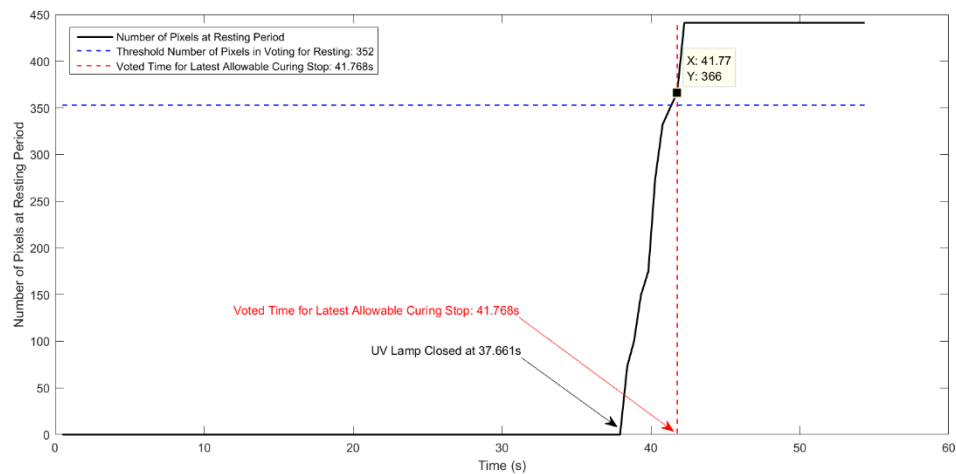


Figure 76. ICM&M voting for ECPL process stage (a) incubation; (b) resting.

### 9.5.2.2 Outlier detection and treatment

The majority voting assisted ICM&M algorithms mentioned above would output an initial height profile such as Figure 75 (b). In this study, outliers in the initial results are defined as these measured heights that are 1-sigma away from the robust fitted average. Detected outliers are replaced by the median filtered ( $3 \times 3$  filter span) values in the matrix of initial ICM&M measurement profile. The same example as in Section 9.5.2.1 is used to demonstrate the effect of applying the outlier removal algorithm. Figure

77 displays a more uniform profile with a sigma of 4.51  $\mu\text{m}$  which is reduced effectively from these estimated in Figure 75, and closer to the standard deviation of 5.07  $\mu\text{m}$  estimated from the microscope data.

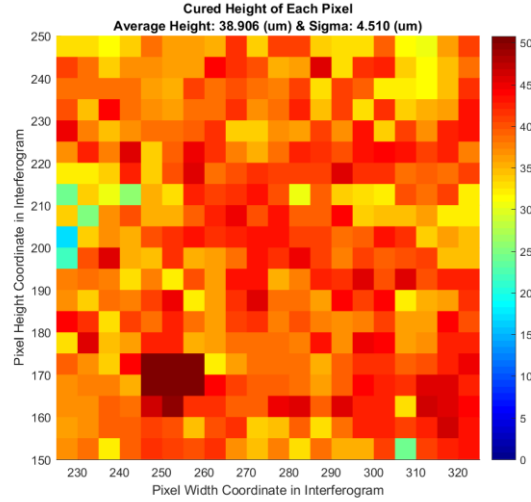


Figure 77. An example of final height profile estimated by the ICM&M with voting and outlier removal schemes

### 9.5.2.3 Summary

The robust ICM&M algorithms which incorporate the methods of majority voting and outlier removal, are applied to the real-time acquired interferogram video for each part cured in the experiments, and the estimated height profile of average height ( $z_{ICM\_off}$ ) and standard deviation is used as the offline ICM&M result in this study.

## 9.6 Experiment design for real-time ECPL process measurement and control

Theoretically, one could deploy the ECPL-M&C codes onto the physical system, conduct an in-process measurement of the height profile for an entire region of interest, and simultaneously apply online a control method with the accessible measurement result to cure a part with desired height. The ideal approach of real-time implementation of ECPL process feedback control demands prohibitively large computing memory and fast computing speed, in order to synchronize the ICM&M analysis with the real-time

interferogram data acquisition, as well as to realize timely hardware (i.e., the UV lamp in the ECPL system) responses to the feedback control algorithm with minimal delay. In general, a reliably fast measurement and actuation for real-time process control would be computationally expensive.

Given the restricted computing resource, only a limited number of pixels are able to be measured online as a demonstration of the ICM&M method's qualification as a real-time process metrology. A fast curing process can sustain an online measuring for one pixel, which does not demand much computation time. In a slow curing process, however, a relatively long measurement interval would not affect the measurement accuracy significantly, and could support a multi-pixel measurement without hindering the software thread for acquisition. Multi-pixel measurement is preferable, since it is more robust and more representative in the estimation of cured height than one single pixel is. With the current system and software, in a fairly slow curing process, three pixels could be measured online simultaneously between two consecutive measurements without causing severe latency between the ICM&M acquisition and analysis. In the designed experiments, in addition to measuring and control a normal ECPL process under a moderate exposure intensity, another set of experiments with a relatively slow process is planned, altogether, to demonstrate the ICM&M method's potentiality in real-time measurement both locally and globally, as well as to validate the On-Off control method's capability of controlling the process with different set points and different dynamics (e.g., curing speed).

Another consideration in the experiment design is to relax the constraint of measurement latency which actually could be well unleashed in a high performance computing system, in order to provide a fairer and truer evaluation of the developed real-time system's performance. Because of the observation that severe measurement latency occurs at the onset of ICM&M and lasts for a while before settling down to an acceptable level, in this study, a target height is selected to be sufficiently large so that its required

exposure time could overcome the troublesome window of high measurement latency. The chosen target height is expected to take the process to where the thread of measurement and control analysis could catch up with that of data acquisition, thereby the assumption of negligible ICM&M latency in the controller design (Section 9.4.5.2) can be justified.

Specifically, in this study, two groups of experiments, with different exposure intensities corresponding to different UV iris levels at 22% and 5%, respectively, are designed to demonstrate the capability of the developed methodology of real-time measurement and control for the ECPL process. It has been found that the curing process under lower-intensity exposure is slower [92], therefore, an ECPL process at 22% UV iris level is adopted for the first group of experiments (denoted as “normal process”), and the 5% UV iris level is used in the second group of experiments (referred to as “slow process”). In each single run of experiment, under a constant UV exposure intensity (i.e., fixed UV iris level), a square bitmap of 250×250 pixels is displayed on the DMD to cure a flat-top block of desired height. The target height is set to be 80 μm in the “normal process” experiment and 40 μm in the “slow process” experiment. The ICM&M method and the On-Off feedback controller are applied in unison to measure and control the cured height in real time. An ex-situ confocal laser microscope is used to measure the cured part for obtaining the actual process output of cured height  $z_p$ . The designed experiments are as shown in Table 18 with the varying factors accentuated.

Table 18. Experimental design for real-time ECPL process measurement and control

		Experiment Groups		
		Group #1: Normal Process	Group #2: Slow Process	
			Subset #1	Subset #2
ECPL Process Conditions	Exposure Intensity (UV Iris level)	22%	5%	5%
	Exposure Pattern Bitmap Size (Pixels × Pixels)	250×250	250×250	250×250
ICM&M Settings	Measurement Interval (Frames/Run)	10	10	30
	Number of Pixels Measured Real Time	1	1	3
Controller Settings	Set Point of Target Height $z_s$	80 $\mu\text{m}$	40 $\mu\text{m}$	40 $\mu\text{m}$
	Ratio of Dark and Total Cured Heights $\gamma_D/\tau$	0.1	0.1	0.1
	Tolerance of Controlled Height $z_{tol}$	0.5 $\mu\text{m}$	0.5 $\mu\text{m}$	0.5 $\mu\text{m}$

## 9.7 Experiment results and implications

For each of the three sets of experiments in Table 18, six trials of ECPL curing with real-time measurement and control are implemented resulting in six sample cured parts. Two samples have to be discarded (i.e., the yielding rate is about  $16/18 = 89\%$ ), because of some severe damages during the postprocessing (washing and cleaning) and failed microscope measurement due to the chromatic dispersion of residual soap water. Herein, the study reports result for six samples in Group #1, six sample in Group #2 Subset #1 and four samples in Group #2 Subset #2.

Offline measurements for these samples, including microscope measurement of the real cured parts and offline ICM&M analysis of the real-time acquired interferogram videos, are presented in Section 9.7.1.

The experiments results are interpreted centering on the two essential real-time elements of in-process measurement and closed-loop control, presented in 9.7.2 and Section 9.7.3, respectively. The analysis primarily involves multiple pairwise comparisons among four quantities of total height: target cured height  $z_s$ , actual cured height – microscope measurement of the process output of cured part’s height  $z_p$ , real-time ICM&M measurement  $z_m$ , and offline ICM&M measurement  $z_{ICM\_off}$ . As the feedback controller (Figure 71) aims to monitor the exposure height only, an investigation into the exposure height measurement results, including the trigger point of

target exposure height  $z_t$ , real-time ICM&M measured sampling pixel(s)'s exposure height  $z_{E\_RT}$ , and offline ICM&M measured average exposure height  $z_{E\_Off}$ , is also necessary for evaluating the overall process measurement and control accuracy.

### **9.7.1 Offline measurement**

#### **9.7.1.1 Results of the offline measurement for ECPL process output**

With the methods presented in Section 9.5, the offline measurement results, including both the microscope and the ICM&M measurements, are shown in Table 19. As a reference for more details about the implementation of the offline ICM&M method (Section 9.5.2) to analyze the interferogram videos in the real-time measurement and control experiments, analysis resultant figures of the curing window identification, the selected ROI, the area profile of cured height, and the process dynamics, are displayed in Appendix A. In Group #1, a ROI of 130-by-130 pixels is measured at an interval of every 5 pixels, thus a total of 729 pixels are measured to evaluate the height profile across the cured part. In Group #2, a ROI of 100-by-100 pixels is measured at an interval of every 5 pixels, thus a total of 441 pixels are measured to evaluate the height profile across the cured part.

As could be observed in Table 19, the ICM&M method is versatile in measuring not only the total height (yellow columns) but also the exposure and dark curing heights (blue columns), as well as in estimating the curing window length that is the difference between the estimated curing start and the estimated curing stop (brown columns). The offline measurement results are used in the succeeding reports of real-time measurement and control results (e.g., Sections 9.7.2 to Section 9.7.5) for validation of the ECPL process measurement and control method as well as for the analysis of overall error in the process output of total height.

Table 19. Offline measurement results for the samples cured in the real-time measurement & control experiments

Part 1: Total height measurement									
Experiment Index			Microscope Measurement		Offline ICM&M Measurement		Offline ICM&M Vs. Microscope		
Experiment Group	Experiment Subgrouping based on Online Measurement Setting	Sample NO.	Total Height-Average (µm)	Total Height-Standard Deviation (µm)	Total Height Average (µm)	Total Height Standard Deviation (µm)	Absolute Error in Total Height (µm)		
Group #1 (Normal Process: UV iris level 22%)	10 frames / run of online measurement for 1 pixel	Sample 1	76.85	4.93	80.30	3.76	3.45		
		Sample 2	83.51	5.83	88.81	4.17	5.30		
		Sample 3	82.61	6.16	86.32	5.03	3.71		
		Sample 4	83.12	4.03	88.36	3.40	5.25		
		Sample 5	78.99	5.15	81.88	3.44	2.89		
		Sample 6	79.63	4.68	82.70	4.52	3.08		
Group #2 (Slow Process: UV iris level 5%)	Subset #1 (10 frames / run of online measurement for 1 pixel)	Sample 1	45.05	6.39	44.15	4.14	-0.90		
		Sample 2	36.90	5.52	36.12	3.55	-0.77		
		Sample 3	44.87	7.05	41.36	3.69	-3.51		
		Sample 4	39.12	6.29	39.21	3.15	0.09		
		Sample 5	33.29	5.01	28.59	3.68	-4.71		
		Sample 6	44.20	5.07	38.91	4.51	-5.30		
	Subset #2 (30 frames / run of online measurement for 3 pixel)	Sample 1	40.02	5.64	38.77	3.57	-1.25		
		Sample 2	42.71	4.89	42.05	3.99	-0.66		
		Sample 3	43.93	5.01	39.11	4.39	-4.82		
		Sample 4	41.60	4.79	42.16	5.87	0.56		

Part 2: Exposure height measurement									
Experiment Index			Offline ICM&M Measurement						
Experiment Group	Experiment Subgrouping based on Online Measurement Setting	Sample NO.	Exposure Height - Average (µm)	Exposure Height - Standard Deviation (µm)	Dark Cured Height (µm)	Ratio of Dark Height to Total Height	Estimated Curing Start Time (s)	Estimated Curing Stop Time (s)	Estimated Curing Window Length (s)
Group #1 (Normal Process: UV iris level 22%)	10 frames / run of online measurement for 1 pixel	Sample 1	73.65	3.35	6.62	8.2%	3.806	19.249	15.443
		Sample 2	84.36	3.49	4.37	4.9%	3.468	21.913	18.445
		Sample 3	81.53	3.89	4.96	5.7%	3.466	21.193	17.727
		Sample 4	82.87	2.84	5.36	6.1%	3.779	22.926	19.147
		Sample 5	74.44	2.83	7.60	9.3%	3.545	19.501	15.956
		Sample 6	76.18	3.56	6.82	8.2%	3.695	20.165	16.470
Group #2 (Slow Process: UV iris level 5%)	Subset #1 (10 frames / run of online measurement for 1 pixel)	Sample 1	40.47	3.63	3.50	7.9%	18.079	44.114	26.035
		Sample 2	32.40	3.23	3.51	9.7%	18.327	39.545	21.218
		Sample 3	37.56	3.08	3.68	8.9%	17.703	41.867	24.163
		Sample 4	35.33	2.99	3.68	9.4%	17.946	40.595	22.649
		Sample 5	25.48	3.51	2.95	10.3%	18.187	36.936	18.750
		Sample 6	36.51	4.07	2.09	5.4%	17.914	41.768	23.854
	Subset #2 (30 frames / run of online measurement for 3 pixel)	Sample 1	35.62	3.37	3.00	7.7%	18.148	41.098	22.950
		Sample 2	38.29	3.58	3.64	8.7%	17.952	42.422	24.470
		Sample 3	36.00	4.28	2.63	6.7%	18.336	43.365	25.029
		Sample 4	36.18	4.71	5.29	12.5%	17.169	44.141	26.972



#### 9.7.1.2 Measurement of the total cured height to evaluate the ICM&M system accuracy

The total cured height of each sample is measured by both the microscope and the ICM&M method. Compared against the microscope results, the ICM&M shows good agreement despite some minor errors which are mostly within 5  $\mu\text{m}$ . The spread (i.e. the standard deviation) of the height profile measured by the ICM&M method is also close to that measured by the microscope. Actually, the ICM&M method measures a relatively smaller deviation than the microscope does, which is attributed to some possible deviation introduced in the postprocessing such as cleaning and washing.

The measurement discrepancies may primarily stem from the refractive index calibration error and the interferogram data deficiency. Notably, in Group #1 - a normal process that cures parts under an exposure intensity of 22% UV iris level, the total heights measured by the ICM&M method are all larger than these got by the microscope with a positive average bias of  $(3.95 \pm 1.07 \mu\text{m})$ , which reveals a systematic error that is due to the underestimated refractive index for larger height (e.g., 80  $\mu\text{m}$ ) in the calibration. Group #2 shows closer agreement between the ICM&M method and microscope yet with a negative average bias of  $(-2.13 \pm 2.22 \mu\text{m})$ , indicating that the refractive index might be more accurate but overestimated in the smaller-height zone (e.g., 40  $\mu\text{m}$ ). It is worth to point out that the refractive index used in this real-time experiment is obtained directly from the previous offline ICM&M validation experiment (Section 8.3.1.4) which uses a different batch of materials, and the batch-to-batch variances in the materials could induce differences in refractive index. The results of Group #1 and Group #2 demonstrate the necessity of calibration for an accurate refractive index of a new batch of materials even though it has nominally the same formulation. Furthermore, a similar measurement error pattern of overestimated height in above-80  $\mu\text{m}$  measurement and underestimated height in under-50  $\mu\text{m}$  measurement has also been observed in previous offline ICM&M validation experiments in Section 8.2.4, testifying that the refractive index is evolving significantly over the curing process and a more

accurate refractive index model is needed to reflect the changes and to enhance the ICM&M accuracy.

To conclude, firstly, the offline measurement results provide a further validation, on top of the previous validation experiments as presented in Chapter 8, of the ICM&M method in a different scenario with a relative sparse data acquisition and lower data quality due to the real-time computation limitation. Secondly, this offline ICM&M measurement validation demonstrates that the ICM&M method could provide more reliable online measurement results given more pixels being able to be measured online with sufficient computation resource. Thirdly, the resultant measurement errors (the rightmost column in Table 19) of the offline ICM&M provide an evaluation of the ICM&M system measurement error which could be used to estimate the real-time measurement accuracy as presented in Section 9.7.5.

#### 9.7.1.3 Measurement of exposure curing and dark curing to assess compensation accuracy

As developed in the ICM&M algorithms (Section 6.4) [103], the ICM&M method has an inbuilt ability to measure not only the part at the end but also the part in process by detecting and differentiating the process stages of exposure curing and dark curing. For the parts cured in the real-time control experiments, the exposure height (i.e., the cured height under exposure) and the dark height (i.e., the cured height in dark curing) are estimated by the ICM&M method offline, and Table 19 shows the results.

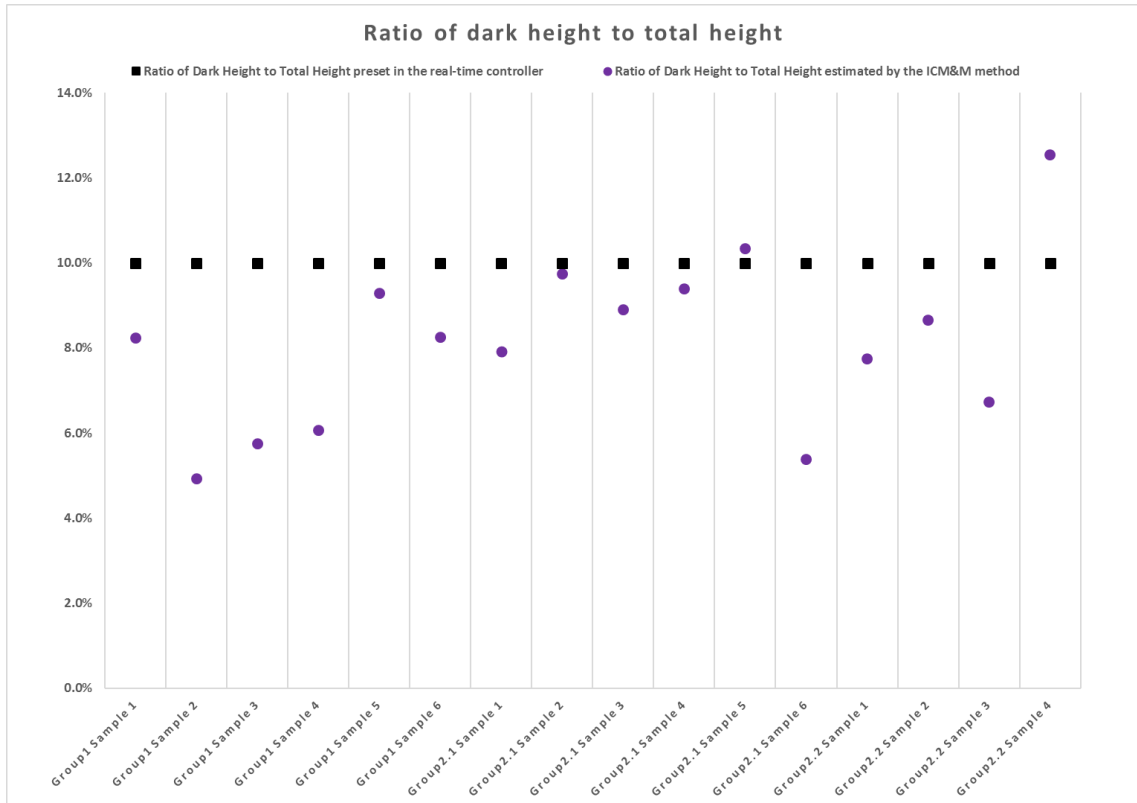


Figure 78. Ratio of dark height to exposure height for the parts cured in the real-time measurement and controls experiments

The ratios of dark height to exposure height for the parts cured in the real-time measurement and controls experiments are shown in Figure 78, and compared with the preset ratio of 10% that is adopted in the controller design in Figure 71 (Section 9.4) and in the experiments. As observed in Figure 78, the ratio of dark to exposure height is not ideally the preset amount. It is possible that the limitations of the ICM&M method present some errors in estimating the exposure height and dark height. Nevertheless, the observed deviations between the column of “Dark Cured Height” in Table 19 and the preset target dark height (i.e., 10% of the target total height) can still indicate a significant error source for the process control due to a potential inaccurate compensation in the controller. The effect is addressed later in Section 9.7.5 about the process control accuracy.

#### 9.7.1.4 Potentiality of the ICM&M method for modeling the ECPL process

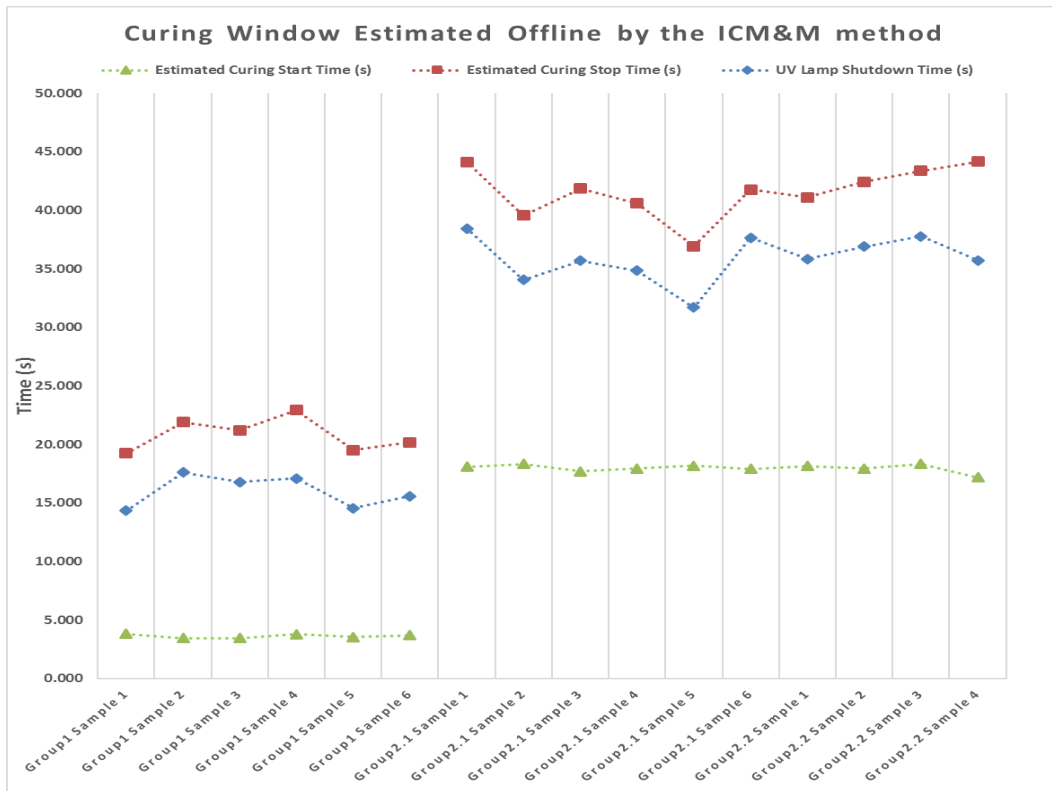
With the ability to identify the start of exposure curing and the end of dark curing, the ICM&M method possess a unique utility in estimating the entire curing window length which is directly related to the cured height. Intuitively, the longer the curing window is, the larger the cured height is. Theoretically, there is a logarithmic model between the exposure time and the cured height [79]. However, the exposure window is different from the curing window due to the existence of incubation and dark curing stages in photopolymerization process; and there is no revelation yet about the relationship between the net curing window length and the cured height for a lack of in-process metrology.

Herein, as shown in Figure 79(a), the results provide a convincing demonstration that the ICM&M method is capable of identifying the curing window consistently and accurately. The normal process in Group #1 and slow process in Group #2 show a very similar curing start time within each group, respectively, and together show an expected long incubation for the slow process. It is also desired that the same process in each group should have similar curing stop time. However, in Figure 79 (a), unlike the curing start time, the curing stop time shows obvious variations. The actual time when the UV lamp shut down is also shown in Figure 79 (a), explaining that the variations of the curing stop time stem from the variations of the actual exposure time which is determined by the real-time controller. Though inherent process and material variations could induce some slight difference in the curing window, the especially rugged pattern of the estimated curing stop time indicate that the real-time control is not accurate sometimes, leading to either earlier or later than the desired curing stop and causing significant variations in the curing window length. Please note that the performance of the real-time control will be evaluated further in an upcoming discussion. One main finding reported in Figure 79 (a) is that the ICM&M method is sensitive to the process input of exposure, and can estimate the curing window of start time and stop time consistently and

accurately. Figure 79 (b) shows that the longer the curing window is, the higher the cured part is, which validates further the ICM&M method's capability of estimating the curing window correctly.

In summary, the ICM&M method's capability of in-process measurement for the exposure curing and dark curing, together with the demonstrated correlation between the curing window length and cured height, could be explored in the future work of the modeling of photopolymerization based additive manufacturing process.

(a)



(b)

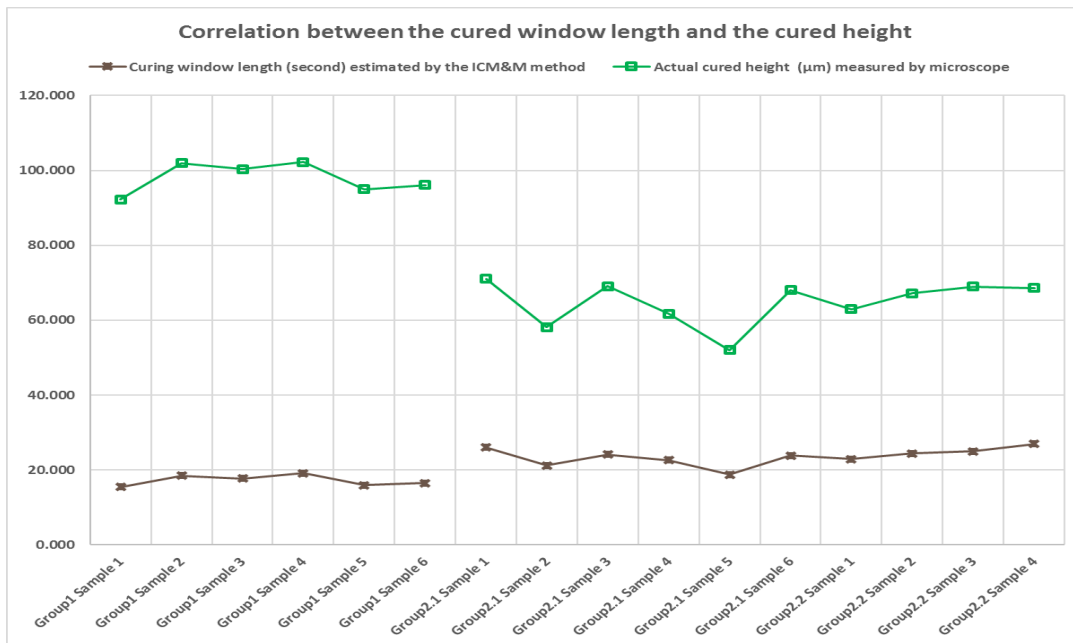


Figure 79. Explore the ICM&M method's utility in ECPL process modeling: (a) capability of identifying the curing window; (b) vivid correlation between the estimated cured window length and the actual cured height

## 9.7.2 Real-time in-process measurement

### 9.7.2.1 Results of the real-time ICM&M for ECPL process

To test the performance of the ICM&M method in real time measurement for the ECPL process, one representative pixel is measured online in Experiment Group #1 and in the first subset of Experiment Group #2. To further demonstrate the measurement capability and to investigate the effect of online sampling bias, more than one pixels (i.e., three pixels due to the limited computation power) are measured and a robust average of the multiple measurements is used as final measurement in a second subset of Experiment Group #2. The real-time data acquisition and measurement results for all the samples are available in Appendix B. A summary of the real-time measurement results, particularly for the exposure height (blue columns) and total height (yellow columns) measured online, are displayed in Table 20. Herein, a series of figures (Figure 80 - Figure 83) are available to provide comprehensive comparisons between the offline (Table 19) and the real-time (Table 20) measurement results of exposure height (Figure 80 and Figure 81 for Group #1 and #2, respectively) and total height (Figure 82 and Figure 83 for Group #1 and #2, respectively).

The observed measurement deviations are mainly caused by spatial sampling bias, data noise, and inability to perform the robust ICM&M method (9.5.2) due to real-time computation limits. Another hidden measurement error is attributed to the online measurement latency as investigated in Section 9.7.2.3. The real-time ICM&M errors and online measurement latency would peril the process control accuracy as discussed further in Section 9.7.3.

Table 20. Real-time measurement results for the samples cured in the real-time measurement & control experiments

Experiment Index			Target ( $\mu\text{m}$ )		Real-time ICM&M Estimation ( $\mu\text{m}$ )		Absolute Error ( $\mu\text{m}$ ) in Real-time Estimation			
Experiment Group	Real-time Measurement Setting	Sample NO.	Total Height	Exposure Height	Exposure Height	Total Height	Exposure Heights		Total Height	
							Vs. Target	Vs. offline ICM&M	Vs. offline ICM&M	Vs. Microscope
Group #1 (Normal Process: UV iris level 22%)	10 frames / run of online measurement for 1 pixel	1	80	72	73.17	80.03	1.17	-0.48	-0.27	3.18
		2	80	72	78.08	86.44	6.08	-6.27	-2.37	2.93
		3	80	72	74.22	74.22	2.22	-7.31	-12.10	-8.39
		4	80	72	80.90	80.90	8.90	-1.97	-7.46	-2.22
		5	80	72	78.41	89.59	6.41	3.97	7.71	10.60
		6	80	72	75.31	86.33	3.31	-0.87	3.63	6.71
Group #2 (Slow Process: UV iris level 5%)	Subset #1 (10 frames / run of online measurement for 1 pixel)	1	40	36	39.85	42.51	3.85	-0.62	-1.63	-2.54
		2	40	36	37.24	43.13	1.24	4.83	7.01	6.24
		3	40	36	36.80	42.57	0.80	-0.76	1.21	-2.30
		4	40	36	35.93	38.41	-0.07	0.60	-0.80	-0.71
		5	40	36	36.86	36.86	0.86	11.38	8.27	3.57
		6	40	36	35.94	41.38	-0.06	-0.58	2.47	-2.82
	Subset #2 (30 frames / run of online measurement for 3 pixel)	1	40	36	38.57	46.63	2.57	2.95	7.86	6.60
		2	40	36	36.10	42.60	0.10	-2.19	0.55	-0.11
		3	40	36	37.46	40.91	1.46	1.46	1.81	-3.01
		4	40	36	37.25	53.76	1.25	1.07	11.59	12.16



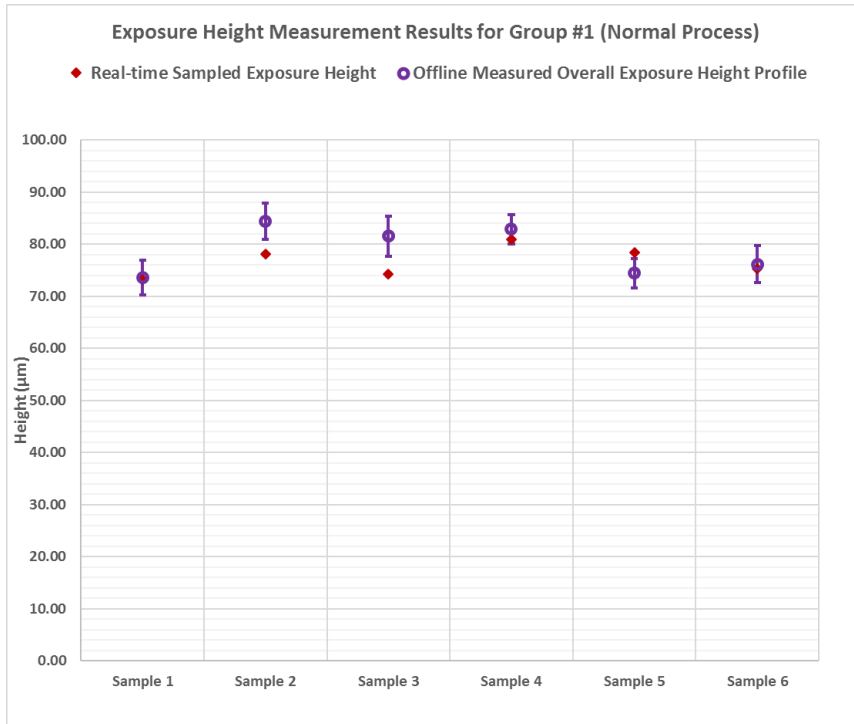


Figure 80. Measurement results of exposure height for the parts cured in the real-time measurement and control experiments Group #1

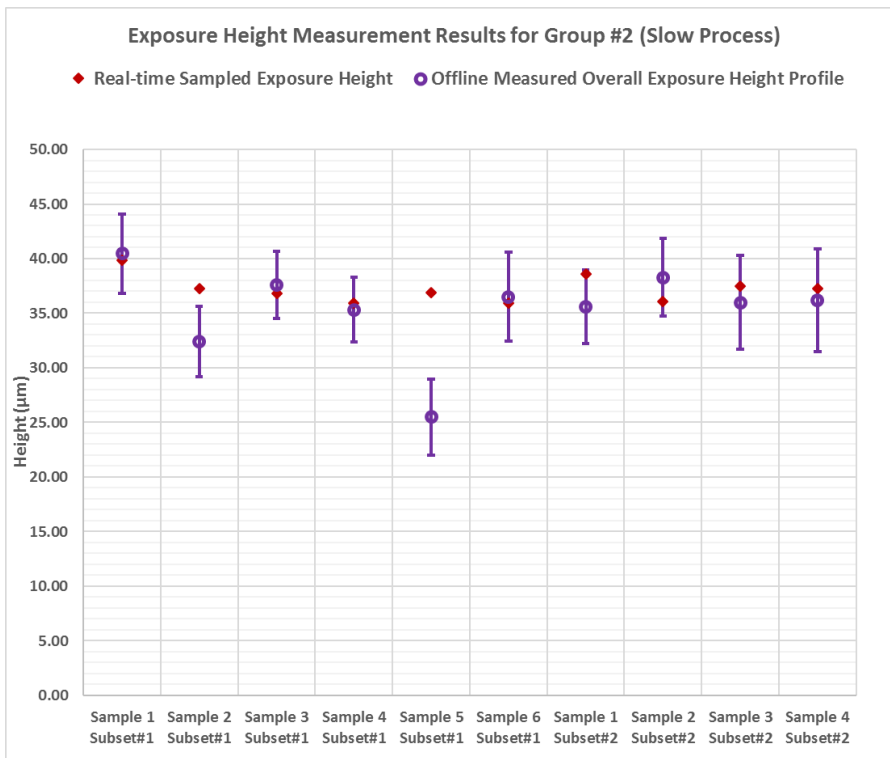


Figure 81. Measurement results of exposure height for the parts cured in the real-time measurement and control experiments Group #2

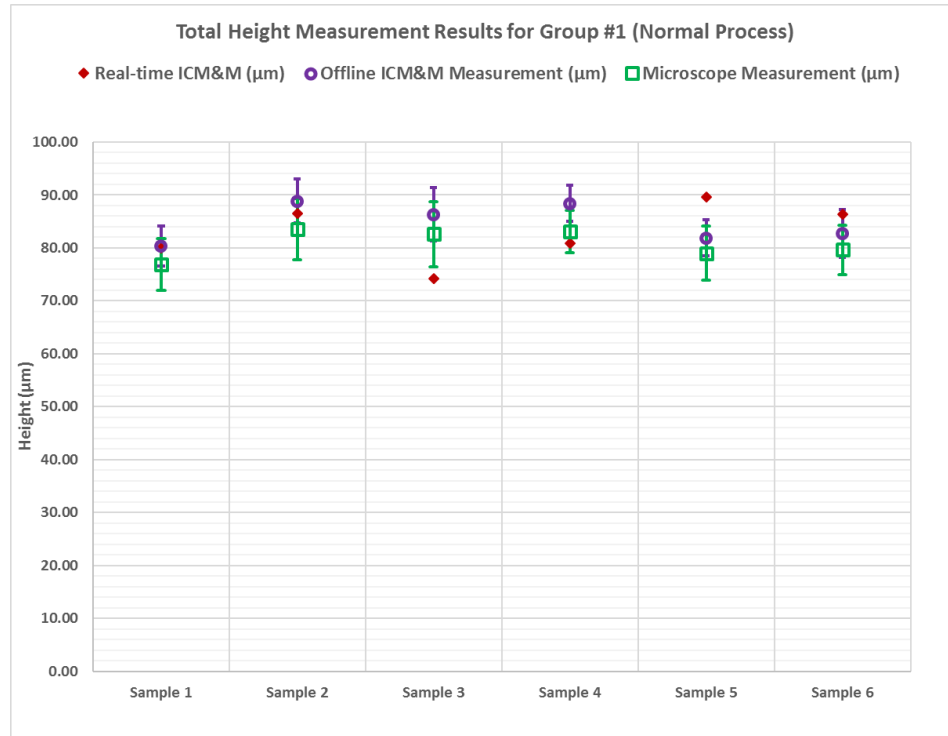


Figure 82. Measurement results of total height for the parts cured in the real-time measurement and control experiments Group #1



Figure 83. Measurement results of total height for the parts cured in the real-time measurement and control experiments Group #2

### 9.7.2.2 Real-time measurement bias and accuracy

In this study, the real-time ICM&M error, defined as the deviation between the real-time ICM&M and microscope results, is broken down into two independent parts as below.

(1) The first part is real-time measurement bias, which is estimated as the deviation between the real-time sampled and the offline ICM&M measured population results as listed in the corresponding columns in Table 20. Comparing with the offline ICM&M implementation which is able to measure a significantly more pixels (i.e., 729 pixels in Group #1 and 441 pixels in Group #2) and to deploy more robust algorithms that require data of more pixels, the real-time ICM&M results obtained from a limited spatial sampling of only one or three pixels due to computation constraints, is prone to misrepresent the overall population height thereby causing a measurement bias.

(2) The second part is the ICM&M system error, which is estimated as the deviation between the offline ICM&M and microscope results as listed in the corresponding columns in Table 19. The offline ICM&M results is more comparable with the microscope in terms of average and standard deviation across the entire cured part and could reveal better the inherent error of the ICM&M method (including the error due to the calibration error and the refractive index modeling inaccuracy) as discussed in Section 9.7.1. Please note that, since the microscope cannot measure out the exposure height, for estimating the ICM&M system error in measuring the exposure height, a value of 90% (approximated ratio of exposure height to total height) of the deviation in measured total heights (listed in Table 19) is used for process control error analysis in Section 9.7.3.

In addition to online sampling bias, low signal noise ratio (SNR) of the online measured pixel's time sequence of grayscales is another significant error source in real-time measurement. Notably, the noise is especially evident in the slow process (Group #2) that employs a low exposure intensity, as shown in the figures in Appendix B. For

example, Sample 5 in Group #2 Subset#1 displays a quite flat data curve of low SNR and results in the worst estimation of exposure height among all the samples in both Group #1 and Group #2, as shown in Figure 81. Sample 4 in Subset#2 presents obvious misleading cycles in the supposed-to-be resting period, and results in the largest error between real-time and offline measured total heights as shown in Figure 83.

To evaluate fairly the real-time measurement performance, as shown in Figure 80 - Figure 83, with the presence of spatial variance across the cured part, the real-time sampled measurement is considered acceptably accurate as long as the real-time result (red diamond) falls within the offline ICM&M resultant range centered on the average (purple circle) and bracketed by the standard deviation (error bar). Based on this criterion, in the real-time measurements of the exposure height, 3 out of 6 (50%) parts in Group #1 and 8 out of 10 (80%) parts in Group #2 are measured inaccurately compared to the offline ICM&M results as shown in Figure 80 and Figure 81. In real-time measurement of the total height, 3 out of 6 (50%) parts in Group #1 and 6 out of 10 (60%) parts in Group #2 exhibit severe errors as shown in Figure 82 and Figure 83. Interestingly, in Group #2 of the slow process, compared with Subset #1, there is no significant improvement in Subset #2 by measuring more pixels, and one possible explanation is that the benefits of measuring more pixels are offset by the cost of longer measurement interval due to the limited computing resource in the system setup.

To conclude from the real-time measurement of both normal and slow ECPL process, it is anticipated based on the worst-case scenario, that using the current ICM&M system in real time, at least 50% ECPL parts could be measured accurately for exposure height and for total height. The real-time measurement errors stem primarily from measurement bias due to the limited spatial sampling, and in case of slow process also stem from real-time data's low SNR. In the future, the real-time measurement error due to the limited and unknowingly biased ROI could be solved by select a more representative and complete set of ROI provided that more computation power is

available. Also, the real-time measurement accuracy could be further improved with better quality data from a better camera.

### 9.7.2.3 Online measurement latency results in over exposure

As introduced in Section 9.4.4, the ICM&M latency  $\tau_{meas}$  refers to the lag between the two parallel threads of real-time interferogram acquisition and online measurement analysis, and depends heavily on the computing power and camera speed. Currently due to some dynamic uncertainty in the computer system and potential deficiency in the parallel computing software, the measurement latency  $\tau_{meas}$  is fairly unpredictable varying significantly by one order of magnitude throughout a single ECPL process for curing one part, for example, as shown in Appendix B.3, it could fluctuate rather randomly from less than 0.1 second up to more than 2 second. Normally, there is a large latency at beginning of each run of measurement, and the latency time would decrease (ideally could decrease to negligible amount) before the next run of measurement thus the analysis would not affect acquisition much. The measurement latency usually decreases as the measurement computation gets smoother and more synchronized with the acquisition, yet it is prone to hike with stochastic environment factors such as other exhaustive background programs running in the computer or electronics glitches. The latency time could also vary significantly, among different experiments, with the changes in the number of online measured pixels and in the measurement interval.

Results of latency and measurement error due to the corresponding over exposure are shown in Figure 86 and Table 21, along with other sources of delay, in the succeeding section that analyzes the real-time control accuracy. For more details about the real-time latency, please refer to Figure B4 in Appendix B.3, which show the experimental latency curves and potential effects of the latency on the ensuing delays in control and actuation.

It is found that Group #1 tends to have large latency and the slow process in Group #2 mostly (9 out of 10 samples) have almost zero latency, which is mainly because the slow process is not that computationally intensive thus the delay is mitigated. Also, specifically in Subset #2 of Group #2, the measurement interval is long enough to avoid a significant latency. Both slow process and long measurement interval aim to parallelize the concurrent process and measurement, and the results demonstrate that the strategy works; however, please note that the root cause lies in the computation limits.

The over-cured height under exposure due to the measurement latency for each sample is also presented in Table 22 in Section 9.7.5. The final output of cured height is partially correlated with the measurement latency induced control error as discussed in Section 9.7.5.

### **9.7.3 Examine the performance of real-time feedback control for exposure height**

As the real-time ECPL process measurement by the ICM&M method being examined above, another key issue is to evaluate the feedback control accuracy in the closed loop as shown in Figure 71. The system delays including measurement latency, feedback control delay and actuation delay, as introduced in Section 9.4.4, could induce significant additional exposure curing in the ECPL process and thus errors in the exposure height. Therefore, this section will firstly present the results of the single part of real-time feedback control node that compares the reference point of target exposure height and the real-time measured height, which outputs an error defined as feedback control error. The follow-up subsections (9.7.3.2, 9.7.3.3) reports the analysis of the experimental system delays and consequential errors in exposure height, providing estimations for the measurement latency induced error, feedback control error and actuation error. Meanwhile, the estimated feedback control errors in Section 9.7.3.3 provide a sound explanation about the experimental result of errors in Section 9.7.3.1. The overall delay effects could be reduced with optimized software and faster hardware.

### 9.7.3.1 Results of the real-time feedback control for ECPL process

Frequently, it makes more sense to describe the performance objective in terms of measurement  $z_m$  rather than the process output  $z_p$ , since often the only knowledge of process output is obtained from the online measurement [101]. The On-Off feedback control loop's performance should be fairly evaluated by assuming that the target exposure height  $z_t$  is accurately provided by the leading compensator and that the real-time measurement is accurate. Please note that the errors in feedforward compensator and online measurement will be incorporated into a comprehensive analysis later in Section 9.7.5.

Therefore, to evaluate purely the feedback control ability in presence of measurement noise and process disturbance within the time interval of UV exposure, the online measurement at triggering time point  $t_{trg}$  is compared against the provided reference point  $z_t$ . Results are plotted in Figure 84 and Figure 85 for Group #1 and Group #2, respectively. Generally speaking, the normal process shows larger errors in exposure height control than the slow process does, which is understandable as slow process is less sensitive to process delays. The observed deviation reflects the error in the feedback control for exposure height, which is accounted by the feedback control delay due to the discrete measurement (i.e., measurement interval effect) and the transmission and controller computation delays as shown in Figure 86. For each sample in the two groups of experiments, the estimation result of the over-cured height due to the feedback control delay (as shown in Table 21) matches well with and accounts for the deviation observed in Figure 84 and Figure 85.

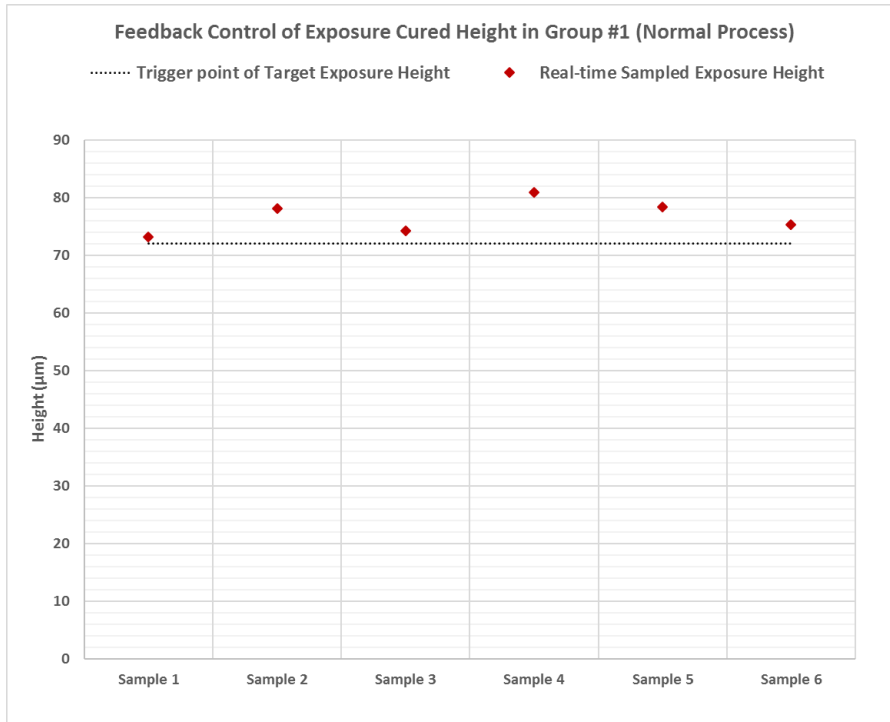


Figure 84. Real-time feedback control results for exposure height in the real-time measurement and control experiments Group #1

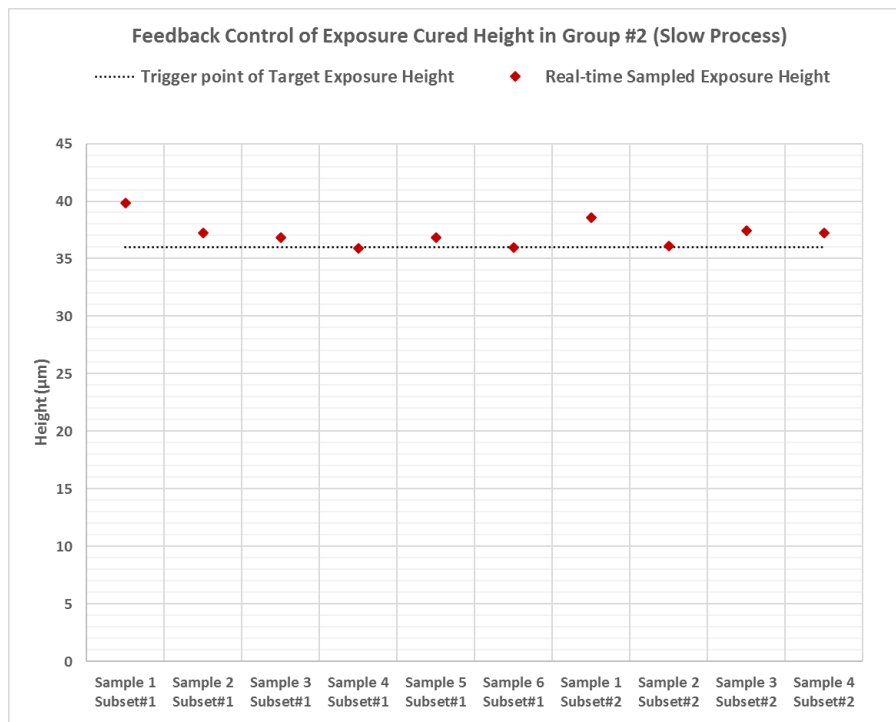


Figure 85. Real-time feedback control results for exposure height in the real-time measurement and control experiments Group #2



### 9.7.3.2 Results of delays in measurement, control and actuation

With the real-time measurement - either of 1 pixel for curing at 22% UV iris level or of 3 pixels for curing at 5% UV iris level, the average image acquisition speed shows a similar rate about 18 frames per second (Table B1 in Appendix B), in other words, the average acquisition interval is 55ms per frame consistently in the experiments. Therefore, Group 2.2 (Group #2 Subset #2) which conduct measurement every 30 frames has a longer measurement interval of approximately 1.68s, compared with other experiments which conduct measurement every 10 frames corresponding to an interval of 0.55s.

As per the concepts and methods presented in Section 9.4.4, the online measurement latency, the control delay and the actuation delay in the experiments are estimated. Details about how the discrete measurement and transmission delay induce the control delay in the real-time measurement, and about the latency reflecting the computing environment fluctuations that cause the delays, are all shown in Appendix B3.

Delays in the real-time process measurement and control experiments are displayed in Figure 86. The measurement latency tends to be smaller for the slower process in Group #2 compared with that in Group #1.

The feedback control delay is comprised of two parts – one due to the discrete measurement and the other due to the transmission and controller computation effort. As observed in Figure 86, in the experiments which has an measurement interval of 0.55 s for measuring only one pixel online (Group #1 and Group #2 Subset #1), the control delay due to the transmission and controller computation dominates. In the experiments with a triple interval to enable measuring multiple pixels (Group #2 Subset #2), the control delay due to missed detection by the discrete measurement or the measurement interval effect is significantly hiking, while the other part of control delay is negligibly small because the long measurement interval allows abundant time for transmitting the feedback signal as well as for performing the control algorithm.

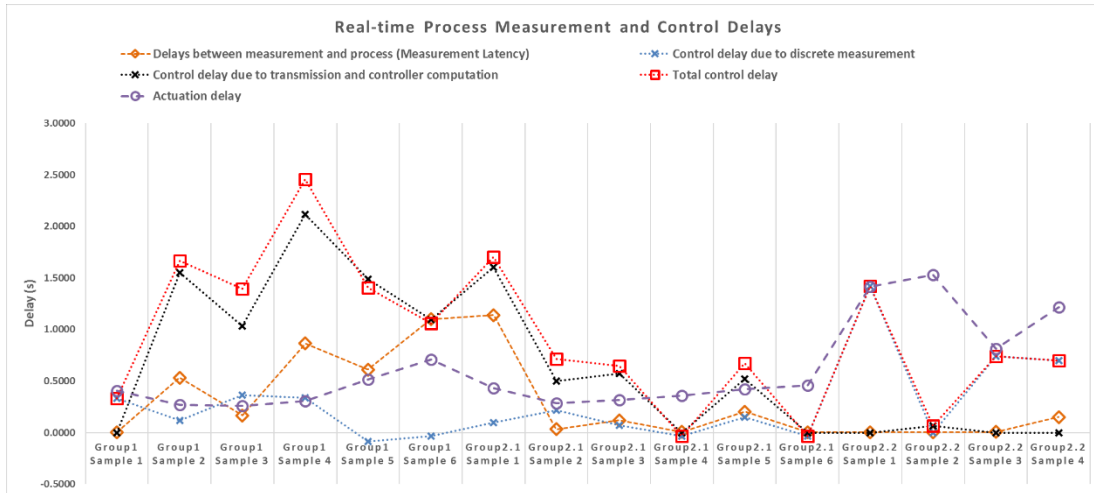


Figure 86 Delays in the real-time process measurement and control experiments

As a summary, the time lapse between the process and measurement, the extended exposure time due to the delay in the feedback control and actuation, are listed in Table 21 (blue columns). Real-time measurement with longer measurement interval is prone to postpone detecting the measurement and delay the control. Regardless of the process speed, sufficiently fast measurement and fast computation is demanded to detect process deviation so that exposure time and intensity adjustment can be done to rectify the problem in a timely manner [104]. Computing power limitation is the root cause for the delays and should be addressed to unleash the potentiality of the real-time control system.

### 9.7.3.3 Over-cured heights due to extended exposure

The over-cured height output by an extended exposure due to the delays in measurement, control and actuation could be estimated with the characterized ICM&M sensitivity model. Specifically, Equation ( 39 ) is used to estimate the over-cured height caused by the delays, and parameters used in this study are provided. It is worth to point out that the estimated period of ICM&M data  $T_{Process}$  is easily identified from the experimental output data of grayscale time sequence. Specifically,  $T_{Process}$  is estimated as being 3.2 s for the normal process in Group #1 and 6.5 s for the slow process in Group

#2. The good agreement between the estimated and observed over-cured heights due to the feedback control delay, as shown in Table 21, provides a verification of the estimated values of  $T_{Process}$ , which thus could be used in Equation ( 39 ) to estimate the over-cured heights for other types of delays. Particularly, the over-cured height due to measurement latency cannot be measured out, hence, has to be estimated by Equation ( 39 ). The actuation delay could be inferred from the real-time measurements, but not reliably enough especially in case of too much noise, for example, several experiments' (e.g., Group#1 Sample 3 and 4) real-time measurements show unrealistic zero value of over-cured height due to considerably non-zero actuation delay. Therefore, the over-cured height due to actuation delay is rather to be estimated by Equation ( 39 ).

$$z_{oc} \approx \frac{1}{2} \times \left( z_{cycle} \times \frac{\tau}{T_{Process}} \right) \quad (39)$$

where,  $z_{cycle}$  is characterized to be 12  $\mu\text{m}$  as in Equation ( 28 );  $T_{Process}$  is roughly 3.2 s for the normal process in Group #1 and 6.5 s for the slow process in Group #2;  $\tau$  is the delay in measurement or control or actuation for estimating the corresponding result of over-cured height  $z_{oc}$  under extended exposure.

As a summary in Table 21, the over-cured heights (highlighted in red) due to the system delays (shown in the blue columns), are estimated by the online measurement results directly to account for the feedback control delay, and by the ICM&M characteristic of sensitivity model in Equation ( 39 ) to account for the measurement and actuation delays. The results are incorporated in the ultimate error analysis in Section 9.7.5.

Table 21. Real-time measurement and control system delays and resultant errors in the process output of cured height

Experiment Group	Online Measurement Setting	Sample NO.	Measurement Latency		Feedback Control Delay					Actuation Delay		
			$\tau_{meas}$	$Z_{OC\_RT}$	$\tau_{ctrl\_s}$	$\tau_{ctrl\_sec}$	$\tau_{ctrl}$	$Z_{OC\_RT}$	$Z_{OC\_ICM}$	$\tau_{act}$	$Z_{OC\_RT}$	$Z_{OC\_ICM}$
Group #1 (Normal Process: UV iris level 22%)	10 frames / run of online measurement for 1 pixel	1	0.004	0.02	0.332	0.000	0.332	1.17	1.25	0.406	1.44	1.52
		2	0.533	2.00	0.118	1.550	1.668	6.08	6.26	0.272	0.97	1.02
		3	0.165	0.62	0.364	1.032	1.396	2.22	5.24	0.257	0.00	0.96
		4	0.865	3.24	0.339	2.114	2.453	8.90	9.20	0.305	0.00	1.14
		5	0.611	2.29	-0.084	1.490	1.406	6.41	5.27	0.515	2.20	1.93
		6	1.100	4.12	-0.033	1.094	1.061	3.31	3.98	0.710	2.57	2.66
Group #2 (Slow Process: UV iris level 5%)	Subset #1 (10 frames / run of online measurement for 1 pixel)	1	1.137	2.10	0.097	1.605	1.702	3.85	3.14	0.433	0.55	0.80
		2	0.033	0.06	0.216	0.499	0.715	1.24	1.32	0.285	0.51	0.53
		3	0.118	0.22	0.071	0.575	0.646	0.80	1.19	0.318	0.41	0.59
		4	0.006	0.01	-0.033	0.000	-0.033	-0.07	-0.06	0.356	0.69	0.66
		5	0.203	0.37	0.151	0.522	0.673	0.86	1.24	0.422	0.00	0.78
		6	0.005	0.01	-0.035	0.000	-0.035	-0.06	-0.13	0.460	0.76	0.85
	Subset #2 (30 frames / run of online measurement for 3 pixel)	1	0.005	0.01	1.420	0.000	1.420	2.57	2.62	1.413	2.22	2.61
		2	0.004	0.01	0.000	0.064	0.064	0.10	0.12	1.528	2.03	2.82
		3	0.006	0.01	0.741	0.000	0.741	1.46	1.37	0.812	1.25	1.50
		4	0.150	0.28	0.696	0.000	0.696	1.25	1.28	1.214	2.14	2.24
Notes: symbols and definitions												
$\tau_{meas}$	Measurement Latency at Trigger point (s)											
$\tau_{ctrl}$	Total Feedback Control Delay (s)											
$\tau_{ctrl\_s}$	Feedback Control delay due to Discrete Measurement (s)											
$\tau_{ctrl\_sec}$	Feedback Control delay due to Transmission & Controller Computation (s)											
$\tau_{act}$	Actuation Delay (s)											
$Z_{OC\_RT}$	Over-cured Height inferred from Real-time Measurement ( $\mu\text{m}$ )											
$Z_{OC\_ICM}$	Over-cured Height estimated by ICM&M Characteristic ( $\mu\text{m}$ )											

#### 9.7.4 Examine the performance of real-time control for total height

As presented in Figure 71, the overall process control system consists of two parts – compensation for dark height and On-Off feedback control for exposure height. The most direct and desired metric for the entire control system’s performance is to check whether the process output  $z_p$  approximates the set point of target total height  $z_s$  in the presence of measurement errors and uncertainty due to process disturbance  $d_p$  and measurement noise  $n_m$ .

Therefore, to evaluate the overall control ability (including both compensator and feedback controls) with the uncertainties and noises in both the ECPL process and the ICM&M sensor, the ultimate error for total height control is estimated by comparing the process output  $z_p$  that is measured by an ex-situ microscope against the setpoint of desired total height  $z_s$ . Results are plotted in Figure 87 and Figure 88 for Group #1 and Group #2, respectively. In the normal process measurement and control (Group #1), the setpoint of total height falls in the range of the actual height profile measured by the microscope for each of the 6 samples, and the errors are all below  $4\ \mu\text{m}$  (i.e., the relatively errors are all under 5%). In the second group of slow process control, 7 out of 10 samples have a deviation from the measured average height less than  $4\ \mu\text{m}$ , that is, about 70% of the samples have a relative error under 10%. Main reasons for less control accuracy in the slow process measurement and control include larger measurement interval and notably lower SNR in the grayscale data. Especially, the worst sample - Sample 5 in Group #2 Subset #1, is completely off the spread of the measured height and has the biggest error of  $(-6.71)\ \mu\text{m}$ , which is caused by the real-time measurement error due to poor data quality and measurement bias. Moreover, Sample 1 in Group #2.1 has the second largest error of  $5.05\ \mu\text{m}$  which attributes to the feedback control delay induced by the measurement interval effect. A comprehensive analysis for the final process output of cured height is performed in Section 9.7.5 and presented in Table 22 and Figure 89.

Another important finding is that the integrated system of measurement and control achieves good repeatability at maintaining the process output around the target setpoint, despite process variations in each individual experiment. As is shown clearly in Appendix B, the process dynamics reflected by the time sequence of grayscales of the online measured pixels (Figure B1-B3 in Appendix B.2) exhibit difference among repeated experiments in the same group. Moreover, the latency and system delays also vary from run to run of experiment as shown in Figure B4 and Figure B5 in Appendix B.3. Altogether, the observed part-to-part (repeated experiments under the same settings)

and batch-to-batch (different settings) variations in the real process, are probably attributed to non-uniformity in exposure and materials disturbances and uncertainties in the process (especially dark curing), noises and errors in the ICM&M system, and instability in the computation system. Nevertheless, the measurement and control system is designed to behave with the presense of these variations by tracking the process dynamics and manipulating the input accordingly to obtain a desired output.

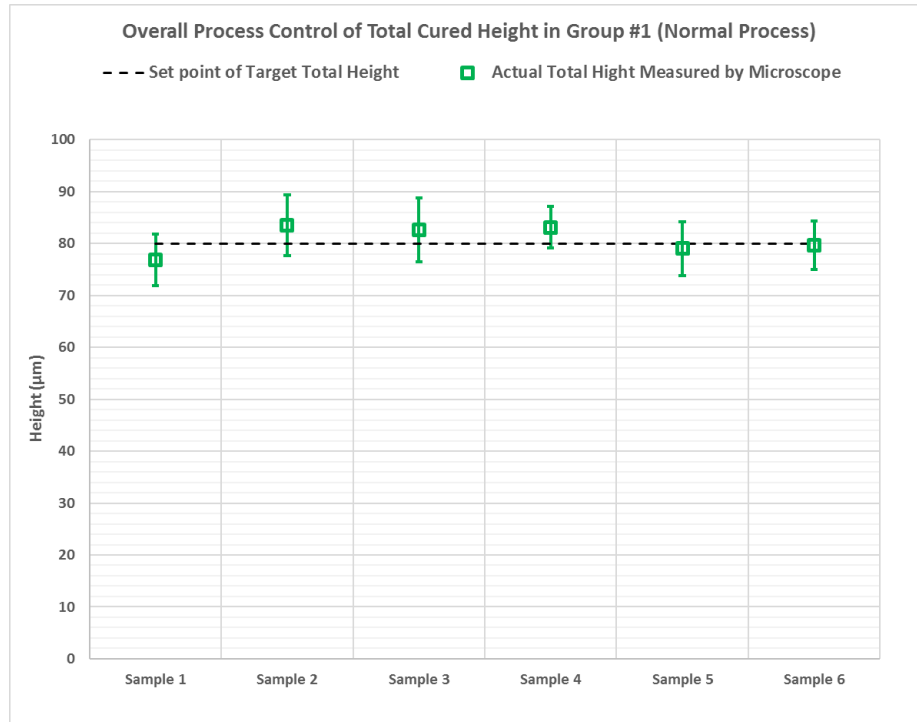


Figure 87. Overall process control results for the parts cured in the real-time measurement and control experiments Group #1

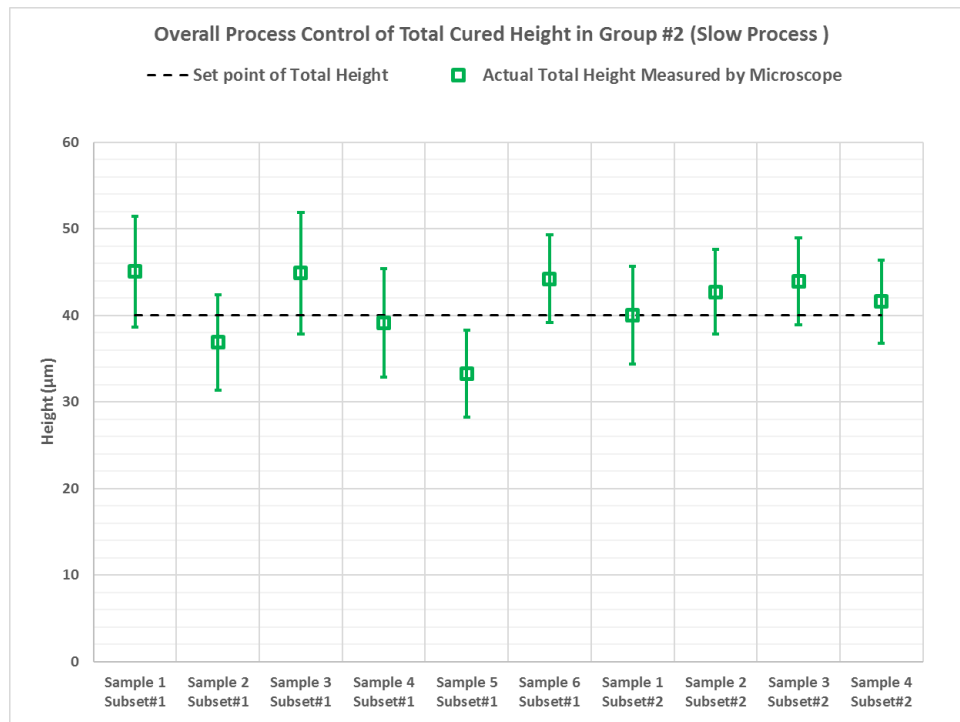


Figure 88. Overall process control results for the parts cured in the real-time measurement and control experiments Group #2

### **9.7.5 Error analysis for the real-time process measurement and control system**

To evaluate the performance of the entire system for ECPL process measurement and control, a variety of performance objectives, including the abovementioned ICM&M measurement performance (both offline and real-time) and feedback control performance, are considered to interpret the experimental results. In the developed real-time measurement and control system for the ECPL process, the ultimate error in total height is broken down into two parts – error in exposure height and error in dark height. The former is attributed to two main categories of causes – real time measurement error and system delays, while the later is caused by inaccurate compensation. A comprehensive set of error sources includes the following six factors, and estimations of the corresponding errors are summarized in Table 22.

1. Real-time measurement bias which is estimated by the deviation between online sampled and offline ICM&M measured population exposure heights as shown in Table 20.
2. ICM&M system error which is estimated by the absolute deviation between the offline ICM&M estimation and the microscope result as shown in Table 19.
3. Over-cured height under extended exposure due to online measurement latency as shown in Table 21.
4. Over-cured height under extended exposure due to feedback control delay as shown in Table 21.
5. Over-cured height under extended exposure due to actuation delay as shown in Table 21.
6. Compensation error which is estimated by the deviation between the offline ICM&M measured dark height (results as shown in Table 19) and the preset dark height (Table 18) by the compensator (Section 9.4.5.1).

Given the independent error sources of bias in online sampling, system error in ICM&M method, latency in real-time measurement, delays in real-time control and



actuation, and uncertainty in the dark curing, the method of multiple linear regression is employed for error analysis about the developed ECPL process feedback control system. In the multiple linear regression, predictors are the six types of errors identified and estimated above (as shown in Column 2 – Column 7 in Table 22), and the response is the actual error in total height (as shown in the red Column in Table 22); thus the regression coefficients are computed by a function of “regress” in MATLAB [105].

Results of the multiple regression analysis of the error sources in the entire process measurement and control system is shown in Table 22. To visualize the error sources and effects in the process measurement and control system, Figure 89 shows the breakdown analysis for the overall error with the six error sources in the process measurement and control system, presents their contributions in the form of “weight” which is the coefficient of corresponding type of error in the multiple regression error model, and illustrates how these factors interplay to output the ultimate error.

The coefficients of the multiple regression indicate how influential the corresponding error source is in the resultant error; hence the larger the absolute value of the weight, the more deviation the source could cause in the final output of total height. It is found that the most significant error sources are real-time measurement bias due to limited spatial sampling and data noises, ICM&M error, feedback control delay, and compensation for dark curing. It is noted that all the measurement related sources (measurement bias, ICM&M error, measurement latency) have negative weights, which is anticipated in a negative feedback control system. The actuation delay has the least weight, which makes sense as the control system is designed with a “height tolerance” (Figure 71) to at least partially (if not fully) account for its potential effect of introducing a deadband (Section 9.4.5.3). The measurement latency turns out to have a small weight of (-0.13), which is justified by the intentional target height that is chosen to be big enough to achieve a better synchronization between the acquisition and the analysis loops as introduced in the design of experiments (Section 9.6). It is reasonable to think that with

sufficient computation power, the developed system can output arbitrary target height that falls in the measurement range (experimentally verified range is 0 to at least 200  $\mu\text{m}$ ) of the current ICM&M system with accuracy and precision.

Table 22. Error analysis for the real-time measurement and control of the ECPL process

Exp. Index	Error in Exposure Height ( $\mu\text{m}$ )					Error in Dark Height ( $\mu\text{m}$ )	Overall Error in Total Height ( $\mu\text{m}$ )		
	Real-time measurement error		Over-cured height ( $\mu\text{m}$ ) under extended exposure due to ***			Feedforward Compensation Error ****	Actual Observation *****	Multiple Resgression Estimation ( $\mu\text{m}$ )	
	Real-time Measurement Bias *	ICM&M System Error **	Measurement Latency	Feedback Control Delay	Actuation Delay			Fitted Error	Residual (Actual vs. Fitted )
Group1 Sample 1	-0.48	3.11	0.02	1.17	1.52	-1.38	-3.15	-3.21	0.06
Group1 Sample 2	-6.27	4.77	2.00	6.08	1.02	-3.63	3.51	3.37	0.14
Group1 Sample 3	-7.31	3.34	0.62	2.22	0.96	-3.04	2.61	2.71	-0.10
Group1 Sample 4	-1.97	4.72	3.24	8.90	1.14	-2.64	3.12	3.01	0.11
Group1 Sample 5	3.97	2.60	2.29	6.41	1.93	-0.40	-1.01	-0.70	-0.31
Group1 Sample 6	-0.87	2.77	4.12	3.31	2.66	-1.18	-0.37	-0.34	-0.03
Group2.1 Sample 1	-0.62	-0.81	2.10	3.85	0.80	-0.50	5.05	4.99	0.06
Group2.1 Sample 2	4.83	-0.70	0.06	1.24	0.53	-0.49	-3.10	-3.22	0.12
Group2.1 Sample 3	-0.76	-3.16	0.22	0.80	0.59	-0.32	4.87	4.99	-0.12
Group2.1 Sample 4	0.60	0.08	0.01	-0.07	0.66	-0.32	-0.88	-1.07	0.19
Group2.1 Sample 5	11.38	-4.23	0.37	0.86	0.78	-1.05	-6.71	-6.76	0.05
Group2.1 Sample 6	-0.58	-4.77	0.01	-0.06	0.85	-1.91	4.20	4.13	0.07
Group2.2 Sample 1	2.95	-1.13	0.01	2.57	2.61	-1.00	0.02	0.25	-0.23
Group2.2 Sample 2	-2.19	-0.60	0.01	0.10	2.82	-0.36	2.71	2.85	-0.14
Group2.2 Sample 3	1.46	-4.34	0.01	1.46	1.50	-1.37	3.93	3.82	0.11
Group2.2 Sample 4	1.07	0.51	0.28	1.25	2.24	1.29	1.60	1.16	0.44
Weights of Error	-1.013	-1.165	-0.130	1.081	0.074	1.050	Coefficients result from Multiple Regression		
Notes: explanation about how the corresponding error item is estimated									
*	Data (Real-time vs. Offline ICM&M) in Table 19								
**	Data (Offline ICM&M vs. Microscope) in Table 18 multiplied by 0.9 (estimated ratio: exposure height /total height)								
***	Data (the red columns) in Table 20								
****	Data (Offline ICM&M Estimated Dark Height) in Table 18 subtracted by Desired Dark Height								
*****	Data (Microscope) in Table 18 subtracted by Target Total Height								

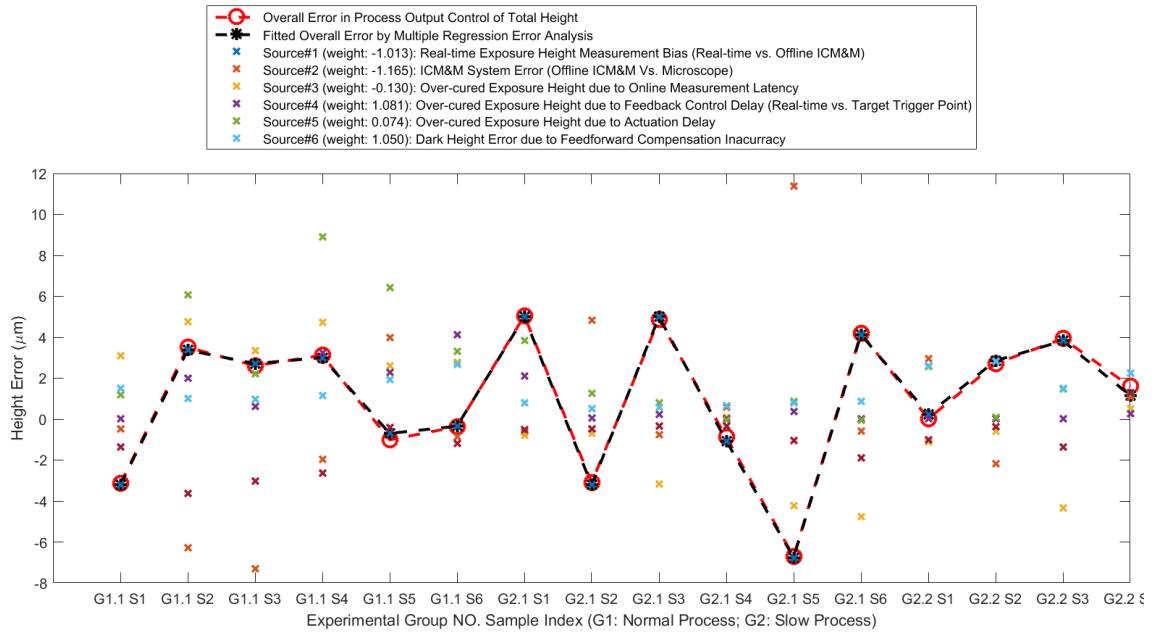


Figure 89. Error analysis for the real-time process measurement and control system

To verify the error model for the cured height with the weighted error sources, the fitted error and residual are calculated as shown in the two rightmost columns in Table 22. It indicates that various possible error sources have been well identified and understood. With this understanding and appropriate improvements in hardware, it is conceivable that the real-time control method with the aid of the developed ICM&M system could achieve a sub-micron control accuracy. Furthermore, the close to zero residuals for all the samples demonstrate vividly that the error analysis is accurate and adequate with all possible sources incorporated, hence implications for the significant error sources can bolster an in-depth discussion of the work and can justify the recommendations for future improvement as in Section 9.8.

## 9.8 Discussion and recommendation

The experiment results and ultimate error analysis provide a thorough and detailed investigation about the capabilities and limitations in the current real-time measurement and control system for the ECPL process, shedding light onto research

directions for improving the system. Future research effort is aimed to solve the real-time measurement bias and system delays by boosting the computing software and hardware , to improve the ICM&M system by better calibration, and to address the compensation by modeling the process (especially the dark curing part) more accurately, so that the current process control error of 5% is anticipated to be reduced greatly down to 1%. Furthermore, the section will present some more thoughts about improving the control accuracy.

### **9.8.1 Online compensation for the measurement latency**

Measurement latency is caused by the inevitable delay in the measurement analysis and the process data acquisition, and could be reduced with a better equipped platform of optimized software and improved hardware. The existence of ICM&M latency indicates that it is an asynchronous metrology, which inevitably could induce some control errors.

As noted in Section 9.4, the preliminary On-Off controller design does not consider about latency in the measurement, and by selecting a proper set point (in Section 9.6) that requires sufficiently long exposure time to allow the latency to drop to an acceptable level (e.g., less than 0.1s), one could assume that the received measurement is synchronized with the ongoing ECPL process. Even though, experimental results still show that sometimes the latency spikes right before the trigger point and induce control error significantly.

Although the error analysis for this specific groups of experiments show an insignificant weight of measurement latency (Section 9.7.5) due to the purposefully-selected target heights, it could actually have the same level of significance as the feedback control delays do in case of process control for outputting arbitrarily desired height. Therefore, measurement latency is still needs to be addressed.

In addition to fastening the computing, some computation strategy could be adopted to compensate for the asynchronous loop. Notably, in this study, the developed

software actually can provide the controller easy access to each acquired frame's timestamp so that it knows how old the received measurement is. This information can then be used by the controller in the control signal calculation. Specifically, future work is recommended to calculate the control signal using a current cured height estimated by extrapolating the received measurement feedback that is probably outdated.

### **9.8.2 A predictive on-off feedback control to address discrete measurement issue**

Due to the ICM&M sensing failure or communication problem or simply a considerably long measurement interval, the discrete measurement effect is pronouncing in the feedback control delay. There is a need to introduce the concept of “timeout” from a control perspective [100]. As it is not always beneficial to wait for a new measurement before doing control, and a controller that uses a timeout can be designed to stop the exposure upfront when the predicted height would reach the target before the arrival of next measurement. Furthermore, a process equipped with the on-off control will constantly overshoot its setpoint [46]. It is recommended to combine a predictive control with the feedback control to manipulate the input around the reference point.

Specifically, in the EPCL process control, the “timeout” is defined as an automatic upfront cessation of exposure before a new measurement is available, when the remaining exposure time for reaching the target height predicted at the current measurement time point is smaller than one measurement period. The key problem is to determine how long the residual exposure is before a timeout should be executed in-between the two measurements.

Therefore, one can augment the existing design of the On-Off feedback controller with a predictive model which can determine online when a timeout is needed. An evolutionary cycle to cycle (EC2C) controller is designed, and a linear predictive model with online adaptively estimated parameters is developed to predict the remaining exposure time. The timeout is decided to be activated at the end of a predicted under-one-

measurement-period residual exposure time, which is calculated by the predictive model using exponentially weighted historic measurement data. The EC2C is actually proposed in Section 3.7.1, and elaborated in one of the author's journal publications [70]. The simulation study of the designed EC2C demonstrates that performance in the ECPL process closed-loop measurement and control can be increased by use of timeout. The described methodology can be extended to other layer-by-layer additive manufacturing process feedback control.

EC2C combines the advantages of real-time On-Off feedback control with model prediction control (MPC), in order to improve the ECPL process control accuracy. To implement EC2C experimentally, the two most important prerequisites are the availability of online measurement, as well as a precise timing of measurement (i.e. constant or at least predictable measurement period) that helps the controller to estimate the necessary remaining exposure time for achieving target cured height [70].

Based on the previous real-time implementation of the On-Off controller, efforts were made to achieve the more advanced On-Off control with EC2C. Unfortunately, the timer object used for real-time ICM&M is subject to the limitations of the hardware, operating system and software, and cannot guarantee the demanded uniformly-spaced image acquisition and constant measurement analysis. Actually, it is noted by MathWorks that timer objects should be avoided for real-time applications [106], because (1) Matlab is implemented in Java and may execute some indefinitely long computation, and (2) Windows operating systems have no real-time guarantees. Therefore, the current MATLAB platform based ECPL-M&C software in the windows operating system is not well suited for real-time precise timing control which is however required by EC2C. Consequently, experimental implementation and investigation of the EC2C for ECPL process is not able to be materialized in this study. Yet the simulation study [70] of the EC2C shows its promising capability of achieving a better control of the cured height compared to the basic On-Off control studied above.

To enhance confidence in deterministic execution for real-time process measurement and control, in future work, the entire system should adopt a real-time operating system (RTOS) for data acquisition and measurement analysis to ensure reliability and repeatability of process control.

### **9.8.3 Control dark curing in the ECPL process**

In this study, as introduced in Section 9.4.5.1, the compensator adopts an empirical process model that assumes a constant ratio of dark height to exposure height (1/9 in the experiments) to determine the reference point for the feedback controller. An inadequate or excessive compensation would be a significant error source in the ECPL process control for the final cured part accuracy, as demonstrated in the error analysis in Section 9.7.5. As dark curing is shown to present disturbing uncertainties and errors in the ECPL process control, in addition to improving the process model thus the compensation accuracy, alternative effective control strategy for dark curing could be considered in future development of more advanced control system for the ECPL process. This section provides some possible solution to address dark curing in ECPL process control.

Radical-based photopolymerization is characterized by a rapid cessation of polymerization when the photo-curing light source is extinguished, and theoretically it is possible to reduce or minimize the dark curing period because radical based active center could have a shorter propagating time with more efficient termination reactions [107]. There exists some research on purposely extending dark curing, since effective dark curing would be useful to reduce processing times and lower initiator concentrations, as well as to achieve photo-curing in shadow regions which finds application in dark curing polymerizable dental composition [107]. The other control direction of shortening the dark curing stage is desired in case of ECPL process control. Such a controlled radical polymerization in which the radical active centers are terminated when the light source is

extinguished can be envisioned by manipulating the chemical formulation in-situ, because the extent of dark curing depends on the chemical composition of the resin [50].

Generally, the speed of the dark reaction depends also on the sensitivity of the photopolymer, which can be controlled by many factors such as the materials of monomer and matrix [96, 107]. Specifically, the dark curing in photopolymerization process could be reduced by rapid oxygen-scavenging of radicals [66]. The current ECPL process neither adds polymerization inhibitor in the resin purposefully, nor prevents atmospheric oxygen which plays the role of inhibitor from diffusing into the chamber. There is some but not sufficient inhibitor to stop the photopolymerization immediately for effective control of the dark curing.

Therefore, for the ECPL process, to improve the On-Off control accuracy, oxygen could be introduced into the resin chamber at the time when UV lamp shuts down so that dark curing could be suppressed. Notably, as one disruptive photopolymerization based AM technology, the continuous liquid interface production successfully achieves high-speed and high-resolution 3D printing of complex microstructures, fundamentally by establishing and controlling an oxygen-inhibited dead zone [108]. Similarly, herein, the proposed “rapid quenching” method of manipulating the inhibitive oxygen via adjusting online the chemical composition in the reaction chamber, is expected to increase the process controllability by reducing the error and uncertainty in the controller’s reference value thereby to improve the control accuracy at the total cured height.

Additionally, another approach to mitigate dark curing effect is to gradually decrease the intensity (i.e., iris level) toward the end of the process so that as the process approaches the target height, there should be little to no dark reaction. Such a strategy could be used with a trade-off of manufacturing speed, hence it might not be suitable in applications where a fast process is desired.



## 9.9 Chapter summary

In this chapter, a real-time feedback control system consisting of a compensator and a facile On–Off feedback control loop that is combined with the ICM&M system is developed, and deployed onto the physical ECPL system. The experimental results provide a validation of the ICM&M system’s real-time capability in capturing the process dynamics and in sensing the process output, as well as a demonstration of the feedback control system’s capability in controlling the cured height with the presence of ECPL process disturbances and uncertainty, ICM&M noises and errors, and computation system instability. Altogether, the study exemplifies how a well-established real-time closed-loop measurement and control system can help realize an accurate, repeatable and robust photopolymerization based additive manufacturing process.

A basic feedback controller is developed to control the ECPL process cured height in real time. The goal is to cure a part with desired height by the real-time measurement and control system. The system’s performance is evaluated with two groups of experiments that cures square blocks with different desired cured heights under different exposure intensity. In the first group of normal ECPL process, a mild UV intensity at 22% lamp iris level was applied; and in the second group, a much lower UV intensity at 5% iris level was used corresponding to a much slower curing process. The rationale for designing such two experiment groups of different curing rate includes three considerations in order to examine both the measurement system’s and the control system’s capabilities at: (1) adapting to different processes dynamics; (2) adapting to different setpoints; (3) global measurement and control with multiple pixels measurement online; and (4) performing well with the presence of system delays and dark curing process uncertainties. A thorough analysis of the real-time measurement and control results assisted with the offline ICM&M and microscope is carried out to validate the system’s capability in measuring and controlling online the part’s vertical height. It demonstrates further that the ICM&M system could benefit the process modeling with its

capability of revealing the process dynamics such as process stages, curing speed and dark curing height which cannot be obtained by offline metrology. The measurement and control system's performance is satisfactory in achieving the desired cured height with an error in order of several microns (less than 5  $\mu\text{m}$ ), which is reasonable and accountable due to the system constraints in real-time. A comprehensive error analysis unveils the major error sources in the current system, including measurement and controls delays and dark curing process uncertainties, and recommendations of future work for unleashing the system's potentiality are made accordingly.

This proof-of-concept implementation demonstrates that one can implement the real-time ECPL process measurement and control with the developed ICM&M method on the currently resource-constrained prototyping ECPL system in the lab. It can be extended with more advanced devices and more computation power to a full-fledged ECPL machine. The measurement feedback control reported here might be the first of its kind in the photopolymerization based AM industry, since it can produce a part with desired cured height under various exposure intensities in real-time. Provided a multi-core computer with larger RAM and higher speed, the ICM&M could run faster online for more pixels measurement simultaneously with minimal latency, and thereby could enable a better in-process estimation of the cured height; meanwhile the On-Off feedback control loop can sense, compute, trigger and actuate all in a timely manner to control the exposure time with minimal delay. The real-time process measurement and control system demonstrates great potentiality to perform even better, and intrinsically 1% error (or less than 1  $\mu\text{m}$  error) can be anticipated without compromising to the computation limit.

Besides, since the On-Off feedback control is confronted with the challenges from dark curing in the ECPL process, more control actions should be incorporated to address the uncertainty brought by dark curing. One possible solution is to suppress the part of dark curing via online formulation adjustment. The EC2C, a subtler predictive on-off

feedback controller, is expected to improve the control accuracy with its online prediction model which could add more robustness and accuracy to the basic On-Off controller. However, the current computing software and hardware system could not guarantee a precise and constant measurement period that is required in implementing EC2C for the ECPL process [70, 109]. It is recommended that in the future one could start with EC2C for cured height control in the ECPL process with an advanced real-time operating system.

Furthermore, in the future, given the limitations of the simple on-off control method, to achieve more comprehensive and capable control, manipulating the exposure intensity at intermediate levels, that is, an exposure intensity control system such as PID control and advanced adaptive control methods could be explored to control the geometrical dimensions and optical properties desired for ECPL applications in micro-optics.

To conclude, this study opens up an avenue for real-time closed-loop advanced control of photopolymerization based additive manufacturing processes to facilitate their applications for precision fabrication in a wide spectrum of industries.

One major part of this chapter is involved with real-time measurement using the developed ICM&M method, answering directly Research Question 1 and validating fully Research Hypothesis 1. Another major part of this chapter is control system design which answers Research Question 2, and the real-time control experiments results validate Research Hypothesis 2. Especially, the through error analysis at the end (Section 9.7.5) indicate that various possible error sources have been well identified and understood. With this understanding and appropriate improvements in hardware, it is conceivable that the real-time control method with the aid of the developed ICM&M system could achieve a sub-micron control accuracy, providing a strong support for Research Hypothesis 2.

## CHAPTER 10 CLOSURE AND FUTURE WORK

This chapter summarizes the previous chapters' conclusions and presents potential benefits from the dissertation research. The research questions and hypothesis evaluated in this thesis are revisited in Section 10.1. The entire work presented in this dissertation is summarized in Section 10.2. In Section 10.3, the intellectual and developmental/engineering contributions of this work are presented. With some limitations of the research identified in Section 10.4, the chapter ends with Section 10.5, which presents the scope of long-term work and recommendations for future research areas to pursue in order to further mature the ECPL technology.

### 10.1 Revisiting Research Questions

This section presents the research questions investigated and the hypothesis evaluated in this thesis. The objective of this research presented in Chapter 4, is restated here:

*“To develop a real-time process measurement and control method for ECPL”.*

In order to achieve this objective several research questions were identified and hypotheses were proposed for each of them. The validity of the hypotheses is tested in this section.

#### 1. Research Question 1

**Question:** How to develop a real-time metrology for the ECPL process based on the existing in-situ interferometric curing monitoring system to measure the cured part dimensions, specifically the cured heights across the curing area?

**Hypothesis:** A real-time metrology for cured part dimensions could be achieved by processing a time series of pixel intensities in a sequence of interferograms, which are provided by the existing in-situ interferometric curing monitoring (ICM) system, based on interference optics and online parameter estimation algorithms.

**Validation of Hypothesis:** Four research tasks were performed to validate the hypothesis about real-time metrology: (1) to establish a sensor model that can interpret the dynamics of interference pattern for the desired measurand of cured height (Chapter 5); (2) to develop fast and robust algorithms for estimating online the sensor model parameters and computing the cured height (Chapter 6); (3) to experimentally validate and characterize the real-time metrology of ICM&M (Chapter 8) in an offline implementation mode; (4) to examine the real-time measurement performance and errors with the ICM&M method (part of Chapter 9, especially, Sections 9.3, 9.7.2).

Firstly, as presented in Chapter 5, the ICM&M sensor model of instantaneous frequency based on interference optics was built to interpret the fringes in-situ automatically, and a fundamental algorithm of online parameter estimation adopting moving horizon exponentially weighted Fourier curve fitting and numerical integration was developed to extract the phase change underlying the fringes in order to measure cured object shape and height.

Challenged by large volume of stream data with process dynamics signals and noises, a comprehensive data mining approach (Chapter 6) for evaluating the ICM&M sensor model was developed to equip the basic online algorithm with denoising, statistical learning and rule-based classification, adaptive fitting, robust regression, and outlier detection and correction, leading to an intelligent, accurate, robust and efficient measurement method. Algorithms parameters effects were studied, and empirical values obtained from experimental observations were incorporated to guarantee realistic solutions derived.

As a summary of the first part of validation for Hypothesis 1, the established ICM&M sensor model and algorithms underpin the hypothesis, by fundamental physics model and data mining approach, and preliminary experimental study.

1. Accurate single voxel measurement with quality data
2. Full-field measurement : 70% voxels can be measured accurately

3. Robustness: 30% outlier voxels would not affect height profile estimation
4. Real-time Feasibility: computation time < 200 ms

For experimental validation, an application program in MATLAB to integrate the ECPL and ICM&M systems for real-time image acquisition and online measurement analysis was developed (Chapter 7).

Initially, given the limited computing power, as a preliminary study, the ECPL process interferograms were acquired real time and analyzed off line (Chapter 8). A coherent series of experiments were performed curing square samples by varying the factors of exposure time and intensity, and a representative full-field height profile was measured for each cured sample by both the in-house ICM&M and a commercial confocal microscope, to evaluate the measurement characteristics including traceability, comparability, accuracy, repeatability, sensitivity, uncertainty, resolution and range. Results showed that the ICM&M could provide a cost-effective measurement for cured heights with excellent accuracy and reliability, and decent capability of estimating lateral dimensions. It can measure multiple voxel heights consistently and simultaneously, and features the capability of full-field measurement which is desired in global measurement and control of ECPL.

As a summary of the second part of validation for Hypothesis 1, the offline implementation of the ICM&M for measuring a series of samples provides a fair evaluation of the measurement characteristics and a benchmark for the real-time metrology, to support the hypothesis. The substantial experiment results and findings are listed below.

1. With initial sensor model assuming constant refractive index
  - (1) Best traceability for same-condition cured samples (error  $\approx 1 \mu\text{m}$ );
  - (2) Good traceability for generally cured samples (20 out of 22 samples have error  $\leq 5 \mu\text{m}$ )

2. With modified sensor model using evolving refractive index

At least 75 % (i.e., 18 out of 22 samples in the reported experiments) of the ECPL parts could be measured accurately (error  $\leq 2 \mu\text{m}$ ).

3. Well understood characteristics and utilities of the ICM&M method

A series of subsequent experiments implementing the ICM&M method in real time were conducted.

As a summary of third third part of validation for Hypothesis 1, the real-time measurement experiments provide a direct and reasonably good proof-of-concept support the hypothesis, although real-time ICM&M is prone to be more erroneous due to a longer acquisition interval (e.g., 55 ms vs. 33 ms) and limited pixels measured online which does not sustain some robust algorithms. The worst-case scenarios (i.e. current limited system) found that at least 50% (actually  $\geq 60\%$  in the experiments) ECPL parts could be measured online accurately (error  $\leq 5 \mu\text{m}$ ) for exposure height and for total height. The real-time measurement errors stem primarily from measurement bias due to the limited spatial sampling, and in case of slow process also stem from real-time data's low SNR. The real-time measurement error due to the limited and unknowingly biased ROI could be solved by select a more representative and complete set of ROI provided that more computation power is available. Also, the real-time measurement accuracy could be further improved with better quality data from a better camera.

In addition to geometrical measurement, a model of evolving effective refractive index for the in-process curing part was developed. Both the trend and magnitude order (0.001) of the refractive index change found by the ICM&M analysis for the ECPL process agreed with the literature reported finding of a gradual increase in refractive index as the photopolymer resin cures. An enhanced ICM&M sensor model with growth-dependent effective refractive index was thereby developed to improve its measurement

accuracy. The ICM&M method has a potentiality in estimating both dimensions and refractive index for the photopolymerized part.

Furthermore, the ICM&M method successfully illustrated the ECPL curing process dynamics in terms of instantaneous frequency which is associated with the curing velocity, i.e., growing rate in units of  $\mu\text{m}$  per second. It was shown to be responsive to the curing start / stop, curing speed, and curing area as shown in the designed experiment series varying exposure time, intensity and pattern size. It can also estimate exposure cured height and dark cured height which cannot be measured by commercial offline metrology systems. The evidence of the relationship between UV intensity and photo curing process dynamics, along with the relationship between the exposure and dark curing, can be utilized for photopolymerization-based additive manufacturing process modeling and control. An insightful process model and thereby an effective process control system could be developed in future with the evidence of the relationship between UV intensity and photo curing process dynamics. The new thinking of exposure intensity control could be a ground-breaking complement to the traditional exposure time control, to realize an ultimate control of the ECPL process for better accuracy.

To conclude, corresponding to the research question and hypothesis, an interferometric curing monitoring and measuring (ICM&M) method that consists of a sensor model (Chapter 5) and online measurement algorithms (Chapter 6) was well established for full field measurement across the entire cured area, and was successfully applied to measure the height of cured part with good accuracy and precision both in off line (Chapter 8, Section 9.7.1) and real time (Section 9.7.2). It also holds promising potentiality in process modeling for innovative exposure intensity control of photopolymer additive manufacturing.



## 2. Research Question 2

**Question:** As a baseline control, without a constitutive process model of first principle differential equations, what is an applicable ECPL process control approach, which could utilize the real-time measurement system to improve the process accuracy?

**Hypothesis:** Using an empirical compensation model for dark curing, a basic On-Off control approach with the online measurement feedback of exposure height, is applicable in ECPL process to control the height of cured part in real time without requiring sophisticated process model.

### **Validation of Hypothesis:**

Corresponding to this part of research, in Chapter 9, a real-time control system consisting of a compensator and a facile On–Off feedback control loop that is combined with the ICM&M system is developed, and deployed onto the physical ECPL system. A MATLAB based software system integrating real-time acquisition, measurement and control by parallel computing was created (Chapter 7), to implement the developed real-time measurement and control system for the ECPL process.

As a summary of the third part of validation for Hypothesis 2, the development and experimental deployment of a feedback controller fully supports the hypothesis by a series of experiments demonstrating the controller’s capability of

- (1) adapting to different processes dynamics
- (2) adapting to different setpoints
- (3) global control potential with multiple pixels measurement online;
- (4) performing well (error  $\leq 5 \mu\text{m}$ ) with the presence of system delays and process uncertainties (e.g. dark curing)
- (5) submicron control with the well-understood error sources to enhance the system in the future.

To conclude, the study in Chapter 9 validates the hypothesis for a simple but effective feedback control system without requiring a sophisticated process model. Under

constrained system, it could control the ECPL process output of cured height with decent accuracy (i.e., deviation is within 5  $\mu\text{m}$ ) despite significant system delays and various process disturbances and uncertainties. The developed methodologies hold even greater potentiality in reducing the error further with an enhanced software and hardware system.

## 10.2 Conclusion

Polymer-based additive manufacturing (AM) is poised to be one advanced manufacturing technology that positively affects major industry such as polymeric electronics and biomedical devices in the world. The vision of polymer-based AM, and the resulting applications that use the revolutionary parts made via AM, is inspirational. However, this vision is not fully a reality today due to several technical challenges, including the challenges associated with process modeling, process measurement and control, materials characterization, and part functional performance for polymer AM. A portfolio of research and development being undertaken by industry, academia, and the government will help overcome these challenges and fulfill the vision, leading to greater proliferation of polymer AM technologies. The lack of real-time sensors critical to process monitoring and control has been identified as one of the major challenges that are currently impeding large-scale deployment of polymer additive manufacturing (AM) processes.

This research is focused on real-time measurement and control for a photopolymer AM process using an in-house exposure controlled projection lithography (ECPL) machine, which is a layerless mask-projection stereolithographic apparatus and could cure a 3D part on a stationary resin chamber with ultra violet exposure from beneath the transparent substrate. To improve the process accuracy with advanced closed-loop control, the study developed an interferometric curing monitoring and measuring (ICM&M) method that consists of a sensor model and online measurement algorithms,

and successfully applied it to measure the height of cured part with good accuracy and precision both in real time and off line.

The ICM&M sensor model of effective interface and instantaneous frequency based on interference optics was built to interpret the fringes in-situ automatically. Challenged by the speed, size and noise of the stream data from the ICM&M system, a comprehensive data mining approach for evaluating the ICM&M sensor model was developed to boost the basic online algorithm and realized an intelligent, accurate, robust and efficient measurement method. Algorithms parameters effects were studied, and empirical values obtained from experimental observations were incorporated to guarantee realistic solutions derived. Besides, a model of evolving effective refractive index for the in-process curing part was developed, enabling the ICM&M method to estimate both dimensions and refractive index for the photopolymerized part. An application program in MATLAB was created to integrate the ECPL process, ICM&M system and controller for real-time image acquisition, online measurement analysis and control computation, providing a human-machine interface to automate and monitor the ECPL process, and a test platform to validate and operate the developed measurement and control systems.

For experimental validation of the developed measurement method (Research Hypothesis 1), two parts of experiments were performed and analyzed – one is offline ICM&M and the other is real-time ICM&M. To begin with, a coherent series of experiments were performed to evaluate the measurement characteristics including traceability, comparability, accuracy, repeatability, sensitivity, uncertainty, resolution and range. Results showed that the ICM&M could provide a cost-effective measurement for cured heights with excellent accuracy and reliability, and decent capability of estimating lateral dimensions. Furthermore, the ICM&M method successfully illustrated the ECPL curing process dynamics in terms of instantaneous frequency which is associated with the growing rate ( $\mu\text{m/s}$ ). It was shown to be responsive to the curing start / stop, curing speed, and curing area. The unfolded dynamics can be utilized to develop an insightful

process model and advanced control system for photopolymerization-based additive manufacturing in future. The new thinking of exposure intensity control could be a ground-breaking complement to the traditional exposure time control, to realize an ultimate control of the ECPL process for better accuracy. As a more advanced experimental validation, the real-time measurement enabled by the parallel computing technique, shows that the ICM&M method could measure multiple voxel heights simultaneously in real time, featuring the capability of real-time full-field measurement which is desired in global measurement and control of ECPL. The real-time measurement results are mixed due to the uncertainties in the limited samples measured online and camera data noises; however, the worst scenarios still demonstrate that the ICM&M method can measure with great accuracy for more than 50% of the samples. The real-time ICM&M method shows very promising potential to be able to measure more accurately with enhanced hardware and computation.

For validation of a basic real-time process control method with accessible measurement feedback (Research Hypothesis 2), a feedback controller is designed and deployed physically. With the real-time measurement and control experiment, the integrated system shows proven capabilities in: (1) adapting to different processes dynamics; (2) adapting to different setpoints; (3) global measurement and control with multiple pixels measurement online; and (4) performing well with the presence of system delays and dark curing process uncertainties. Under the constrained hardware system and limited computation environment, the developed control system could still control the ECPL process output of cured height at a reasonably small error under 5  $\mu\text{m}$ , despite multiple influential error sources including system delays, process disturbances and uncertainties (e.g. dark curing). Substantive recommendations are provided to further augment the fundamental control system reported in the dissertation. It is promising that the developed real-time control method with the aid of the developed ICM&M system

could achieve a sub-micron control accuracy given enhanced hardware and computing system in the future.

As a result of this research effort, an economical and effective real-time measurement system has been developed allowing for the implementation of a feedback control. A cyber-physical system of real-time measurement and control is developed and implemented in the ECPL process in replacement of previous problematic open-loop process planning methods. The developed real-time system features online parameter estimation and adaptive learning of the process model, which is essential for controlling black/grey-box ECPL process with unmeasurable variations and disturbances. The closed-loop control strategy in unison with real-time metrology are exemplified to be able to achieve the target part's height with good accuracy, repeatability and robustness in the presence of process uncertainties and disturbances, reducing the part-to-part and batch-to-batch variability in the ECPL process.

Although a global measurement and control of the ECPL process has not been fully materialized due to several practical engineering problems (e.g., limited computation power, to-be-optimized software coding, and to-be-upgraded hardware), the validity and potentiality of the developed ICM&M method along with the feedback control method have been demonstrated by a facile On-Off control system and representative experimental cases presented in the dissertation. Both the ICM&M system and the real-time control method are shown to be able to measure and control at submicron level accuracy with improved hardware and software systems.

### **10.3 Contribution**

Investigation of Instrumentation and control methodologies, which will be needed to meet the evolving needs of photo polymerization based processes and other additive manufacturing processes, could be a challenging and vibrant area for academic researchers and industrial practitioners alike.

### 10.3.1 Summary of novelty

The new methods, findings, results and implications obtained from this research are summarized as below.

1. A novel and cost-effective method (i.e., ICM&M method) for both real-time and offline dimensional measurement in photopolymer based AM process is developed. Specifically,
  - (1) a new sensor model utilizing novel concepts of “effective interface” and “instantaneous frequency” based on interference optics is developed;
  - (2) a new paradigm of fast, accurate and robust data analytics for in-situ measurement for AM is established.
2. Newly identified characteristics of the developed ICM&M method.
3. Newly unveiled photopolymerization process dynamics in terms of growing speed, cured height and refractive index, which are not reported before.
4. Newly quantified dark curing height, which is not available due to a lack of in-process measurement tool.
5. A new software with parallel computing and user interface is created, realizing a cyber-physical system that can integrate and automate the hardware system, and can visualize, measure and control the ECPL process.
6. Real-time On-Off control for ECPL
  - (1) New knowledge about the On-Off feedback control capabilities, as well as the fully identified error sources for improvement, are obtained through experiment.
  - (2) A New Evolutionary Cycle-to-Cycle Control (EC2C) scheme, which is a predictive on-off feedback control aimed to address discrete measurement issue, is developed and studied via simulation [70].
7. With the new knowledge obtained from the developed ICM&M method,

- (1) new photopolymer AM process modeling is enabled;
- (2) new process control methodology to manipulate exposure intensity for desired properties is envisioned.

### 10.3.2 Overall contribution

Generally speaking, the most significant contribution of the dissertation is having *delivered a systematic and paradigmatic research for developing a real-time additive manufacturing process measurement and control system, including sensor modeling and data mining, dynamics visualization and control, system integration and process automation, along with software development, experiment validation and applications exploration. The outcome of this research not only improves the particular ECPL process but also inspires the general AM community. Several impacts are perceived in multiple areas of AM process metrology, control and modeling. (1) It pioneers to address the gap of lacking traceable in-process measurement methods for polymer additive manufacturing. (2) It enables a real-time feedback control which has been envisioned for years by the AM industry but just got some emerging materialization. (3) It unveils photopolymerization dynamics from a unique perspective that can bridge the molecular reactions and the microscale forming, and the enabled modeling advance could facilitate precision polymer additive manufacturing by upscaling molecules and nanoscale materials for real-world applications.*

To elaborate, the outcome and impact of this research is presented in details from two perspectives: (1) the direct benefits for the ECPL process – the particular AM process being studied for in the dissertation (Section 10.3.3); (2) the inspiration for the general AM community (Section 10.3.4).

### 10.3.3 Contributions to the particular AM process - ECPL

With the theoretical research on metrology and control, the research culminates in delivering a functional ECPL measurement and control software to integrate the ECPL system, the ICM&M system and the control system, *realizing a cyber-physical system for the ECPL - a photopolymer additive manufacturing process - with good accuracy and robustness.*

Specifically, the contributions of this research to the ECPL process could be expanded as below.

- 1) Established a real-time metrology (ICM&M method) for ECPL process, which can provide online feedback to enable advanced controls and can provide an offline measurement method to examine the process data and dynamics.
- 2) Performed an in-depth research on the ICM&M algorithms, and made constructive recommendations for future improvement.
- 3) Characterized and validated experimentally the developed ICM&M system's performance in measuring vertical height.
- 4) Built an evolving refractive index model during the ECPL process, which could expand the ICM&M's capability in measuring optical property of refractive index.
- 5) Revealed the ECPL process dynamics including exposure curing and dark curing, cured speed and height evolution, enhanced the understanding about the process, provided a powerful tool for building a more accurate and control-oriented process modeling.
- 6) Created a software using MATLAB that provides a computing platform to implement the developed metrology and control methods, to conduct experiments of real-time measurement & control for the ECPL process, to



implement offline ICM&M implementation for calibration, process data analysis and modeling.

- 7) Designed and implemented a basic closed-loop control system with the online ICM&M system to measure and control the ECPL process in real time.
- 8) Improved the accuracy, precision, robustness and reliability of the ECPL process, which is nonlinear and prone to process variations and disturbances with the developed real-time metrology and closed-loop control system.
- 9) Demonstrated that real-time sensor and feedback controller is applicable for ECPL and promising for other photopolymerization based additive manufacturing processes.
- 10) Investigated literature on controls of relevant manufacturing process and proposed some conceptual design of advanced control methods for the black/grey-box ECPL process.

#### **10.3.4 Contributions to the general AM research**

From a broader perspective of the overall AM industry, this section firstly concludes the contribution for general polymer AM research as ECPL is essentially an photopolymerization based AM process. Furthermore, it reviews the challenges and needs which are confronting the existing research on the two key technology nodes in AM processes - measurement and control, respectively, and highlights the contribution of this study accordingly.

##### **10.3.4.1 To the research for polymer additive manufacturing**

This research could be generalized and extended to sense and control a variety of photopolymerization based additive manufacturing processes. The reported real-time measurement system has the potential to break through the technological limitations (dimensional accuracy and process repeatability) of the existing photopolymer AM

systems. Notably, it can add knowledge in photopolymerization related processes for advanced process modeling and control. Insights gained from this study could help extend the use of additive manufacturing in more polymer and soft material research and applications.

(1) Metrology for polymerization process

The lack of real-time sensors critical to process monitoring and control has been identified as one of the major challenges that are currently impeding large-scale deployment of polymer additive manufacturing (AM) processes [6]. *The reported ICM&M method provides a potential metrology tool for estimating both geometry property (dimensions) and optical property (refractive index) for the photopolymerized part.*

(2) Modeling for polymerization process

Key to a successful application of control to a manufacturing process is the availability of appropriate mathematical models, which range from empirical forms such as from design of experiments (DOE) to system identification to analytical forms such as detailed fundamental physics and first principle differential equations. Existing photopolymerization based AM process models usually assume that the cured height is determined by lumped sum exposure dose, and seldom acknowledge the individual effect of intensity, which however might be critical in the photopolymerization process to form delicate features (e.g. edges and curves) and even to affect the final part's properties (e.g. refractive index, strength). It is unavoidable to combat the complicated process dynamics for better understanding and control of the system. Hence, a more sophisticated process model could be developed with the intensity as one of the process parameters, and an in-process metrology is necessary to aid the modeling.

In this study, the developed ICM&M method can unveil the photo-curing process dynamics in terms of instantaneous frequency which is associated with the growing rate ( $\mu\text{m/s}$ ). *The dynamics unfolded for the developed metrology can be utilized to develop an*

*insightful polymerization process model that bridges the molecular level reactions and the microscale structures. The reported metrology tool and accompanied modeling advance could facilitate one interesting polymer research area on upscaling molecules and nanoscale materials (e.g., nano particle) by means of precision additive manufacturing to real world applications.*

(3) Control for polymerization process

Though intensity is thought to affect the process behavior, the influence is not clearly recognized. Few formal or quantitative study has been reported on the effect of intensity magnitude in curing.

*This dissertation reveals some initial findings in such effect of exposure intensity on photopolymerization. It not only confirms vividly that higher intensity exposure can cure an object faster, but also quantifies eloquently how the growing speed evolves over the curing process.*

*The new thinking of exposure intensity control enabled by the developed metrology could be a ground-breaking complement to the traditional exposure time control, in order to realize a comprehensive control for geometry accuracy and other properties (e.g., optical properties, mechanics strength) in photopolymer additive manufacturing of functional parts.*

10.3.4.2 To the metrology research for additive manufacturing

Broadly speaking, this research provides an exemplification that real-time metrology in unison with closed-loop control strategies can reduce layer-to-layer, part-to-part and batch-to-batch variability in AM processes.

(1) Real-time metrology

The primary AM researches that focus on in-process monitoring have been associated with determining the geometry and the temperature profile of the metal AM process. Infrared thermography and pyrometry are two well-developed non-intrusive

techniques for the measurement of surface temperatures. There are also some reported works on in-process monitoring of the dimensional accuracy, errors and defects during the build process. A few reports also discuss the in-process measurement of strain–stress.

However, little of such in-process measurement is reported for non-metal (e.g. polymer) AM process. *This study aims to fill in this gap in real-time measurement by providing an in-process metrology for a photopolymer AM process.*

#### (2) Reliable metrology

Even for the considerably developed metal AM process, it is still in urgent need for continual research effort in finding new traceable metrology with better accuracy and repeatability as well as in identifying new measurable process signatures. Similar challenges are confronting the non-metal AM processes, for which the research and development of measurement science and controls technology is under-developed.

*This study pioneers in the existing research to address this gap of lacking traceable measurement methods, by achieving accurate and repeatable measurements as presented in the experimental validation (Chapter 8), and gaining a comprehensive understanding of measurement characteristics including traceability, sensitivity and uncertainty.*

#### 10.3.4.3 To the control research for additive manufacturing

##### (1) Control loops and architecture

It is well known that the relationships between parameters in the AM processes are complex. For example, in powder bed fusion (PBF) process, process maps will be a key tool to organize and communicate the complex, multidimensional parameter relationship topology [110]. These maps will be essential for multi-input, multi-output (MIMO) control algorithm design, and model-based predictive controller design. The metal AM process control design landscape is still so far limited in variety, with most examples using melt-pool temperature and/or size to control laser power or speed. This

method could very well be the most effective; however, there is wider potential for different levels of control loops. For example, control loops may occur discretely between completion of each build layer rather than continuously.

Furthermore, a better understanding of measurement uncertainty would assist system controller design by identifying the necessary level of precision required to attain the goals of the control system. Taking the metal AM for example, it is yet unclear which signatures are best modelled or measured, and which input parameters are best controlled for which timescale (either continuously or discrete inter-layer). Further work should involve the development of monitoring techniques through the use of new sensors and measurement methods that will enable the integration of materials, process control and feedback [9].

As a conclusion from the research status and needs, it is a worthwhile endeavor to create an AM control loop architecture that identifies the multiple potential control loops, and provides a basis for identifying which loops are optimal for controlling which parameter-quality relationship.

*This study initiates an investigation for lithography based AM processes control (Chapter 3) [111], and proposes a framework of promising process control architecture at different levels for the photopolymer AM processes. Furthermore, it exemplifies such a piece of work in identifying the to-be-improved nodes for optimal control, by designing and implementing of a facile control system with a thorough identification for error sources and possible solutions (Chapter 9).*

## (2) Control platform

As the process control research is still in a theory study stage with ideal conceptual designs, there are scant reports on some materialized real-time control systems for AM processes. Future work should involve the development of AM research platform to test and demonstrate the in-process measurement and control methods.

*This research establishes such a platform (i.e., the ECPL-M&C software application) that materializes a cyber-physical system for the ECPL process measurement and control in real time. Specifically, it integrates a friendly user interface with the developed process metrology – ICM&M system and the designed On-Off control system, for testing the measurement and control algorithms as well as for improving the ECPL process automation and accuracy. Remarkably, it enables a macroscopic (micro-scale) visualization of the molecular-level photopolymerization process and could aid advanced process modeling and control.*

#### 10.3.4.4 To the commercial photopolymer AM systems

The ICM&M system is not directly applicable to measure parts cured on commercial photopolymer AM systems (e.g., stereolithography) due to different system setups. However, it could be used to characterize the commercial photopolymer materials' photopolymerization dynamics such as growth speed (unit:  $\mu\text{m/s}$ ) in an ex-situ system. The unveiled curing behavior in microscale could help the companies develop a more powerful process plan that is capable of fabricating parts more accurately and precisely on the commercial photopolymer based AM machines.

### **10.4 Limitations**

The 3D printing machine under study (ECPL) is an in-house additive manufacturing process as described in the introduction part of the dissertation. It was designed for continuous structures such as microlens and microfluidic channels, which does not have overhanging features, and is not able to print lattice structure. The ICM&M system was designed specifically for ECPL process measurement and assumed correspondingly a measurand as a continuous bulk. Real-time monitoring of lattice structures printing is not within the research scope but could still benefit from the research approaches and methodologies. For intricate structures such as lattice, a different

optics metrology using sophisticated configuration and principle might be needed rather than the Mach-Zehnder interferometer based ICM&M method in this dissertation.

## **10.5 Future work**

### **10.5.1 Long-term goal**

3D printing and additive manufacturing is facing challenges in resolution, robustness and reliability. Investigation of Instrumentation and control methodologies, which will be needed to meet the evolving needs of this industry, could be a challenging and vibrant area for academic researchers and industrial practitioners alike.

The long-term goal of this research is to fully understand and control the ECPL processes for fabricating complex micro parts in micro-optics, micro-fluidics, MEMS and bio-manufacturing. Insights from this research could help the ECPL system to be deployed for practical applications. Furthermore, this research will aid control-oriented modeling and simulation, sensor and controller development and implementation in various additive manufacturing processes. This research will help extend the use of 3D printing and additive manufacturing in more advanced technology applications where both structural integrity and functional properties are demanded.

### **10.5.2 Recommendation for Future Work**

Future work includes engineering design and development of both the hardware and software system. Extension and explore to global measurement and control also presents an interesting challenge. Applications of a full-fledged fabrication machine integrating both the ECPL and ICM&M system need to be materialized. The following lists several specific research tasks that could be considered in the future work to improve the modeling, measurement and control for the ECPL process.

10.5.2.1 To develop a constitutive and control-oriented process model of ECPL with the aid of ICM&M and COMSOL

A good understanding of the polymerization kinetics is essential in designing a robust and effective reactor control strategy. The key to building a reliable model is to mathematically describe the chemical and physical phenomena involved in a process and to derive the necessary material, energy and momentum balances [24]. These mathematical descriptions involve nonlinear algebraic and differential equations. The rigor and correctness of a dynamic polymerization model are strongly related to the availability of accurate information on the thermodynamic and transport properties of the polymerization system. Therefore, a constitutive model of the ECPL process could be available with chemical reactions and transport which has been simulated in COMSOL [17, 112].

In the broad picture of the entire ECPL project, it has been envisioned to utilize the current research on process measurement together with COMSOL multiphysics model [112] to develop a more constitutive ECPL process modeling useful for control purpose.

The future work could include a new project having to do with the relationship between the scientific theory of polymerization and the ECPL process as measured by the ICM&M. More specifically, one would like to establish a constitutive process model by connecting the macroscopic interferogram pattern dynamics of phase shifting, the microscale cured bulk height evolution and the refractive index changes in the order of magnitude of 0.001, all of which can be provided by the ICM&M method, with the molecular-level polymerization reaction theory which can be simulated in COMSOL. The COMSOL program to model the changing height and refractive index throughout the reaction could be developed, and compared with the cured height and refractive index determined by the ICM&M. The COMSOL model provide chemical and physics theory

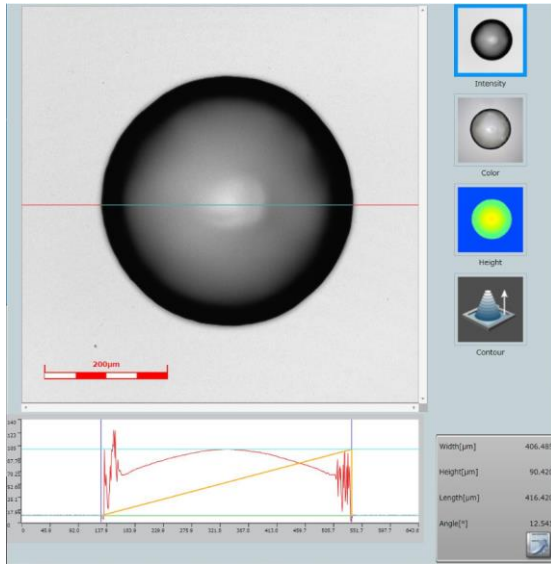


insights, which could be combined with the ICM&M measurement data, to develop a sophisticated and control-oriented process model for better control of the ECPL process.

Some preliminary research has been conducted by using ICM&M to measure some ECPL cured samples of microlens. Prior to the experiment, a COMSOL Multiphysics photopolymerization model was developed and simulated to plan for the ECPL process inputs of a timed sequence of size-varying circular bitmaps to output a microlens of desired shape and target dimensions (i.e., base diameter is 200  $\mu\text{m}$  and center-top height is 80  $\mu\text{m}$ ). The process planning method and process input details are reported in the literature [112], and two repeated experiments were conducted resulting in two microlens referred as Sample #1 and #2 in this section. During the experiment, the ICM&M system was used to record online in parallel with the ECPL curing process for a microlens. After the experiment, the cured microlens was measured by an ex-situ confocal laser microscope and results are shown in Figure 90. Meanwhile, the ICM&M method was performed with the real-time acquired video of interferogram for the microlens curing process, to obtain an estimation of the cured height in the center of curing area, and results are shown in Figure 91.

Moreover, in the particular application case of curing microlens with a sequence of circular bitmap pattern, the center voxel is of great interest for investigating the process dynamics as it contains the curing from the very beginning to the end of the entire exposure duration with all the bitmaps. Voxels at the edges, for instance, do not necessarily get exposed as the bitmap patterns shrink into smaller circles.

(a) Sample #1:



(b) Sample #2:

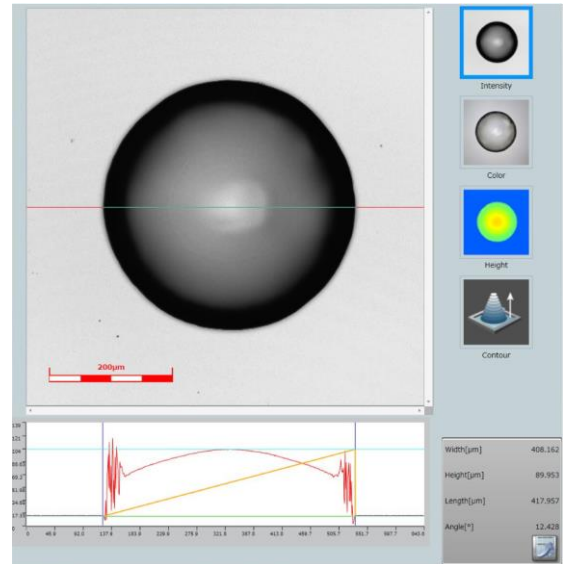
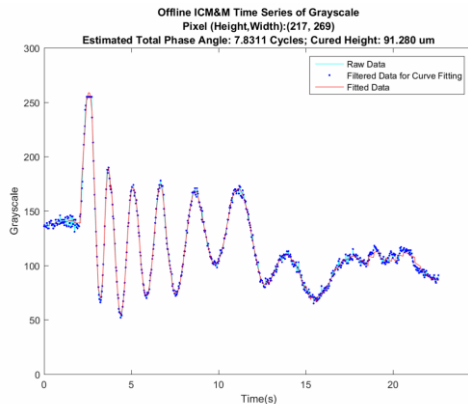


Figure 90. Confocal microscope (Objective Lens Magnification 25 $\times$ , edges could be clearly imaged and measured under a higher magnification lens e.g. 50 $\times$ ) measured centerline profile for the ECPL cured microlens (a) Sample #1; (b) Sample #2.

(a) Sample #1:



(b) Sample #2:

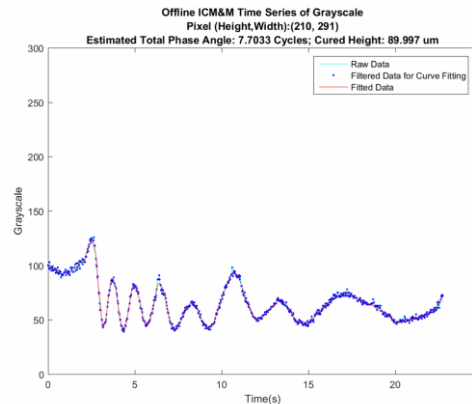


Figure 91. ICM&M estimation results for the center voxel in the EPCL cured microlens (a) Sample #1; (b) Sample #2.

Therefore, the center voxel which represents the topmost point in the cured part will be studied to unveil a comprehensive process in COMSOL simulation and ICM&M estimation, as shown in Figure 92. The top-center height of the cured part is also easily available under the microscope observation – 90.420 µm for Sample #1 and 89.953 µm

for Sample #2 as shown in Figure 90, which are in good accordance with the ICM&M estimated center height - 91.280  $\mu\text{m}$  for Sample #1 and 89.997  $\mu\text{m}$  for Sample #2 as shown in Figure 91. Hence, the ICM&M method is demonstrated to be able to detect the real process dynamics and measure the cured height accurately (at least for the center voxel as compared herein).

However, comparing the COMSOL simulation with the ICM&M estimation in Figure 92, it seems that the developed COMSOL model [112] severely underestimated the microlens's center height, probably because the real process conditions and materials are slightly different from these in the simulation while the COMSOL model [112] is known to be extremely sensitive to process variations. It is noted in Figure 92 that the ICM&M system, however, successfully captures the real physical process dynamics and provides a pretty accurate measurement result that is close to the actual height measured by the microscope.

(a) Sample #1:

(b) Sample #2:

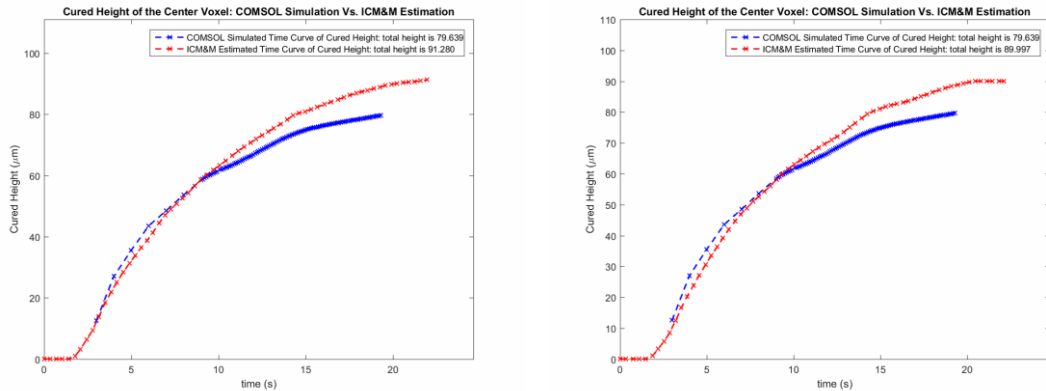


Figure 92. Process simulation by COMSOL and measurement by the ICM&M method for the center voxel in the EPCL cured microlens (a) Sample #1; (b) Sample #2.

The discrepancies observed (Figure 92) between the COMSOL simulation and the ICM&M estimation, suggest that an improved Multiphysics model could be developed with the aid of the ICM&M method that has been validated to agree with the microscope.

Inspired by the preliminary research results as presented above, in the future, research by comparing more experimental results from the COMSOL Multiphysics process simulation, the ICM&M estimation and the microscope measurement, could be performed to explore their connections for a potential constitutive and control-oriented process model, which can incorporate both the prediction from the molecular / polymer science and the observation by the optical metrology.

It is worth to point out that a high fidelity process model will be mainly used to complement the measurement system to provide a more robust estimation of the measurands (e.g., height, mechanical properties), since the metrology system is usually susceptible to noise especially in real-time implementation. If a comprehensive and robust measurement method is developed in the future, chance is that one needs only a simple or even no process model for controlling the corresponding properties that could be measured well.

#### 10.5.2.2 To improve the experiment design for ICM&M calibration / validation / characterization

The ICM&M method is essentially about a sensor model and estimation algorithms; hence a model validation technique such as cross validation is applicable to the calibration for refractive index value and to the validation and characterization of the ICM&M method. The holdout method is the simplest kind of cross validation [113]. The data set corresponding to the experiment set is separated into two sets, called the training set as calibration experiment and the testing set as validation experiment.

This study actually adopts the holdout method to calibrate and validate the ICM&M off line as presented in Chapter 8. Specifically, with multiple experiments, one should decide which experiment is used to calibrate for refractive index, so that the others are used to validate the ICM&M method. The calibration experiment plays the role as a training set, while the validation experiment plays the role as a testing set. Firstly, in the

calibration process, the ICM&M model uses the training set data to obtain refractive index that is going to be used in the validation. Then in the validation experiment, with the calibrated refractive index, the ICM&M model is used to predict the output values of cured height for the experiment data in the testing set, and the errors between the prediction and observation are used to evaluate the ICM&M model and algorithm. The advantage of this method is that it is straightforward and economical. However, its evaluation can have a high variance. The evaluation may depend heavily on which experiment end up in the training set and which end up in the test set, and thus the evaluation may be significantly different depending on how the division is made. The holdout estimate of error rate will be misleading if one happens to get an “unfortunate” split, especially in the ICM&M case where the calibrated refractive index might have a wide distribution due to the ROI selection and stochastic noises and process uncertainty.

For more accurate calibration of the refractive index in the ECPL process, instead of single calibration experiment currently used in the study, more repeated experiments should be conducted and variations could be observed among the obtained refractive indices from the same-conditioned experiments

The machine learning experiment design technique called “K-fold cross validation”, might improve over the holdout method statistically and does not depend much on how the experiments are split for training and testing, though it is more computationally expensive. Inspired by the “K-fold cross validation”, a better design for ICM&M calibration and validation could be employed to characterize the ICM&M system and the refractive index model, and it does not need to specify which experiment is used as calibration. The advantage of the new experiment design based on K-Fold cross validation is that all the experiments in the dataset are eventually used for both calibration and validation. For large datasets, even 3-Fold cross validation will be quite accurate.

It is recommended that even just for the calibration purpose to develop an accurate refractive index model, a set of three experiments can be used so that a 3-fold cross validation can be conducted to estimate the refractive index more accurately. A precisely identified refractive index model is critical in the succeeding experiments to measure the ECPL process in real time or the cured parts off line. This experiment method should be more accurate than the one used in Chapter 8 that used only a single small subset of the experiments to estimate the refractive index.

Furthermore, the improved experiment design for ICM&M calibration and validation can be beneficial for a better characterization of the metrology in terms of traceability, accuracy and repeatability.

#### 10.5.2.3 To quantify the in-process refractive index changes

In addition to the improved calibration experiment (Section 10.5.2.2) for modeling better the evolution of refractive index in the ECPL process, it would be interesting to directly measure and model the real refractive index of solid cured part, to replace or complement the calibration procedure. In future, provided capable measurement equipment available for direct measurement of refractive index over the cured part, it is recommended to verify and quantify the in-process refractive index changes so as to improve the ICM&M sensor model accuracy.

#### 10.5.2.4 To upgrade the ICM&M hardware system

Noise would be a big concern for the ICM&M performance. A filter technique was applied to preprocess the data and the experiment reported in the dissertation showed that 30 fps was working well. So far, the ICM&M has been proven to be a very cost effective approach by using a common camera. A high-performance camera with higher image quality and measurement resolution would be recommended in future improvement to cope with rising quality requirements.

#### 10.5.2.5 To develop a three-dimensional (3D) ICM&M system

For the current research stage, we focus on measuring and controlling the cured height in vertical dimension only. In this study, the lateral boundary in the interferograms was approximated manually by human eyes, and the chosen ROI was aimed to measure the main part height for a direct comparison with the microscope measurement.

Theoretically, by measuring voxels height profile, the lateral shape could be defined naturally. However, this approach of realizing a 3D ICM&M method demands a high-resolution and high-performance system of camera and computer.

In the future, image processing and analysis technologies such as image segmentation, edge detection, and pattern recognition could be explored to estimate the cured shape and sizes in the lateral dimensions, and then can be combined with the vertical height measurement method as reported in this study to realize a 3D ICM&M method.

Thereby, algorithms for ICM&M could be extended to 2D and 3D measurement and enable more comprehensive measurement and control.

#### 10.5.2.6 To employ a real-time operating system for fast precise and reliable process control

As is pointed out in Section 9.8.2, a real-time operating system is envisioned to enable a more advanced and accurate process control method such as EC2C. For many engineers and scientists, running a measurement or control program on a standard PC with a general-purpose OS installed (such as Windows) is unacceptable. At any time, the operating system might delay execution of a user program for many reasons: to run a virus scan, update graphics, perform system background tasks, and more. For programs that need to run at a certain rate without interruption (for example the ECPL process measurement and control system), this delay can cause process errors.

Note that this behavior is by design: general-purpose operating systems are optimized to run many processes and applications at once and provide other features like rich user interface graphics. In contrast, real-time operating systems are designed to run a single program with very precise timing. Specifically, real-time operating systems can allow one to [114]:

- Perform tasks within a guaranteed worst-case timeframe
- Carefully prioritize different sections of the program
- Run loops with nearly the same timing each iteration (typically within microseconds)
- Detect if a loop missed its timing goal

Real-time computing systems can be categorized as "hard real-time" and "soft real-time". To clarify, hard real-time systems are designed to absolutely guarantee that a task will execute within a certain worst-case timeframe. Therefore, for projects involving safety or systems that could result in a large investment in the event of failure, hard real-time is often a requirement. On the other hand, soft real-time systems are designed to satisfy the timing requirements most of the time but without absolute certainty. This can be acceptable for operations like video processing, where a lost data frame is not good but may not necessarily be a critical problem. For example, the developed ECPL-M&C software in MATLAB is a "soft real-time" system. However, MATLAB is not traditionally used to do real-time analysis. Instead, LabVIEW is widely adopted for demanding real-time analysis which can be fulfilled with appropriate hardware.

There have been literature reporting a successful real-time microstructure control of a metal additive manufacturing process by using National Instruments (NI) real-time operating system and LabVIEW for online camera image acquisition and processing and an NI motion module for applying controller signals to the system (e.g. CNC traveling speed, laser power and laser spot size) [5]. The ECPL system could also benefit from



using a more professional and more advanced software platform and real-time operating system for process measurement and control.

For future work, it is recommended to adopt real-time operating system to improve the real-time measurement and control of ECPL in terms of computation speed, precision and reliability. Even in the case where precise timing and long term reliability are not absolute requirements, building a real-time system can provide added peace of mind that the program will continue to run without interrupting the measurement or control process [114]. Also, please note that the use of software synchronization was not problematic at the low image acquisition rate (1 Hz); however, the use of hardware synchronization, which provides resolution in the order of nanoseconds, will be used when higher collection rates are desired.

#### 10.5.2.7 To develop a comprehensive ECPL control for both geometry and properties

Firstly, it is worthwhile to deepen the existing research on the basic process control as presented in Chapter 9. The corresponding future work to leverage the bootstrapping research is elaborated in Section 9.8.

So far there has been no characterization work to identify the ECPL process parameters (i.e., chemical composition of photo initiator concentration and oxygen concentration, exposure time and exposure intensity) effects on the final cured part mechanical properties such as residual stress, hardness and strength, or on the optical properties of refractive index. One factor influencing the mechanical properties is the relaxation of the polymer matrix that occurs after exposure and continues after dark curing. As in most polymerization cases, in the ECPL process the chemical reactions usually occur faster than mechanical relaxation and other effects of physical processes, which suggests that mechanical properties could vary with time after cure and the post-cure changes of mechanical properties such as modulus depend on materials used in the

polymerization process [115]. Additional in-situ measurement technologies are required to characterize the polymer part properties, and the evolution of properties after cure should also be modeled with the online measured properties to achieve a potential real-time comprehensive multi-input multi-output (MIMO) process control for the ECPL process.

As a start of this part of research, thorough investigations are needed to understand which of the process variables should be used as a comprehensive control action besides the single exposure time as described in the study. It has been found that exposure intensity could affect the curing rate significantly, and chance is that it also affects other properties other than geometry dimensions. Therefore, intensity control might dominate in the comprehensive control strategy for final part properties.

Results indicate that the exposure intensity has a more critical effect on the curing rate [92]. Hence, the future work is recommended to start with a simplified problem that only uses exposure intensity as a controlling action to manipulate the curing rate to fabricate a micro part of desired properties. Such advanced control methods, with closed-loop feedback control, have various embodiment designs based on different schemes and algorithms. A preliminary investigation has been conducted to identify some potential control methods for the exposure intensity in the ECPL system, which showed that classical PID control and adaptive neural network control might be good candidates [111]. With the advanced controller being designed, a methodology could be finalized to control the microstructure and properties in real-time during the ECPL process. Real-time curing rate, cured height and refractive index values can be extracted from the ICM&M method developed in this thesis. The target is to obtain a functional gradient part by controlling the output microstructural variations in geometry, residual stress and refractive index based on curing rate changes during the process. The developed closed-loop control system measures the curing rate and cured height in real-time and feeds it to a real-time controller. The controller, utilizing a to-be identified correlation between the

curing rate and part properties, feeds in the required curing speed to reach the desired properties such as optical refractive index.

Towards the end of this future research path, a controlled microstructure with desired mechanical and optical properties will be expected with controlled curing rates through the ECPL process. The comprehensive ECPL process control could help achieve its promising application as a novel additive manufacturing method for fabricating gradient-index lenses [116].

## APPENDIX A

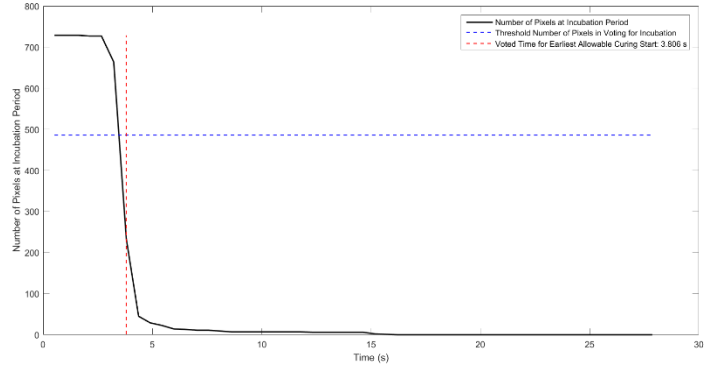
### OFFLINE ICM&M ANALYSIS RESULT FOR THE SAMPLES CURED IN THE REAL-TIME CONTROL EXPERIMENTS

#### A.1 Voting scheme for identifying curing window in global measurement

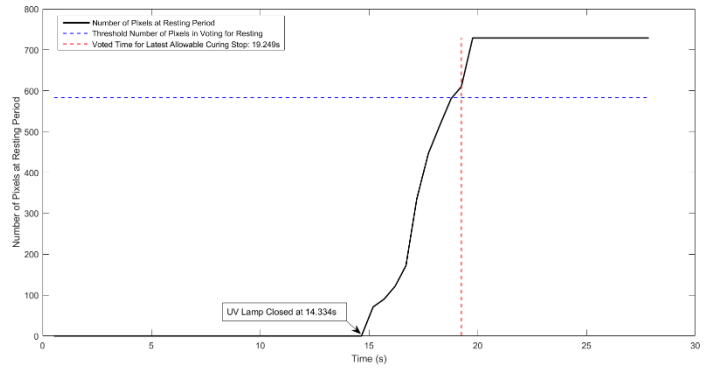
Introduced in Section 9.5.2.1, the majority voting method is employed to boost the robustness of the offline ICM&M algorithms for a full-field profile measurement of the parts cured in the real-time controls experiment in Chapter 9. Figure A1, Figure A2 and Figure A3 display the details of how the globally allowable curing start and curing stop are determined for each sample in Group #1, Group #2 Subset #1 and Group #2 Subset #2, respectively. The artificial enforcement of earliest allowable curing start and latest allowable curing stop in defining the longest curing window, effectively suppresses the interferogram noises in the non-curing stages of the ECPL process, thereby improves the overall profile measurement robustness and accuracy.

Group #1: Sample #1

1(a)  
 Voting for the  
 earliest  
 beginning of  
 curing in the ROI

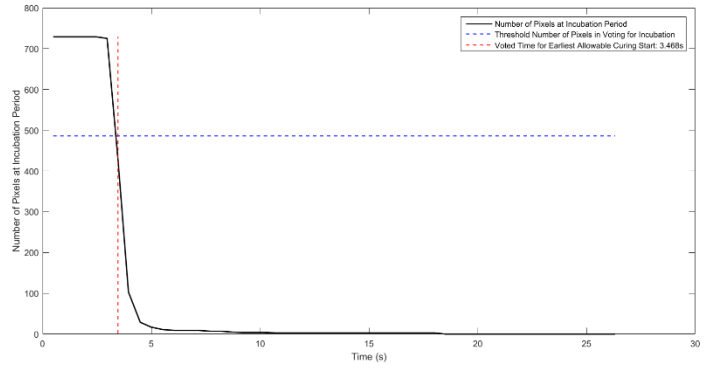


1(b)  
 Voting for the  
 latest end of  
 curing in the ROI

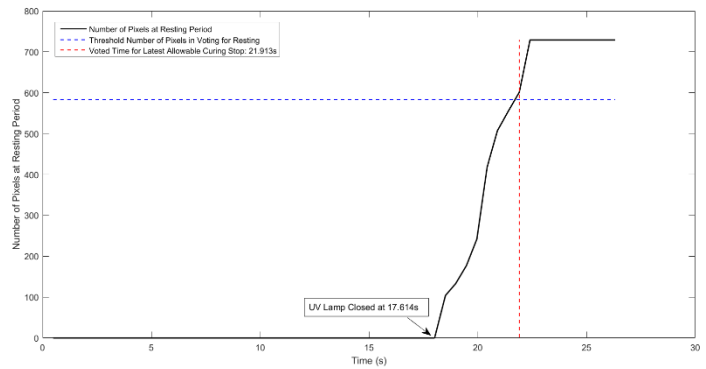


Group #1: Sample #2

2(a)  
 Voting for the  
 earliest  
 beginning of  
 curing in the ROI

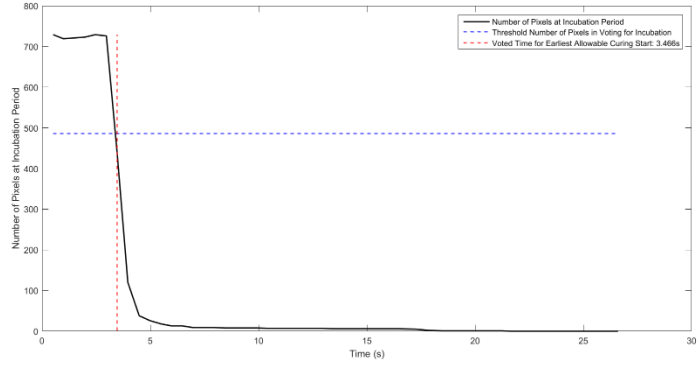


2(b)  
 Voting for the  
 latest end of  
 curing in the ROI

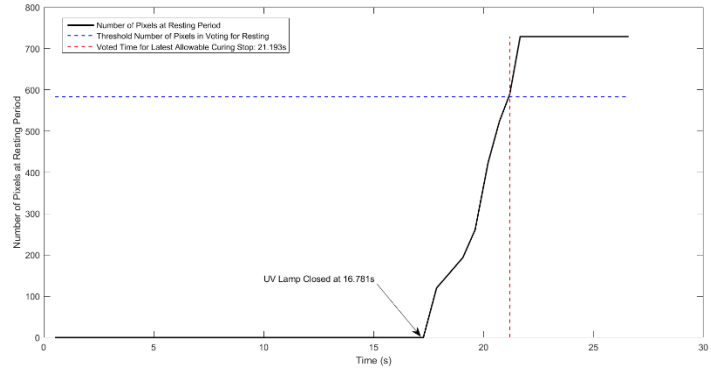


Group #1: Sample #3

3(a)  
Voting for the  
earliest  
beginning of  
curing in the ROI

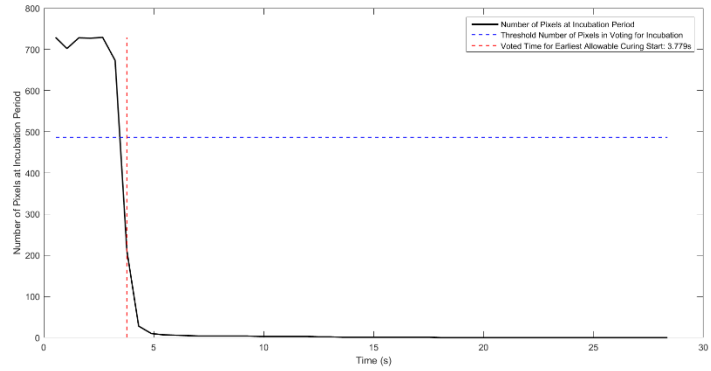


3(b)  
Voting for the  
latest end of  
curing in the ROI

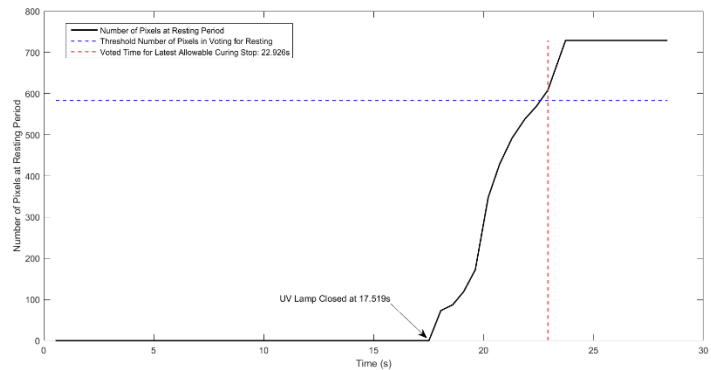


Group #1: Sample #4

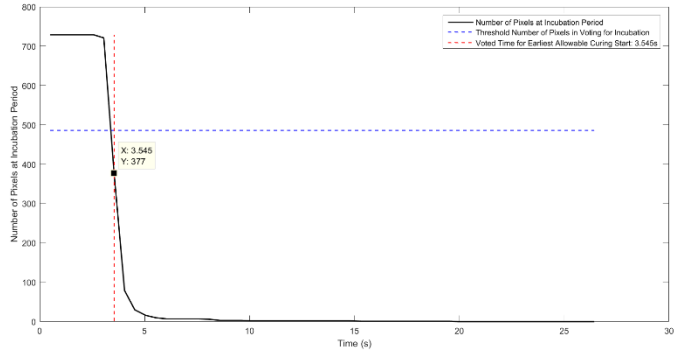
4(a)  
Voting for the  
earliest  
beginning of  
curing in the ROI



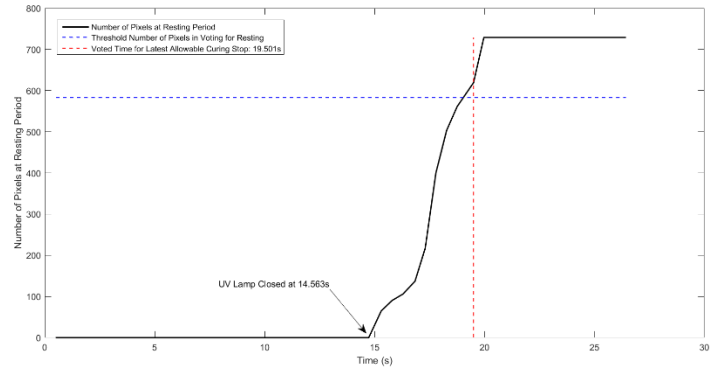
4(b)  
Voting for the  
latest end of  
curing in the ROI



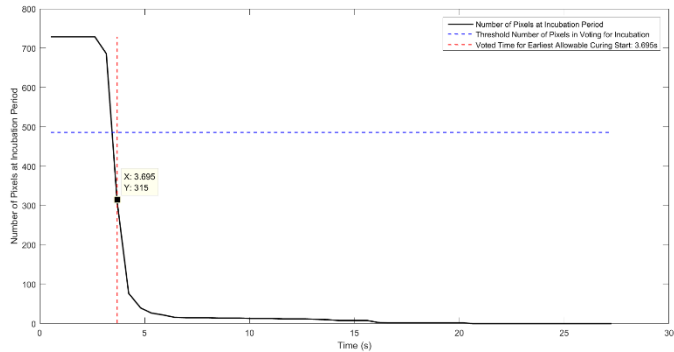
5(a)  
 Voting for the  
 earliest  
 beginning of  
 curing in the ROI



5(b)  
 Voting for the  
 latest end of  
 curing in the ROI



6(a)  
 Voting for the  
 earliest  
 beginning of  
 curing in the ROI



6(b)  
 Voting for the  
 latest end of  
 curing in the ROI

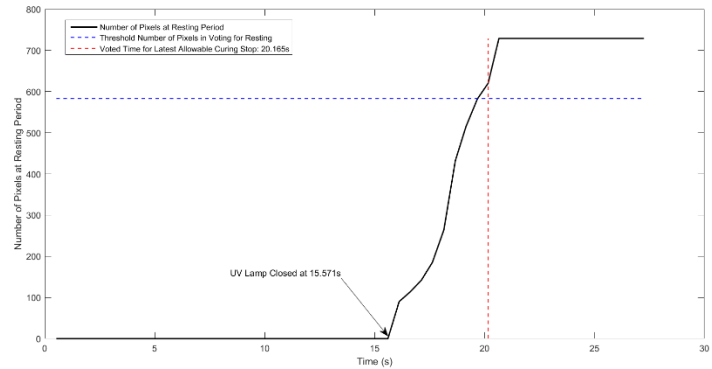
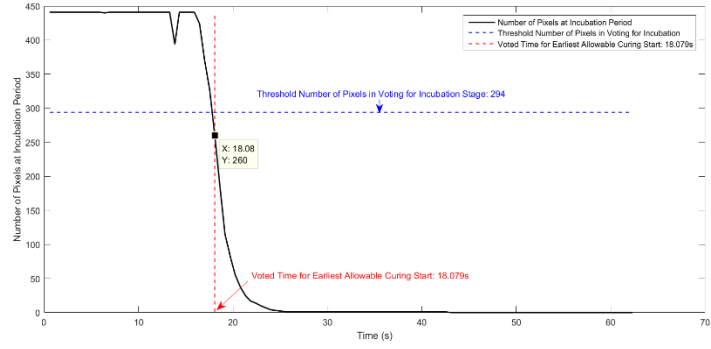


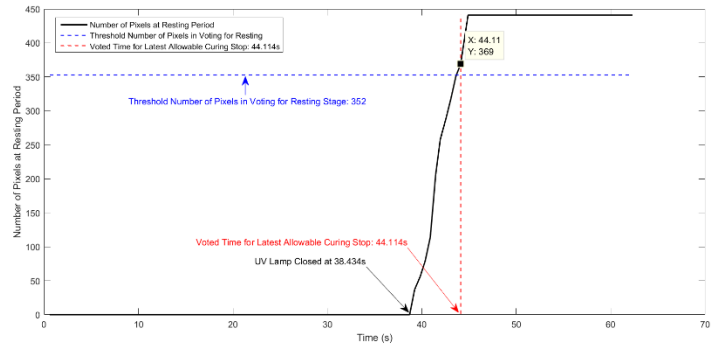
Figure A1. Majority voting in the offline ICM&M analysis (Real-time Group #1)

Group #2 Subset #1: Sample #1

1(a)  
 Voting for the  
 earliest  
 beginning of  
 curing in the ROI

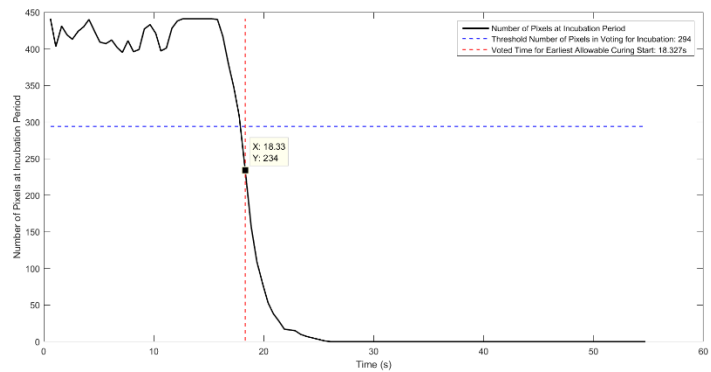


1(b)  
 Voting for the  
 latest end of  
 curing in the ROI

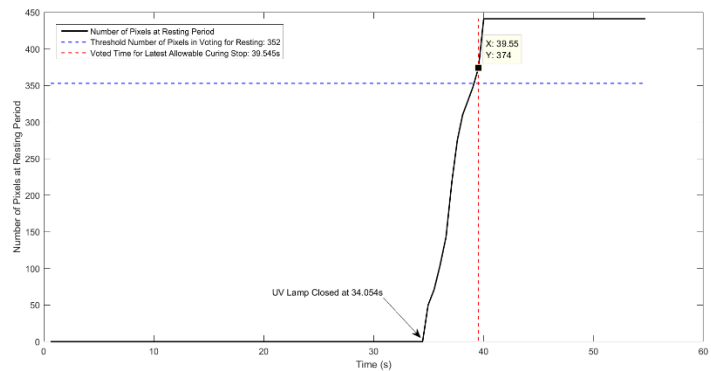


Group #2 Subset #1: Sample #2

2(a)  
 Voting for the  
 earliest  
 beginning of  
 curing in the ROI



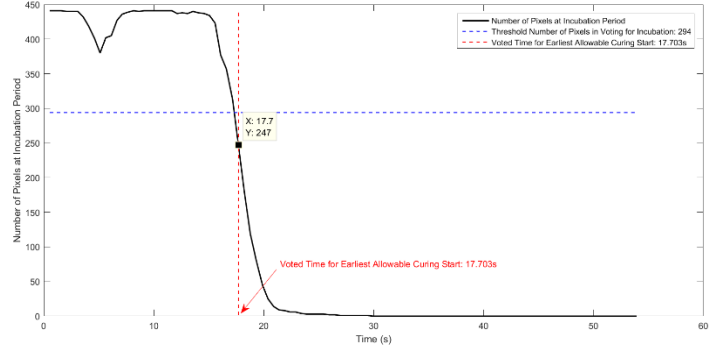
2(b)  
 Voting for the  
 latest end of  
 curing in the ROI



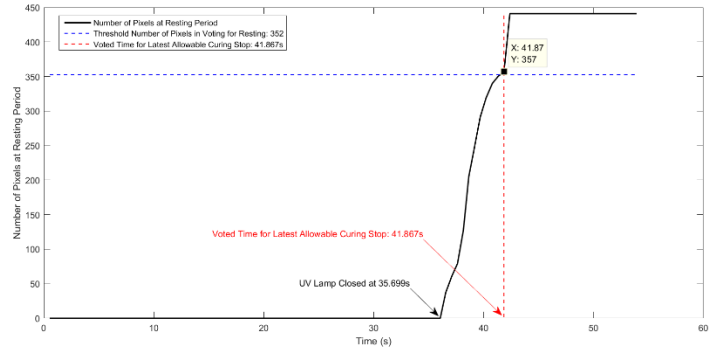


Group #2 Subset #1: Sample #3

3(a)  
 Voting for the  
 earliest  
 beginning of  
 curing in the ROI

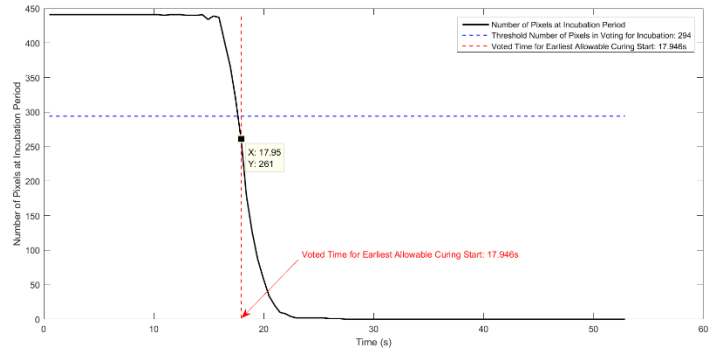


3(b)  
 Voting for the  
 latest end of  
 curing in the ROI

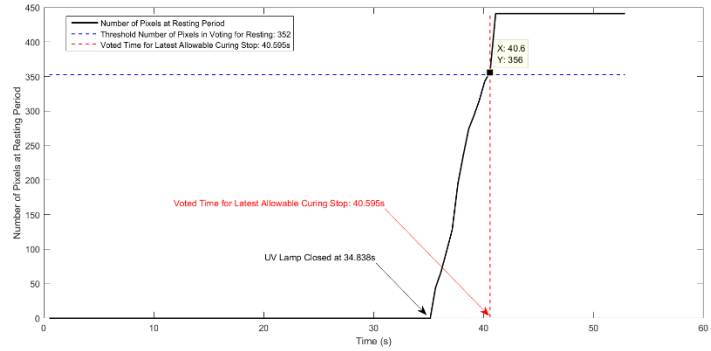


Group #2 Subset #1: Sample #4

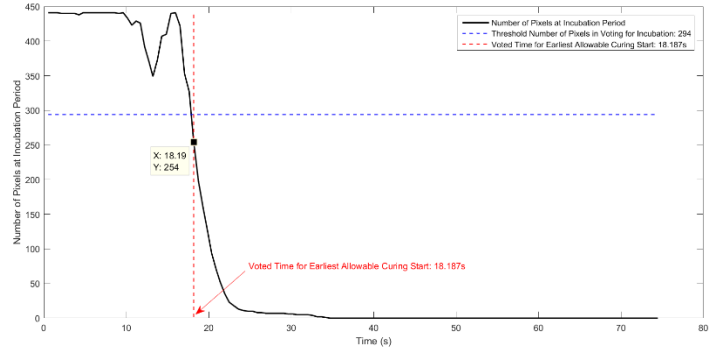
4(a)  
 Voting for the  
 earliest  
 beginning of  
 curing in the ROI



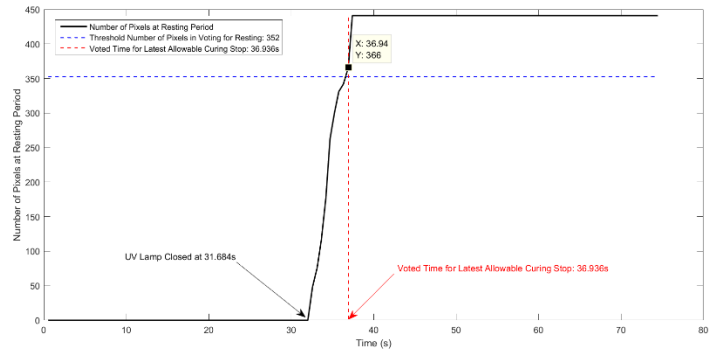
4(b)  
 Voting for the  
 latest end of  
 curing in the ROI



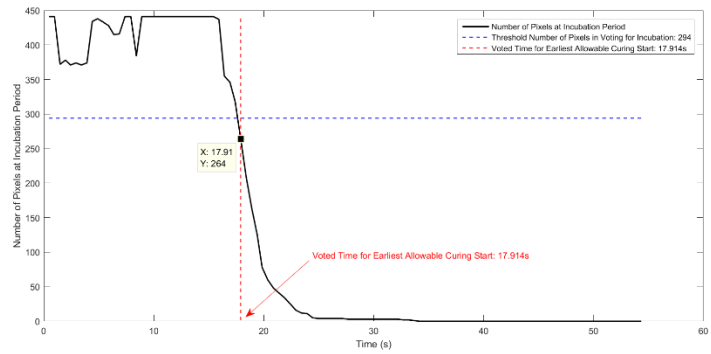
5(a)  
 Voting for the  
 earliest  
 beginning of  
 curing in the ROI



5(b)  
 Voting for the  
 latest end of  
 curing in the ROI



6(a)  
 Voting for the  
 earliest  
 beginning of  
 curing in the ROI



6(b)  
 Voting for the  
 latest end of  
 curing in the ROI

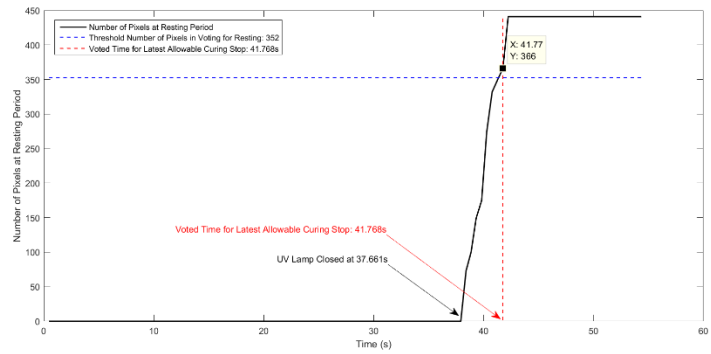
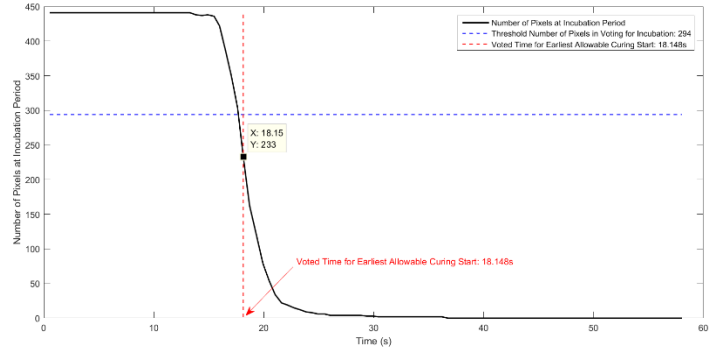


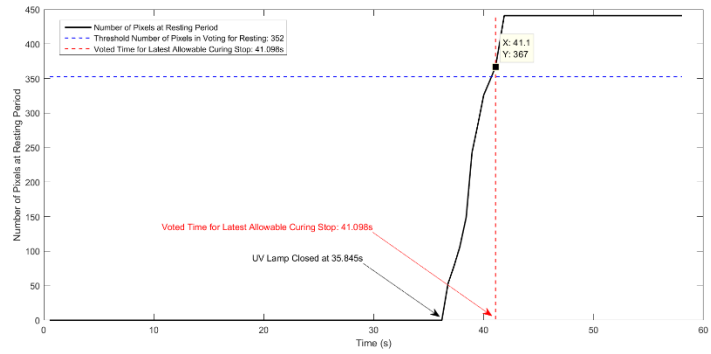
Figure A2. Majority voting in the offline ICM&M analysis (Group #2 Subset #1)

Group #2 Subset #2: Sample #1

1(a)  
Voting for the  
earliest  
beginning of  
curing in the ROI

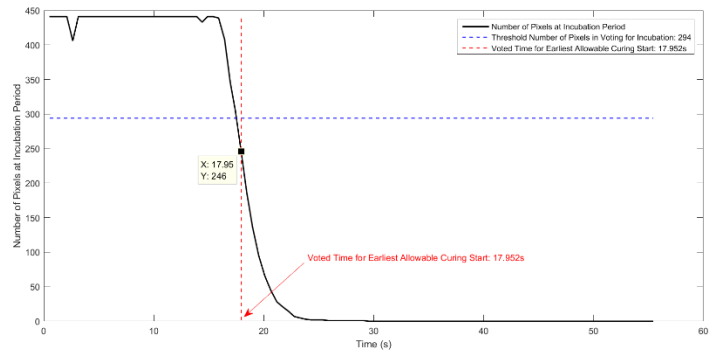


1(b)  
Voting for the  
latest end of  
curing in the ROI

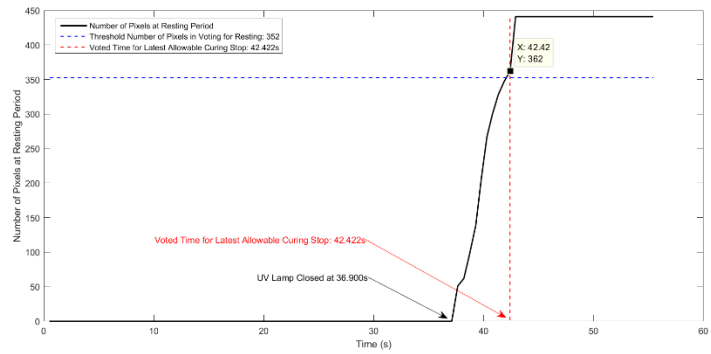


Group #2 Subset #2: Sample #2

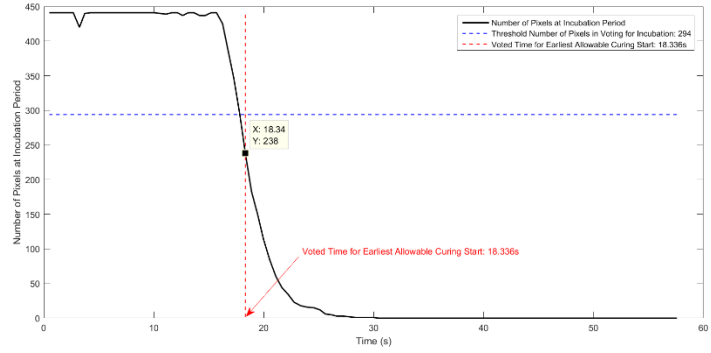
2(a)  
Voting for the  
earliest  
beginning of  
curing in the ROI



2(b)  
Voting for the  
latest end of  
curing in the ROI

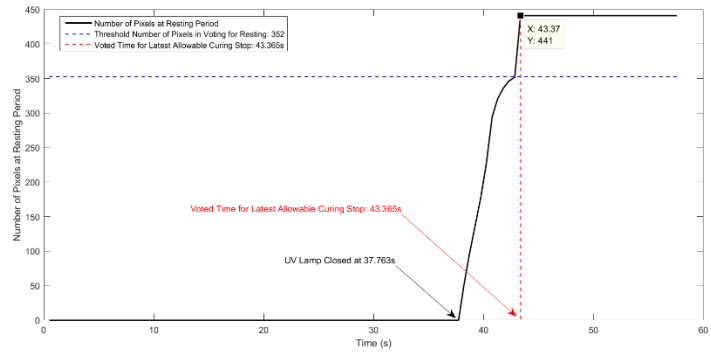


3(a)  
 Voting for the  
 earliest  
 beginning of  
 curing in the ROI

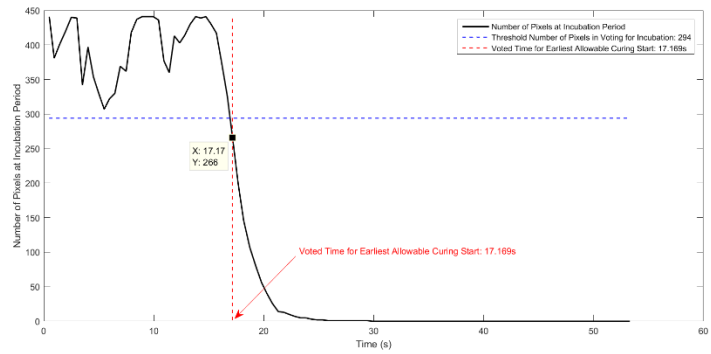


Group #2 Subset #2: Sample #3

3(b)  
 Voting for the  
 latest end of  
 curing in the ROI



4(a)  
 Voting for the  
 earliest  
 beginning of  
 curing in the ROI



Group #2 Subset #2: Sample #4

4(b)  
 Voting for the  
 latest end of  
 curing in the ROI

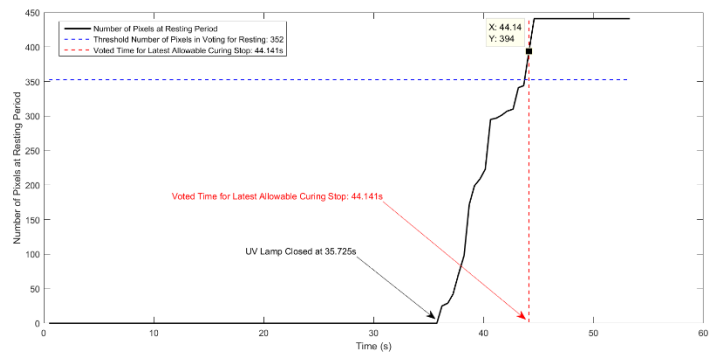
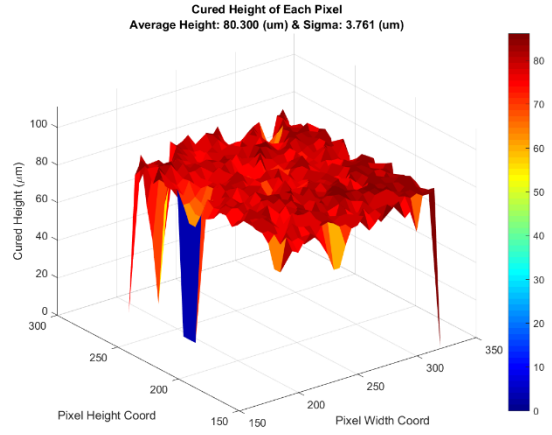
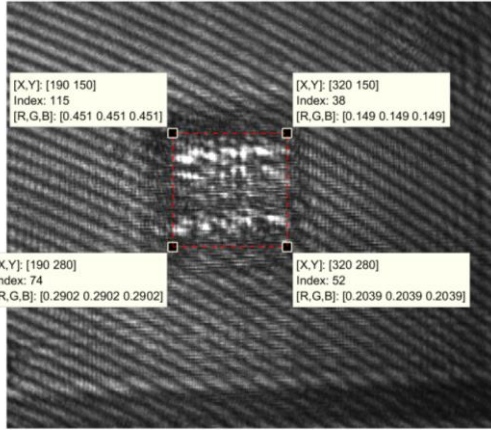


Figure A3. Majority voting in the offline ICM&M analysis (Group #2 Subset #2)

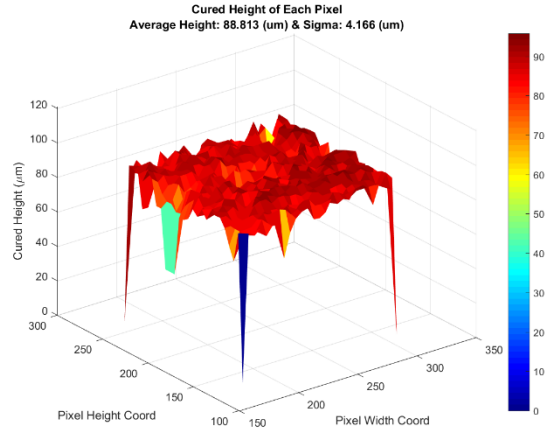
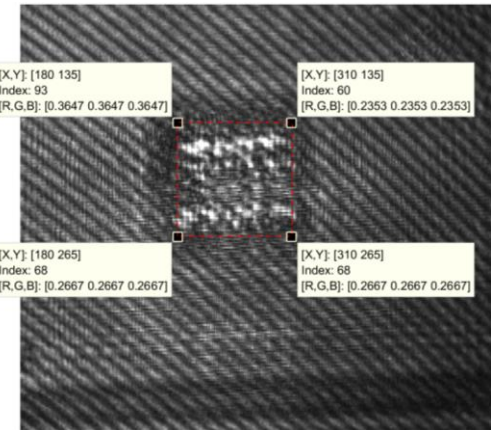
## **A.2 Measured region and results by the offline ICM&M method**

In the offline ICM&M analysis of the real-time acquired interferogram videos in Chapter 9 (Section 9.7.1), the region of interest (ROI) selected in the interferogram video and the corresponding area profile of cured height for each sample in the designed experiments (Table 18. Experimental design for real-time ECPL process measurement and control), are displayed in Figure A4, Figure A5, and Figure A6 for Group #1, Group #2 Subset #1 and Group #2 Subset #2, respectively.

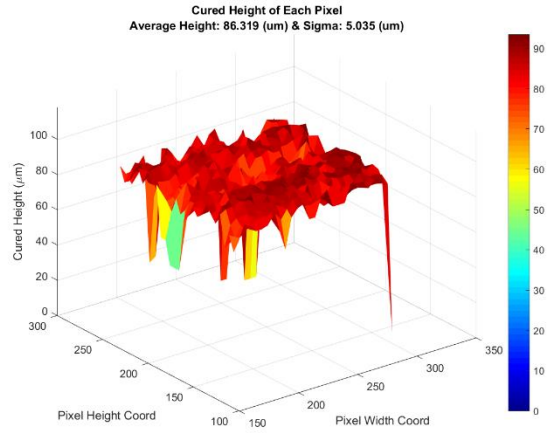
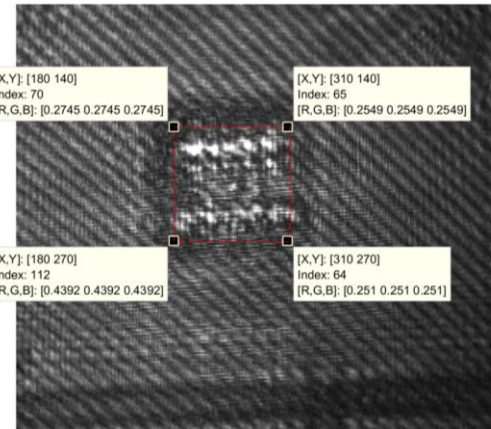
Sample #1



Sample #2



Sample #3



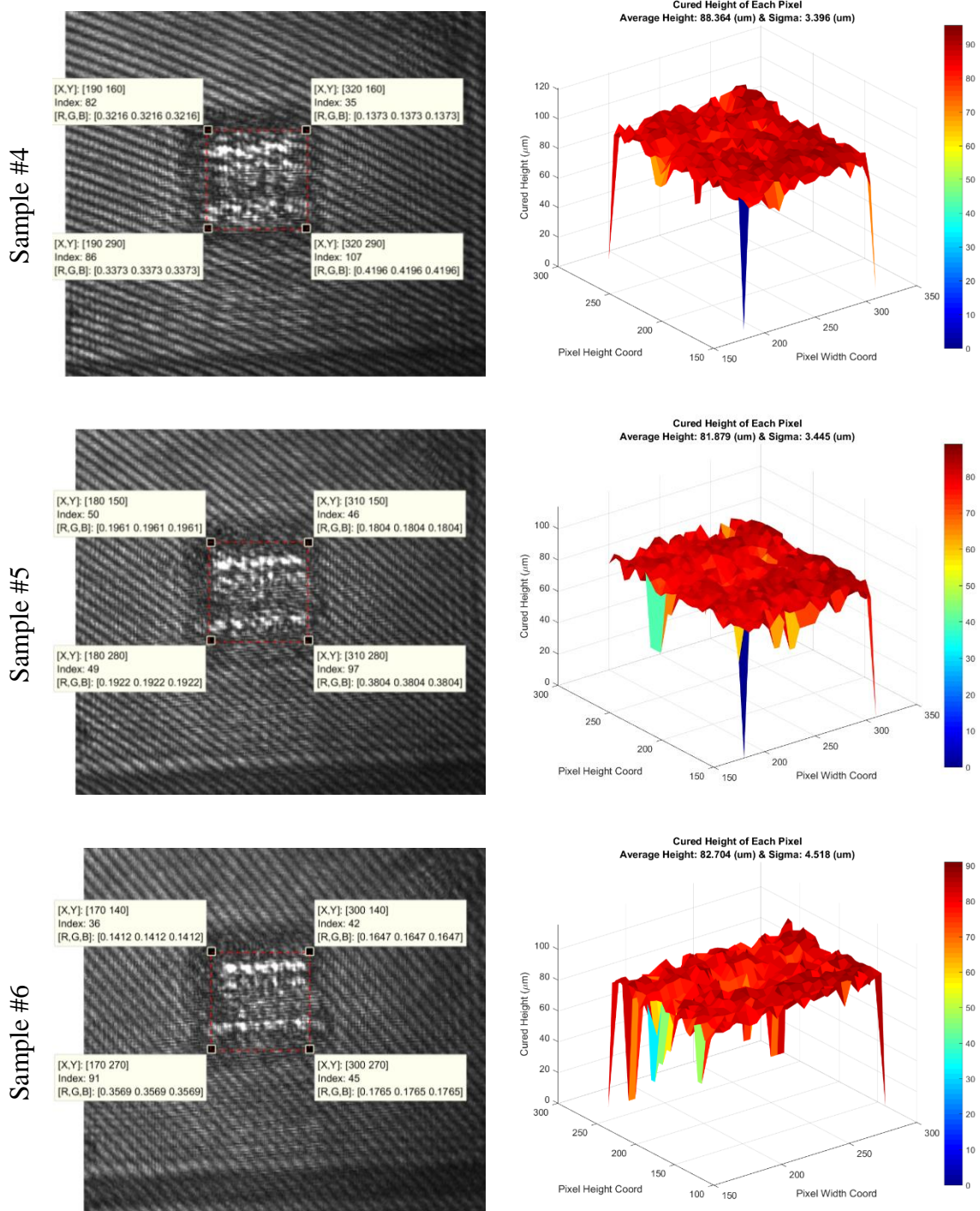
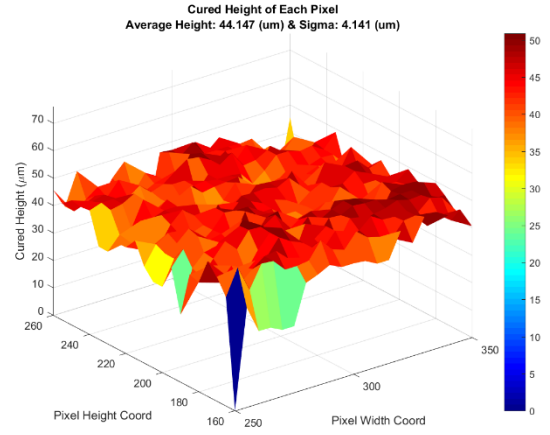
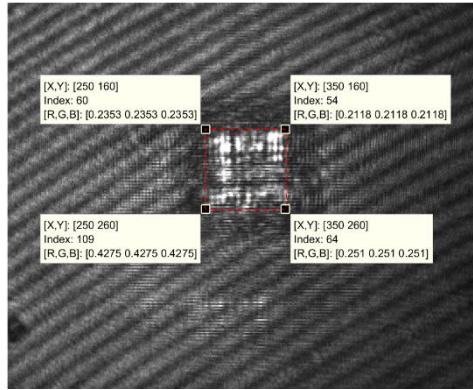
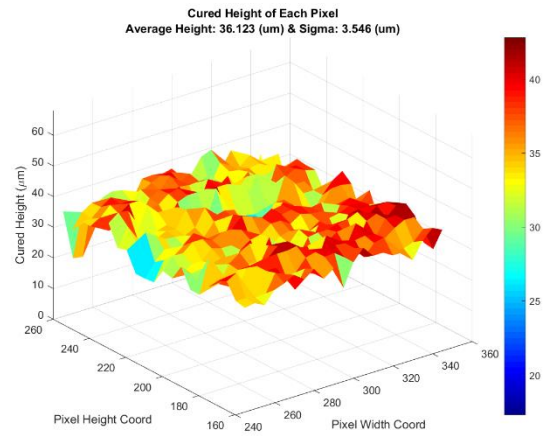
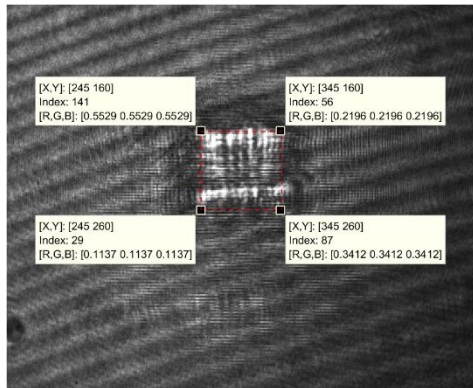


Figure A4. Offline ICM&M analysis of the samples cured in the real-time experiments (Group #1) - Left: region of pixels selected in the interferogram video to be measured; Right: corresponding area profile of cured heights across the selected region

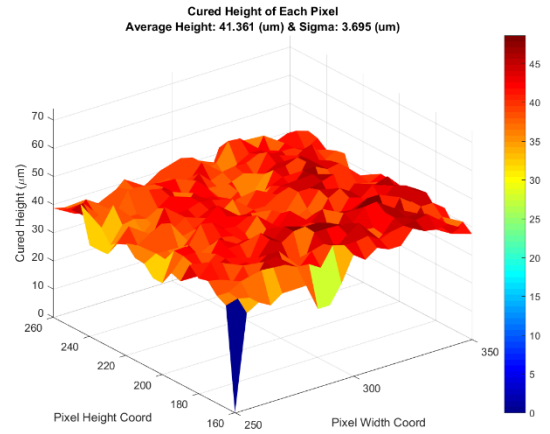
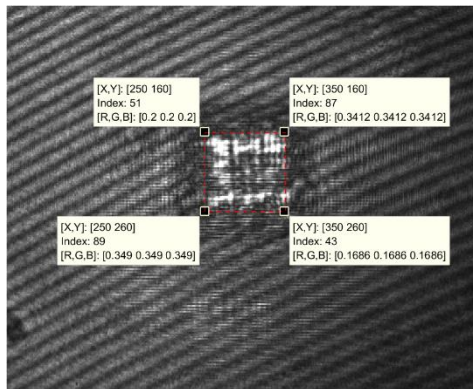
Sample #1



Sample #2

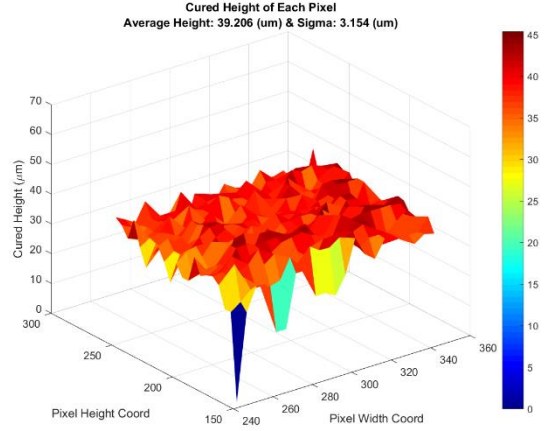
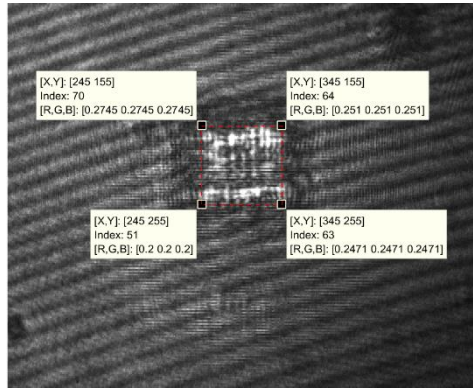


Sample #3

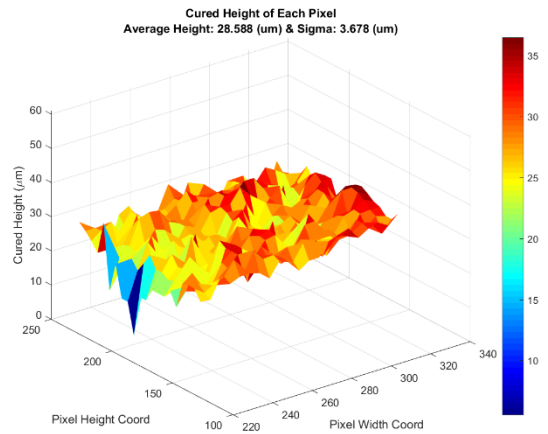




Sample #4



Sample #5



Sample #6

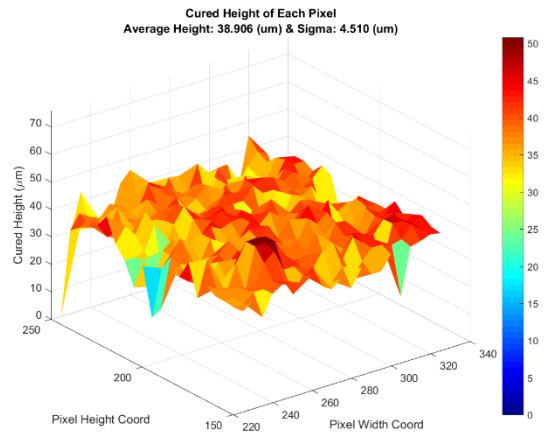
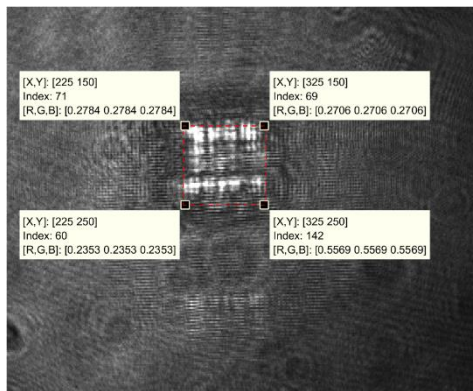
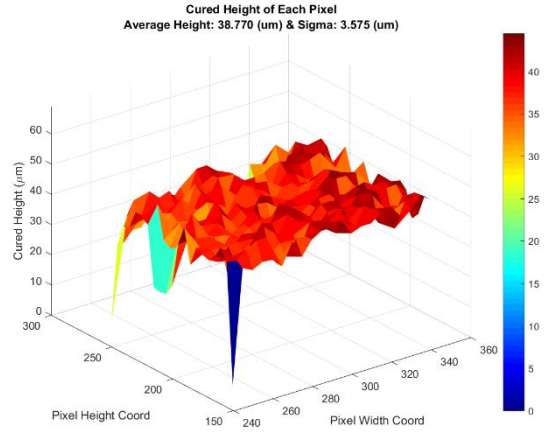
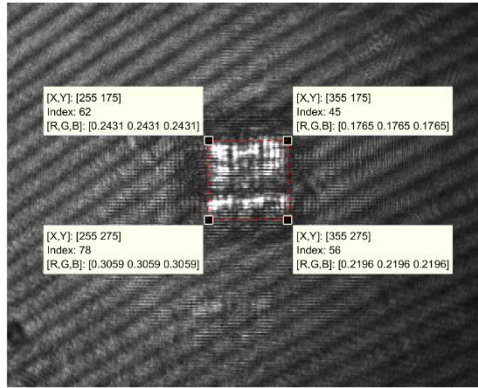
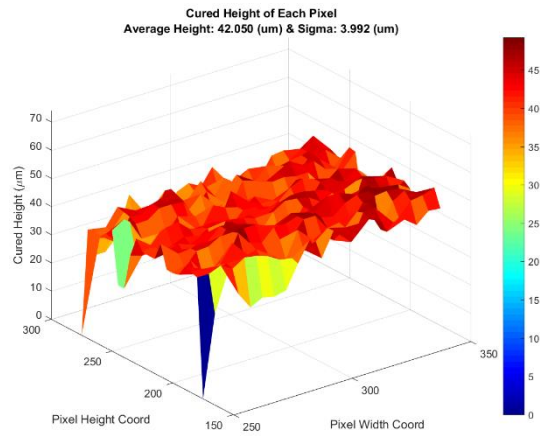
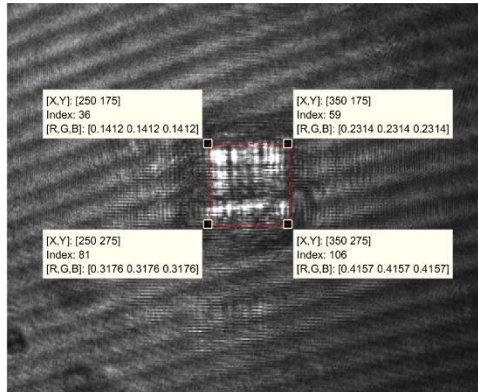


Figure A5. Offline ICM&M analysis of the samples cured in the real-time experiments (Group #2 Subset #1) - Left: region of pixels selected in the interferogram video to be measured; Right: corresponding area profile of cured heights across the selected region

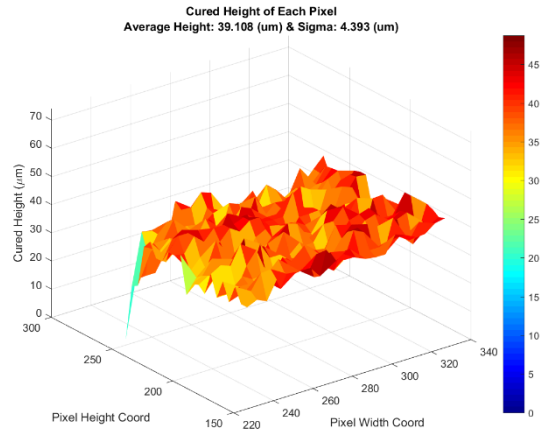
Sample #1



Sample #2



Sample #3



Sample #4

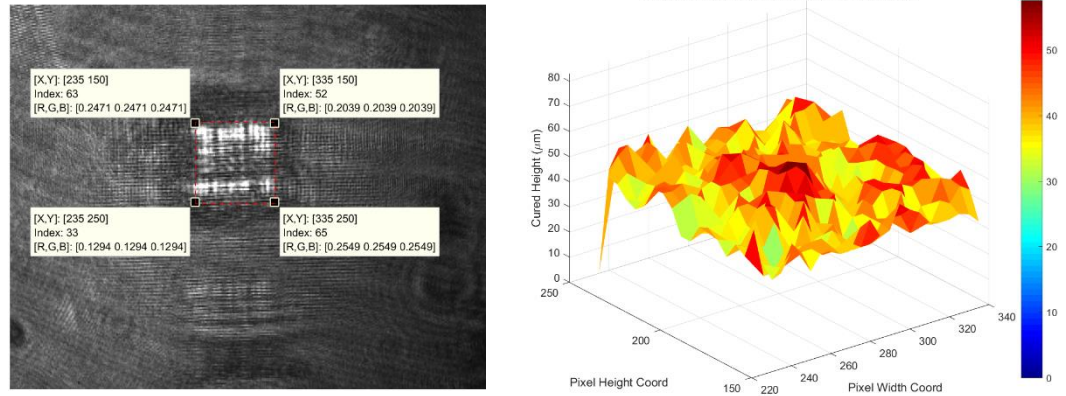


Figure A6. Offline ICM&M analysis of the samples cured in the real-time experiments (Group #2 Subset #2) - Left: region of pixels selected in the interferogram video to be measured; Right: corresponding area profile of cured heights across the selected region

### **A.3 Selected example pixel measured by the offline ICM&M method**

In the implementation of the ICM&M method, firstly each individual pixel is measured, and then the aggregate of individual measurements would be used to evaluate the overall height profile for the measured region. As a demonstration of the detected and measured process dynamics, one representative pixel in the ROI (as shown in Figure A4 – A6) is selected for each sample, and the corresponding data and analysis result is presented in Figure A7, Figure A8, and Figure A9 for Group #1, Group #2 Subset #1 and Group #2 Subset #2, respectively.

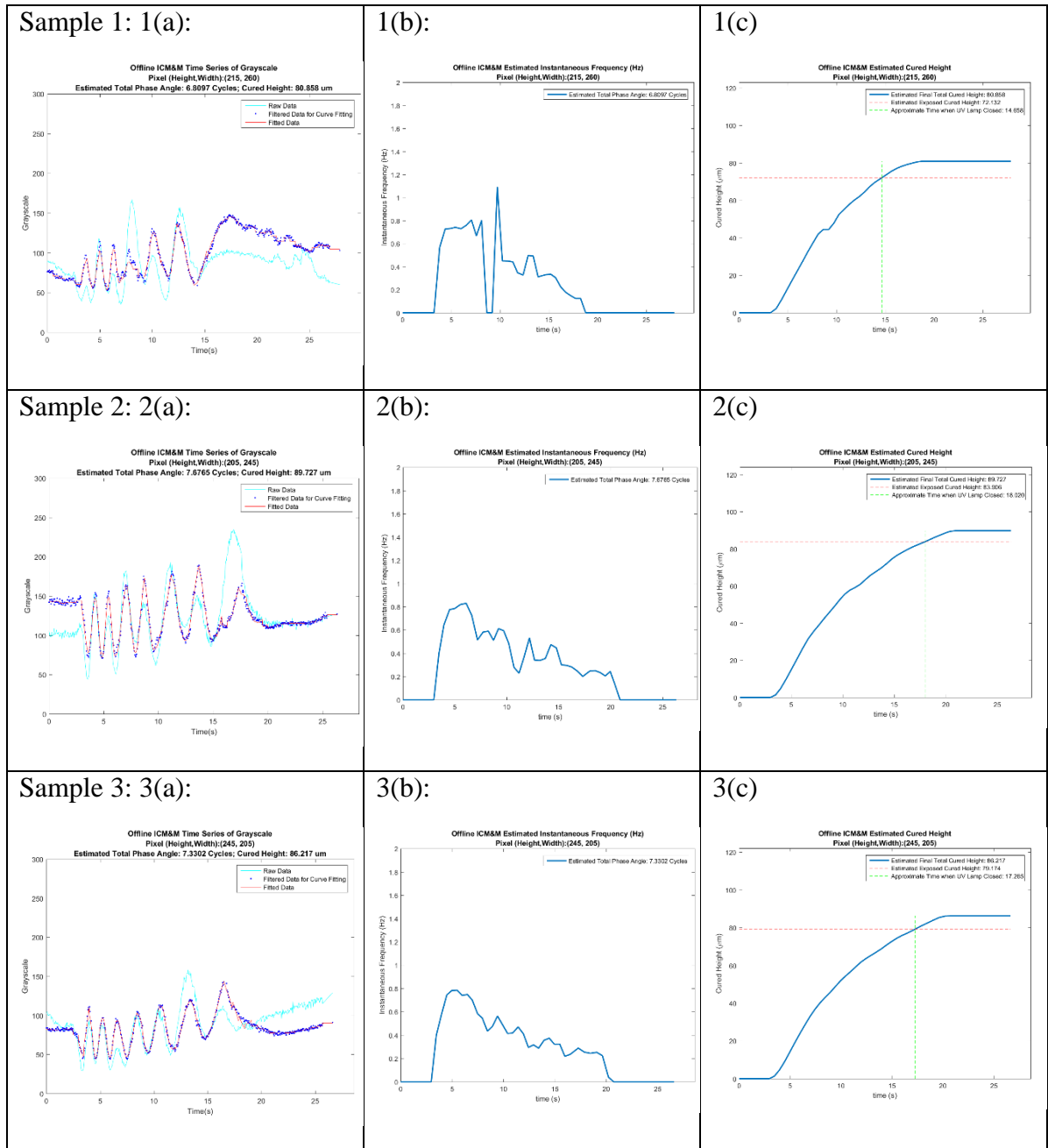


Figure A7 (Part 1). Example of individual pixel's data dynamics and

measurement results in the offline ICM&M analysis (Real-time Group #1): (a) time sequence of pixel's grayscale and data analysis; (b) estimated evolution of the instantaneous frequency; (c) estimated time curve of cured height.



Figure A7 (Part 2). Example of individual pixel's data dynamics and measurement results in the offline ICM&M analysis (Real-time Group #1): (a) time sequence of pixel's grayscale and data analysis; (b) estimated evolution of the instantaneous frequency; (c) estimated time curve of cured height.

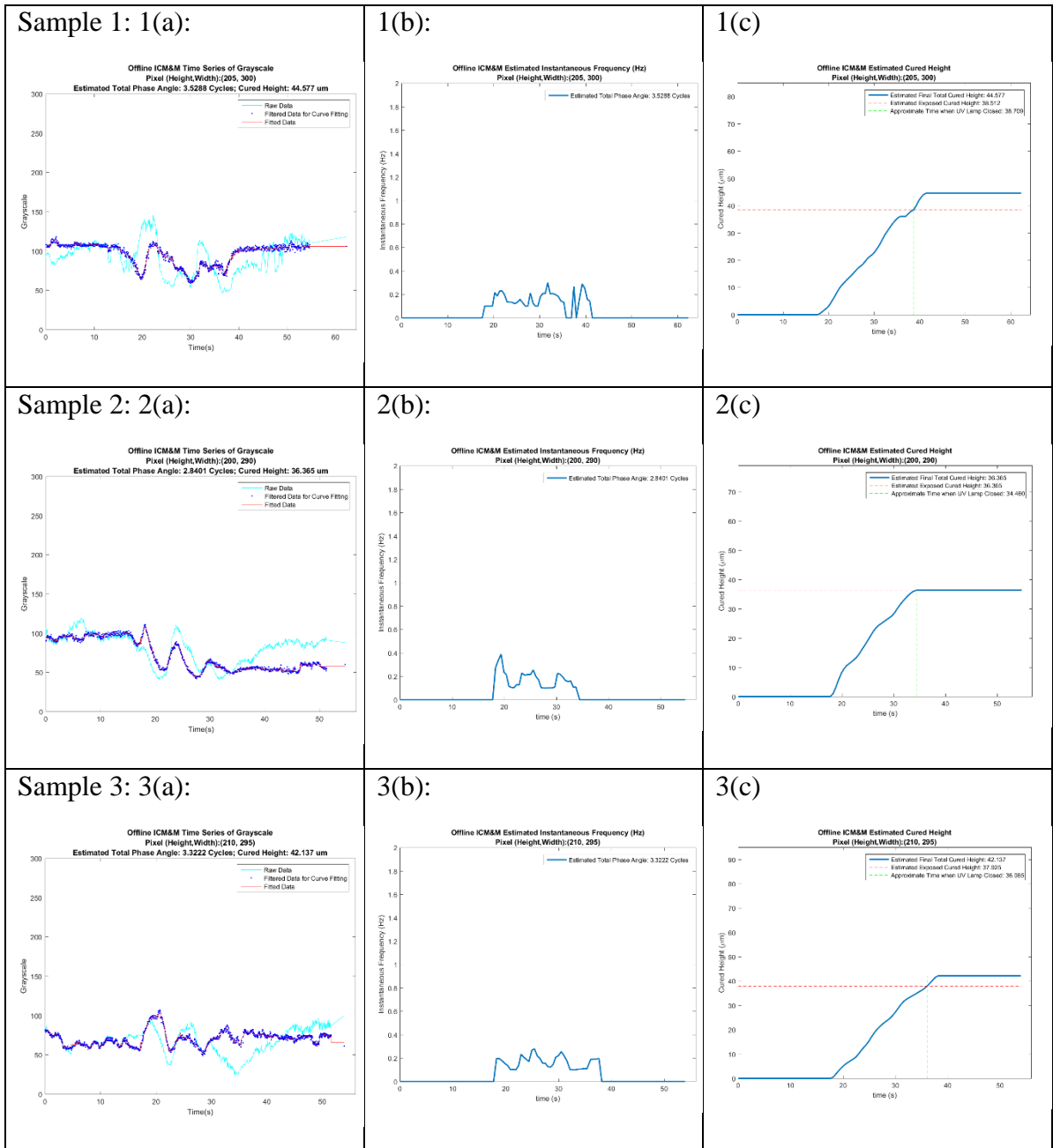


Figure A8 (Part 1). Example of individual pixel's data dynamics and

measurement results in the offline ICM&M analysis (Real-time Group #2 Subset #1): (a) time sequence of pixel's grayscale and data analysis; (b) estimated evolution of the instantaneous frequency; (c) estimated time curve of cured height.

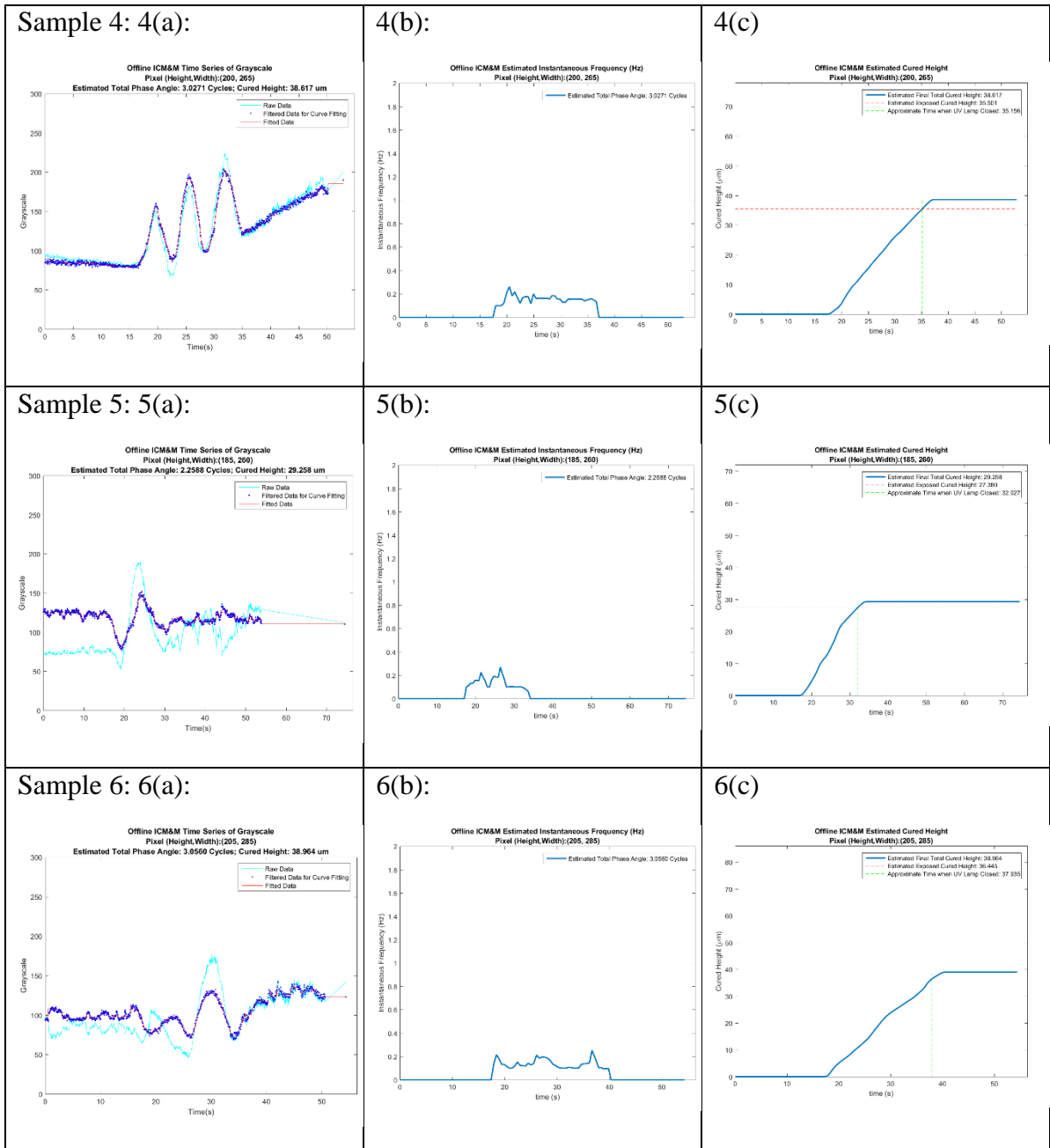


Figure A8 (Part 2). Example of individual pixel's data dynamics and

measurement results in the offline ICM&M analysis (Real-time Group #2 Subset #1): (a) time sequence of pixel's grayscale and data analysis; (b) estimated evolution of the instantaneous frequency; (c) estimated time curve of cured height.



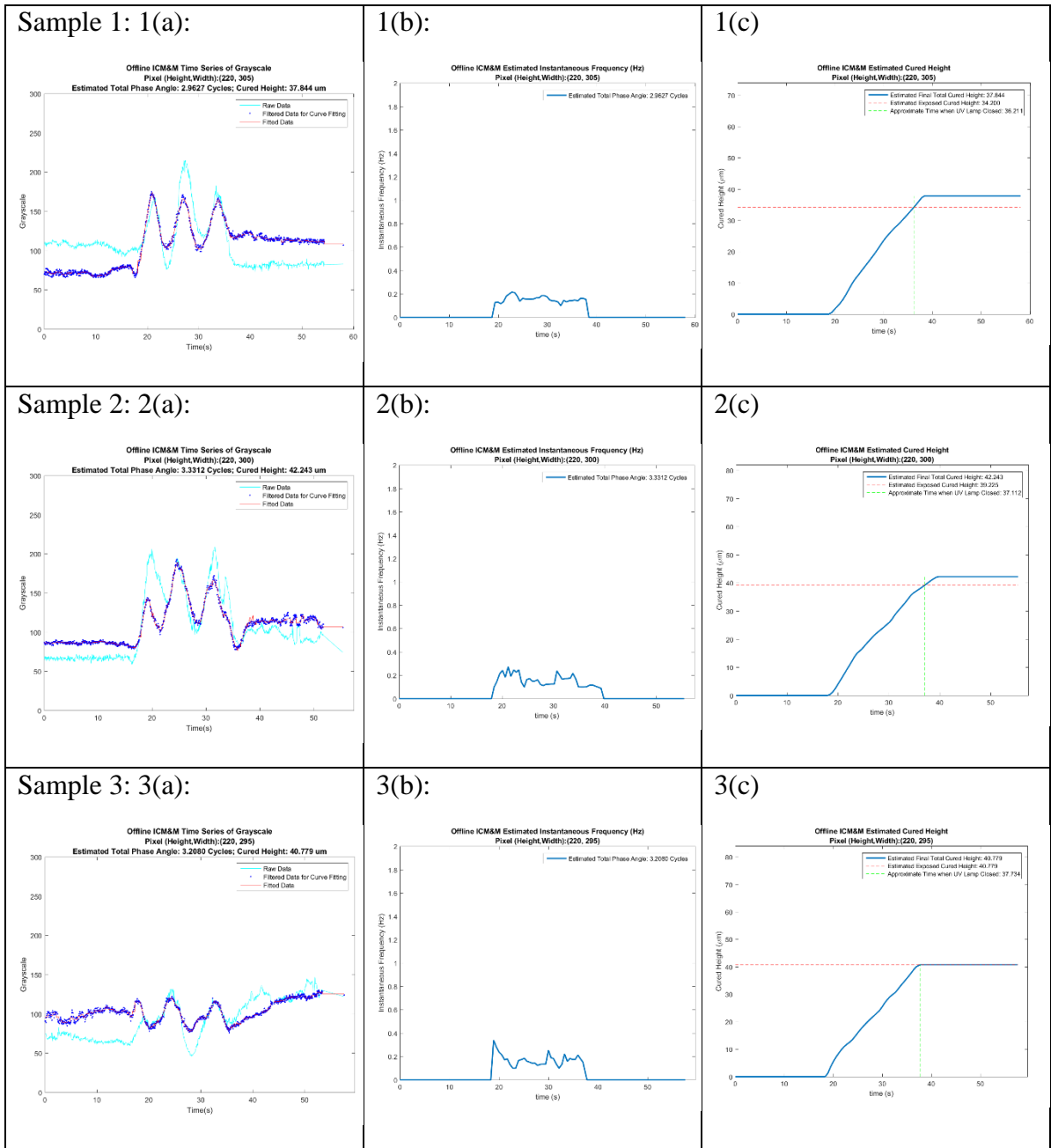


Figure A9 (Part 1). Example of individual pixel's data dynamics and measurement results in the offline ICM&M analysis (Real-time Group #2 Subset #2): (a) time sequence of pixel's grayscale and data analysis; (b) estimated evolution of the instantaneous frequency; (c) estimated time curve of cured height.

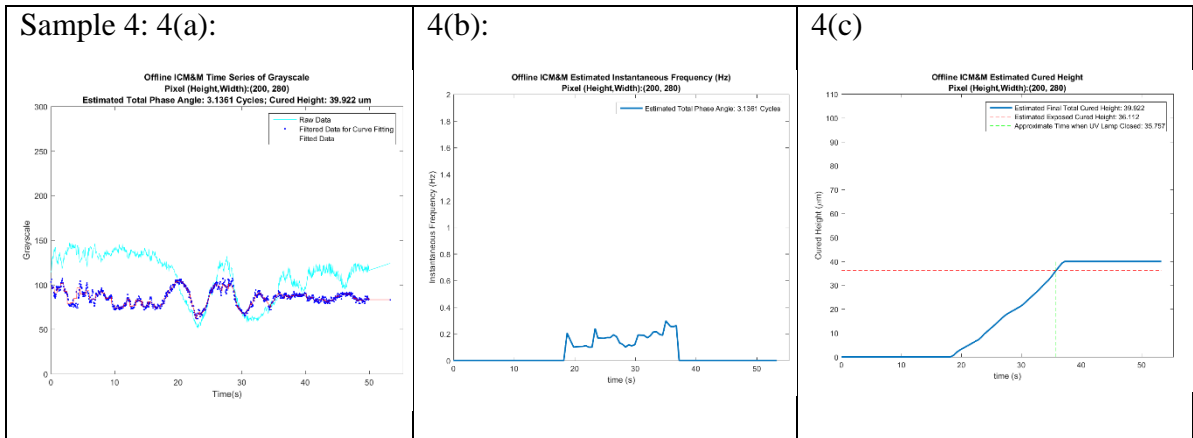


Figure A9 (Part 2). Example of individual pixel's data dynamics and

measurement results in the offline ICM&M analysis (Real-time Group #2 Subset #2): (a) time sequence of pixel's grayscale and data analysis; (b) estimated evolution of the instantaneous frequency; (c) estimated time curve of cured height.

## APPENDIX B

### REAL-TIME ICM&M DATA ACQUISITION AND ANALYSIS RESULT FOR THE SAMPLES CURED IN THE REAL-TIME CONTROL EXPERIMENTS

#### B.1 Real-time data acquisition and logging

The interferogram acquisition is performed in parallel with the measurement analysis in the real-time process measurement and control experiments. The data logging records each interferogram’s image data and time stamps, as well as the process flags of “UV Open Frame Index” and “UV Close Frame Index” which mark the frame when the UV lamp opens and when the UV lamp closes respectively.

Table B1: Real-time acquisition results and logging of UV lamp status

Experiment Index			Real-time Acquisition and Logging of Interferogram						
Experiment Group	Experiment Subgrouping based on Online Measurement Setting	Sample NO.	Number of Frames Acquired	Acquisition Time (s)	Average Frame Interval (s)	Average Acquisition Speed (FPS: Frames/Sec)	UV Open Frame Index	UV Close Frame Index (Nominal)	UV Close Frame Index (Actual)
Group #1 (Normal Process: UV iris level 22%)	10 frames / run of online measurement for 1 pixel	Sample 1	502	27.896	0.056	18	1	260	263
		Sample 2	502	26.351	0.052	19	1	340	341
		Sample 3	502	26.628	0.053	19	1	330	331
		Sample 4	502	28.396	0.057	18	1	310	311
		Sample 5	502	26.461	0.053	19	1	280	286
		Sample 6	502	27.283	0.054	18	1	280	289
Group #2 (Slow Process: UV iris level 5%)	Subset #1 (10 frames / run of online measurement for 1 pixel)	Sample 1	1002	62.317	0.062	16	1	700	704
		Sample 2	1002	54.743	0.055	18	1	660	661
		Sample 3	1002	53.953	0.054	19	1	690	692
		Sample 4	1002	52.897	0.053	19	1	690	693
		Sample 5	1002	53.959	0.054	19	1	580	583
		Sample 6	1002	54.390	0.054	18	1	740	745
	Subset #2 (30 frames / run of online measurement for 3 pixel)	Sample 1	1002	58.095	0.058	17	1	630	652
		Sample 2	1002	55.469	0.055	18	1	690	715
		Sample 3	1002	57.623	0.058	17	1	690	700
		Sample 4	1002	53.340	0.053	19	1	690	709

## **B.2 Online measured pixels' time sequence and measurement results**

Corresponding to Section 9.7.2, Figure B1, Figure B2 and Figure B3 display the details about the online measured pixel(s)'s data dynamics and analysis results for each sample in Group #1 (1 pixel measured online), Group #2 Subset #1(1 pixel measured online), and Group #2 Subset #2 (3 pixels measured online), respectively.

Please note that the time curve of real-time measured cured height represented by the real-time measurement of the pixel(s) for each sample in Figure B1, Figure B2 and Figure B3, is shown in the Figure B5.

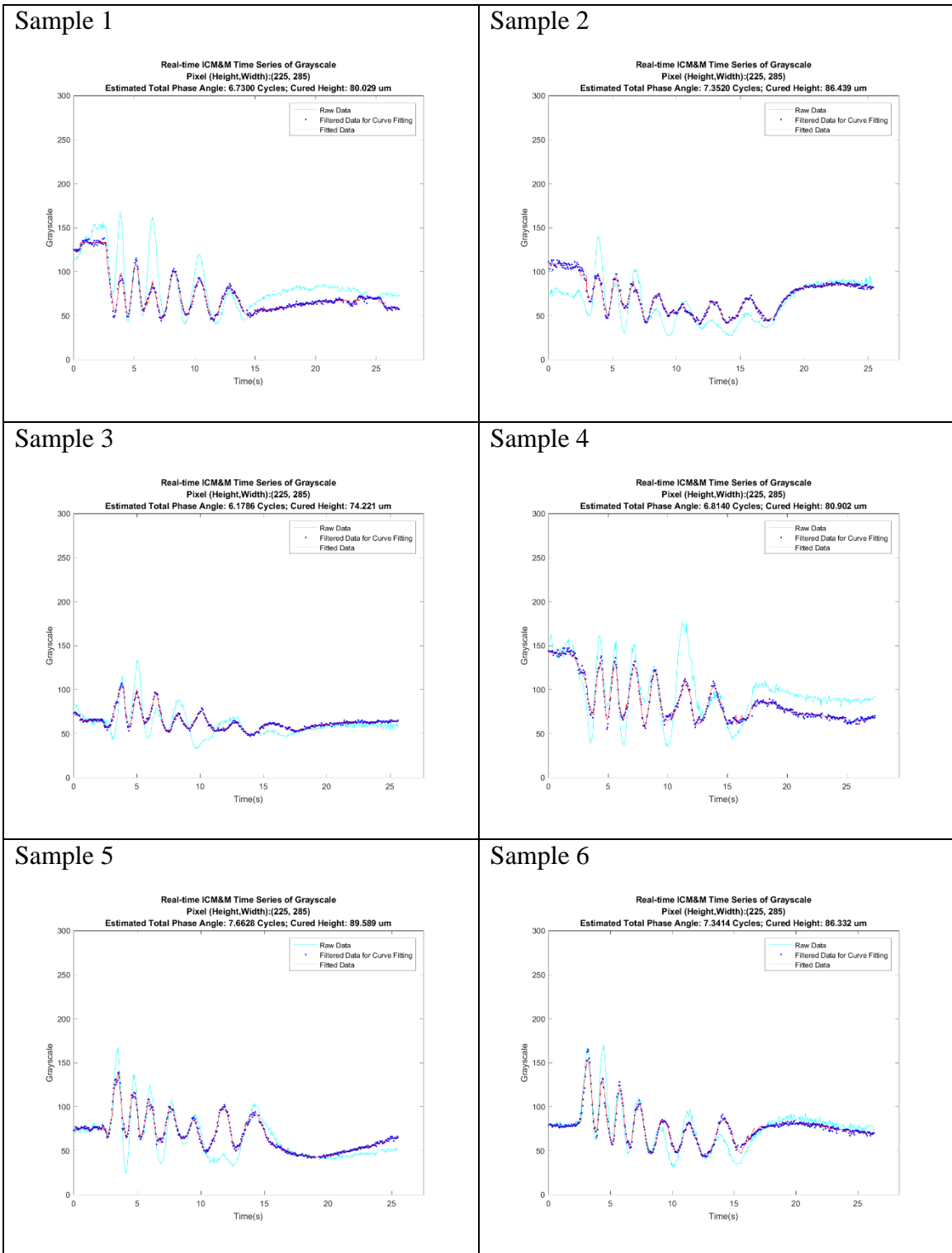


Figure B1. Online measured pixel's data dynamics and measurement results in the real-time ICM&M analysis (Real-time Group #1)

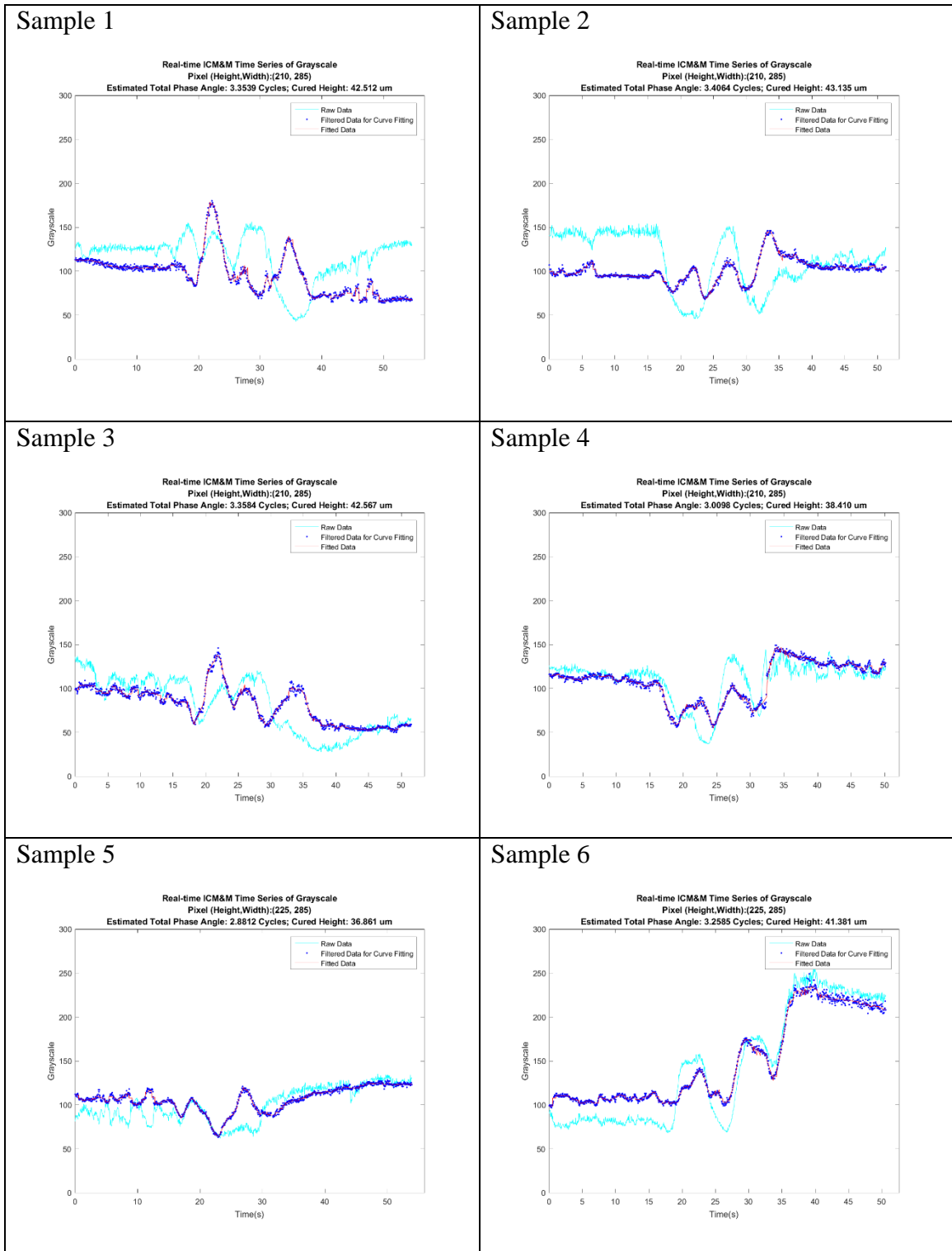


Figure B2. Online measured pixel's data dynamics and measurement results in the real-time ICM&M analysis (Real-time Group #2 Subset #1)

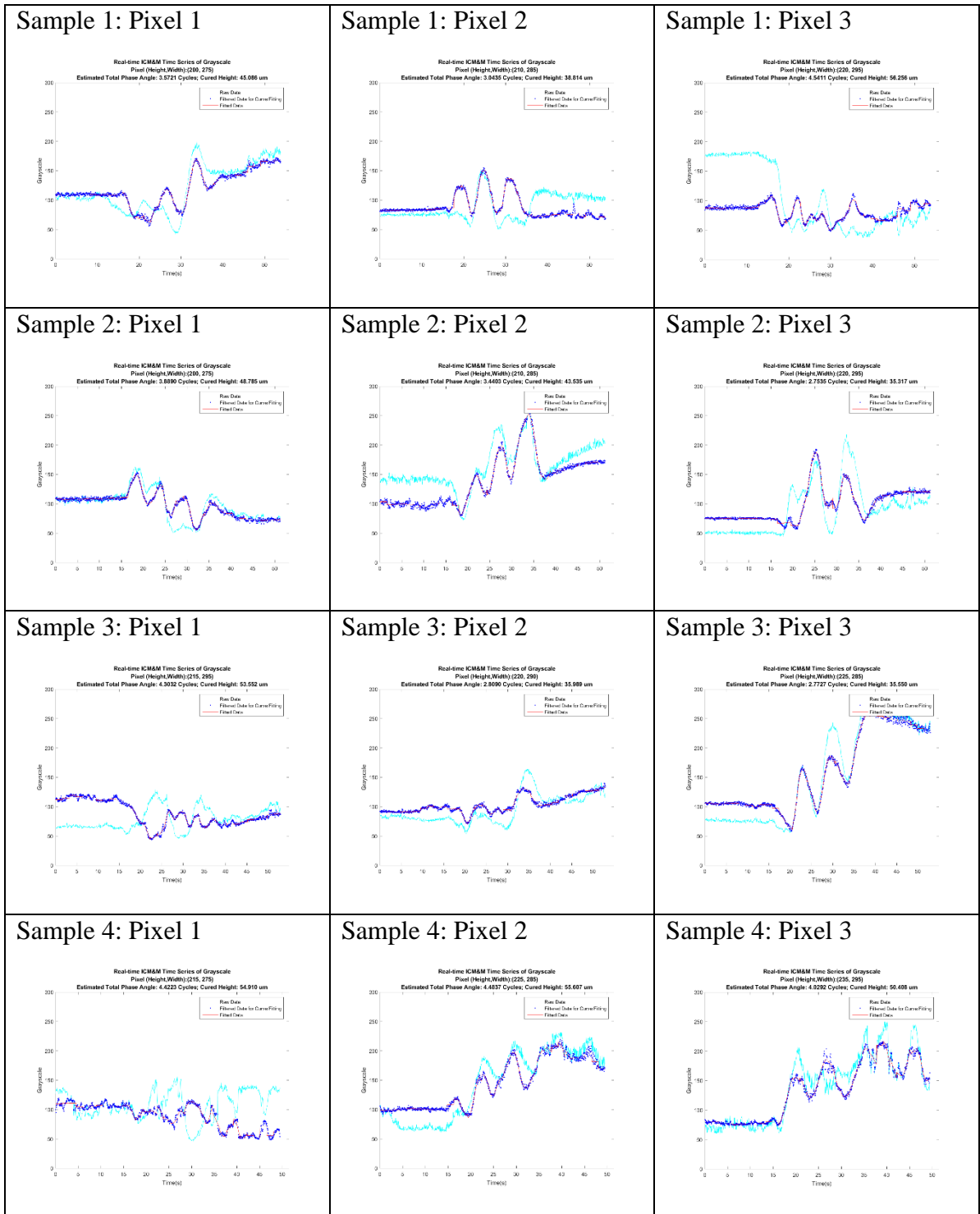


Figure B3. Online measured pixels' data dynamics and measurement results in the real-time ICM&M analysis (Real-time Group #2 Subset #2)

### **B.3 Real-time measurement latency and control system delays**

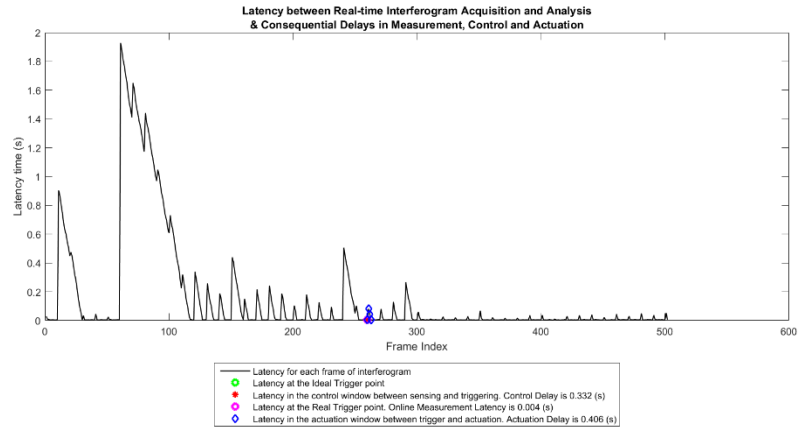
As per the concepts and methods presented in Section 9.4.4, the results of online measurement latency, control delay and actuation delay are estimated for each run of experiment.

To support 9.7.2.3, Figure B4 display the real-time latency for each frame of interferogram and analyzes the measurement latency at trigger point. Please note that the latencies in the control window and actuation window of frames can reveal the fluctuations of the computing environment which could account for the observed delays in control and actuation. Sometimes, a spike in latency time occurs at the frame when the ideal trigger point is reached, indicating a possible computing strain in the background. As the subsequent frames analysis gradually catch up with the acquisition till the analysis thread resumes synchronized with the acquisition, the real triggering usually takes place later than the ideal time point resulting in a control delay (details shown in Figure B5). After triggering, the hardware response in the UV lamp takes some time, leading to actuation delay. In turn, the UV lamp shutting down process could also occupy some computation resource, and thus could hinder the analysis and drag down the analysis speed further. Altogether, the racing of multithreads could randomly lead to delays in the measurement, control and actuation, as shown in Figure B4.

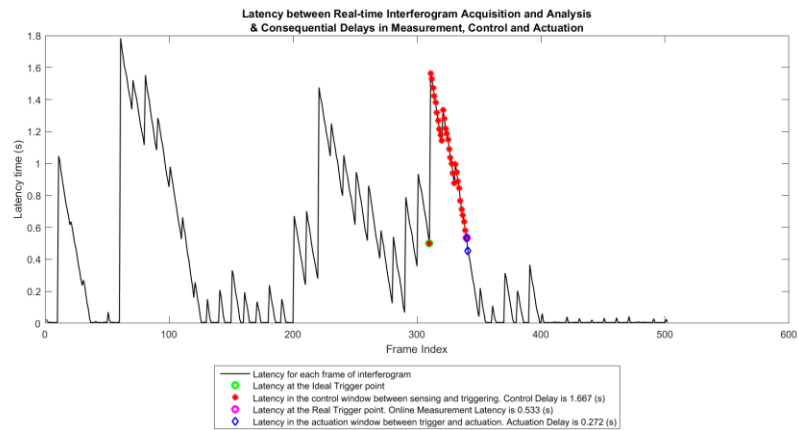
As introduced in Section 9.7.3.2, Figure B5 illustrates the two components of the total control delay, which are caused by the discrete measurement (i.e. measurement interval effect) and the delays in transmission and controller computation, respectively. The real-time cured height evolution which is estimated by evaluating the real-time measurement of the pixel(s) for each sample in Figure B1, Figure B2 and Figure B3, is shown in the Figure B5.



(1) Group#1 Sample 1: Normal process (UV iris level 22%), 1 pixel measured online



(2) Group#1 Sample 2: Normal process (UV iris level 22%), 1 pixel measured online



(3) Group#1 Sample 3: Normal process (UV iris level 22%), 1 pixel measured online

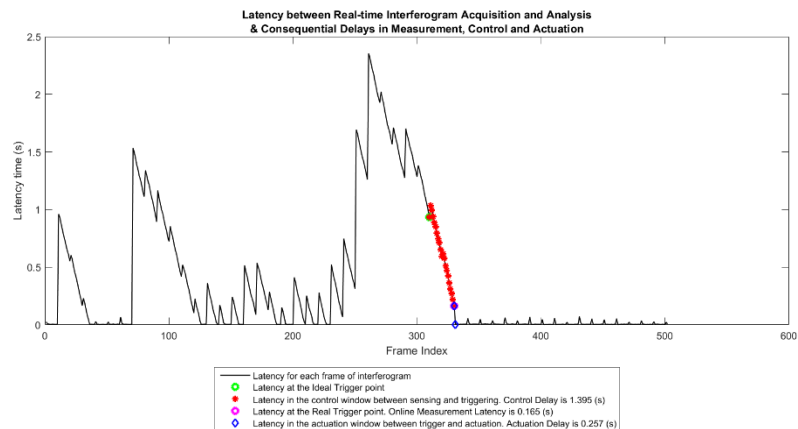
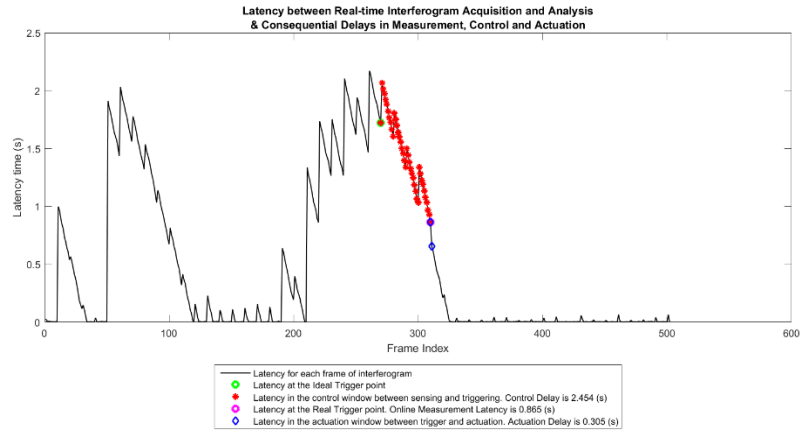
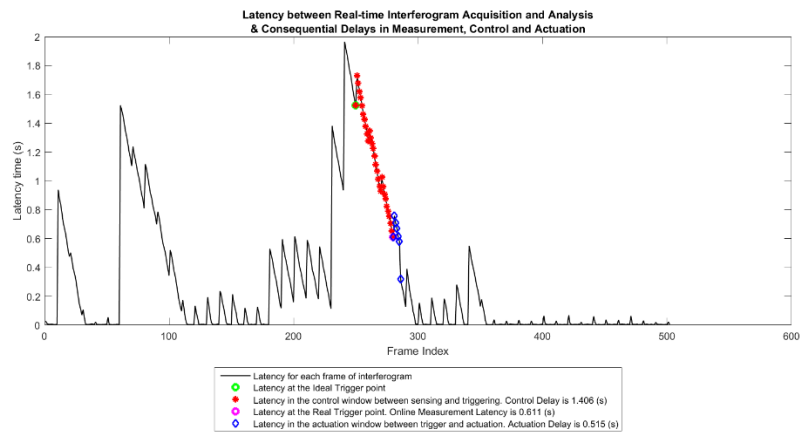


Figure B4. Real-time latency and indication for computation fluctuations that could account for delays in measurement, control and actuation

(4) Group#1 Sample 4: Normal process (UV iris level 22%), 1 pixel measured online



(5) Group#1 Sample 5: Normal process (UV iris level 22%), 1 pixel measured online



(6) Group#1 Sample 6: Normal process (UV iris level 22%), 1 pixel measured online

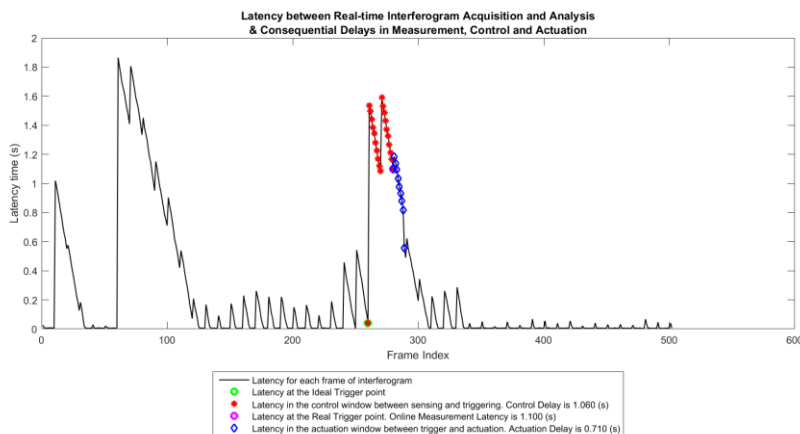
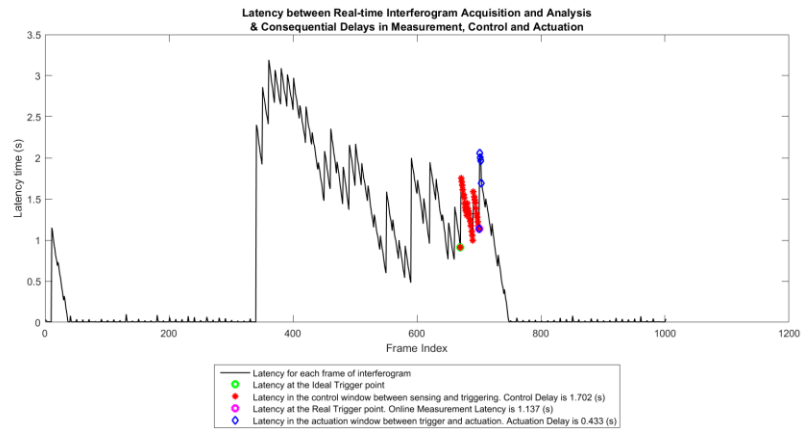
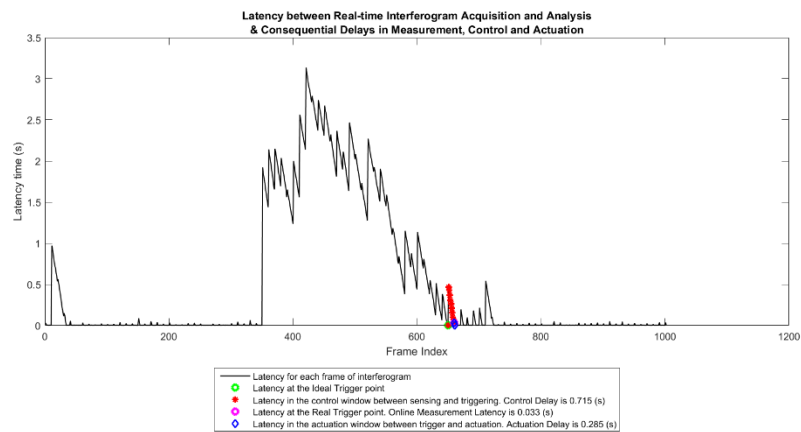


Figure B4 (continued). Real-time latency and indication for computation fluctuations that could account for delays in measurement, control and actuation

(7) Group#2 Subset#1 Sample 1: Slow process (UV iris 5%), 1 pixels measured online



(8) Group#2 Subset#1 Sample 2: Slow process (UV iris 5%), 1 pixels measured online



(9) Group#2 Subset#1 Sample 3: Slow process (UV iris 5%), 1 pixels measured online

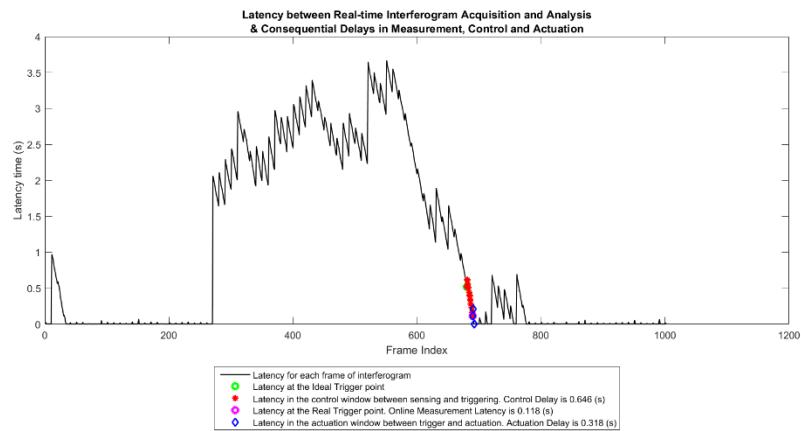
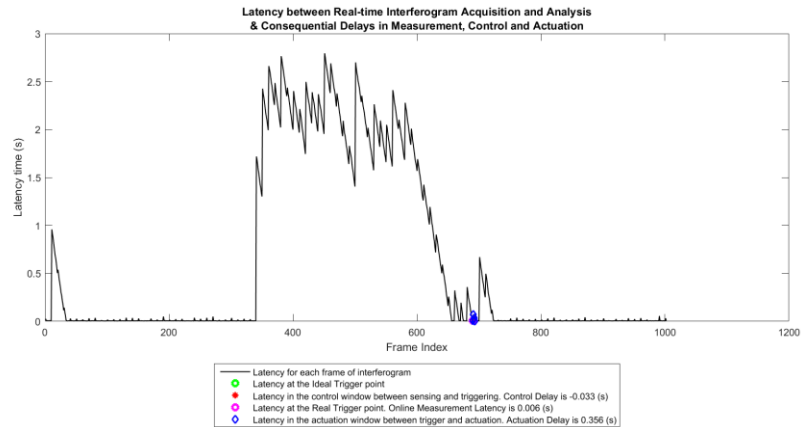
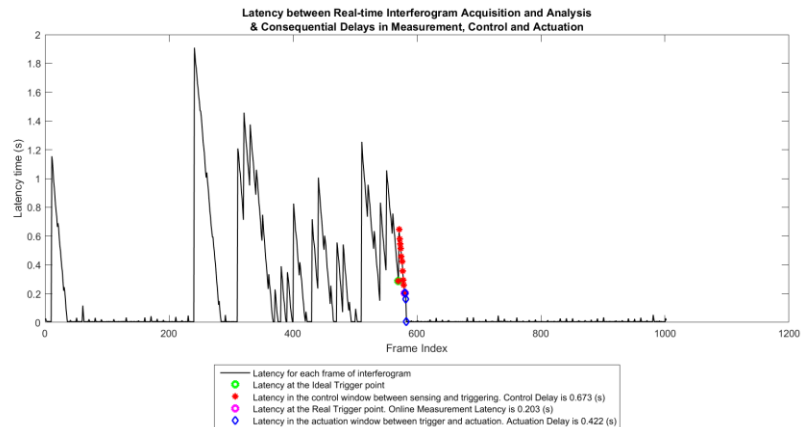


Figure B4 (continued). Real-time latency and indication for computation fluctuations that could account for delays in measurement, control and actuation

(10) Group#2 Subset#1 Sample 4: Slow process (UV iris 5%), 1 pixels measured online



(11) Group#2 Subset#1 Sample 5: Slow process (UV iris 5%), 1 pixels measured online



(12) Group#2 Subset#1 Sample 6: Slow process (UV iris 5%), 1 pixels measured online

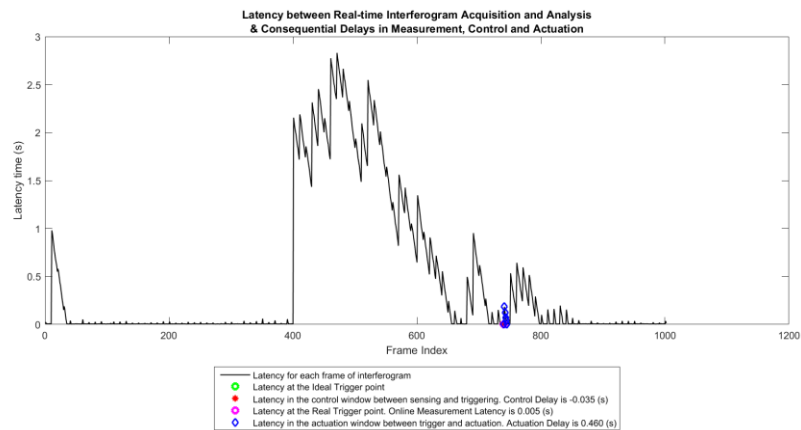
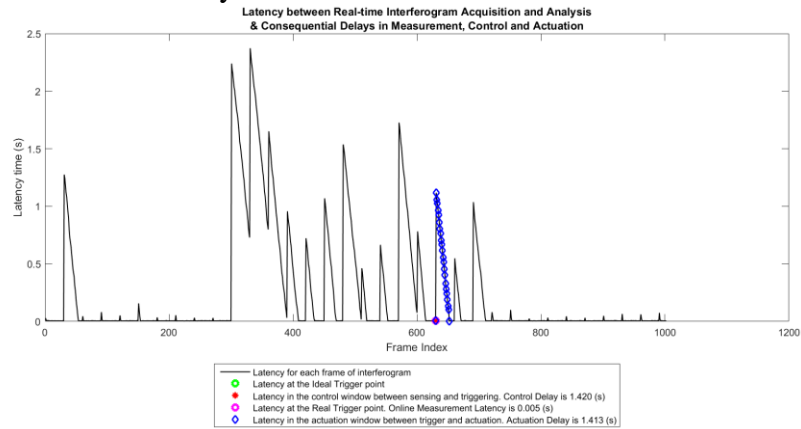


Figure B4 (continued). Real-time latency and indication for computation fluctuations that could account for delays in measurement, control and actuation

(13) Group#2 Subset#2 Sample 1: Slow process (UV iris 5%), 3 pixels measured online, measurement run every 30 frames



(14) Group#2 Subset#2 Sample 2: Slow process (UV iris 5%), 3 pixels measured online, measurement run every 30 frames

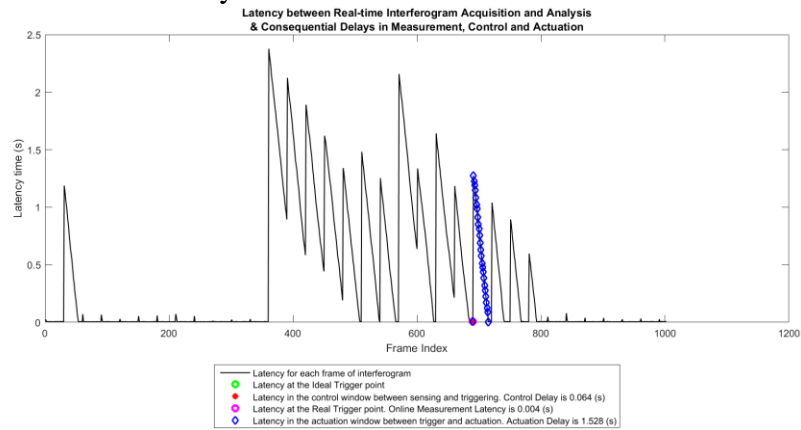
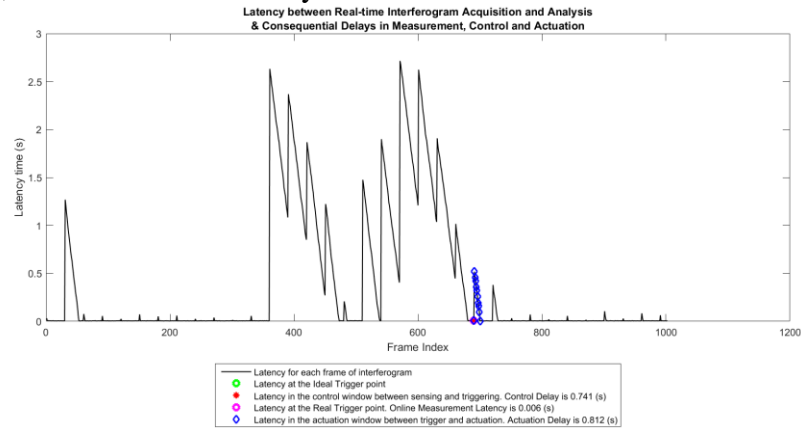


Figure B4 (continued). Real-time latency and indication for computation fluctuations that could account for delays in measurement, control and actuation

(15) Group#2 Subset#2 Sample 3: Slow process (UV iris 5%), 3 pixels measured online, measurement run every 30 frames



(16) Group#2 Subset#2 Sample 4: Slow process (UV iris 5%), 3 pixels measured online, measurement run every 30 frames

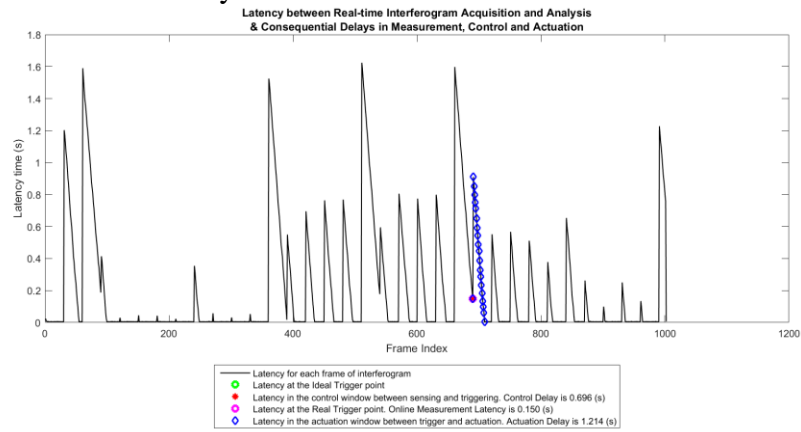
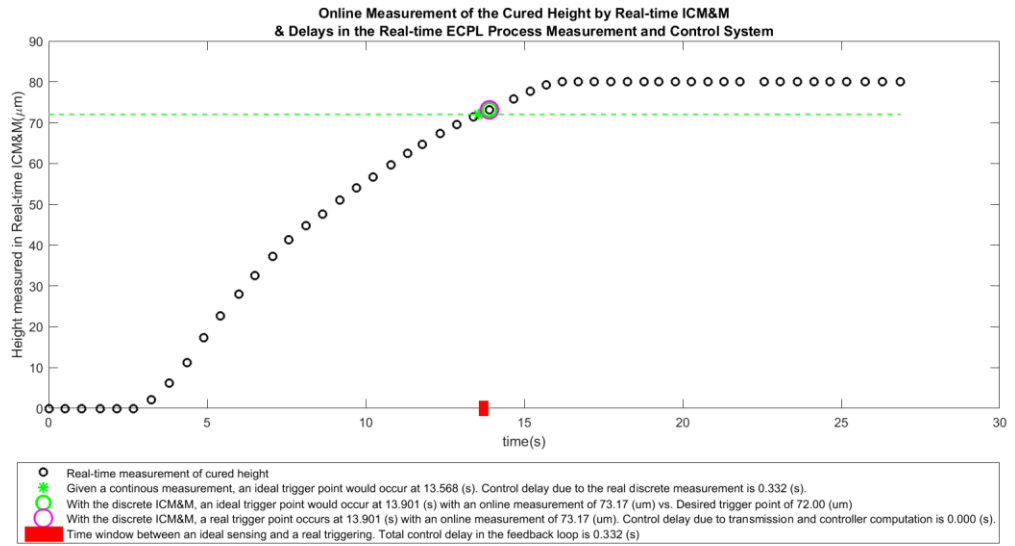


Figure B4 (continued). Real-time latency and indication for computation fluctuations that could account for delays in measurement, control and actuation

(1) Group#1 Sample 1: Normal process (UV iris level 22%), 1 pixel measured online



(2) Group#1 Sample 2: Normal process (UV iris level 22%), 1 pixel measured online

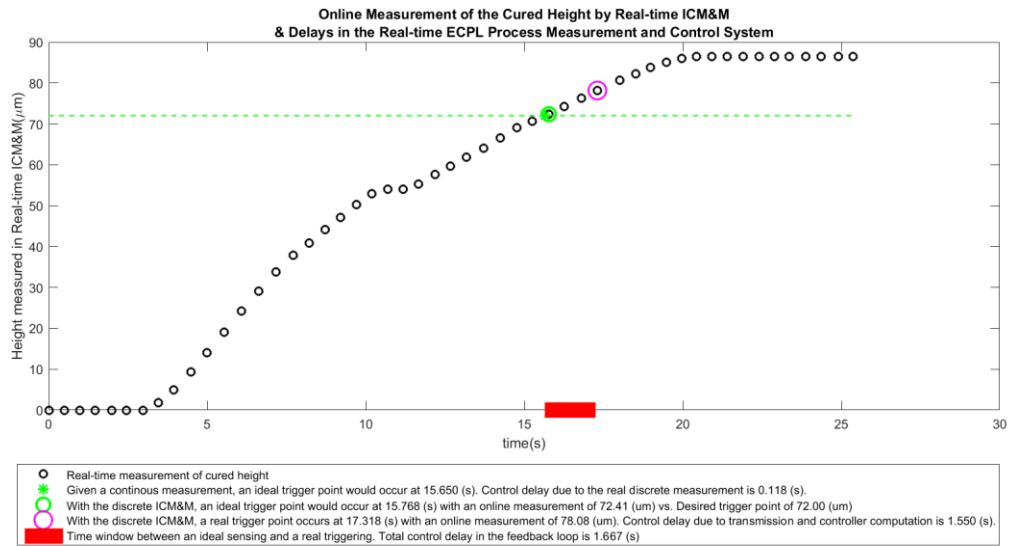
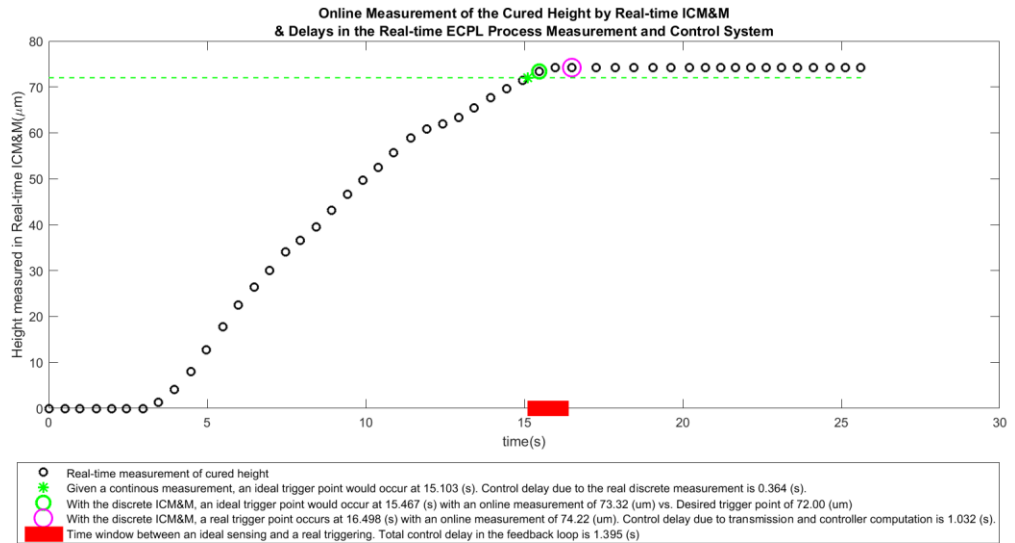


Figure B5. Real-time ICM&M measurement and analysis for online delays in the ECPL process measurement and control system

(3) Group#1 Sample 3: Normal process (UV iris level 22%), 1 pixel measured online



(4) Group#1 Sample 4: Normal process (UV iris level 22%), 1 pixel measured online

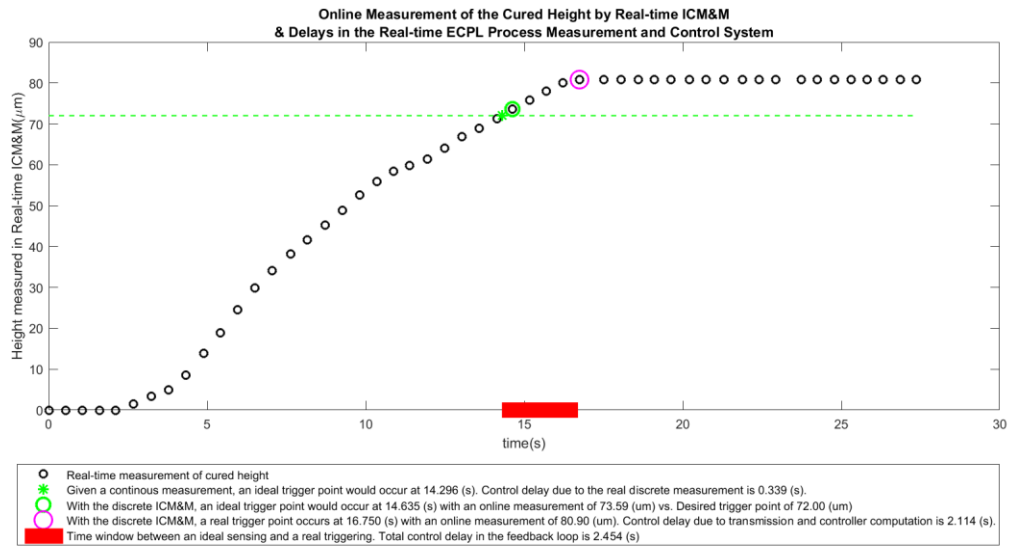
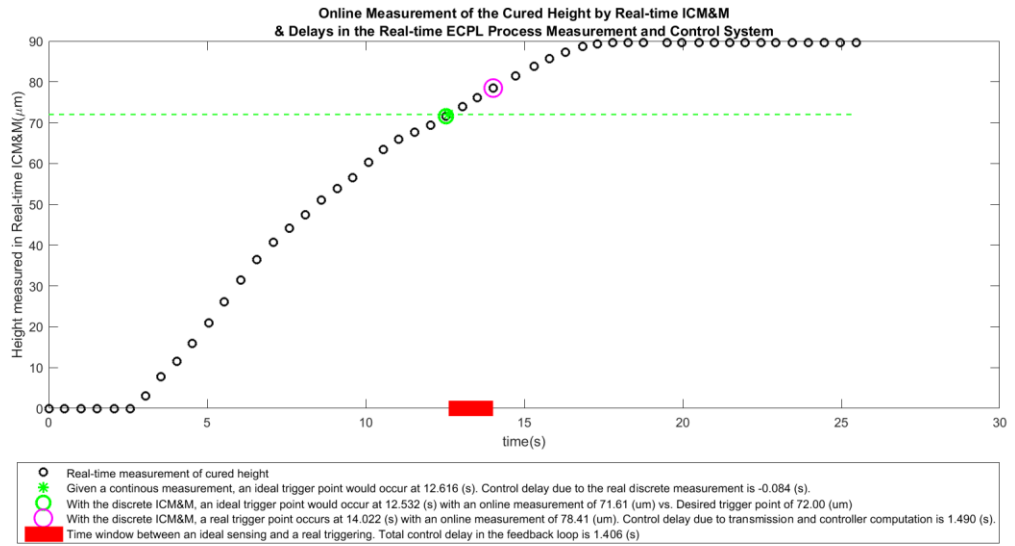


Figure B5 (continued). Real-time ICM&M measurement and analysis for online delays in the ECPL process measurement and control system



(5) Group#1 Sample 5: Normal process (UV iris level 22%), 1 pixel measured online



(6) Group#1 Sample 6: Normal process (UV iris level 22%), 1 pixel measured online

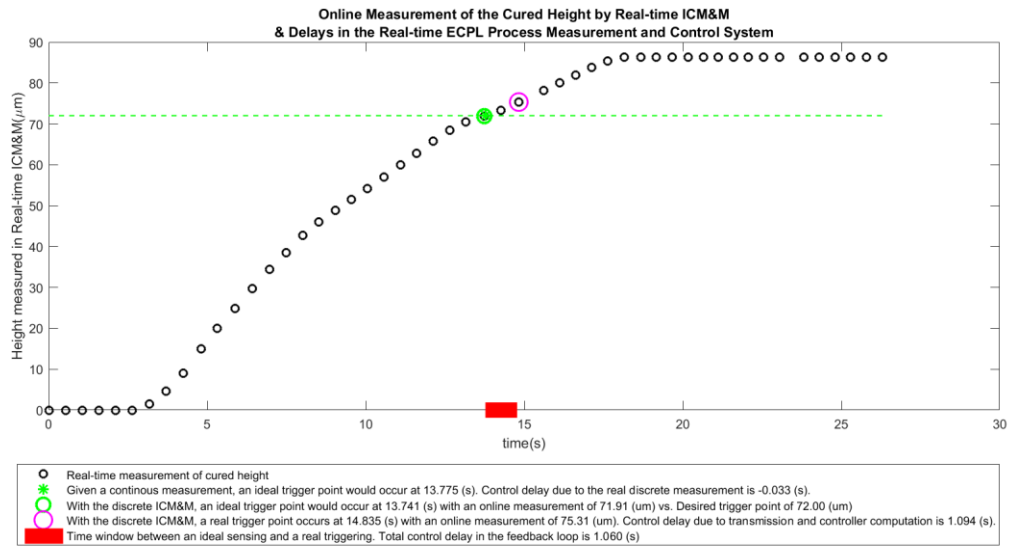
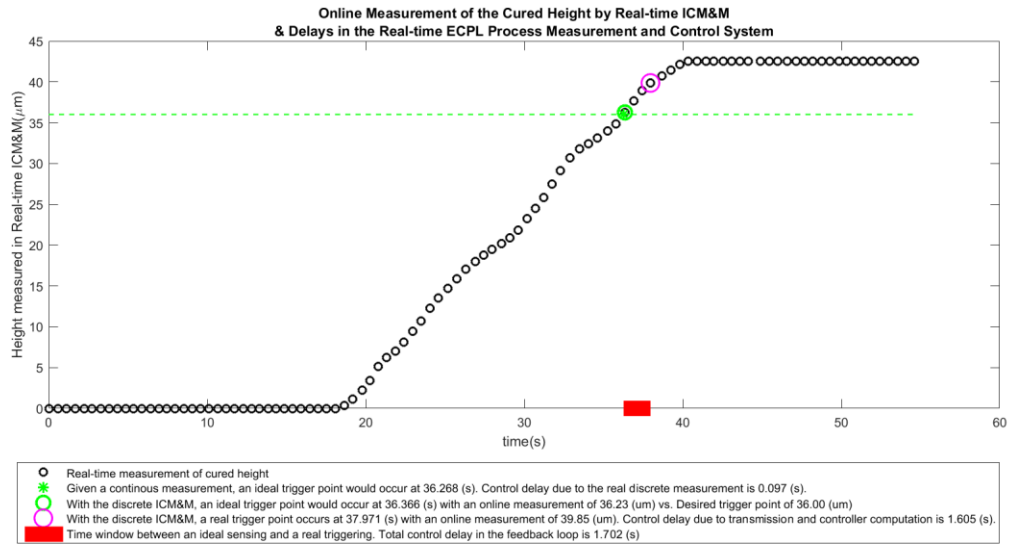


Figure B5 (continued). Real-time ICM&M measurement and analysis for online delays in the ECPL process measurement and control system

(7) Group#2 Subset#1 Sample 1: Slow process (UV iris 5%), 1 pixels measured online



(8) Group#2 Subset#1 Sample 2: Slow process (UV iris 5%), 1 pixels measured online

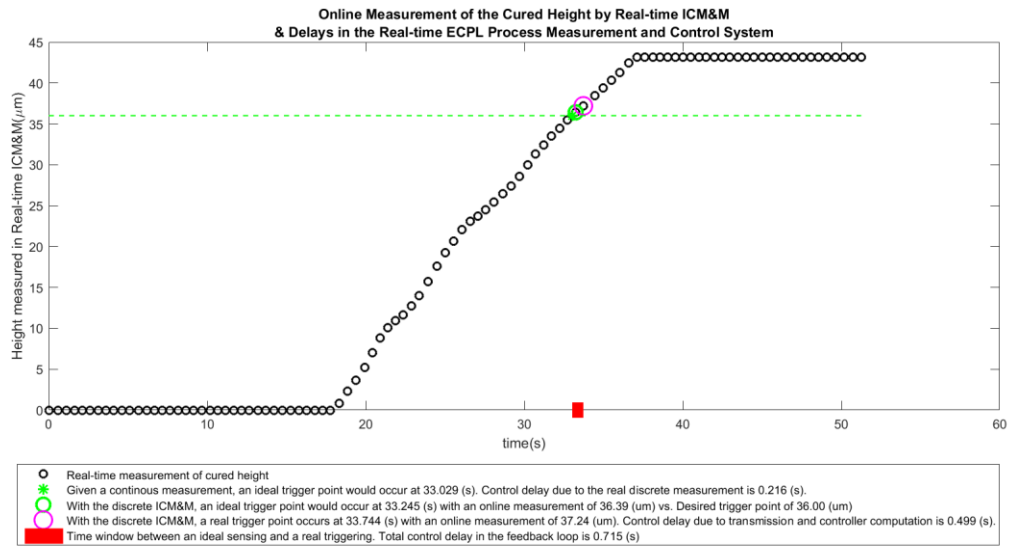
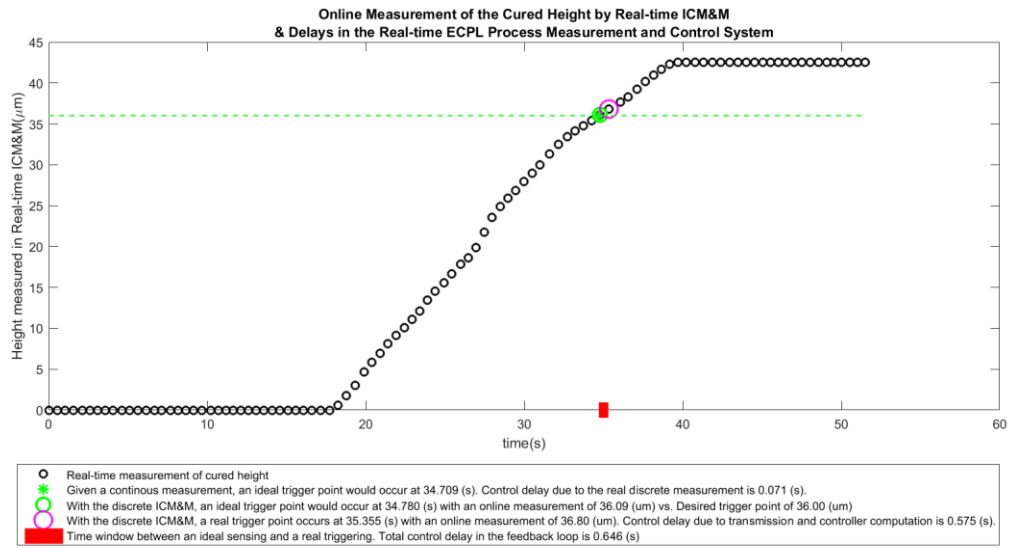


Figure B5 (continued). Real-time ICM&M measurement and analysis for online delays in the ECPL process measurement and control system

(9) Group#2 Subset#1 Sample 3: Slow process (UV iris 5%), 1 pixels measured online



(10) Group#2 Subset#1 Sample 4: Slow process (UV iris 5%), 1 pixels measured online

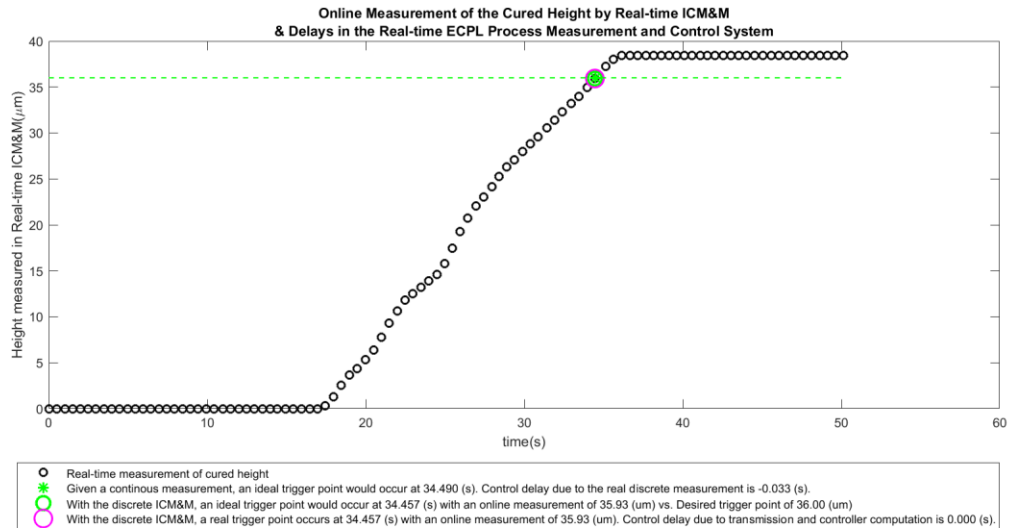
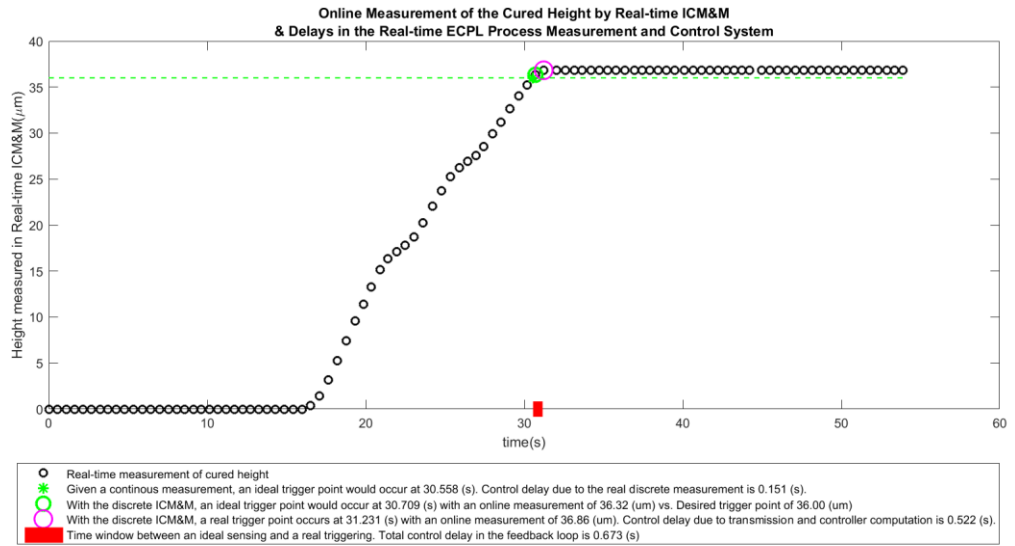


Figure B5 (continued). Real-time ICM&M measurement and analysis for online delays in the ECPL process measurement and control system

(11) Group#2 Subset#1 Sample 5: Slow process (UV iris 5%), 1 pixels measured online



(12) Group#2 Subset#1 Sample 6: Slow process (UV iris 5%), 1 pixels measured online

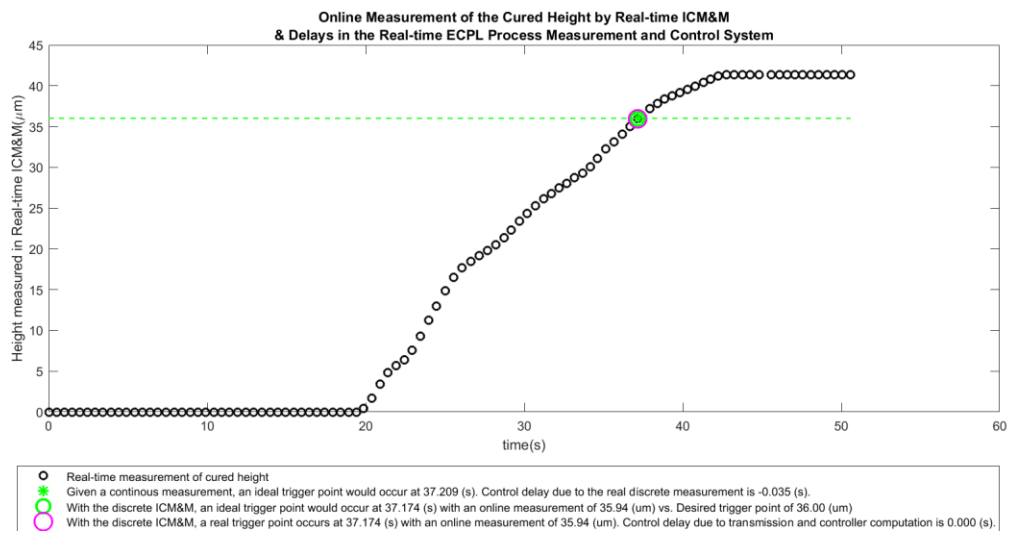
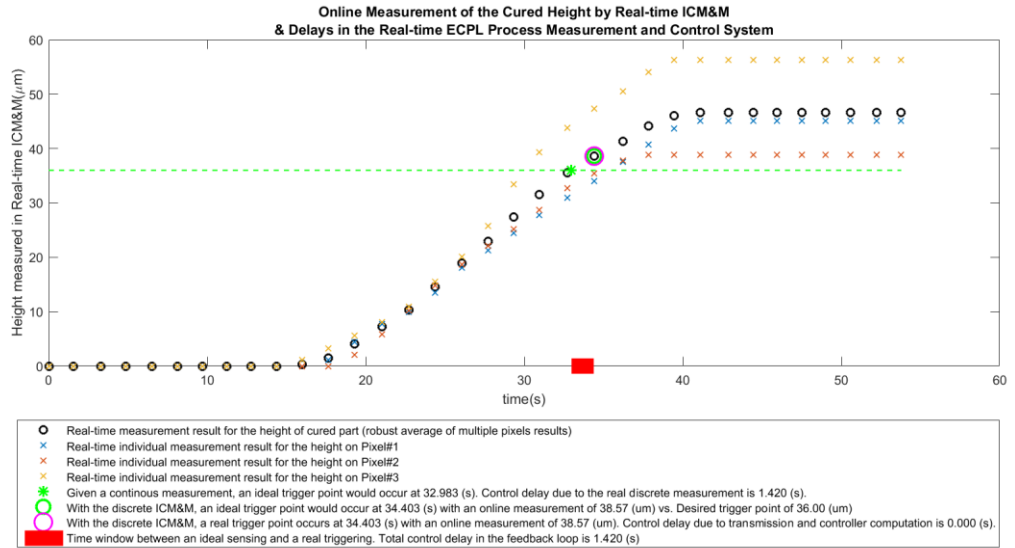


Figure B5 (continued). Real-time ICM&M measurement and analysis for online

delays in the ECPL process measurement and control system

(13) Group#2 Subset#2 Sample 1: Slow process (UV iris 5%), 3 pixels measured online, measurement run every 30 frames



(14) Group#2 Subset#2 Sample 2: Slow process (UV iris 5%), 3 pixels measured online, measurement run every 30 frames

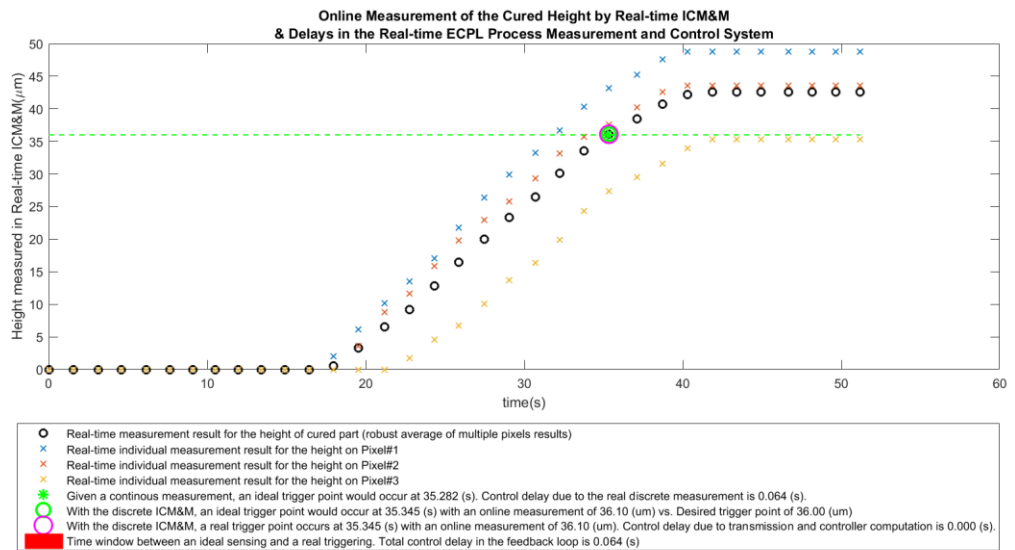
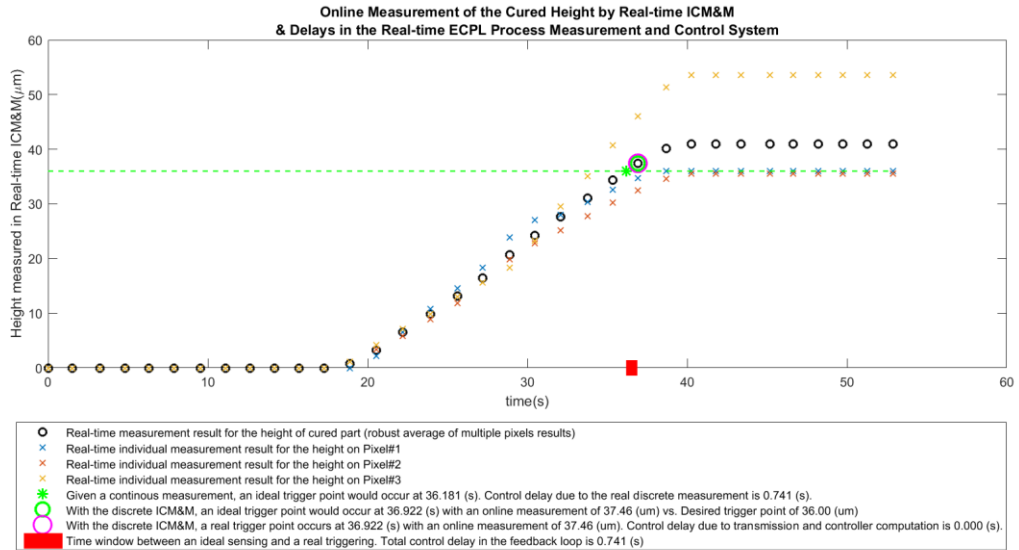


Figure B5 (continued). Real-time ICM&M measurement and analysis for online delays in the ECPL process measurement and control system

(15) Group#2 Subset#2 Sample 3: Slow process (UV iris 5%), 3 pixels measured online, measurement run every 30 frames



(16) Group#2 Subset#2 Sample 4: Slow process (UV iris 5%), 3 pixels measured online, measurement run every 30 frames

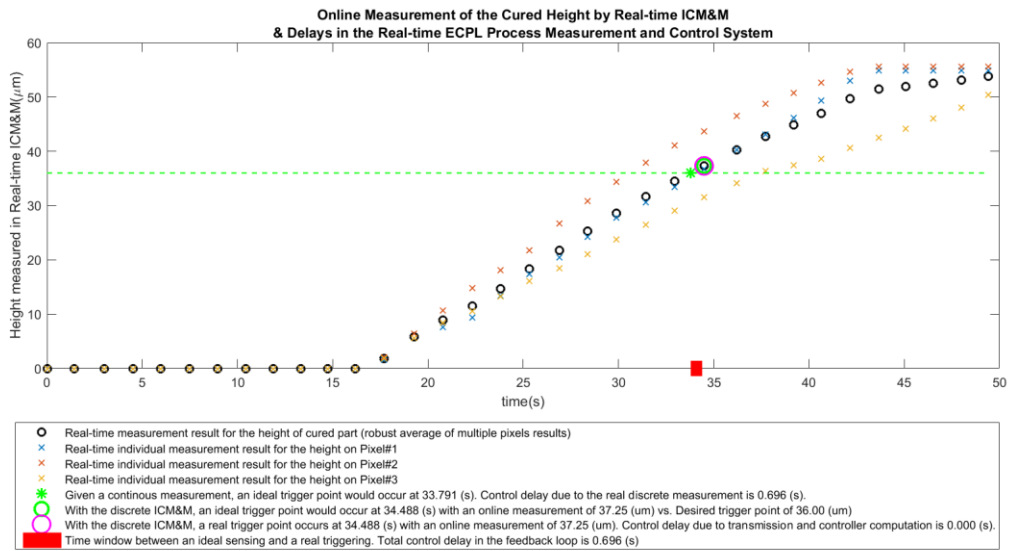


Figure B5 (continued). Real-time ICM&M measurement and analysis for online delays in the ECPL process measurement and control system

# APPENDIX C

## ECPL-M&C SOFTWARE

### C.1 Software Manual

Two example instruction for performing a real-time measurement and control experiment (Chapter 9) with the software is presented as below, using the GUI described previously.

- Experiment Group # 1: 1 pixel, 22% UV

Sample 1: 250×250 square

Instructions:

1. Connect UV lamp, camera, and DMD
2. Open Matlab, run "Real\_Time\_ICM", measure & control online by following the steps as below.

(1) Set the measurement period box value "10" (default already), UV light "22"

(2) The online acquired interferograms are simultaneously written into the global variable "g\_all\_frame", which is initialized in the matlab code "pb\_AcquireAVI\_Callback.m", and user could set the number of maximum frames to be acquired in that code.

For UV=22% and curing 80um, 500 frames will do. Hence, one could change the frame number at Line 72 (highlighted in blue) to be "500".

```
pb_AcquireAVI_Callback.m  X +
51  %% Start the icm main worker
52  disp('Starting ICM main worker')
53  set(handles.st_InterferogramStatusBar,'String','Starting ICM main worker');
54  pause(0.5);
55  g_job = batch(@icm_main_worker, 1, (handles.cp),...
56  'Pool', handles.cp.numFitter,...
57  'AttachedFiles', {'icmFit2.m'}...
58  );
59  wait(g_job, 'running');
60  disp('ICM main worker started, wait until worker is ready')
61  set(handles.st_InterferogramStatusBar,'String','ICM main worker started, wait until worker is ready');
62  while g_mmf.Data(1).status(3) == 0
63      pause(1)
64  end
65  disp('icm main worker is ready!')
66  set(handles.st_InterferogramStatusBar,'String','ICM main worker is ready! Click "Open UV" to start ECPL and ICM&M.');
```

```
67
68
69  g_frameIdx = 0;
70  g_acquiring = 1;
71  g_uvstatus = 0;
72  g_all_frame = zeros(handles.cp.imH, handles.cp.imW, 1, 1000); % HOME computer & camera
73
74  set(handles.pb_OpenCloseUV,'Enable','on');
```

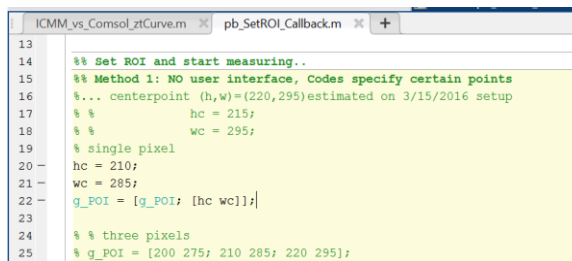
(3) Input "250" in the boxes of "Rectangle Width" and "Rectangle Height" , and "Generate DMD bitmap"

(4) Make sure to CHECK "Target Cured Height" and UNCHECK "Target Exposure Time", this is already by default but better make sure. Set the Target Cured Height as "80" .

(5) "Start Camera"

(6) "Set ROI" (1 pixel: H=210, w=285)

Step: In "pb\_SetROI.m", change the g\_POI as below

A screenshot of a MATLAB script editor window showing the code for the 'pb\_SetROI\_Callback.m' function. The code is as follows:

```
13  
14 %% Set ROI and start measuring..  
15 %% Method 1: NO user interface, Codes specify certain points  
16 %... centerpoint (h,w)=(220,295) estimated on 3/15/2016 setup  
17 %%          hc = 215;  
18 %%          wc = 295;  
19 % single pixel  
20 hc = 210;  
21 wc = 285;  
22 g_POI = [g_POI; [hc wc]];  
23  
24 %% three pixels  
25 g_POI = [200 275; 210 285; 220 295];
```

(7) "Start Acquisition" and wait until the pushbutton "Open UV Light" is enabled. This may take one minute or longer.

(8) "Open UV Light"

(9) After UV light is off, wait for 3 seconds, click "Stop Acquisition", and hold on till the status bar under the image shows "Main worker Returned measurement and analysis results."

Note: Do NOT click "Stop Acquisition" again if it still continues acquiring because the acquisition will stop automatically when 500 frames are acquired.

(10) Close the app.



## C.2 MATLAB Codes

This section lists all the key functions in the MATLAB based ECPL-M&C software.

### 1. Function: “icmFit2.m”

The function is for adaptive curve fitting. The codes are as below.

```
function ret = icmFit2(dataX, dataY, params,
prevRet)
%% Function returns the following parameters:
...ret.fitobject = fitobjects{iFitTrial}; % fitting
trial which outstands
    ...ret.fitgof = gofs{iFitTrial};
    ...ret.movingHorizon =
movingHorizons(iFitTrial);
    ...ret.halfLife = halfLives(iFitTrial);
    ...ret.frameIdx = frameIdx_local =
length(rawY);
    ...ret.firstValidFoiIdx: curing starts,i.e.,end
of threshold
    ...ret.fitStatus: 0:not started; 1:fail;
2:valid
    ...ret.fittype: "fourier 1"
    ...ret.fitoptions
    ...ret.I0: baseline amplitude (DC)
    ...ret.I1: oscillation amplitude (AC)
    ...ret.freqW: angular frequency in
Im=I0+I1*cos(W*t+phi)
    ...ret.freq: frequency = W/2/pi (unit:Hz)
    ...ret.time: relative time (s) from beginning
of measurement = dataX(end)

%% Smooth time sequence of grayscale
dataY = smooth(dataY);
dataLen = length(dataY);
frameIdx_local = dataLen;

%%--if want to use different criterions for
threshold and dark period, use below
if isempty(params.uvIris) || (params.uvIris >= 10)
```

```

    Threshold_I1 = 10;
    % 1.5s range to detect dark curing
    darkWindowLen = 44;
    darkRange = 20;
else % set empirical frequency range [0.1 Hz,0.5
Hz]for uvIris=5
    Threshold_I1 = 10;
    % 2.5s range to detect dark curing
    darkWindowLen = 44;
    darkRange = 10;
end

%%-----

%% Initialize fitting options
if params.RunNo == 1

    %  $y = a_0 + a_1 \cos(w \cdot x) + b_1 \sin(w \cdot x)$ , where  $x$  is
    actually time "t"
    % Coefficients = [a0;a1;b1;w];
    opts = fitoptions('fourier1');
    opts.Display = 'Off';

    % note: setting reasonable limit is very
    important!
    % set limits of the coefficients "a0,a1,b1,w"
    % If FPS of video is 30, maximum detectable
    frequency is  $30/2=15$ , while
    %  $w_{Max} = 2 * \pi * \text{params.FPS}/2$ ;
%  $w_{Max} = 2 * \pi *$ 
min(params.FPS/2,params.f_max);
    aMax = 255 * 1;

    %%--- 1st curve fitting, bound frequency to get
    a good start, starting point is important
    % set empirical frequency range [0.4 Hz,1.2 Hz]
for uvIris>5
    if isempty(params.uvIris) || (params.uvIris >=
10)
        opts.Lower = [0 -aMax/2 -aMax/2 0.4*2*pi];
        opts.Upper = [aMax aMax/2 aMax/2 1.2*2*pi];

```

```

else % updated on 07-22-2016: set empirical
frequency range [0.1 Hz,0.5 Hz]for uvIris=5
    opts.Lower = [0 -aMax/2 -aMax/2 0.1*2*pi];
    opts.Upper = [aMax aMax/2 aMax/2 0.5*2*pi];
end
%%-----

opts.MaxIter = 400;
%     opts.TolFun = 1.0e-6;
%     opts.TolX = 1.0e-6;
opts.TolFun = 1.0e-3;
opts.TolX = 1.0e-5;
% opts.StartPoint = [0 0 0 0];

else % if previous fitting exists, keep using it
opts = prevRet.fitoptions;
% note: setting reasonable limit is very
important!
% set limits of the coefficients "a0,a1,b1,w"
% If FPS of video is 30, maximum detectable
frequency is 30/2=15, while
wMax = 2 * pi *min(params.FPS/2,params.f_max);
%     wMax = 2 * pi *params.f_max;
aMax = 255 * 1;

% Set frequency range [0.1,15 Hz] for curing
period before UV closes
if (prevRet.fitStatus ~= 0) &&
(isempty(params.RunNo_uvClose) || (params.RunNo <=
params.RunNo_uvClose))
    opts.Lower = [0 -aMax/2 -aMax/2 0.1*2*pi];
    opts.Upper = [aMax aMax/2 aMax/2 wMax];
elseif ~isempty(params.RunNo_uvClose) &&
(params.RunNo > params.RunNo_uvClose) % dark curing
period, fitting frequency could be low to 0
    opts.Lower = [0 -aMax/2 -aMax/2 0];
    opts.Upper = [aMax aMax/2 aMax/2 wMax];
end

% use the previous starting point to save time

```

```

        if prevRet.fitStatus == 2 || prevRet.fitStatus
== 42 || (prevRet.fitStatus ~= 0 &&
prevRet.fitgof.rsquare >= 0.75 &&
prevRet.fitgof.rsquare ~= 1)
            opts.StartPoint =
coeffvalues(prevRet.fitobject);
        end
    end

%% At threshold period, useless fitting, simply
return
if (prevRet.fitStatus == 0) &&
(std(dataY(prevRet.frameIdx+1:end)) <
5)&&(range(dataY(1:end)) < 20)% previously use 10
    ret.fitobject = [];
    ret.fitgof.rsquare = 1;
    ret.movingHorizon = params.MHL;
    ret.halfLife = params.halfLife;
    ret.frameIdx_dummy = frameIdx_local;
    ret.frameIdx = params.frameIdx;
    ret.firstValidFoiIdx = 0; % NOT curing frame
yet
    ret.fitStatus = 0; % NO fitting yet
    ret.fitoptions = opts;
    % retrun DC (Direct Current) values
    ret.I0 = mean(dataY((prevRet.frameIdx+1):end));
    ret.I1 = 0;
    ret.freqW = 0;
    ret.freq = 0;
    ret.time = dataX(end);
    return
end

%% At the dark curing period, when the curve flats
out, no need fitting
if (~isempty(params.RunNo_uvClose) &&
(std(dataY(prevRet.frameIdx+1:end)) < 5) ...
&&(range(dataY(end-darkWindowLen:end)) <=
darkRange)) ...%% updated on 07-22-2016
    || (prevRet.fitStatus == 3)
    ret = prevRet;

```

```

ret.fitobject = [];
ret.fitgof.rsquare = 1;
ret.movingHorizon = params.MHL;
ret.halfLife = params.halfLife;
ret.frameIdx_dummy = frameIdx_local;
ret.frameIdx = params.frameIdx;
ret.fitStatus = 3; % Dark curing, NO fitting
ret.fitoptions = opts;
ret.I0 = mean(dataY((prevRet.frameIdx+1):end));
ret.I1 = 0;
ret.freqW = 0;
ret.freq = 0;
ret.time = dataX(end);
return
end

%% Start fitting
% R-square threshold value for fitting goodness
rsqTh = params.rSquare;

nMaxTrial = 2;
halfLifes = params.halfLife* [1,1];
movingHorizons =
min(dataLen,round(params.MHL*[1,1.5]));
% if dark curing period, extend the window length
to estimate the lower frequency
if ~isempty(params.RunNo_uvClose) &&
(params.RunNo >= params.RunNo_uvClose)
    halfLifes = round(params.halfLife* [2,3]);
    movingHorizons =
min(dataLen,round(params.MHL*[2,3]));
end

% uvIris level too low, e.g., uvIris=5, curing
frequency is 0.2Hz, need
...longer MHL to estimate the frequency accurately
if params.uvIris < 10
    halfLifes = params.halfLife* [1,2];
    movingHorizons =
min(dataLen,round(params.MHL*[2,3]));

```

```

    % dark curing, longer MHL
    if ~isempty(params.RunNo_uvClose) &&
        (params.RunNo >= params.RunNo_uvClose)
        halfLives = round(params.halfLife* [2,3]);
        movingHorizons =
min(dataLen, round(params.MHL*[4,6]));
    end
end

fitobjects = cell(nMaxTrial, 1);
gofs = cell(nMaxTrial, 1);

fitStatus = 1;
for iFitTrial = (1:nMaxTrial)
    halfLife = halfLives(iFitTrial);
    movingHorizon = movingHorizons(iFitTrial);

    trainLen = movingHorizon;
    trainIdxs = ((dataLen - trainLen + 1) :
dataLen)';
    trainX = dataX(trainIdxs);
    trainY = dataY(trainIdxs);

    weights = exp((trainIdxs - trainIdxs(end)) /
halfLife * log(2));
    opts.Weights = weights;

    [fitobject, gof] = fit( trainX, trainY,
'fourier1', opts );
    fitobjects{iFitTrial} = fitobject;
    gofs{iFitTrial} = gof;

    if round(gof.rsquare,2) >= rsqTh
        fitStatus = 2;
        break;
    else
        if iFitTrial > 1 && gof.rsquare <
gofs{Idx_PrevTrial}.rsquare
            iFitTrial = Idx_PrevTrial;
            break;
        else

```

```

        % otherwise keep going
        Idx_PrevTrial = iFitTrial;
    end
end
end

%% Return values
ret.fitobject = fitobjects{iFitTrial};
ret.fitgof = gofs{iFitTrial};
ret.movingHorizon = movingHorizons(iFitTrial);
ret.halfLife = halfLives(iFitTrial);

ret.frameIdx_dummy = frameIdx_local;
ret.frameIdx = params.frameIdx;
ret.firstValidFoiIdx = prevRet.firstValidFoiIdx;

if fitStatus ~= 0 && prevRet.firstValidFoiIdx == 0
    ret.firstValidFoiIdx = prevRet.frameIdx+1;
end

coeffs = coeffvalues(fitobject);
I0 = coeffs(1); % estimated baseline amplitude (DC)
I1 = sqrt(coeffs(2)^2+coeffs(3)^2); % estimated
fringe amplitude (AC)
freqW = coeffs(4); % estimated angular frequency
"w"
freq = coeffs(4) / 2 / pi;% estimated frequency "f"
(unit:Hertz)

ret.fitStatus = fitStatus;
ret.fitoptions = opts;

ret.I0 = I0;
ret.I1 = I1;
ret.freqW = freqW;
ret.freq = freq;
ret.time = dataX(end);

%% Frequency outliers detection & correction
...In the threshold period, correct the frequency
artificially by using previous

```

```

% the following is especially useful in low uvIris
when threshold
% period is long and fluctuating, to identify the
threshold correctly is
% very important in the overall process parameters
estimation
% if (prevRet.fitStatus == 0) && ((ret.I1 <
10)|| (ret.freq < 0.05))
if (prevRet.fitStatus == 0) && (ret.I1 <
Threshold_I1)
    ret = prevRet; % use previous returned fitting
    ret.fitgof.rsquare = 0;
    ret.frameIdx_dummy = frameIdx_local;
    ret.frameIdx = params.frameIdx;
    ret.fitStatus = 0;
    ret.fitoptions = opts;

    % retrun DC (Direct Current) values
    ret.I0 = mean(dataY((prevRet.frameIdx+1):end));
    ret.I1 = 0;
    ret.freqW = 0;
    ret.freq = 0;
    ret.time = dataX(end);
end

% the following is especially useful in low uvIris
when threshold
% period is long and fluctuating, to identify the
threshold correctly is
% very important in the overall process parameters
estimation
if (prevRet.fitStatus == 0) && (ret.freq < 0.1)
    ret.fitStatus = 0;
end

%--- in the curing period, if too noisy, use zero
frequency directly.
if (prevRet.fitStatus ~= 0) && (ret.I1 < 5)
    ret = prevRet; % use previous returned fitting
    ret.fitgof.rsquare = 0;
    ret.frameIdx_dummy = frameIdx_local;

```



```

    ret.frameIdx = params.frameIdx;
    ret.fitStatus = 40; % outlier frequency due to
failed fitting

    % retrun DC (Direct Current) values
    ret.I0 = mean(dataY((prevRet.frameIdx+1):end));
    ret.I1 = 0;
    ret.freqW = 0;
    ret.freq = 0;
    ret.time = dataX(end);
end

end

```

## 2. Function: “Real\_Time\_ICM\_processMeasureTimer.m”

The function is used for real time ICM&M data acquisition (i.e., interferogram acquisition) and logging. The codes are as below.

```

%% process measurement timer func
function Real_Time_ICM_processMeasureTimer(vid,
event, hObject)

global hImage
global g_all_frame
global uv
global g_uvStatus
global hdvp
global g_acquiring
global g_mmf
global g_frameIdx
global g_tImaqStart
global g_previewFrameIdx

%% Communication variables
global g_mmfWriteIdx

handles = guidata(hObject);
if ~isrunning(vid)
    return

```

```

end

%% Real-time Preview video
% if user does NOT push the button to acquire and
log AVI, just preview
frame = getsnapshot(vid);
g_previewFrameIdx = g_previewFrameIdx + 1;
if g_previewFrameIdx == 1
    hImage = imshow(frame, 'Parent',
handles.Interferogram);
else
    set(hImage, 'CData', frame);
end

if g_acquiring == 0 || g_uvStatus == 0
    return
end;

if g_mmf.Data(1).status(1) == 0
    % capture stopped
    fprintf('Timer get msg that capture is
stopped!\n')
    guidata(hObject, handles);
    return
end

if g_mmf.Data(1).status(3) == 2 && g_uvStatus == 1
    % shutdown uv
    icm_set_uv_status(0,handles.cp.uvIris);

    % display exposure time dynamically till UV
closed
    set(handles.ed_ExposureTime, 'string',
toc(g_tImaqStart));

    % Change button string
    set(handles.pb_OpenCloseUV, 'String', 'Open UV
Light');
    set(handles.pb_OpenCloseUV, 'Enable', 'off');

    % update the Interferogram Status Bar for info

```

```

set(handles.st_InterferogramStatusBar,'String','ON
Target. Controller closed UV shutter. Click "Stop
Acquisition" when ready.');
```

end

```

%% now we are acquiring and uvStatus is 1
if g_frameIdx == 0
%   g_tImaqStart = tic;
    fprintf('Measurement starts...\n')
    disp(handles.cp)
    g_mmfWriteIdx = 0;
end

%% Real-time acquisition:get latest frame and
display
% if user has started to acquire AVI, start
acquiring and logging data
% trigger(handles.video);
% frame = getdata(handles.video,1); % takes 27ms,
slower than "getsnapshot"
% frame = getsnapshot(vid); % takes 7ms, much
faster than "getdata"
% tImaqStart = tic; % start time of imaq
frameTime = toc(g_tImaqStart); % absolute elapsed
time from start to current frame
g_frameIdx = g_frameIdx + 1;

%% process mmf
% read status

g_mmfWriteIdx = mod(g_mmfWriteIdx,
handles.cp.maxNumCache) + 1;
% fprintf('g_mmfWriteIdx=%d\n', g_mmfWriteIdx)

% write frame
fprintf('Writing frame %d to cache %d\n',
g_frameIdx, g_mmfWriteIdx)
if g_mmf.Data(g_mmfWriteIdx).frameIdx(1) ~= 0
```

```

    fprintf('Previous frame %d at cache %d is not
processed yet!!!\n',
g_mmf.Data(g_mmfWriteIdx).frameIdx(1),
g_mmfWriteIdx)
end
g_mmf.Data(g_mmfWriteIdx).frame = frame;
g_mmf.Data(g_mmfWriteIdx).frameIdx(1) = g_frameIdx;
g_mmf.Data(g_mmfWriteIdx).frameTime(1) = frameTime;
g_mmf.Data(g_mmfWriteIdx).uvIris(1) =
handles.cp.uvIris;
g_mmf.Data(g_mmfWriteIdx).snapTic(1) = tic;
g_mmf.Data(g_mmfWriteIdx).uvStatus(1) = g_uvStatus;

% update status
g_mmf.Data(1).status(2) = g_frameIdx;
set(hObject, 'CData', frame);
g_all_frame(:, :, 1, g_frameIdx) = frame;

set(handles.st_DisplayedFrame, 'String', sprintf('Fra
me %d', g_frameIdx));

% display exposure time dynamically till UV closed
if g_uvStatus == 1
    set(handles.ed_ExposureTime, 'string',
frameTime);
end

set(handles.ed_ICM_MeasuredHeight, 'String', g_mmf.Da
ta(1).avgTotalHeight(1));
set(handles.ed_Phase2Pi, 'String', g_mmf.Data(1).avgT
otalPhase(1));
%%
guidata(hObject, handles);

```

### 3. Function: “icm\_main\_worker.m”

The function is used for real time ICM&M data analysis, measurement and control computation. The codes are as below.

```
function ret = icm_main_worker(cp)
```

```

disp('icm main worker thread starts');

%% init memory map file for gui session
clearFile = 0;
mmf = icm_init_mem_file(cp, clearFile);

mmfReadIdx = 1;
mmfMaxNumCache = size(mmf.Data, 1);
fprintf('mmfMaxNumCache=%d\n', mmfMaxNumCache);

%% init

RunNo = 0;
RunNo_uvClose = [];

% nPOI-by-1 structure array of all points
measurement
nPOI = size(cp.POI, 2);
MeasStruct = icm_init_measure_ret(cp);
MeasureRet = repmat(MeasStruct, nPOI, 1);
for iPoint = 1:nPOI
    % single point identification by coordinations
    (height, width)
    MeasureRet(iPoint).PixelHeightWidth = cp.POI(:,
iPoint);
end

lastReadFrameIdx = 0;
nCache = 0;
statPts = zeros(2, 5000);

% tell GUI that worker is ready now
mmf.Data(1).status(3) = 1;

%% start parsing
while mmf.Data(1).status(1) == 1 ||
lastReadFrameIdx < mmf.Data(1).status(2)

    if lastReadFrameIdx >= mmf.Data(1).status(2)
        % keep iterating until there's new frame
        coming
        continue
    end
end

```

```

end

% If there's new frame, read it
cacheData = mmf.Data(mmfReadIdx);
nCache = nCache + 1;
frameIdx = cacheData.frameIdx;
frameTime = cacheData.frameTime;
frame = cacheData.frame;
snapTic = cacheData.snapTic;
uvIris = cacheData.uvIris;
uvStatus = cacheData.uvStatus;

% fixme: preallocate
cacheDataVec(nCache) = cacheData;
frameTimeVec(nCache) = frameTime;

if frameIdx ~= nCache
    warning('frameIdx %d should equal to
nCache %d', frameIdx, nCache);
end

% update cache
mmf.Data(mmfReadIdx).frameIdx(1) = 0;
lastReadFrameIdx = frameIdx;

t = toc(snapTic);
fprintf('received frame %d from cache %d,
t=%.3f\n', frameIdx, mmfReadIdx, t);
statPts(:, nCache) = [double(frameIdx); t];

mmfReadIdx = mod(mmfReadIdx, mmfMaxNumCache) +
1;

%% prepare fit data
for iPoint = 1:nPOI
    % single point identification by
    coordinations (height, width)
    h = cp.POI(1, iPoint); % height coordinate
    w = cp.POI(2, iPoint); % width coordinate

    area = frame((h-2):(h+2), (w-2):(w+2)); %
5X5 filter

```

```

        dataY_foi = double(median(area(:)));
        MeasureRet(iPoint).rawY =
[MeasureRet(iPoint).rawY; double(frame(h, w))];
        MeasureRet(iPoint).dataY =
[MeasureRet(iPoint).dataY; dataY_foi];
    end

    if (frameIdx < cp.SamplesNumB4Measure) ||
(mod(frameIdx-cp.SamplesNumB4Measure,
cp.MeasPeriodSamples) ~= 0)
        continue
    end

    RunNo = RunNo + 1; % Run number of rolling
fit&prediction
    fprintf('Run rolling fit no. %d\n', RunNo);

    dataX = frameTimeVec' - frameTimeVec(1); % time
of each foi relative to start of measurement

    % Curve fitting parameters
    params.rSquare      = cp.GOF_rSquare;
    params.FPS          = cp.FPS;
    params.halfLife    = cp.HalfLife;
    params.MHL         = cp.MovingHorizonL;
    params.MeasPeriod  = cp.MeasPeriodSamples;
    params.f_max       = cp.f_max;
    params.f_diff_max  = cp.f_diff_max;

    params.uvIris      = uvIris;
    params.RunNo       = RunNo;
    params.frameIdx    = frameIdx;
    params.RunNo_uvClose = RunNo_uvClose;

    %% point-by-point analysis
    %   for iPoint = 1:nPOI
    parfor iPoint = 1:nPOI
        % single point identification by
coordinates (height, width)
        h = cp.POI(1, iPoint); % height coordinate
        w = cp.POI(2, iPoint); % width coordinate
    end
end

```

```

        fprintf('fitting point %d [%d %d]\n',
iPoint, h, w);

        MeasureRet(iPoint).dataX = dataX;

        % time series of intensity data
        dataY = MeasureRet(iPoint).dataY; % without
missing data imputation

        %% Curve Fitting
        % Rolling fit with "fourier1" returns 4
coefficients  $y=a_0+a_1\cos(px)+b_1\sin(px)$ 
        % fitRollRet = icmFit(trainX, trainY,
trainW);
        % save the fitting coefficients, i.e.,
online estimates of parameters
        prevFitRet = MeasureRet(iPoint).lastFitRet;
%         fprintf('dataX %d dataY %d\n',
size(dataX), size(dataY));
        fitRollRet = icmFit2(dataX, dataY, params,
prevFitRet);
        MeasureRet(iPoint).lastFitRet = fitRollRet;

        % save the fitting coefficients, i.e.,
online estimates of parameters
        coeffs =
[fitRollRet.fitStatus, fitRollRet.fitgof.rsquare, ...
        fitRollRet.I0, fitRollRet.I1,
fitRollRet.freqW, fitRollRet.freq, ...
        fitRollRet.movingHorizon,
fitRollRet.halfLife];

        MeasureRet(iPoint).FittedCoeffs =
[MeasureRet(iPoint).FittedCoeffs; coeffs];
        MeasureRet(iPoint).Freq_w =
MeasureRet(iPoint).FittedCoeffs(:,5);
        MeasureRet(iPoint).Freq =
MeasureRet(iPoint).FittedCoeffs(:,6);

        if isfield(fitRollRet, 'fitobject')

```



```

        if (fitRollRet.fitStatus ~=0 &&
fitRollRet.fitStatus ~=3 && fitRollRet.fitStatus
~=40) ...
                ||(fitRollRet.fitStatus ==0 &&
fitRollRet.freq~=0 ) % small freq (<0.1Hz) in
threshold acceptable
                newFitY =
feval(fitRollRet.fitobject,
dataX( (prevFitRet.frameIdx+1):fitRollRet.frameIdx)
);
                %
newFitY = feval(fitRollRet.fitobject, dataX( end-
cp.MeasPeriodSamples+1:end));
                MeasureRet(iPoint).fitY =
[MeasureRet(iPoint).fitY; newFitY];
                else
                newFitY =
fitRollRet.I0*ones(fitRollRet.frameIdx-
prevFitRet.frameIdx,1);
                MeasureRet(iPoint).fitY =
[MeasureRet(iPoint).fitY; newFitY];
                end
                else
                newFitY =
fitRollRet.I0*ones(fitRollRet.frameIdx-
prevFitRet.frameIdx,1);
                MeasureRet(iPoint).fitY =
[MeasureRet(iPoint).fitY; newFitY];
                end

                % Mark the start of curing, i.e., the end
of threshold
                if
(MeasureRet(iPoint).CureFlags.CureFlag_RunNo==0) &&
(fitRollRet.firstValidFoiIdx~=0)

MeasureRet(iPoint).CureFlags.CureFlag_RunNo =
RunNo;

MeasureRet(iPoint).CureFlags.CureFlag_FrameIdx =
fitRollRet.firstValidFoiIdx;

```

```

        end
        % Flag the runs of failed curve fitting,
which has low R-square and may yield frequency
outlier
        if fitRollRet.fitStatus ~= 2
            MeasureRet(iPoint).Idx_FailFit =
[MeasureRet(iPoint).Idx_FailFit; RunNo];
        end

        %% Height Estimation: growth by integration
T_Int = dataX(end)- prevFitRet.time;
        % array of measurement time(s) per point,
RunNo-by-1 matrix
        MeasureRet(iPoint).Times =
[MeasureRet(iPoint).Times;dataX(end)];

        MeasureRet(iPoint).Phase2Pi =
MeasureRet(iPoint).Phase2Pi+T_Int*(fitRollRet.freq+
prevFitRet.freq)/2;
        n_m_evolve =
0.00041*(MeasureRet(iPoint).Phase2Pi)+1.49191;%
calculate evolving refractive index with the model
in thesis
        z = cp.Wavelength/(2*(n_m_evolve-
cp.n_L))*MeasureRet(iPoint).Phase2Pi; % evolving
refractive index
        MeasureRet(iPoint).Heights =
[MeasureRet(iPoint).Heights;z];

    end % end of point-by-point analysis

    %% Evaluate the average height of a line
profile
    heightsALL = [MeasureRet.Heights];
    heights = heightsALL(end,:);
    if length(MeasureRet) < 3
        zNorminal = mean(heights);
        meanPhase2Pi = mean([MeasureRet.Phase2Pi]);
    else

```

```

        zNorminal_fit=
robustfit(ones(length(heights),1),heights);
        zNorminal = max(0, zNorminal_fit(1));
        meanPhase2Pi_fit =
robustfit(ones(length([MeasureRet.Phase2Pi]),1),[Me
asureRet.Phase2Pi]);
        meanPhase2Pi = max(0, meanPhase2Pi_fit(1));
    end

    mmf.Data(1).avgTotalHeight(1) = zNorminal;
    mmf.Data(1).avgTotalPhase(1) = meanPhase2Pi;

    %% control after receiving new frame & Exposed
    Curing
    % Real-time control:for target exposure time or
    target height
    % Turn off UV immediately when measured time or
    height hits target

    if uvStatus == 1
        % Simple control stopwatch time control
        if cp.targetMode == 2 && ((cp.targetExpTime
- frameTime) <= cp.MeasPeriodSamples*0.03)
            sprintf('frameTime %.2f exceeds
targetExpTime %.2f, sending msg to shutdown uv',
frameTime, cp.targetExpTime)
            mmf.Data(1).status(3) = 2;
            R.targetExpTime = cp.targetExpTime; %
setpoint of epxosure time

            tExpDuration_Ideal = frameTime;

            %%---- Mark the end of exposed curing
            frameIdx_uvClose_Ideal = frameIdx; %
flag the frame number in acquired video when UV
closes

            RunNo_uvClose = RunNo;
            if exist('MeasureRet','var') &&
~isempty(MeasureRet)
                for iPoint = 1:length(MeasureRet)

```

```

        MeasureRet(iPoint).zExposed =
MeasureRet(iPoint).Heights(end);
        end
        % average using robustfit to remove
outliers
        if length(MeasureRet) < 3
            zExposedNorminal =
mean([MeasureRet.zExposed]);
        else
            zExposedNorminal_fit=
robustfit(ones(length([MeasureRet.zExposed]),1), [Me
asureRet.zExposed]);
            zExposedNorminal = max(0,
zExposedNorminal_fit(1));
        end
    end

    end

    % Measurement feedback control
    if cp.targetMode == 1 &&
(cp.targetCuredHeight*0.9-zNorminal <= 0.5)
        sprintf('measured height %.2f exceeds
targetHeight %.2f, sending msg to shutdown uv',
zNorminal, cp.targetCuredHeight)
        mmf.Data(1).status(3) = 2;
        R.targetCuredHeight =
cp.targetCuredHeight; % Save above already:
setpoint of cured height

        tExpDuration_Ideal = frameTime;
        %%---- Mark the end of exposed curing
        frameIdx_uvClose_Ideal = frameIdx; %
flag the frame number in acquired video when UV
closes

        RunNo_uvClose = RunNo;

        if exist('MeasureRet','var') &&
~isempty(MeasureRet)
            for iPoint = 1:length(MeasureRet)

```

```

        MeasureRet(iPoint).zExposed =
MeasureRet(iPoint).Heights(end);
        end
        % average using robustfit to remove
outliers
        if length(MeasureRet) < 3
            zExposedNorminal =
mean([MeasureRet.zExposed]);
        else
            zExposedNorminal_fit=
robustfit(ones(length([MeasureRet.zExposed]),1), [Me
asureRet.zExposed]);
            zExposedNorminal = max(0,
zExposedNorminal_fit(1));
        end
        % to-do: display the exposed
cured height in GUI
        %
set(cp.ed_ExposedCuredHeight,'String',zExposedNormi
nal);
        end
    end

end
%%----- End of control -----
-----

%% ----- Dark curing -----
-----%
    if uvStatus == 2 % display dark curing height
    for iPoint = 1:length(MeasureRet)
        MeasureRet(iPoint).zDark =
MeasureRet(iPoint).Heights(end)-
MeasureRet(iPoint).zExposed;
    end

    % average using robustfit to remove outliers
    if length(MeasureRet) < 3
        zDarkNorminal = mean([MeasureRet.zDark]);
    else

```

```

        zDarkNorminal_fit=
robustfit(ones(length([MeasureRet.zDark]),1), [MeasureRet.zDark]);
        zDarkNorminal = max(0,
zDarkNorminal_fit(1));
    end
%     % to-do: display the dark cured height in GUI
%
set(cp.ed_DarkCuredHeight,'String',zDarkNorminal);
    end

end

%% Calculates latence time between acquiring and
analyzing a frame
statPts = statPts(:, 1:nCache);

frames = statPts(1,:);
meanDelay = mean(statPts(2,:));

R.rtFramesLatence = statPts;
R.rtProcessedFrames = length(frames);
R.rtMeanDelayAcqAnl = meanDelay;

ret = MeasureRet;
fprintf('icm main worker thread stops, processed %d
frames, average delay %.3f\n', length(frames),
meanDelay);

clear mmf;

%% Saving results
if cp.isRT == 1 % Real-time

    fn = strcat(cp.ResultFolder,...

strcat('\RT_ECPL_ICM_',datestr(now,'yyyymmdd_HHMMSS
'),...
        sprintf('_H%03d_W%03d', cp.POI(1, 1),
cp.POI(2, 1)), '.mat'));

```

```

    fprintf('saving ret to file %s', fn);
    R.MeasureRet = MeasureRet;

    R.frameIdx_uvClose_Ideal =
frameIdx_uvClose_Ideal;
    uvStatusVec = [cacheDataVec.uvStatus];
    uvStatusVec_diff = diff(uvStatusVec);
    frameIdx_uvClose = find(uvStatusVec_diff~=0)+1;
    R.frameIdx_uvClose = frameIdx_uvClose;
    R.tExpDuration_Ideal = tExpDuration_Ideal;
    R.tExpDuration =
frameTimeVec(frameIdx_uvClose);
    R.RunNo_uvClose = RunNo_uvClose;

    R.zExposedNorminal = zExposedNorminal; %
average exposed height evaluated for the line
    R.zDarkNorminal = zDarkNorminal; % average dark
height evaluated for the line
    R.zNorminal = zNorminal; % average height
evaluated for the line
    R.cp = cp;
    R.dp = cacheDataVec;
    R.imageTime = [cacheDataVec.frameTime]'; %
image time which is required in offline ICM
    save(fn, '-struct', 'R');
end

%% Report results
reportMeasureRet_RT(MeasureRet, RunNo_uvClose);

```

#### 4. Function: “icm\_init\_measure\_ret.m”

The function is to initialize the structure array of measurement result for the chosen POI. The codes are as below.

```

function MeasStruct = icm_init_measure_ret(cp)

%% Initialize the structure array of measurement
result for the chosen POI
    ...Will be used in the
"Real_Time_ICM_processMeasureTimer.m"

```

```

% data structure for each point measurement with
all the fields above
MeasStruct = struct(...
    'PixelHeightWidth', [], ... % point coordination
    [height;width]
    'dataX', [], ... % point data: array of time (s)
in curve fitting
    'rawY', [], ... % point data: time-series of
pixel grayscale
    'dataY', [], ...
    'fitY', [], ... % fitted data using curve fitting
    'FittedCoeffs', [], ... % Curve fitting
coefficients at initial run per point
    'CureFlags',
struct('CureFlag_RunNo', 0, 'CureFlag_FrameIdx', 0), ...
.% Flag the curing window, i.e., mark the beginning
of curing
...RunNo and frame index that mark the begin of
curing
    'Idx_FailFit', zeros(1,1), ... % Flag the runs of
failed curve fitting, which has low R-square and
may yield frequency outlier Idx_FailFit = [failed
RunNO]
    'Times', [0], ...% array of run time per point,
will grow to be a RunNo-by-1 matrix
    'Heights', [0], ...% height estimation at initial
run per point, will grow to be a RunNo-by-1 matrix
    'zExposed', [], ...% ICM Measured Cured Heights
when UV closes
    'zDark', [], ...% ICM Measured Cured Heights
after UV closes at the end of acquisition
    'Freq_w', [], ...% frequency of  $I_m = I_0 + I_1 \cos(wt + \phi)$ , Freq_w: angular frequency in
 $I_m = I_0 + I_1 \cos(W*t + \phi)$ 
    'Freq', [], ...% Freq: frequency = Freq_w/2/pi
(unit:Hz)
    'Phase2Pi', 0, ...% the phase (unit: 2Pi),
i.e., time cumulative sum of frequencies to measure
height
    'lastFitRet', icm_init_fit_ret(cp)...

```



```
);
```

#### 5. Function: “icm\_init\_mem\_file.m”

The function is to initialize the memory map file for logging the real time data which can be fetched by the parallel thread of measurement analysis and controller computation. The codes are as below.

```
function m = icm_init_mem_file(cp, clearFile)

filename = fullfile(pwd, 'icm_comm.dat');

numFitter      = cp.numFitter;
W              = cp.imW;
H              = cp.imH;
numImageCache  = cp.maxNumCache;

frame = zeros(H, W);
frameIdx = 0;
frameTime = 0.0;
tic = 0;

% global status, only use first one of the array
% (1): measurement status. 1: running, 0 stopped.
% (2): lastWriteFrameIdx
% (3): workerStatus. 0: not running, 1: started,
2: targetReached
status = [1 0 0]';

if clearFile && exist(filename, 'file')
    disp(['remove file ', filename])
    delete(filename)
end

% Create the communications file if it is not
already there.
if ~exist(filename, 'file')
    disp(['init file ', filename])
    [f, msg] = fopen(filename, 'wb');
    if f ~= -1
        for i = 1:numImageCache
```

```

        fwrite(f, frame, 'uint8');
        fwrite(f, frameIdx, 'uint32');
        fwrite(f, frameTime, 'double');
        fwrite(f, 0, 'uint64'); % snapTic
        fwrite(f, 0, 'uint8'); % uvIris
        fwrite(f, 0, 'uint8'); % uvStatus
        fwrite(f, 0, 'double'); %
    avgTotalHeight
        fwrite(f, 0, 'double'); % avgTotalPhase
        fwrite(f, status, 'int32');
    end
    fclose(f);
else
error('MATLAB:demo:send:cannotOpenFile', ...
      'Cannot open file "%s": %s.',
filename, msg);
    end
end

% Memory map the file.
disp(['creating memmapfile for', filename])
m = memmapfile(filename,...
    'Writable', true,...
    'Format', {...
        'uint8', size(frame), 'frame';...
        'uint32', size(frameIdx), 'frameIdx';...
        'double', size(frameTime), 'frameTime';...
        'uint64', [1 1], 'snapTic';...
        'uint8', [1 1], 'uvIris';...
        'uint8', [1 1], 'uvStatus';...
        'double', [1, 1], 'avgTotalHeight';...
        'double', [1, 1], 'avgTotalPhase';...
        'int32', size(status), 'status';...
    },...
    'Repeat', numImageCache...
);

fprintf('init status = %d\n', m.Data(1).status);

return;

```

#### 6. Function: “icm\_init\_fit\_ret.m”

The function is to initialize the structure array of curve fitting result for one measurement cycle. The codes are as below.

```
function fitRet = icm_init_fit_ret(cp)

fitRet = struct(...
    'fitobject', [], ...
    'fitgof', struct(), ...
    'movingHorizon', cp.MovingHorizonL, ...
    'halfLife', cp.HalfLife, ...
    'frameIdx_dummy', 0, ...
    'frameIdx', 0, ...
    'firstValidFoiIdx', 0, ...
    'fitStatus', 0, ...
    'fitoptions', fitoptions('fourier1'), ...
    'I0', [], ...
    'I1', [], ...
    'freqW', 0, ...
    'freq', 0, ...
    'time', 0);
```

#### 7. Function: “icm\_set\_uv\_status.m”

The function is to display UV pattern on DMD, and to control UV lamp “On/Off”. The codes are as below.

```
function icm_set_uv_status(onOrOff, uvLevel)

% result folder
global uv
global g_tImaqStart
global g_uvStatus
global hdvp
global DMDimage

if onOrOff == 1
    %% Prepare DMD as a 2nd monitor to display the
    upcoming image
```

```

    % Get monitors (including DMD which is also a
monitor) information
    % use get(0,'MonitorPosition') to get the
locations and size of the monitors
    % for details
http://www.mathworks.com/help/vision/ref/vision.deployablevideoplayer-class.html
    % a = [Left-bottom width, Left-bottom height,
screen width, screen height]
    a = get(0,'MonitorPosition');
    hdvp = vision.DeployableVideoPlayer;
    hdvp.Size = 'Full-Screen'; % this command set
the video to be displayed in full-screen
    hdvp.Location = a(2,1:2); % this defines the
DMD location where the image should display.
    % hdvp.Location = a(1,1:2); % this tests the
code on primary monitor

    %% Display DMD bitmap
step(hdvp,DMDimage);

    %% UV lighting and exposure finally begins here
uv = UVConn('COM3');
UVSetIrisLevel(uv, uvLevel);
UVShutterOpen(uv);
g_tImaqStart = tic;
g_uvStatus = 1; % flag UV light is on
disp('open uv')

else
    % Close UV Shutter
UVShutterClose(uv);

    % flag UV light is off again after being "on",
not "0" so that acquisition and measurement could
go on to capture dark curing
g_uvStatus = 2;
disp('close uv');

    % Disconnect UV
UVDisc(uv);end

```

## REFERENCES

- [1] Huang, Y. and M.C. Leu, *Frontiers of Additive Manufacturing Research and Education*, in *An NSF Additive Manufacturing Workshop Report*. 2014: An National Science Foundation (NSF) Additive Manufacturing Workshop Report.
- [2] Bikas, H., P. Stavropoulos, and G. Chryssolouris, *Additive manufacturing methods and modelling approaches: a critical review*. The International Journal of Advanced Manufacturing Technology, 2016. 83(1-4): p. 389-405.
- [3] Frazier, W.E., *Metal Additive Manufacturing: A Review*. Journal of Materials Engineering and Performance, 2014. 23(6): p. 1917–1928.
- [4] Hu, D. and R. Kovacevic, *Sensing, modeling and control for laser-based additive manufacturing*. International Journal of Machine Tools & Manufacture, 2003. 43: p. 51–60.
- [5] Farshidianfar, M.H., A. Khajepour, and A. Gerlich, *Real-time control of microstructure in laser additive manufacturing*. International Journal of Advanced Manufacturing Technology, 2016. 82(5): p. 1173–1186.
- [6] *Measurement Science Roadmap for Polymer-Based Additive Manufacturing*. 2016, National Institute of Standards and Technology (NIST)
- [7] Gibson, I., D.W. Rosen, and B. Stucker, *Additive Manufacturing Technologies: 3D Printing, Rapid Prototyping, and Direct Digital Manufacturing*. 2nd ed. 2014: Springer-Verlag New York. XXI, 498.
- [8] *Measurement Science Roadmap for Metal-Based Additive Manufacturing*. 2013, National Institute of Standards and Technology (NIST)
- [9] Jurrens, K. *NIST Measurement Science for Additive Manufacturing*. 2013 [cited 2016 05-18-2016]; Available from: [http://www.nist.gov/el/msid/infotest/upload/Jurrens-NIST-AM\\_Projects\\_March2013.pdf](http://www.nist.gov/el/msid/infotest/upload/Jurrens-NIST-AM_Projects_March2013.pdf).
- [10] Rubenchik, A., et al., *Direct measurements of temperature-dependent laser absorptivity of metal powders*. Applied Optics, 2015. 54(24): p. 7230-7233.
- [11] Teng, C., et al., *The effects of material property assumptions on predicted meltpool shape for laser powder bed fusion based additive manufacturing*. Measurement Science and Technology, 2016. 27(8): p. 085602.
- [12] Evertona, S.K., et al., *Review of in-situ process monitoring and in-situ metrology for metal additive manufacturing*. Materials and Design, 2016. 95(5): p. 431–445.
- [13] Thompson, A., I. Maskery, and R. Leach, *X-ray computed tomography for additive manufacturing: a review*. Measurement Science and Technology, 2016. 27(7): p. 072001.
- [14] Spears, T.G. and S.A. Gold, *In-process sensing in selective laser melting (SLM) additive manufacturing*. Integrating Materials and Manufacturing Innovation, 2016. 5(2).
- [15] Mani, M., et al., *A review on measurement science needs for real-time control of additive manufacturing metal powder bed fusion processes*. International Journal of Production Research, 2016: p. 1-19.

- [16] Nassar, A.R., et al., *Intra-layer Closed-loop Control of Build Plan during Directed Energy Additive Manufacturing of Ti-6Al-4V*. Additive Manufacturing, 2015. 6: p. 39-52.
- [17] Jariwala, A.S., *Modeling And Process Planning For Exposure Controlled Projection Lithography*. Ph.D. thesis, Mechanical Engineering, Georgia Institute of Technology, Atlanta, USA, 2013.
- [18] Jariwala, A.S., R.E. Schwerzel, and D.W. Rosen, *Real-Time Interferometric Monitoring System For Exposure Controlled Projection Lithography*. Proceedings of the 22nd Solid Freeform Fabrication Symposium, 2011: p. 99-108.
- [19] Zhao, X., *Process Planning For Thick Film Mask Projection Micro Stereolithography*. M.S. thesis, Mechanical Engineering, Georgia Institute of Technology, Atlanta, USA, 2009.
- [20] Jones, H.H., A.S. Jariwala, and D.W. Rosen, *Towards Real Time Control Of Exposure Controlled Projection Lithography*. Proceedings of International Symposium on Flexible Automation, 2014.
- [21] Jones, H.H., et al., *Real-Time Selective Monitoring Of Exposure Controlled Projection Lithography*. Proceedings of the 24th Solid Freeform Fabrication Symposium, 2013: p. 55-65.
- [22] Limaye, A.S. and D.W. Rosen, *Process planning method for mask projection micro-stereolithography*. Rapid Prototyping Journal, 2007. 13: p. 76-84.
- [23] Crisalle, O.D., et al., *Adaptive Control Of Photolithography*. SPIE: Integrated Circuit Metrology, Inspection, and Process Control, 1991. 1464.
- [24] Kiparissides, C., *Challenges in particulate polymerization reactor modeling and optimization: A population balance perspective*. Journal of Process Control, 2006. 16(3): p. 205-224.
- [25] Richards, J.R. and J.P. Congalidis, *Measurement and control of polymerization reactors*. Computers & Chemical Engineering, 2006. 30(10-12): p. 1447-1463.
- [26] Seborg, D.E., T.F. Edgar, and D.A. Mellichamp, *Process dynamics and control*. 2nd ed. 2004, New York: Wiley.
- [27] Jakatdar, N.H., *Deep Sub-Micron Photolithography Control through In-line metrology*. Ph.D., Engineering - Electrical Engineering and Computer Sciences, University Of California at Berkeley, USA, 2000.
- [28] Wu, C.-F., et al., *Advanced Process Control of the Critical Dimension in Photolithography*. International Journal of Precision Engineering and Manufacturing, 2008. 9(1): p. 12-18.
- [29] Sammons, P.M., D.A. Bristow, and R.G. Landers. *FREQUENCY DOMAIN IDENTIFICATION OF A REPETITIVE PROCESS CONTROL ORIENTED MODEL FOR LASER METAL DEPOSITION PROCESSES* in *International Symposium on Flexible Automation*. 2014. Awaji-Island, Hyogo, Japan.
- [30] Kwan, C. and S. Member, *Robust backstepping control of nonlinear systems using neural networks*. IEEE TRANSACTIONS ON SYSTEMS, MAN, AND CYBERNETICS—PART A: SYSTEMS AND HUMANS, 2000. 30(6): p. 753-766.
- [31] Yahui Li, S.Q., Xianyi Zhuang, and Okyay Kaynak, *Robust and Adaptive Backstepping Control for Nonlinear Systems Using RBF Neural Networks*. IEEE TRANSACTIONS ON NEURAL NETWORKS, 2004. 15(3): p. 693-701.

- [32] Musacchio, J., *Run to Run Control in Semiconductor Manufacturing*. M.S., Department of Electrical Engineering and Computer Sciences, University of California at Berkeley, 1998.
- [33] Kurfess, T.R. and T.J. Hodgson, *Metrology, Sensors and Control*, in *Micromanufacturing*. 2007. p. 89-109.
- [34] Creath, K., *Phase-measurement interferometry techniques*. Progress in optics, 1988. 26(26): p. 349-393.
- [35] Huntley, J.M. and H. Saldner, *Temporal phase-unwrapping algorithm for automated interferogram analysis*. Applied Optics, 1993. 32(17): p. 3047-3052.
- [36] Kaufmann, G.H. and G.E. Galizzi, *Phase measurement in temporal speckle pattern interferometry: comparison between the phase-shifting and the Fourier transform methods*. Applied Optics, 2002. 41(34): p. 7254-7263.
- [37] Colonna de Lega, X., *Processing of non-stationary interference patterns - adapted phase-shifting algorithms and wavelet analysis. Application to dynamic deformation measurements by holographic and speckle interferometry*. Ph.D. dissertation, Swiss Federal Institute of Technology, 1997.
- [38] Gao, W., et al., *Real-time 2D parallel windowed Fourier transform for fringe pattern analysis using Graphics Processing Unit*. Optics Express, 2009. 17(25): p. 23147-23152.
- [39] Kemao, Q., H. Wang, and W. Gao, *Some Recent Developments of Windowed Fourier Transform for Fringe Pattern Analysis*. AIP Conference Proceedings, 2010. 1236(1): p. 106-111.
- [40] Takeda, M., H. Ina, and S. Kobayashi, *Fourier-transform method of fringe-pattern analysis for computer-based topography and interferometry*. Journal of the Optical Society of America, 1982. 72(1): p. 156-160.
- [41] Schwerzel, R.E., A.S. Jariwala, and D.W. Rosen, *A simple, inexpensive, real-time interferometric cure monitoring system for optically cured polymers*. Journal of Applied Polymer Science, 2013. 129(5): p. 2653-2662.
- [42] Federico, A. and G.H. Kaufmann, *Robust phase recovery in temporal speckle pattern interferometry using a 3D directional wavelet transform*. Optics letters, 2009. 34(15): p. 2336-2338.
- [43] Kai, L. and Q. Kemao, *Dynamic phase retrieval in temporal speckle pattern interferometry using least squares method and windowed Fourier filtering*. Optics Express, 2011. 19(19): p. 18058-18066.
- [44] Fu, Y., et al., *Kinematic and deformation parameter measurement by spatiotemporal analysis of an interferogram sequence*. Applied Optics, 2007. 46(36): p. 8645.
- [45] Edwards, C. and S.K. Spurgeon, *Sliding mode control : theory and applications*. Systems and control book series. Vol. 7. 1998, London: Taylor & Francis.
- [46] Haber, R., R. Bars, and U. Schmitz, *Predictive On-Off Control*, in *Predictive Control in Process Engineering : From the Basics to the Applications (1)*. 2012, Wiley-VCH. p. 103-134.
- [47] Rzepniewski, A.K., *Cycle-to-Cycle Control of Multiple Input-Multiple Output Manufacturing Processes*. Ph.D., Mechanical Engineering, Massachusetts Institute of Technology, 2005.

- [48] Leang, S., et al., *A Control System For Photolithographic Sequences*. IEEE Transactions On Semiconductor Manufacturing, 1996. 9(2).
- [49] Wayne F. Reed and A.M. Alb, *Monitoring Polymerization Reactions: From Fundamentals to Applications*. 2013: John Wiley & Sons.
- [50] Chartoff, R.P. and J. Du. *Photopolymerization reaction rates by reflectance real time infrared spectroscopy: application to stereolithography resins*. in *Solid Freeform Fabrication Symposium*. 1999. Austin, TX.
- [51] Duner, G., E. Thormann, and A. Dedinaite, *Quartz Crystal Microbalance with Dissipation (QCM-D) studies of the viscoelastic response from a continuously growing grafted polyelectrolyte layer*. J Colloid Interface Sci, 2013. 408: p. 229-34.
- [52] Jeon, H., et al., *Chemical patterning of ultrathin polymer films by direct-write multiphoton lithography*. J Am Chem Soc, 2011. 133(16): p. 6138-41.
- [53] *Q-sense QCM-D*. [cited 2017; Available from: <http://cleanroom.iem.gatech.edu/equipment/190/q-sense-qcm-d/>].
- [54] Orski, S.V., et al., *Design and implementation of two-dimensional polymer adsorption models: evaluating the stability of Candida antarctica lipase B/solid-support interfaces by QCM-D*. Biomacromolecules, 2013. 14(2): p. 377-86.
- [55] Fu, Y., G. Pedrini, and X. Li, *Interferometric Dynamic Measurement: Techniques Based on High-Speed Imaging or a Single Photodetector*. The Scientific World Journal, 2014: p. 14.
- [56] Li, X., et al., *High-precision large deflection measurements of thin films using time sequence speckle pattern interferometry*. Measurement Science And Technology, 2002. 13(8): p. 1304-1310.
- [57] Breiland, W.G. and K.P. Killeen, *A virtual interface method for extracting growth rates and high temperature optical constants from thin semiconductor films using in situ normal incidence reflectance*. Journal of Applied Physics, 1995. 78(11): p. 6726-6736.
- [58] Meneses-Fabian, C. and U. Rivera-Ortega, *Phase-Shifting Interferometry by Amplitude Modulation*. Interferometry – Research and Applications in Science and Technology, ed. I. Padron. 2012: InTech. 171-194.
- [59] Tang, Y., *Stereolithography Cure Process Modeling*. PhD, School of Chemical & Biomolecular Engineering, Georgia Institute of Technology, Atlanta, 2005.
- [60] Stanković, L., et al., *Instantaneous frequency in time–frequency analysis: Enhanced concepts and performance of estimation algorithms*. Digital Signal Processing, 2014. 35: p. 1-13.
- [61] Guldin, S., *Optical Aspects of Thin Films and Interfaces*, in *Inorganic Nanoarchitectures by Organic Self-Assembly*. 2013, Springer.
- [62] *The LEXT OLS4000 3D Laser Measuring Microscope*. 09-10-2016]; Available from: <http://www.olympus-ims.com/en/metrology/ols4000/>.
- [63] Grover, M.A. and R. Xiong, *A Modified Moving Horizon Estimator for In Situ Sensing of a Chemical Vapor Deposition Process*. Control Systems Technology, IEEE Transactions, 2009. 17(5): p. 1228 - 1235.
- [64] Soroush, M., *State and parameter estimations and their applications in process control*. Computers and Chemical Engineering, 1998. 23: p. 229-245.



- [65] *Evaluating Goodness of Fit*. [cited 2016; Available from: <http://www.mathworks.com/help/curvefit/evaluating-goodness-of-fit.html>.
- [66] Lee, J.H., R.K. Prud'homme, and I.A. Aksay, *Cure depth in photopolymerization: Experiments and theory*. *Journal of Materials Research*, 2001. 16(21): p. 3536-3544.
- [67] Xiong, R. and M.A. Grover, *In Situ Optical Sensing and State Estimation for Control of Surface Processing*, in *Feedback Control of MEMS to Atoms*. 2012, Springer US. p. 45-67.
- [68] Zhao, X. and D.W. Rosen, *Real-time interferometric monitoring and measuring of photopolymerization based stereolithographic additive manufacturing process: sensor model and algorithm*. *Measurement Science and Technology*, 2017. 28(1).
- [69] Zhao, X. and D.W. Rosen, *Parameter Estimation Based Real-Time Metrology for Exposure Controlled Projection Lithography*. *Proceedings of the 26th Annual International Solid Freeform Fabrication Symposium*, 2015: p. 1294-1312.
- [70] Zhao, X. and D.W. Rosen, *Simulation Study on Evolutionary Cycle to Cycle Time Control of Exposure Controlled Projection Lithography*. *Rapid Prototyping Journal*, 2016. 22(3): p. 456-464.
- [71] Kamath, C. and Y.J. Fan, *Data Mining in Materials Science and Engineering*, in *Informatics for Materials Science and Engineering : Data-driven Discovery for Accelerated Experimentation and Application*, K. Rajan, Editor. 2013, Butterworth-Heinemann. p. 17-36.
- [72] Esmailian, B., S. Behdad, and B. Wang, *The evolution and future of manufacturing: A review*. *Journal of Manufacturing Systems*, 2016. 39: p. 79–100.
- [73] O'Neil, C. and R. Schutt, *Doing Data Science*. 2014: O'Reilly Media, Inc.
- [74] Han, J., J. Pei, and M. Kamber, *Mining Stream, Time-Series, and Sequence Data*, in *Data Mining: Concepts and Techniques*. 2006, Morgan Kaufmann. p. 467-497.
- [75] Han, J., M. Kamber, and J. Pei, *Data Mining: Concepts and Techniques*. 3rd ed. 2012: Morgan Kaufmann.
- [76] Xiong, H., et al., *Enhancing Data Analysis with Noise Removal*. *IEEE Transactions on Knowledge and Data Engineering*, 2006. 18(3): p. 304 - 319.
- [77] Derryberry, D.R., *Basic Data Analysis for Time Series with R*. 2014: Wiley.
- [78] Moeslund, T.B., *Introduction to Video and Image Processing-Building Real Systems and Applications*. 2012: Springer London.
- [79] Jacobs, P.F., *Rapid Prototyping and Manufacturing: Fundamentals of StereoLithography*. 1992: Society of Manufacturing Engineers. 434.
- [80] Boddapati, A., *Modeling Cure Depth during Photopolymerization of Multifunctional Acrylates*. MS, School of Chemical & Biomolecular Engineering, Georgia Institute of Technology, Atlanta, 2010.
- [81] Alexander, F.J. and T. Lookman, *Novel Approaches to Statistical Learning in Materials Science*, in *Informatics for materials science and engineering : Data-driven discovery for accelerated experimentation and application*, K. Rajan, Editor. 2013, Butterworth-Heinemann. p. 37-51.
- [82] Han, J., M. Kamber, and J. Pei, *Data mining: concepts and techniques: concepts and techniques*. 2011: Elsevier.

- [83] Han, J., M. Kamber, and J. Pei, *Outlier Detection*, in *Data Mining: Concepts and Techniques*. 2012, Morgan Kaufmann. p. 543-584.
- [84] *Evaluating Goodness of Fit*. 2016 09/19/2016]; Available from: <http://www.mathworks.com/help/curvefit/evaluating-goodness-of-fit.html>.
- [85] Nisbet, R., G. Miner, and J. Elder, IV, *Handbook of Statistical Analysis and Data Mining Applications*. 2009: Academic Press.
- [86] Chapra, S.C. and R.P. Canale, *Numerical methods for engineers*. 7th ed. 2014, Boston: McGraw-Hill Higher Education.
- [87] Slaev, V.A., A.G. Chunovkina, and L.A. Mironovsky, *Metrology and Theory of Measurement*. de Gruyter Studies in Mathematical Physics. 2013: Walter de Gruyter.
- [88] Barnett, V. and T. Lewis, *Outliers in Statistical Data*. 3rd ed. 1994: Wiley.
- [89] Tomlins, P.H., et al., *Time-resolved simultaneous measurement of group index and physical thickness during photopolymerization of resin-based dental composite*. Journal of biomedical optics, 2007. 12(1): p. 014020.
- [90] Rousseeuw, P.J. and A.M. Leroy., *Robust regression and outlier detection*. Vol. 589. 2005: John Wiley & Sons.
- [91] *Statistics and Machine Learning Toolbox: User's Guide (R2016b)*. 2016 09/27/2016]; Available from: <https://www.mathworks.com/help/stats/robustfit.html>.
- [92] Zhao, X. and D.W. Rosen, *Experimental validation and characterization of a real-time metrology system for photopolymerization based stereolithographic additive manufacturing process*. International Journal of Advanced Manufacturing Technology, 2016.
- [93] MathWorks. *Perform parallel computations on multicore computers, GPUs, and computer clusters*. 2016; Available from: <https://www.mathworks.com/products/parallel-computing.html>.
- [94] MathWorks. *Batch (Run MATLAB script or function on worker)*. 2016; Available from: <http://www.mathworks.com/help/distcomp/batch.html>.
- [95] Asaad, W.F., et al., *High-performance execution of psychophysical tasks with complex visual stimuli in MATLAB*. Journal of Neurophysiology, 2013. 109(1): p. 249-60.
- [96] Arimoto, H., et al., *Measurement of refractive index change induced by dark reaction of photopolymer with digital holographic quantitative phase microscopy*. Optics Communications, 2012. 285(24): p. 4911-4917.
- [97] Korpelainen, V., *Traceability for nanometre scale measurements - Atomic force microscopes in dimensional nanometrology*. Department of Physics, University of Helsinki, Finland, 2014.
- [98] Hadis, M.A., et al., *Dynamic monitoring of refractive index change through photoactive resins*. Dental Materials, 2010. 26(11): p. 1106-1112.
- [99] Lambert, J.R., *Control Modes - On/Off Control*, in *Contemporary Measurement Concepts*. 2014, Lulu.com.
- [100] Nilsson, J., *Real-Time Control Systems with Delays*. Department of Automatic Control, Lund Institute of Technology, 1998.
- [101] Doyle, J.C., B.A. Francis, and A.R. Tannenbaum, *Feedback control theory*. 2013: Courier Corporation.

- [102] Ross, S.M., *Introduction to Probability Models*. 11th ed. 2014: Academic Press. 784.
- [103] Zhao, X. and D.W. Rosen, *A data mining approach in real-time measurement for polymer additive manufacturing process with exposure controlled projection lithography*. Journal of Manufacturing Systems, 2017. Special Issue: Cybermanufacturing.
- [104] Ngo, Y.S., K.T. Ang, and A. Tay, *Method for real-time critical dimensions signature monitoring and control: Sensor, actuator, and experimental results*. Review of Scientific Instruments, 2013. 84(1): p. 015116.
- [105] MathWorks. *Multiple linear regression*. 2016; Available from: <https://www.mathworks.com/help/stats/regress.html>.
- [106] MathWorks. *Timer class*. 2016 [cited 2017 01-2017]; Available from: <http://www.mathworks.com/help/matlab/ref/timerclass.html>.
- [107] Stansbury, J.W. and D. Kim, *Methods For Extensive Dark Curing Based on Visible-Light Initiated, Controlled Radical Polymerization*. 2011, Stansbury Jeffrey W  
Dongkwan Kim: USA.
- [108] Tumbleston, J.R., et al., *Continuous liquid interface production of 3D objects*. Science, 2015. 347(6228): p. 1349-1352.
- [109] Zhao, X. and D.W. Rosen, *Process Modeling and Advanced Control Methods for Exposure Controlled Projection Lithography*, in *IEEE American Control Conference*. 2015, American Automatic Control Council: Chicago. p. 3643-3648.
- [110] Beuth, J., et al. *Process Mapping for Qualification Across Multiple Direct Metal Additive Manufacturing Processes*. in *International SFF Symposium - An Additive Manufacturing Conference*. 2013. Austin, TX.
- [111] Zhao, X. and D.W. Rosen, *Investigation of Advanced Process Control Methods for Exposure Controlled Projection*. Proceedings of the 25th Solid Freeform Fabrication Symposium, 2014.
- [112] Zhang, Y., *Empirical process planning for exposure controlled projection lithography*. M.S., Mechanical Engineering, Georgia Institute of Technology, Atlanta, USA, 2016.
- [113] Alpaydin, E., *Design and Analysis of Machine Learning Experiments*, in *Introduction to Machine Learning*. 2010, MIT Press. p. 475 - 515.
- [114] Instruments, N. *Do I Need a Real-Time System*. 2013; Available from: <http://www.ni.com/white-paper/14238/en/>.
- [115] Khudyakov, I.V., *Post-Polymerization*, in *RadTech Report*. November/December 2010. p. 47-52.
- [116] Roper, D.A., et al., *Additive manufacturing of graded dielectrics*. Smart Materials and Structures, 2014. 23(4): p. 045029.

## **VITA**

### **XIAYUN ZHAO**

Xiayun Zhao was born in a scenic town on the bank of Li River in Guilin, China. She received a B.Sc. in Precision Engineering with a major of “Measurement Science and Control Technology” from Tsinghua University in Beijing, China in 2006. She earned her M.Sc. in Mechanical Engineering from Georgia Institute of Technology, Atlanta, USA in 2009. After graduation she worked as an instrumentation and controls engineer at an EPC (Engineering, Procurement & Construction) company for Oil & Gas industry clients. In 2014 she went back to Georgia Institute of Technology and continued to pursue a doctorate degree in Mechanical Engineering. When she is not working on her research, Ms. Zhao enjoys playing with her two lovely children – Larry and Jerry.